Amphilic fatty acid conjugates of pyridylporphyrins in photodynamic therapy of melanoma cell lines

Mušković, Martina

UNIVERSITY OF RIJEKA

FACULTY OF BIOTECHNOLOGY AND DRUG DEVELOPMENT

Martina Mušković

AMPHIPHILIC FATTY ACID CONJUGATES OF PYRIDYLPORPHYRINS IN PHOTODYNAMIC THERAPY OF MELANOMA CELL LINES

DOCTORAL THESIS

Rijeka, 2025.

UNIVERSITY OF RIJEKA

FACULTY OF BIOTECHNOLOGY AND DRUG DEVELOPMENT

Martina Mušković

AMPHIPHILIC FATTY ACID CONJUGATES OF PYRIDYLPORPHYRINS IN PHOTODYNAMIC THERAPY OF MELANOMA CELL LINES

DOCTORAL THESIS

Supervisor: Prof. Nela Malatesti, PhD

Co-supervisor: Assis. Prof. Ivana Ratkaj, PhD

Rijeka, 2025.

SVEUČILIŠTE U RIJECI
FAKULTET BIOTEHNOLOGIJE I RAZVOJA LIJEKOVA

Martina Mušković

AMFIFILNI KONJUGATI MASNIH KISELINA PIRIDILPORFIRINA U FOTODINAMIČKOJ TERAPIJI NA STANIČNIM LINIJAMA MELANOMA

DOKTORSKI RAD

Mentorica: Prof. dr. sc. Nela Malatesti
Ko-mentorica: Izv. prof. dr. sc. Ivana Ratkaj

Rijeka, 2025.

This doctoral thesis was completed at the Faculty of Biotechnology and Drug Development, University of Rijeka, as a part of the postgraduate doctoral program Medicinal Chemistry, under the supervision of Prof. Nela Malatesti, PhD and Assoc.Prof. Ivana Ratkaj, PhD.
The research was supported by projects *"Preparation of lipid-pyridylporphyrin conjugates, their characterisation and photodynamic activity"* and *"Preparation of N-oxide derivatives of pyridylporphyrins, their characterisation and photodynamic activity"* by University of Rijeka, awarded to Nela Malatesti, PhD.

Doctoral thesis supervisor: Prof. Nela Malatesti, PhD (Faculty of Biotechnology and Drug Development, University of Rijeka)

Doctoral thesis co-supervisor: Assis. Prof. Ivana Ratkaj, PhD (Faculty of Biotechnology and Drug Development, University of Rijeka)

Doctoral thesis was defended on February 6th, 2025, at the University of Rijeka, Faculty of Biotechnology and Drug Development, in front of the Evaluation Committee:

1. Assoc. prof. Toni Todorovski, PhD (Faculty of Biotechnology and Drug Development, University of Rijeka)
2. Prof. Ivo Piantanida, PhD (Ruđer Bošković Institute)
3. Dubravko Jelić, PhD (Selvita d.o.o.)

Acknowledgments

My heartful gratitude goes to my supervisor, Nela. Thank you for introducing me the world of photodynamic therapy, for your guidance and support from the first steps in the lab work for the master thesis to this point in my career. Thank you for all the knowledge and experience you have passed on to me, for the encouragement and for being there for me. I couldn't wish for a better supervisor.

I am deeply grateful to my co-supervisor Ivana. Thank you for teaching me everything I know about cell culture and biological experiments. I really appreciate your patience and encouragement towards my academic and personal development.

A big thank you goes to the collaborators, Dr. Martin Lončarić, Dr. Iva Džeba and Dr. Nikola Basarić. Thank you for the warm welcome every time I arrived in Zagreb, for the knowledge you passed on to me, for all the support and for all the discussions we had about the results and beyond.

To my current and ex- colleagues, Nikolina, Beti, Bobana, Patrizia, Robert, Dario, Eda, Andrea, Maja, Pegi, Maja, Matea and Ena. Thank you for making my PhD days full of laugh and joy. I am grateful for every coffee, every conversation and every meeting we had. Also, thank you for taking care of me every time when I overdid my work and for bringing me back down to earth.

To my two closest friends, Lucija and Leda. Thank you for your care, support and for being there for me all these years. I would also like to thank Tomi, Butko, Antonela, Ana, Dani and Peki for all weekends together full of laughs that took my mind off work.

My deepest gratitude goes to my family, my mum, my dad and my brother Dado, who have been a huge support throughout my life. Thank you for your unwavering faith in me and for always giving me the strength and motivation I needed. This thesis would not have been possible without your encouragement and understanding. I would like to thank Vicky, my dog, who came into my life at the beginning of my PhD and whose companionship and unconditional love have brought me comfort and joy on this journey.

And finally, a special thanks to my wonderful future husband, Antun. Thank you for being by my side all these years, being my biggest support, for lifting me up when I needed it most, and for always being my sanity every time when I lost mine. Thank you, I love you <3.

Abstract

Amphiphilic porphyrins are widely used photosensitisers (PSs) in photodynamic therapy (PDT), an antitumor treatment in which the PS is combined with light irradiation of appropriate wavelength and oxygen in the vicinity within the treated lesions to induce the cytotoxic effect and consequently tumour destruction. In addition to their beneficial properties as antitumour agents, they are also used to treat viral, bacterial or fungal infections. The hydrophobic parts of the molecule facilitate the passage through the membrane bilayer, while the hydrophilic parts enable water solubility and thus the possibility of easier administration of the PS. Although the amphiphilic porphyrins have shown great efficacy as PSs, the hydrophilic-lipophilic balance, which utilises all the advantageous properties of this type of PSs and avoids the disadvantages such as aggregation or low cellular uptake, is somewhat less studied.

The main goal of this doctoral thesis was to study the hydrophilic-lipophilic balance on different groups of asymmetric A_3B pyridylporphyrins and its content is divided into four parts. In the first part, *N*-methylated (pyridinium-3-yl) porphyrins and Zn(II) analogues with alkyl chains of different lengths (7-17 C-atoms) were compared. The Zn(II)-porphyrin with a 13 C-atom alkyl chain showed the highest cytotoxicity and selectivity towards the melanoma cell line when irradiated with orange light. The second part involved the synthesis of amphiphilic *N*-oxidised pyrid-3-ylporphyrins, where porphyrins with a 13 and 17 C-atom chain showed to be promising against melanoma cell line, diminishing the melanin obstruction. In the last part, amphiphilic (pyridinium-3-yl)porphyrins were chelated with ^{68}Ga(III) and ^{nat}Ga(III) to obtain the PET/PDT agents, and their distribution was analysed in PET-CT scan. It was found that the hydrophilic-lipophilic balance not only affects cytotoxicity and selectivity *in vitro*, but also exhibits differential biodistribution *in vivo*. These findings on A_3B pyridylporphyrins will give us a deeper insight into the importance of the amphiphilicity of the molecule and lead us to the further development of an “ideal PS” for use in PDT.

Keywords: amphiphilic porphyrins, pyridinium porphyrins, melanoma, photodynamic therapy, hydrophilic-lipophilic balance

Sažetak

Amfifilni porfirini su široko korišteni fotosenzibilizatori (PS-ovi) u fotodinamičkoj terapiji (PDT), antitumorskom tretmanu u kojem se PS kombinira sa svjetlošću odgovarajuće valne duljine i kisikom u blizini liječenih lezija kako bi se izazvao citotoksični učinak i posljedično uništenje tumora. Osim što se koriste kao antitumorski ljekovi, također je poznata njihova upotreba protiv virusnih, bakterijskih i fungalnih infekcija. Hidrofobni dijelovi u molekuli olakšavaju prolazak kroz membranski dvosloj, dok hidrofilni dijelovi omogućuju topljivost u vodi, a time i mogućnost lakše administracije PS-a. Iako su amfifilni porfirini pokazali veliku učinkovitost kao PS-ovi, ravnoteža hidrofilnih i lipofilnih dijelova, koja omogućava sva povoljna svojstva i izbjegava nedostatke kao što su agregacija ili niska stanična internalizacija, manje je izučavana.

Glavni cilj ovog doktorskog rada bio je proučavanje ravnoteže hidrofilnih i lipofilnih dijelova različitih skupina asimetričnih A_3B piridilporfirina, podijeljenih u četiri dijela. U prvom dijelu uspoređeni su *N*-metilirani (piridin-3-ij)porfirini i njihovi Zn(II) analozi s alkilnim lancima različitih duljina (7-17 ugljikovih atoma). Zn(II)-porfirin s alkilnim lancem od 13 C-atoma pokazao je najveću citotoksičnost i selektivnost prema staničnoj liniji melanoma nakon osvjetljavanja narančastom svjetlošću. Drugi dio uključivao je sintezu amfifilnih *N*-oksidiranih pirid-3-ilporfirina, gdje su se porfirini s lancem od 13 i 17 C atoma pokazali obećavajućima protiv stanične linije melanoma, smanjujući utjecaj pigmenta melanina. U posljednjem dijelu amfifilni (piridinij-3-il)porfirini kelirani su s ^{68}Ga(III) i ^{nat}Ga(III) kako bi se dobili PET/PDT agensi, a njihova distribucija analizirana je PET-CT skeniranjem. Utvrđeno je da ravnoteža hidrofilnih i lipofilnih dijelova ne samo da utječe na citotoksičnost i selektivnost *in vitro*, već pokazuje i različitu biodistribuciju *in vivo*. Ovaj rad i saznanja dobivena na temelju rezultata o A_3B piridilporfirinima dat će nam dublji uvid o utjecaju amfifilnosti molekule i dovesti nas do daljnjeg razvoja "idealnog fotosenzibilizatora" za upotrebu u PDT-u.

Ključne riječi: amfifilni porfirini, piridinijevi porfirini, melanom, fotodinamička terapija, ravnoteža hidrofilnih i lipofilnih dijelova molekule

Content

1. Introduction

Photodynamic therapy (PDT) is one of the emerging therapies against malignant and non-malignant diseases. It consists of a photoactive molecule, called photosensitiser (PS), oxygen and light of an appropriate wavelength[1,2]. When these components are combined, i.e. when PS surrounded with oxygen molecules is irradiated, reactive oxygen species (ROS) are generated, which subsequently lead to strong oxidative stress in cells and the tumour ablation. Porphyrins and other tetrapyrrolic molecules (chlorins and bacteriochlorins) are the most studied group of the PSs for PDT in tumours, as they possess many characteristics of an "ideal PS", such as a single molecule of high (photo)stability, negligible toxicity without irradiation, good absorption in the red region of the electromagnetic (EM) spectrum and they have been shown to selectively accumulate in tumour cells [3].

Among porphyrins, the group of amphiphilic porphyrins has attracted great attention from scientists because they have hydrophilic parts in their structure that enable the solubility of a PS in biological aqueous media and hydrophobic parts that facilitate passage through the membrane bilayer and thus increase cellular internalisation[4,5]. However, to date there is very little research addressing the optimal balance between hydrophilicity and lipophilicity to achieve all desirable properties of amphiphilic porphyrins while avoiding undesirable effects such as prolonged photosensitivity and inflammation or, on the other hand, reducing PDT efficiency.

Furthermore, melanoma is one of the most commonly diagnosed cancers, especially in the younger population, with the number of new cases and deaths increasing dramatically every year [6,7]. Current therapies against melanoma are ineffective, as metastatic melanoma represents the group of the most aggressive metastatic tumours due to many resistance mechanisms. Some of these are the presence of melanin pigment, defects in the apoptotic pathway and increased DNA recovery mechanisms blocking the action of many anti-tumour therapies, including PDT[6,8].

Therefore, this doctoral thesis is focused on study of four different groups of amphiphilic porphyrins, which, within each group, differ in the length of the alkyl chain as the hydrophobic part of the molecule, to investigate the proper hydrophilic-lipophilic balance of each group for use in PDT against melanoma cell lines. The first part describes two groups of amphiphilic porphyrins: *N*-methylated tricationic (pyridinium-3-yl)porphyrins as free-base and Zn(II) porphyrins with an alkyl chain of 7, 9, 11, 13, 15 and 17 C atoms at the acetamidophenyl substituent in the fourth *meso*-position of the porphyrin ring. Their photophysical and photochemical properties in different solvents (MeOH, H_2O and phosphate buffer) were investigated as well as lipophilicity and singlet oxygen ($^1O_2$)

production. *In vitro* studies included the investigation of the cellular uptake, localisation and cytotoxicity against melanotic (MeWo) and amelanotic (A375) cell lines using irradiation with standard red wavelength (λ = 643 nm) and orange wavelength (λ = 606 nm).

The second part of the thesis involves the study of *N*-oxidation of (pyrid-3-yl)porphyrin precursors of amphiphilic porphyrins from the previous group and introduction of the pyridyl *N*-oxide moieties as the hydrophilic parts of the PS molecule. The use of *N*-oxide substituents in the porphyrin structure not only increases the hydrophilicity of a molecule, but also serves as a moiety of hypoxia-activated prodrugs (HAPs), which are commonly used as a strategy to overcome hypoxia in the tumour microenvironment (TME)[9]. This part also includes the photophysical properties and photochemical reactivity of the newly synthesised porphyrins as well as their $^1O_2$ production and lipophilicity. The *in vitro* study was performed in comparison to the previously mentioned *N*-methylated analogues and also includes cellular uptake and localisation of the synthesised porphyrins as well as cytotoxicity on two melanoma cell lines, however, this time under conditions of normoxia and $CoCl_2$-induced hypoxia.

The third part includes the attempts of reduction of one or two peripheral double bonds of the porphyrin ring of the parent pyridyl porphyrins to obtain corresponding chlorin and bacteriochlorin derivatives, tetrapyrrolic PSs that, compared to porphyrins, have better absorption in the red region of the EM spectrum, which is preferable for use in PDT. The reduction was studied by two procedures, using the most studied Whitlock's diimide reduction and $SnCl_2$ reduction in hot acidic solution.

The last part of the thesis was the study of the use of amphiphilic (pyridinium-3-yl)porphyrins as potential theranostic molecules that can be used both as PDT therapeutic agents and as radiotracers for PET imaging. In this part, the synthesis of Ga(III)-(pyridinium-3-yl)porphyrins, three amphiphilic with an alkyl chain of 9, 13 and 17 C-atoms and one hydrophilic porphyrin with acetamido group as PDT agents is presented, and the radiolabelling of the *N*-methylated free-base analogues with $[^{68}Ga]GaCl_3$ performed to obtain the PET imaging radiotracers. Furthermore, the preparation of ^{68}Ga porphyrins of high and low specific activity (high and low SA) in both PBS and carrier-added formulations (bovine serum albumin (BSA) and low-density lipoprotein (LDL)), their stability in serum and towards biological chelators, and their lipophilicity were investigated. The *in vitro* experiments included the study of the cellular uptake of the synthesised Ga(III) porphyrins and the cytotoxicity against the breast cancer cell line (MDA-MB 231). *In vivo* experiments studied the biodistribution of [^{68}Ga]gallium porphyrins using PET/CT scanning in the naïve mouse based on their lipophilicity.

1.1. Hypotheses and aims

The main hypothesis is that the optimal lipophilicity-hydrophilicity ratio in the structure of the newly synthesised amphiphilic PSs will increase cellular uptake and selectivity towards the melanoma cell lines and thus improve PDT efficiency in melanoma.

The main aim of this doctoral thesis was the synthesis and evaluation of photophysical properties and photochemical reactivity of different groups of amphiphilic pyridyl porphyrins conjugated with acyl-chlorides of fatty acids to introduce alkyl chains of different length, and with different ways of pyridyl *N*-quaternisation.

As the different groups of amphiphilic pyridinium porphyrins were studied, the thesis is divided into four groups with different specific aims:

1. **HYPOTHESES:**
   - The Zn(II) porphyrins of the optimal hydrophilic-lipophilic balance will show improved photophysical properties required for PSs in PDT.
   - Orange irradiation wavelength (λ = 606 nm) will suit better Zn(II) *N*-methylated (pyridinium-3-yl)porphyrin group.
   - Chelation of *N*-methylated pyridiniumporphyrins with Zn(II) results in a increased lipophilicity of the PSs.

   AIM: Investigation of the impact of hydrophilic-lipophilic balance and the light irradiation wavelength (606 and 643 nm) of the same fluence rate (2 mW/cm^2) of the two groups of pyridinium porphyrins, free-base *N*-methylated and their Zn(II) analogues substituted with an alkyl chain of 7, 9, 11, 13, 15 and 17 C-atoms on melanoma cell lines (A375 and MeWo).

2. **HYPOTHESIS:** *N*-oxidised (pyridyl-3-yl)porphyrins of the optimal hydrophilic-lipophilic balance will show high PDT potential against melanoma cells, also under induced hypoxia conditions.

   AIM: Investigation of the group of amphiphilic *N*-oxidised (pyridinium-3-yl)porphyrins with an alkyl chain of 9, 13 and 17 C-atoms for use in PDT and comparison of their activity with *N*-methylated analogues on melanoma cell lines (A375 and MeWo) under normoxia and $CoCl_2$-induced hypoxia.

3. **HYPOTHESIS:** Successfully prepared chlorins and bacteriochlorins will have improved absorption in the red region of the EM spectrum and thus better biological efficiency on melanoma cell lines.

   AIM: Synthesis and purification of novel chlorins and bacteriochlorins by Whitlock's diimide or $SnCl_2$ reduction of pyridylporphyrins.

4. **HYPOTHESES:**
   - *N*-methylated(pyridinium-3-yl) porphyrins with different alkyl chain can be prepared as potential PET/PDT agent by chelating with $^{68}Ga/^{nat}Ga$.
   - Different hydrophilic-lipophilic balance of the ^{68}Ga radiotracers will lead to the different biodistribution of porphyrins which will be observed by PET-CT scanning in the mouse model.

   AIM: Investigation of the group of *N*-methylated ^{68}Ga- and Ga(III)-(pyridinium-3-yl)porphyrins as potential PET/PDT agents and analysis of the impact of hydrophilic-lipophilic balance on their *in vivo* biodistribution by PET-CT scanning.

2. Literature review

2.1. Photodynamic therapy (PDT)

According to the World Health Organization, cancer is one of the leading causes of death in the world [10]. Current therapies include surgery (60%), chemotherapy, radiotherapy or immunotherapy, depending on the type of tumour and the stage of tumour progression [10]. However, current treatments are either ineffective or cause numerous side effects on normal tissue. Therefore, there is an urgent need to develop new treatments that will be affordable and easily accessible.

Although it was discovered in 1905 by Oscar Raab as an antimicrobial therapy, today, photodynamic therapy (PDT) is considered as emerging therapy for the treatment of malignant and non-malignant diseases [1,11]. It consists of three main components: a photoactive molecule called photosensitizer (PS), light of an appropriate wavelength and endogenous molecular oxygen in the surrounding tissue. These components are non-toxic on their own, but in combination produce oxidative stress and highly cytotoxic events. The clinical protocol involves two steps: the first is the administration of a PS, intravenously, topically or orally, and the second step is the irradiation of the diseased tissue with a light of appropriate wavelength [2,11,12]. Between the two steps there is a period of time during which a PS can accumulate or persist in the target tissue. This period is called the drug-light interval (DLI), and the length of this period depends on the PS design and the type of targeting, which can be cellular or vascular [13]. A short DLI indicates vascular effects predominantly, where vascular collapse may be the first tumour death mechanism that will occur, while a DLI favours the effect on tumour cells and destroys the tumour through cell death mechanisms such as apoptosis or necrosis, which will be discussed in the following chapters [2,11,14].

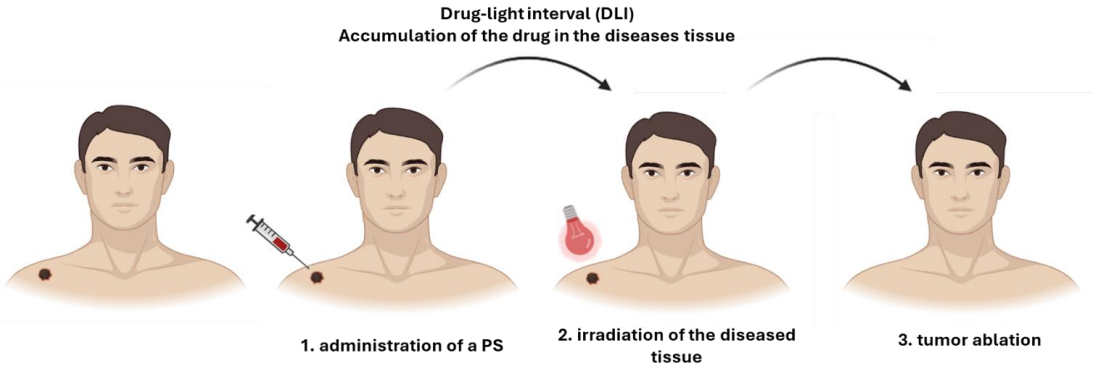

Figure 1. The clinical procedure for photodynamic therapy (PDT). Created with BioRender®.

The advantages of PDT include less side effects and low systemic toxicity as well as the excellent cosmetic outcome, with minimal or no scars or inflammation after the therapy. It is a short treatment that can be applied several times to the same area if necessary, and it can also be used as an individual or adjuvant therapy. In addition, it has a high selectivity for cancer and a low potential for resistance development. On the other hand, there are some disadvantages: the limited penetration depth of the light into deep-seated tumours, the photosensitivity of the skin after the treatment, oxygen supply to the tissue and low possibility of treating metastatic cancers [11,15].

Although the term "photodynamic" was introduced by von Tappiener and A. Jodlbauer in 1907 and the first treatment in humans took place in 1913 when Friedrich Meyer Betz injected himself with hematoporphyrin - both more than 100 years ago[1,16] - the number of approved PSs and those undergoing clinical trials is still limited and the treatment is still underutilized in everyday clinical practice [16].

2.1.1. The mechanism underlying the PDT

The mechanism underlying photodynamic therapy is explained by the Jablonski diagram (**Figure 2**). The photosensitizer in the ground state (S_0) has two paired electrons with opposite spin (S=0) in their lowest occupied energy orbital. When irradiated, PS absorbs a photon, transfers an electron to the higher unoccupied energy orbital, whereby the spin of an electron remains the same, and reaches the first excited singlet state ($^1PS^*$). The excited singlet state is very unstable and short-lived (10^{-12} s) and a molecule can return to the ground state by releasing energy through fluorescence or heat. The decay of a molecule can also be observed via non-radiative processes, through the vibrational relaxation. However, PSs are molecules that preferentially undergo the spin-forbidden transition pathway, intersystem crossing (ISC), to reach excited triplet state ($^3PS^*$) [17,18]. This transition from the singlet to the triplet state is associated with a change of electronic state. Therefore, the lifetime of the triplet state is about 10^4 longer than that of the singlet state [19]. The PS in the triplet state has two unpaired electrons of the same spin and can decay by radiative relaxation known as phosphorescence. The PS in the excited triplet state can trigger chemical changes in neighbouring molecules by two competing pathways that form reactive oxygen species (ROS) [12,17,18].

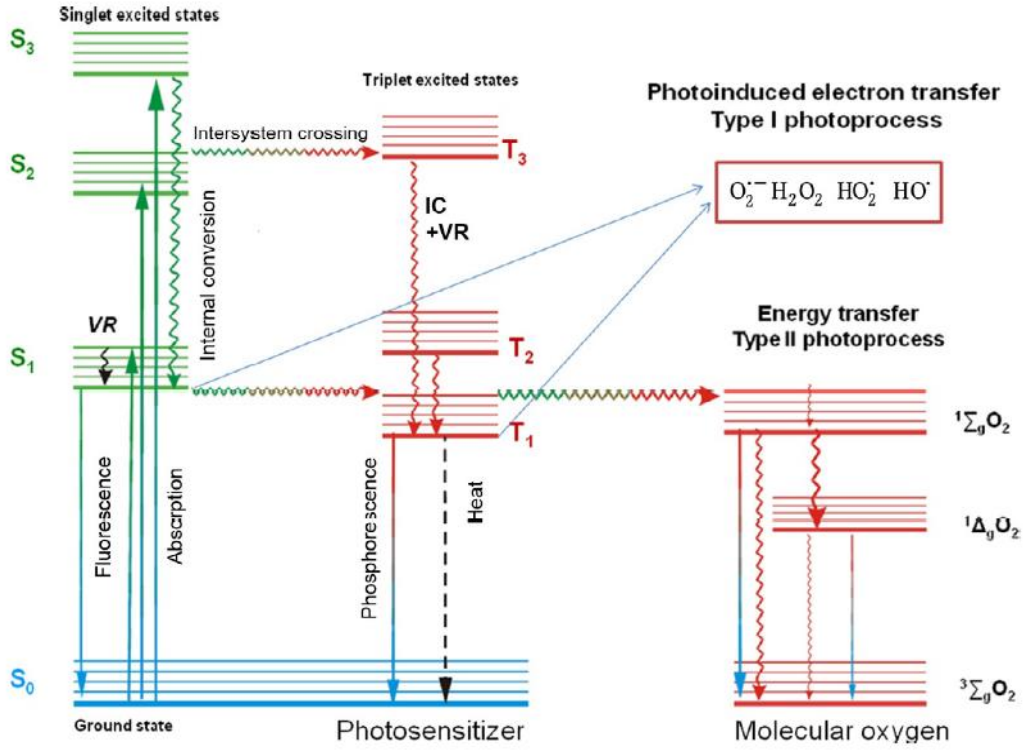

Figure 2. Photophysical and photochemical processes described by Jablonski diagram. Adapted from[20].

The ratio of Type I and Type II (**Figure 2**) that is likely to occur depends on the nature of PS used, the concentrations of $^3O_2$ available in the environment and the nearest cell substrates present. Type I involves proton or electron transfer to the biomolecules or oxygen in the surrounding tissue. A weak oxidizing agent, the superoxide ion ($O_2^{\bullet-}$), is formed by the transfer of one electron from a reducing agent in the environment (**Figure 3**, equations 1 and 2) or to the oxygen (**Figure 3**, equation 3). In this way, a cascade of reactions is set in motion, followed by the formation of the perhydroxyl radical ($HO_2^{\bullet}$), a stronger oxidant capable of oxidizing back the superoxide ion, leading to the formation of hydrogen peroxide (H_2O_2) (**Figure 3**, equations 4 and 6). Compared to superoxide ions and perhydroxyl radicals, H_2O_2 has a much longer lifetime and can penetrate the membrane bilayer, damaging other cell organelles in the process [14,17,20].

The strongest ROS in the Type I reaction is the hydroxyl radical, which can be formed by the reaction of superoxide ions or perhydroxyl radicals with hydrogen peroxide (**Figure 3**, equations 7 and 8). In biological systems where ferrous ions are present, hydroxyl radicals and iron(III) ions are formed by a one-electron reduction from hydrogen peroxide in a Fenton reaction (**Figure 3**, equations 9 and 10) [18,20].

Initiation reactions:

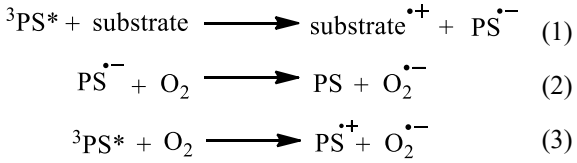

Formation of hydrogen peroxide:

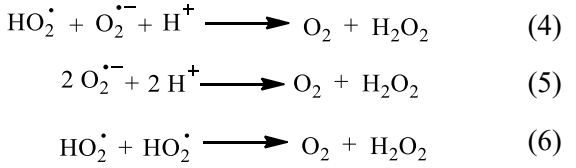

Formation of hydroxyl radical:

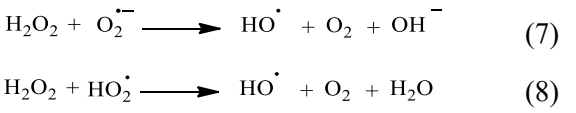

Fenton reaction:

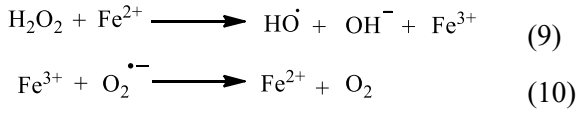

Reaction with PS:

Figure 3. Formation of ROS by Type I mechanism[20].

Type II is a photophysical process in which triplet-triplet annihilation takes place. The energy is transferred from PS in the triplet excited state (^{3}PS*) to the oxygen in the ground triplet state, forming two singlet excited states $^1\Delta_g$ and $^1\Sigma_g^+$; 95 kJ mol^{-1} (22.5 kcal mol^{-1}) and 158 kJ mol^{-1} (31.5 kcalmol^{-1}), respectively, which differ in the structure of the π-antibonding orbitals. The first singlet excited state, $^1\Delta_g$, is the most important for reactions in biological systems due to its relatively long lifetime (10^{-6} to 10^{-3} s in water), while the second excited state, $^1\Sigma_g^+$, has a very short lifetime (10^{-11} to 10^{-9} s in water) and has no effect in biological systems, but transfers relatively easily to the $^1\Delta_g$ due to the allowed spin transition [21,22].

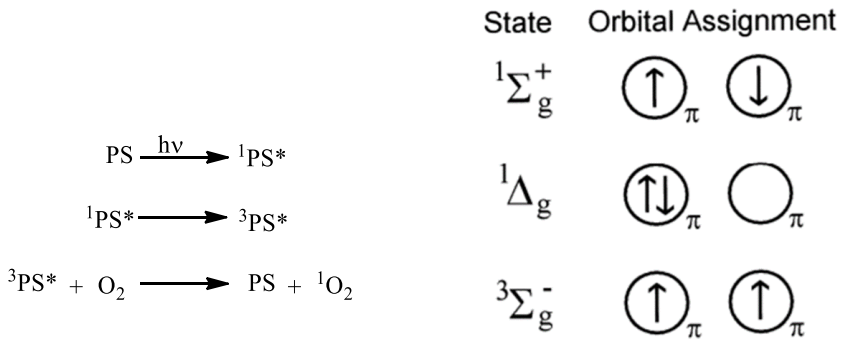

Figure 4. Formation of ROS by Type II mechanism and the π-antibonding spin orbital configuration [17,21].

Both type I and type II processes occur in parallel, and the ratio depends on many factors described above. However, singlet oxygen ($^1O_2$) is thought to be the predominant product of the many PSs in PDT, as type II chemistry is mechanistically simpler compared to Type I photochemistry [2,23,24]. Moreover, the distinction between the Type I and II processes is mainly based on the photophysical properties of the PS, as the Type II efficiency mainly depends on the triplet state lifetime and triplet state quantum yield of the PS [25].

2.1.2. Biological targets of ROS produced by PDT

Among the radicals generated, hydroxyl radicals ($OH^•$) and singlet oxygen in the $^1\Delta_g$ state are the main oxidising agents that cause the most damage in cells. In water, both $OH^•$ and $^1\Delta_g$ $^1O_2$ have similar lifetimes and diffusion distance, with determined lifetimes of 3.3 μs for $^1O_2$ and 2.7 μs for $OH^•$ and distances of 270 and 309 nm for $^1O_2$ and $OH^•$, respectively [26,27]. These lifetimes and distances are much shorter in cells due to the direct interaction with biomolecules in the environment. In contrast to $OH^•$, that is a strongly oxidising reagent and reacts non-selectively with almost all biomolecules, singlet oxygen has been shown to react selectively with biomolecules that possess double bonds in their structure, where it can undergo a [2+4] Diels-Alder or [2+2] cycloaddition reaction or "ene"-type reaction to form endoperoxides, dioxetanes or allyl hydroperoxides [27]. Some of the atomic targets of the generated ROS are “electron-rich” sulphur-containing molecules usually found in the amino acids like cysteine and methionine, selenium in seleno-cysteine, or carbon in nucleosides or some amino acids such as lysine, arginine or polyunsaturated fatty acids. Molecular targets, which we will discuss in more detail, include lipids, DNA and proteins [27,28].

The lipid oxidation can be triggered by both radical and non-radical ($^1O_2$) oxidation, with lipid hydroperoxides (LOOH) being the primary oxidation products in both cases [28] (**Figure 5**). In radical oxidation, the reaction begins with the abstraction of a hydrogen atom,

which leads to the formation of the carbon-centred radical, which in turn reacts with oxygen forming the peroxyl radical [29]. The peroxyl radical formed is then the trigger for the radical chain reaction, in which it reacts with another lipid molecule, forming a lipid hydroperoxide and another carbon-centred lipid radical. The reaction can take a different pathway in which the peroxyl radical can form different oxidised products with functional groups such as alcohols, aldehydes, ketones or carboxylic acids [29]. On the other hand, in a non-radical reaction, $^1O_2$ reacts directly with the unsaturated double bond by an "ene" addition mechanism, where an oxygen is inserted at both ends of the double bond, which is shifted to an allylic position and isomerised to the *trans* configuration [28,30]. Lipid peroxidation leads to morphological changes in biological membranes by forming "gaps" in the membrane or leading to "cross-linking" of fatty acids and proteins or two fatty acids, which increases the fluidity of the membrane and its permeability. In addition, toxic by-products can be a result of lipid peroxidation, directly inducing apoptosis or acting as second messengers to other biological targets [29,31].

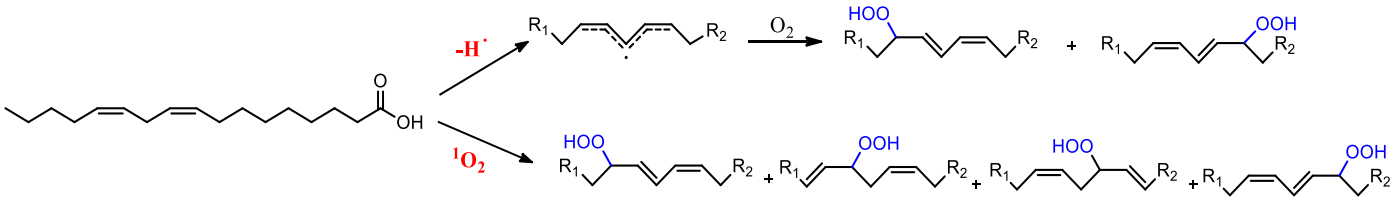

Figure 5. Formation of different lipid hydroperoxides by lipid peroxidation of unsaturated fatty acids (e.g. linoleic acid) by reaction with radical type ROS and singlet oxygen ($^1O_2$).

Although the nucleus is not a common target of PSs, the $^1O_2$ and $OH^{\bullet}$ produced can react with DNA, leading to strand breaks and the formation of altered bases [29,32]. Due to its redox potential, the guanine molecule serves as the main target for oxidation with $^1O_2$ or free radicals. In a reaction with $^1O_2$, oxidation occurs mainly via a [4+2] cycloaddition, which ends in the formation of 8-oxoguanosine, which can be further oxidised [28]. The formation of oxidation products such as 8-oxoguanosine leads to DNA-DNA or DNA-protein cross-linking, which results in termination of replication. Therefore, oxidation of DNA has genotoxic and mutagenic potential and radical or non-radical oxidation may be involved in the multistep process of chemically induced carcinogenesis [29,31,33].

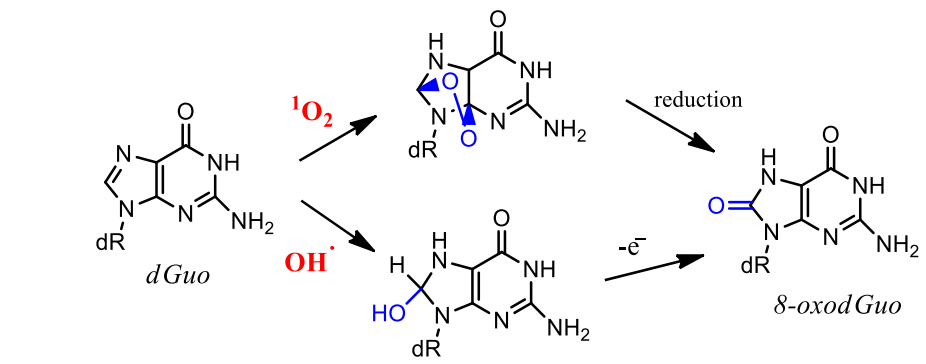

Figure 6. The main oxidative degradation pathways of 2-deoxyguanosine induced by $^1O_2$ and OH•.

It has been found that amino acids such as methionine, histidine and tryptophan are the main targets in proteins and are oxidised to a considerable extent by $^1O_2$, producing hydroperoxides and endoperoxides [29]. In the case of cysteine, an example of a sulphur- containing amino acid, the reaction with $^1O_2$ leads to the formation of cystine (**Figure 7a**), which contains a disulfide bond via the persulfoxide intermediate. When radical oxidation occurs, cysteic acid and H_2O_2 are detected. Histidine reacts with $^1O_2$ via a [4+2] cycloaddition reaction forming endoperoxides, which further rearrange to form different hydroperoxides (**Figure 7b**) [28]. Hydroperoxides can then decompose either by the loss of water molecules or by reduction to the diol molecule. The last example is tryptophan, where $^1O_2$ reacts with the indole substituent forming dioxetanes by cycloaddition or hydroperoxides by an "ene" type reaction. Although the "ene" reaction was predominant in the oxidation of tryptophan, the hydroperoxides formed can easily decompose to dioxetanes and lead to *N*-formylkynurenine by cleavage of the O-O bond (**Figure 7c**) [28]. Photooxidation of amino acids leads to loss of activity of proteins and peptides, changes in their mechanical properties, aggregation site and affinities to ligands. Moreover, the oxidation of the first protein or peptide can trigger a further oxidation reaction of other proteins, either by a radical propagation reaction or by a further reaction of the oxidised molecules [29,31].

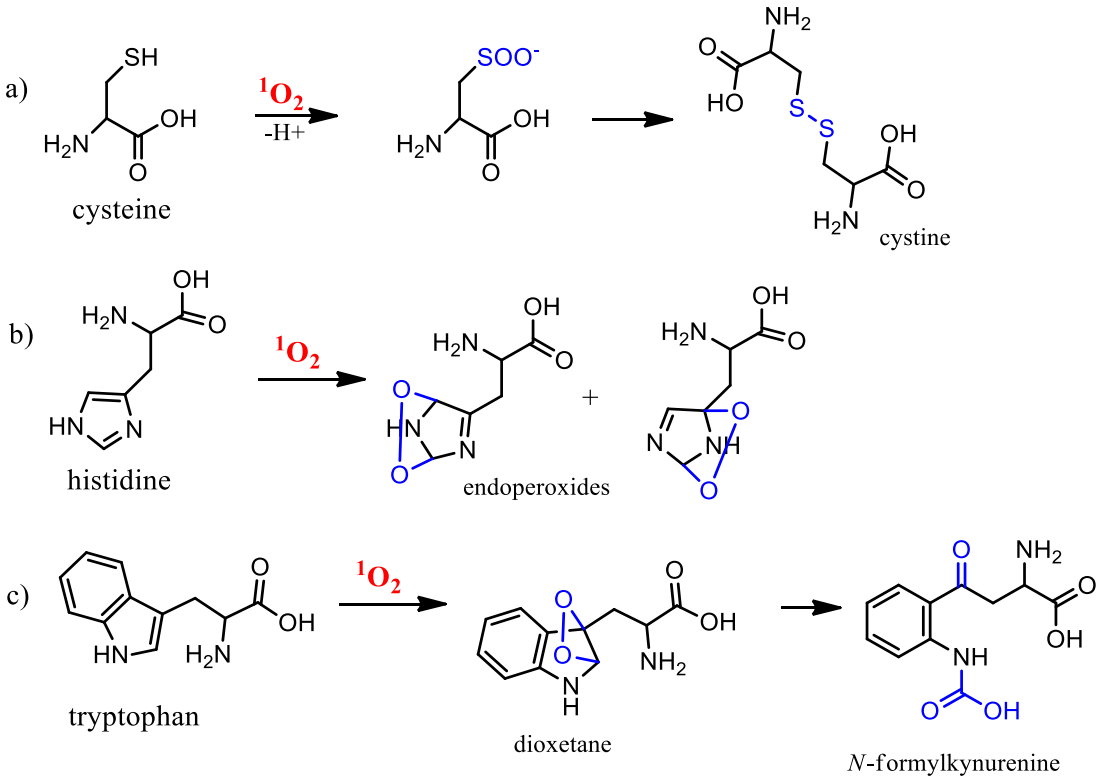

Figure 7. Reaction of singlet oxygen with amino acids: a) cysteine b) histidine and c) tryptophan.

2.1.3. Cell death in PDT

As described above, oxidative stress induced by PDT can damage numerous biomolecules. Therefore, cells have found a way to combat oxidative stress and have developed "survival mechanisms" that can remove or repair the damaged molecules and restore cellular homeostasis and viability. The regulation of this mechanism is mediated by different transcription factors such as eukaryotic translocation initiation factor 2 subunit α (eIF2), nuclear factor erythroid 2-related factor 2 (NRF2), hypoxia-inducible factor (HIF-1), nuclear factor kB (NF-κB) and several others (ATF4 and XBP1) [14,34]. In addition, pigment melanin, heat shock proteins, antioxidant enzymes such as superoxide dismutase (SOD), catalase and glutathione peroxidase or even some small molecules such as glutathione and vitamins E and C can play an important role in the fight against ROS in cells [14].

However, when oxidative stress is persistent or severe, the repair mechanisms and other ROS defence mechanisms are unable to restore cellular homeostasis, so cell death pathways are induced instead [35]. In PDT, there are three main mechanisms of cell death - apoptosis,

necrosis and autophagy. Different factors govern which cellular death mechanism will be triggered, such as the type and concentration of PS, its physicochemical properties and cellular internalisation and subcellular localisation, as well as the oxygen concentration in the biological targets [14,36]. In addition, light fluence and light dose play an important role. It has been shown that light of high fluence, preferably in combination with a high PS concentration, probably leads to necrosis, whereas light with a low fluence rate leads to cell death by apoptosis [13,35]. The same PS can trigger all three types of cell death simultaneously. However, the rate of each type of death will depend on the properties of PS and light described above and on tissue characteristics [35].

Apoptosis is known as a "regulated form" of cellular death, which can manifest itself through changes in cellular morphology seen as shrinkage, cell surface blebbing, chromatin condensation and DNA fragmentation[14]. Depending on the localisation of the PS, it undergoes two distinct pathways: the intrinsic (mitochondrial) and the extrinsic (death receptor) pathway [34,35,37]. The extrinsic pathway is usually involved when a disturbance is detected in the extracellular environment and involves the activation of caspase 8, which in turn leads to the activation of other effector caspases. The intrinsic pathway, on the other hand, is triggered intracellularly either by direct damage to the mitochondria or indirectly by damage to other organelles, which indicates the signalling pathway and causes the perturbation of the mitochondrial membrane. This signalling pathway is regulated by the B-cell lymphoma 2 family (BCL-2), which is divided into two groups of anti- and pro-apoptotic proteins. As a result, the perturbation of the mitochondrial membrane can lead to its irreversible permeabilization, which induces changes in mitochondrial membrane potential ($\Delta\Psi_m$) and consequently leads to the leakage of mitochondrial proteins into the cytosol, of which cytochrome *c* is the best known. The released cytochrome *c* then activates caspase 9 and this in turn mediates the proteolytic activation of caspases 3 and 7, which is an indicator of the morphological and biochemical changes associated with apoptosis mentioned above [34,35,38].

In contrast to apoptosis, necrosis is considered the non-regulated form of cellular death, which is usually activated by a high dose of PDT and/or the activation site of PS at the plasma membrane [14,37]. It is characterised by the leakage of intracellular contents into the extracellular environment due to loss of membrane integrity, cellular and organelle swelling, cytoplasm blebbing and clumping of chromatin, resulting in complete degradation of the cell [35]. As a result of the loss of membrane integrity, an ion imbalance occurs, leading to a decrease in ATP levels and an increase in cell volume due to the passive influx of Ca^{2+}, Na^{+} and water [14,34]. The release of the cellular contents leads to a strong inflammation, an activator of the immune system.

The last of the conventional cell-death types is autophagy, a process that can act both as a cytoprotective mechanism (adaptive autophagy) or as a death mechanism (autophagy-dependent cell death). The extent of photodamage when this death mechanism is activated is not yet fully understood. However, it has been shown to be activated together with apoptosis and necrosis or when the apoptosis mechanism in the cells is impaired. It is determined by the formation of autophagosomes, the double-membrane vesicles containing damaged material that separate the contents from the rest of the cytoplasm [35,38]. The second step includes the formation of the autophagolysosome by fusion of the autophagosome with the lysosome, which is further degraded by the lysosomal hydrolases [34]. The formation of the autophagosome and later the autolysosome is a highly regulated process in which numerous proteins and signalling pathways are involved. These include the unc-51-like autophagy-activating kinase 1 (ULK1) complex, the phosphatidylinositol 3-kinase catalytic subunit type 3 (PIK3C3)-Beclin 1 complex and other autophagy-related genes (ATG). Autophagy also plays an important role in activating the immune response by exposing antigens during the process of autolysosome formation [14,34].

In addition to the three "conventional" mechanisms commonly reported as cellular death pathways, new "non-conventional" mechanisms have recently been recognised in the last decade as a form of cellular death induced by PDT, known as necroptosis, ferroptosis, pyroptosis, parthanatos and mitotic catastrophe [36]. The non-conventional mechanisms have different morphological, biochemical, genetic and functional characteristics from the well-accepted conventional mechanisms and have attracted the interest of scientists, especially necroptosis and ferroptosis, as they can activate the immunological cell death (ICD) [36,39].

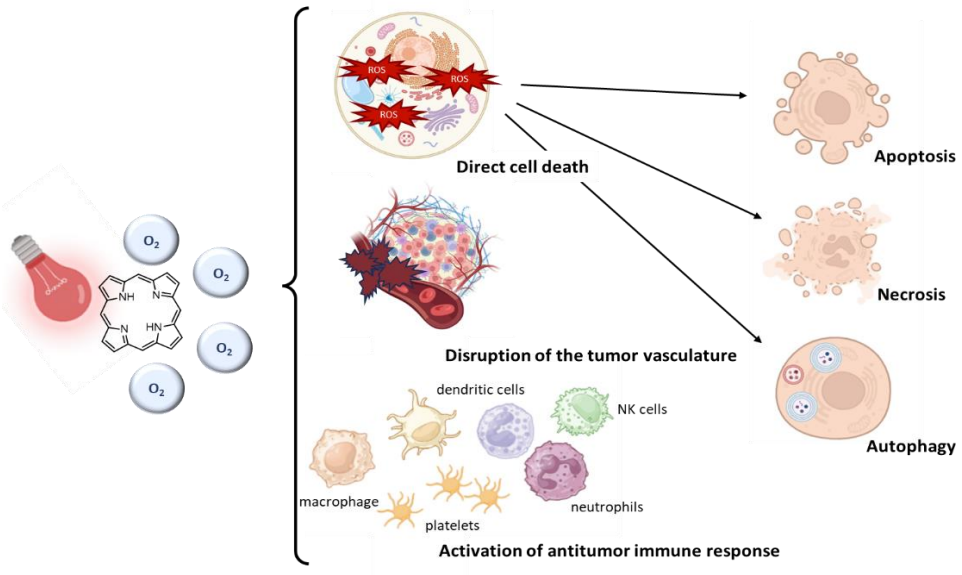

Figure 8. The tumour ablation pathways activated after oxygen-consumed PDT. The pathways include direct tumour cells killing, destruction of tumour vasculature and induction of inflammation and immune response. Modified according to the literature [40]. Created with BioRender©.

In addition to the direct mechanism of tumour destruction through cellular death, there are also indirect mechanisms, such as the disruption of the tumour's microvasculature, leading to the deprivation of oxygen and nutrients and consequently to tumour infarction [41]. PDT damages the endothelial and subendothelial cells in the vessels, leading to the formation of junctions in the interendothelial cell wall. In addition, under normal conditions, endothelial cells balance the production of the vasodilatation (prostacyclin and endothelium derived growth factor) and vasoconstriction (endothelin-1) factors. When PDT-induced damage occurs, a cascade of eicosanoids and other inflammatory agents are released, shifting the balance towards vasoconstriction of the vessels [33]. In addition, clotting factors are also released (von Willebrand factor), leading to platelet activation and the release of tromboxane, which causes platelet aggregation, thrombus formation and the build-up of vessels that block the blood flow of tumour vessels. Vascular targeted PDT with a DLI < 1 h has many potential advantages as it uses the highly hydrophilic PS, which can be rapidly eliminated from the body and can be applied in just one short session [14].

Indirect tumour destruction also includes the activation of the immune response by PDT, which has attracted much attention in recent years. The activation of the immune response is a complex process involving different immune cells, such as dendritic cells, macrophages, NK cells and others [42]. In brief, upon PDT photodamage, cellular death (especially apoptosis, necroptosis and ferroptosis) [36] leads to the release of immunostimulatory molecules called damage-associated molecular patterns (DAMPs), which in turn are recognised by pattern recognition receptors (PRRs) on the immune cells. The DAMPs that are released extracellularly or exposed on the surface of the dying cell include ATP, calreticulin (CRT), high mobility groups Box 1 (HMGB1), heat shock proteins 70 and 90 as well as different cytokines and chemokines [39]. Binding of DAMPS to PRRs expressed by macrophages leads to their activation and release of TNFα, a cytolytic cytokine that may mediate indirect cytotoxicity [42]. In addition, the release of DAMPs can promote the maturation of dendritic cells (DC), which are known as antigen-presenting cells. The cells treated with PDT show increased expression of the major histocompatibility complex class 1 (MHC class 1) and molecules MICA and NKG2D. Mature dendritic cells are therefore responsible to activate the adaptive immune response through the cross-presentation of exogenous antigens on the MHC class 1 molecules to the effector $CD8^+$ T cells of the

adaptive immune system, which is the main regulatory mechanism for the effective control of tumour destruction and the activation of long-term immunity [36,39,42].

2.2. Photosensitisers

As described above, a photosensitiser (PS) is a molecule that preferentially accumulates in diseased tissue and generates cytotoxic species (ROS) upon irradiation, thereby producing a desired biological effect in the diseased tissue. Together with oxygen and light, it represents one of the main characters in PDT [2,11,25]. Therefore, one of the main focuses of this work is the design and characterisation of a series of new PSs for use in PDT.

The first approved PS is the purified derivative of hematoporphyrin (HpD), first synthesised by Thomas Dougherty in 1978 and approved by Canadian Health Agency and later in Japan and America under the name Photofrin® for the treatment of esophageal and non-small lung cancer [43]. However, major disadvantages of Photofin® such as prolonged photosensitivity (up to 90 days) and weak absorption in the red region of the electromagnetic (EM) spectrum (λ = 630 nm) were observed. Disadvantages of Photofrin® significantly reduced the ability to further investigate this treatment for a broader range of diseases and forced scientists to develop new PSs with improved properties for use in PDT and to consider them as a second generation of PSs. The key characteristics that scientists have proposed for a PS to be an "ideal PS" for PDT adhere to the following criteria [25,44,45]:

- a single pure compound of relatively high-yielding synthesis route
- high absorption in the red region of the EM spectrum (600-800 nm)- allowing the deeper tissue penetration of light and minimisation of the damage of surrounding healthy tissue
- efficient generation of ROS, particularly singlet oxygen
- preferable photophysical properties with high intersystem crossing yield (Φ_{ISC} 0.5), lifetime of a triplet state (τ_T) in microsecond scale and relatively high triplet state energy (94 KJ/mol)
- selective accumulation in cancer cells minimizing the death of the normal, healthy cells
- preferable administration, distribution, metabolism and excretion (ADME) properties reducing the side effects and long photosensitivity of healthy tissue
- to have a simple drug formulation with high biocompatibility to minimise the adverse reaction
- high photodynamic index (PI) showing high toxicity of a compound when irradiated and negligible or no toxicity in the dark

- photostability of the compound allowing the repeated cycles of photoactivation without degradation or loss of the photodynamic properties
- solubility and stability in biological media allowing the intravenous administration of the PS and successful transport to the target

Among the second-generation PSs, 5-aminolevulinic acid (5-ALA) was approved under the name Levulan® for the treatment of basal cell carcinoma and other skin diseases such as actinic keratosis, psoriasis, Bowen's disease and acne. Although not a PS itself, it undergoes the pathway of heme biosynthesis *in vivo* and produces protoporphyrin IX (PPIX), a successful PS which has a much rapid accumulation and clearance compared to Photofrin®, resulting in a shorter photosensitivity of the patient [15,25,37,46]. In addition to 5-ALA, ester derivatives such as methy-ALA ester (Metvix®) for basal cell carcinoma and other skin lesions and hexyl (Hexvix®) and benzyl (Benvix®) for gastrointestinal or bladder cancer have been developed due to the poor bioavailability of Levulan® when applied topically. Another approved PS is the benzoporphyrin derivative, monoacid ring A (BDP-MA), known under the trade names Visudyne® or Verteporfin®. It showed a strong red-shifted absorption at λ = 690 nm and, similar to Levulan, was rapidly accumulated in the tumour and excreted from the body. The most potent second-generation PS approved is considered to be tetra-(*m*-hydroxylphenyl)chlorin (***m*-THPC**), known as Temoporfin, or commercially as Foscan®, which is approved for squamous cell carcinoma of the head and neck and for prostate and pancreatic cancer and has a high absorption peak at 652 nm, making it 100 times more potent than Photofrin®. However, the lack of selectivity for normal cells and the prolonged photosensitivity (two weeks) are considered to be the main disadvantages of therapy with Foscan® [15,25,46].

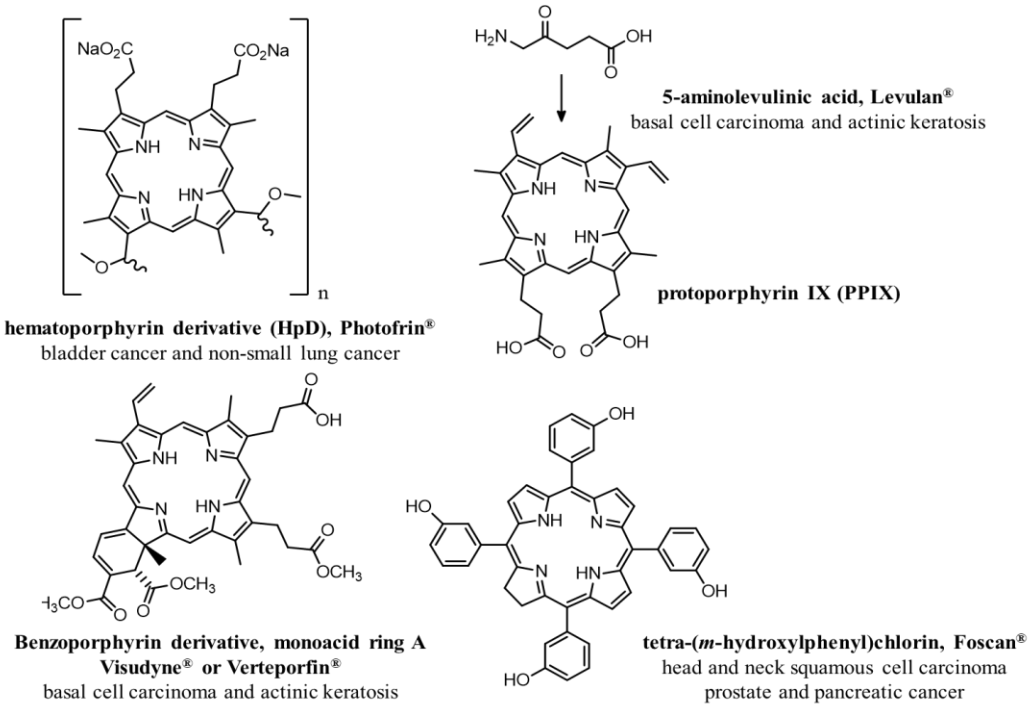

Figure 9. Some approved PSs for clinical use (commercial and chemical name) with the type of cancer for which they are approved.

Although the properties of the second generation were improved, the poor solubility of the approved PSs and the lack of selective accumulation in cancer cells were the focus of the third generation of PSs. Selectivity of PS could be achieved by adding a targeting component in the design of the PS, which is known as active targeting, or by relying on the pathophysiological and morphological differences of tumours compared to normal tissue, which allows passive accumulation [47–50]. In active targeting, peptides, aptamers, sugars, antibodies and other small molecules are used to target the receptors that are usually overexpressed in the tumours while their expression is minimal in normal tissue, such as human epidermal growth factor receptor 2 (HER 2), endothelial growth factor receptor (EGFR), integrin receptor or folate receptor [50,51]. Although active targeting should theoretically lead to higher specificity and selectivity towards cancer cells, it has been shown that maintaining the functionality and stability of PS with an active targeting component is challenging, as the potential interaction with non-targeted components in *in vivo* systems affecting the overall effect [52].

In contrast, passive targeting, as mentioned above, relies on accumulation based on the so-called enhanced permeability and retention (EPR) effect, which is based on the differences of tumours compared to normal tissue. Those differences include massive irregular neovascularisation with structural abnormalities of tumour blood vessels with disorganised,

loosely connected or branched endothelial cells [49,50]. Furthermore, solid tumours show a lack of efficient drainage of the lymphatic system and an acidic microenvironment due to anaerobic glycolysis, which is a result of tumour hyperproliferation, as well as increased expression of pro-inflammatory factors (prostaglandins, bradykinin, nitric oxide, interleukin 1β, interleukin 2, and others) [49,53]. In addition to PSs with moderate hydrophobicity, different biodegradable (liposomes) or non-biodegradable (silica, gold, polyacrylamide and others) nanoparticles have been investigated as passive uptake strategies [49,54]. Disadvantages of passive targeting include differences in EPR efficacy between tumours, leading to inconsistent accumulation of the PS in different tumours, and accumulation of the PS in normal tissues, potentially leading to side effects of therapy [55].

In general, among these two approaches, passive targeting, which relies on the EPR effect and the structure-activity relationship (SAR) of PS, was shown to have much greater potential for the development ofapplication *in vivo*, while the active targeting approach, which relies on the overexpression of targeting receptors in tumours, showed limited activity with a lack of tumour selectivity [45].

2.2.1. Porphyrins and related tetrapyrrolic PSs

The most studied PSs, with the highest number in preclinical and clinical trials and the PSs approved for PDT are porphyrins and related tetrapyrrolic PSs [14,56,57]. Porphyrins are a group of macrocyclic compounds usually found in and involved in biological systems, e.g. as a chlorophyll molecule in plants involved in photosynthesis or as heme molecule in humans or animals involved in oxygen transport. In addition to their role in biological systems, they are used in numerous scientific fields and can serve in solar systems or as analytical reagents for the detection of anions, as fluorescent molecules in fluorescence diagnostics or for therapeutic purposes as PSs in PDT [58,59], which is a topic of this thesis. The porphyrins are aromatic macrocycles which, as their name suggests, consist of four pyrrole subunits linked by methine bridges. The macrocycle itself consists of 22 π electrons, 18 of which, according to Hückel's rule, are responsible for the aromaticity of the structure. The standard nomenclature comes from Hans Fischer, who named the structure porphine. However, their derivatives with substituents at methine bridges, known as *meso*-substituents, or at pyrrolic, known as *β*-positions, or coordinated metal in the centre of the ring are called porphyrins or metalloporphyrins (**Figure 10**) [1,41,45,57,60].

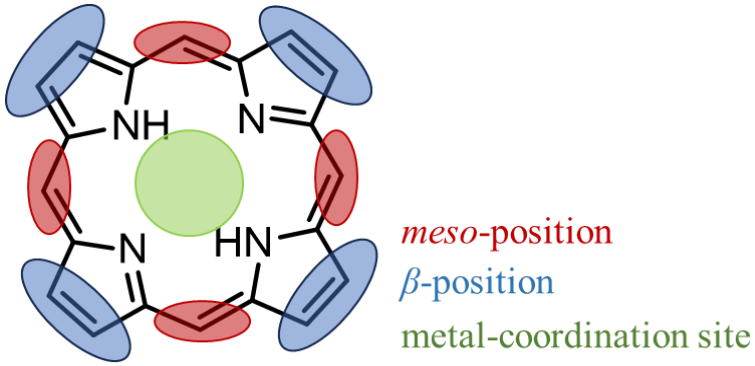

Figure 10. The porphyrin core (porphine) with the modification sites.

Porphyrins have been intensively studied as PSs in PDT due to the aromatic stability of the structure and the efficient absorption in the red part of the EM spectrum, known as therapeutic window (for more details see Section 2.3.). Photoexcitation of porphyrins leads to the photoinduced processes and the formation of high amount of ROS that causes strong oxidative stress in cells. Furthermore, porphyrins and their derivatives have shown intrinsic affinity to tumours and have been found to selectively accumulate in tumour tissue [3,61].

In addition to their advantageous properties for use in PDT, porphyrin structures can be modified to alter amphiphilicity, solubility in biological media, p*K*a, and stability of the molecule. These parameters contribute to the biological distribution of the compounds in tissue, cellular uptake and intracellular localisation as well as pharmacokinetic properties, making them even better for use in PDT [45]. The modifications of the structure can be made at the *meso*-position, the most electronically active site of the molecule, or at the *β*-position, the most sterically accessible site of the molecule for the reactions of electrophilic aromatic substitution, additions or radical reactions (**Figure 10**). In addition, porphyrins can be readily metalated within the metal coordination site (**Figure 10**), leading to an inductive effect of the chelated metal on the π-electron system of the porphyrins, thereby strongly influencing the photophysical properties, chemical reactivity and biological function of the porphyrins[62]. The reduction of one *β*-*β*'-double bond in the porphyrin macrocycle results in a macrocycle with 20 π electrons, known as chlorin, or the reduction of two opposite *β*-*β*'-double bonds results in a macrocycle with 18 π electrons, known as bacteriochlorin. Both chlorin and bacteriochlorin, from the group of tetrapyrrolic macrocycles, have gained a lot of interests for applications in PDT due to their better absorption in the region of the EM spectrum > 600 nm compared to porphyrins [60,63].

This work focuses on the modification of the *meso*-substituted amphiphilic A_3B porphyrins to study the balance between the lipophilicity and hydrophilicity of the molecule. The amphiphilic metalloporphyrins chelated with Zn(II) and Ga(III) are also prepared and their

properties investigated. The design of the porphyrins is described in more detail in the following sections.

2.2.1.1. Amphiphilic porphyrins

Amphiphilic porphyrins have attracted a lot of attention in the study of the optimal PSs to use for therapeutic purposes as they overcome the drawbacks of the highly hydrophobic or hydrophilic molecules, keeping their positive characteristics to achieve the efficient therapeutic outcome. The PS of predominantly hydrophobic structures, as it is the porphyrin core itself, have sufficient affinity to interact with biomolecules and can efficiently pass through the biological membranes via passive diffusion. However, their lower solubility in aqueous media usually results in aggregation making them non-ideal PSs unless a suitable carrier is used. Aggregation facilitates internal conversion (IC), which leads to insufficient ISC and lower ^{3}PS* yield required for generation of ROS [4,5]. On the other hand, hydrophilic PSs are known to have low tendency to aggregate in aqueous media which allows them to be administered intravenously into the body and they can be decomposed or eliminated from the body faster, lowering the possibility to cause side effect. In addition, it was seen that hydrophilicity in PSs can increase bioavailability and *in vivo* distribution due to the solubility in water. However, drawbacks of the hydrophilic PSs include low penetration through the membrane bilayer leading to the poor cellular internalization of those PSs and they showed low stability under reductive biological conditions [4,5].

Amphiphilic porphyrins are often designed by adding long alkyl chains to increase the hydrophobicity of the molecule and thus improve cellular internalization, while various non-charged polar groups (hydroxyl or alkoxy groups) or positively (pyridinium or quaternary ammonium salts) or negatively (sulfonatophenyl) charged groups are added to increase water solubility [64,65].

Extensive research on different amphiphilic tetracationic *meso*-tetrakis(*N*-alkylpyridiniumyl)porphyrins was conducted by Benov research group [66,67]. In the work by Odeh et al, the alkyl chain length on the quaternised pyridyl rings (**ZnTM-2-PyP, ZnTBu-2-PyP** and **ZnTHex-2-PyP, Figure 11**) and their impact on cellular uptake and intracellular localisation was investigated [66]. It was shown that an increase in the hydrophobic chain length has increased cellular uptake and suppressed the localization in lysosomes, shown for the hydrophilic analogue, and increased the localization in the mitochondria and ER [66].

The various lipophilic derivatives of cationic porphyrins were investigated on colorectal adenocarcinoma cell line (HT-29) and their structure-activity relationship (SAR) was investigated by Hudson *et al.* [68]. The nature of the cation substituents was shown to affect

the cellular uptake and intracellular retention and distribution. In addition, along with the nature of substituents bounded to cation having an impact, their ability to delocalise the positive charge was found to be an essential property of potential PSs for PDT [68].

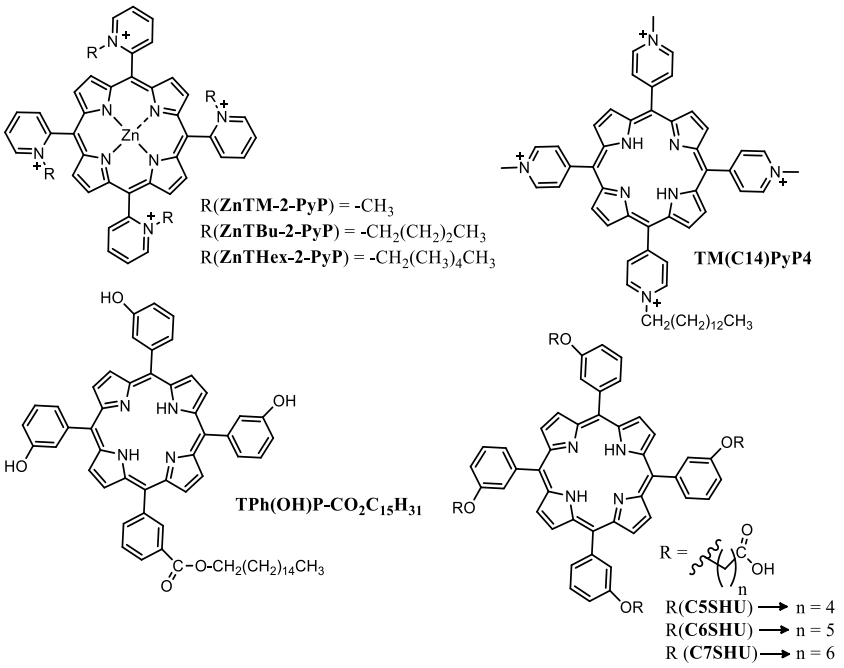

Figure 11. Examples of the amphiphilic porphyrins described in the literature.

Compared to symmetric (A_4) porphyrins, porphyrins containing one different, usually hydrophobic substituent (A_3B) on one side of the molecule and the remaining hydrophilic substituents on the opposite side of the molecule proved to be more effective for PDT. The literature showed that the asymmetry of the structure not only improves the penetration of the PS into the cells, but also increases the production of singlet oxygen ($^1O_2$) [5,69]. Moreover, cellular uptake of amphiphilic and asymmetric PS with higher affinity to membrane phospholipids or apoproteins is usually mediated by two carriers, albumin and high-density lipoprotein (HDL), which are overexpressed in tumours [41].

As the example of Rapozzi and colleagues shows, the addition of only one alkyl chain with 14 carbon atoms to the tetracationic (*N*-methylpyridinium-4-yl)porphyrin (**TM(C14)PyP4**, F**igure 11**) dramatically improved both the *in vitro* and *in vivo* properties [70]. For the *in vitro* analysis, the amelanotic melanoma cell line B78-H1 from mice was used, in which the porphyrin **TM(C14)PyP4** was found to be more effective when irradiated with a halogen lamp with a light dose of 7.2 J/cm^2 compared to the hydrophilic tetracationic analogue without alkyl chain, which showed a 25-fold higher cellular uptake and consequently higher cytotoxic events (IC_{50} (**TM(C14)PyP4**) = 10 nM, IC_{50} (**TMPyP4**) = 200 nM). These results

were also confirmed *in vivo* in 6-week-old C57/BL6 mice with inoculated B78-H1 tumours, where a 10-fold lower dose of the porphyrin **TM(C14)PyP4** (3 mg/Kg) compared to the hydrophilic analogue TMPyP4 (30 mg/Kg) was required for the same therapeutic effect [70].

The synthesis of the novel derivatives of the approved second generation with the 16-carbon atom alkyl chain was achieved by Rojkiewicz and colleagues when studying the derivatives of the approved second-generation PS, Foscan®[71]. They also concluded that an alkyl chain on the porphyrin ring (**TPh(OH)P-$CO_2C_{15}H_{31}$**, **Figure 11**) increases lipophilicity compared to the hydrophilic analogues, giving amphiphilic PS better properties for PDT. In the same study, it was shown that the ester and amide functionality used to attach the hydrophobic part to the porphyrin ring increased the hydrophilic character, resulting in better metabolic stability and faster elimination after PDT treatment, which in turn results in fewer side effects [71].

Based on these findings, our research group investigated the effects of substitution with the 17 C-atom alkyl chain. The result was a high cytotoxic effect on all tested tumour cell lines of both *N*-oxidised and *N*-methylated tripyridyniumporphyrin derivatives compared to their hydrophilic analogues without the alkyl chain on different tumour cell lines (MCF-7, HTC116, HepG2, HeLa and u87MG). It was also shown that among the derivatives with a long alkyl chain, all 3-pyridyl derivatives of both *N*-oxidised and *N*-methylated porphyrins are more effective than 4-pyridyl derivatives. However, the *N*-methylpyridiniumporphyrins (for both 3 and 4-pyridyl groups) substituted with an alkyl chain also showed slightly lower toxicity at a concentration of less than 10 μM (HeLa and u87MG) [72,73].

It was shown in the literature that balancing the lipophilic and hydrophilic parts of the porphyrins has a remarkable impact on their pharmacokinetic and pharmacodynamic characteristics, as well as their role in tumour cellular internalisation and the biodistribution [74,75]. Just recently, Malacarne *et al.* investigated the group of *N*-alkylated tetracationic (pyridinium-4-yl)porphyrins, pointing out the importance of the study of the lipophilic balance in the design of the porphyrin-based PS to achieve the highest efficacy of PDT. As reported, higher cellular uptake correlated with log*P* values, however, PDT efficacy did not correlate with the results of cellular uptake, indicating that the porphyrin with the longest alkyl chains conjugated to all four pyridyl units was not the most PDT efficient among the PSs tested on HCT116, SKOV3 and MCF-7 cell lines [74].

Continuing the work of our research group, the aim of this thesis is to investigate the hydrophilic-lipophilic balance of A_3B porphyrins by varying the length of a long alkyl chain on the acetamidophenyl substituent (B). The alkyl chain, introduced by a nucleophilic acid substitution reaction, is the hydrophobic part of the molecule, forming a fatty acid-porphyrin conjugates [72,73]. Fatty-acid conjugates have been widely investigated as anti-tumour agents, as the fatty acid moiety utilises the normal lipid metabolic processes and successfully

delivers drugs across lipid membranes via passive diffusion or through the fatty acid transport protein [76]. The increased metabolic activity and uncontrolled proliferation of the tumour cells requires the increased uptake of various metabolites, including free fatty acids[77]. Although it is not well defined as cancer cell glucose and amino acid mechanism (Warburg effect), the need for lipids in cancer cells is increased since the lipids serve as the building blocks that support the replication of the cells and the formation of new membranes or as substrates for various intracellular mechanisms, such as mitochondrial ATP synthesis or post-translational protein-lipid modification of the signalling proteins [78,79]. In addition, overexpression of the free fatty acid receptors and fatty acid synthase enzymes in cancers, associated with their invasive proliferation and aggressiveness, is helpful for the selective targeting and enhanced cellular uptake in tumours [76,80,81].

The porphyrin-fatty acid conjugates, with varied alkyl chain length, was investigated by Bonsall and colleagues, where the porphyrin with the shortest chain length (**C5SHU**, n = 4, **Figure 11**) and the lowest hydrophobic surface area was the most efficient PS, with the highest toxicity towards lung biphasic mesothelioma (MSTO-211H) and the minimal toxicity towards the normal Met-5a cell line [82]. Although porphyrins of higher hydrophobicity were expected to be more effective, due to the increased molecular recognition of the cell surface based on the lipophilicity of the molecule, the porphyrin was overall non-charged molecule of higher hydrophobicity and the derivative of the shortest alkyl chain provided the least evidence of aggregation in aqueous solution, which was a determining factor for effectiveness [82].

In contrast to hydrophobic parts, hydrophilic parts of the porphyrins include positively charged substituents, achieved by quaternisation of the nitrogen on the pyridyl groups in the *meso* position of the porphyrin ring, either by *N*-methylation or the *N*-oxidation. Along with the chelation with Zn^{2+} and Ga^{3+}, increasing the solubility of the porphyrin molecule will be discussed in the following sections.

2.2.1.2. Cationic porphyrins

Cationic porphyrins are of great interest because they increase the solubility of the molecule and positively charged PS are more likely to target mitochondria through electrostatic interactions than negatively charged or non-charged molecules [37,41]. It is also believed that positively charged PSs penetrate the cell more efficiently as they interact electrostatically with negatively charged membranes with higher affinity, leading to better efficiency in PDT [83].

In this work, the positive charge of the molecule is achieved by alkylation, more precisely *N*-methylation, of the nitrogen atoms on the *meso*-substituted pyridyl rings. A similar procedure

was utilised as with one of the most investigated cationic molecules, 5,10,15,20-tetrakis(*N*-methylpyridinium-4-yl)porphyrin (**TMPyP4**), which showed high photodynamic efficiency against different cell lines *in vitro* [84]. However, it localises preferentially in the cell nucleus[84], where it has shown strong interactions with DNA [85].

The importance of the charge position on the pyridinium ring was shown by Ezzedine *et al.*, on the example of *N*-methylpyridinium porphyrins where changing from *ortho* to *para* isomers resulted in different intracellular localisation, with the *para*-isomer being localised mostly in the nucleus, which is not favourable for PSs in PDT, while *meta* and *ortho* isomers were mostly found outside the nucleus, localised on the organelles in cytosol, especially in mitochondria [67]. Furthermore, Engelmann *et al.* showed that the stereochemistry of *para*-isomers of pyridiniumporphyrins favours π-π stacking due to the symmetry of the molecule, leading to a higher aggregation of these molecules and consequently to a lower production of $^1O_2$ [86].

In addition to the position of the charges, the number of charges attached to the *meso* position of the porphyrin core also plays an important role in the solubility of the molecule and its cellular internalisation. Among the *N*-methylpyridinium porphyrins with net charge 0 to 4^+, those with two or more charges are the most effective due to their increased hydrophilicity and affinity to target mitochondria [4,87]. In addition, the *cis*-isomer of dicationic porphyrin was found to be the most effective due to the highest cellular uptake and preferential mitochondrial targeting [87].

2.2.1.3. Metal insertion to porphyrins

Chelation of the pyrrolic nitrogen atoms in the porphyrin core was shown to be another method to modify the properties of porphyrins for PDT. Among the most investigated metalloporphyrins are those chelated with Zn(II), In(III), Mn(III), Fe(III), Cu(II) and Ag(II) [88]. Depending on the nature of chelated metal, they can alter the photophysical and photochemical properties of a chromophore [4,44,89]. As seen in the literature, chelation with diamagnetic metals such as Zn(II) and In(III) is expected to increase quantum yield of singlet oxygen production, as a result of higher quantum yield of intersystem crossing and a longer lifetime of the triplet excited state (τ_T) [3,63]. Therefore, there is a higher possibility for these porphyrins to interact with oxygen and biomolecules and produce higher cytotoxic effects. In contrast, chelation with paramagnetic metals such as Mn(III), Fe(III) or Cu(II) leads to an attenuation of $^1O_2$ production due to the lower quantum yield of ISC and the shorter lifetime of the triplet excited state, as the energy obtained from the absorption of light is dissipated as heat [89]. In practice, however, chelation of porphyrins with diamagnetic metals was shown to result in, unexpectedly, lower singlet oxygen production. Although

having worse photophysical properties required for efficient inactivation, paramagnetic metals can improve the solubility and stability of the porphyrin core, which is also beneficial for a PS [57]. Furthermore, Mn(III), Fe(III) and Cu(II) have been extensively studied as redox-active molecules and as mimics of the superoxide dismutase [4,88].

In this work, two different series of cationic metalloporphyrins chelated with Zn(II) and Ga(III), both diamagnetic metals, were investigated. In addition to their preferential photophysical properties mentioned above, the complete *d*-shell of Zn(II) favours the type II mechanism of ROS of Zn(II) porphyrins and thus a higher formation of $^1O_2$ compared to their metal-free analogues [63]. The chelation with Zn(II) in the work of Pavani *et al*., who studied a group of tetracationic porphyrins, results in stronger binding to biological membranes leading to an overall better photoefficiency [90]. Furthermore, Cuoto and co-workers showed that chelation with Zn(II) increases affinity for low density lipoprotein (LDL) receptors and interaction with human serum albumin (HSA), both of which are overexpressed in many tumour cell lines [91]. This led to a higher selectivity for the amelanotic melanoma cell line A375 compared to the metal-free analogue [91]. Another advantage is their positive charge, which has been shown to be a favoured feature for the *in vivo* efficiency of PS [92,93].

The similar situation is for Ga(III)porphyrins, where in addition to their beneficial photophysical properties, Ga(III) in complexes can mimic Fe(III) in cells, leading to the antineoplastic effect in cells. This strategy is often referred to as the "Trojan horse strategy", as Ga(III) complexes can serve as a competitive inhibitor of Fe(III) *in vitro* and *in vivo*. They are taken up by the cells through transferrin pathway and later are stored in ferritin, disrupting the Fe-dependent processes in the cells, leading to the cytotoxic events [94].

However, despite all the beneficial properties of both Zn(II) and Ga(III) porphyrins for use as PSs in PDT, they have been more investigated as antimicrobial agents rather than photosensitisers in PDT [95]. In addition, Ga(III) porphyrins, particularly [^{68}Ga]Ga(III) porphyrins, have been investigated as potential radiotracers for PET imaging, which will be discussed in more detail in the following sections.

2.2.1.4. *N*-oxide moiety in porphyrins

In addition to *N*-methylation, *N*-oxidation of the nitrogen atoms from the pyridyl substituents in the *meso*-position of the porphyrin was investigated as another strategy to increase the hydrophilicity of the molecule. The *N*-oxide functionality has recently become very attractive in medicinal chemistry and is used for a wide range of applications in the healthcare-related fields, e.g. magnetic resonance imaging, anticancer and antibacterial drug development [96]. Some of the favourable characteristics of *N*-oxides include the high polarity of the N^+-O^-

bond, which forms strong hydrogen bonds that can be both inert and reactive, depending on the rest of the molecules. Furthermore, the *N*-oxide group is often used to increase the solubility of the molecule and to decrease the membrane permeability [96,97]. Aromatic *N*-oxides, as in our case, are characterised by a shorter but more stable N^+-O^- bond with a high dipole moment. Due to the stable N^+-O^- bond, they are generally stable at room temperature and in a solution, they are generally stabilized by polar protic solvents such as alcohols [96,97].

In addition to its favourable properties for increasing the solubility of a drug, the *N*-oxide moiety on the pyridine substituents in the structure of porphyrins is inspired by the structure of tirapazamine (TPZ), a hypoxia-activated prodrug (HAP). Hypoxia is a condition of deficiency of oxygen (< 2%) in tissue and represents one of the major limitations of conventional cancer therapies (chemotherapy and radiotherapy). It also contributes to the tumour aggressiveness, as hypoxic tumours have more malignant phenotype, a higher number of gene mutations and a stronger expression of prometastatic genes compared to oxygenated solid tumours [98]. Hypoxia-activated prodrugs (HAPs) have emerged as potential anticancer agents that exploit hypoxia and are used to treat deep-seated solid tumours [99]. They are used as deactivated or "masked" cytotoxins that undergo bioreduction by cellular enzymes under hypoxia conditions and transform into toxic radicals or active drugs [99,100]. The aromatic *N*-oxide, tirapazamine (TPZ) was the first type of HAPs discovered, showing 300-fold greater toxicity *in vitro* under hypoxic than normoxic conditions and 3- to 5-fold higher cytotoxicity *in vivo*, depending on the tumour type. Although further investigation and final clinical approval of TZP was halted in phase III clinical trials due to limited accumulation at the tumour site [100,101], it proved to be a perfect proof-of-concept for the development of new antitumour agents selective for hypoxia. In addition to the aromatic *N*-oxides studied in this work, the class of hypoxia-activated prodrugs also includes aliphatic *N*-oxides, quinones, nitroaromatics and transition metal complexes.

The cellular mechanism of enzymatically activated one-electron or two-electron bioreduction of HAPs is explained in **Figure 12**. In one-electron reduction, which is an oxygen-sensitive reaction, a cytotoxic metabolite, a nitroxide radical, is generated under hypoxic conditions. The process can be inhibited by oxygen, producing superoxide ($O_2^{\bullet-}$), which is readily detoxified by superoxide dismutase and converts the intermediate back to the starting prodrug. The two-electron reduction bypasses the formation of the oxygen-sensitive radical and reduces the prodrug into the corresponding amine. This releases the cytotoxic radicals that can disrupt the surrounding biomolecules, including DNA [102–104]. The enzymes involved in two-electron reduction belong to a family of oxidoreductases, with cytochrome P450 oxidoreductase (CYP) having been shown to be primarily responsible for one-electron reduction, while several oxidoreductases, such as DT-diaphorase (NQO1) and aldo-keto

reductase 1C3 (AKR1C3), which are usually overexpressed in tumours, are involved in the two-electron reduction of aromatic *N*-oxides [103,105].

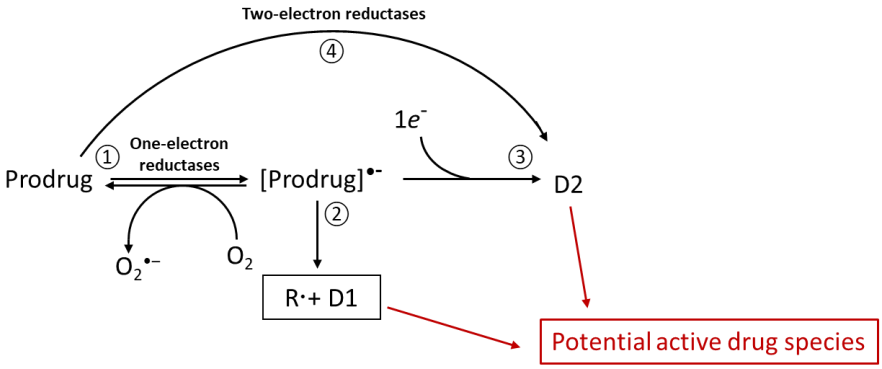

Figure 12. Mechanism of *N*-oxide based bioactive prodrug reduction under hypoxia conditions [104].

In PDT, poorly oxygenated tissue resulting from TME and/or PDT action in the tissue is an obstacle for oxygen-dependent Type II photophysical process. In this way, the use of a hypoxia-responsive moiety in the structure of the porphyrins provides the opportunity to exploit the unfavourable hypoxic environment and overcome the Achilles heel of PDT, known as the "turn corruption into wonder" approach [40]. Some of the recent works based on the formulation of nanoparticles with a bioreductive prodrug and a PS have shown that the combination of PS and HAP in nanoparticles is a promising strategy that not only reduces the side effects of chemotherapy but also enhances the biocompatibility of PS [106,107]. Dai *et al.* prepared a liposome using a chlorine e6 (Ce6) as PS and adding indocyanine green (ICG) and TPZ as photothermal agent and HAP molecule, respectively [108]. Illumination in the near infrared range (NIR) achieves a photothermal and photodynamic effect due to the presence of ICG and Ce6. The formation of hypoxia during PDT reduces TPZ to a radical and further enhances the cytotoxic effect. The efficacy of this combination was confirmed *in vitro* and *in vivo* on the lung tumour cell line (A549), where successful complete eradication of the tumour without recurrence was observed within the 15 days after the treatment [108]. Another work was performed by Zhu *et al.* who encapsulated the hyaluronic acid-chlorin e6 (HA-Ce6) and TZP molecule into self-assembling amphiphilic hypoxia-dissociable nanoparticles based on amphiphilic polyethylenimine−alkyl nitroimidazole [PEI−ANI, (PA)] [109]. The effective synergistic potential of the nanoparticles was observed upon irradiation with red light (660 nm) *in vivo* on 4TI xenograft tumours, increasing the survival rate of mice twofold. In addition, biocompatibility studies showed no weight loss in mice, diminishing the systemic toxicity of the nanoparticles tested [109].

Although nanoparticles are highly investigated with numerous papers that show their potential for use as drug delivery systems in anticancer therapy, the number of published

research papers is disproportionate to the number of clinical studies with nanoparticles. The reason for this lies in their likely hazardous effects *in vivo*. It was shown that the efficiency of nanomaterials decreases with increasing body size, leading to the accumulation of nanoparticles in unwanted organs such as the liver and causing undesirable health problems [110]. A golden standard in medicinal chemistry is therefore still to obtain all the preferred properties in a single molecule. The first porphyrins with *N*-oxide functionality were prepared by Posakony and colleagues and by Andrews and colleagues, who were motivated by the idea of modifying porphyrin molecules according to the TPZ molecule [111,112]. Posakony and colleagues were the first to successfully synthesise and optimise purification methods for several groups of porphyrins containing *N*-oxides in their structure, such as (oxidopyridyl)porphyrins and TPZ-porphyrin conjugates, for use under hypoxic conditions [111]. Following these syntheses approaches, our work will include the preparation of a group of amphiphilic porphyrins with an *N*-oxide moiety and an *in vitro* study to evaluate their potential use under hypoxic conditions.

2.3. Light in PDT

In addition to the design of PS, the light is also an important parameter in PDT, and optimising the light characteristics has proven to be a decisive parameter for the outcome of the therapy. For optimal light delivery, various parameters such as irradiation wavelength, light fluence and total light dose are required to be optimised[113]. The red and infrared regions of the EM spectrum are considered the most suitable for the activation of porphyrin-type PS. Red and infrared light have been shown to penetrate the deepest into the tissue, while blue light was the least efficient. Moreover, the shorter wavelengths (< 580 nm) are not efficient due to the absorption of oxy/deoxyhemoglobin and, in the case of melanoma tumours, the pigment melanin in the tissue. Longer wavelengths (> 850 nm) are not efficient due to the absorption of water and the inefficiency of longer wavelengths to trigger a photodynamic reaction. Therefore, the optimal irradiation range between 600 and 850 nm is considered, which is often referred to as the "phototherapeutic window" [2,37,113]. However, the choice of light irradiation depends on several factors, such as the choice of PS for treatment and its optical properties (absorption), the tumour to be treated and its size, location, accessibility and tissue characteristics. The last, but no less important point in the optimisation is the usability of the light source and its cost, size and handling [114].

In addition to the wavelength of the irradiation, the light fluence and the total dose of light must also be optimised when applied to the tumours. The light fluence is described as the power of the irradiation energy per second to the selected treated area (W/m^2), while the total light dose is considered as the total energy of the exposed light to the treated area [45,115]. The total light dose is calculated by multiplying the fluence rate by the irradiation time in

seconds and expressed as energy per unit area of irradiated light (J/m^2). In clinics, a high fluence is often used to achieve the desired photodynamic effect. However, this may not be the right choice because at high fluence rates oxygen depletion occurs faster, resulting in less production of ROS and thus reducing cytotoxic events [37,45,114,115].

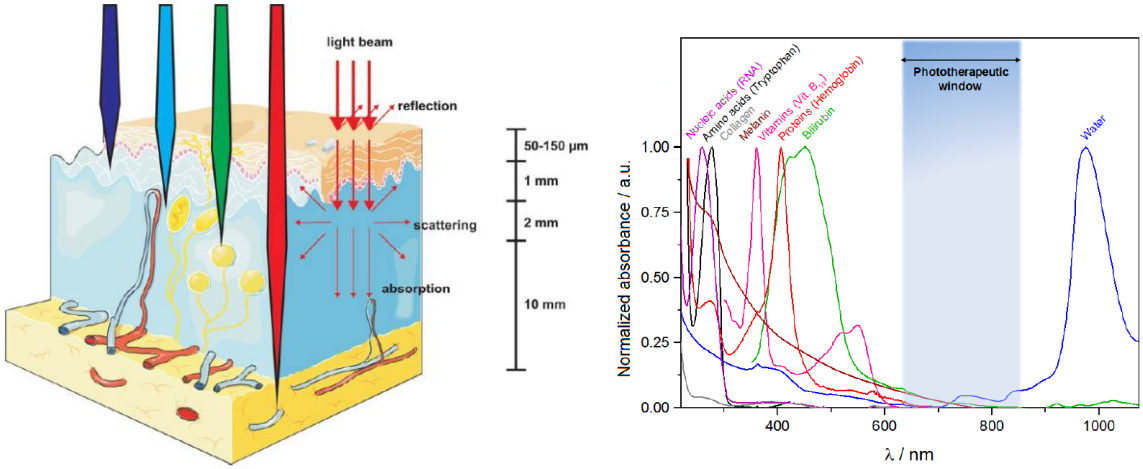

Figure 13. Light irradiation wavelength properties: penetration depth based on the irradiation wavelength (left) and "phototherapeutic window" from 630 to 850 nm (right). Figures adapted from [2,63].

Irradiation devices such as lamps, lasers and light-emitting diodes (LEDs) are often used to emit light. Lamps were the first irradiation devices used in PDT. Although they are relatively simple and easy to use, they have numerous disadvantages for their use. They have a broad irradiation spectrum and therefore have a lower forward scattering of light, making them unsuitable for treating deeper lesions. In order to achieve a narrower spectrum of irradiation and to remove unnecessary ultraviolet and infrared wavelengths when using lamps, additional optical filters are also used [114,116]. In contrast to lamps, lasers offer high optical power and narrow wavelength irradiation that can be controlled and adjusted to the characteristics of the PS. Furthermore, lasers are radiation sources that can be adapted to different source fibres. However, the main disadvantage of using lasers for PDT is their cost and poor handling, as they are often large and require high maintenance. Nowadays, the focus is on the development and perfection of LEDs, which are semiconductor devices in which the electron-hole combination is responsible for generating light. They are small, adaptable, relatively inexpensive and easy to handle. LEDs can generate the light of the desired wavelength, whereby the width of the spectrum is slightly greater (5%) compared to lasers. The only disadvantage of using LEDs is their sometimes relatively low power for clinical use and the thermal effects resulting from the low electrical to optical conversion rate [114,116].

2.4. Tumour microenvironment

As mentioned at the beginning, solid tumours are not just a growing cluster of malignant cells. In addition to the malignant cells present, the tumour is considered a “rouge organ” composed of extracellular matrix (ECM), immune cells such as dendritic cells, T or B cells, endothelial cells, myofibroblasts, activated fibroblasts, pericytes, and an impaired blood and lymphatic vascular network [117,118]. The components such as adipocytes, proteoglycans, hyaluronan and fibrous proteins are also found in the tumour stroma. The interaction and communication between malignant and non-transformed cells is a complex mechanism involving cytokines, chemokines, growth factors and inflammatory signals [119,120]. The different cells and their interaction in the formation and growth of the tumour are referred as the tumour microenvironment (TME) [119]. Abnormal growth and increased proliferation of tumours lead to tumour stiffening, which is associated with mechanical forces that induce abnormal solid and fluid stresses on the tumour that promote tumour progression and increase resistance to numerous treatments [121,122]. Solid stress are mechanical forces exerted by the non-liquid components in tumours that affect tumour pathophysiology by compressing the cancer and stromal cells and deforming the blood and lymphatic vessels [122–124]. In contrast, the fluid pressure induced by the fluid components of the TME is divided into two groups: microvascular and interstitial fluid stress (MV and IFP, respectively) [119,122,125]. It is determined by the structure of the tumour vessels and compression of the blood and lymph vessels. Vascular hyperpermeability, which is a consequence of angiogenesis, leads to increased fluid flow into the interstitial space (i.e. fluid leakage), resulting in tumour perfusion and consequently increased IFP [122].

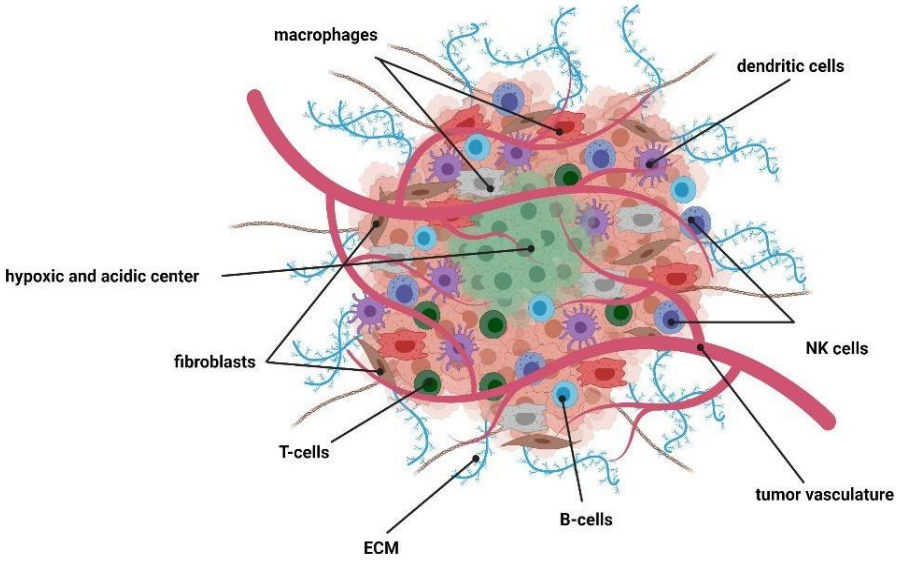

Figure 14. Cells that form tumour microenvironment and the hypoxic and acidic center of the TME [117].

The increased density and stiffness of the ECM play the decisive role in tumour progression. The increased solid stress within the deep-seated tumours leads to a pressure effect on the blood and lymphatic vessels, which in turn leads to a reduced supply of nutrients and oxygen in the tumour. This leads to hypoxia and an acidic environment as a further characteristic of TME [119,121].

As described above, hypoxia is a condition of low oxygen levels. In tumours, hypoxia contributes to angiogenesis, chemoresistance and metastasis of tumours. Hypoxic conditions primarily lead to upregulation of hypoxia-inducible factor (HIF), a protein family of transcription factors known to regulate and facilitate cell adaptation to deprived conditions [101,117,126] through the upregulation of more than 100 genes. Furthermore, hypoxia creates an immunosuppressive environment and facilitates the escape of cancer cells from the primary tumour by increasing IFP [119].

In PDT, hypoxia is considered the "Achilles's heel" and numerous approaches have been developed to either overcome or utilise hypoxia to achieve a positive outcome in PDT. In this work, as previously mentioned, the HAP moiety is used in a combination with porphyrin as PS to overcome hypoxia, while some other mechanisms include: modification of TME, suppression of hypoxia-related proteins, oxygen-independent PDT or release of hypoxia-triggered cargos [101,106,107,127].

2.4.1. Melanoma

This doctoral thesis focuses on the efficacy of porphyrin-PSs in PDT against melanoma cell lines. Melanoma is one of the most serious skin cancers with the highest potential for metastatic development. Among all cancers, it is the third most commonly diagnosed cancer in the United States and the sixth most commonly diagnosed cancer in Europe [128]. According to GLOBOCAN 2020 data, more than 325,000 new cases with more than 57000 deaths were estimated for 2020 [128,129]. The most serious issue is that, according to the statistics, the rates of melanoma are raising rapidly, especially among younger population. Over the last ten years (2014 to 2024), the number of new cases has increased by 32% and is expected to increase even by 51% by 2040, with an estimated increase in new cases for more than 510,000 per year and a 68% increase in deaths, with 96,000 deaths of patients diagnosed with melanoma expected in 2040 [130]. The main cause of the rise in cases is increasing exposure to UV radiation, either from sunlight or artificial sources, with 86% of total cases shown to be due to exposure to the sun. People who have had more than five sunburns are twice as likely to develop melanoma cancer. Intense exposure and accumulation of the UV-damage in melanocytes triggers to the different mutations in their DNA and development of

tumour. The most abundant oncogenic mutations implicated in melanoma are BRAF and NRAS mutation, with mutations of BRAF gene responsible for more than 50% skin melanomas [8,117].

2.4.1.1. Characteristics of melanoma tumours

Melanomas are tumours composed of melanocytes, the dendritic type of cells located in the basal layer of the epidermis where, together with keratinocytes and fibroblasts, form the melanoma unit. Melanocytes differ from keratinocytes as they have specific lysosome-related organelles called melanosomes, which are responsible for the synthesis and storage of the pigment melanin [131,132]. These cell types communicate with each other via secreted factors such as growth factors, hormones, inflammatory mediators and cell-cell contacts (E-cadherin and integrins) [133]. Furthermore, melanocyte proliferation and pigmentation are directly regulated by secretory factors released by fibroblasts, such as Dickkopf-related protein 1 (DKK1) and neureoregulin 1 (NRG 1), which regulate melanocyte growth and proliferation. Moreover, the regulation of melanocyte proliferation and thus protein expression in melanocytes is carried out by the microphthalmia-associated transcription factor (MITF) [133,134].

The process of melanogenesis, known as maturation of the melanosome, is derived into the three main steps: the biogenesis of the melanosome, the synthesis of the pigment melanin and homeostasis-associated endogenous melanogenic cytotoxicity (EMC) [8]. The biogenesis of melanosomes occurs in 4 stages, where the first two stages are considered "premelanosomes", while stages III and IV are known as "late melanosomes". Premelanosomes in stages I and II are spherical vacuoles with proteins derived from the ER, lysosomes and endosomes, without structural components capable of trapping and exporting drugs such as cisplatin [8,133]. Stage II differs from stage I in the formation of the visible fibrillar matrix by the glycoproteins Pmel17 and MART-1 and the presence of the tyrosinase enzyme required for melanin synthesis. In stage III, active melanin synthesis begins and the melanins formed are deposited on the inner fibrillar network [133]. The nascent melanin formed has the highest capacity to trap cytotoxic drugs. Therefore, stage III melanosomes are the most resistant to many antitumor drugs [8]. Stage IV is characterised by the filling of melanosomes with melanin and the activation of autophagy to eliminate the by-products of endogenous melanin synthesis. After stage IV, the fully formed melanosomes are forming melanin granules that are transferred by the melanocyte dendrites to the keratinocytes in the surrounding area [8,131].

As already mentioned, the synthesis of the pigment melanin takes place in stages III and IV of melanosome biogenesis. This is a highly cytotoxic process, also for the melanocytes.

Therefore, an overexpression of BCL-2, the proapoptotic protein, as well as of tyrosinase and tyrosinase related protein 1 (TRP1), the main proteins required for melanin synthesis, were found in melanoma [133,134]. The melanosomes produce two types of the pigment melanin, pheomelanin, which is known as the yellow to red pigment, and eumelanin, the brown to black pigment [131,133].

The simplified biosynthesis of melanin is described further. It starts with the amino acid L-tyrosine and the key enzyme is tyrosinase [133]. Tyrosinase can undergo two different pathways, the first of which is hydroxylation to 3,4-dihydroxyphenylalanine (L-DOPA) and the second is the oxidation of *o*-diphenol to dopaquinone. Thiol-containing compounds such as cysteine or glutathione (GSH) are responsible for the synthesis of pheomelanin, as they conjugate with dopaquinone and initiate the oxidation process that leads to the formation of pheomelanin. In the absence of thiol-containing compounds, dopaquinone cyclizes to cyclodopa and undergoes redox disproportionation to dopachrome. Further steps include the spontaneous decarboxylation of dopachrome to 5,6-dihydroxylindole (DHI) and 5,6-dihydroxyindole-2-carboxylic acid (DHICA) [131]. The final step in the formation of eumelanin involves the oxidation of DHI and DHICA either by tyrosinase or TRP1 or by oxygen or ROS generated in the previous steps or present in the environment [134]. Pheomelanin and eumelanin differ not only in pigmentation but also in their role in the melanosome. Eumelanin has an antioxidant, photoprotective function, while pheomelanin has a phototoxic, prooxidant effect and can serve as a PS that generates large amounts of ROS and leads to undesirable events [131,133,134]. Melanin and its synthesis generate ROS via multiple mechanisms, therefore melanocytes in which melanin synthesis is active are able to maintain high levels of ROS, which are much higher compared to other tumour cell types.

The cellular ROS produced can result in a variety of cellular responses that may contribute to melanoma progression and aggressiveness [135].

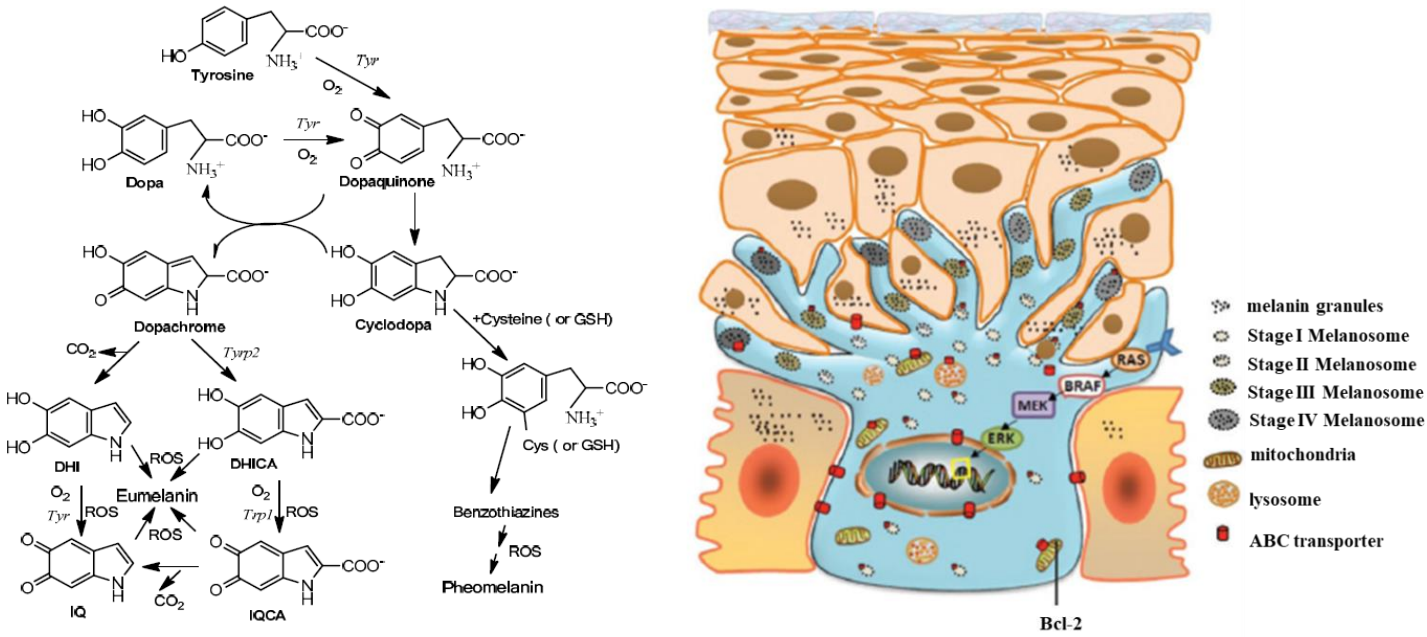

Figure 15. The melanin synthesis pathway (left) [131] and the four-stage process of melanogenesis (right) and maturation of melanosomes [8].

As we have seen, intrinsic mechanisms such as melanogenesis and melanin synthesis unfortunately cause melanoma to respond poorly to conventional anti-tumour therapies such as chemotherapy and radiotherapy. There is therefore an urgent need to find new alternative treatment methods, including PDT [8].

2.4.1.2.Resistance of melanoma to conventional therapies and PDT

Multidrug resistance (MDR) to anti-tumour agents in melanoma depends primarily on the chemotherapeutic agent used and the tumour entity and can occur via two pathways: disruption of the drug-target interaction by the modulation of the target site and/or drug-target mechanism or by dysregulation of the cellular death pathway (e.g. apoptosis) in the prevention of the cellular death [8]. First and foremost is the MDR of melanogenesis, which has been observed in each stage, from premelanosomes, that have a high capacity to trap drugs, to later stages where newly synthesised melanin is capable of trapping cytotoxic drugs. ATP-binding cassette (ABC) transporters are found in the cells, mainly on the cell membranes or on some organelles, and have the task of expelling cytotoxic drugs from the

cells. In melanoma, the most frequently found ABC transporter is ABCB5, which is therefore most responsible for the MDR of melanoma [136].

Another mechanism detected is the hyperactivation of the DNA repair mechanism, which can occur either by upregulation of repair genes or by overexpression of enzymes responsible for the removal of DNA alkylation damage. Moreover, dysregulation of cellular apoptotic death has also been observed, and found that this may be due to inhibition or deletion of apoptosis protease-activation factor 1 (APAF-1), one of the effectors of p53-dependent apoptosis pathways, or overexpression of anti-apoptotic proteins of the BCL-2 family [8].

In PDT, although melanomas appear to be easy to target as they are accessible to irradiation and PS can be administered topically, resistance mechanisms to chemotherapeutic agents have also proven to be a problem for PDT [7,137]. These include the presence of the ATP-binding cassette, which reduces the concentration of PS entering cells by expelling them into the extracellular space, and melanosomes, which can act as drug scavengers or sequestrants [137]. In addition, the pigment melanin and its optical and antioxidant properties have been shown to be a major obstacle to the PDT treatment [6]. Melanin absorbs in the visible part of the EM spectrum (λ_{max} = 500-600 nm), so it overlaps with the absorption spectrum of most PSs and therefore acts as an optical shield. Melanin is also an intracellular antioxidant that scavenges free radicals in its environment [6,134,138]. Therefore, it competes with PS for the photons and reduces PS activation. It has also been shown to prevent deep light penetration and scatter the therapeutic light, resulting in insufficient irradiation of some deep-seated melanomas and poor treatment [139]. The scavenging properties of melanoma in the presence of oxidising and reducing radicals were investigated by Rozanowska and colleagues using pulse radiolysis [140]. It was shown that the synthetic melanins, DOPA-melanin, obtained by auto-oxidation of L-DOPA, and cysteinyldopa-melanin, obtained by tyrosinase-catalysed oxidation in the presence of cysteine, can interact with oxidising radicals. The reaction with both melanin pigments occurs via a simple one-electron transfer process in the presence of oxidising and reducing radicals. It was found that the pheomelanin precursor is more efficient at oxidising the reducing radicals opposite to the eumelanin precursor, which interacts more efficiently with oxidising radicals [140].

2.4.1.3. Porphyrins in treatment of melanoma

Despite the mechanisms of resistance of melanoma tumours to PDT, there are more than 50 PSs, mostly from the tetrapyrrolic group, that have been studied *in vitro* and show high potential for the use of PDT on melanoma. These studies have highlighted the properties

required for a PS in PDT against melanomas, especially high absorption in the red part of the spectrum and selective accumulation in tumour tissue [137].

The clinical trials were conducted with chlorin e6 (Ce6), hematoporphyrin derivative (HpD) and Malvix® and showed complete regression of the tumour after one or multiple PDT treatments. However, tumour recurrence was seen in a significant number of patients, suggesting that further development of a PSs for use in melanoma is needed [117,137].

There are only a few studies in the literature in which synthetic porphyrins have been tested *in vitro* for melanoma. One of those include the study described by Baldea *et al.* on the PDT activity of tetraphenylporphyrin derivatives, 5,10,15,20-tetrakis(4-hydroxyphenyl)porphyrin (**THOPP, Figure 16**) and 5-(4-hydroxyphenyl)-10,15,20-methoxyphenyl)porphyrin (**THOMPP, Figure 16**) [141,142]. The study proved both **THOPP** and **THOMPP** to be very effective PSs, much higher compared to 5-ALA, with a reduced antioxidant effect of the melanin pigment and with an effective ROS-induced DNA destruction [141,142].

Furthermore, the studies involving *in vitro* analysis on melanomas and other tumour cell lines, conducted by Kramer-Marek *et al.*, describe the influence of an alkyl chain with 16 C-atoms on the PDT activity of two A_3B porphyrins with pyridyl or tolyl substituents (**TPP-C16** and **TPyP-C16, Figure 16**) [143]. The results showed a high efficacy of both derivatives, although somewhat lower in melanoma cell lines (Me45 and B16-F10) compared to the colon adenocarcinoma cell line (Hct116), which is due to the presence of the antioxidant pigment melanin. The paper further states that a derivative with pyridyl groups (**TPyP-C16**) at the *meso*-positions has a longer-lived triplet state, as groups with electron non-bonded orbitals favour the conversion from the excited singlet to triplet state, thereby increasing ISC [143].

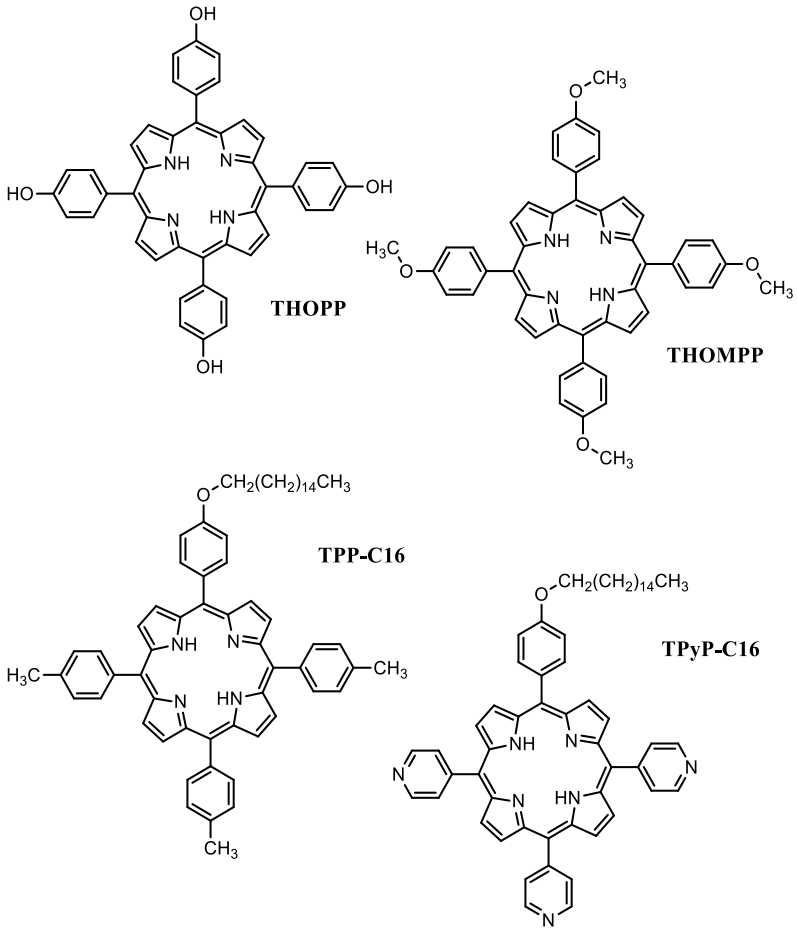

Figure 16. Structures of several porphyrins tested in the treatment of melanoma.

Although there is a high potential of the use of porphyrins in PDT against melanoma, there is still a need to design a PS closer to an "ideal PS" that will have characteristics required to combat the obstacles from the melanoma TME.

2.5. Porphyrins as theranostic agents

In addition to their therapeutic purposes, as PSs in PDT, porphyrins have also been developed as potential imaging agents due to their photophysicochemical properties, their low cytotoxicity in the absence of light, and their preferential tumour uptake [144,145] Theranostics is the term used when the diagnostic and therapeutic modalities are contained in a single molecule. In personalised medicine, there is increasing interest in the development of theranostic agents as they can significantly improve treatment [89,146]. Tumour detection, more precisely tumour imaging, plays an important role in the optimisation of the therapy as it can be used in all stages of cancer management, from diagnosis and screening prior to

treatment, to dose optimisation and response monitoring during therapy, to monitoring of possible recurrence and post-treatment recovery [146–148].

The porphyrins could serve as diagnostic agents as they have intrinsic fluorescence and easily chelate various metal ions. Intrinsic luminescence properties serve them to be used in fluorescence imaging, which allows monitoring of the treatment outcome [149]. Furthermore, porphyrins have a central cavity to chelate different metals, or radionuclides, therefore potentially serve as imaging agents for techniques such as magnetic-resonance imaging (MRI), x-ray radiography, photoacoustic imaging (PAI), single-photon emission computed tomography (SPECT) and positron emission tomography (PET) that is investigated in this work; thus it will be further described in following chapter [144,149].

2.5.1. PET imaging

At the beginning of the 20th century, the first theoretical observations of the positron were postulated by Paul Dirac and experimentally demonstrated by Carl Anderson. Later, in 1933. and 1936. respectively, both scientists were honoured with the Nobel Prize in Physics for their discovery of the positron (e^+). In theory, the positron is considered as an "anti-electron", which has the same mass and opposite charge to the electron (e^-) and when in contact with electron, they annihilate each other [150].

Today, the positron is commonly used in PET scanning, a functional nuclear imaging technique based on the use of biologically active molecules labelled with positron-emitting radionuclides (radiotracers) to monitor metabolic changes in the human body in real time [151,152]. Furthermore, radiotracers are administered intravenously and PET imaging can be used to study their distribution within the different tissues depending on the characteristics of the carrier. Radiotracers undergo a beta-plus decay (β^+), which produces a positron (e^+) that, after losing its kinetic energy, reacts with an electron (e^-) in a rapid annihilation reaction, producing two gamma rays (γ) (511 keV) of opposite direction that are detected by scintillation crystals in the PET scanner [151,153]. PET scanning is used in combination with CT scanning (PET/CT) to obtain both functional and morphological images in a single scan [152].

The choice of radionuclide for PET imaging depends on its nuclear properties, such as the type of radiation, decay half-life and energy. Furthermore, the conditions of the radiolabelling protocol, radionuclide production and specific activity and co-emission of other gamma rays play an important role in the radiolabelling. In PET imaging, the current clinical gold standard is ^{18}F-labeled fluorodeoxyglucose (^{18}F-FDG), which localises preferentially in the tumour due to increased glucose uptake by tumours, known as Warburg effect [148]. Although ^{18}F being the most popular radionuclide for the development of new PET imaging

agents, the first examples of chelating porphyrins and preparation of radiolabelled metalloporphyrins were performed with another popular radionuclide, ^{64}Cu. The great popularity of ^{64}Cu lies in its relatively long half-life of 12.7 hours, the high positron abundance of 61% and the simple production in cyclotron by photon bombardment of stable ^{64}Ni [149,153].

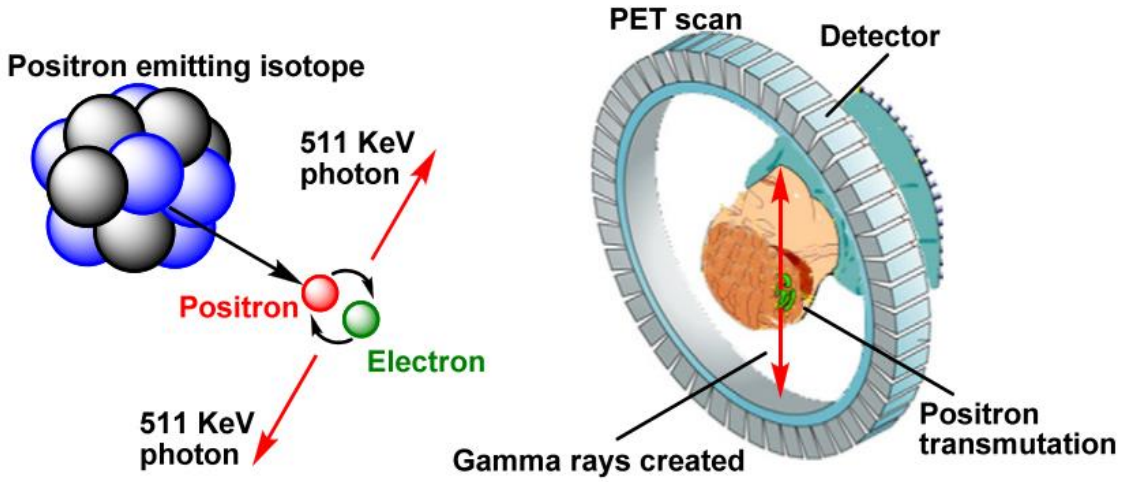

Figure 17. The basic principle of positron emission tomography (PET) scanning. Figure adapted from [154].

Interest in [^{68}Ga]gallium, the radionuclide used in this work, has increased greatly in the last 15 years, most likely due to the development of the ^{68}Ge/^{68}Ga generator, which allows facile "on-site" elution of the radionuclide from a resin containing the parent ^{68}Ge nuclide [146,155]. The decay characteristics of ^{68}Ga include its high positron abundance (89%) with negligible photon emission and a half-life of 68 minutes, which is compatible with the pharmacokinetic profile and biological half-life of small molecules with rapid biodistribution [149].

Compared to other radionuclides, ^{68}Ga is an attractive option for the radiolabelling of porphyrins, as the ionic radius of the radionuclide (62 pm) allows for easy chelation of porphyrin and the formation of highly stable metalloporphyrin [148,149]. Moreover, the diamagnetic nature of ^{68}Ga keeps the preferential phototherapeutic properties of a metal-free porphyrin, allowing the porphyrins to be used as theranostic PET/PDT agents, unlike ^{64}Cu, a paramagnetic isotope, that quenches the therapeutic effect of the porphyrin [149,156].

The first example of ^{68}Ga radiolabelling was performed by Azad and colleagues on a protoporphyrin IX-arginylglycylaspartic acid (**PPIX-RDG**) derivative, in which the tripeptide served as a targeting moiety for $\alpha_v\beta_3$ integrins, which are overexpressed in numerous cancers [157]. They showed that the best radiolabelling conditions were achieved with an acetic acid/H_2O solution with a pH adjusted to 4.5 microwaved at 120 °C for 45

minutes. The radiochemical yield (RCY) obtained was 33±3% with a purity of the radiotracer of > 97% [157]. Fazaeli et al. successfully radiolabelled two groups of porphyrins, one with pentafluorophenyl substituents at all four *meso*-positions (**^{68}Ga-TFPP**) and one with 2,4,6-trimetoxyphenyl substituents also on all four *meso*-units (**^{68}Ga-TTMPP**) [158,159]. Successful radiolabelling of ^{68}Ga-TFPP was achieved in 60 minutes at 100 °C, resulting in a radiochemical yield of > 97% and a specific activity of 13-14 GBq/mmol [159]. In the case of **^{68}Ga-TTMPP,** successful radiolabelling with a radiochemical yield of >96% was achieved within 15 minutes at 100 °C in 0.1 M sodium acetate buffer with pH = 2.3 [158]. It should be emphasised that both **^{68}Ga-TFPP** and **^{68}Ga-TTMPP** were analysed *in vivo* in a mouse with fibrosarcoma tumours, where porphyrin **^{68}Ga-TTMPP** showed preferential tumour uptake within 1 hour of incubation (> 50 tumour/muscle ratio and > 7 tumour/blood ratio), while porphyrin **^{68}Ga-TFPP** showed some accumulation in the body, but much of the radiotracer was excreted within 1 hour [158,159].

The first example of labelling of cationic porphyrins was performed by Bhadwal *et al*. on the symmetrical (*N*-methyltetrapyrdinium-1-yl)porphyrin (**^{68}Ga-TMPyP4**) [160]. Successful radiolabelling was achieved by incubating the radionuclide and porphyrin in sodium acetate buffer (pH = 4) in boiling water for 45 minutes. The radiochemical purity after purification of the radiotracer was >99%. The *in vivo* studies showed that the majority of the radiotracer was either excreted (>30%) or in the kidneys (>16%) within 30 minutes of incubation. The results are consistent with the observed partition coefficient of log*P* = –4.3, indicating that the high solubility of the radionuclide results in a relatively easy excretion from the body [160].

Following the work of Bhadwal *et al.*, Guleria *et al.* investigated the changes in the biodistribution properties of the ^{68}Ga radiotracer observed by changing a pyridinium substituent to a carboethoxymethyleneoxyphenyl substituent (**TMPyP4-COOHP**) [161]. The radiolabelling of both **TMPyP4** and **TMPyP4-COOHP** was performed in a 2 M sodium acetate solution of pH 5.5 boiling in water for 30 minutes. Changes in the lipophilicity of the molecule (log*P*(TMPyP4-COOHP) = –1.55) did not show an improved tumour uptake or reduced excretion of the radionuclide. In addition, the PDT activity against the A549 cell line was investigated. Surprisingly, a higher cytotoxicity of the more hydrophilic TMPyP4 derivative was found (cell proliferation: TMPyP4 = 43.98 ± 0.42%; TMPyP4-COOHP = 61.30 ± 4.59% at a light dose of 0.4 kJ/cm^2) [161]. Another example of the development of PET/PDT theranostics was done by Bryden *et al.* [156]. Here, the tricationic porphyrin was conjugated to the docapeptide TWYKIAFQRNRK, which is known to target the $\alpha 6\beta 1$ integrin, involved in cellular migration and adhesion in normal tissue and is overexpressed in tumours. The radiolabelling was performed on a precursor and was successful in a microwave reaction for 7 minutes at 110 °C (100 W, MW), resulting in a radiochemical yield of > 95%. The phototoxicity of the non-radioactive analogue was investigated in the HeLa

cell lines and the U87 cell line with minimal integrin expression. This showed a decrease in cell proliferation of > 80 % in the HeLa cell line, demonstrating the high potential of porphyrins both as PS for PDT and PET imaging [156].

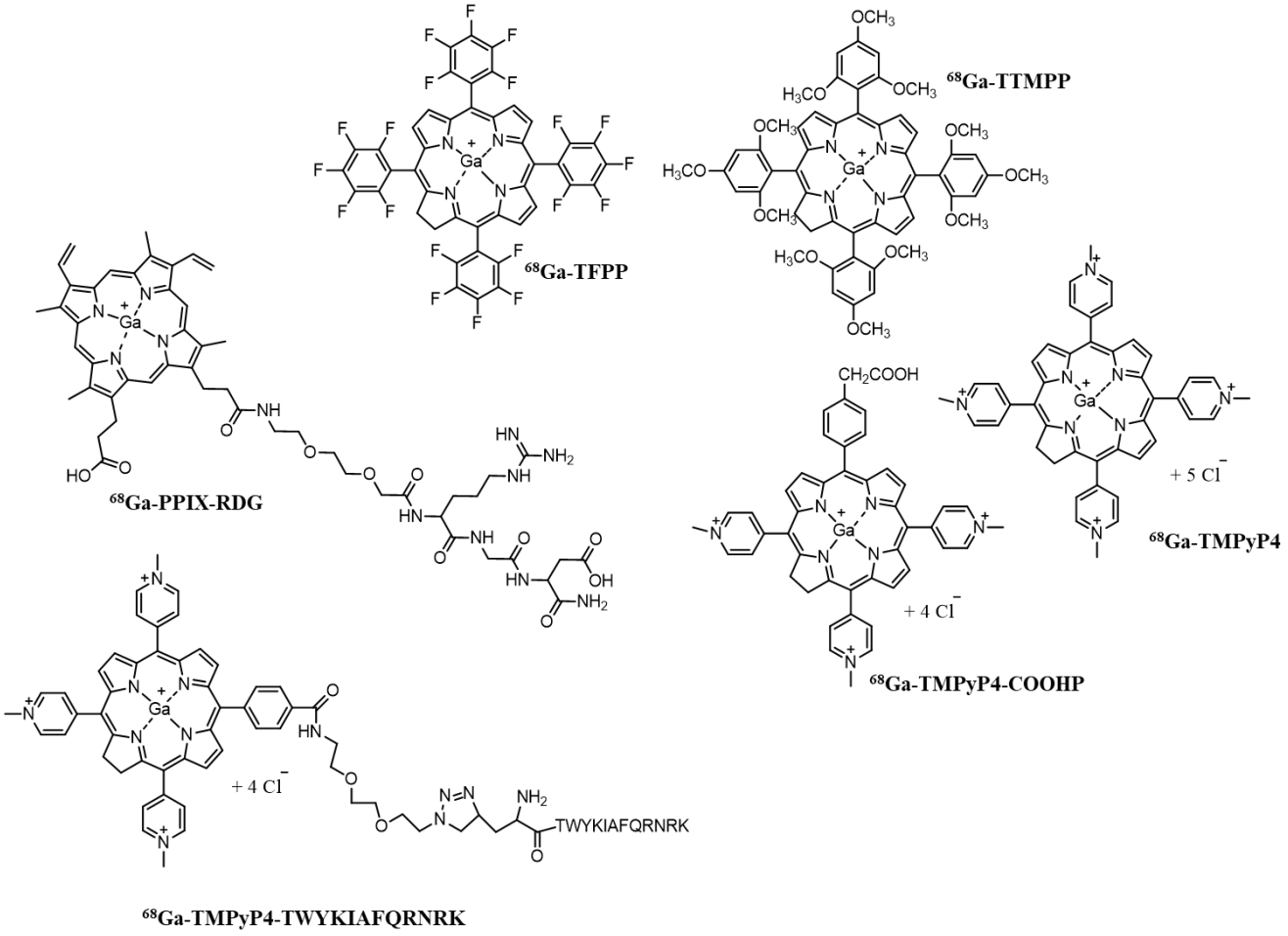

Figure 18. The structures of porphyrin ligands (with the abbreviations used in the text) from the literature complexed with ^{68}Ga(III) for use in PET imaging.

There are numerous papers in the literature demonstrating the success of radiolabelling porphyrins with the radionuclide ^{68}Ga and using them as potential radiotracers in PET imaging [89,148,149]. However, the lack of literature on the development of PET/PDT theranostics provides an opportunity to develop new agents. Moreover, the current literature describes work on 1 to 2 agents that minimally describe their tumour targeting properties, and the role of hydrophilic-lipophilic balance in the study of biodistribution or tumour targeting properties has not yet been investigated.

3. Materials and methods

3.1. General

All reagents were purchased from Sigma Aldrich or Alfa Aesar and used without further purification, except for pyrrole, which was redistilled before every use. Solvents were purchased from BDP Prolabo and GramMol. To obtain dry solvents {dichloromethane (DCM) and pyridine}, solvents were kept on an activated molecular sieve 4 Å (Sigma Aldrich) in N_2 atmosphere for at least 24 hours before use. For activation of molecular sieves, sieves were heated in an oven for gravimetry at 500 °C for 5 hours and, after heating, they were cooled down in a desiccator. After addition of the sieves to the solvent, solvents were purged with 5.0 N_2 (purity ≥ 99.99%) for 15-20 minutes and kept in N_2 atmosphere until use.

Silica gel and thin-layer chromatography (TLC) plates were purchased from Macherey-Nagel. For the TLC, silica (0.2 mm) plates on aluminium foil with the UV_{254} fluorescence indicator were used, and for the column chromatography silica gel 40-63 μm (230-400 mesh). Porphyrins, tetraphenylporphyrin (**TPP**) and zinc(II) tetraphenylporphyrin (**ZnTPP**) were purchased from Porphychem and used as standards in calculations of fluorescence quantum yield (Φ_{FL}) and in the experiments of laser flash photolysis (LFP).

NMR spectra were recorded on a Bruker Advance DPX 600 spectrometer in the Laboratory for NMR spectroscopy, Chemical Department, Faculty of Science at University of Zagreb. All ^1H NMR spectra were recorded at 400 or 600 MHz, and ^{13}C at 100 or 150 MHz (specified in each spectrum). Methanol-d_4 was used as a solvent for all *N*-methylated porphyrins and deuterated chloroform for porphyrins with non-quaternised pyridyl groups. The spectra of *N*-oxidized porphyrins were recorded in methanol-d_4 and few drops of deuterated chloroform was added in cases of low solubility in methanol. 5-(4-acetamidophenyl)-10, 15, 20-(3-pyridyl) porphyrin (**7**) dissolved in deuterated chloroform was used to investigate the temperature effect on the structure and the existence of rotamers using ^1H NMR (400 Hz). The spectra were first recorded at 25 °C, then at 5 °C, followed by heating up to 50 °C, and then cooling back to the starting point at 25 °C. ATR-IR spectra were recorded on Cary 630 FTIR spectrophotometer from Agilent Technologies.

Mass spectra of porphyrins were recorded using a high-resolution mass spectrometer (HRMS) 6546 LC/Q-TOF (Agilent, Santa Clara, CA, SAD) equipped with a high-performance liquid chromatography 1290 Infinity II HPLC (Agilent, Santa Clara, CA, SAD) at the Laboratory for Bioanalytics at the Ruđer Bošković Institute. Non-cationic porphyrins, **6** to **10**, were dissolved in acetonitrile (MeCN) while free-base *N*-methylated porphyrins (**13** to **17**) and their Zn(II) complexes (**18** to **26**) were dissolved in methanol (MeOH). Spectra were recorded in ESI+ ionization mode and the data collected every second in the range 100-1100 Da.

Mass spectra of gallium(III) porphyrins (**33-36**) was recorded on the MALDI-MS spectrometer at the Department of Chemistry at the University of Hull. The samples (0.5 μL) were dissolved in MeOH with 1 μL matrix (HABA; MeOH:CH_3CN: H_2O, 40:20:20) and 1 μL of 0.1% TFA was added. The samples were recorded in 1000 Hz in positive ion reflector mode (1000 shots per spectrum in the mass range 200 to 2500 Da).

3.2. Synthesis of porphyrins

3.2.1. Synthesis of the starting material-porphyrins 1, 2 and 3

3.2.1.1. 5,10,15,20-tetrakis(3-pyridyl) porphyrin (1) [73] and 5-(4-acetamidophenyl)-10,15,20-tris(3-pyridyl)porphyrin (2) [73]

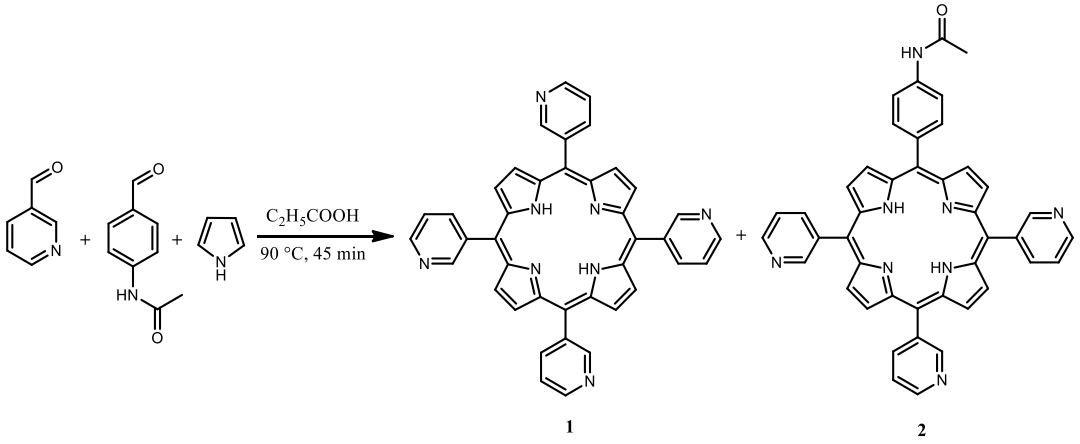

Scheme 1. Synthesis of porphyrins **1** and **2**.

3-Pyridinecarboxyaldehyde (1.78 g, 0.02 mol, 3 equiv.) and 4-acetamidobenzaldehyde (0.90 g, 5.52 mmol, 1 equiv.) were dissolved in propionic acid (70 mL). Freshly distilled pyrrole (1.54 mL, 0.02 mol, 4 equiv.) was added dropwise over 10 min, gradually heated and under constant stirring. After reaching 90 °C, reaction was stirred for another 45 min, under light and presence of air, keeping the same temperature. Upon completion of the reaction, solvent was removed and product was purified by column chromatography twice on silica gel using DCM/MeOH (30:1) as a mobile phase. Porphyrin **1** was the first purple fraction and it was isolated from the column after precipitation in *n*-hexane (177 mg, 5%).

^{1}H NMR (CD_3Cl, 400 MHz): δ/ppm -2.81 (s, 2H, pyrrole N*H*), 7.81 (dd, J = 7.8 Hz, 4.9 Hz, 3H, Py-5-*H*), 8.56 (d, J = 7.8 Hz, 3H, Py-6-*H*), 8.89 (br s, 8H, β-*H*), 9.10 (dd, J = 4.9 Hz, 2.0 Hz, 3H, Py-4-*H*), 9.49 (d, J = 2.0 Hz, 3H, Py-2-*H*);

The second fraction was porfirin **2** and it was isolated as a purple solid after precipitation in *n*-hexane (140 mg, 4%).

^{1}H NMR (CD_3Cl, 400 MHz): *δ*/ppm -2.81 (s, 2H, pyrrole N*H*), 2.37 (s, 3H, C*H*$_3$), 7.59 (s, 1H, amide N*H*), 7.76 (t, *J* = 6.9 Hz, 3H, Py-5-*H*), 7.93 (br s, 2H, Ar-3,5-*H*), 8.17 (d, *J* = 8.0 Hz, 2H, Ar-2,6-*H*), 8.52 (d, *J* = 6.9 Hz, 3H, Py-6-*H*), 9.01 – 8.78 (m, 8H, β-*H*), 9.14 – 9.02 (m, 3H, Py-4-*H*), 9.46 (s, 3H, Py-2-*H*).

3.2.1.2. 5-(4-aminophenyl)-10,15,20-tris(3-pyridyl)porphyrin (**3**) [73]

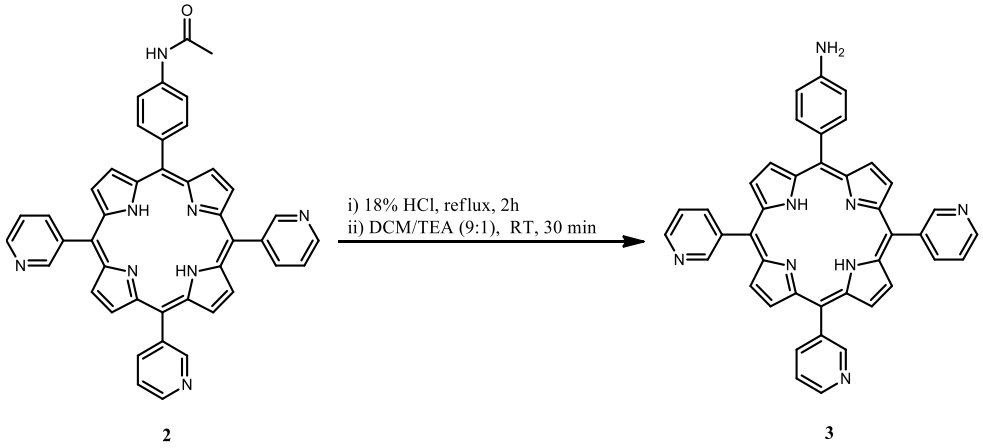

2 **3**

Scheme 2. Synthesis of porphyrin **3**.

Porphyrin **2** (325 mg, 0.48 mmol, 1 equiv.) was dissolved in 100 mL of 18% HCl. Reaction was stirred under reflux for 2 h. Solvent was removed, and the crude product was dissolved in 70 mL of DCM/TEA (9:1) and stirred for 30 minutes at room temperature. The reaction mixture was then washed with H_2O (3 × 50 mL) and with brine (1 × 50 mL). After drying over Na_2SO_4, reaction mixture was filtered, and solvent removed *in vacuo*. The product was purified with a column chromatography on a silica gel with DCM/MeOH (30:1) as mobile phase. Product **3** was isolated as a purple crude after the precipitation in *n*-hexane (261 mg, 87%).

^{1}H NMR (CD_3Cl, 400 MHz): *δ*/ppm -2.76 (s, 2H, pyrrole N*H*), 4.09 (s, 2H, -N*H*$_2$), 7.11 (d, *J* = 8.2 Hz, 2H, Ar-3,5-*H*), 7.79 (d, *J* = 7.8 Hz, 3H, Py-5-*H*), 8.02 (d, *J* = 7.9 Hz, 2H, Ar-2,6-*H*), 8.55 (d, *J* = 7.7 Hz, 3H, Py-4-*H*), 9.19 – 8.74 (m, 8H, β-*H*), 9.49 (d, *J* = 2.2 Hz, 3H, Py-2-*H*).

3.2.2. Synthesis of products 4 and 5

3.2.2.1. Decanoyl chloride

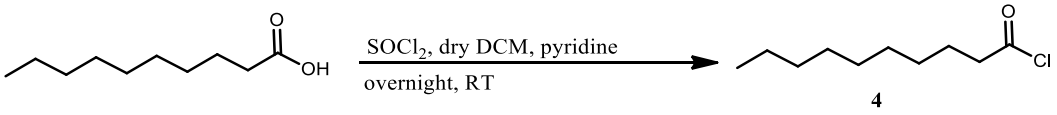

Scheme 3. Synthesis of decanoyl chloride **4**.

Decanoic acid, $C_9H_{19}COOH$ (556 mg, 3.22 mmol, 1 equiv.) was dissolved in 25 mL of dry DCM and a few drops of pyridine. Thionyl chloride, $SOCl_2$ (1.4 mL, 2.29 g, 0.019 mol) was added and the reaction was stirred overnight at room temperature. Solvent was removed, and the reaction mixture re-dissolved in DCM (25 mL). Reaction mixture was washed with H_2O (3 × 25 mL) and organic layer died over Na_2SO_4 for 30 min. Solution was filtered to remove Na_2SO_4 and after removal of the solvent, product **4** was isolated as a viscose yellow liquid (600 mg, 98%).

^{1}H ($CDCl_3$, 400 MHz): δ/ppm 0.90 (t, 3H, J = 6.9 Hz, -CH_3),1.24-1.42 (m, 12 H, C$^3H_2$-C$^9H_2$), 1.63-1.79 (m, 2H, C$^2H_2$), 2.90 (t, 2H, J = 7.3 Hz, COCH_2);

ATR-IR (cm^{-1})**:** 1800 (C=O); 2850 and 2900 (C-H).

3.2.2.2. Tetradecanoyl chloride (5)

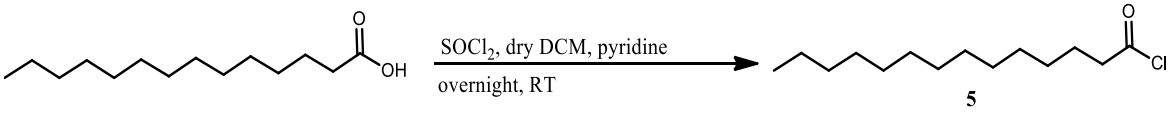

Scheme 4. Synthesis of tetradecanoyl chloride **5**.

The tetradecanoyl chloride, **5**, was synthetised following the same protocol as decanoic chloride, product **4**. Tetradecanoic acid, $C_{13}H_{27}COOH$ (396 mg, 3.22 mmol, 1 equiv.) was stirred overnight in DCM and pyridine with $SOCl_2$ (755 µL, 1.24 g, 0.01 mol). After the purification, product **5** was isolated as a viscose yellow liquid (343 mg, 80%).

^{1}H ($CDCl_3$, 400 MHz): δ/ppm 0.91 (t, 3H, J = 6.8 Hz, -CH_3),1.23-1.46 (m, 20 H, C$^3H_2$-C$^{13}H_2$), 1.62-1.78 (m, 2H, C$^2H_2$), 2.90 (t, 2H, J = 7.2 Hz, COCH_2);

ATR-IR (cm^{-1})**:** 1800 (C=O); 2850 and 2900 (C-H).

3.2.3. Conjugation of acyl chlorides with the porphyrin 3

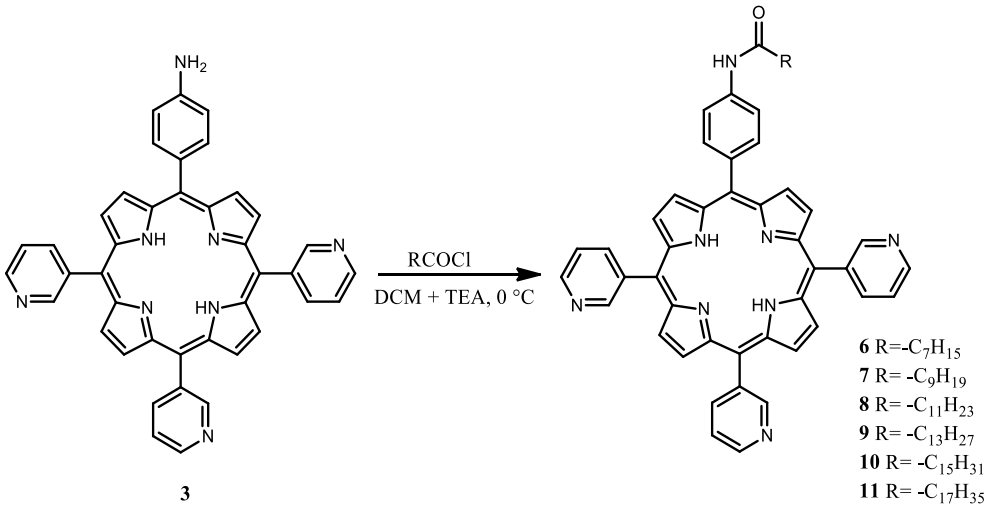

Scheme 5. Synthesis of porphyrins **6-11**.

The same general procedure for the nucleophilic acyl substitution with acyl chlorides of alkyl chains of different length was used to obtain porphyrins **6-11**. Porphyrin **3** was dissolved in dry DCM (10-20 mL) with the addition of 1 mL of triethylamine. The solution was cooled down to 0 °C and under N_2 atmosphere desired acyl chloride previously dissolved in 5 mL of dry DCM was added dropwise over 30 min. Reaction was monitored using TLC silica plates with DCM/MeOH (9:1) as a mobile phase. Upon completion of the reaction, solvent was removed, and the product was dissolved in DCM (20 mL). The product was washed with H_2O (3 × 20 mL), and organic layer was dried over Na_2SO_4 for 30 min. Obtained product was purified twice using column chromatography on silica gel with different DCM and MeOH ratios. After precipitation in *n*-hexane porphyrins were isolated as dark purple solids.

Table 1. Summarized reaction and purification (column chromatography) conditions and obtained mass and yields for porphyrin **6-11**.

Porphyrin	Mass & molarity of porphyrin **3**	Mass & molarity of acyl chloride	Column chromatography condition (DCM:MeOH)	Mass & yield of obtained product
6	56 mg, 0.09 mmol	95 mg, 0.58 mmol ($C_7H_{15}COCl$)	1st 30:1 2nd 40:1	55 mg, 82%
7	45 mg, 0.08 mmol	97 mg, 0.51 mmol ($C_9H_{19}COCl$)	1st 30:1 2nd 40:1	49 mg, 87%

8	90 mg, 0.14 mmol	187 mg, 0.85 mmol ($C_{11}H_{23}COCl$)	1st 30:1 2nd 40:1	102 mg, 88%
9	61 mg, 0.10 mmol	160 mg, 0.65 mmol ($C_{13}H_{27}COCl$)	1st 30:1 2nd 35:1	73 mg, 89%
10	39 mg, 0.06 mmol	146 mg, 0.53 mmol ($C_{15}H_{31}COCl$)	1st 30:1 2nd 35:1	47 mg, 87%
11	89 mg, 0.14 mmol	265 mg, 0.88 mmol ($C_{17}H_{35}COCl$)	1st 35:1 2nd 40:1	103 mg, 82%

3.2.3.1. 5-(4-octanamidophenyl)-10,15,20-tris(3-pyridyl)porphyrin (6)

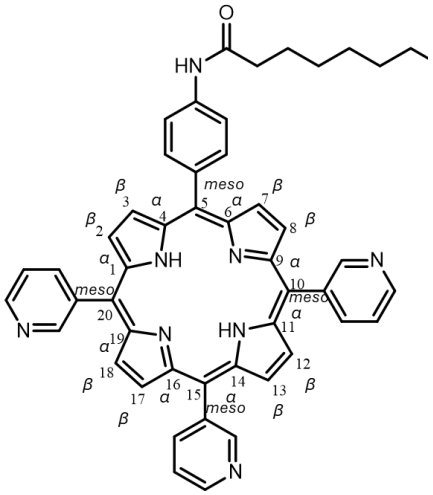

6

^{1}H NMR (CDCl$_3$, 400 MHz): δ/ppm 2.79 (br s, 2H, pyrrole N*H*), 0.97 (t, 3H, J = 7.2 Hz, -C^8*H$_3$*), 1.35-1.59 (m, 8H, overlapping C^4*H$_2$*(C*H$_2$*)$_2$C^7*H$_2$*), 1.86-1.96 (m, 2H, J = 7.3 Hz, C^3*H$_2$*), 2.58 (t, 2H, J = 7.5 Hz, -COC^2*H$_2$*), 7.57 (s, 1 H, amide N*H*), 7.77-7.82 (m, 3H, Py-5-*H*), 7.89-8.10 (m, 2H, Ar-3,5-*H*), 8.0 (d, 2H, J = 8.8 Hz, Ar-2,6-H), 8.55 (d, 3H, J = 7.4 Hz, Py-6-*H*), 8.81-8.91 (m, 6H, β-2,8,12,13,17,18-*H*), 8.98 (d, 2H, J = 4.9 Hz, β-3,7-*H*), 9.09 (dd, 3H, J = 3.3 Hz,1.7 Hz, Py-4-*H*), 9.48 (br s, 3H, Py-2-*H*);

^{13}C NMR (CDCl$_3$, 100 MHz): δ/ppm 14.1 (-*C*^{8}H$_3$), 22.7, 25.8, 29.2, 29.4, 29.7, 29.8, 31.8 (-*C*^{3}H$_2$), 38.1 (*C*^{2}H$_2$), 116.1 (*meso*-5-*C*), 116.4 (*meso*-10,15,20-*C*), 118.1(Ar-3,5-*C*), 120.9 (Py-1-*C*), 122.1 (Ar-2,6-*C*), 135.2 (Py-5-*C*), 137.3 (Ar-1-*C*), 137.8 (*α*-*C*), 137.9 (*α*-*C*), 138.2 (Ar-4-*C*), 140.7 (Py-6-*C*), 149.21 (Py-4-*C*), 153.6 (Py-2-*C*), 171.9 (*C*=O);

HRMS: *m/z* theor. calcd. for $C_{49}H_{42}N_8O$ $[M+H]^+$ 759.3560; exp. 759.3562.

3.2.3.2. 5-(4-decanamidophenyl)-10,15,20-tris(3-pyridyl)porphyrin (7)

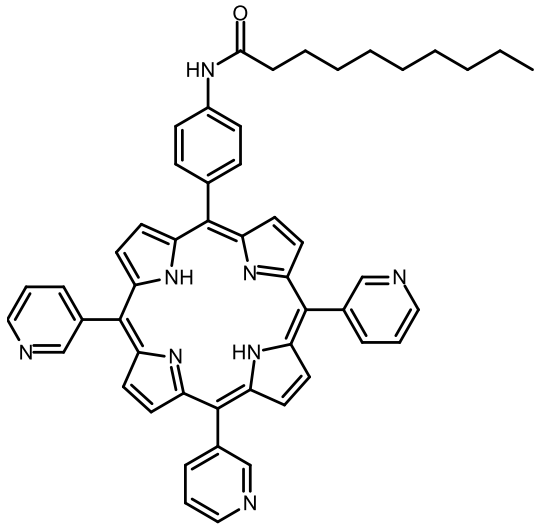

7

^{1}H NMR ($CDCl_3$, 400 MHz): δ/ppm 2.78 (s, 2H, pyrrole N*H*), 0.93 (t, 3H, J = 6.8 Hz, -$C^{10}H_3$), 1.25-1.58 (m, 12H, $C^4H_2(CH_2)_4C^9H_2$), 1.85-1.97 (m, 2H, C^3H_2), 2.58 (t, 2H, J = 7.5 Hz, COC^2H_2), 7.74-7.82 (m, 4H, overlapping amide N*H*, Py-5-*H*), 7.86-8.12 (m, 2H, Ar-3,5-*H*), 8.2 (d, 2H, J = 8.9 Hz, Ar-2,6-*H*), 8.52-8.59 (m, 3H, Py-6-*H*), 8.81-8.92 (m, 6H, β-2,8,12,13,17,18-*H*), 8.98 (d, J = 3.2 Hz, 2H, β-3,7-*H*), 9.07-9.11 (m, 3H, Py-4-*H*), 9.49 (br s, 3H, Py-2-*H*);

^{13}C NMR ($CDCl_3$, 100 MHz): δ/ppm 14.2, 22.7, 25.8, 29.3, 29.4, 29.5, 29.5, 31.9, 38.1, 45.8, 116.4, 118.2, 122.2, 135.2, 137.4, 137.9, 138.1, 140.9, 149.3, 153.5, 171.8;

HRMS: *m/z* theor. calcd. for $C_{51}H_{46}N_8O$ $[M+H]^+$ 787.3873; exp. 787.3876.

3.2.3.3. 5-(4-dodecanamidophenyl)-10,15,20-tris(3-pyridyl)porphyrin (8)

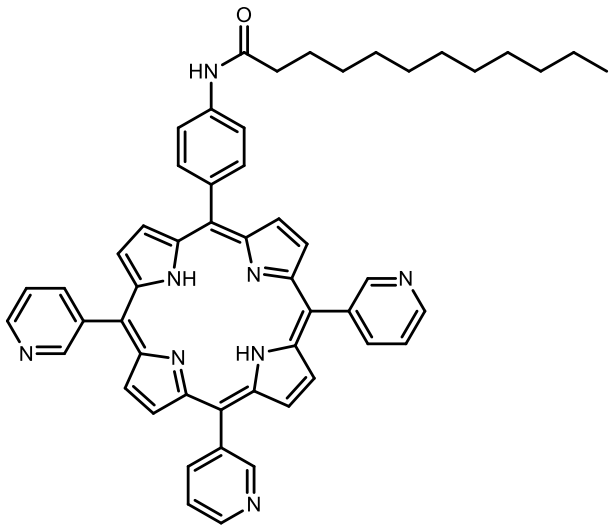

8

^{1}H NMR ($CDCl_3$, 400 MHz): δ/ppm 2.78 (s, 2H, pyrrole N*H*), 0.92 (t, 3H, -C^{12}*H*$_3$), 1.24-1.58 (m, 16H, C^{4}*H*$_2$(C*H*$_2$)$_6$C^{11}*H*$_2$), 1.85-1.96 (m, 2H, C^{3}*H*$_2$), 2.57 (t, 2H, J = 7.5 Hz, COC^{2}*H*$_2$), 7.74 (s, 1H, amide N*H*), 7.76-7.82 (m, 3H, Py-5-*H*), 7.84-8.14 (m, 2H, Ar-3,5-*H*), 8.20 (d, 2H, J = 8.6 Hz, Ar-2,6-*H*), 8.51-8.58 (m, 3H, Py-6-*H*), 8.80-8.92 (m, 6H, β-2,8,12,13,17,18-*H*), 8.98 (d, 2H, J = 4.6 Hz, β-3,7-*H*), 9.06-9.13 (m, 3H, Py-4-*H*), 9.49 (br s, 3H, Py-2-*H*);

^{13}C NMR ($CDCl_3$, 100 MHz): δ/ppm 14.1, 22.7, 25.8, 29.4, 29.4, 29.5, 29.6, 29.7, 31.9, 38.1, 116.4, 118.1, 120.9, 122.1, 135.2, 137.4, 137.8, 138.1, 140.9, 149.2, 153.6, 171.8;

HRMS: *m/z* theor. calcd. for $C_{53}H_{50}N_8O$ $[M+H]^+$ 815.4186; exp. 815.4190.

3.2.3.4. 5-(4-tetradecanamidophenyl)-10,15,20-tris(3-pyridyl)porphyrin (9)

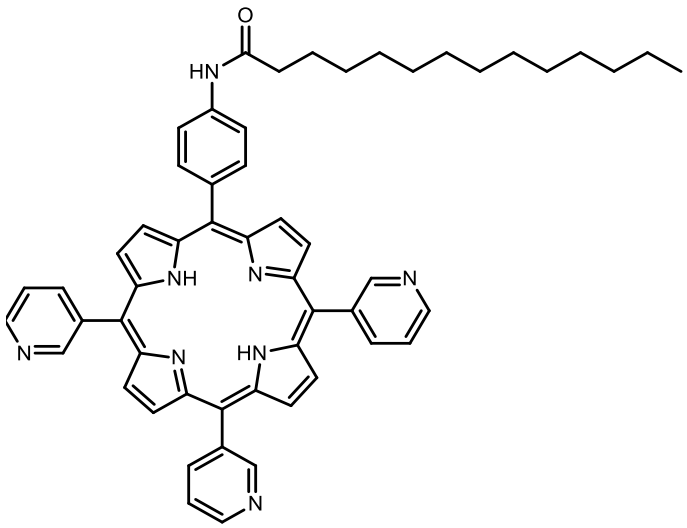

9

^{1}H NMR ($CDCl_3$, 400 MHz): δ/ppm 2.78 (s, 2H, pyrrole-N*H*), 0.91 (t, 3H, J = 6.8 Hz, -$C^{14}H_3$), 1.25-1.58 (m, 20H, -$C^{4}H_2(CH_2)_8C^{13}H_2$), 1.85-1.96 (m, 2H, -$C^{3}H_2$), 2.72 (t, 2H, J = 7.5 Hz, -$COC^{2}H_2$), 7.71 (s, 1H, amide N*H*), 7.75-7.84 (m, 3H, Py-5-*H*), 7.85-8.14 (m, 2H, Ar-3,5-*H*), 8.20 (d, 2H, J = 8.7 Hz, Ar-2,6-*H*), 8.52-8.59 (m, 3H, Py-6-*H*), 8.80-8.91 (m, 6H, β-2,8,12,13,17,18-*H*), 8.98 (d, 2H, J = 4.7 Hz, β-3,7-*H*), 9.06-9.12 (m, 3H, Py-4-*H*), 9.49 (br s, 3H, Py-2-*H*);

^{13}C NMR ($CDCl_3$, 100 MHz): δ/ppm 14.2, 22.7, 25.8, 29.4, 29.5, 29.6, 29.7, 31.9, 38.1, 116.1, 116.4, 118.1, 120.9, 122.1, 135.2, 137.9, 138.1, 140.9, 149.2, 153.6, 171.8;

HRMS: *m/z* theor. calcd. for $C_{55}H_{54}N_8O$ $[M+H]^+$ 843.4499; exp. 843.4497.

3.2.3.5. 5-(4-hexadecanamidophenyl)-10,15,20-tris(3-pyridyl)porphyrin (10)

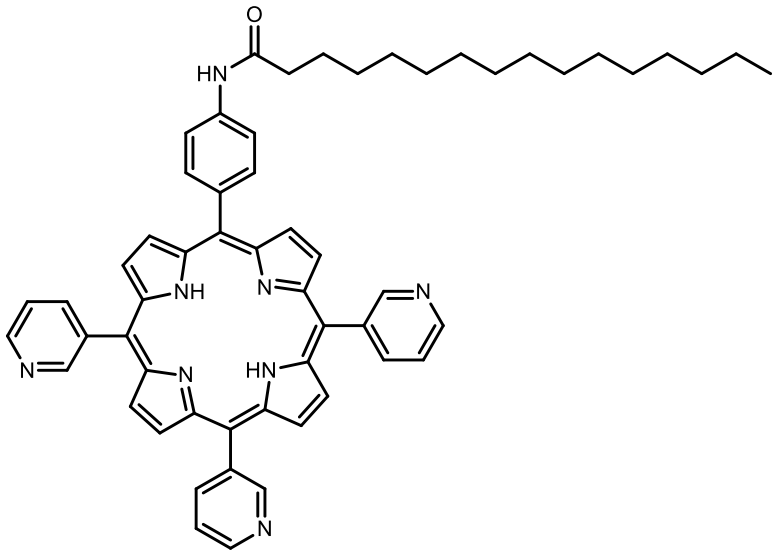

10

^{1}H NMR (CDCl$_3$, 400 MHz): δ/ppm 2.78 (s, 2H, pyrrole-N*H*), 0.91 (t, 3H, J = 6.8 Hz, -C^{16}*H$_3$*), 1.23-1.58 (m, 24H, -C^{4}*H$_2$*(C*H$_2$*)$_{10}$C^{15}*H$_2$*), 1.85-1.96 (m, 2H, -C^{3}*H$_2$*), 2.57 (t, 2H, J =7.5 Hz, -COC^{2}*H$_2$*), 7.69 (s, 1H, amide N*H*), 7.75-7.83 (m, 3H, Py-5-*H*), 7.85-8.12 (m, 2H, Ar-3,5-*H*), 8.20 (d, 2H, J = 8.5 Hz, Ar-2,6-*H*), 8.51-8.59 (m, 3H, Py-6-*H*), 8.81-8.92 (m, 6H, β-2,8,12,13,17,18-*H*), 8.98 (d, 2H, J = 4.7 Hz, β-3,7-*H*), 9.07-9.12 (m, 3H, Py-4-*H*), 9.50 (br s, 3H, Py-2-*H*);

^{13}C NMR (CDCl$_3$, 100 MHz): δ/ppm 14.2, 22.7, 25.8, 29.4, 29.5, 29.6, 29.7, 31.9, 38.1, 116.1, 116.4, 118.1, 120.9, 122.1, 135.2, 137.3, 137.8, 138.1, 140.9, 149.2, 153.6, 171.9;

HRMS: *m/z* theor. calcd. for $C_{57}H_{58}N_8O$ $[M+H]^+$ 871.4812; exp. 871.4816.

3.2.3.6. 5-(4-octadecanamidophenyl)-10,15,20-tris(3-pyridyl)porphyrin (11)[73]

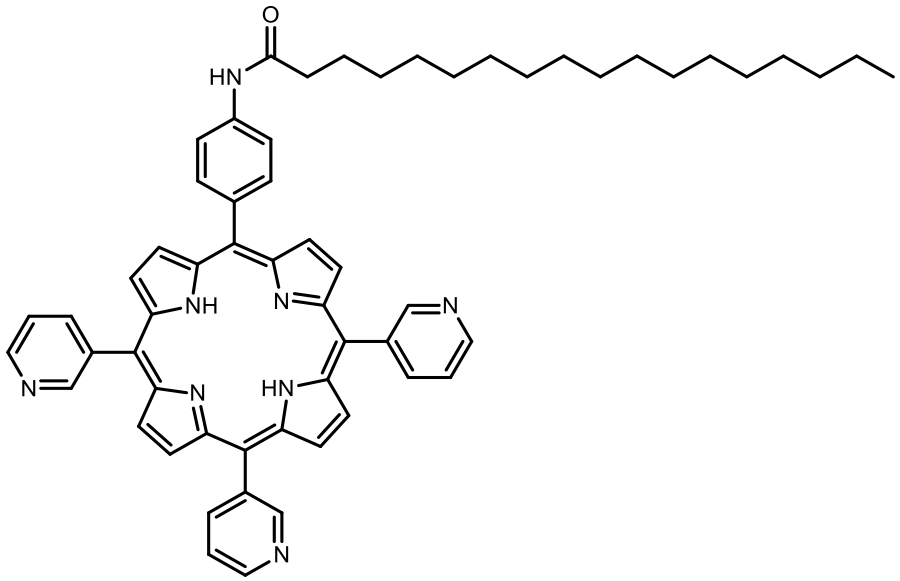

11

^{1}H NMR agrees with the previously published data:

^{1}H NMR ($CDCl_3$, 400 MHz): δ/ppm 2.79 (s, 2H, pyrrole-N*H*), 0.90 (t, 3H, J = 6.9 Hz -$C^{18}H_3$), 1.24-1.58 (m, 28H, -$C^{4}H_2(CH_2)_{12}C^{17}H_2$), 1.85-1.96 (m, 2H, -$C^{3}H_2$), 2.58 (t, 2H, J = 7.5 Hz, -$COC^{2}H_2$), 7.58 (s, 1H, amide N*H*), 7.76-7.83 (m, 3H, Py-5-*H*), 7.86-8.11 (m, 2H, Ar-3,5-*H*), 8.20 (d, 2H, J = 8.7 Hz, Ar-2,6-*H*), 8.52-8.59 (m, 3H, Py-6-*H*), 8.81-8.91 (m, 6H, β-2,8,12,13,17,18-*H*), 8.98 (d, 2H, J = 4.6 Hz, β-3,7-*H*), 9.07-9.12 (m, 3H, Py-4-*H*), 9.49 (br s, 3H, Py-2-*H*).

3.2.4. *N*-methylation of porphyrins 2, 6-11

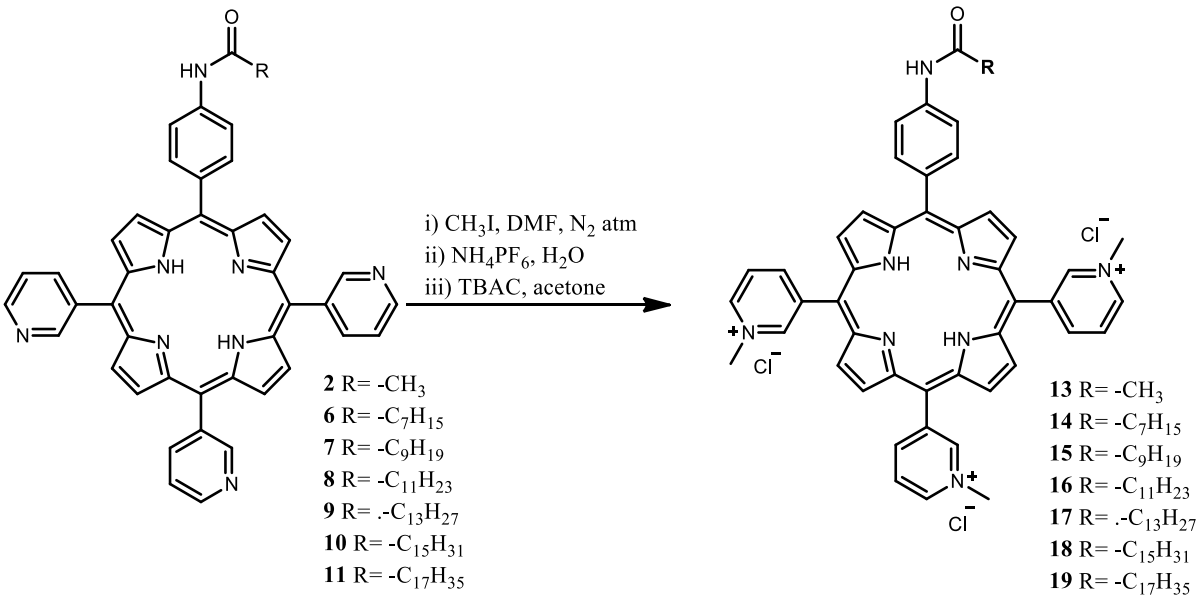

Scheme 6. Synthesis of porphyrins **13**-**19**.

The same general procedure for pyridyl *N*-methylation was used to obtain porphyrins **12**-**19** [162]**.** The reaction protocols and obtained masses and yields for porphyrins **13**-**19** are summarized in **Table 2.** Porphyrin **1**, **2** or **6-11** (1 equiv.) was dissolved in dry dimethylformamide (DMF) and the solution was purged with nitrogen for 15 minutes. Methyl iodide (CH_3I) (200 equiv.) was added and the reaction was stirred at room temperature overnight, under N_2 atmosphere, protected from light. Reaction was monitored using silica TLC plates with MeCN:water:$KNO_{3(sat.)}$ (8:1:1) as a mobile phase. After the reaction was completed, the solvent was removed *in vacuo* and the crude product underwent two precipitations to change the counter ion (from I^- to Cl^-). The first step was precipitation in ammonium hexafluorophosphate (NH_4PF_6) after dissolving the crude porphyrin in water, and the second precipitation in tetrabutylammonium chloride (TBAC) in acetone. In both precipitations, the obtained solid was washed (3×) with solvent. Final step was dissolving the crude in MeOH and addition of diethyl ether (Et_2O) until precipitation. After washing the crude in Et_2O and collecting by filtration, products were isolated as dark purple to brown solids.

Table 2. Summarized reaction conditions and obtained masses and yields for porphyrins **12**-**19**.

Porphyrin	Mass & Molarity, Porphyrin code	Volume & Molarity of CH_3I	Mass & Yield of obtained product
12	60 mg, 0.097 mol (**1**)	1.2 mL, 0.02 mol.	60 mg, 75%
13	78 mg, 0.12 mmol (**2**)	1.4 mL, 0.02 mol	80 mg, 84%
14	39 mg, 0.05 mmol (**6**)	610 µL, 9.80 mmol	43 mg, 97%
15	47 mg, 0.06 mmol (**7**)	700 µL, 9.80 mmol	51 mg, 96%
16	57 mg, 0.07 mmol (**8**)	870 µL, 0.02 mol	62 mg, 91%
17	41 mg, 0.06 mmol (**9**)	610 µL, 9.80 mmol	46 mg, 95%
18	47 mg, 0.05 mmol (**10**)	670 µL, 0.01 mmol	49 mg, 90%
19	34 mg, 0.04 mmol (**11**)	470 µL, 7.50 mmol	35 mg, 89 %

3.2.4.1. 5,10,15,20-tetrakis(*N*-methylpyridinium-3-yl)porphyrin tetrachloride (12) [162]

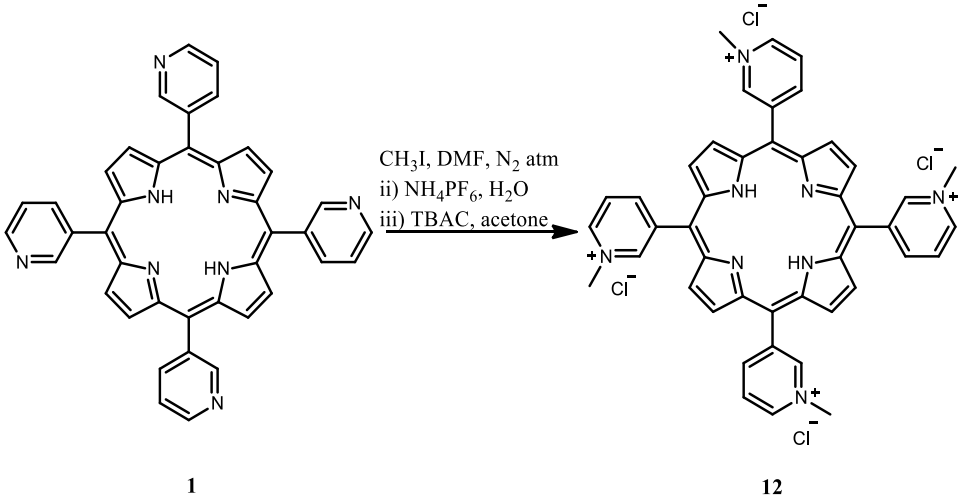

Scheme 7. Synthesis of porphyrin **12**.

^{1}H NMR of **12** agrees with the previously published data:

^{1}H NMR (DMSO, 400 MHz): δ/ppm 4.73 (s, 12H, 4 N-C*H*$_3$), 8.64 (t, 4H, *J* = 7.0 Hz, Py-5-*H*), 9.22-9.38 (m, 12H, overlapping β-*H* and Py-6-*H*), 9.64 (d, 4H, *J* = 6.2 Hz, Py-4-*H*), 10.10 (br s, 4H, Py-2-*H*).

3.2.4.2. 5-(4-acetamidophenyl)-10,15,20-tris(*N*-methylpyridinium-3-yl)porphyrin trichloride (**13**) [162]

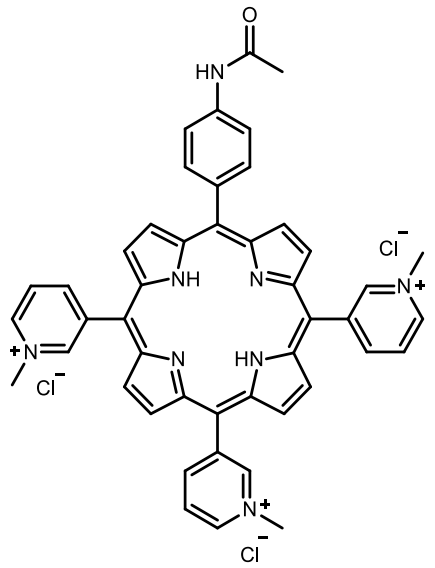

13

^{1}H NMR of **13** agrees with the previously published data:

^{1}H NMR (CD_3OD, 400 MHz): δ/ppm 2.35 (s, 3H, -COC*H*$_3$), 4.81 (s, 9H, 3N-C*H*$_3$), 8.09 (d, 2H, *J*= 8.1 Hz, Ar-3,5-*H*), 8.21 (d, *J* = 8.7 Hz, Ar-2,6-*H*), 8.57-8.63 (m, 3H, Py-5-*H*), 9.14 (br s, 8H, β-*H*), 9.38-9.44 (m, 3H, Py-6-*H*), 9.47 (d, 3H, *J* = 6.2 Hz, Py-4-*H*), 9.97 (br s, 3H, Py-2-*H*).

3.2.4.3. 5-(4-octanamidophenyl)-10,15,20-tris(*N*-methylpyridinium-3-yl)porphyrin trichloride (14)

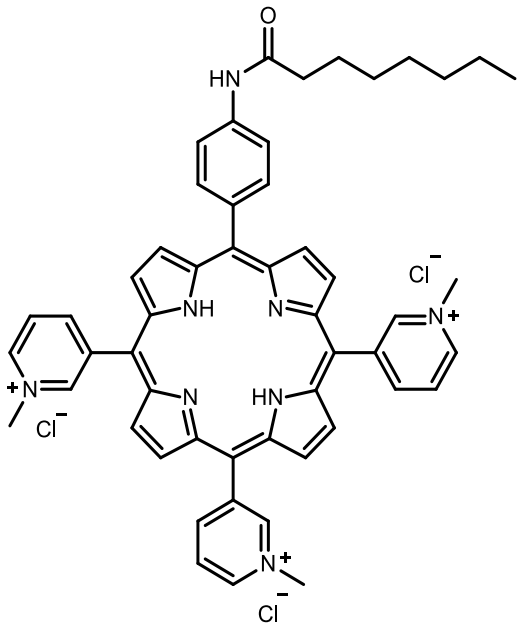

14

^{1}H NMR (CD_3OD, 600 MHz): δ/ppm 0.96 (t, 3H, J = 7.6 Hz, -C$^{8}H_3$), 1.37-1.55 (m, 8H, C$^{4}H_2$(CH_2)$_2$C$^{7}H_2$), 1.82-1.88 (m, 2H, C$^{3}H_2$), 2.57 (t, 2H, J = 7.5 Hz, -COC$^{2}H_2$), 4.78 (s, 9H, 3x N-CH_3), 8.06-8.10 (m, 2H, Ar-3,5-*H*), 8.20 (d, 2H, J = 8.9 Hz, Ar-2,6-*H*), 8.55-8.59 (m, 3H, Py-5-*H*), 9.01 (br s, 8H, β-*H*), 9.35-9.41 (m, 3H, Py-6-*H*), 9.43-9.47 (m, 3H, Py-4-*H*), 9.94 (br s, 3H, Py-2-*H*);

^{13}C NMR (CD_3OD, 150 MHz): δ/ppm 13.1 (-*C*$^{8}H_3$), 22.3 (-*C*$^{7}H_2$), 25.7 (-*C*$^{6}H_2$), 28.8 (-*C*$^{5}H_2$), 29.0 (-*C*$^{4}H_2$), 31.6 (-*C*$^{3}H_2$), 36.8 (-CO*C*$^{2}H_2$), 48.1 (3x N-*C*H$_3$), 111.5 (*meso*-5-*C*), 112.3 (*meso*-10,15,20-*C*), 118.4 (Ar-3,5-*C*), 123.2 (Py-1-*C*), 126.3 (Ar-2,6-*C*), 134.8 (Py-5-*C*), 136.2 (Ar-1-*C*), 139.3(Ar-4-*C*), 141.8 (α-*C*), 145.2 (Py-6-*C*), 147.8 (Py-4-*C*), 148.3 (Py-2-*C*), 173.9 (*C*=O);

HRMS: *m/z* theor. calcd. for $C_{52}H_{51}N_8O$ $[M]^{3+}$ 267.8062; exp. 267.8065.

3.2.4.4. 5-(4-decanamidophenyl)-10,15,20-tris(*N*-methylpyridinium-3-yl)porphyrin trichloride (15)

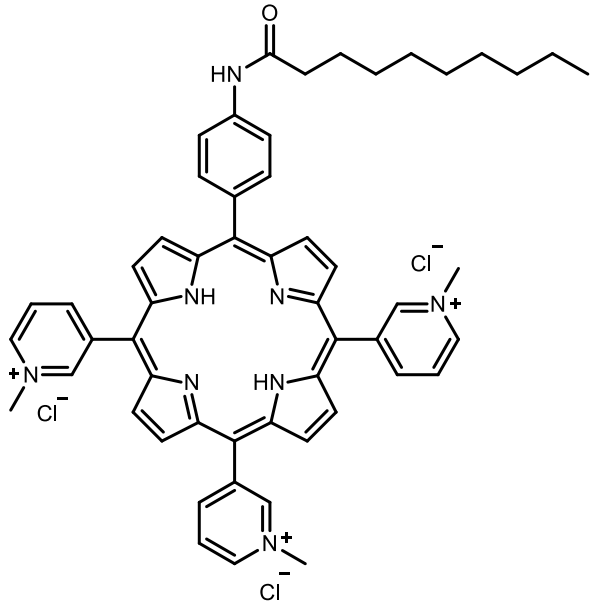

15

^{1}H NMR (CD$_3$OD, 600 MHz): δ/ppm 0.93 (t, 3H, J = 7.1 Hz, -C$^{10}H_3$), 1.31-1.55 (m, 12H, C$^{4}H_2$(CH_2)$_4$C$^{9}H_2$), 1.82-1.88 (m, 2H, C$^{3}H_2$), 2.57 (t, 2H, J = 7.5 Hz, -COC$^{2}H_2$), 4.78 (s, 9H, 3 N-CH_3), 8.05-8.26 (m, 2H, Ar-3,5-*H*), 8.18 (d, 2H, J = 8.6 Hz, Ar-2,6-*H*), 8.55-8.59 (m, 3H, Py-5-*H*), 9.01 (br s, 8H, β-*H*), 9.36-9.41 (m, 3H, Py-6-*H*), 9.45 (d, J = 6.4 Hz, Py-4-*H*), 9.94 (br s, 3H, Py-2-*H*);

^{13}C NMR (CD$_3$OD, 100 MHz): δ/ppm 13.2, 22.5, 25.7, 29.0, 29.1, 29.2, 29.3, 31.7, 36.9, 48.2, 111.6, 112.4, 118.4, 123.9, 126.3, 126.4, 134.9, 136.2, 139.3, 141.8, 145.3, 147.9, 148.3, 173.9;

HRMS: theor. calcd. for $C_{54}H_{55}N_8O$ $[M]^{3+}$ 277.1500; exp. 277.1502.

3.2.4.5. 5-(4-dodecanamidophenyl)-10,15,20-tris(*N*-methylpyridinium-3-yl)porphyrin trichloride (16)

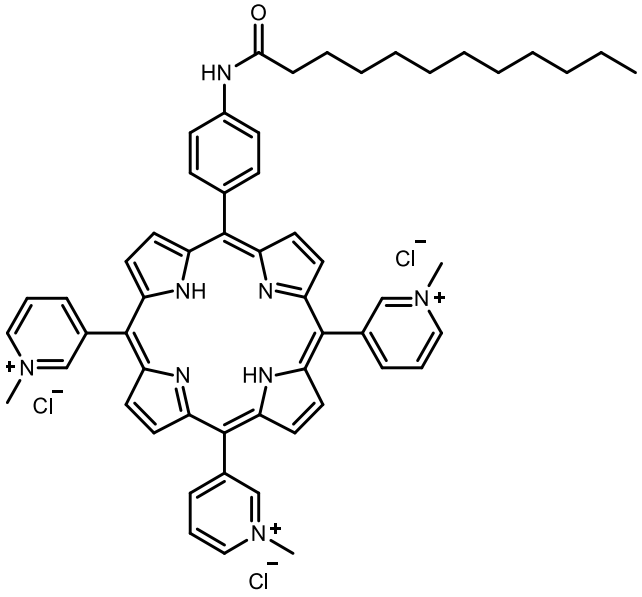

16

^{1}H NMR (CD_3OD, 600 MHz): δ/ppm 0.91 (t, 3H, J = 7.0 Hz, -C$^{12}H_3$), 1.27-1.55 (m, 16H, C$^{4}H_2$(CH_2)$_4$C$^{11}H_2$), 1.82-1.88 (m, 2H, C$^{3}H_2$), 2.57 (t, 2H, J = 7.5 Hz, -COC$^{2}H_2$), 4.78 (s, 9H, 3 N-CH_3), 8.05-8.11 (m, 2H, Ar-3,5-*H*), 8.18 (d, 2H, J = 8.5 Hz, Ar-2,6-*H*), 8.55-8.59 (m, 3H, Py-5-*H*), 9.01 (br s, 8H, β-*H*), 9.35-9.40 (m, 3H, Py-6-*H*), 9.45 (d, J = 6.4 Hz, Py-4-*H*), 9.94 (br s, 3H, Py-2-*H*);

^{13}C NMR (CD_3OD, 150 MHz): δ/ppm 13.1, 22.4, 25.6, 29.0, 29.1, 29.2, 29.3, 29.4, 31.7, 36.8, 482., 111.5, 112.3, 118.4, 123.2, 126.3, 134.9, 136.2, 139.3, 141.8, 145.2, 147.8, 148.3, 173.9;

HRMS: theor. calcd. for $C_{56}H_{59}N_8O$ $[M]^{3+}$ 286.4937; exp. 286.4939.

3.2.4.6. 5-(4-tetradecanamidophenyl)-10,15,20-tris(*N*-methylpyridinium-3-yl)porphyrin trichloride (17)

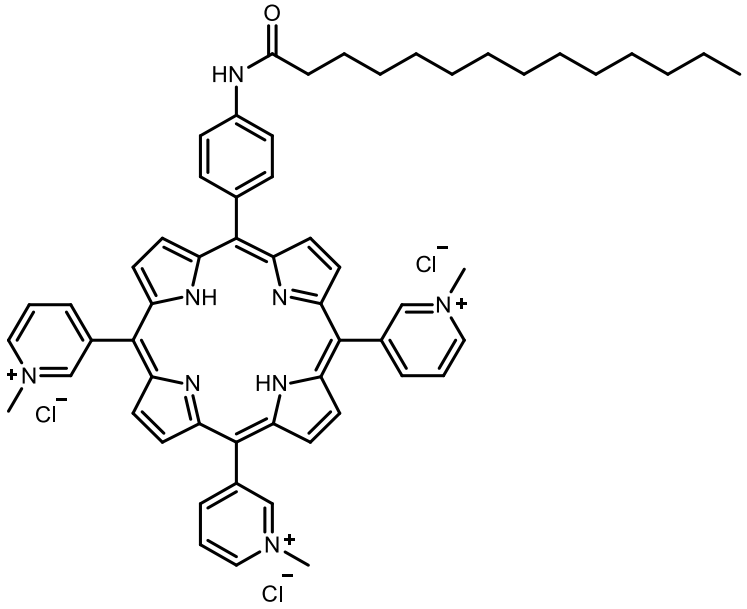

17

^{1}H NMR (CD_3OD, 600 MHz): δ/ppm 0.88 (t, 3H, J = 6.9 Hz, -C$^{14}H_3$), 1.25-1.55 (m, 20H, C$^{4}H_2$(CH$_2$)$_8$C$^{13}H_2$), 1.82-1.88 (m, 2H, C$^{3}H_2$), 2.57 (t, 2H, J = 7.4 Hz, -COC$^{2}H_2$), 4.78 (s, 9H, 3x N-CH_3), 8.05-8.11 (m, 2H, Ar-3,5-*H*), 8.18 (d, 2H, J = 8.4 Hz, Ar-2,6-*H*), 8.55-8.59 (m, 3H, Py-5-*H*), 9.01 (br s, 8H, β-*H*), 9.36-9.40 (m, 3H, Py-6-*H*), 9.45 (d, J = 6.4 Hz, Py-4-*H*), 9.95 (s, 3H, Py-2-*H*);

^{13}C NMR (CD_3OD, 100 MHz): δ/ppm 13.1, 22.4, 25.7, 29.1, 29.2, 29.3, 29.4, 29.5, 31.8, 36.9, 47.5, 111.6, 112.4, 118.4, 126.3, 134.9, 136.2, 139.3, 141.8, 145.3, 147.9, 148.3, 173.9;

HRMS: theor. calcd. for $C_{58}H_{63}N_8O$ $[M]^{3+}$ 295.8375; exp. 295.8379.

3.2.4.7. 5-(4-hexadecanamidophenyl)-10,15,20-tris(*N*-methylpyridinium-yl)porphyrin trichloride (18)

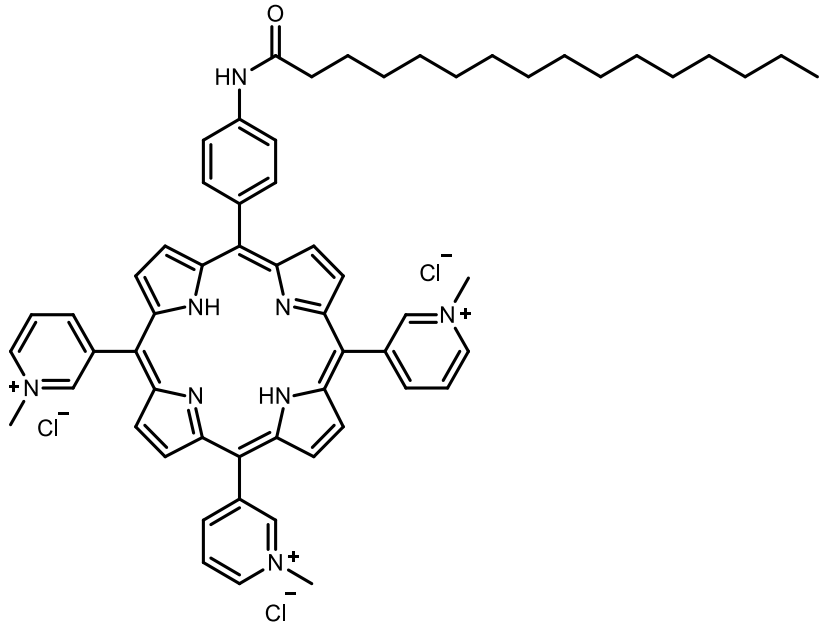

18

^{1}H NMR (CD_3OD, 600 MHz): δ/ppm 0.84 (t, 3H, J = 6.9 Hz, -C$^{16}H_3$), 1.21-1.55 (m, 24H, C$^{4}H_2$(CH_2)$_{10}$C$^{15}H_2$), 1.82-1.88 (p, 2H, C$^{3}H_2$), 2.57 (t, 2H, J = 7.5 Hz, -COC$^{2}H_2$), 4.78 (s, 9H, 3x N-CH_3), 8.05-8.11 (m, 2H, Ar-3,5-*H*), 8.18 (d, 2H, J = 8.6 Hz, Ar-2,6-*H*), 8.55-8.58 (m, 3H, Py-5-*H*), 9.01 (br s, 8H, β-*H*), 9.35-9.41 (m, 3H, Py-6-*H*), 9.45 (d, J = 6.3 Hz, Py-4-*H*), 9.94 (br s, 3H, Py-2-*H*);

^{13}C NMR (CD_3OD, 150 MHz): δ/ppm 13.0, 22.3, 25.6, 29.0, 29.1, 29.2, 29.3, 29.4, 29.5, 31.7, 36.8, 48.1, 111.5, 112.3, 118.4, 123.2, 126.3, 134.9, 136.2, 139.3, 141.8, 145.2, 148.3, 173.9;

HRMS: theor. calcd. for $C_{60}H_{67}N_8O$ $[M]^{3+}$ 305.1813; exp. 305.1815.

3.2.4.8. 5-(4-octadecanamidophenyl)-10,15,20-tris(*N*-methylpyridinium-3-yl)porphyrin trichloride (**19**) [162]

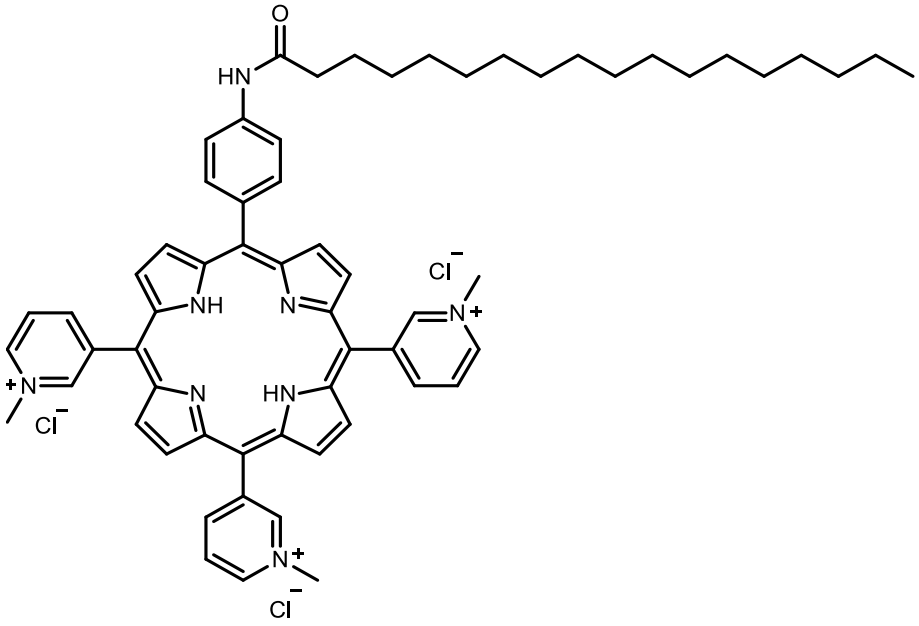

19

^{1}H NMR of **19** agrees with the previously published data [162]:

^{1}H NMR (CD_3OD, 600 MHz): δ/ppm 0.85 (t, 3H, J = 7.0 Hz, -CH_3), 1.19-1.57 (m, 28H, C$^3H_2$-C$^{17}H_2$), 1.83-1.92 (m, 2H, C$^2H_2$), 2.60 (t, 2H, J = 7.5 Hz, -COCH_2), 4.81 (s, 9H, 3 N-CH_3), 8.07-8.14 (m, 2H, Ar-3,5-*H*), 8.21 (d, 2H, J = 8.6 Hz, Ar-2,6-*H*), 8.56-8.62 (m, 3H, Py-5-*H*), 9.04 (br s, 8H, β-*H*), 9.37-9.43 (m, 3H, Py-6-*H*), 9.45 (d, 3H, J = 6.4 Hz, Py-4-*H*), 9.94 (br s, 3H, Py-2-*H*);

3.2.5. Zinc(II) insertion into the porphyrins 12-19

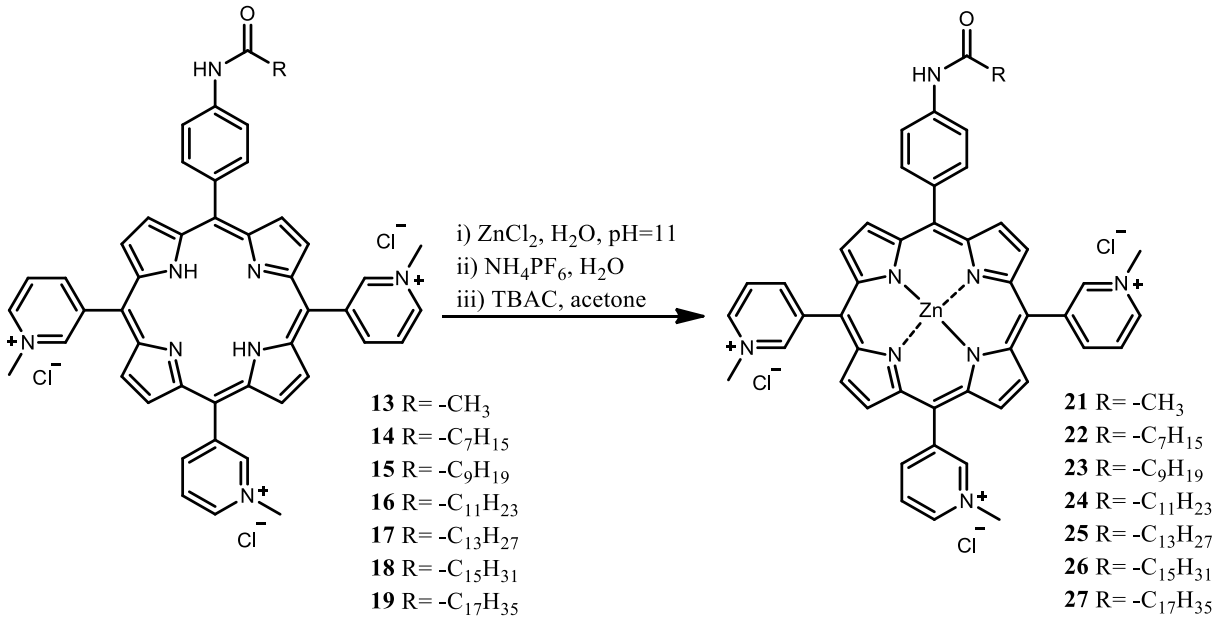

Scheme 8. Synthesis of porphyrins **21**-**27**.

The general method for Zn(II) insertion was applied on porphyrins **13**-**19** after an optimization of the procedure on porphyrin **12** [163]. The reaction conditions and obtained masses and yields for the synthesis of porphyrins **21**-**27** were summarised in the **Table 3**. Free-base porphyrin (1 equiv.) was dissolved in H_2O and the solution was adjusted to pH = 11 using 1 M NaOH. Zinc chloride (10 equiv.) was added and the solution was stirred at room temperature for 1-1:30 h. Reaction was monitored using TLC on silica TLC plates with 8:1:1 MeCN:H_2O:$KNO_{3(sat.)}$ as solvent, as well as following the change in pH of the solution (pH = 11 to pH = 6). Upon completion of the reaction, saturated solution of NH_4PF_6 in H_2O was added until precipitation. Solution was centrifuged and the residue was washed once again with water. The product was collected by filtration, and dissolved in acetone. Tetrabutylammonium chloride (TBAC), previously dissolved in acetone, was added until precipitation. After centrifuge of the solution, the residue was washed with acetone. The washing procedure was repeated three times, and the final product was collected by filtration. After drying, this solid was dissolved in a minimum amount of MeOH, and Et_2O was added until precipitation. The washing procedure was repeated three times with Et_2O and the product was collected by filtration. The products were isolated as dark purple to green solids.

Table 3. Summarized reaction conditions and obtained masses and yields for porphyrins **21**-**27**.

Porphyrin	Mass & Molarity, Porphyrin code	Mass & Molarity of $ZnCl_2$	Mass & Yield of obtained product
21	32 mg, 0.038 mmol (**13**)	53 mg, 0.38 mmol	31 mg, 90%
22	21 mg, 0.023 mmol (**14**)	35 mg, 0.26 mmol	21 mg, 90%
23	27 mg, 0.028 mmol (**15**)	45 mg, 0.33 mmol	22 mg, 78%
24	32 mg, 0.033 mmol (**16**)	56 mg, 0.41 mmol	30 mg, 89%
25	26 mg, 0.026 mmol (**17**)	37 mg, 0.27 mmol	25 mg, 90%
26	24 mg, 0.023 mmol (**18**)	35 mg, 0.26 mmol	24 mg, 96%
27	24 mg, 0.022 mmol (**19**)	42 mg, 0.30 mmol	21 mg, 82%

3.2.5.1. Zinc(II) 5,10,15,20-tetrakis(*N*-methylpyridinium-3-yl)porphyrin tetrachloride (20)

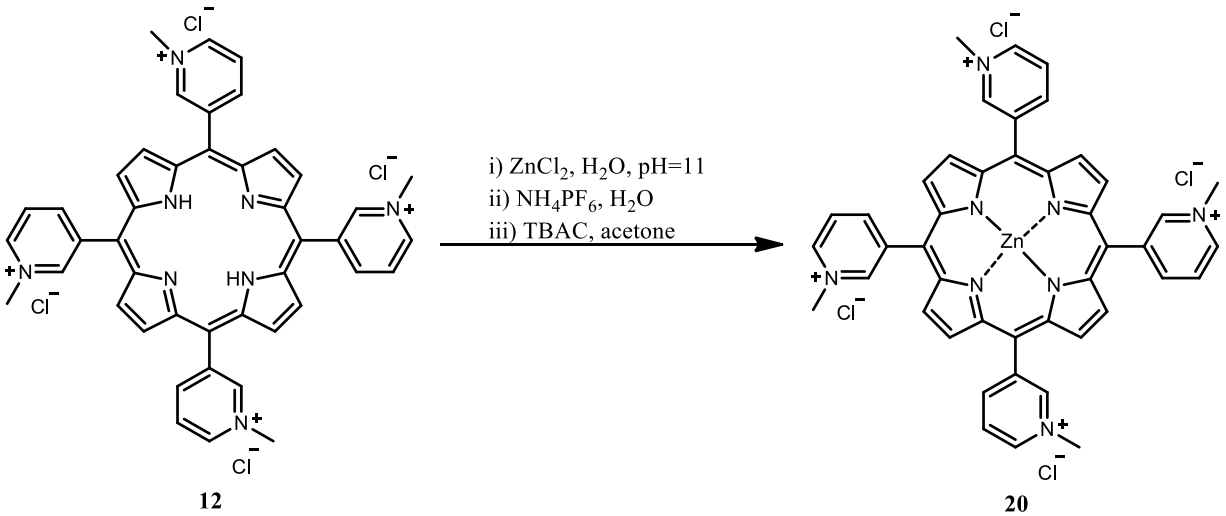

Scheme 9. Synthesis of porphyrin **20**.

Method A: Porphyrin **12** (11 mg, 0.015 mmol, 1 equiv.) was dissolved in 30 mL of DEMI H_2O. Zinc acetate ($Zn(OAc)_2$) (32 mg, 0.17 mmol, 12 equiv.) was added as a solid and the reaction mixture was stirred overnight. Upon completion of the reaction and following the purification procedure as in the general method, porphyrin **20** was isolated as a dark purple-green solid (8 mg, 65%).

Method B: Porphyrin **12** (33 mg, 0.04 mmol, 1 equiv.) was dissolved in 30 mL of H_2O and pH was adjusted to pH = 11. Zinc chloride (59 mg, 0.43 mmol, 11 equiv.) was added as a solid and the reaction mixture was stirred for 1 hour. Upon completion of the reaction and purification procedure carried out as in the general method, porphyrin **20** was isolated as a dark purple-green solid (26 mg, 73%).

^{1}H NMR (DMSO, 600 MHz): δ/ppm 4.71 (s, 12H, 4N-C*H*$_3$), 8.56-8.61 (m, 3H, Py-5-*H*), 8.96 9.06 (s, 8H, β-*H*), 9.20–9.29 (m, 3H, Py-6-*H*), 9.54 (d, 4H, *J* = 6.1 Hz, Py-4-*H*), 9.95 (s, 4H, Py-2-*H*);

3.2.5.2. Zinc(II) 5-(4-acetamidophenyl)-10,15,20-tris(*N*-methylpyridinium-3-yl)porphyrin trichloride (21)[163]

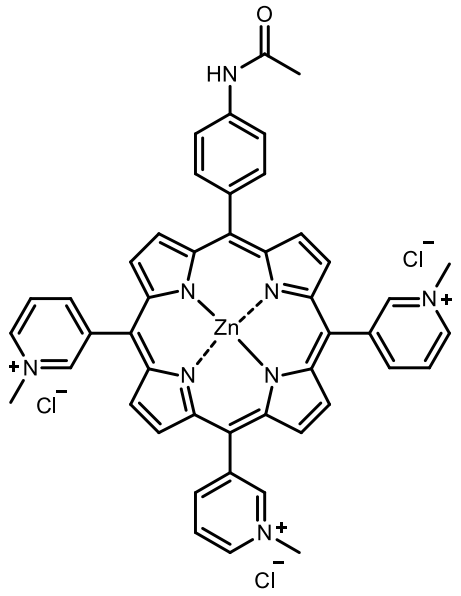

21

^{1}H NMR (CD_3OD, 600 MHz): δ/ppm 2.32 (s, 3H, -COC*H*$_3$), 4.79 (s, 9H, 3 N-C*H*$_3$), 8.00–8.05 (m, 2H, Ar-3,5-*H*), 8.16 (d, 2H, *J* = 8.3 Hz, Ar-2,6-*H*), 8.54-8.58 (m, 3H, Py-5-*H*), 8.96 (d, 2H, *J* = 4.6 Hz, β-3,7-*H*), 9.08–9.11 (m, 6H, β-2,8,12,13,17,18-*H*), 9.31–9.36 (m, 3H, Py-6-*H*), 9.40 (d, 3H, *J* = 5.9 Hz, Py-4-*H*), 9.88 (br s, 3H, Py-2-*H*);

^{13}C NMR (CD_3OD, 150 MHz): δ/ppm 22.7, 111.6, 112.4, 118.1, 123.5, 125.5, 131.2, 131.9, 132.2, 133.7, 134.7, 137.8, 138.7, 143.4, 144.5, 147.4, 148.0, 148.0, 149.6, 150.0, 150.1, 151.5, 170.8;

HRMS (MALDI): theor. calcd. for $C_{46}H_{37}N_8OZn$ $[M–2H]^+$ 781.2382; exp. 781.2407.

3.2.5.3. Zinc(II) 5-(4-octanamidophenyl)-10,15,20-tris(*N*-methylpyridinium-yl)porphyrin trichloride (22)

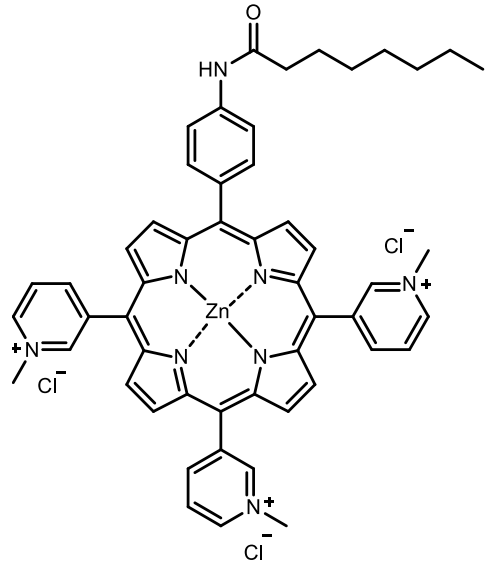

22

^{1}H NMR (CD_3OD, 600 MHz): δ/ppm 0.96 (t, 3H, J = 6.4 Hz, -CH_3), 1.35-1.56 (m, 8H, C$^4H_2$(CH_2)$_2$C$^7H_2$), 1.82-1.89 (m, 2H, C$^3H_2$), 2.57 (t, 2H, J = 7.2 Hz, COC$^2H_2$), 4.77 (s, 9H, 3 N-CH_3), 7.99-8.06 (m, 2H, Ar-3,5-*H*), 8.13-8.18 (m, 2H, Ar-2,6-*H*), 8.50-8.56 (m, 3H, Py-5-*H*), 8.91-9.15 (m, 8H, β-*H*), 9.29-9.46 (m, 6H, overlapping Py-6-*H* and Py-4-*H*), 9.88 (br s, 3H, Py-2-*H*);

^{13}C NMR (CD_3OD, 150 MHz): δ/ppm 13.1, 22.4, 25.7, 28.9, 29.1, 31.6, 36.8, 47.9, 111.6, 112.4, 118.1, 123.6, 125.8, 131.2, 131.9, 132.2, 133.7, 134.7, 137.8, 138.7, 143.4, 144.6, 147.5, 147.9, 147.9, 149.6, 150.0, 150.1, 151.6, 173.9;

HRMS: theor. calcd. for $C_{652}H_{49}N_8OZn$ $[M]^{3+}$ 288.4440; exp. 288.4446.

3.2.5.4. Zinc(II)-5-(4-decanamidophenyl)-10,15,20-tris(*N*-methylpyridinium-yl)porphyrin trichloride (23)

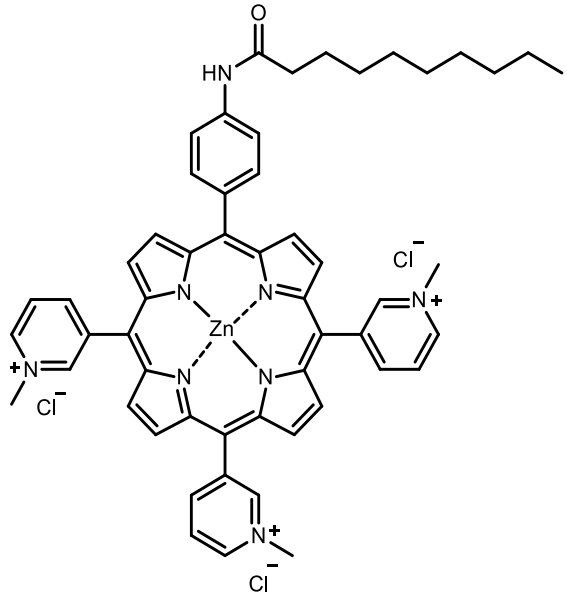

23

^{1}H NMR (CD$_3$OD, 600 MHz): δ/ppm 0.93 (t, 3H, J = 6.9 Hz, -C^{10}*H$_3$*), 1.32-1.55 (m, 12H, C^{4}*H$_2$*(C*H$_2$*)$_4$C^{9}*H$_2$*), 1.80-1.87 (m, 2H, C^{3}*H$_2$*), 2.57 (t, 2H, J = 7.5 Hz, COC^{2}*H$_2$*), 4.77 (s, 9H, 3 N-C*H$_3$*), 8.00-8.06 (m, 2H, Ar-3,5-*H*), 8.15 (d, 2H, J = 8.2 Hz, Ar-2,6-*H*), 8.50-8.55 (m, 3H, Py-5-*H*), 8.96 (d, 2H, J = 4.6 Hz, β-3,7-*H*), 9.04-9.12 (m, 6H, β-2,8,12,13,17,18-*H*), 9.33 (t, 3H, J = 7.2 Hz Py-6-*H*), 9.39-9.42 (m, 3H, Py-4-*H*), 9.88 (br s, 3H, Py-2-*H*);

^{13}C NMR (CD$_3$OD, 150 MHz): δ/ppm 13.1, 22.4, 25.7, 29.1,29.1, 29.2, 29.3, 31.7, 36.8, 47.9, 111.6, 112.4, 118.1, 123.5, 125.8, 131.2, 131.9, 132.2, 133.7, 134.7, 137.8, 138.7, 143.4, 144.6, 147.5, 148.0, 148.0, 149.6, 150.0, 150.1, 151.6, 173.9;

HRMS: theor. calcd. for $C_{54}H_{53}N_8OZn$ $[M]^{3+}$ 297.7878; exp. 297.7882.

3.2.5.5. Zinc(II)-5-(4-dodecanamidophenyl)-10,15,20-tris(*N*-methylpyridinium-3-yl)porphyrin trichloride (24)

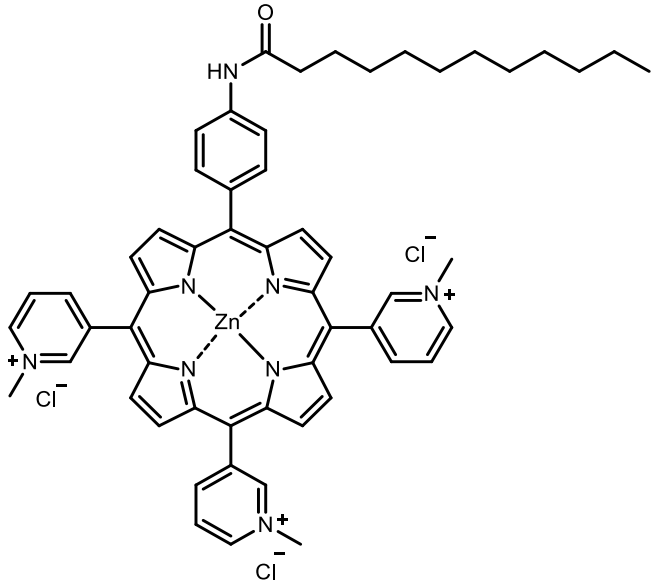

24

^{1}H NMR (CD_3OD, 600 MHz): δ/ppm 0.93 (t, 3H, J = 6.8 Hz, -C$^{12}H_3$), 1.27-1.54 (m, 16H, C$^{4}H_2$(CH_2)$_6$C$^{11}H_2$), 1.82-1.89 (m, 2H, C$^{3}H_2$), 2.56 (t, 2H, J = 7.5 Hz, COC$^{2}H_2$), 4.76-4.80 (m, 9H, 3 N-CH_3), 8.01-8.06 (m, 2H, Ar-3,5-*H*), 8.15 (d, 2H, J = 8.6 Hz, Ar-2,6-*H*), 8.49-8.57 (m, 3H, Py-5-*H*), 8.96 (d, 2H, J = 4.6 Hz, β-3,7-*H*), 9.04-9.12 (m, 6H, β-2,8,12,13,17,18-*H*), 9.30-9.34 (m, 3H, Py-6-*H*), 9.38-9.42 (m, 3H, Py-4-*H*), 9.88 (br s, 3H, Py-2-*H*);

^{13}C NMR (CD_3OD, 150 MHz): δ/ppm 13.1, 22.4, 25.7, 29.0, 29.1, 29.2, 29.3, 29.4(d), 31.7, 36.8, 48.2, 111.6, 112.5, 118.1, 123.5, 125.8, 131.2, 131.9, 132.2, 133.7, 134.7, 137.8, 138.7, 143.4, 144.6, 147.4, 148.0, 149.7, 150.0, 150.1, 151.6, 173.9;

HRMS: theor. calcd. for $C_{56}H_{57}N_8OZn$ $[M]^{3+}$ 307.1316; exp. 307.1320.

3.2.5.6. Zinc(II) 5-(4-tetradecanamidophenyl)-10,15,20-tris(*N*-methylpyridinium-3-yl)porphyrin trichloride (25)

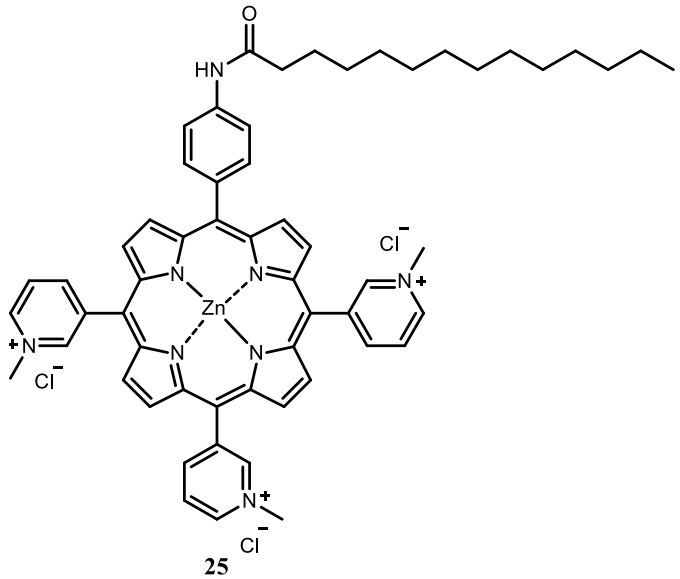

25

^{1}H NMR (CD_3OD, 600 MHz): δ/ppm 0.89 (t, 3H, J = 7.0 Hz -C$^{14}H_3$), 1.25-1.56 (m, 20H, C$^{3}H_2$(CH_2)$_8$C$^{13}H_2$), 1.82-1.89 (m, 2H, C$^{3}H_2$), 2.57 (t, 2H, J = 7.5 Hz, COC$^{2}H_2$), 4.78 (s, 9H, 3 N-CH_3), 8.01-8.06 (m, 2H, Ar-3,5-*H*), 8.15 (d, 2H, J = 8.3 Hz, Ar-2,6-*H*), 8.51-8.56 (m, 3H, Py-5-*H*), 8.96 (d, 2H, J = 4.6 Hz, β-3,7-*H*), 9.04-9.12 (m, 6H, β-2,8,12,13,17,18-*H*), 9.31-9.36 (m, 3H, Py-6-*H*), 9.39-9.42 (m, 3H, Py-4-*H*), 9.88 (br s, 3H, Py-2-*H*);

^{13}C NMR (CD_3OD, 150 MHz): δ/ppm 13.1, 22.4, 25.7, 29.0, 29.1, 29.2, 29.3, 29.4, 29.4, 31.7, 36.8, 47.9, 111.6, 112.4, 118.1, 123.6, 125.8, 131.2, 131.9, 132.2, 133.7, 134.7, 137.8, 138.7, 143.3, 144.5, 147.4, 147.9, 149.6, 150.0, 150.1, 151.6, 173.9;

HRMS: theor. calcd. for $C_{58}H_{61}N_8OZn$ $[M]^{3+}$ 316.4753; exp. 316.4757.

3.2.5.7. Zinc(II) 5-(4-hexadecanamidophenyl)-10,15,20-tris(*N*-methylpyridinium-3-yl)porphyrin trichloride (26)

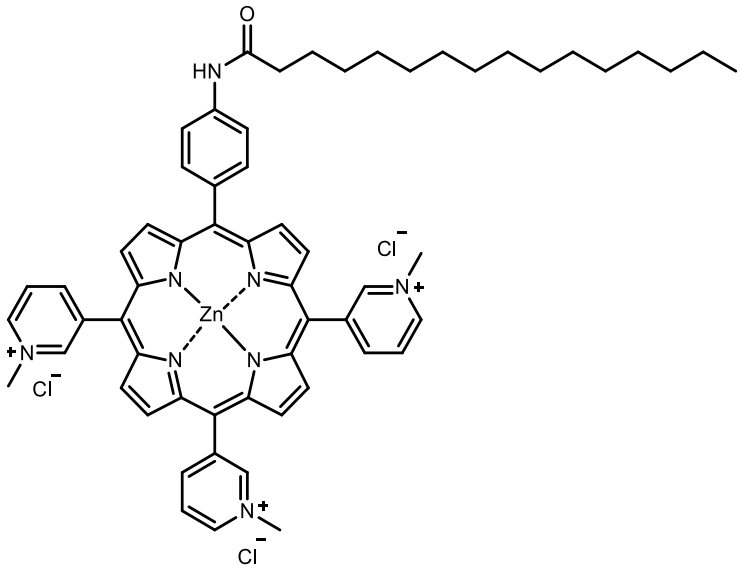

26

^{1}H NMR (CD$_3$OD, 600 MHz): δ/ppm 0.86 (t, 3H, J = 7.0 Hz, -C$^{16}H_3$), 1.22-1.56 (m, 24H, C$^{4}H_2$(CH_2)$_{10}$C$^{15}H_2$), 1.82-1.88 (m, 2H, C$^{3}H_2$), 2.57 (t, 2H, J = 7.5 Hz, COC$^{2}H_2$), 4.77 (s, 9H, 3 N-CH_3), 8.00-8.06 (m, 2H, Ar-3,5-*H*), 8.15 (d, 2H, J = 8.3 Hz, Ar-2,6-*H*), 8.51-8.55 (m, 3H, Py-5-*H*), 8.96 (d, 2H, J = 4.6 Hz, β-3,7-*H*), 9.04-9.12 (m, 6H, β-2,8,12,13,17,18-*H*), 9.30-9.35 (m, 3H, Py-6-*H*), 9.38-9.42 (m, 3H, Py-4-*H*), 9.88 (br s, 3H, Py-2-*H*);

^{13}C NMR (CD$_3$OD, 150 MHz): δ/ppm 13.1, 22.3, 25.7, 29.0, 29.1, 29.2, 29.3, 29.4, 29.4, 31.7, 36.8, 48.0, 111.6, 112.4, 118.1, 123.6, 125.8, 131.2, 131.9, 132.2, 133.7, 134.7, 137.8, 138.7, 143.4, 144.6, 147.4, 148.0, 149.6, 150.0, 150.1, 151.6, 173.9;

HRMS: theor. calcd. for $C_{60}H_{65}N_8OZn$ $[M]^{3+}$ 325.8191; exp. 325.8196.

3.2.5.8. Zinc(II) 5-(4-octadecanamidophenyl)-10,15,20-tris(*N*-methylpyridinium-yl)porphyrin trichloride (27)

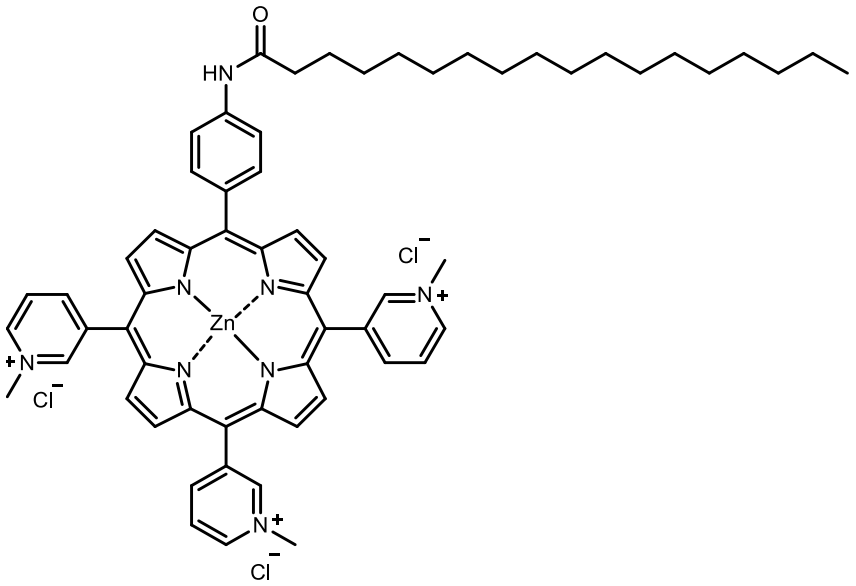

27

^{1}H NMR (CD$_3$OD, 600 MHz): δ/ppm 0.89 (t, 3H, J = 7.0 Hz, -C$^{18}H_3$), 1.20-1.59 (m, 28H, C$^{4}H_2$(CH_2)$_{12}$C$^{17}H_2$), 1.85-1.91 (m, 2H, C$^{3}H_2$), 2.59 (t, 2H, J = 7.5 Hz, COC$^{2}H_2$), 4.80 (s, 9H, 3 N-CH_3), 8.01-8.08 (m, 2H, Ar-3,5-*H*), 8.17 (d, 2H, J = 8.2 Hz, Ar-2,6-*H*), 8.53-8.58 (m, 3H, Py-5-*H*), 8.98 (d, 2H, J = 4.6 Hz, β-3,7-*H*), 9.07-9.13 (m, 6H, β-2,8,12,13,17,18-*H*), 9.33-9.37 (m, 3H, Py-6-*H*), 9.41-9.44 (m, 3H, Py-4-*H*), 9.90 (br s, 3H, Py-2-*H*);

^{13}C NMR (CD$_3$OD, 150 MHz): δ/ppm 13.0, 22.3, 25.7, 29.1, 29.2, 29.3, 29.4(m), 31.7, 36.8, 47.9, 111.6, 112.4, 118.1, 123.6, 125.8, 131.2, 131.9, 132.2, 133.7, 134.7, 137.8, 138.7, 143.4, 144.8, 147.5, 147.9, 149.7, 150.0, 150.1, 151.6, 173.9;

HRMS: theor. calcd. for $C_{62}H_{69}N_8OZn$ $[M]^{3+}$ 335.1629; exp. 335.1632.

3.2.6. *N*-oxidation of the porphyrins 1, 2, 7, 9 and 11

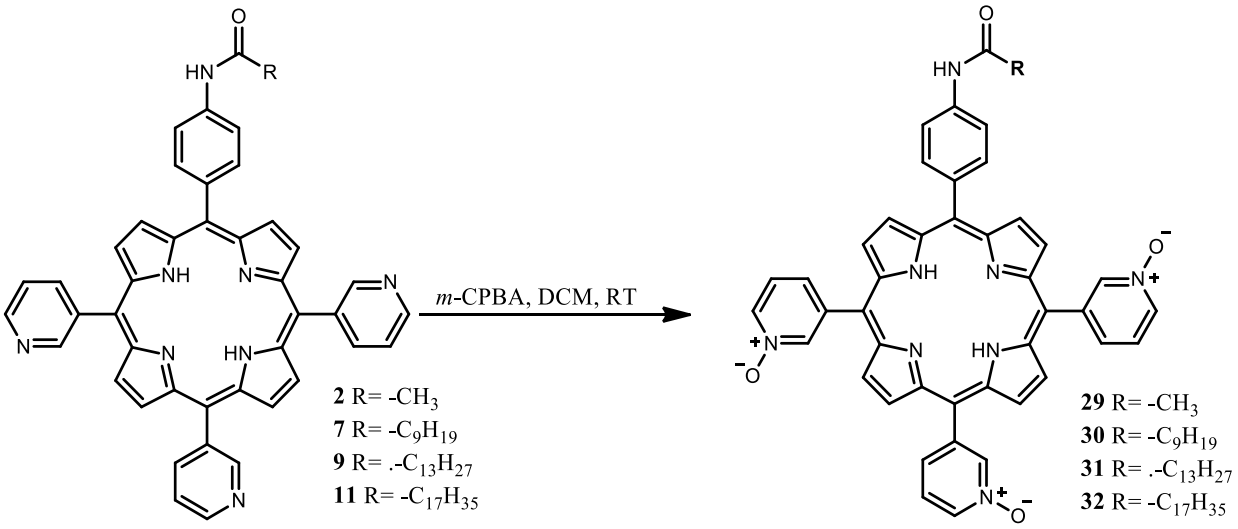

Scheme 10. Synthesis of porphyrin **29**-**31**.

A general method for the synthesis of porphyrins **29**-**31** was applied after optimization of the procedure for porphyrin **28** with modifications in purification steps for each porphyrin. Porphyrin (0.1 mmol, 1 equiv.) was dissolved in dry DCM (15 ml) and *meta*-chloroperbenzoic acid (*m*-CPBA) (2.0 mmol, 20 equiv.) was added gradually over 30 min under constant stirring at room temperature. After the oxidizing agent had been added, the reaction was stirred for a further 30 minutes. The reaction was monitored by TLC on silica gel plates with DCM:MeOH (9:1) as mobile phase. Upon completion of the reaction, propylamine (PrA) (1-2 mL) was added and the reaction was stirred for another 30 minutes. The solvent was removed *in vacuo*.

3.2.6.1. 5,10,15,20-tetrakis(1-oxido-3-pyridyl)porphyrin (28)

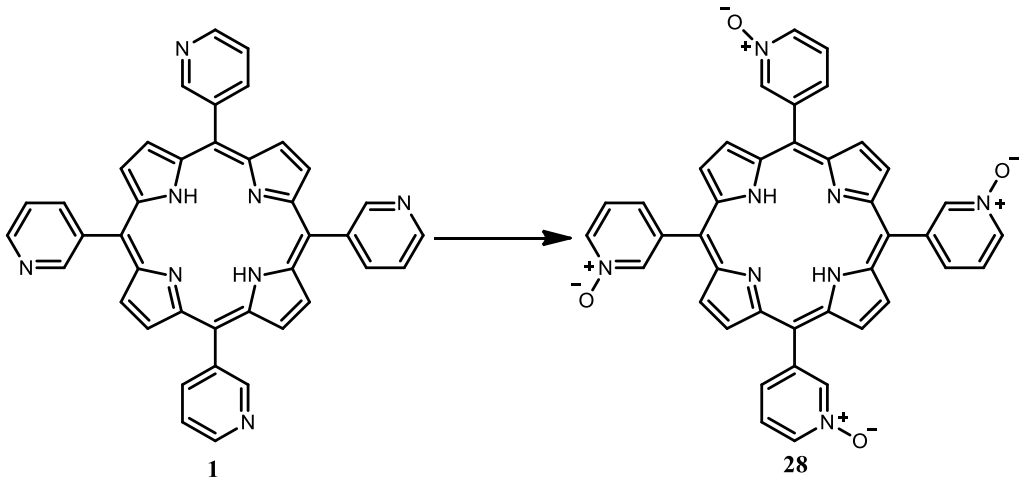

Scheme 11. Synthesis of porphyrin **28**.

Method A: Porphyrin **1** (25 mg, 0.04 mmol, 1 equiv.) was dissolved in DCM. Potassium peroxymonosulfate (OXONE®) (249 mg, 1.62 mmol, 20 equiv.) dissolved in H_2O was added stepwise over 1 hour and the pH of the reaction was adjusted to 7.6 - 7.7 with 1M $NaHCO_3$. Acetone was added to the reaction mixture in three sets of 0.5 mL every 10 minutes. After each addition of acetone (0.5 mL), the pH of the reaction was checked and adjusted if necessary. After addition of all reactants, the reaction was stirred for 2 hours at room temperature. The reaction was monitored by TLC with DCM/MeOH (9:1) as mobile phase. Upon completion of the reaction, the reaction mixture was washed with H_2O (3 × 20 mL) and the organic layer was dried over Na_2SO_4. After filtration, the product was purified by column chromatography with DCM:MeOH 10:1 as eluent. After removal of the solvent *in vacuo*, porphyrin **28** was isolated as a purple solid (18 mg, 66%).

Method B: The synthesis of porphyrin **1** (40 mg, 0.065 mmol, 1 equiv.) was performed following the general protocol described above. The obtained product was purified with column chromatography with DCM:MeOH (9:1) as eluent. After recrystallization in ethanol (EtOH), porphyrin **28** was isolated as purple powder (22 mg, 50%).

^{1}H NMR of **28** agrees with previously published data [72]:

^{1}H NMR (CD_3OD, 400 MHz): δ/ppm 7.75-7.86 (m, 4H, Py-5-*H*), 8.10-8.25 (m, 4H, Py-6-*H*), 8.70 (d, 4H, J = 6.7 Hz, Py-4-*H*), 8.79-9.09 (m, 12H, overlapping β-*H* and Py-2-*H*).

3.2.6.2. 5-(4-acetamidophenyl)-10,15,20-tris(1-oxido-3-pyridyl)porphyrin (29)

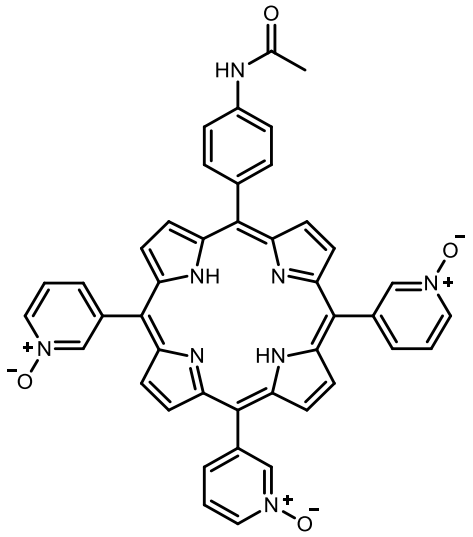

29

Porphyrin **2** (64 mg, 0.095 mmol, 1 equiv.) was dissolved in dry DCM (20 mL) and *m*-CPBA (291 mg, 1.69 mg, 18 equiv.) was added gradually over 30 min. Upon completion of the reaction, 1 mL of PrA and reaction was stirred for another 30 min. Solvent was removed *in vacuo*, and the reaction mixture was dissolved in DCM. The product was purified twice with column chromatography (1st 10: 1 DCM:MeOH, 2nd 5:1 DCM:MeOH). Porphyrin **29** was isolated as purple solid (42 mg, 61%).

^{1}H NMR of **29** agrees with the previously published data [72]:

^{1}H NMR ($CDCl_3$, 600 MHz): δ/ppm 2.95 (s, 2H, pyrrole-N*H*), 2.39 (s, 3H, -CH_3), 7.55 (s, 1H, N*H*-$COCH_3$), 7.67-7.77 (m, 3H, Py-5-*H*), 7.79-8.01 (m, 2H, Ar-3,5-*H*), 8.03-8.21 (m, 5H, overlapping Py-6-*H*, Ar-2,6-*H*), 8.68-8.72 (m, 3H, Py-4-*H*), 8.83-9.03 (m, 8H, β-*H*), 9.06 (s, 3H, Py-2-*H*).

3.2.6.3. 5-(4-decanamidophenyl)-10,15,20-tris(1-oxido-3-pyridyl)porphyrin (30)

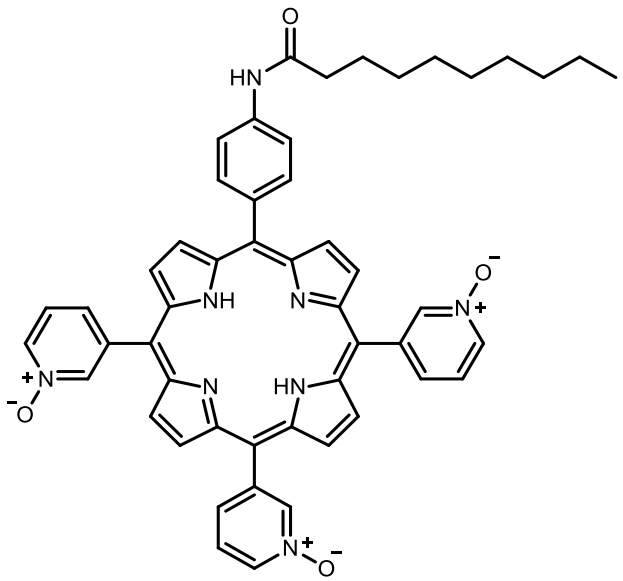

30

Porphyrin **7** (40 mg, 0.051 mmol, 1 equiv.) was dissolved in 15 ml of dry DCM and *m*-CPBA (179 mg, 1.02 mmol, 20 equiv.) was added gradually over 30 minutes. After all *m*-CPBA was added, the reaction was left to stir for another 30 minutes at room temperature. When the reaction was completed, PrA was added (1 mL) and reaction was left to stir for another 30 minutes. Solvent was removed *in vacuo*. Reaction mixture was dissolved in DCM (20 mL), and it was washed with H_2O (3 × 20 mL). Organic layer was dried over Na_2SO_4 and filtered. The product was purified twice with column chromatography with DCM/MeOH 10:1 used as a mobile phase. Porphyrin **30** was isolated as a violet solid (31 mg, 73%).

^{1}H NMR (CD_3OD, 600 MHz): δ/ppm 0.93 (t, 3H, J = 6.9 Hz, -C$^{10}H_3$), 1.24-1.51 (m, 12H, C$^4H_2$(CH_2)$_4$C$^9H_2$), 1.78-1.85 (m, 2H, C$^3H_2$), 2.53 (t, 2H, J = 7.5 Hz, C$^2H_2$), 7.83-8.02 (m, 7H, overlapping Py-5-*H*, Ar-2,6-*H*, Ar-3,5-*H*), 8.25-8.38 (m, 3H, Py-6-*H*), 8.69-9.23 (m, 14H, overlapping Py-4-*H*, β-*H*, Py-2-*H*);

^{13}C NMR ($CDCl_3$, 150 MHz): δ/ppm 13.1, 22.3, 25.6, 29.0, 29.1, 29.2, 29.3, 31.7, 36.8, 112.6, 113.2, 118.1, 122.1, 124.9, 134.2, 134.6, 136.2, 138.7, 138.8, 141.1, 142.5, 173.6;

HRMS: theor. calcd. for $C_{55}H_{54}N_8O_4$ $[M+H]^+$ 835.3720; exp. 835.3720.

3.2.6.4. 5-(4-tetradecanamidophenyl)-10,15,20-tris(1-oxido-3-pyridyl)porphyrin (31)

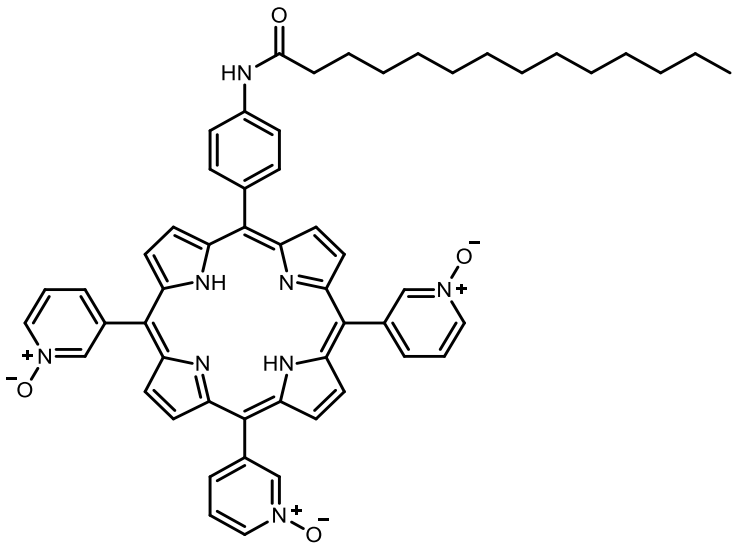

31

Porphyrin **9** (53 mg, 0.06 mmol, 1 equiv.) was dissolved in dry DCM and *m*-CPBA (217 mg, 1.25 mmol, 20 equiv.) was added gradually over 30 min under constant stirring and then stirred for further 30 min at room temperature. Upon completion of the reaction, PrA (2 mL) was added, and reaction was stirred for another 30 min. Solvent was removed under pressure and the reaction mixture was dissolved in H_2O: trifluoroacetic (TFA) (20:1) solution. Reaction was neutralized (pH = 8) and precipitated by adding 1M NaOH. Reaction mixture was extracted with DCM (2×20 mL) and organic layer was further washed with H_2O (2 × 20 mL). Organic layer was dried over Na_2SO_4 and filtered. The product was further purified twice with column chromatography (1st 15:1 DCM:MeOH; 2nd 10:1 DCM:MeOH). Porphyrin **31** was isolated as purple solid (44 mg, 79%)

^{1}H NMR ($CDCl_3$, 600 MHz): δ/ppm -2.94 (s, 2H, pyrrole N*H*), 0.90 (t, 3H, J = 7.0 Hz, -$C^{14}H_3$), 1.22-1.56 (m, 20H, $C^4H_2(CH_2)_8C^{13}H_2$), 1.87-1.95 (m, 2H, C^3H_2), 2.60 (t, 2H, J = 7.6 Hz, C^2H_2), 7.69-7.77 (m, 3H, Py-5-*H*), 7.95-8.25 (m, 7H, overlapping Py-6-*H*, Ar-2,6-*H*, Ar-3,5-*H*), 8.72 (d, 3H, J = 6.3 Hz, Py-4-*H*), 8.85-9.05 (m, 8H, β-*H*), 9.06-9.13 (m, 3H, Py-2-*H*);

^{13}C NMR ($CDCl_3$, 150 MHz): δ/ppm 14.2, 22.7, 25.8, 29.3, 29.5, 29.6, 29.7, 29.8, 31.9, 38.1, 112.8, 113.5, 118.2, 124.3, 131.3, 135.2, 136.6, 138.5, 139.0, 141.0, 143.0, 172.0;

HRMS: theor. calcd. for $C_{55}H_{54}N_8O_4$ $[M+H]^+$ 891.4346; exp. 891.4345.

3.2.6.5. 5-(4-octadecanamidophenyl)-10,15,20-tris(1-oxido-3-pyridyl)porphyrin (32)

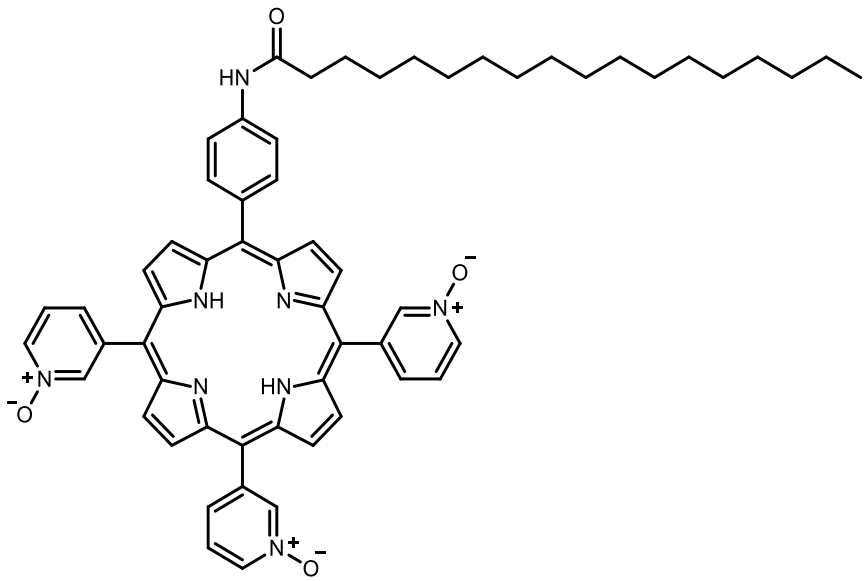

32

Porphyrin **11** (63 mg, 0.07 mmol, 1 equiv.) was dissolved in dry DCM and *m*-CPBA (243 mg, 1.41 mmol, 20 equiv.) was added gradually over 30 min and then stirred for another 30 min at room temperature. Upon completion of the reaction, PrA (1 mL) was added, and the reaction was stirred for another 30 minutes. The solvent was removed under pressure and the reaction mixture was dissolved in H_2O:TFA (20:1). The reaction was neutralized (pH = 8) and precipitated by adding 1M NaOH. The reaction mixture was extracted with DCM (2 × 20 mL) and the organic layer was washed with H_2O (2 × 20 mL). The organic layer was dried over Na_2SO_4 and filtered. The product was further purified twice by column chromatography with DCM/MeOH (15:1) used as a mobile phase. Porphyrin **32** was isolated as a violet solid (26 mg, 39%).

^{1}H NMR of **32** agrees with the previously published data [72]:

^{1}H NMR (CD_3OD, 600 MHz): δ/ppm 0.87 (t, 3H, J = 6.9 Hz, $C^{18}H_3$), 1.20-1.54 (m, 28H, $C^4H_2(CH_2)_{12}C^{17}H_2$), 1.83-1.91 (m, 2H, C^3H_2), 2.56 (t, 2H, J = 7.6 Hz, C^2H_2), 7.79-7.87 (m, 3H, Py-5-*H*), 7.89-8.11 (m, 2H, Ar-3,5-*H*), 8.12-8.18 (m, 2H, Ar-2,6-*H*), 8.18-8.28 (m, 3H, Py-6-*H*), 8.71-8.76 (m, 3H, Py-4-*H*), 8.76-9.17 (m, 11H, overlapping β-*H* and Py-2-*H*).

3.2.7. Gallium(III) insertion to the porphyrins 13, 15, 17 and 19

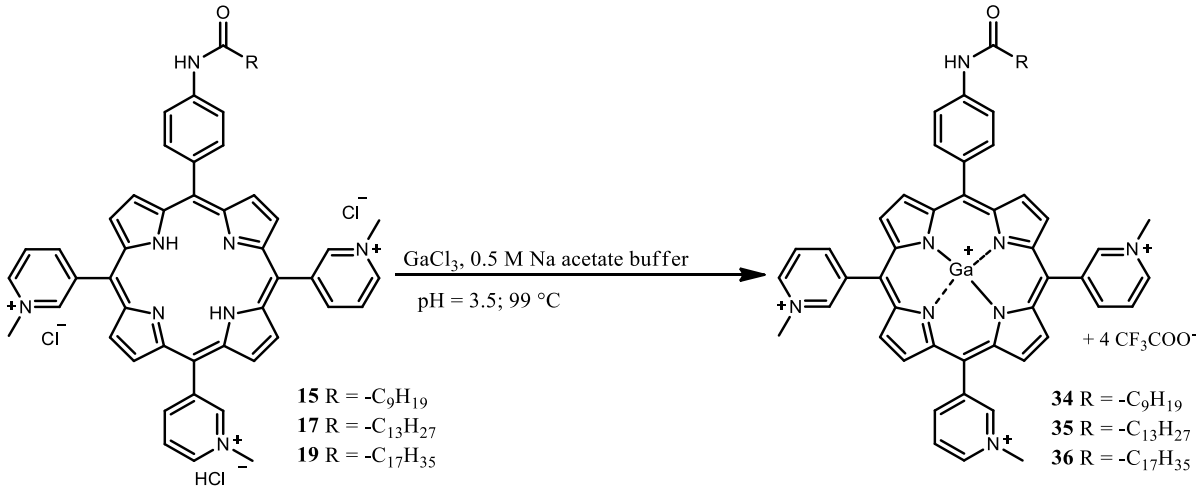

Scheme 11. Synthesis of porphyrins **34**-**36**.

A general procedure was used for Ga(III) insertion into porphyrins **13**, **15**, **17** and **19**, with the purification step modified for each obtained porphyrin. The porphyrins (~0.03 mmol, 1 equiv.) were dissolved in sodium acetate (0.5 M, pH = 3.5) and gallium chloride, $GaCl_3$ (~0.3 mmol, 10 equiv.) was added to the reaction. The reaction was heated to 100 °C and stirred for 30 minutes to 1 hour, monitored by TLC with MeCN:H_2O:$KNO_{3(sat.)}$ (8:1:1) as mobile phase and by analytical high-pressure liquid chromatography (HPLC) with MeOH + 0.1% trifluoroacetic acid (TFA) (Solvent A) and H_2O + 0.1% TFA (Solvent B) (Phenomenex Luna C18, 125 x 4 mm, 5 µm particle size) with the conditions varied for each porphyrin due to their different lipophilicity.

3.2.7.1. Ga(III) 5-(4-acetamidophenyl)-10,15,20-tris(*N*-methylpyridinium-3-yl)porphyrin tetrachloride (33)

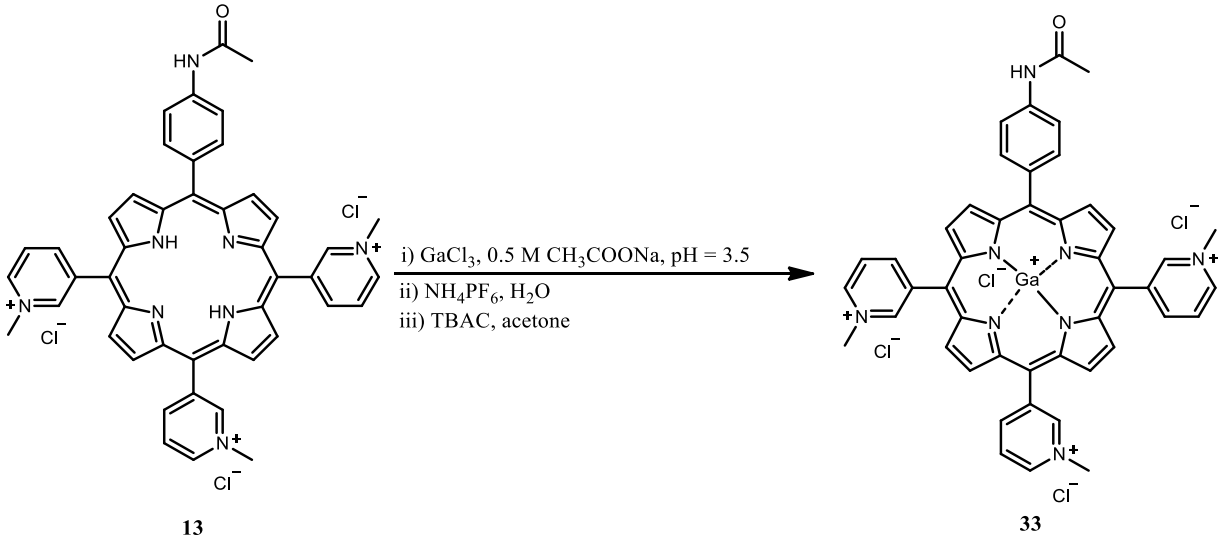

Scheme 12. Synthesis of porphyrin **33**.

Porphyrin **13** (22 mg, 0.026 mmol, 1 equiv.) was dissolved in 15 mL 0.5 M sodium acetate, pH = 3.5. Gallium chloride, $GaCl_3$ (46 mg, 0.26 mmol, 10 equiv.) was added to the solution and the reaction was stirred for 30 minutes at 100 °C. Upon completion of the reaction, monitored using TLC and HPLC, NH_4PF_6 was added to the reaction until precipitation. The reaction mixture was centrifuged, supernatant removed, and precipitate resuspended in H_2O. After this step was repeated, the pellet was collected by filtration and dissolved in acetone. Saturated solution of TBAC was added until precipitation. Precipitate was washed three times with acetone and the solid was collected by filtration. The final step included dissolving the solid in MeOH and addition of the Et_2O until precipitation. After three rounds of washing the precipitate with Et_2O, the porphyrin **33** collected by filtration and isolated as pink powder (27 mg, 84%).

Analytical HPLC conditions: 0 min 20% A, 12 min 70% A, 13 min 100% A, 16 min 100% A, 17 min 20% A, 20 min 20% A;

^{1}H NMR (CD_3OD, 600 MHz): δ/ppm 2.35 (s, 3H, -C*H*$_3$), 4.82 (s, 9H, 3 N-C*H*$_3$), 8.02-8.16 (m, 2H, Ar-3,5-*H*), 8.20-8.26 (m, 2H, Ar-2,6-*H*), 8.56-8.66 (m, 3H, Py-5-*H*), 9.20-9.53 (m, 14H, overlapping Py-6-*H*, β-*H*, Py-4-*H*), 9.98-10.07 (m, 3H, Py-2-*H*);

MALDI-MS (HABA, TFA): *m/z* 783.7 $[M-3H]^+$.

3.2.7.2. Ga(III) 5-(4-decanamidophenyl)-10,15,20-tris(*N*-methylpyridinium-yl)porphyrin tetratrifluoroacetate (34)

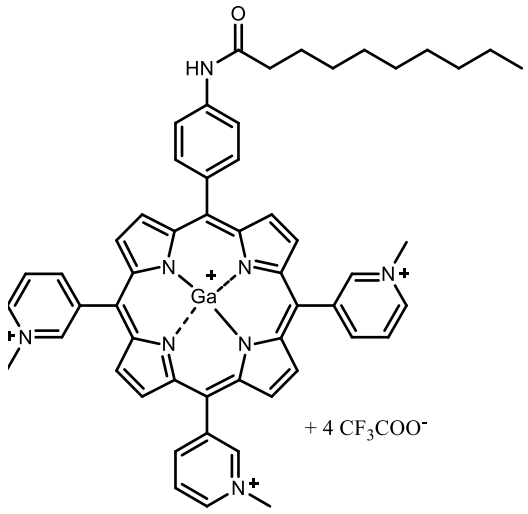

34

Porphyrin **13** (26 mg, 0.027 mmol, 1 equiv.) was dissolved in 0.5 M sodium acetate buffer (15 mL, pH = 3.5) and $GaCl_3$ (95 mg, 0.53 mmol, 20 equiv.) was added to the reaction mixture. The reaction was left to stir at 99 °C for 30 minutes. Upon completion of the reaction, checked by TLC and HPLC, reaction was purified with HPLC, using following conditions: Solvent A: MeOH + 0.1% TFA, Solvent B: H_2O + 0.1% TFA) 0 min 30% A, 5 min 30% A, 6 min 50% A, 20 min 70% A, 22 min 100% A, 26 min 100% A, 27 min 30% A, 30 min- 30% A. After purification, solvent was removed under pressure using the dry-ice rotary evaporator. Excess TFA was removed by purification on tBuC18 SepPak columns. Prior to the purification, tBuC18 Sep-Pak columns were activated by flushing with 1 mL of EtOH and 1 mL of water. After loading the product on column, TFA was extracted with water. Product was eluted from column with MeOH and solvent was removed *in vacuo*. Product was re-dissolved in small amount of H_2O. After lyophilization, porphyrin **34** was isolated as dark pink powder (12 mg, 38%).

Analytical HPLC conditions: 0 min 50% A, 12 min 100% A, 15 min 100% A, 16 min 50% A, 20 min 50% A;

^{1}H NMR (CD_3OD, 600 MHz): δ/ppm 0.96 (t, 3H, J = 6.9 Hz, -C$^{10}H_3$), 1.31-1.59 (m, 12H, C$^4H_2$(CH_2)$_4$C$^9H_2$), 1.84-1.92 (m, 2H, C$^3H_2$), 2.60 (t, 2H, J = 7.4 Hz, C$^2H_2$), 4.80 (s, 9H, 3x N-CH_3), 8.11 (d, 2H, J = 7.8 Hz, Ar-3,5-*H*), 8.23 (d, 2H, J = 7.8 Hz, Ar-2,6-*H*); 8.57-8.63 (m, 3H, Py-5-*H*), 9.19-9.54 (m, 14H, overlapping Py-6-*H*, β-*H*, Py-4-*H*), 9.97 (s, 3H, Py-2-*H*);

MALDI-MS (HABA, TFA): *m/z* 895.9 $[M-3H]^+$.

3.2.7.3. Ga(III) 5-(4-tetradecanamidophenyl)-10,15,20-tris(*N*-methylpyridinium-yl)porphyrin tetratrifluoroacetate (35)

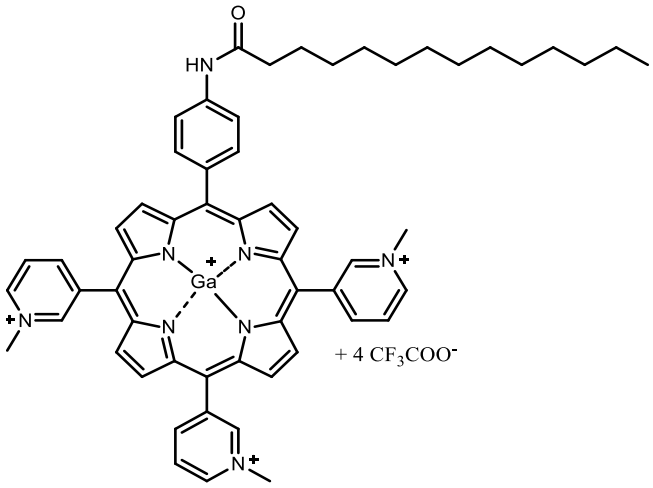

35

Porphyrin **17** (24 mg, 0.024 mmol, 1 equiv.) was dissolved in 15 mL 0.5 M sodium acetate, pH = 3.5 and $GaCl_3$ was added in excess (170 mg, 40 equiv.) and the reaction was stirred at 99 °C for 1 hour. Reaction was monitored using TLC and HPLC, with the following conditions: Solvent A: MeOH+ 0.1% TFA, Solvent B: H_2O + 0.1% TFA) 0 min 30% A, 5 min 30% A, 6 min 70% A, 20 min 100% A, 25 min 100% A, 26 min 30% A, 30 min 30% A. Solution was evaporated using the dry-ice rotary evaporator and the TFA was removed by flushing through, previously activated, tBuC18 Sep-Pak columns. After purification, solvent was removed *in vacuo*. Product was dissolved in water and dried out using lyophilization. Porphyrin **35** was isolated as pink solid (9 mg, 28%).

Analytical HPLC conditions: 0 min 70% A, 12 min 100% A, 16 min 100% A, 17 min 70% A, 20 min 70% A.

^{1}H NMR (CD_3OD, 600 MHz): δ/ppm 0.92 (t, 3H, J = 7.0 Hz, $C^{14}H_3$),1.25-1.60 (m, 20H, $C^4H_2(CH_2)_8C^{13}H_2$), 1.83-1.91 (m, 2H, C^3H_2), 2.60 (t, 2H, J = 7.4 Hz, C^2H_2), 4.80 (s, 9H, 3x N-CH_3), 8.12 (d, 2H, J = 7.7 Hz, Ar-3,5-*H*), 8.23 (d, 2H, J = 7.7 Hz, Ar-2,6-*H*), 8.61 (t, 3H, J = 6.5 Hz, Py-5-*H*), 9.20-9.56 (m, 14 H, overlapping Py-6-*H*, β-*H*, Py-4-*H*), 9.98 (s, 3H, Py-2-*H*);

MALDI-MS (HABA, TFA): *m/z* 951.9 $[M-3H]^+$, 937.9 $[M-CH_3-2H]^+$.

3.2.7.4. Ga(III) 5-(4-octadecanamidophenyl)-10,15,20-tris(*N*-methylpyridinium-yl)porphyrin tetratrifluoroacetate (36)

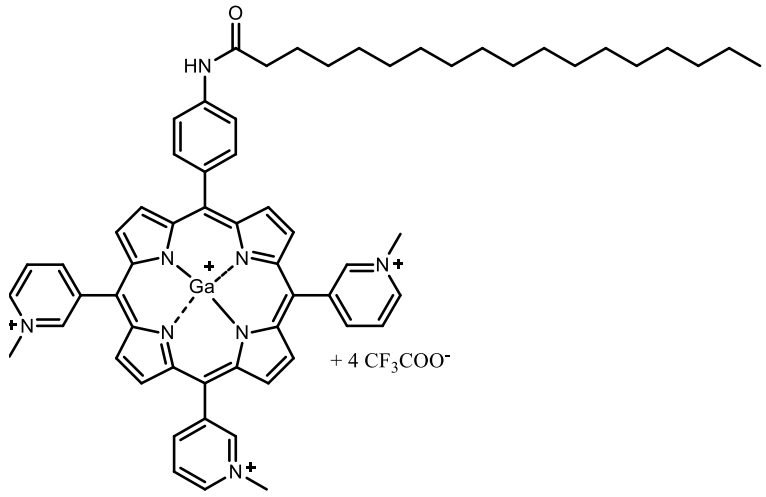

36

Porphyrin **19** (11 mg, 0.01 mmol, 1 equiv.) was dissolved in 5 mL 0.5 M sodium acetate buffer, pH = 3.5 and $GaCl_3$ (74 mg, 0.42 mmol, 40 equiv.) was added to the reaction mixture. Reaction was heated for 30 min at 100 °C under constant stirring. Upon completion of the reaction, reaction mixture was purified with preparative HPLC, using following conditions: Solvent A MeOH + 0.1% TFA, Solvent B: H_2O + 0.1% TFA); 0 min 30% A, 5 min 30% A, 6 min 80% A; 20 min 100% A, 25 min 100% A, 26 min 30% A, 30 min 30% A. Solvent was removed using a dry-ice rotary evaporator. To remove excess acid, the product was loaded on, previously activated, tBuC18 SepPak column. Acid was removed by washing the column with water and then the product was eluted with MeOH. After purification, solvent was removed *in vacuo*. Product was dissolved in water and dried out using lyophilization. Porphyrin **36** was isolated as pink solid (1.9 mg, 20%).

Analytical HPLC conditions: 0 min 80 % A, 12 min 100 % A, 16 min 100 % A, 17 min 80 % A, 20 min 80 % A.

^{1}H NMR (CD_3OD, 600 MHz): δ/ppm 0.92 (t, 3H, J = 6.9 Hz, -CH_3), 1.20-1.58 (m, 28H, C$^4H_2$(CH_2)$_{12}$C$^{17}H_2$), 1.84-1.92 (m, 2H, C$^3H_2$), 2.60 (t, 2H, J = 7.4 Hz, C$^2H_2$), 4.80 (s, 9H, 3 N-CH_3), 8.11 (d, 2H, J = 7.6 Hz, Ar-3,5-*H*), 8.22 (d, 2H, J = 7.6 Hz, Ar-2,6-*H*), 8.60 (t, 3H, J = 6.8 Hz, Py-5-*H*), 9.18-9.51 (m, 14H, overlapping Py-6-*H*, β-*H*, Py-4-*H*), 9.96 (s, 3H, Py-2-*H*);

MALDI-MS (HABA, TFA): *m/z* 994.2 $[M-CH_3-2H]^+$.

3.2.8. Reduction of porphyrin 2- 5-(4-acetamidophenyl)-10,15,20-tris(3-pyridyl)-17,18-dihidroporphyrin (37)

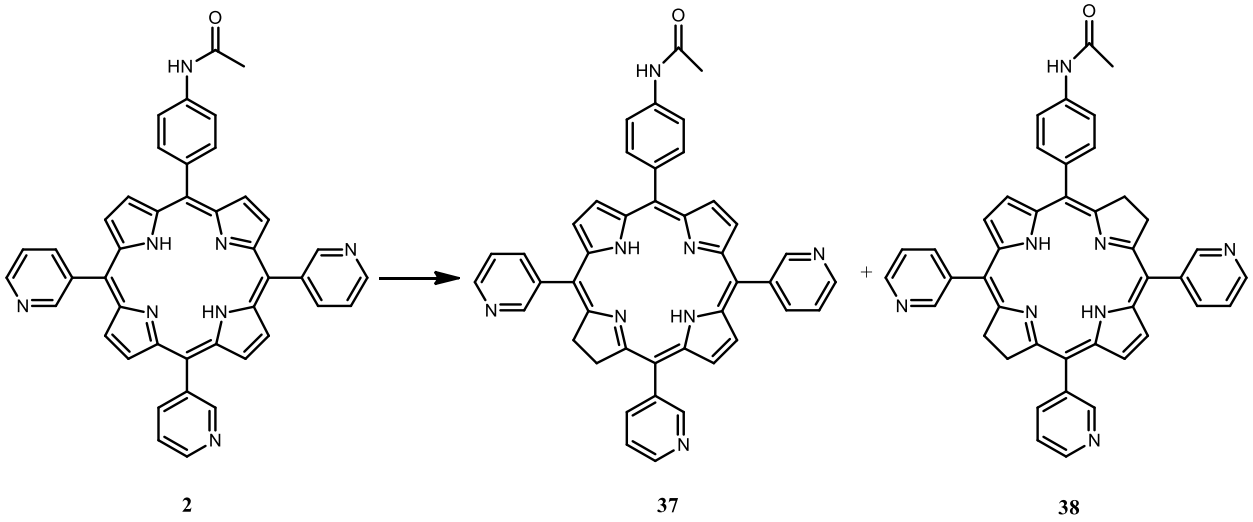

Scheme 13. Synthesis of chlorin **37** and bacteriochlorin **38** by reduction of porphyrin **2**.

Method A: Porphyrin **2** (22 mg, 0.03 mmol, 1 equiv.) was dissolved in dry pyridine (10 mL) and the reaction was purged with N_2 for 15 minutes. After the reaction was heated to 105 °C, *p*-toluenesulfonylhydrazide (*p*-TSH) and K_2CO_3 (46 mg, 0.33 mmol, 10 equiv.) were added to the reaction. The addition of *p*-TSH was carried out in three sets of 8, 8 and then 4 equiv. dissolved in dry pyridine (1 mL), with the first addition at the beginning of the reaction and the other two sets after two hours each. The reaction was refluxed for a total of 6.5 hours and monitored by TLC with DCM and MeOH (9:1) as eluent. Upon completion of the reaction, the solvent was removed *in vacuo*. The reaction mixture was dissolved in DCM (20 mL) and the 2,3-dichloro-5,6-dicyano-1,4-benzoquinone (DDQ) (25 mg, 0.11 mmol, 3.4 equiv.) was added gradually. The oxidation reaction was monitored by TLC and UV-Vis spectroscopy, and the addition of DDQ was stopped at the disappearance of the bacteriochlorin peak at ~720 nm. The reaction mixture was then washed with H_2O (2 × 20 mL) and the organic layer was dried over Na_2SO_4 and filtered. The product was further purified by column chromatography using DCM:MeOH (30:1) as mobile phase. The isolated second fraction was product **37**, chlorin, which was obtained as a red-brown solid with many impurities (3.4 mg).

Method B: Porphyrin **2** (22 mg, 0.03 mmol, 1 equiv.) and tin(II) chloride ($SnCl_2$) (13 mg, 0.07 mmol, 2 equiv.) were dissolved in 6 M HCl (10 mL). The reaction was heated to 65 °C

and stirred for 2 hours. After 2 hours, the heating was turned off and the reaction was stirred overnight at room temperature. The reaction was neutralized by adding Na_2CO_3 until the pH of the reaction was 8. The reaction was then extracted with DCM (2 × 10 mL) and the organic layer was further washed with H_2O (2 × 20 mL). The product was purified by column chromatography with DCM: MeOH in various ratios: the starting porphyrin **2** was isolated with DCM:MeOH (30:1), the product **37** with DCM:MeOH 20:1. Product **37**, chlorin, was isolated as a violet-red solid (4.5 mg, 20%).

^{1}H NMR (CD_3Cl, 600 MHz): δ/ppm 1.43 (s, 2H, pyrrole-N*H*), 1.26 (s, 3H, -NHCO-CH_3), 4.07-4.27 (m, 4H, C β-$^{17}H_2$-C β-$^{18}H_2$), 7.74-7.65 (m, 3H, Py-5-*H*), 8.20 (d, 2H, J = 5.0 Hz, Ar-3,5-*H*), 8.41 (s, 3H, Py-6-*H*), 8.58 (d, 2H, J = 5.0 Hz, Ar-2,6-*H*), 8.87 (s, 1H, β-2,3-*H*), 8.96 (dd, J = 5.0 Hz, 1.62 Hz, 2H, β-12, 13-*H*), 9.00 (dd, J = 5.0 Hz, 1.62 Hz, 2H, β-7,8-*H*), 9.17 (s, 3H, Py-4-*H*), 9.34 (s, 3H, Py-2-*H*).

3.3. Radioactive labelling of porphyrins 13, 15, 17 and 19 with [^{68}Ga]$GaCl_3$

Radioactive labelling of porphyrins **13**, **15**, **17** and **19** was performed in a PET Research Center at University of Hull under the supervision of Dr Juozas Domarkas. Germanium-68/gallium-68 generator (Eckert & Ziegler Cyclotron Co. Ltd.) is used to extract the positron-emitting isotope [^{68}Ga]gallium from a source of decaying [^{68}Ge]germanium. [^{68}Ga]gallium was eluted from Ge-68/Ga-68 generator using 4 mL of 0.05 M HCl. Given reaction mixture was purified using SXC column, to eliminate non-decayed [^{68}Ge]germanium from the solution. First wash was with the 20% of 0.1 M HCl in acetone (1 mL) to elute excess [^{68}Ge]germanium. To elute [^{68}Ga]gallium from the column, 1 mL 2% 0.1 M HCl in acetone was used. Before further manipulation, isolated radionuclide was dried in a vial under argon at 80 °C for few minutes. Porphyrin reaction mixture was prepared by mixing aqueous solution of porphyrin (2 mg/mL) and sodium acetate buffer (0.5 M, pH = 4.3). Reaction mixture was added to the ^{68}Ga with the adjustment of pH (3.5-4.5). Reaction mixture was stirred for 30 min at 100 °C. Completion of the reaction was monitored using radio-HPLC with MeOH+ 0.1% TFA (Solvent A) and H_2O + 0.1% TFA (Solvent B) and radio-ITLC with 0.2 M citric acid as mobile phase. Analytical HPLC was performed following the same conditions as for ^{nat}Ga porphyrins (**33**-**36**) as mentioned above.

The excess of unreacted ^{68}Ga was removed by purification on tBuC18 Sep-Pak cartridge. Before purification, Sep-Pak cartridge was prepared by eluting with 1 mL of EtOH and then with 5 mL of mili-Q water. Reaction mixture was dissolved in 1.5 mL of mili-Q water and added to the column. Unreacted [^{68}Ga]gallium was eluted using 10 mL of mili-Q water, and the product was extracted with 2 × 300 μL of EtOH or 0.01% of 0.1 M HCl in EtOH.

Formula for the calculation of the radioactive decay:

$$A = A_0 e^{-\lambda t} \qquad (\mathbf{1})$$

$\boldsymbol{A}$ – ending activity

$\boldsymbol{A_0}$ – starting activity

$\boldsymbol{\lambda}$ – ($0.693/T_{1/2}$) $T_{1/2}$ – half-life ($T_{1/2}$ [^{68}Ga]gallium = 68 minutes)

$\boldsymbol{t}$ – elapsed time

Calculation of the radiochemical yield (RCY, %):

$$RCY = \frac{A_P}{A_0}\ x\ 100\ \% \qquad (\mathbf{2})$$

$\boldsymbol{A_P}$- product activity

$\boldsymbol{A_0}$- starting activity

Radiochemical efficiency (RCF, %) of the reaction was calculated by dividing the AUC of free-[^{68}Ga]gallium and AUC of the [^{68}Ga]porphyrin obtained from HPLC and expressed as percentage. To obtain high-specific activity of [^{68}Ga]porphyrin, after completion of the reaction with free[^{68}Ga]gallium product was purified using HPLC (Phenomonex Luna, C18, 250 x 10 mm, 5 µm) with MeOH + 0.1 % TFA and H_2O + 0.1% TFA as solvents. Conditions for purification were the same as for ^{nat}Ga(III)porphyrins, **33-36**. After the purification, free [^{68}Ga]gallium was removed using a tBuC18 Sep-Pak column, following the same procedure as mentioned above. Low specific activity (low SA) was obtained using a "hot-cold" method. After completion of the reaction with free[^{68}Ga]gallium, the product was re-dissolved in sodium acetate buffer (pH = 4.3) and 100 µg of $GaCl_3$ was added to the reaction. The reaction was heated for 15 minutes and then checked using both radio-TLC and radio-HPLC. If needed, the product was further purified using HPLC, following conditions used for high-specific activity and ^{nat}Ga(III) porphyrin purification procedure.

Calibration curves comparing the AUC per added mass of porphyrins investigated on ^{nat}Ga(III) porphyrins (**Figure S93**) were used to calculate the mass and concentration of the porphyrin in the sample. Using this information, the amount of the activity in the vial was divided by the mass of the porphyrin in the sample to obtain activity/mass (Bq/g) or activity/mol (Bq/mol) for each low and high specific activity (low and high SA) of each porphyrin.

3.4. Light sources

All the light sources used in this work for photoactivation of porphyrins in PDT experiments and singlet oxygen measurements were designed based on light emitting diodes (LED) and diffuser, and were provided by Dr Martin Lončarić and Anton Radman from the Center of Excellence for Advanced Materials and Sensing Devices at the Ruđer Bošković Institute in Zagreb.

Red light source (λ_{MAX}= 647 nm, $\Delta\lambda_{FWHM}$ = 22 nm) with variable fluence rates 38.0, 22.0, 15.3 and 10.7 mW/cm^2) and orange light source (λ_{MAX} = 606 nm, fluence rate 2 mW/cm^2) (**Figure S74**) were used to determine the production of singlet oxygen by photodegradation of 1,3- diphenylisobenzofuran (DPBF). In addition, violet light source (λ_{MAX} = 411 nm, $\Delta\lambda_{FWHM}$ = 20 nm) with various fluence rates: 38.0, 22.0, 15.3 and 10.7 mW/cm^2) (**Figure S74**) was also used to determine the singlet oxygen production, however by using the photodegradation of a water-soluble dye, 9,10-anthracenediyl-bis(methylene)dimalonic acid (ABMDMA). For the *in vitro* studies, red light source (λ_{MAX} = 645 nm, $\Delta\lambda_{FWHM}$ = 20 nm, fluence rate 2 mW/cm^2) and orange light source (λ_{MAX} = 606 nm, $\Delta\lambda_{FWHM}$ = 14 nm, fluence rate 2 mW/cm^2) prepared for uniform illumination of 12- and 96-well plates were used (**Figure S75**).

The number of photons absorbed by a porphyrin is the key parameter for assessment of the PDT outcome and the actual light dose delivered by a light source to a PS has to be calculated taking into account spectral overlap between the light source emission and the PS absorption[164]. To determine the number of absorbed photons of each porphyrin upon irradiation with light source at certain wavelength, a formula based on Beer-Lambert law was used that combines the optical properties of a porphyrin, namely its absorbance ($A(\lambda)$) at the irradiation wavelength λ, the source radiant power P at this wavelength and an irradiation time Δt:

$$N_{photons\ absorbed} = \Delta t \int_{\lambda} \frac{P(\lambda)}{\frac{hc}{\lambda}} (1 - 10^{-A(\lambda)}) d \quad (3)$$

obtained from:

$$N_{photons\ absorbed}(\lambda) = N_{photons\ incident}(\lambda) - N_{photons\ transmitted}(\lambda) \quad (4)$$

$$A(\lambda) = log_{10} \frac{N_{photons\ incident}(\lambda)}{N_{photons\ transmitted}(\lambda)} \text{ (Absorbance)} \quad (5)$$

$$N_{photons\ transmitted} = N_{photons\ incident}(\lambda) \cdot 10^{-A(\lambda)} \text{ (Beer-Lambert law)} \quad (6)$$

$$P_{source\ radiance}(\lambda) = \frac{N_{photons\ incident}(\lambda) \cdot \frac{hc}{\lambda}}{\Delta t} \quad (7)$$

Note: fluence rate (irradiance) $E = {}^{P}/_{S}$ (P = radiant power, S = irradiated surface)

3.5. Spectroscopic analysis

Absorption spectra of all porphyrins were recorded on a Cary UV 60 (Agilent Technologies). All absorption spectra were recorded in a wavelength range of 300-700 nm. Fluorescence spectra were recorded on a Cary Eclipse (Agilent Technologies) after excitation at the Soret band wavelength in the wavelength range of 500-800 nm. Solvent for all cationic and zwitterionic porphyrins was methanol and for porphyrins **1**-**11** DCM was used. Also, absorption and fluorescence properties of free-base *N*-methylated porphyrins (**13**, **15**, **17** and **19**) and their Zn(II) (**21**, **23**, **25** and **27**) and Ga(III) complexes (**33**-**36**) were obtained in 10× phosphate buffered saline (PBS) prepared by mixing 1.4 M NaCl, 0.03 M KCl, 0.1 M Na_2HPO_4 and 0.02 M NaH_2PO_4 adjusted to pH =7.45. Before use, the solution was diluted to a 10-fold lower concentration (1× PBS).

Steady-state fluorescence spectra of some *N*-oxidized (**28** and **32**), free-base *N*-methylated porphyrins (**13**, **14** and **19**) and their Zn(II) complexes (**21**, **22** and **27**) were obtained on a FS5 Edinburgh Instruments spectrometer. Methanol (HPLC grade), high purity water (mili-Q) and phosphate buffer (0.05 M, pH = 7) were used as solvents. Samples were degassed with high purity N_2 prior to the measurement, and the absorbance was adjusted to <0.1 at the excitation wavelength. Excitation wavelengths were 405 and 550 nm, and emission was recorded from 550 to 800 nm. The slits were set to the bandpass corresponding to 2 nm for the excitation and 3 nm for the emission. All the experiments were conducted at 25 °C.

To study the effect of the temperature on both absorption and fluorescence spectra, samples were first recorded at 25 °C. Changes in the spectra were observed after heating to 60 °C and cooling down to 5 °C. In addition, the effect of solution degassing was investigated, recording all spectra at 25°C.

Fluorescence quantum yield ($\boldsymbol{\Phi}_{\mathbf{FL}}$) was calculated in a comparison to the standards, **TPP** and **Zn-TPP** according to the following equation:

$$\Phi_{\mathrm{FL}}(P) = \Phi_{\mathrm{FL}}(S)\left(\frac{n_P}{n_S}\right)^2 \frac{I_P}{I_S}\frac{A_S}{A_P} \qquad (\mathbf{8})$$

$\boldsymbol{\Phi}_{\mathbf{FL}}$ – fluorescence quantum yield of compound and the standard (**TPP** or **Zn-TPP**)

$\boldsymbol{n}_{\mathbf{P}}$ and $\boldsymbol{n}_{\mathbf{S}}$ – refractive index of the solvent in which porphyrin or the reference was dissolved

$\boldsymbol{A}_{\mathbf{P}}$ and $\boldsymbol{A}_{\mathbf{S}}$ – absorbance of the compound and the reference at the excitation wavelength

$\boldsymbol{I}_{\mathbf{P}}$ and $\boldsymbol{I}_{\mathbf{S}}$ – area under emission curve of the compound and the standard

3.5.1. Absorption properties in cell medium

To determine the impact of the cell culturing media on the absorption properties of the porphyrin, absorption spectra of porphyrins **13** and **19** was recorded in Dulbecco's modified Eagle medium (DMEM) with 1.0 g/L glucose, l-glutamine and 3.7 g/L sodium bicarbonate ($NaHCO_3$) and its dilutions with 1× PBS in ratios 1:1, 1:4 and 1:9 DMEM/PBS. Tested concentrations of porphyrins were 1, 2, 5 and 10 μM. Absorption spectra were recorded from 250-800 nm in a 1 cm quartz cuvette. In addition, absorption spectra were also recorded in a complete DMEM enriched with 1% Penicillin/Streptomycin solution, 1% l-glutamine and 10 % fetal bovine serum (FBS). The measurements in the complete DMEM were repeated in the same conditions as with the DMEM without addition of the supplements.

3.5.2. Absorption properties in addition of bovine serum albumin (BSA)

Impact of BSA in the solution of porphyrins in 1× PBS was tested. In the experiment, free-base porphyrin **19** and its Zn(II) complex **27** were used, with the hydrophilic analogues (**13** and **21**, respectively) as controls. Porphyrin solutions (10 μM) were prepared in PBS with the addition of 0.01%, 0.05%, 0.1%, 0.5% and 1% BSA. Porphyrin in the PBS solution without addition of BSA served as a control. Absorption spectra were recorded in a 350-700 nm wavelength range.

3.5.3. Absorption properties in addition of surfactants (Triton X-100 and sodium dodecyl sulfate (SDS))

N-methylated porphyrins (**13** and **19**) and their Zn(II) complexes (**21** and **27**) were tested in a 1× PBS solution with different concentrations of non-ionic (Triton X-100) or anionic detergent (SDS). Porphyrins were tested in 10 μM concentrations in 1× PBS, and tested detergent concentrations were 50 μM, 0.1 mM, 0.5 mM, 1 mM, 5 mM, 10 mM, 50 mM, 0.1 M. Porphyrin solution without detergents was used as a control. Absorption spectra were recorded in a 350-700 nm wavelength range in a 1 cm quartz cuvette.

3.6. Laser flash photolysis (LFP)

Laser flash photolysis was performed on a LP980 transient absorption spectrometer (Edinburgh Instruments) equipped with an Nd:YAG laser (Quantel, Q-smart 450, 5 ns pulse duration, 10 Hz) in collaboration with Dr. Iva Džeba from the Laboratory of Radiation Chemistry and Dosimetry at the Ruđer Bošković Institute.

The LFP setup consists of an LP980 transient absorption spectrometer (Edinburg Instruments) equipped with a Nd:YAG laser (Quantel, Q-smart 450, 5 ns pulse duration, 10 Hz, excitation wavelengths 266 and 355 nm). A xenon lamp with a continuous light beam (or pulse mode) passes through the sample, while a nanosecond light pulse (5 ns) from a Nd: YAG laser perpendicular to the lamp beam is used to excite the sample. The change in sample absorbance, resulting from the difference in light absorption by the sample before and after laser excitation, is measured in time at a specific wavelength selected by a monochromator, detected by a photomultiplier and converted into an electrical signal displayed by an oscilloscope and transferred to a computer. All set-up parts are time-synchronized and the measurement is triggered by a computer.

LFP is a powerful technique for studying the photophysical properties of molecules and processes described in the Jablonski diagram (**Figure 2**), as well as the photochemical reactivity and mechanisms of transients (short-lived species such as molecules in triplet-excited states, radicals and intermediates) formed after the excitation with a short pulse of laser light. It was first demonstrated in 1949 by Norrish and Porter, who were in 1967 awarded the Nobel Prize [165]. In this thesis, nanosecond laser flash photolysis was used to measure the kinetics of triplet state depopulation (τ_T) and triplet-triplet absorption spectra, and to calculate the ISC quantum yield (Φ_{ISC}) and quenching rate constants of triplet states by molecular oxygen (kq) [166].

Before the analysis, the ground state absorbance of the porphyrins was adjusted to 0.2 at the laser excitation wavelength of 266 nm or 355 nm and the solutions were purged with high purity N_2 or O_2 for at least 15 min before measurements. All measurements were performed at 25 °C in 1 cm quartz cuvettes. Free base and Zn(II) complexes of *N*-methylated porphyrins were measured in MeOH, H_2O and 0.05 M phosphate buffer (pH = 7), and *N*-oxidized porphyrins only in MeOH. Laser energy was adjusted below 5 mJ to avoid triplet-triplet annihilation. Ground state absorption spectra of the samples were also recorded after the purging with N_2 or O_2 and after transient absorption (TAS) measurements to track the differences in every step of measurements to ensure that no photoproducts were formed.

To calculate Φ_{ISC}, the first step was calculation of the molar absorption coefficient of the triplet state by using the singlet depletion method [166,167] and second step was calculation of Φ_{ISC} using a comparative method [168]. When using this procedure, avoiding overlapping in the singlet and triplet excited state was considered. Standards used in calculation of the ISC quantum yield were **TPP** (Φ_{ISC} = 0.87 in toluene [169]) for *N*-methylated and *N*-oxidised porphyrins and **Zn-TPP (**Φ_{ISC} = 0.66 in benzene [170]) for Zn(II) complexes of *N*-methylated porphyrins.

Lifetime of the triplet excited state was calculated using the 1st order decay kinetics with one or two contributions, in case when aggregates are formed:

$$for\ t = 0 \rightarrow y = A_0 \times e^{(-x/\tau)} + y_0; \Delta A = A_0 + y_0 = y \quad \textbf{(9)}$$

$\boldsymbol{\Delta A}$ - changes in the absorption of a triplet maximum

$\boldsymbol{\tau}$ – lifetime of the excited triplet state

$$y = A_1 \times e^{(-x/\tau_1)} + A_2 \times e^{(-x/\tau_2)} + y_0; \Delta A = y = A_1 + A_2 + y_0 \quad \textbf{(10)}$$

$\boldsymbol{A_1 + A_2}$ - changes in the absorption of a triplet maximum (=ΔA)

$\boldsymbol{\tau_1}$ – lifetime of the excited triplet state (τ) of the first contribution of the decay

$\boldsymbol{\tau_2}$ – lifetime of the excited triplet state (τ) of the second contribution of the decay

To account for triplet-triplet annihilation in some cases, the triplet excited state lifetimes were determined by fitting the triplet decays to equation for the mixed 1st and 2nd order decay [163]. Fitting function used:

$$y = \frac{1}{k_2'(e^{k_1 x} - 1) + e^{k_1 x}/A_0} \quad \textbf{(11)}$$

where:

$$k_2' = \frac{2k_2}{\varepsilon l k_1} \quad \textbf{(12)}$$

Parameters used in the function: $k_1 \sim 10^3; k_2' \sim 10;\ A_0 = \Delta A$ [163]

Molar absorption coefficients for the triplet states of tested porphyrins were calculated using the singlet depletion method and calculated according to the equation:

$$\varepsilon_T = \varepsilon_S \frac{\Delta A_T}{\Delta A_S} \quad \textbf{(13)}$$

$\boldsymbol{\varepsilon_T}$ – molar absorption coefficient of the triplet state

$\boldsymbol{\varepsilon_S}$ – molar absorption coefficient of the ground state

$\boldsymbol{\Delta A_T}$ – changes in the absorption at the triplet maximum

$\boldsymbol{\Delta A_S}$ - changes in the absorption at the singlet maximum

Comparative method was used to determine ISC quantum yield according to the equation:

$$\Phi_T^P = \Phi_T^S \frac{\Delta A_T^P}{\Delta A_T^S} \frac{\varepsilon_T^S}{\varepsilon_T^P} \quad \textbf{(14)}$$

$\boldsymbol{\Phi_T^P}$- ISC quantum yield of tested porphyrins

$\boldsymbol{\Phi_T^S}$- ISC quantum yield of a standard

$\boldsymbol{\Delta A_T^P}$- changes in the triplet absorption of a tested porphyrin

$\boldsymbol{\Delta A_T^S}$- changes in the triplet absorption of a standard

$\boldsymbol{\varepsilon_T^P}$- triplet excited state molar absorption coefficient of a tested porphyrin

$\boldsymbol{\varepsilon_T^P}$- triplet excited state molar absorption coefficient of a standard

Quenching rate constant of a triplet excited state by molecular oxygen was calculated using the Stern-Volmer equation:

$$\frac{1}{\tau} = \frac{1}{\tau_0} + k_q\,[O_2] \qquad (\mathbf{15})$$

$\boldsymbol{\tau}$- lifetime of a triplet excited state in the presence of a quencher

$\boldsymbol{\tau_0}$- lifetime of a triplet excited state without the presence of a quencher

$\boldsymbol{k_q}$ – quenching rate constant ($M^{-1}s^{-1}$)

3.7. Time-correlated single photon counting (TC-SPC)

Time-correlated single photon counting method (TC-SPC) was used to obtain the fluorescence decays. All measurements were performed on a FS5 Edinburgh Instruments spectrometer in collaboration with Dr. Nikola Basarić from the Laboratory of Synthetic Organic Chemistry, Ruđer Bošković Institute.

N-oxidized porphyrins (**29** and **32**) were measured only in MeOH, whereas free-base (**13**, **14** and **19**) and Zn(II) complexes of *N*-methylated porphyrins (**21**, **22** and **27**) were also measured in water and 0.05 M phosphate buffer (pH = 7). Prior the measurements, absorbance at the excitation wavelength (λ= 405 nm) was adjusted to 0.1 a.u. and all samples were purged with N_2 for 15 min. For the sample excitation, a pulsed laser at 405 nm with a pulse duration of 60 ps was used. Fluorescence signals were monitored at 660 nm over 1023 channels, with the time increment of ≈ 49 ps/channel. All the decays were collected until they reached 3000 counts in the peak channel. However, 1000 counts were set as a threshold in a peak channel for weekly emitting solutions in water or phosphate buffer. To obtain the instrument response function (IRF) a scattering solution a silica gel suspension in H_2O was used.

The histograms of fluorescence decays were analysed by a nonlinear least-squares deconvolution method using the following expression:

$$F(t) = A + \alpha_1 \exp\left(-\frac{t}{\tau_1}\right) + \alpha_2 \exp\left(-\frac{t}{\tau_2}\right) + \alpha_3 \exp\left(-\frac{t}{\tau_3}\right) + \ \ldots \ \textbf{(16)}$$

Least-squares deconvolution method was in a program software implemented with the spectrometer and the quality of a fit was analyzed by the distribution of the weighted residuals and by the approximation of the reduced χ^2 (expected value $\chi^2 = 1$).

3.8. Singlet oxygen production

The singlet oxygen ($^1O_2$) production was measured by measuring the photodegradation of fluorescent dyes 1,3-diisophenylbenzofurane (DPBF) and 9,10-anthracenediyl-bis(methylene)dimalonic acid (ABMDMA) in combination with porphyrins and light irradiation. For the measurements with DPBF, stock solutions of DPBF and porphyrins were dissolved in dimethylsulfoxide (DMSO) and diluted in MeOH until desired concentrations. In a cuvette, 1 mL of 10 μM porphyrin and 1 mL of 8 μM DPBF (final concentration 5 μM and 4 μM, respectively) were mixed and exposed for 15 min to a red wavelength irradiation (λ = 647 nm; 10.7 mW/cm^2; light dose: 9.63 J/cm^2) at room temperature under constant stirring. When samples were exposed to the orange wavelength irradiation (λ = 607 nm; 2 mW/cm^2; light dose: 1.8 J/cm^2), porphyrin concentration used was 16 μM (final concentration after mixing with DPBF, 8 μM), and for DPBF concentration remained the same. In both measurements, decrease of fluorescent intensity of DPBF was recorded at 453 nm (λ_{ex} = 410 nm) before irradiation and after every 60 seconds of irradiation.

For determination of singlet oxygen production of amphiphilic porphyrins in PBS, photodegradation of ABMDMA was used. Here, free-base *N*-methylated porphyrins and their Zn(II) complexes with an alkyl chain of 10, 14 and 18 C atoms and porphyrin with acetamido group were tested. Stock solution of both porphyrins and ABMDMA were prepared in DMSO (20 mM) and diluted in 1x PBS until desired concentrations (1 μM porphyrin and 2 μM ABMDMA). Samples were mixed in a cuvette in 1:1 ratio and irradiated with violet wavelength light for 5 min (λ = 411 nm, 3.5 mW/cm^2, 1.05 J/cm^2). The decrease of fluorescence intensity of the ABMDMA was recorded at λ = 432 nm (λ_{ex} = 380 nm) before the irradiation and after every 30 seconds during irradiation. In all singlet oxygen experiments, control represents photodegradation of the fluorescent dye in the same conditions with addition of solvent without porphyrins.

From the obtained photodegradation curves, area under the curve (AUC) was calculated according to the formula below. The given result was divided with the elapsed time in seconds and subtracted from 1 to give the percentage of fluorescence decrease. All results were presented as an average of three individual measurements with the standard deviation in error bars.

Formula for the calculation of the AUC [163]:

$$AUC = \frac{(\left(I/I_0\right)\mathrm{s}+\left(I/I_0\right)\mathrm{f})}{2\,(t_\mathrm{f}-t_s)} \qquad (17)$$

$(I/I_0)_\mathrm{s}$ – ratio of the fluorescence intensity and initial fluorescence intensity at the beginning of the tested interval

$(I/I_0)_\mathrm{f}$ - fluorescence intensity and initial fluorescence intensity ratio at the end of the tested interval

t_s – time at the beginning of the interval of the measurement

t_f - time at the end of the interval of the measurement

3.9. Lipophilicity of porphyrins

3.9.1. R_f determination

Thin-layer chromatography of purified compounds was used to determine the R_f values of free-base *N*-methylated porphyrins and their Zn(II) complexes. Silica plates on aluminum foil were used as a stationary phase, and solvent mixture MeCN:H_2O:$KNO_{3(sat.)}$ (8:1:1) was used as a mobile phase. Typically, 1 µl of 0.1 mM samples dissolved in methanol was applied at 0.5 cm from the strip border and the solvent front was allowed to run ~7 cm. The measurements were performed in duplicate, and the results are shown as an average with the standard deviation.

3.9.2. Modified shake-flask method

The shake-flask method was used to determine the partition coefficient between *n*-butanol (*n*-BuOH) and water. The method was modified according to the procedure by Kos and colleagues[171]. Before measuring the lipophilicity, absorption of each porphyrin was determined in few concentrations in both demineralised water and *n*-BuOH to determine molar absorption coefficient in each layer. In each test tube 1 mL of *n*-BuOH and 900 µL of water were added, followed by addition of 100 µL of 100 µM porphyrin previously dissolved in a water. The test tube was vortexed for 5 min and then centrifuged for 5 min at 6000 rpm to separate layers. By recording absorption spectra, concentration in each layer was determined. LogP_BW was calculated using the following equation:

$$logP_{BW} = \log(\frac{c_\mathrm{n-BuOH}}{c_{\mathrm{H_2O}}}) \qquad (18)$$

$c_\mathrm{n\text{-}BuOH}$-concentration of porphyrin in *n*-BuOH layer

c_H2O-concentration of porphyrin in water layer

To calculate logP_{OW}, a correlation formula provided by Kos and colleagues was used [171]:

$$logP_{OW} = 1.55\ (logP_{BW}) - 0.54 \qquad (\mathbf{19})$$

Shake flask measurements were performed in triplicate, and the results are shown as an average of repeated measurements with standard deviation as error bars.

3.9.3. clog*P*

To compare experimental data with the theoretical online calculations, structure-based calculations of log*P* were observed using *Chemicalize* from ChemAxon where all molecules were provided as SMILES (https://chemicalize.com/).

3.10. Analysis of the [^{68}Ga]gallium porphyrins

3.10.1. Log*D* calculation

Dried radiolabelled porphyrin (~ 5 MBq) was dissolved in 700 µL of 1× PBS (0.14 M NaCl, 3 mM KCl, 10 mM Na_2HPO_4 and 2 mM NaH_2PO_4, pH = 7.4). Eppendorf tubes were prepared by addition of 500 µL of 1-octanol and 300 µL of PBS, followed by addition of 200 µL radiolabelled porphyrin (~ 0.5 MBq) solution. Prepared solutions were vigorously shaken for 12 min followed by 3-minute centrifuge to separate the layers. After separation each layer (fixed volume, 100 µL) is added to the gamma tubes previously filled with ~ 1 mL acetonitrile (MeCN) and read on γ- counter. To calculate log*D* the following equation was used:

$$\log D = \log\left(\frac{radioactivity\ in\ organic\ phase\ (1-octanol)}{radioactivtiy\ in\ aqueous\ phase}\right) \qquad (\mathbf{20})$$

3.10.2. Serum stability

To investigate stability of a [^{68}Ga] porphyrin in mouse serum, to a [^{68}Ga] porphyrin (~ 10 MBq) a 30% mouse serum (200 µL) (Sigma Aldrich, MA, USA) was added and incubated at 37 °C for 2 hours. Stability was tested using radio-HPLC and radio-ITLC (in the same conditions as described in the 4.3. Radiolabelling of porphyrins) in following time points: 0, 15, 30, 60 and 120 min. Samples for HPLC were prepared by mixing the serum aliquots (20 µL at time points 0, 15 and 30 min or 40 µL or time points 60 and 120 min) with 40 µL of MeCN with 0.1 % TFA to precipitate. After precipitation, suspension was centrifuged for 3 min at maximum speed and supernatant was analysed using radio-HPLC and radio-ITLC.

3.10.3. *Apo*-transferrin studies

Dried [^{68}Ga] porphyrin (8-9 MBq) was dissolved in 200 µL of previously prepared solution of *apo*-transferrin (1 mg/mL) (Sigma Aldrich, MA, USA) in 1× PBS (pH = 7.4). Solution was incubated at 37 °C for 3 hours, and stability was measured using radio-HPLC and radio-ITLC after 30, 60, 120 and 180 minutes of incubation as well as in the beginning of the experiment.

3.10.4. BSA and LDL binding studies

Dried [^{68}Ga] porphyrin (8-9 MBq) was dissolved in 500 µl of 3 % BSA in 1× PBS or 0.5 mg/mL low density lipoprotein (LDL) in PBS. The high specific activity of radiotracers **[^{68}Ga]34** and **[^{68}Ga]35** and low specific activity **[^{68}Ga]33** was used for the LDL binding studies. Prepared solution was analysed by size exclusion liquid chromatography (SE-HPLC) with PBS as solvent and 0.5 mL/min flow rate. Binding to BSA or LDL was tested at the time point 0 and after incubation for 30 minutes, 1 hour and 2 hours. Solutions of BSA or LDL alone and with the addition of [^{68}Ga] acetate were used as controls.

3.11. *In vitro* studies

3.11.1. Chemicals and reagents used in *in vitro* studies

Table 4. List of chemicals and reagents used for *in vitro* experiments with the manufacturer and catalogue number.

Reagent	Catalogue Number	Manufacturer, Country
Dulbecco's Modified Eagle Medium (DMEM)	P04-05550	PAN- Biotech GmbH, Germany
Dulbecco's phosphate-buffered saline (DPBS)	P04-35500	PAN- Biotech GmbH, Germany
FBS Standard	P30-3306	PAN- Biotech GmbH, Germany
L-glutamine 200 mM	P04-80100	PAN- Biotech GmbH, Germany
Penicillin (10 000 U/mL)/Streptomycine (10 mg/mL) solution	PO6-07100	PAN- Biotech GmbH, Germany
(10×) Trypsin 0.5%/EDTA 0.2% in DPBS	P10-024100	PAN- Biotech GmbH, Germany

Glycine	BP381500	Thermo Fisher Scientific, Massachsetts, USA
Albumine from bovine serum	A2153	Sigma-Aldrich, Massachsetts, USA
Sodium hydroxide (NaOH)	567530 (250g)	Sigma-Aldrich, Massachsetts, USA
Sodium dodecyl sulfate (SDS)	BP8200100	Fischer Chemicals, Thermo Fisher Scientific, Massachsetts, USA
Sodium chloride (NaCl)	S9888	Sigma-Aldrich, Massachsetts, USA
Paraformaldehyde (PFA)	441244	Sigma-Aldrich, Massachsetts, USA
4',6-diamidino-2-phenylindole (DAPI)	D9542	Sigma-Aldrich, Massachsetts, USA
3,3-diehyloxacarbocyanine ($DIOC_6(3)$)	sc-205905	Santa Cruz Biotechnology, Inc., Santa Cruz, USA
Fluoroshield®, histology mounting medium	F6182	Sigma-Aldrich, Massachsetts, USA
Thiazolyl Blue Tetrazolium Bromide (MTT)	M2128	Sigma-Aldrich, Massachsetts, USA
Cobalt chloride ($CoCl_2$) 0.1 M solution	15862	Sigma-Aldrich, Massachsetts, USA
Dimethyl sulfoxide (DMSO)	97063-136	VWR Chemicals, VWR International, Pennsylvania, USA

3.11.2. Cell lines and culturing conditions

Human malignant melanoma cell lines A375 and MeWo, representing melanoma tumour cells and human dermal fibroblast (HDF), representing normal cell line, were tested in the *in vitro* experiments. In addition to the melanoma cell lines used in *in vitro* experiments with *N*-methylated (both free-base and Zn(II)) and *N*-oxidised porphyrins, the triple-negative breast cancer cell line (MDA-MB-231) was used in *in vitro* experiments of Ga(III) *N*-methylated porphyrins. All cell lines used in this thesis are a kind donation from the Prof. Dubravka Švob Štrac from the Laboratory of Molecular Neuropsychiatry at the Ruđer Bošković Institute. Cell lines were cultured in Dulbecco's Modified Eagle Medium (DMEM) supplemented with

10% FBS, 1% L-glutamine and 1% Penicillin-Streptomycin solution and incubated in a humified atmosphere at 37 °C and 5% CO_2 and passaged at 80-90% confluency. For the subculturing of the cells, media was removed, and cells were rinsed with DPBS to remove any excess of the serum that could inactivate the activity of the trypsin. Trypsin-EDTA was added to the flask (1-1.5 mL), and after incubation for 2-3 min at 37 °C DMEM was added. An aliquot of cells remained in the flask, resuspended in a fresh medium.

3.11.3. Cellular internalization

Cells were seeded in 96-well plates in a concentration of 5000 cells/well and left to attach and reach their full morphology for 48 hours. After incubation, porphyrin was added to each well to reach the final concentration of 1 μM/well. Porphyrin stocks were prepared in DMSO (20 mM) and diluted in medium until the desired concentrations. Porphyrins were tested at incubation points 0.5, 1, 2, 4, 6, 12 and 24 h and incubated at 37 °C or 4 °C. After incubation, the media was removed, and cells were washed twice with 1x PBS. To remove all molecules bound to membrane, ice-cold acid buffer (50 mM glycine in 0.1 M NaCl, pH = 2.8) was added followed by incubation on ice for 5 minutes. After treatment cells were washed with PBS [172–174]. For lysis, cells were treated with 1% SDS in 0.1 M NaOH and incubated for 15 minutes at room temperature. The treatment was repeated. In the last step, wells were washed with 1× PBS. Steps with lysis buffer and PBS wash were collected in separate sterile 96-well plates for measuring fluorescence (BD Falcon Microtest Assay Plate (Becton Dickinson & Company Biosciences (New Jersey, USA) for Ga(III) porphyrins and FluoroNunc black, F bottom, Thermo Fisher Scientific (Massachusetts, USA) for *N*-methylated, *N*-oxidised and Zn(II) porphyrins). The fluorescence was measured at microplate reader, Tecan Infinite 200Pro (Tecan Life Sciences, Switzerland). Fluorescence intensity of free-base *N*-methylated porphyrins and *N*-oxidized porphyrins was measured at λ= 650 nm, bandwidth 20 nm (λ_{ex} = 420 nm; bandwidth 9 nm) and for *N*-methylated Zn(II) and Ga(III) complexes at λ= 600 nm, bandwidth 20 nm (λ_{ex}= 600 nm, bandwidth 9 nm). Controls were performed in the same conditions, without the addition of porphyrins.

Calibration curves for each porphyrin in 1% SDS in 0.1 M NaOH (**Figures S76, S77, S78** and **S79**) were prepared prior to the experiments. Concentration in each well was calculated by dividing the measured fluorescence intensity with the slope of the calibration curve. Obtained concentration was then divided with 5 to obtain the concentration (nM) per 1000 cells. All measurements were performed in triplicate and given data is an average of repeated measurements with standard deviation in error bars. Statistical analysis was performed using a GraphPad Prism 8 and included standard Two-way ANOVA test with *post-hoc* Tuckey analysis and confidence level was $\alpha = 0.05$. Significance was $p < 0.0001$ and it was shown

using the following signs: **** < 0.0001; 0.0001 <*** < 0.001; 0.001 < ** < 0.01; 0.01 < * < 0.1; ns (not significant) > 0.1.

3.11.4. Intracellular localization

Intracellular localization of porphyrins was evaluated using fluorescence microscopy. In a 12-well plate, with previously added cover glass, cells were seeded in a concentration 50 000 cells/well. After 48 h, cells reached their full morphology. Medium was replaced with fresh medium containing 5 μM porphyrin. Porphyrin stock solutions was prepared in DMSO (20 mM) and diluted in media until desired concentration. In a non-treated, control well medium was changed, without addition of porphyrins in a new media.

Cells were incubated with porphyrins for 6 hours in the incubator. 3,3'-dihexyloxacarbocyanine iodide ($DIOC_6(3)$), a marker for staining endoplasmic reticulum, mitochondria, and vesicle membranes, was added to the media in concentration 500 nM 30 min before the end of the incubation. After incubation, cells were washed with 1x PBS and fixed with 4% paraformaldehyde for 8 min at room temperature, followed with addition of 4′,6-diamidino-2-phenylindole (DAPI), nuclear marker dilute 1:10 000 in 1× PBS from 5 mg/mL, and incubation for another 3-5 min at room temperature. Cover slips were washed with 1× PBS and Fluoroshield® mounting media was used to connect the slips. Fluorescence microscopy of porphyrins chelated with Ga^{3+}, **34**-**36**, were performed using the same protocol, without addition of ER marker, $DIOC_6(3)$.

Colocalization with Golgi was tested with porphyrin **11**. After incubation for 6 hours with 5 μM porphyrins, cells were washed 3x with 1x PBS. Fixation of membranes was achieved using ice-cold MeOH and incubation for 8 min at -20 °C. Cells were then washed with 1x PBS. After washing, 3% BSA in PBS was added and cells were further incubated for 30 minutes at room temperature. After washing with 1× PBS (3×), primary antibody for Golgi apparatus, Anti-GM130 (Cat. No. 610822, Becton Dickinson & Company Biosciences (New Jersey, USA)) (1:2500 in 5% BSA in 1× PBS) was added and cells were incubated for 1 hour at room temperature. Cells were again washed with 1× PBS (3×). Secondary antibody, Goat anti-mouse Alexa Flor™ 488 (Cat. No. A-11001, Invitrogen, Thermo Fisher Scientific (Massachusetts, USA)) (1: 1000 in 5% BSA in 1× PBS) was added and cells were incubated for another 1 hour at room temperature. After final wash with 1× PBS (3×), cells were treated with DAPI, and the slips were connected with Mountain Media for histology (Sigma Aldrich) using the protocol described above.

Images were observed with fluorescence microscopy (Olympus IX83 equipped with camera Hamamatsu Orca R2) at 20× magnification. Porphyrins, $DIOC_6(3)$ and DAPI were respectively excited at the red (λ = 530-550 nm), green (λ = 460-495 nm) and blue (λ = 360-

370 nm) wavelength. All images were analysed using the *ImageJ* program, while Pearson's correlation coefficient was calculated the *CellSense* program, a software by Olympus implemented with the fluorescence microscope.

3.11.5. (Photo)cytotoxicity

MTT assay was used to determine the proliferation of the cells upon the treatment with porphyrins. Cells were seeded in 96-well plates in a concentration 5000 cells/well and incubated at 37 °C and 5% CO_2 for 48 h to allow the cells to attach and reach their full morphology. Porphyrins stocks were prepared in a DMSO (all porphyrins) or EtOH (*N*-oxidized porphyrins) and dissolved in DMEM until the desired concentration. Porphyrins in the different concentrations were added to wells (up to 100 μM) and allowed to uptake for 6 h. After the incubation, media was replaced with the fresh media (200 μL) to remove all the porphyrin that didn't enter the cells. Cells were then irradiated for 30 min with a light of desired wavelength. Both *N*-methylated free-base, Zn(II) and Ga(III) porphyrins were irradiated with a light or red wavelength (645 nm, 2 mW/cm^2, 3.6 J/cm^2) or orange wavelength (606 nm, 2 mW/cm^2, 3.6 J/cm^2) and for the irradiation *N*-oxidized porphyrins only red light wavelength was used. Nonirradiated cells were used to investigate the dark toxicity.

In addition, *N*-oxidized porphyrins were tested in a condition of normoxia and hypoxia. To obtain the hypoxia conditions, cell media was replaced with media containing $CoCl_2$ (100 μM) 2-3 h before the porphyrin treatment, and after the incubation with porphyrins, fresh media with $CoCl_2$ was added to the cells.

Number of viable cells was determined 36-48 hours after the irradiation using 3-(4,5-dimethylthiazol-2-yl)-2,5-diphenyltetrazolium bromide (MTT dye). Enzymes in viable cells, NAD(P)H dependent oxidoreductase, can reduce the yellow tetrazolium MTT dye in a purple insoluble formazan. The intensity of purple dye is considered proportional to the cell viability. After the removal of the media, 40 μL od MTT dye, previously diluted 40× in DMEM (from the starting 5 mg/mL in 1×PBS), was added. Cells were incubated with the dye for 3 h, covered in tin foil, at 37 °C. After the incubation, DMSO (160 μL) was added to the each well. Absorption was recorded on a Tecan Sunrise at λ= 570 nm, the maximum of the formazan absorption.

Proliferation of the cells were calculated using the following equation:

$$\%\, proliferation = \frac{A_t - A_{blank}}{A_{control} - A_{blank}} \times 100 \qquad (\mathbf{21})$$

$\boldsymbol{A_t}$ – average of the absorption in wells with treated cells with the same concentration

A_{blank}- average of the absorption in wells with MTT dye and DMSO

$A_{control}$- average of the absorption in wells with control, non-treated cells

All measurements were performed in three individual experiments and results were shown as proliferation of the cells at 1 μM concentration or calculated concentration at 50% of inhibition (IC_{50}). All results are shown as an average with the standard deviation in error bars. Statistical analysis was performed using a *GraphPad Prism 8* and included standard Two-way ANOVA test with *post-hoc* Tukey analysis and confidence level was $\alpha = 0.05$. Significance was $p < 0.0001$ and it was shown using the following signs: **** < 0.0001; 0.0001 <*** < 0.001; 0.001 < ** < 0.01; 0.01 < * < 0.1, ns (not significant) > 0.1.

3.12. *In vivo* PET imaging of the [^{68}Ga]gallium porphyrins (33-36)

3.12.1. Formulation preparation, mouse and PET imaging

Dried [^{68}Ga]gallium porphyrin (~ 5 MBq) was dissolved in PBS or 3% BSA in PBS (1 mL). *In vivo* scans were performed by John D Wright, Animal Technician at the PET Research Centre, University of Hull. Prior to measurements, mice (CD1 strain, female) were anaesthetized with isoflurane and a catheter was inserted into the tail vein. The mouse was placed in the PET/CT scanner (Bioscan BIO-PET/CT). Dynamic imaging was performed with the start time coinciding with the intravenous injection of the radiotracer. Whole-body PET scans usually last 90 minutes, followed by whole-body CT. The given scans were analysed with the AMIDE program.

3.12.2. Analysis of metabolites

After the PET/CT scan, mice were sacrificed and the samples of blood, urine and liver were taken for analysis. Each sample was prepared following procedure:

- Blood sample- blood sample (1 mL) was taken and centrifuged for 5 min at 14000 rpm to remove blood cells from the plasma. Sample of blood cells was treated with MeCN in ratio 1:2. Suspension was shaken for 1 min followed by centrifuge for 5 min (4 °C) at 14000 rpm to separate supernatant and precipitate. Supernatant was taken and analysed using radio-HPLC following conditions for the porphyrin **35** described above.
- Liver sample- After removing from the mouse, liver was treated with liquid nitrogen and crashed into powder. Liver powder (50 μg) was dissolved in MeCN: H_2O solution (70% MeCN/ 30% H_2O) and shaken. Solution was centrifuged for 5 min (4 °C) at

14000 rpm. Supernatant was taken and analysed using radio-HPLC following conditions for the porphyrin **35** described above.

- Urine sample- Urine was mixed in the Eppendorf tube with of MeCN: H_2O (70% MeCN and 30% H_2O) in a 1:2 ratio. Solution was shaken for 1 minute followed by centrifuge for 5 min (4 °C) at 14000 rpm. Supernatant was analysed using radio-HPLC following conditions for the porphyrin **35** described above.

4. Results and discussion

4.1. Comparison of the free-base and Zn(II) (*N*-methylpyridinum-3-yl)porphyrins with an alkyl chain of different length

4.1.1. Synthesis of *N*-methylated porphyrins (13-19) and their Zn(II) complexes (21 to 27)

The synthesis of porphyrins involves a reaction of pyrroles and aldehydes. The first attempts to synthesize porphyrins from individual pyrroles were done by Rothemund in 1935 [175,176]. In this reaction, pyrrole and benzaldehyde, dissolved in pyridine, were involved in a one-pot synthesis in a sealed tube at 150 °C for 24 hours [176]. The reaction led to the formation of *meso*-tetraphenylporphyrin (**TPP**) in a yield of 10%, which was heavily contaminated with the corresponding chlorine. A simpler reaction procedure and better yields were obtained in a reaction proposed by Adler, Longo and co-workers in 1967 [177], in which they carried out an acid-catalysed (with propionic acid) reaction of benzaldehyde and pyrrole under reflux for 30 minutes. The reaction was carried out under atmospheric air to allow the oxygenation of porphyrinogen to porphyrin. The reaction gave a yield of 20% with minor chlorine impurities, which could easily be washed with methanol (**Scheme 14**) [177].

The Adler-Longo synthesis proved successful for more than 70 aldehydes tested, and it is still used as the first method for the synthesis of many *meso*-substituted porphyrins [177,178]. However, Lindsey and co-workers revised the methods for porphyrin synthesis and proposed a two-step synthesis under milder conditions suitable for all aldehydes with different functional groups and protecting groups. The reaction is carried out under room temperature conditions with equimolar concentrations of pyrrole and acid, followed by oxidation with *p*-chloranil. Under these conditions, 50% **TPP** is formed, and if other aldehydes are used, the reaction yield is 30-40%, depending on the aldehyde used [179].

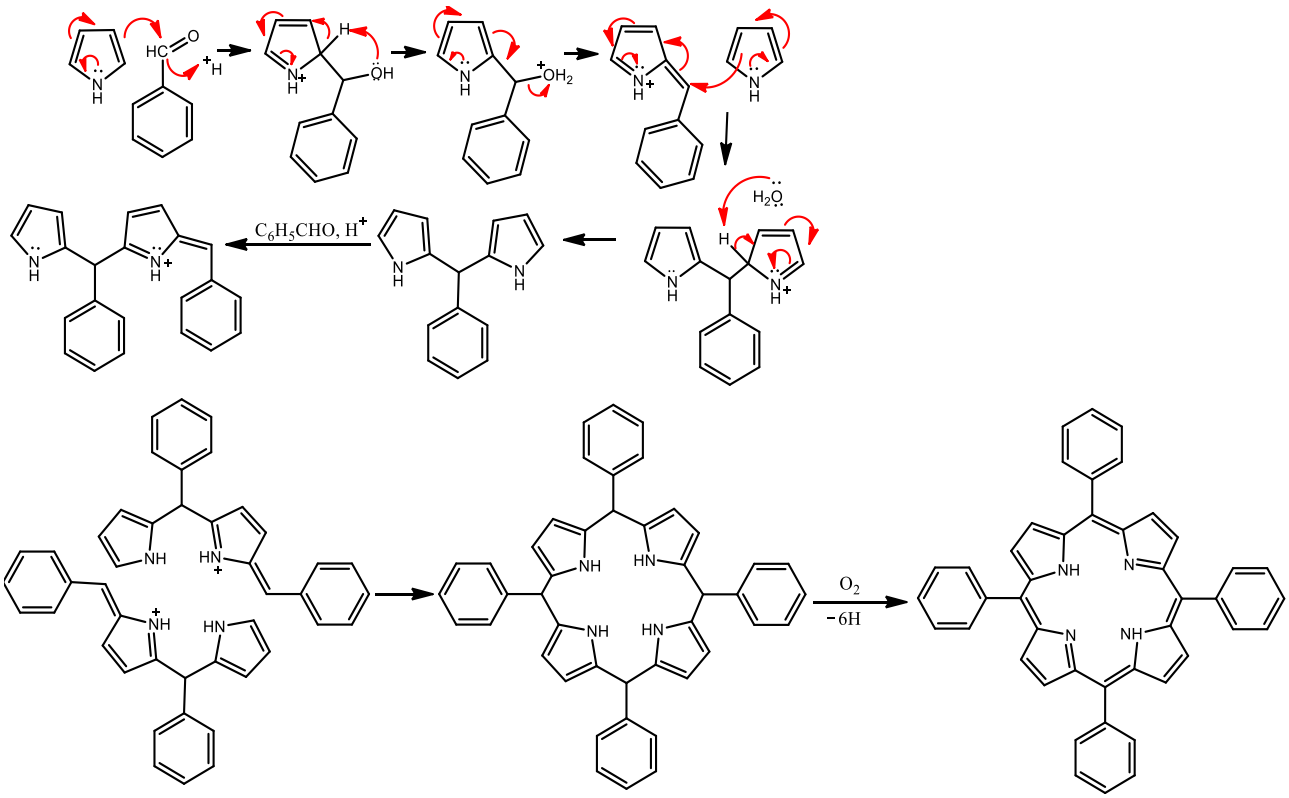

Scheme 14. A mechanism of Adler-Longo porphyrin condensation reaction on the example of *meso*-tetraphenylporphyrin.

The condensation reaction in this work was carried out with a mixture of aldehydes, 3-pyridinecarboxyaldehyde and 4-acetamidobenzaldehyde, and pyrrole in propionic acid according to the Adler-Longo procedure. The resulting crude product yields four different porphyrins, that can be separated by column chromatography. However, only porphyrins **1** and **2** were successfully isolated and used in further synthesis (**Scheme 15**). The symmetrical 5, 10, 15, 20- tetra-(pyrid-3-yl)porphyrin was porphyrin **1**, which was isolated as the first fraction with a yield of 5%, and the asymmetrical porphyrin with one acetamidophenyl group was porphyrin **2**, which was isolated as the second fraction with a yield of 4%. The structures of the obtained porphyrins **1** and **2** were confirmed by ^{1}H NMR spectroscopy (**Figure S1**). The acetamido group in porphyrin **2** is further hydrolysed to an amino group in a reaction carried out in refluxing aqueous HCl (18%) for two hours, followed by neutralization with DCM and triethylamine (TEA) (9:1), yielding 87% of porphyrin **3** (**Scheme 15**).

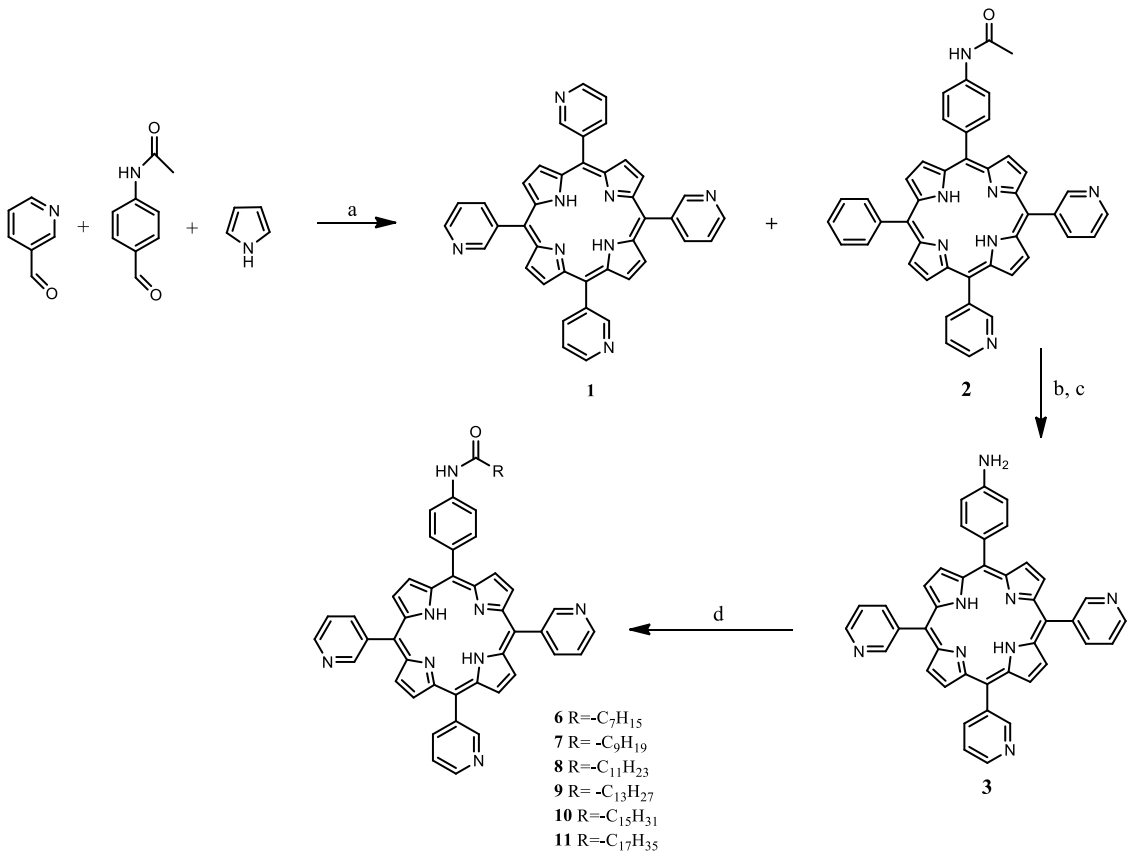

Scheme 15. Synthesis route of porphyrins **6-11**. Conditions of the reaction: a) propionic acid, 90 °C, 45 minutes; b) 18 % HCl, reflux, 2 hours; c) DCM/TEA, 9:1, r.t., 30 minutes; d) RCOCl, 0 °C, DCM + TEA, 1.5 hours.

In a previous study by our group, conjugation of a porphyrin to an acyl chloride with a 17 C-atom long alkyl chain increased efficiency against HeLa cell lines [73]. Our intention was to synthesize porphyrins with different hydrophilic-lipophilic ratio, with three quaternised pyridinium groups as the hydrophilic part and conjugated acyl chloride of different fatty acids with different alkyl chain length to obtain different lipophilicity. Therefore, porphyrin **3** underwent a series of nucleophilic acyl substitution reactions with different acyl chlorides to synthesize porphyrins **6** to **11**, whose alkyl chains with 7 to 17 C atoms differ in only two C atoms between two porphyrins of the group. The successful purification of porphyrins **6-11** was achieved by eluting twice by column chromatography with different ratios of DCM and MeOH and precipitation with *n*-hexane. The porphyrins **6-11** were obtained in high yields (> 82%) and their structure was confirmed by ^{1}H and ^{13}C NMR spectroscopy and the mass of the product by HRMS (**Figures S3-S17**).

The *N*-methylation of porphyrins **1**, **2** and **6** to **11** was carried out using methyl iodide (CH_3I) in dimethylformamide (DMF) at room temperature overnight, resulting in porphyrins **12** to

19 (**Scheme 6 and 7**), as described in the literature [67]. All porphyrins **12** to **19** were obtained in yields > 90%. To increase the solubility of the porphyrins in aqueous solutions, a counterion exchange (from I^- to Cl^-) was performed [180]. Furthermore, among the drugs approved by the FDA (in the period from 2015 to 2019), 43% are pharmaceutical salts, and in this group, chloride salts (29%) predominate, having the best aqueous solubility, pharmacokinetic and toxicokinetic profile and ADME (absorption, distribution, metabolism and excretion) properties [181]. Compared to iodine salts, that are only used to a limited extent, chloride salts are known to be preferable in drug development and are used without restrictions [181]. Previously, in a work by our research team[72,73], an Amberlite IRA 400 in DCM/MeOH or MeOH was used, which resulted in successful counterion exchange, however, impurities were sometimes found in the aliphatic part of the ^{1}H NMR spectrum.

A new method using precipitation with ammonium hexafluorophosphate (NH_4PF_6) and tetrabutylammonium chloride (TBAC) was applied following the procedure of Ezzedine and colleagues [67]. In the first step, the obtained dry *N*-methylated porphyrin was dissolved in H_2O and a saturated solution of NH_4PF_6 was added until the product precipitated. The precipitate is the result of the exchange of counterions from I^- to $NH_3PF_6^-$, resulting in the precipitation of a porphyrin with a large counterion in water. The precipitate obtained was washed vigorously with H_2O to remove all water-soluble impurities and the excess of NH_4PF_6. After the product was collected by filtration, it was dissolved in acetone and TBAC was added until precipitation. The change of a counterion, from $NH_3PF_6^-$ to Cl^- in this step, resulted in the formation of a water-soluble product that precipitates in organic solvents. The precipitate was then washed with acetone and diethyl ether, and the final product was obtained as a purple solid. With this method, a simple counterion exchange was achieved that successfully removed both water-soluble and organic impurities in the product. The structures of all porphyrins obtained were confirmed by ^{1}H NMR. This clearly showed a new peak at 4.80 ppm, which was assigned to the methyl groups on all quaternised nitrogen atoms, as well as a broadening of the β-protons at ~9.10 ppm. In the ^{13}C NMR, the peak of the methyl groups on the pyridine rings was observed at ~ 48 ppm (**Figures S21**, **S24**, **S27**, **S30** and **S33**).

The next step in the synthesis was the metalation of the porphyrins with Zn^{2+} cation. It is important to emphasize that the metalation must be carried out after the quaternisation of the pyridine nitrogen for two reasons. The first reason is that the Zn^{2+} chelation takes place in aqueous media, so the porphyrin must be water-soluble for a successful reaction. The second reason is the polymerization of the Zn(II) pyridylporphyrins when the nitrogen atoms are not quaternised because upon chelation, a coordination bond is formed between the nitrogen at the peripheral pyridyl substituents and the zinc metal centre, resulting in an insoluble product [182,183].

For Zn^{2+} chelation, zinc(II) acetate dihydrate ($Zn(CH_3COO)_2 \times 2\ H_2O$) and zinc chloride ($ZnCl_2$) were used according to the procedures described by Giuntini *et al*. for zinc(II) acetate [184] and the procedure of Ezzedine *et al*. [67], who used $ZnCl_2$ for Zn(II) chelation. When $Zn(CH_3COO)_2$ was used, the salt was used in 10-fold excess and diluted in water. The reaction was stirred overnight and completion of the reaction was confirmed by TLC in 8:1:1 MeCN: H_2O:$KNO_{3(sat.)}$ and UV-Vis spectroscopy.

In the case of $ZnCl_2$, the salt was diluted in 10-fold excess water and the pH of the solution was adjusted to 11 using 1M NaOH. The reaction was stirred for 1 hour at room temperature and completion of the reaction was confirmed by TLC and UV-Vis spectroscopy and by change in the pH from 11 to 6. Both products were analysed by ^{1}H NMR spectroscopy, and it was found that $ZnCl_2$ served as a better zinc(II) salt for chelation. Although chelation was carried out much longer than with $ZnCl_2$, the reaction with zinc(II) acetate was not complete. This was confirmed by ^{1}H NMR spectroscopy, where the peaks at 8.65 (Py-5-*H*), 9.33 (Py-6-*H*), 9.62 (Py-4-*H*) and 10.07 (Py-2-*H*) are residues of the unreacted free-base porphyrin found in the product (**Figure 19**).

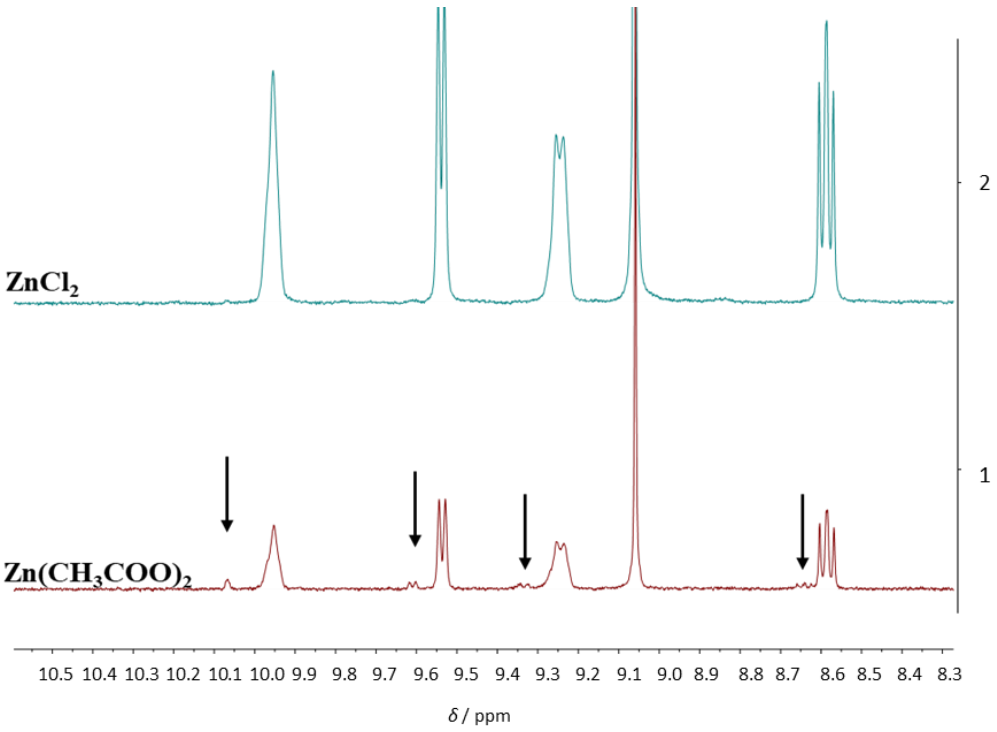

Figure 19. Comparison of the ^{1}H NMR spectra after using $ZnCl_2$ for 1 hour and $Zn(CH_3COO)_2$ for metalation of porphyrin **12** to obtain porphyrin **20**.

After chelation with $ZnCl_2$, the product was purified using the same procedure as for the *N*-methylated porphyrins. Zn(II) chelation of porphyrins **12** to **19** was achieved in very high yields (> 82%) (**Table 3**) and the compounds **20** to **27** were confirmed by ^{1}H NMR and ^{13}C NMR spectroscopy. The broad signal of the *β*-protons at 9.14 ppm shown for the free-base porphyrins, changes in the structure of the Zn(II) complex and becomes a doublet at 8.96 ppm, assigned to the two *β*-protons at positions 3 and 7, and a multiplet from 9.08 to 9.11 ppm, assigned to the remaining *β*-protons. In addition to NMR analysis, the mass of novel Zn(II) porphyrins was observed by HRMS as further confirmation of the successful synthesis (**Figures S36-S56**, ^{1}H and ^{13}C NMR and HRMS).

4.1.2. ^{1}H NMR analysis of porphyrin isomers

The porphyrin structure, a macrocycle with the π-extended electron system, has various isomers, with the tautomers, which are formed by a shift of the inner pyrrole protons in a structure [185,186], being the most studied isomers in the porphyrin structure. The two best known are *syn*- and *anti*-isomers, in which the inner pyrrole hydrogens are arranged in adjacent or opposite positions. Experimentally and according to theoretical calculations, the *anti*-tautomer has been shown to be the most stable, with an energy 7.6 kcal/mol lower than the *syn*-isomer.

The presence of tautomers was investigated using the example of the *N*-methylated asymmetric free-base porphyrin **13** and its Zn(II) complex, porphyrin **21**, both measured in deuterated methanol (MeOH-d_4) at room temperature (25 °C). As mentioned above, the broadening of the *β*-pyrrole protons at ~ 9.10 ppm can be detected in the ^{1}H NMR spectrum of porphyrin **13** (**Figure 20**, red line). The broadening of the *β*-protons is a result of the exchange of the inner N-H protons of the pyrrole by the deuterons in the solvent, which led to a relatively slow tautomerisation of the di-deuterated porphyrins and caused the broadening of the normally sharp signal of the protons in *β*-pyrroles [187]. Chelation with Zn^{2+} replaces the inner N-H protons with a metal cation, resulting in sharp signals of the *β*-pyrrole protons (**Figure 20**, blue line) [187]. This confirms that our porphyrins undergo such N-H tautomerisation, as the chelation with the metal cation leads to the loss of hydrogen atoms, whereby a slow tautomerisation of the deuterons and a broadening of the signal can no longer be seen [163].

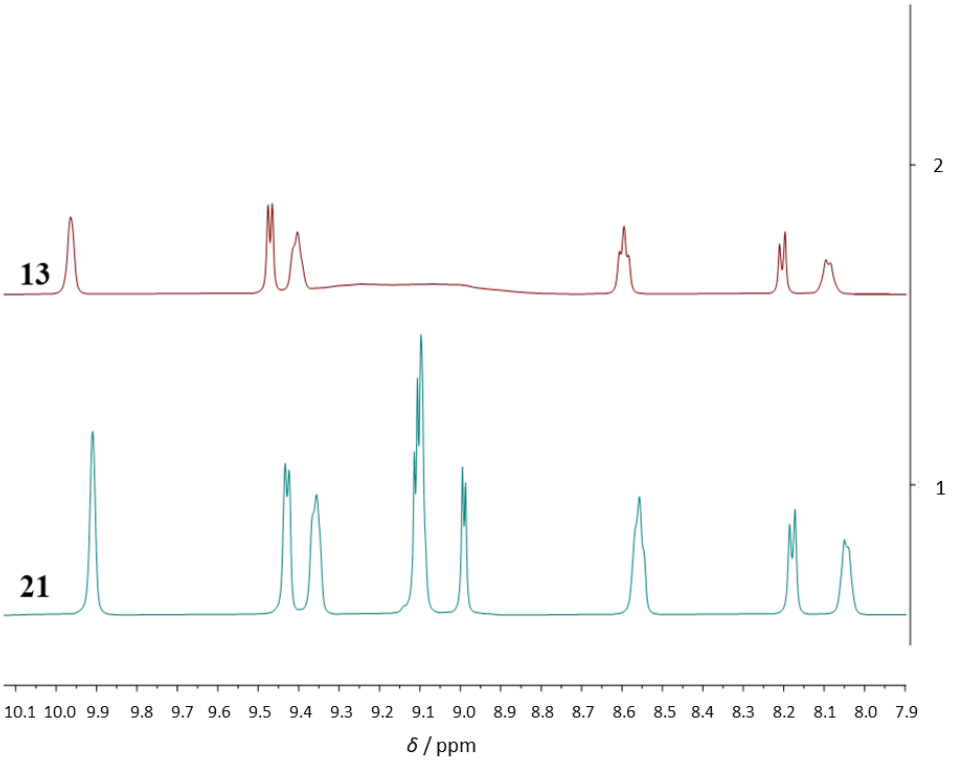

Figure 20. Comparison of the ^{1}H NMR spectra of *N*-methylated free-base porphyrin (**13**) and its Zn(II) complex (**21**).

In addition to tautomers, in the structure of the asymmetric porphyrins tested, the rotamers occurring by the rotation of the amide bond and the pyridine bond can be found. Since the presence of rotamers is difficult to detect after the *N*-methylation of porphyrins, an asymmetric porphyrin **2** was used to detect amide bond rotamers that occur due to rotation of the C-N bond. A temperature-dependent ^{1}H NMR was observed in which porphyrin **2** dissolved in $CDCl_3$ was first measured at room temperature (25 °C), then the sample was analysed after cooling to 5 °C, then after heating to 50 °C, and finally at room temperature to detect the changes.

As can be seen in **Figure 21**, three signals from 7.80 to 8.05 assigned to Ar-3,5-protons were detected at room temperature, which were very broad and overlapping with the amide proton signal (red line). After cooling the sample to 5 °C, the signal became more complex, with sharper and more defined signals (green line), suggesting that the mixture of conformers is present as a result of the restricted rotation of the C-N bond, while after heating to 50 °C the signal appeared as a single broad peak, indicating a much faster exchange between the conformers [163]. After cooling to room temperature, the spectrum again shows three broad peaks, as at the beginning of the experiment, indicating that these changes are reversible.

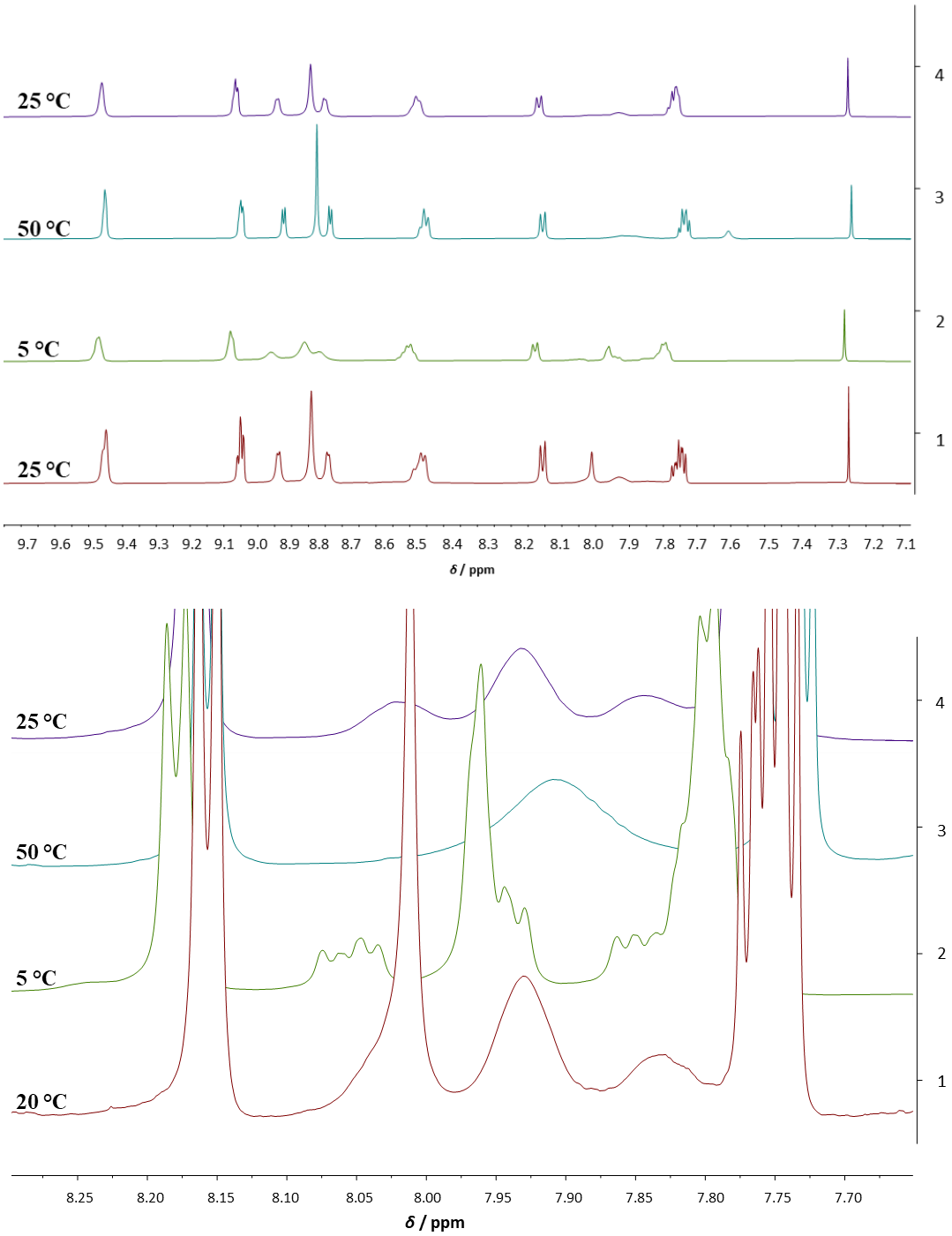

Figure 21. The aromatic part of the ^{1}H NMR ($CDCl_3$, 400 MHz) spectrum of porphyrin **2** (upper spectrum) and enlarged part of the spectrum between 6.95 and 8.30 ppm (lower spectrum) measured first at 25 °C (red line), then after cooling to 5 °C (green line), followed by heating to 50 °C (blue line) and cooling back to 25 °C (purple line).

In the temperature-dependent ^{1}H NMR analysis, especially at low temperatures, dynamic processes of both the NH tautomers and the rotamers, which would be formed by rotation of the pyridine groups, could not be detected. This was also confirmed in the literature investigating the isomers of symmetric porphyrin **1** [188]. Using DFT calculations, it was shown that the peripheral pyridyl groups of porphyrin **1** in the crystal state are twisted out of the plane of the planar porphyrin ring and follow the *ααββ* conformation of the molecule (**Figure 22**) [188].

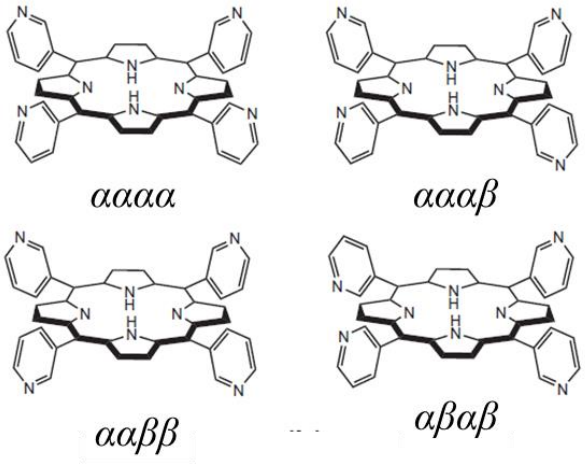

Figure 22. Perspective view of four possible conformations of porphyrin **1** [188].

4.1.3. Spectroscopic properties of *N*-methylated porphyrins and their Zn(II) complexes

The absorption and fluorescence properties of free-base and Zn(II) porphyrins measured in methanol (MeOH) are shown on **Figure 23** and in **Table 1**. The characteristic absorption spectrum of free-base porphyrins is explained by the "four-orbital theory" (with two highest occupied π orbitals and two unoccupied π^* orbitals) proposed by Martin Gouterman in the early 1960s [189,190]. It is divided into two distinct regions, where the transition from the ground state to the second excited state ($S_0 \rightarrow S_2$) can be seen as a strong Soret or B band in a range of 400-450 nm. In the second region between 500 and 650 nm, there are four Q bands that indicate the transition from the ground state to the first excited state ($S_0 \rightarrow S_1$) [191]. The intensity of the Q bands can vary depending on the porphyrin structure and the position (*β* or *meso*) or type of substituents. In the literature, there are *ethio*, *rhodo*, *oxo-rhodo* and *phyllo* type of the free-base porphyrin spectrum [60,185]. In our case, with *meso*-substituted porphyrins, the *phyllo* type of absorption spectra is expected, with the intensity of the Q bands in the order IV> II > III> I. Furthermore, it has been shown that the type of *meso* substituents

has an influence on the absorption and fluorescence spectra, due to the interaction between the substituents and the porphyrin ring. Some of the features that can influence the spectral properties are the electronic and inductive effect of the substituents and the dihedral angles between the planes of the outlying moieties and the porphyrin ring [192].

Here, all the synthesized free-base *N*-methylated (pyridinium-3-yl)porphyrins show a strong Soret band at 422 nm with calculated ε = 2.5-2.9 10^5 $M^{-1}cm^{-1}$ and four Q bands from 514 nm to 645 nm with calculated ε = 1.7-2.0 10^4 $M^{-1}cm^{-1}$ for Q_y (1-0) to 1.0-1.7$10^3$ $M^{-1}cm^{-1}$observed for Q_x (0-0) (**Table 5**). The incorporation of the metal cation into the porphyrin core leads to a change in electron density, which in turn alters the absorption and fluorescence properties of the porphyrin. The metal ion accepts the lone pair of electrons of the *N*-atoms of the pyrrole, substituting the hydrogen atoms and forming delocalized π bonds, which permit the easy electron flow within the delocalised π system. Metalation with Zn^{2+} increases the symmetry of the molecule from rectangular (D_{2h}) to square (D_{4h}), resulting in a simpler spectrum and reducing the number of Q bands from four to two [63,193]. In addition, chelation with Zn^{2+} to porphyrins generally showed a small red shift of the Soret band due to the delocalization of the π-bands by the lone electrons of Zn(II) porphyrins, which increases the average electron density of the porphyrin, resulting in a lower energy for electron transfer and thus causing a bathochromic shift of the Soret band [194]. In addition, out-of-plane and border-line metalloporphyrins (as Zn(II)) do not perturb the molecular orbital upon metal chelation, so their change in the electronic spectrum resembles the spectrum of the deprotonated form of the free-base porphyrin [195,196].

Porphyrins **21** to **27** showed strong Soret band at 432 nm $\varepsilon = 2.2 \times 10^5$ $M^{-1}cm^{-1}$ and two distinct Q bands in MeOH (**Table 5B**), Q (1-0) at 560 nm with observed $\varepsilon = 1.4\text{-}1.8 \times 10^4$ $M^{-1}cm^{-1}$ and Q (0-0) at 600 nm with observed $\varepsilon = 1.8\text{-}3.0 \times 10^5$ $M^{-1}cm^{-1}$. Compared to the free base analogues, a reduction in the number of Q bands from four to two and a bathochromic shift of the Soret band by 10 nm were observed, as expected (**Figure 23**). In addition, the observed molar absorption coefficients (ε) of the Zn(II) porphyrins at the Soret band wavelength was much lower compared to their free-base analogues. These results are consistent with the changes of other standard *meso*-substituted porphyrins and their chelation with Zn^{2+}, such as tetraphenylporphyrin and zinc(II) tetraphenylporphyrin [63,197].

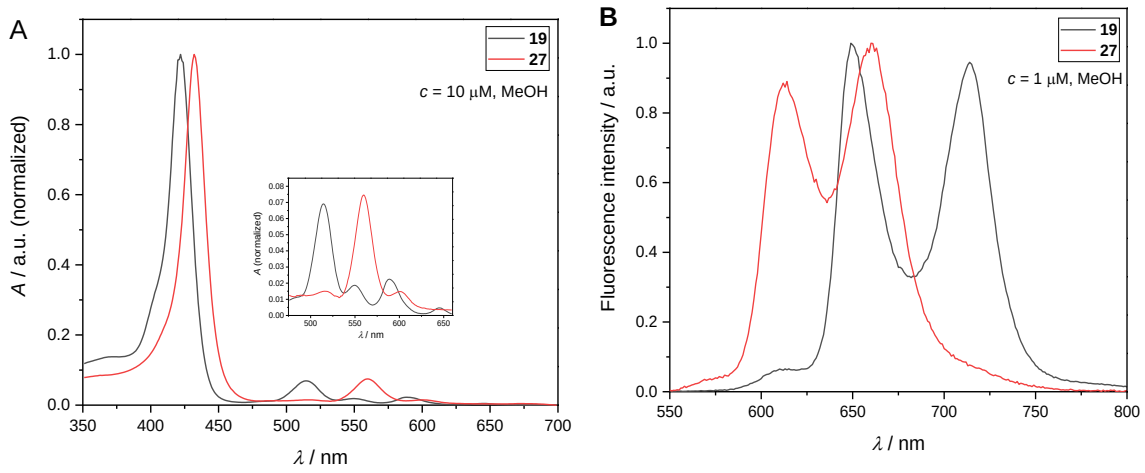

Figure 23. Comparison of the normalised absorption (A) and fluorescence (B) spectrum of *N*-methylated free-base and Zn(II) porphyrins on the example of porphyrins **19** and **27**, both conjugated with an alkyl chain with 17 C atoms. Measurements were performed in MeOH and Soret band wavelength (λ = 419 nm (**19**) and λ = 432 nm (**27**)) was used for the excitation.

The fluorescence spectra of the free-base porphyrins **13**-**19** and their Zn(II) complexes **21**-**27** were recorded in MeOH (**Table 5**). All spectra of the free base porphyrins are characterised by two distinct maxima at 650 nm for Q (1-0) and 715 nm for Q (0-0) with additional "shoulder" at 610 nm. Upon metalation with Zn^{2+}, two maxima are observed at ~ 615 nm and 660 nm, with a hypsochromic shift compared to the free-base analogues of 35 nm for Q (0-0) and 55 nm for Q (1-0). The Stokes shift was calculated as the λ-difference in nm between the absorbance Q_x (0-0) in the case of free base porphyrins and Q (0-0) for metalloporphyrin and the fluorescence band Q (0-0). For free base porphyrin, the calculated Stokes shift was between 4 and 6 nm, while for Zn(II) porphyrins a slightly larger Stokes shift of ~ 12 nm was observed (**Table 5**).

The quantum yield of fluorescence (Φ_{FL}) provides information on the efficiency of the fluorescence that occurs. It is defined as the ratio of the number of emitted photons to the number of photons absorbed in the sample. Here, the Φ_{FL} of the free-base porphyrins **13**, **14** and **19** and their Zn(II) complexes **21**, **22** and **27** was determined according to equation 8 using **TPP** (for free-base porphyrins) and **ZnTPP** (for metalloporphyrins) as reference compounds. The literature values for Φ_{FL} for **TPP** and **ZnTPP** were 0.11 and 0.03 [198], respectively. Free-base porphyrins exhibit a higher Φ_{FL} compared to their Zn(II) complexes with the same alkyl chain length. The hydrophilic porphyrin **13** had a Φ_{FL} = 0.072 and its

Zn(II) analogue 0.051, while a lower Φ_{FL} of 0.021 was observed for both amphiphilic Zn(II) porphyrins (**22** and **27**) compared to the free-base analogues, porphyrins **14** (0.045) and **19** (0.105). Increased intersystem crossing (ISC) rate for Zn(II) porphyrins results in their lower Φ_{FL} and has already been described in the literature [63,196,199].

Table 5. Absorption and fluorescence properties of *N*-methylated porphyrins and their Zn(II) complexes recorded in MeOH. *Soret band wavelength was used for the excitation.

A	λ_{abs} / nm (ε / $\times 10^3$ $M^{-1}cm^{-1}$)					λ_{em} / nm*		Φ_{FL}
	Soret (B)	Q_y (1-0)	Q_y (0-0)	Q_x (1-0)	Q_x (0-0)	Q (0-0)	Q (1-0)	
13	422 (267.1)	515 (17.7)	552 (6.2)	588 (6.1)	645 (1.5)	649	714	0.072
14	422 (258.4)	514 (16.9)	551 (4.4)	598 (5.4)	645 (1.5)	648	713	0.045
15	422 (249.1)	515 (16.5)	552 (5.9)	588 (5.7)	645 (1.8)	650	715	-
16	422 (289.4)	514 (19.4)	550 (5.6)	589 (6.4)	644 (1.5)	650	714	-
17	422 (251.7)	514 (15.7)	550 (4.5)	589 (4.9)	646 (0.7)	651	714	-
18	422 (274.6)	514 (18.3)	551 (5.4)	589 (6.1)	644 (1.4)	649	715	-
19	422 (268.7)	514 (17.9)	551 (5.5)	589 (4.1)	645 (1.5)	650	714	0.105

B	λ_{abs} / nm (ε / $\times 10^3$ $M^{-1}cm^{-1}$)			λ_{em} / nm*		Φ_{FL}
	Soret (B)	Q (1-0)	Q (0-0)	Q (0-0)	Q (1-0)	
21	432 (203.3)	560 (15.1)	600 (2.5)	614	659	0.051
22	432 (241.9	560 (17.6)	602 (2.4)	613	660	0.021
23	432 (227.0)	560 (17.0)	600 (1.7)	614	660	-
24	432 (223.2)	560 (16.9)	601 (2.8)	611	660	-
25	432 (220.7)	560 (16.6)	599 (2.8)	612	660	-
26	432 (189.5)	560 (14.3)	602 (2.5)	614	660	-
27	432 (211.1)	554 (18.2)	601 (3.0)	614	660	0.021

In addition to the absorption and fluorescence properties recorded in MeOH, the solvation effect on the absorption properties in water and 0.05 M phosphate buffer of hydrophilic porphyrin **13** and its Zn(II) complex, porphyrin **21**, as well as on porphyrins **19** and **27**, its Zn(II) complex, both substituted with the 17 C-atom alkyl chain, were investigated (**Figure 24**).

The porphyrin **13** showed similar absorption spectra in both water and phosphate buffer, with a hypsochromic shift of 2 nm for the Soret band and a bathochromic shift of 4 nm for the Q (1-0) band when the porphyrins are dissolved in aqueous solutions compared to MeOH. In addition, a hyperchromic shift was observed in MeOH for the Q (1-0) and Q (0-0) bands

compared to spectra in water or buffer (**Figure 24A**). For Zn(II) porphyrin **21**, hypsochromic shifts of the Soret band and Q (1-0) for 2 nm were observed for a porphyrin dissolved in water compared to MeOH (**Figure 24B**). The changes in the absorption spectra of symmetric **TMPyP4** were previously studied in both water and alcoholic solutions (MeOH, EtOH and propanol (PrOH)), where similar changes were observed [200]. These solvent polarity-dependent changes were linked to the impact of charge transfer (CT) between the porphyrin core and the side groups, which contributes to the formation of the lowest absorption maximum. This CT state is dependent on the polarity of the solvent and the degrees of freedom achieved by the co-planarity of the porphyrin-π system [163,200]. Although expected, it was found in this work that the influence of hydrogen bonding on the changes in the absorption spectrum is insignificant [200].

A more complex situation was observed for amphiphilic porphyrins **19** and **27** (**Figure 24C and 24D**), where similar changes were observed between the spectra in water and MeOH. However, in 0.05 M phosphate buffer, a much lower intensity and a broadening of the Soret band was observed. Furthermore, a hyposchromic shift and a decrease in intensity was also observed in the Q bands. These changes are known to be the first indications of aggregate formation. In porphyrins, different types of aggregates are known, such as face-to-face dimers, cyclic arrangements and H- and J-aggregates, and were investigated, in particular describing their effects on the steady state electronic absorption and fluorescence spectral properties as well as the changes in time-resolved spectra [201,202]. The influence of ionic strength in solution has already been observed for certain cationic porphyrins, where it has been shown that the addition of salt, such as KNO_3, enhances the self-aggregation of water-soluble porphyrins. This is due to the “salting out” effect, that influences the orientation of the water molecule and thus increases the hydrophobic interaction between the porphyrin molecules [203]. This was confirmed in a study of a porphyrin with similar structure, where it was found that porphyrins of higher hydrophobicity tend to aggregate more easily, allowing them to form more stable vesicle-like aggregates [204]. The changes in time-resolved spectroscopy by laser pulse photolysis (LFP) and time-correlated single photon counting (TC-SPC) using these solvents are described in the following chapters.

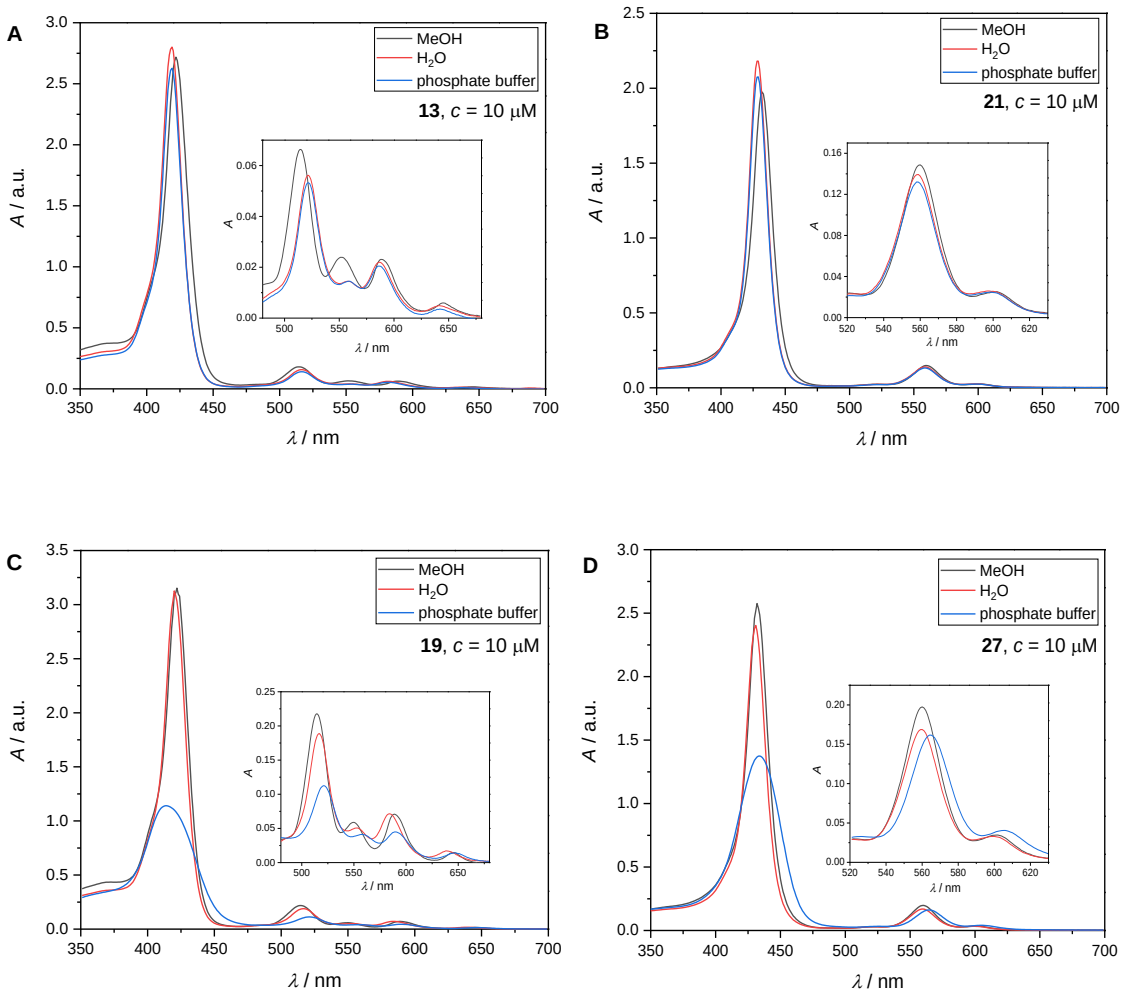

Figure 24. Comparison of the absorption spectra of *N*-methylated free-base porphyrins **13** (A) and **19** (C) and their Zn(II) complexes **21** (B) and **27** (D) in MeOH, H_2O and 0.05 M phosphate buffer.

The influence of solvation on the fluorescence spectra of porphyrins **13** and **21** in water, phosphate buffer and MeOH was also investigated. Porphyrin **19** showed the broadening of Soret band and its lower intensity in phosphate buffer (**Figure 24**), which indicates the possible formation of aggregates [201], therefore, the tendency of hydrophilic porphyrins to form aggregates was studied at different excitation wavelength (**Figure S80**), different concentrations (**Figure S81**), at different temperatures (**Figure 25**) and before and after purging the 1 μM solution with N_2 (**Figure S82**). In addition, porphyrin **13** showed a bathochromic shift of 10 nm at concentrations > 10^{-4} M in MeOH, indicating the formation of aggregates (**Figure S83**).

In the fluorescence spectra, the vibrionic structure of free-base porphyrin **13** is better resolved in MeOH than in buffer and water, while the changes in the resolution of Zn(II) porphyrin **21** were negligible. The impact of different solvents and their mixture (H_2O, H_2O: MeOH 1:1, MeOH) and different alcohols (EtOH and PrOH) has previously been investigated with isomers of symmetric free-base pyridiniumporphyrins, which vary in the position of the nitrogen in the pyridyl ring and show similar effects [200,205]. The spectral changes in the vibrionic structure in H_2O and buffers may be due to the formation of stronger hydrogen bonds in the structure and to the mixing of the S1 state with the nearby CT state formed by charge translocation from the porphyrin ring [163,200]. A better resolution of the spectra in H_2O can be achieved by increasing the temperature, adding organic solvents or surfactants or diluting the solution to $< 10^{-7}$ M [205].

The temperature-dependent fluorescence spectra were recorded after cooling to 5 °C, then after heating to 60 °C and finally after cooling back to room temperature (25 °C) (**Figure 25**). As indicated above, increasing the temperature resulted in well-resolved vibrionic spectra in water and phosphate buffer compared to spectra recorded at 5 °C or 25 °C (**Figure 25B** and **25C**). For both porphyrins **13** and **21**, no bathochromic or hypsochromic shifts were observed in water or phosphate buffer, indicating that no aggregates are formed. However, a small temperature-dependent hypsochromic shift was detected in MeOH (**Figure 25A** and **25D**), indicating the formation of H-type aggregates even in hydrophilic porphyrins.

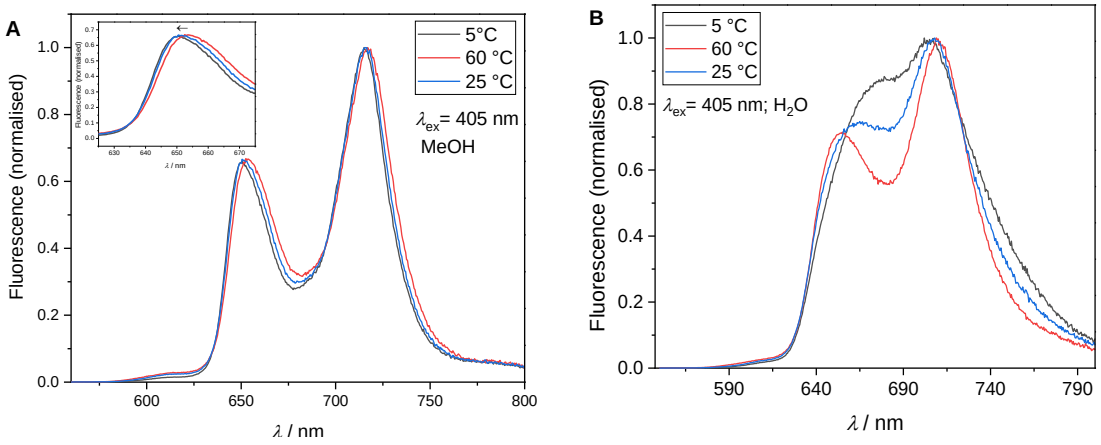

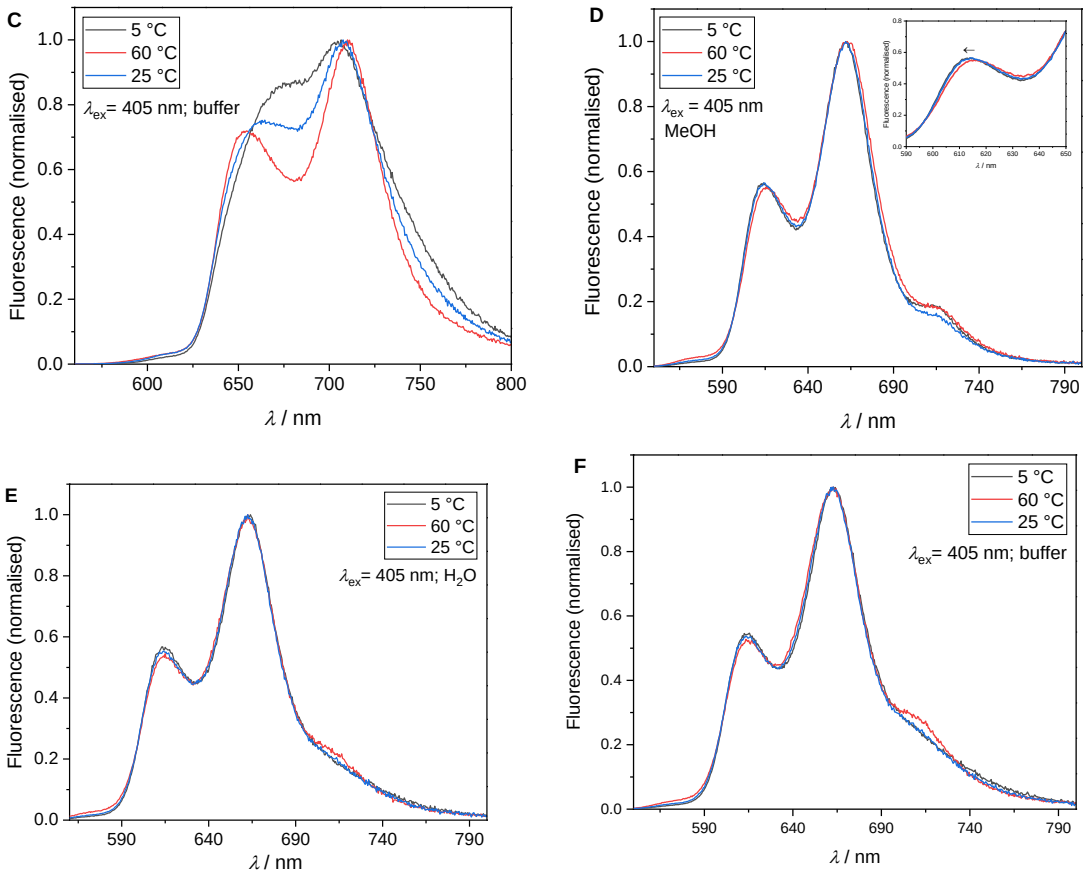

Figure 25. Comparison of the temperature effect (5 °C, 25 °C and 60 °C) on the fluorescence spectra of porphyrin **13** (A, B and C) and its Zn(II) complex **21** (D, E and F) (1 μM) in MeOH (A, D), H_2O (B, E) and 0.05 M phosphate buffer (C, F).

Furthermore, the absorption properties of the free-base porphyrins and their Zn(II) complexes with alkyl chains of 1, 9, 13 and 17 C atoms were investigated in phosphate buffer saline (1× PBS, pH = 7.45) (**Figure 26 and Table 6**), a buffer used in many biological experiments. For the hydrophilic porphyrins **13** and **27**, similar results were shown in PBS as in phosphate buffer, with a slightly larger hypsochromic shift (3 nm) in the Zn(II) analogue, probably due to the presence of a higher ionic strength. Porphyrin **15**, with an alkyl chain of 9 C atoms, showed a similar spectrum to porphyrin **13**, while porphyrins **17** and **19**, substituted with an alkyl chain of 13 and 17 C atoms, respectively, exhibited a larger hypsochromic shift (6 nm) and a broadened Soret band with lower intensity, suggesting the formation of aggregates.

Similar to the hydrophilic analogue, porphyrin **23** substituted with an alkyl chain of 9 C atoms showed a hypsochromic shift of 3 nm, with a decreased intensity of the Soret band. In contrast to the hydrophilic analogue **21**, the Zn(II) porphyrins **25** and **27**, substituted with an alkyl chain of 13 and 17 C atoms, respectively, showed a bathochromic shift of 1 nm and 5 nm

(**Figure 26B**). As with the free-base porphyrins, Zn(II) porphyrins **25** and **27** showed a broadened Soret band with a strong decrease in absorption intensity, indicating that aggregation occurs in aqueous solutions upon addition of inorganic salt.

The emission spectra recorded in PBS with maxima at 655 nm and 715 nm for the free-base porphyrins and at 613 and 660 nm for the Zn(II) porphyrins correspond to the poorly resolved spectra in water and phosphate buffer shown above (**Figure 27** and **Table 6**). As can be seen from the absorption spectra, a longer alkyl chain leads to a lower fluorescence intensity, which can plausibly be explained by the formation of aggregates, especially for the free-base porphyrins **17** and **19** and their Zn(II) complexes **25** and **27** (**Figure 27**).

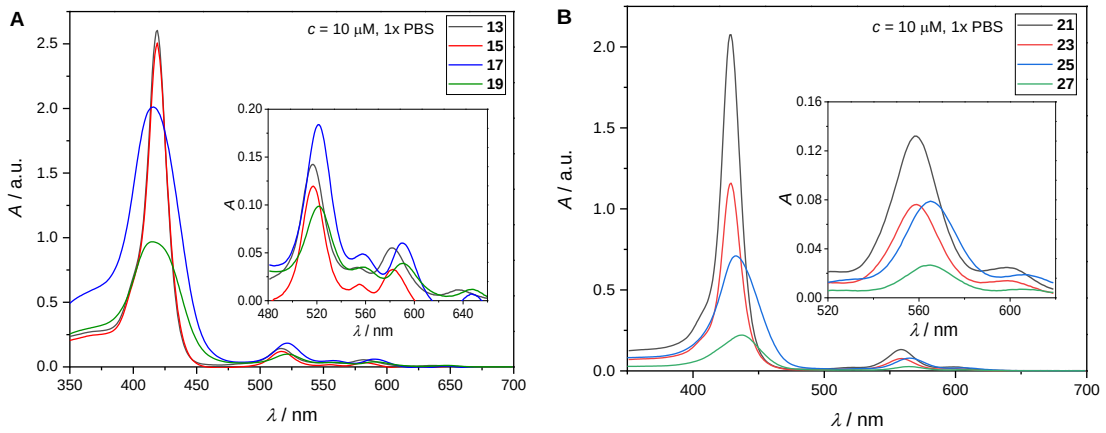

Figure 26. Absorption spectra of the *N*-methylated free-base porphyrins (**13**, **15**, **17** and **19**) (A) and their Zn(II) complexes (**21**, **23**, **25** and **27**) (B) recorded in 1× PBS.

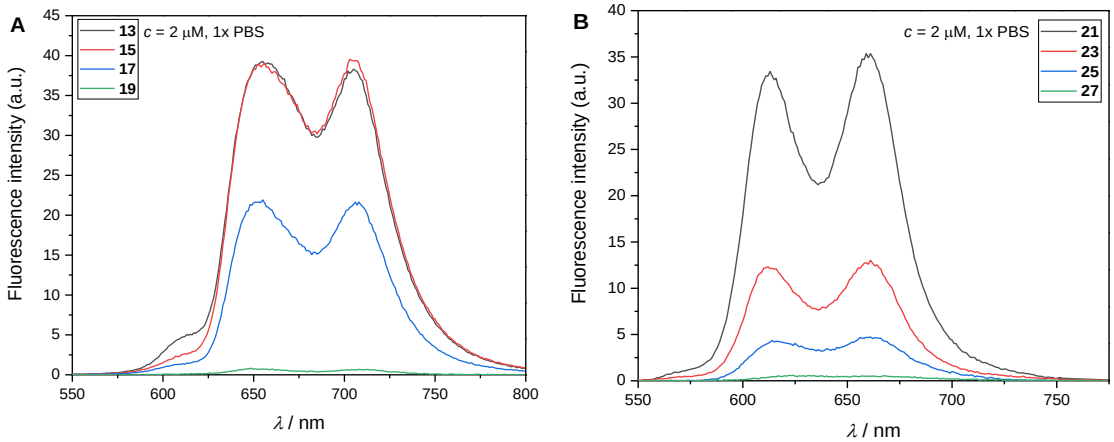

Figure 27. Emission spectra of the free-base porphyrins (**13**, **15**, **17** and **19**) (A) and their Zn(II) complexes (**21**, **23**, **25** and **27**) (B) recorded in PBS. Excitation wavelength used for free-base *N*-methylated porphyrins was 420 nm, and for Zn(II) complexes 430 nm.

Table 6. Absorption and fluorescence properties of the selected A) *N*-methylated porphyrins and their B) Zn(II) complexes obtained in 1× PBS.

A	λ_{abs} / nm (ε / × 10^3 $M^{-1}cm^{-1}$)					λ_{em} / nm*	
	Soret (B)	**Q_y(1-0)**	**Q_y(0-0)**	**Q_x(1-0)**	**Q_x(0-0)**	**Q (0-0)**	**Q (1-0)**
13	419 (263.9)	517 (15.1)	552 (3.5)	581 (5.6)	638 (1.1)	654	705
15	419 (264.7)	517 (13.1)	555 (2.6)	583 (3.1)	639 (0.8)	656	703
17	416 (199.4)	521 (19.0)	557 (6.9)	590 (8.0)	646 (2.3)	655	706
19	416 (95.1)	522 (9.9)	558 (3.4)	590 (3.8)	648 (1.1)	655	708

B	λ_{abs} / nm (ε / × 10^3 $M^{-1}cm^{-1}$)			λ_{em} / nm*	
	Soret (B)	**Q (1-0)**	**Q (0-0)**	**Q (0-0)**	**Q (1-0)**
21	428 (212.9)	557 (13.5)	598 (2.5)	611	659
23	429 (117.4)	559 (7.7)	599 (1.4)	612	661
25	433 (71.7)	565 (8.4)	606 (1.9)	614	661
27	437 (22.5)	565 (2.7)	604 (0.7)	615	662

* Soret band wavelength was used as the excitation wavelength.

4.1.4. Time-correlated single photon counting (TC-SPC) of free-base *N*-methylated porphyrins (13, 14 and 19) and their Zn(II) complexes (21, 22 and 27)

Time-correlated single photon counting (TC-SPC) is a technique with the highest recording efficiency and the best time resolution among the known time-resolved techniques and is mainly used to measure fluorescence lifetime from the picosecond (ps) to microsecond (μs) time range and the related time-resolved fluorescence properties [206]. Nowadays, it can also provide information on the kinetics of the excited state of a photochemical reaction and can be used for photon migration measurements in scattering or absorbing media and for time-resolved fluorescence imaging [207]. The method is based on the detection of single photons and the measurement of the time from the pulsed excitation to the arrival of the photon to the detector. The relatively high repetition of the short flash of light triggered by an LED or a laser pulse (10 kHz to 100 MHz) is synchronised with the time of arrival of the photons at a detector, the photomultiplier tube (PMT). Timing electronics in the form of a time-to-digital converter or time-to-amplitude converter (TAC) are used to record the signals. The registration of the single photon arrivals results in a histogram whose decay behaviour is then fitted to an exponential function that represents that represents the luminscence decay of an excited state, usually singlet excited state that decays by fluorescence (^{1}PS*) [207].

The fluorescence decays were studied for porphyrins **13**, **14** and **19** as well as for their Zn(II) complexes **21**, **22** and **27** in MeOH and phosphate buffer (**Table 7**). All decays were typically were fit to a sum of two exponents, indicating dual fluorescence in the sample. This could be tentatively explained by the isomers present in the structure, e.g. NH tautomers or rotamers formed by the rotation of the pyridinium ring. In addition, the multiexponential fluorescence decay may also be a consequence of aggregation [163,201].

In methanol, none of the compounds tested showed changes in the absorption or fluorescence spectrum that would indicate the formation of aggregates in the ground state in 10 μM concentration at room temperature (25 °C) (**Table 5**). However, all fluorescence decays of free-base porphyrins (**13**, **14** and **19**) were fit to a sum of two exponents, with a shorter decay component of 1.4 ns and a smaller contribution and the longer decay component of ∼10 ns with a larger contribution (**Figure 28A**, **28C** and **28E**). Note that the contribution of the shorter decay increases with the length of the alkyl chain of the porphyrins tested. The contribution of the hydrophilic porphyrin **13** substituted with the acetamido group was only 5%, while for porphyrin **14** substituted with an alkyl chain of 7 C atoms was 17% and for porphyrin **19**, with an alkyl chain of 17 C-atoms was 19%. This indicates that the shorter component probably belongs to a porphyrin in the aggregated form, with the amount of aggregates increasing with the length of the alkyl chain, and that the longer contribution probably belongs to the porphyrin in its monomeric form. The longer contribution of the fluorescence decay of 10 ns is consistent with literature data of other free-base porphyrins in MeOH, where a lifetime of 10.6 ns was observed for the monomeric form of the symmetric tetraypyridinium-3-ylporphyrin in MeOH [200,205] and 10.8 ns is estimated for symmetric tetra-(3-hydroxyphenyl)porphyrins (**THOPP**) [208]. In addition, the fluorescence lifetime of a reference compound, **TPP** in toluene is 11 ns [198].

Two exponential fluorescence decays were also observed for Zn(II) porphyrins, confirming the hypothesis that the contributions of the decay are due to the presence of aggregates in the sample or rotamers but not to tautomers as mentioned above as one of the possible reasons of multiexponential decay [163]. Among the Zn(II) porphyrins, decay with a lifetime of ~ 1.5 ns was observed for all porphyrins tested, suggesting that this lifetime may correspond to a non-aggregated molecule of a porphyrin. Furthermore, the reported lifetimes for Zn(II) porphyrins are usually in the range of 1-3 ns, confirming this assignment [198,209]. The other, longer component of the fluorescence decay for hydrophilic Zn(II) porphyrin **21** was estimated to be 3.88 ns and corresponds to 7% of the decay. In the case of amphiphilic porphyrin, short decay times were observed, with an estimated 0.7 ns for **22** (with a contribution of 13%) and 1.15 ns for **27** (with a contribution of 49%). As with free-base porphyrin, the contribution of the shorter decay is larger with the length of the alkyl chain. This confirms that the smaller contribution of the decay with variable decay lifetime can be

attributed to the aggregates and that even for Zn(II) porphyrins the amount of aggregates in solution increases with the length of the alkyl chain (**Figure 28B**, **28D** and **28E**).

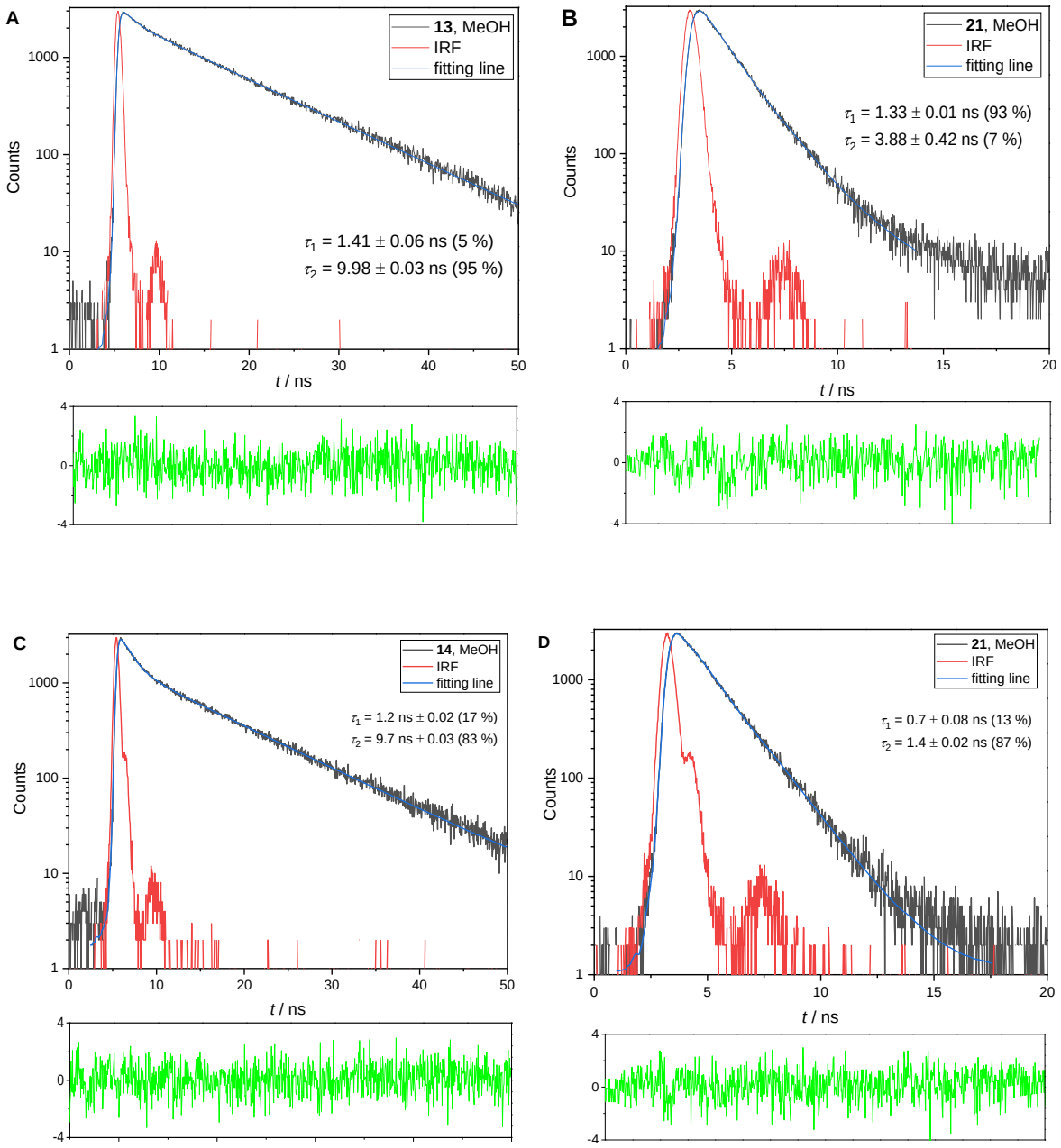

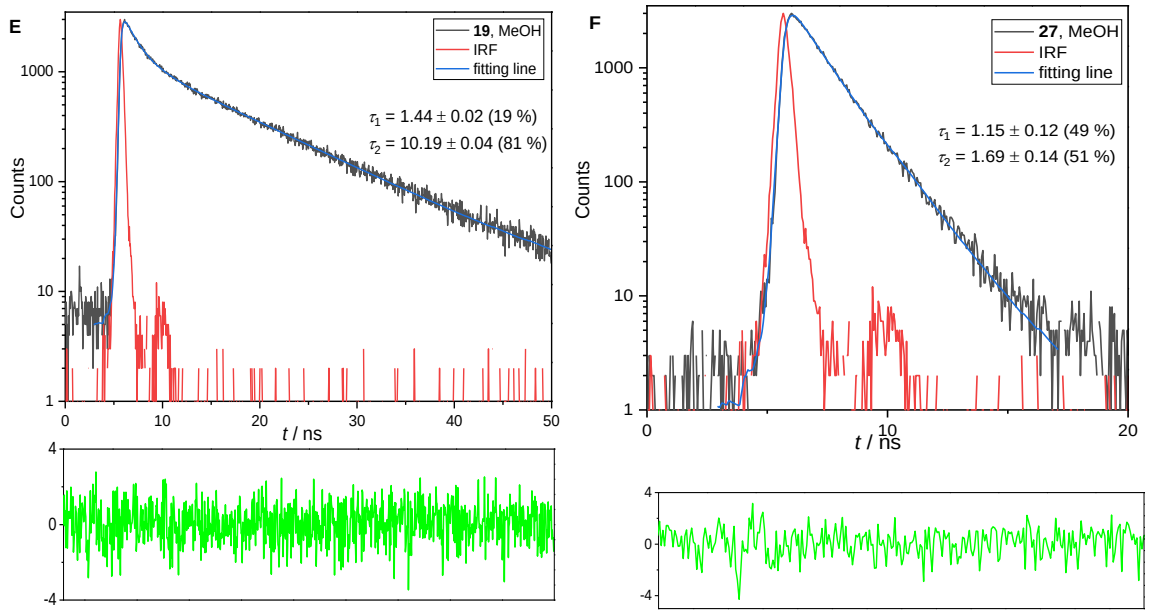

Figure 28. Fluorescence decay at 650 nm (λ_{ex} = 405 nm) for free-base porphyrins **13** (A), **14** (C) and **19** (E) their Zn(II) complexes **21** (B), **22** (D) and **27** (F) measured in MeOH (N_2) using time-correlated single photon counting (TC-SPC) (black line) and fit to a sum of two exponents (red line). The bottom panel of the figures correspond to the weighted residuals between the experimental and the fitted values.

It is worth emphasizing that the longest decay times were found for all monomeric forms of free-base porphyrins in MeOH. Compared to the decay times measured in H_2O and phosphate buffer, the decay times in MeOH were ~ 3 ns longer. This result agrees with the lifetimes obtained for symmetric tetrapyridinium-3-yl porphyrin shown by Vergeldt and colleagues [205]. There it was shown that the lifetime of the monomer in H_2O is 7.9 ns and increases to 9.0 ns when a mixture of H_2O and MeOH (4:1) is used as solvent and to 10.6 ns when only MeOH is used as solvent [205]. Goncalves and colleagues also showed similar result for tetra(pyridinium-4-yl)porphyrin, with 5.4 ns τ_S observed in H_2O, and > 10 ns τ_S observed in alcoholic solutions as MeOH, EtOH or propanol (PrOH) [200]. In addition, the contributions of a shorter decay, that are thought to come from a porphyrin in aggregated form, are smaller than in MeOH, with 1% observed for porphyrin **13** and 5% for porphyrin **14** in phosphate buffer (**Table 3**). Since both water and MeOH are polar protic solvents and their alteration is not expected to affect the equilibrium of the isomers such as rotamers and tautomers, this confirms that the two exponential decays may be due to the formation of aggregates in MeOH and, to a lesser extent, in phosphate buffer [163].

Only fluorescence decay of porphyrin **19**, which also showed broadened peaks of lower intensity in the ground state, indicating formation of aggregates (**Figure 24**), was fit to a sum

of three exponents, with only 31% of the porphyrin in monomeric form, with an estimated lifetime of 7.54 ns. The other two short components of 0.35 ns with a contribution of 44% to the decay and 1.10 ns with a contribution of 25% to the decay could be due to different types of aggregates present in the sample (**Table 7**).

Table 7. Fluorescence decay times (τ_F) obtained using TC-SPC (λ_{ex} = 405 nm) of free-base porphyrins **13**, **14** and **19** and their Zn(II) complexes **21**, **22** and **27** in MeOH and phosphate buffer, 0.05 M, pH = 7 at 1 μM concentration after degassing the solution with N_2. For porphyrins **13** and **21** the water was also used as solvent.

A	**Solvent**	**τ_S / ns (%)**
13	**MeOH**	1.41 ± 0.06 (5 %) 9.97 ± 0.03 (95 %)
	H_2O	7.34 ± 0.01 (100 %)
	phosphate buffer, 0.05 M	0.6 ± 0.1 (1 %) 7.29 ± 0.02 (99 %)
14	**MeOH**	1.25 ± 0.02 (17 %) 9.74 ± 0.03 (83 %)
	phosphate buffer, 0.05 M	1.10 ± 0.06 (5 %) 7.40 ± 0.02 (95 %)
19	**MeOH**	1.44 ± 0.02 (19 %) 10.19 ± 0.04 (81 %)
	phosphate buffer, 0.05 M	0.35 ± 0.02 (44 %) 1.10 0.08 (25 %) 7.54 0.13 (31 %)
B		**τ_S / ns (%)**
21	**MeOH**	1.33 ± 0.01 (93 %) 3.88± 0.04 (7 %)
	H_2O	1.32 ± 0.01 (93 %) 3.8 ± 0.4 (7 %)
	phosphate buffer, 0.05 M	1.31 ± 0.01 (85 %) 3.1 ± 0.1 (15 %)
22	**MeOH**	0.73± 0.08 (13 %) 1.44 ± 0.02 (87 %)
	phosphate buffer, 0.05 M	0.60 ± 0.08 (9 %) 1.40 ± 0.01 (91 %)
27	**MeOH**	1.15 ± 0.12 (49 %) 1.69 ± 0.14 (51 %)
	phosphate buffer, 0.05 M	-

4.1.5. Laser flash photolysis (LFP) of free-base *N*-methylated porphyrins (13, 14 and 19) and their Zn(II) complexes (21, 22 and 27)

The excited triplet state of a PS (^{3}PS*) is the most important PS state for producing ROS. Therefore, the excited triplet state of porphyrin and its photophysical properties are of interest for the design of an ideal PS for use in PDT. To generate and investigate the ^{3}PS* properties, the nanosecond laser flash photolysis (LFP) method described in Section 3.6 was used.

The properties measured in this work using laser flash photolysis (LFP) include the quantum yield of the intersystem crossing (Φ_{ISC}), the lifetime of the ^{3}PS* (τ_T) and the quenching rate constant (k_q) of the ^{3}PS* by molecular oxygen. The representative TA spectra assigned to the ^{3}PS* and the triplet decay kinetic profile for the free-base porphyrins **13**, **14** and **19** and for their Zn(II) complexes **21**, **22** and **27** obtained in MeOH (**13**, **21**, **19** and **27**) or in 0.05 M phosphate buffer (**14** and **22**) are shown in **Figure 29** and **Figure 30**. As can be seen in all spectra, the maximum of the triplet absorption can be observed at 450 nm for the free-base and 460 nm for their Zn(II) complexes, while the maximum of the ground state bleach is at 420 and 440 nm, respectively (**Figure 29**).

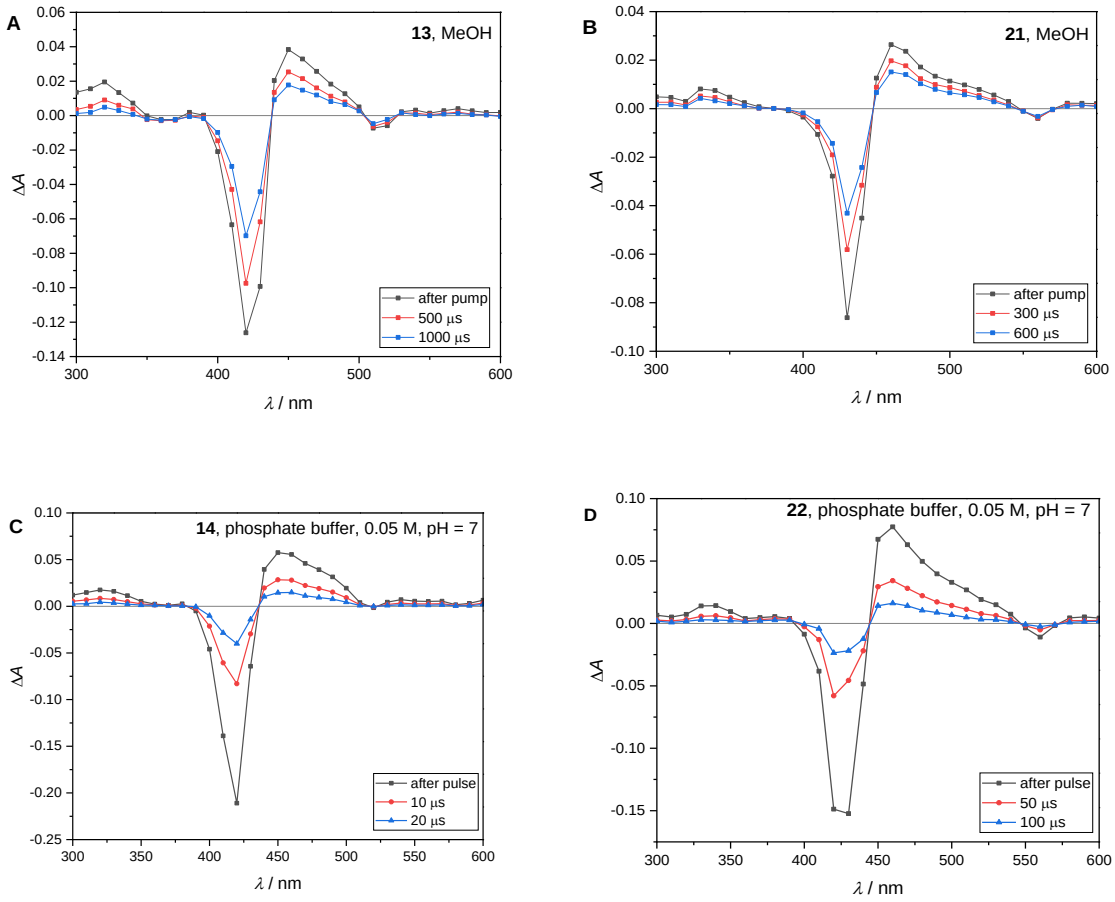

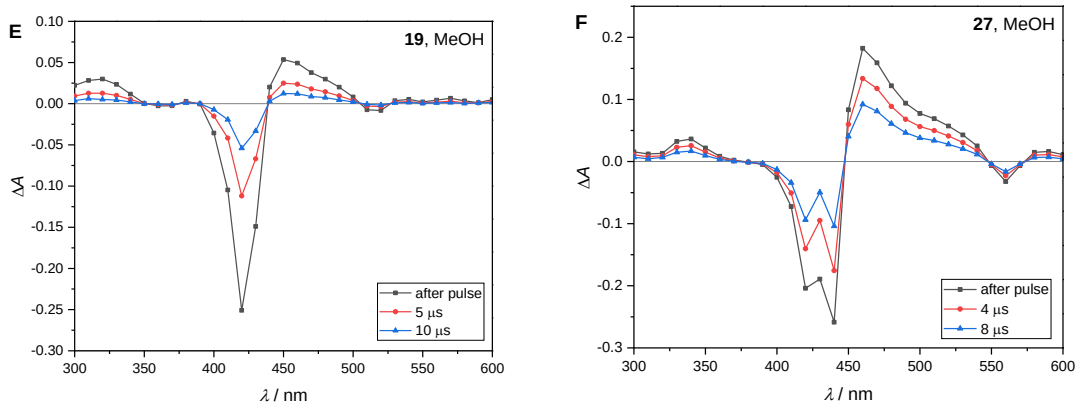

Figure 29. Triplet-triplet absorption spectra or Transient absorption spectra after laser excitation of free-base *N*-methylated porphyrins **13** (A), **14** (C) and **19** (E) and their Zn(II) complexes **21** (B), **22** (D) and **27** (F). ^{3}PS* of **13** and **21** were recorded in MeOH after laser excitation at 266 nm ($E_{266\ nm}$ = 2 mJ. $A_{266\ nm}$ = 0.20), ^{3}PS* of **14** and **22** in phosphate buffer (0.05 M, pH = 7) after laser excitation at 355 nm ($E_{355\ nm}$ = 2 mJ. $A_{355\ nm}$ (14) = 0.23; $A_{355\ nm}$ (22) = 0.25) and ^{3}PS* **19** and **27** in MeOH after laser excitation at 355 nm ($E_{355\ nm}$ = 2 mJ. $A_{355\ nm}$ = 0.25).

The lifetimes of the excited triplet states were determined by fitting the triplet decays with the single exponential function (Eq. 9). The obtained lifetimes (τ_T) in MeOH for the free base porphyrins **13**, **14** and **19** are 0.77, 1.2 and 0.74 ms, respectively. The slightly shorter lifetime of porphyrin **19** could be due to the formation of different types of aggregates, as indicated by the multi-exponential decays (τ_F) obtained by TC-SPC. Compared to the free base porphyrins, a longer lifetime was observed for the Zn(II) porphyrins **21** and **22** with values of 1.1 and 1.7 ms, respectively. Furthermore, the triplet states of hydrophilic porphyrins **13** and **21**, measured in MeOH, were fit to a mixed first- and second-order decay function following equations 11 and 12, that accounts for the self-quenching of the decay due to the triplet-triplet annihilation [159]. The estimated lifetimes were slightly longer when the mixed first- and second- order decay function was used, with 1.1 ms for free-base porphyrin **13** and 1.7 ms for porphyrin **21**. The decay of transient absorption for porphyrin **27** was fit only to the mixed first- and second- order function, as this function was a better fit, and the estimated lifetime was 3.5 ms. The results obtained are in agreement with literature data for the similar porphyrin, 5,10,15,20-tetrakis(1-methylpyridinium-4-yl)porphyrin (**TMPyP4**) and its Zn(II) complex (**Zn-TMPyP4**) with lifetimes of 0.17 ms and 2 ms, respectively [210]. The effects found for the excited singlet state, such as shorter fluorescence lifetime and lower quantum yield of fluorescence for Zn-chelated porphyrins, can be attributed to the chelation of the metal ion, which is known as the "heavy" atom effect [63,199]. The triplet state lifetimes of free-base porphyrins **13** and **14** were also observed in 0.05 M phosphate buffer, with estimated 200 μs for porphyrin **13** and 170 μs for porphyrin **14**, a much shorter lifetime

compared to lifetimes in MeOH. This is consistent with the literature, where a decrease in lifetime for **TMPyP4** from 1.7 ms in EtOH to 0.2 ms in H_2O was observed[200]. With the shorter fluorescence lifetimes shown previously, this is additional confirmation that the nitrogen atoms in the porphyrin ring are more strongly hydrogen-bonded to the surrounding water molecules in the excited state than in the ground state. This could be tentatively explained by the appearance of new vibrational levels and the subsequent increase in the rates of non-radiative transitions, thus, as observed experimentally, the decreased rate of fluorescence and phosphorescence [200].

All obtained ^{3}PS* were efficiently quenched when the decays were measured in air or in O_2-purged solutions. Their quenching rate constants (k_q) were calculated using the Stern-Volmer equation **15**, comparing the decay constant ($k = 1/\tau$) with the concentration of the O_2 in solution, and the results are shown in **Table 8**. The quenching rate constants obtained are a one order of magnitude lower than the diffusion limit (**Figure S87**).

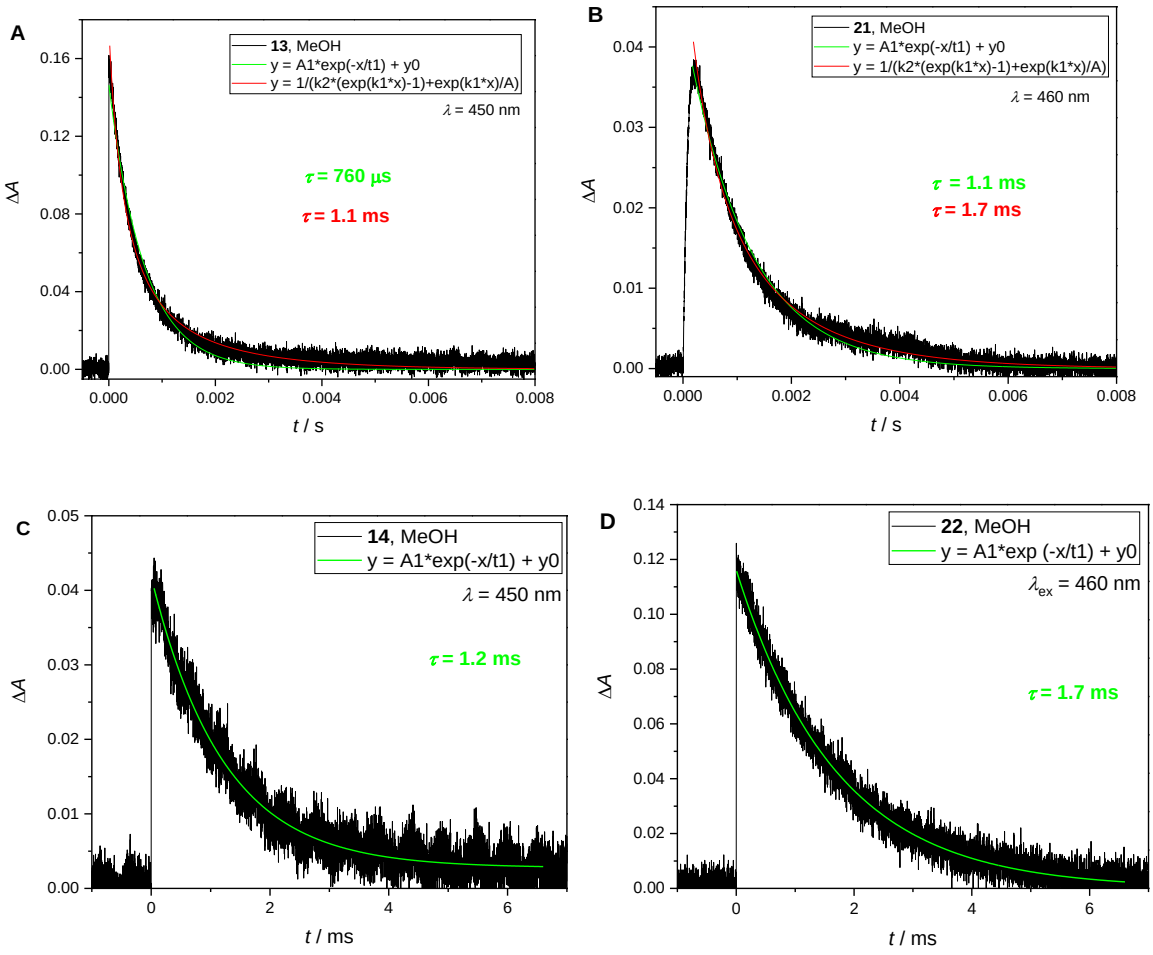

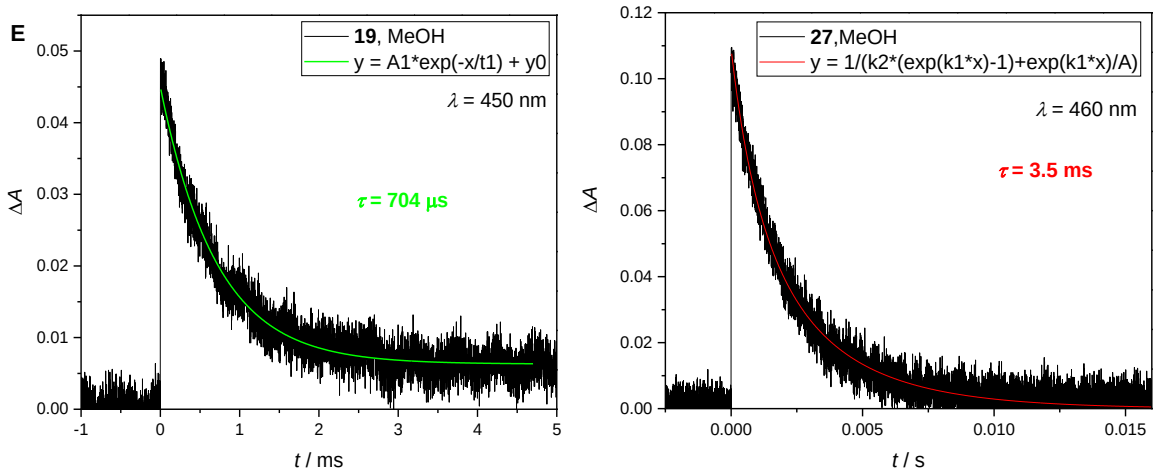

Figure 30. Transient absorption kinetics of *N*-methylated free-base porphyrins **13**, **14** and **19** (A, C and E) and their Zn(II) complexes **21**, **22** and **27** (B, D and F) at 450 nm (free-base porphyrins) or 460 nm (Zn(II) porphyrins) after 355 nm laser excitation in MeOH saturated with N_2. $A_{355\ nm} = 0.2$; $E_{355\ nm} = 3$ mJ.

The tendency of a PS to populate the triplet state was measured by the quantum yield of intersystem crossing (Φ_{ISC}), which measures the probability of triplet state formation per photon absorbed [211]. The quantum yield of intersystem crossing (Φ_{ISC}) was calculated in two steps. The first step involved the singlet depletion method to calculate the molar absorption coefficients of the excited triplet state ($\varepsilon_{T\text{-}T}$) of porphyrins according to equation **13**. This technique uses flash photolysis excitation and involves comparing the loss of ground state absorption (in our case at 420 nm) with the increase in triplet absorption (measured at 450 nm). Although this technique is not widely used, it can be applied to molecules such as PS where the singlet to triplet quantum yield is relatively high, and the triplet lifetime is reasonably long [166,167,211]. This is a simple method to measure the molar absorption coefficient when the ΔA of the triplet formed does not spectrally overlap with the singlet state and the singlet state only depopulates to S_0 and triplet, i.e. the rate constant of the triplet state depopulation is the same as the singlet state recovery [166,167]. The obtained molar absorption coefficients of the excited triplet state ($\varepsilon_{T\text{-}T}$) observed in MeOH and for some in 0.05 M phosphate buffer are summarised in **Table 8**.

The second step in the determination of the quantum yield of intersystem crossing (Φ_{ISC}) was carried out using the comparative method with **TPP** in benzene and **ZnTPP** in toluene as reference compounds according to Equation 14. (**Table 8**). The hydrophilic porphyrins **13** and **21** showed a Φ_{ISC} values of 0.34 and 0.41, respectively. These results are in agreement with the literature data, where it was observed that diamagnetic metals such as Zn(II) can enhance singlet-triplet conversion and thus increase ISC [44,63,199]. The fluorescence quantum yield (Φ_{FL}) for the corresponding porphyrins agrees with the Φ_{ISC} results.

The impact of alkyl chain length was not observed. However, contrary to the hydrophilic porphyrins, the free base porphyrins **14** and **19** showed higher Φ_{ISC} values (0.44 and 0.38, respectively) compared to their Zn(II) complexes, porphyrins **22** and **27** (0.27 and 0.29, respectively). A possible reason for these unexpected values is the choice of the singlet depletion method to calculate the molar absorption coefficient of the triplet due to the small gap between the ground state bleach maximum (420 nm) and the triplet maximum (450 nm) and a possible overlap of the spectra, which can lead to errors in the calculation of $\varepsilon_{T\text{-}T}$, and consequently of Φ_{ISC} calculation by the comparative method. To avoid these contradictory results in further calculations, an energy transfer method with benzophenone could be used [167]. The obtained results of the tested porphyrins with long τ_T and a relatively high Φ_{ISC}, show that they have photophysical properties suitable to use as PSs for PDT.

Table 8. Photophysical parameters of *N*-methylated porphyrins **13**, **14** and **19** (A) and their Zn(II) complexes **21**, **22** and **27** (B) measured in MeOH and phosphate buffer (0.05 M, pH = 7) at 25 °C. A lifetime of the ^{3}PS* ($\boldsymbol{\tau_T}$) and quantum yield of intersystem crossing (Φ_{ISC}), molar absorption coefficient of the ^{3}PS* ($\boldsymbol{\varepsilon_{T\text{-}T}}$), and quenching rate constant of the ^{3}PS* by O_2 ($\boldsymbol{k_q}$ **(O_2)**). Tetraphenylporphyrin in C_6H_6 (**TPP**) and its Zn(II)complex, **ZnTPP** in toluene were used as standards.

A	***Solvent***	τ_T / μs	$\varepsilon_{T\text{-}T}$ / $M^{-1}cm^{-1}$	Φ_{ISC}	k_q (O_2) / $M^{-1}s^{-1}$
TPP[208]	C_6H_6	90	66 600	0.67	/
13	MeOH	7678 ± 5	54000 ± 3400	0.34 ± 0.05	1.3×10^9
	phosphate buffer, 0.05M	17	-	0.33 ± 0.05	1.7×10^9
14	MeOH	1206 ± 2	43000 ± 2300	0.44 ± 0.01	1.2×10^9
	phosphate buffer, 0.05M	170 ± 19	50000 ± 1700	0.59 ± 0.02	1.6×10^9
19	MeOH	740 ± 50	57000 ± 3000	0.38 ± 0.02	1.3×10^9
	phosphate buffer, 0.05M	-	-	-	-
B	**Solvent**	τ_T / μs	$\varepsilon_{T\text{-}T}$ / $M^{-1}cm^{-1}$	Φ_{ISC}	k_q (O_2) / $M^{-1}s^{-1}$
ZnTPP[170]	toluene	30	69 000	0.88	/
21	MeOH	1100 ± 3	129 000 ± 13000	0.41 ± 0.06	5.1×10^9
	phosphate buffer, 0.05M	150 ± 22	-	0.43 ± 0.08	1.9×10^9
22	MeOH	1697 ± 2	151 000 ± 9100	0.27 ± 0.01	6.6×10^8
	phosphate buffer, 0.05M	-	-	-	-
23	MeOH	3516 ± 5	121 000 ± 2900	0.29 ± 0.02	6.6×10^8
	phosphate buffer, 0.05M	-	-	-	-

4.1.6. Spectroscopic properties of *N*-methylated free-base porphyrins 13 and 19 and their Zn(II) complexes after addition of detergents (SDS and Triton X-100)

One of the preferable characteristics of porphyrins is their interaction with biological membranes. Therefore, the studies on the interaction of porphyrins with biological membranes and the factors that influence this relationship are of great interest. To study this interaction, surfactants and spectroscopic analysis of the interaction have proven to be the most promising approach [212].

In previous experiments, the changes in the ground state absorption spectra were attributed to the possible aggregation of porphyrins in aqueous solutions with higher ionic strength, possibly due to the hydrophobic interactions of the long alkyl chain in the structure. The aggregation led to a strong decrease in absorbance and a broadening of the Soret band. Previously, it was observed that the presence of surfactants can dissociate aggregates of some amphiphilic porphyrins and protoporphyrin IX into monomers [201,204]. To investigate the possible interactions of the synthesized compounds with surfactants at different concentrations, two hydrophilic porphyrins, **13** and **21** (free base and Zn(II) complex) and their analogues substituted with an alkyl chain with 17C atoms, porphyrins **19** and **27**, all at a concentration of 10 μM, were studied. The surfactants used were non-ionic 2-[4-(2,4,4-trimethylpentan-2-yl)phenoxy]ethanol (Triton X-100) and anionic sodium dodecyl sulfate (SDS) at concentrations ranging from 50 μM to 0.1 M at neutral pH.

Minimal changes in hydrophilic porphyrins **13** and **21** were observed when Triton-X was used (**Figure 31**). At concentrations > 5 mM, a small bathochromic shift (2 nm) and a decrease in absorbance were observed. This could be due to the small electrostatic interactions of a porphyrin with a surfactant molecule [200,204,213]. Porphyrins **19** and **27** showed broadening of the Soret band of decreased intensity indicating aggregation in PBS, which my be due to the formation of micelle-like vesicles [204], as previously seen with porphyrins of similar structure. When Triton-X was added, an increase and narrowing of the Soret band was already observed at a concentration of 50 μM. At a concentration of 1 mM Triton X-100, both free base and Zn(II) porphyrins resemble spectra of porphyrins in monomeric form (**Figure 31**). This shows that the hydrophobic part also plays an important role in the interaction with surfactants, since the increased interaction of amphiphilic porphyrin with Triton X-100 could be due to the higher lipophilic character of the molecule, leading to an enhanced hydrophobic interaction with Triton X-100, which results in the dissociation of the porphyrin aggregates in monomeric form [213].

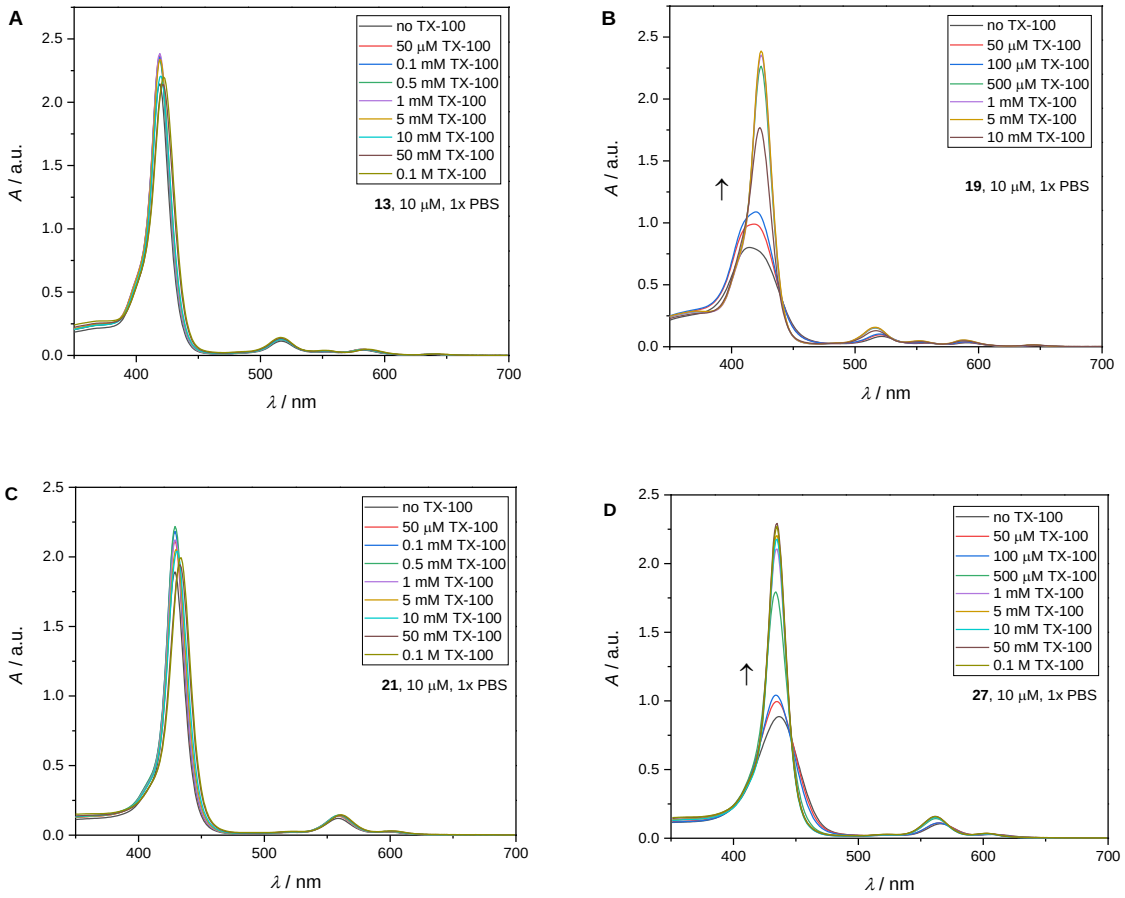

Figure 31. Absorption spectra of free base porphyrins 13 (A) and 19 (B) and their Zn(II) complexes 21 (C) and 27 (D) in PBS alone and after addition of TX-100 in different concentrations to the PBS solution.

The solubilisation of porphyrins was also investigated using SDS, as an anionic detergent, at different concentrations (**Figure 32**). Porphyrin **13**, which showed no signs of aggregation in the ground state in PBS, exhibited a significant decrease in absorption intensity, a broadening of the spectrum and a red shift when SDS was added at concentrations of 0.1 and 0.5 μM, indicating the formation of J-type aggregates (**Figure 32A**). Similar phenomenon was observed with tetra(4-hydroxyphenyl)porphyrin and its amphiphilic A_3B derivative substituted with a 14 C-atom alkyl chain in the concentration range of 1-5 mM SDS [214]. In the literature, this phenomenon is attributed to the formation of porphyrin-surfactant complexes due to the electrostatic stabilisation of the inner pyrrole protons by the formation of hydrogen bond between the oxygen atoms in the sulfonate groups of the surfactant and the pyrrole protons in the porphyrin core [214,215]. Gonçalves and colleagues came to a similar conclusion when studying **TMPyP4**. They concluded that the hydrogen bond formed

between the pyrrolic nitrogen atom and the water plays a key role in the photophysical properties of this molecule, while the side groups determine the localization in the hydrophobic part of the micelle [200]. Upon addition of the higher SDS concentration (> 5 mM), a "recovery" of the Soret band was observed, with a red shift compared to the porphyrin in PBS. This could be the result of two porphyrin-surfactant interactions that depend on the SDS concentration. The first is the J-type aggregates formed by the porphyrin-surfactant interaction, which is based on the porphyrin interaction with premicellar SDS that occurs at the critical aggregation concentration (CAC) of SDS, which is lower than the critical micellization concentration (CMC). When the SDS concentration used is higher than the CMC, the premicellar surfactant−porphyrin aggregates dissociate and form porphyrin-bound, micellar-encapsulated monomers with a red shift in the porphyrin spectrum [216–218].

A bathochromic shift in the spectrum can also be observed in the Zn(II) complex, porphyrin **21**, but to a lesser extent and without evidence of Soret band broadening. In this porphyrin, Zn^{2+} is bound to two pyrrole nitrogen atoms and reduces the probability of hydrogen bond formation leading to a porphyrin-surfactant assembly (**Figure 32C**) [219]. However, the red shift of the absorption spectrum at higher SDS concentrations is due to electrostatic interactions between SDS micelles and Zn(II) porphyrin.

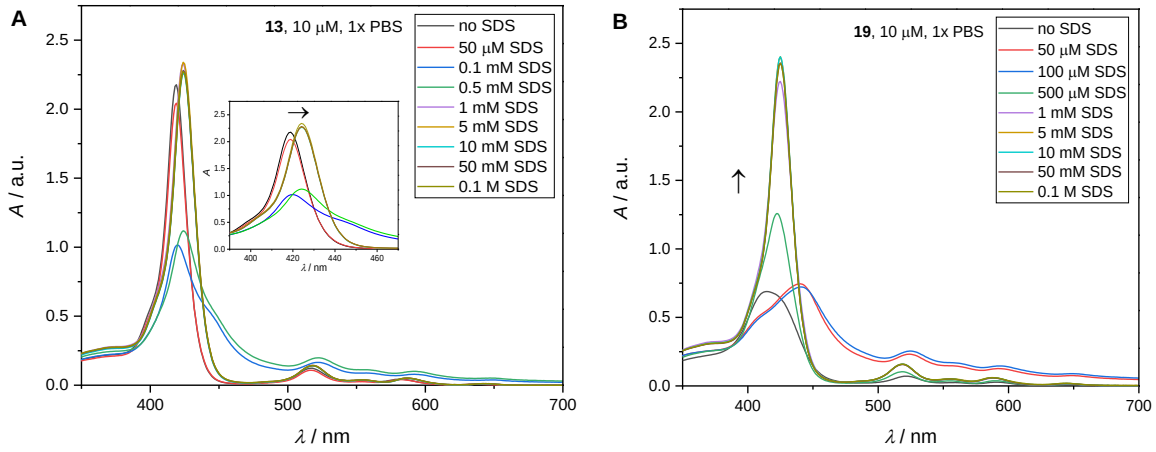

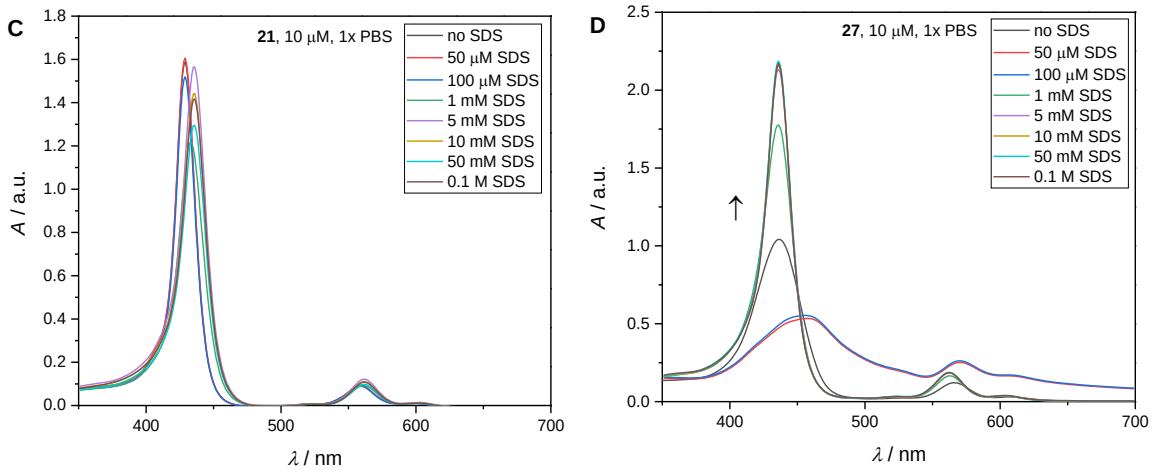

Figure 32. Absorption spectra of free base porphyrins (**13** (A) and **19** (B)) and their Zn(II) complexes (**21** (C) and **27** (D)) in PBS alone and after addition of SDS in different concentrations to the PBS solution.

A similar pattern to porphyrin **13** was also observed for porphyrins **19** and **27** (**Figure 32C** and **32D**), with the Soret band additionally "recovering" after SDS addition in concentrations above the CMC. This suggests that at the premicellar concentration of SDS, porphyrin-surfactant aggregates are formed due to hydrogen bonding, whereas at higher concentrations, when SDS micelles are formed, porphyrin aggregates formed in PBS dissociate into monomeric form due to the electrostatic interaction on the surface of the micelles and the hydrophobic interaction with the dodecyl chain inside the micelle.

4.1.7. Spectroscopic properties in cell medium and after addition of BSA

Dulbecco's modified Eagle Medium (DMEM) is a basal medium frequently used in biology to maintain cells in the tissue culture. It consists of various salts, including sodium bicarbonate used to maintain the pH of the culture, various amino acids, vitamins and glucose. When used in tissue culture, it is supplemented with fetal bovine serum (FBS) (usually 10%), antibiotics and L-glutamine to support the cell growth and viability. It has been shown that DMEM, together with MEM, is the most used basal medium in cancer cell research. More than half of the published cell culture-based studies use one or the other medium, as the cells are supplied with the nutrients essential for their continuous proliferation and viability when kept in these media [220].

In biological experiments, porphyrin is prepared at different concentrations in the cell medium before it is added to the cells. Since aggregation of porphyrins with a longer alkyl chain is observed in an aqueous solution with higher ionic strength, such as PBS, porphyrins

13 and **19** were investigated at a concentration of 10 μM in DMEM before (DMEM) and after the addition of FBS, L-glutamine and antibiotics (DMEM 2) **(Figure 33**).

Similar to the results in PBS, porphyrin **19** conjugated with a long alkyl chain shows a strong decrease in the absorption spectrum and a broadening of the Soret band, which can indicate formation of aggregates. When the porphyrin is prepared at the same concentration in the supplemented medium (DMEM 2), a "recovery" of the Soret band is observed, indicating the porphyrin in monomeric form (**Figure 33B**). No changes in the absorption spectrum, at Soret band wavelength, were detected for porphyrin **13**, as expected.

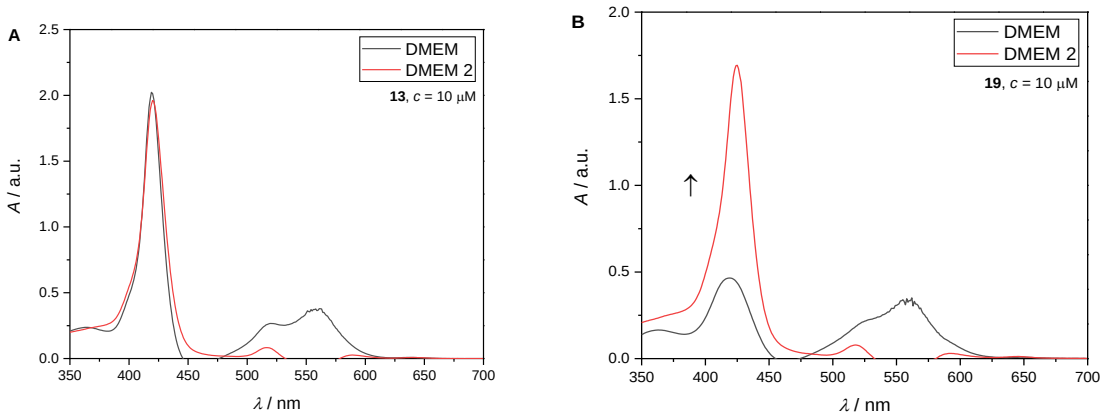

Figure 33. Absorption spectra of free-base porphyrin **13** (A) and porphyrin **19** (B) in pure DMEM cell medium and DMEM medium after completion of the medium with 1 % penicillin/streptomycin solution, 1 % L-glutamine and 10 % fetal bovine serum (FBS) (DMEM 2). Spectra were compared at 10 μM concentration.

Albumin is the most abundant protein in human serum, occurring at a concentration of 0.6 mM in blood plasma, and can serve as an excellent carrier of drugs, in our case porphyrins [25,51]. It has been shown that albumin can accumulate in tumour cells both passively, due to the lack of effective lymphatic drainage in TME and an increased EPR effect, and by active uptake due to the overexpression of tumour-specific membrane receptors, such as glycoprotein 60 and secreted protein acidic and rich in cysteine (SPARC), which have been found to increase the uptake of albumin and albumin-bound drugs [221].

With its special three-dimensional ellipsoidal structure, which has three homologous structural domains (I, II and III) divided into two independent helical substructures (A and B), albumin has been shown to be an excellent carrier as it can bind many drugs of moderate hydrophobicity. The major binding sites in the albumin structure are site I (IIA) and site II (IIIA) [222], with binding site I serving only for binding through hydrophobic interactions, while binding site II is responsible for a combination of interactions that include hydrogen bonding, electrostatic and hydrophobic interactions, or a combination thereof [223,224].

Based on the results in DMEM, the potential of porphyrin binding to bovine serum albumin (BSA), as a model for human serum albumin (HSA), was evaluated for porphyrins **13** and **19** tested in DMEM, and their Zn(II) complexes **21** and **27** (**Figure 34**). The hydrophilic porphyrins **13** and **21** showed negligible changes when BSA was added to PBS. Both amphiphilic porphyrins, which exhibited aggregation in pure PBS, showed a "recovery" of the Soret band in the absorption spectrum upon addition of BSA, indicating dissolution of the aggregates formed in PBS. The synthesized amphiphilic porphyrins **19** and **27**, which showed high albumin binding, are synthesized as fatty acid conjugates of porphyrins. The primary role of albumin in the blood is the transport of fatty acids, which bind to albumin through hydrophobic tunnels closed by basic amino acid residues such as arginine or lysine [225]. It has been shown that there are six fatty acid binding sites in the albumin structure and that the binding enables not only the transport of hydrophobic molecules but also their colloidal solubilization [223,225]. This shows that the dissociation of porphyrins **19** and **27** into monomers may be a consequence of the hydrophobic binding of a long alkyl chain as moiety of a fatty acid in the porphyrin structure.

The presence and impact of an alkyl chain length in porphyrins on albumin binding has already been investigated by Ben Dror *et al*. [226]. Protoporphyrin IX and hematoporphyrin were synthesized with different lengths of a carboxylate chain (1, 2, 4 and 6 C atom long). Tests with albumin showed that a longer carboxylate chain could increase the protein binding constant, with the deeper insertion of the PS into the BSA cavity through hydrophobic interactions[226], confirming our assumptions.

Using the tetracationic porphyrins **TMPyP4** and **TMPyP3** as examples, it was shown that positive charges in the porphyrin structure can also interact electrostatically with the negative amino acid residues in the BSA structure [227]. The porphyrins **TMPyP4** and **TMPyP3** bind to the albumin at sites IB and IIA, preferentially with the tryptophan residues in the structure. **TMPyP3** showed stronger binding compared to **TMPyP4**, due to the steric barriers in the pyridine rotation of **TMPyP3**, which leads to greater disruption of the planarity of the porphyrin ring, allowing better binding with the interactions within the hydrophobic internal cavity and electrostatic interactions with the entrance of the BSA cavity [228]. Although negligible changes were observed for hydrophilic porphyrin **13**, with only a small decrease in the intensity of the Soret band (**Figure 34A**), that can be attributed to small electrostatic interactions with BSA, its Zn(II) complex, porphyrin **21**, showed a small red shift of a Soret band (**Figure 34C**). A similar effect has been shown in the literature where Zn(II) porphyrins exhibit a higher binding constant, possibly due to the additional electrostatic interaction with BSA and the formation of an additional bond at the protein surface [229,230].

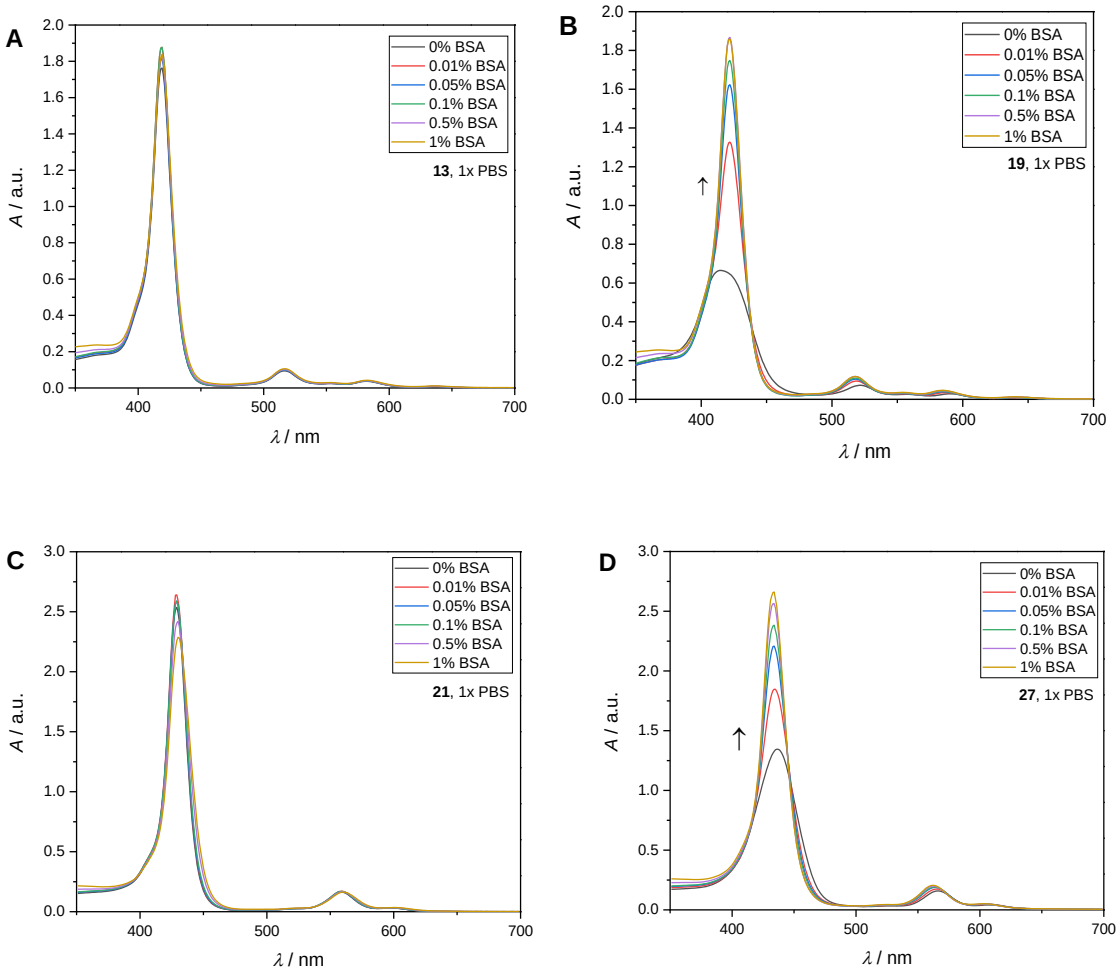

Figure 34. Absorption spectra of free-base porphyrins **13** and **19** (A and B) and their Zn(II) complexes, **21** and **27** (C and D) measured in PBS with the addition of bovine serum albumin (BSA).

Nevertheless, the ability of a porphyrin to bind to albumin has proven to be an advantageous feature for improving porphyrin characteristics for use as PS. Albumin has been shown to be a good target due to its good biocompatibility, its increased accumulation in tumours through passive and active targeting mechanisms, and its promotion of non-lysosomal delivery [25,51,224]. The strong binding of amphiphilic porphyrins via their fatty acid pockets has been shown to be a good strategy to enhance their cellular uptake and accumulation in tumours and thus increase their PDT outcome.

4.1.8. Singlet oxygen production of *N*-methylated free-base (13-19) and Zn(II) porphyrins (21-27)

One of the features of an ideal PS is its ability to generate high amounts of reactive oxygen species (ROS), especially singlet oxygen ($^1O_2$), upon irradiation. The method of choice for the detection of $^1O_2$ is direct photoactivation based on the measurement of $^1O_2$ phosphorescence at 1270 nm. This method is still a gold standard for detection, but due to the high background noise, the efficiency is significantly lower with a low quantum yield of $^1O_2$ compared to indirect methods [27]. In addition, the method strongly depends on the medium used, as the lifetime of singlet oxygen differs depending on the medium (e.g. $\tau(D_2O)$ = 30 μs; $\tau(H_2O)$ = 3 μs) [21,231].

Other methods include the detection of radical species by electron spin resonance or, as used here, by fluorescent probes that undergo a chemical reaction with certain ROS, resulting in a change in the absorption and fluorescence properties of the probe. Since 1970. 1,3-diphenylisobenzofuran (DPBF) is known as a $^1O_2$ trap. The production of $^1O_2$ is proportional to the photodegradation of DPBF, which occurs as a loss of the extended π-electron system and is usually detected by measuring the decrease of absorbance at 410 nm or, as was done here, a decrease in fluorescence at 455 nm of DPBF [20,27]. When DPBF reacts with $^1O_2$, the furan ring undergoes a [4+2] cycloaddition reaction at the 2,5-positions to form endoperoxide [27,232]. The final product, 1,2-dibenzoylbenzene, is the result of the reduction of the endoperoxide by cleavage of the O-O bond and loss of oxygen (**Scheme 16**) [232]. Moreover, the same product was observed upon degradation of DPBF with other ROS, such as H_2O_2, $HO^{\bullet}$, $RO^{\bullet}$, $ROO^{\bullet}$, showing that DPBF can serve as a ROS trap that is not specific only for singlet oxygen [233–235].

1.)

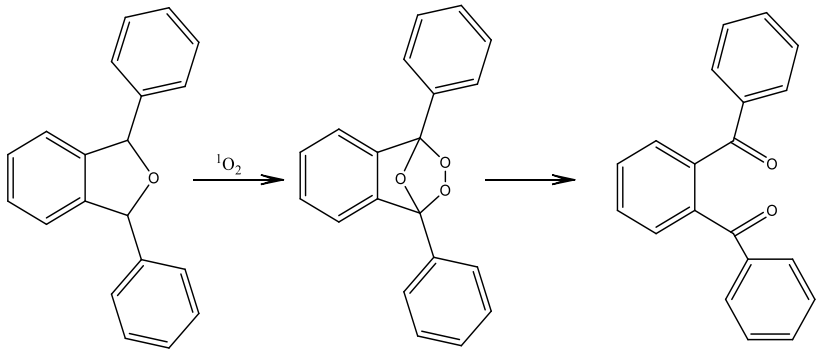

DPBF **DBB**

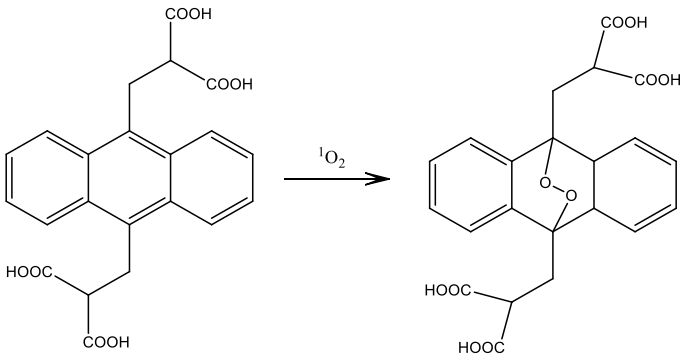

2.) **ABMDMA**

Scheme 16. Photodegradation reactions of the fluorescent probes, 1,3-diphenylisobenzofuran (DPBF) and 9,10-anthracenedilylbisdimalonic acid (ABMDMA), upon reaction with $^1O_2$, used in this work.

Singlet oxygen production measured by photodegradation of DPBF, was performed on all synthesized *N*-methylated free-base porphyrins (**13**-**19**) and their Zn(II) complexes (**21**-**27**) (**Figure 35**). Photodegradation was tested during a 15-min irradiation with an LED-based light source for cuvette irradiation with red light (λ = 647 nm) and orange light (λ = 606 nm). As expected, the length of the alkyl chain had no effect, while the wavelength of irradiation had a large effect on $^1O_2$ production, due to the different optical properties of porphyrin groups. A stronger photodegradation of DPBF after irradiation with red light (λ = 647 nm) was observed for free-base porphyrins (60-70%) compared to their Zn(II) analogues (30-40 %) due to the higher absorption of free-base porphyrins at this wavelength (**Figure 35A**). The number of absorbed photons of all porphyrins at the tested concentration (5 μM) in MeOH was calculated according to the equations **3-7** at both irradiation wavelengths (**Table 9**). After irradiation at 647 nm, the number of absorbed photons of the free-base porphyrins **13**-**19** (4.2 - 8.7 × 10^{26} ph/cm^2) was found to be up to 8 times higher compared to their Zn(II) analogues, porphyrins **21**-**27** (0.3 - 1.3 × 10^{26} ph/cm^2).

Irradiation with orange light (λ = 606 nm) was used to study the $^1O_2$ production and cytotoxicity of porphyrins, as the absorbance of both porphyrin groups (*N*-methylated free-base and Zn(II) complexes) is similar. The number of absorbed photons after irradiation at 606 nm, as expected, was very similar with observed 1.8 - 3.2 × 10^{26} ph/cm^2 for the *N*-methylated free base porphyrins and 2.1 - 3.0 × 10^{26} ph/cm^2 for their Zn(II) complexes (**Table 9**). Moreover, $^1O_2$ production increased to ~70% for all Zn(II) porphyrins **21**-**27**, while the photodegradation of DPBF by *N*-methylated free-base porphyrins slightly dropped to 55-60% after irradiation with orange light. All the obtained results can be linked to the calculated number of absorbed photons. The slightly higher production of singlet oxygen by Zn(II) porphyrins in MeOH at 606 nm correlates with their longer lifetime of ^{3}PS* obtained by LFP (**Table 8**).

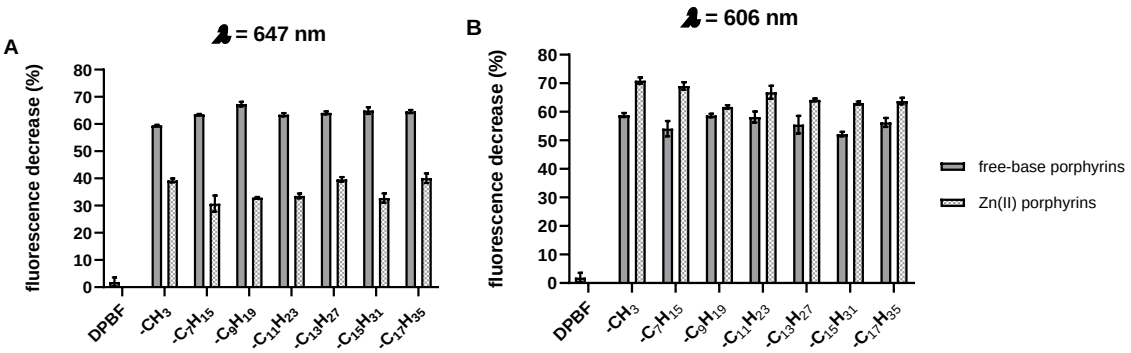

Figure 35. Singlet oxygen production ($^1O_2$) of the *N*-methylated free-base (**13**-**19**) porphyrins and their Zn(II) complexes (**21**-**28**) determined by photodegradation of DPBF after irradiation for 15 min with red light (λ = 647 nm, 10.7 mW/cm^2, 9.63 J/cm^2) (A), and orange light (λ = 606 nm, 2 mW/cm^2, 1.8 J/cm^2) (B). Results are presented as percentage of fluorescence decrease calculated from area under the curve after the photodegradation of DPBF. All results are presented as an average of measurements in triplicate with the standard deviation in error bars.

Table 9. Number of photons absorbed by *N*-methylated free-base (**13**-**19**) and their Zn(II) complexes (**21**-**27**) during the measurement of $^1O_2$ production, calculated according to the equations **3**-**7.** Porphyrins were tested in 5 μM concentration dissolved in MeOH and irradiated with orange light (606 nm, 2 mW/cm^2, 1.8 J/cm^2) or red light (647 nm, 10.7 mW/cm^2, 9.63 J/cm^2) for 15 minutes.

	N_{ph} (×10^{26}) [ph/cm^2]			N_{ph} (×10^{26}) [ph/cm^2]	
	606 nm 2 mW/cm^2	647 nm 10.7 mW/cm^2		606 nm 2 mW/cm^2	647 nm 10.7 mW/cm^2
13	3.2	8.7	**21**	2.3	1.1
14	2.8	7.7	**22**	2.1	0.7
15	2.2	5.4	**23**	2.3	0.3
16	2.2	5.1	**24**	2.3	0.5
17	1.8	4.2	**25**	2.4	0.7
18	2.2	4.7	**26**	2.1	0.5
19	3.1	8.3	**27**	3.0	1.3

In addition to DPBF, 9,10-anthracenediyl-bis(methylene)dimalonic acid (ABMDMA) was also used as a water-soluble probe to study the production of $^1O_2$, this time in PBS. Like DPBF, the photodegradation of ABMDMA is based on the formation of a non-fluorescent endoperoxide via a Diels-Alder [4+2] cycloaddition reaction [27,235], and the amount of endoperoxide formed is assumed proportional to the $^1O_2$ produced. ABMDMA is known to

react preferentially with $^1O_2$, but only captures 5% of the $^1O_2$ [235], whereas DPBF captures more than 70% of the $^1O_2$ produced and it doesn't react only with $^1O_2$.

The $^1O_2$ production by photodegradation of ABMDMA was tested with the free-base porphyrins (**13**, **15**, **17** and **19**) and their Zn(II) complexes (**21**, **23**, **25** and **27**), the same porphyrins whose absorption properties were tested in PBS (**Figure 36**). The samples were irradiated with a LED-based light source for cuvette irradiation with violet light (λ = 411 nm) for 5 minutes and the fluorescence decrease was measured before and after 30 seconds of irradiation. A small decrease in fluorescence was only observed in the control alone, which is due to the overlap of the irradiation wavelength with the absorption spectra of ABMDMA. Compared to the decrease in the control (5%), a small decrease in fluorescence was observed in the hydrophilic porphyrins (**13** and **21**) (11% and 8%, respectively). In addition, among the amphiphilic porphyrins, porphyrins **15** and **23**, substituted with an alkyl chain with 9 C atoms, showed a small decrease of ABMDMA of 12% and 8%, respectively (**Figure 36**). By increasing the number of C atoms in the alkyl chain, the production of $^1O_2$ increased to 62% for **17** and to 21% for **25**, its Zn(II) analogue, and to 69% and 40% for **19** and **27**, its Zn(II) complex, respectively. This agrees with our previously published results where two hydrophilic porphyrins, **12** and **13**, and the amphiphilic porphyrin **19**, were tested in waters of different hardness [162]. The significantly higher production of $^1O_2$ for amphiphilic porphyrin compared to the hydrophilic analogues suggests the formation of micelle-like structures which could capture $^1O_2$ over a longer period and thus increase the possibility of reacting with ABMDMA and detection by fluorescence spectroscopy. Furthermore, these results confirm the findings from the absorption spectra obtained for porphyrins **13**, **15**, **17** and **19** and their Zn(II) complexes in PBS, as well as the changes in their absorption after the addition of detergents and BSA, which also indicates the formation of aggregates, such as micelle-like vesicles [204,236], in aqueous media of increased ionic strength.

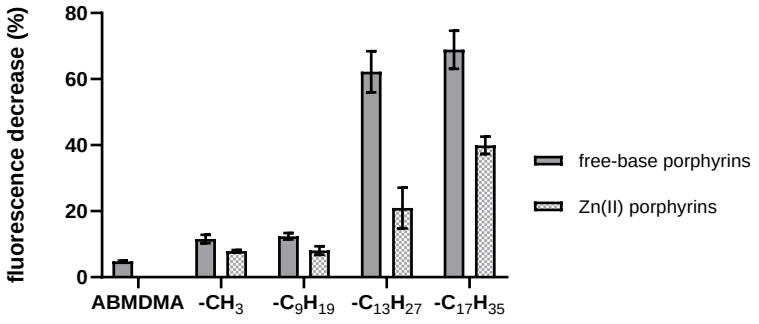

Figure 36. Singlet oxygen production ($^1O_2$) of the *N*-methylated free-base (**13**, **15**, **17** and **19**) and Zn(II) porphyrins (**21**, **23**, **25** and **27**) (1 μM) determined by photodegradation of ABMDMA in PBS after irradiation with violet light (λ = 411 nm, 3.5 mW/cm^2, 1.05 J/cm^2). Results are presented as average of measurements in triplicate showing a percentage of

fluorescence decrease calculated from area under the curve after the photodegradation of 1,3-diphenylisobenzofurane (DPBF).

According to the literature, Zn(II) porphyrins mainly undergo the type II mechanism, producing mainly $^1O_2$, whereas free-base porphyrins can undergo both type I and type II mechanisms [237]. Here, however, the differences in the production of $^1O_2$ between the porphyrin groups cannot be observed because the experiments were performed with the same concentration of all porphyrins and the porphyrins have different absorption at the irradiation wavelength. The number of absorbed photons by free-base porphyrins at λ = 411 nm is up to 4 times higher (2.2 - 4.3 × 10^{26} ph/cm^2) compared to their Zn(II) complexes (0.3 - 1.1 × 10^{26} ph/cm^2) in PBS (**Table 10**).

Table 10. Number of photons absorbed by *N*-methylated free-base (**13**, **15**, **17** and **19**) and their Zn(II) complexes (**21**, **23**, **25** and **27**) during the measurement of singlet oxygen production. Porphyrins (1 μM) were dissolved in PBS and irradiated with violet light (λ = 411 nm, 3.5 mW/cm^2, 1.05 J/cm^2) for 5 min.

	N_{ph} (× 10^{26}) [ph/cm^2]		
13	3.5	**21**	1.1
15	3.5	**23**	0.6
17	4.3	**25**	0.7
19	2.2	**27**	0.3

4.1.9. Lipophilicity of free-base *N*-methylated (13-19) porphyrins and their Zn(II) complexes (21-27)

It has been shown that the lipophilicity of a molecule is an important feature for a PS in PDT. The balance between the hydrophobic and hydrophilic parts is not only important for cellular uptake, but also for determining water solubility to avoid the formation of aggregates [64,238]. The porphyrin ring itself is hydrophobic and its degree of lipophilicity can be modified by adding hydrophilic and hydrophobic substituents at the *meso*- or *β*-positions of the ring [238].

Amphiphilic porphyrins, as mentioned above, have attracted much attention for PDT due to the possible arrangement of the hydrophobic and hydrophilic parts of the molecule for achieving their best ratio. The standard method for calculating lipophilicity is to determine the logarithm of the partition coefficient (log*P*) between the aqueous and organic phases. The partition coefficient for amphiphilic porphyrins is generally considered between -0.1 and 0.4 [64]. Although this information is oversimplified and cannot be used as a definitive prediction of molecular partitioning between an aqueous phase and lipid membranes, it can provide initial information about the lipophilicity of a porphyrin [64].

The shake-flask method, modified according to Kos and colleagues [171], was used to determine the partition coefficient between *n*-butanol and water (logP_{BW}), as the synthesized porphyrins are more soluble in *n*-butanol than in *n*-octanol. Finally, to obtain logP_{OW} values from logP_{BW}, a correlation equation **19** proposed by Kos and colleagues was used [171]. The calculated logP_{BW} and logP_{OW} values are listed and plotted in **Figure 37**. As expected, hydrophilic porphyrins substituted with an acetamido group showed the lowest partition coefficients (logP_{BW}), with obtained values of –1.73 and –1.01 for porphyrins **13** and **21**, respectively. The increased logP_{BW} and logP_{OW} values obtained for both the free-base porphyrins and their Zn(II) complexes are related to the length of the alkyl chain. For the free-base porphyrins, the logP_{BW} value increases from –0.82 for porphyrin **14** with an alkyl chain of 7 C atoms to -0.07 for porphyrin **19** with an alkyl chain of 17 C atoms. The situation is similar with their Zn(II) analogues, where the logP_{BW} value is calculated –0.67 for porphyrin **22**, also substituted with an alkyl chain of 7 C atoms, and it increases to 0.37 for porphyrin **27**, with an alkyl chain of 17 C atoms. As mentioned above, porphyrins with amphiphilic character are those with a calculated log*P* between –0.1 and 0.4 [64]. According to this ratio and the logP_{BW} value obtained, porphyrins **17** to **19** of the free base porphyrins and **25** to **27** of the Zn(II) porphyrin group are considered amphiphilic. If the logP_{OW} value is used, only porphyrin **27** can be considered amphiphilic.

The Zn(II) analogues showed higher logP_{BW} and logP_{OW} values compared to their free base analogues substituted with an alkyl chain of the same length, indicating a higher lipophilicity due to Zn(II) insertion (**Figure 37**). The impact of Zn(II) chelation on lipophilicity has already been evidenced by Malarcane et al. on the groups of symmetric tetracationic pyridiniumporphyrins, where no difference between the porphyrin groups was observed [74]. In our case, the difference between the hydrophilic porphyrins **13** and **21** in the logP_{OW} value is 1.12, while the difference between porphyrins **19** and **27** is 0.69. This shows that the difference in lipophilicity among amphiphilic porphyrins is much smaller than the difference between the hydrophilic analogues, indicating that the effect of Zn(II) is much smaller than the substitution with a long alkyl chain. This is in agreement with the previously mentioned results of Malarcane *et al.,* as their tetracationic porphyrins were substituted with four long alkyl chains at all pyridyl positions, which likely completely reduced the effects of Zn(II) chelation, thus did not affect the overall lipophilicity of the molecule [74].

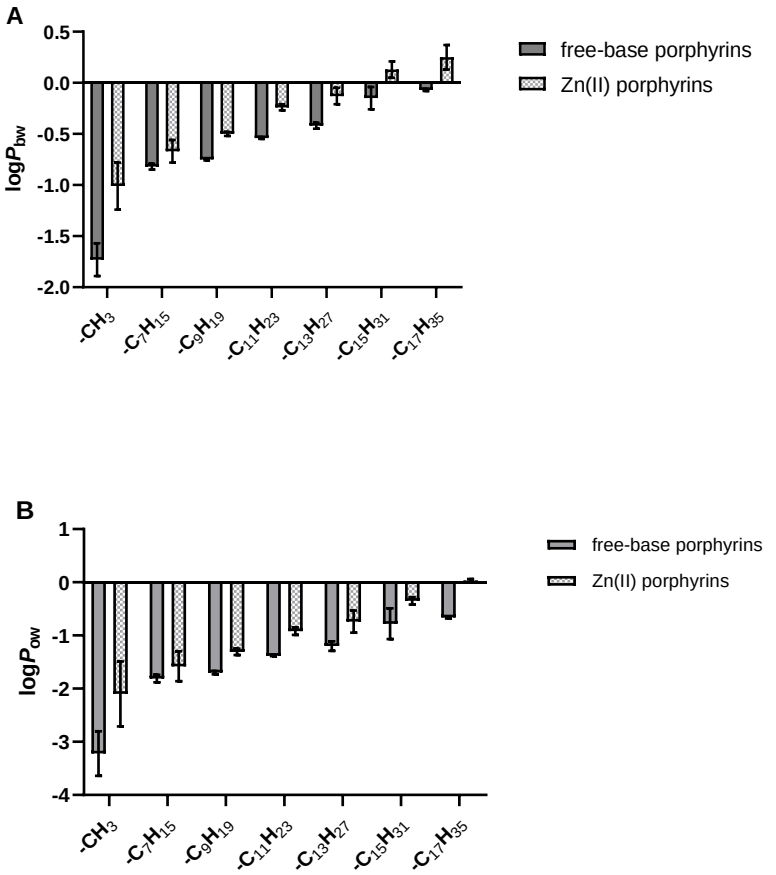

	LogP_{BW}
13	-1.73 ± 0.16
14	-0.82 ± 0.03
15	-0.75± 0.01
16	-0.54 ± 0.01
17	-0.42 ± 0.03
18	-0.15 ± 0.11
19	-0.07 ± 0.01
21	-1.01 ± 0.23
22	-0.67 ± 0.11
23	-0.50 ± 0.02
24	-0.24 ± 0.03
25	-0.13 ± 0.08
26	0.13 ± 0.11
27	0.37 ± 0.01

	LogP_{ow}
13	-3.22 ± 0.42
14	-1.81 ± 0.07
15	-1.70 ± 0.03
16	-1.38 ± 0.01
17	-1.20 ± 0.09
18	-0.78 ± 0.29
19	-0.66 ± 0.02
21	-2.10 ± 0.61
22	-1.58 ± 0.28
23	-1.31 ± 0.06
24	-0.92 ± 0.07
25	-0.74 ± 0.21
26	-0.35 ± 0.07
27	0.03 ± 0.03

Figure 37. Obtained logP_{BW} (A) and logP_{OW} (B) with corresponding tables showing calculated values obtained by modified shake-flask method. log*P*ow was calculated from the logP_{BW} values using a correlation formula **19**. All results are shown as an average of duplicate measurements with standard deviation in error bars.

In addition to calculating the partition coefficient (log*P*) following the modified shake-flask method, the differences in lipophilicity were also tested using thin-layer chromatography on silica plates to obtain R_f values, following the procedure previously described by Kos and colleagues (**Figure 38**) [171]. In these experiments, a mixture of acetonitrile (MeCN), water and saturated potassium nitrate solution (KNO_3) in a ratio of 8:1:1 was used as an eluent. For porphyrin **13** and its Zn(II) analogue, porphyrin **21**, which are both hydrophilic, the calculated R_f values were 0.4 and 0.47, respectively (**Figure 38**), significantly lower than for the other porphyrins with an alkyl chain. Similar to the results obtained with the shake-flask method, an increased R_f value was proportional to the length of the alkyl chain and was observed for both the free-base porphyrins **14** to**19** and their Zn(II) analogues **22** to **27**. For the free-base porphyrins, the R_f value increased from 0.57 for porphyrin **14** to 0.62 for porphyrin **19**. For the Zn(II) analogues, an R_f value of 0.58 for porphyrin **22** was increased

to 0.63 for porphyrin **27**. Similar to the results of the shake-flask method, the Zn(II) porphyrins also showed a slightly higher R_f value, confirming a slightly higher lipophilicity of the Zn(II) analogues of the pyridinium porphyrins.

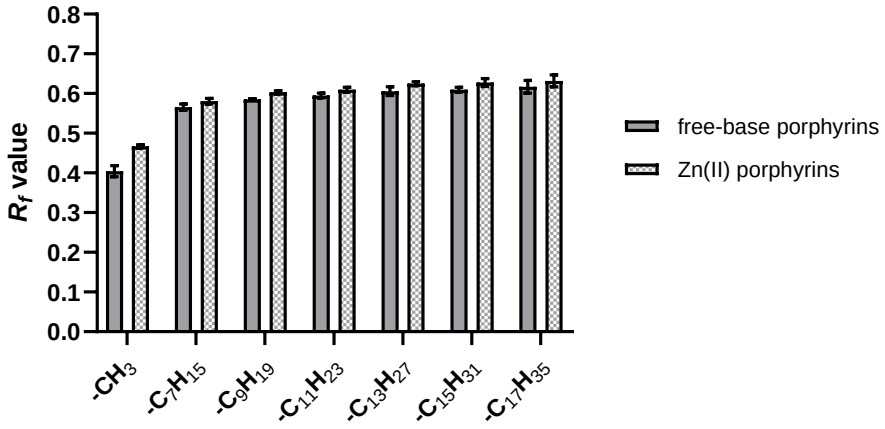

Figure 38. R_f values determined by thin layer chromatography (TLC) on silica gel plates with MeCN: H_2O: $KNO_{3(sat.)}$ (8:1:1) used as a mobile phase. Results represent an average of measurements in duplicate with standard deviation in error bars.

In addition to the experimentally determined values, theoretical calculations were carried out using Chemicalize, an online tool from Chemaxon. Chemicalize provides structure-based calculations and predictions for any molecular structure, based on a method proposed by Viswanadhan *et al.* [239]. This method uses a pool of pre-calculated fragments and a log*P* value for a single atom, taking into account the delocalization of electrons, the hydrogen bonding effect and the contribution of ionized atoms or fragments [240]. To calculate log*P*, the molecules were provided as SMILES. The results provided by Chemicalize are summarized in **Table 11**. The calculated results are not consistent with the experimentally obtained results, with much larger differences in the clog*P* value between two porphyrins in both series (free-base and Zn(II) porphyrins) that differ only by two C atoms in the alkyl chain length. According to the above-mentioned ratio for amphiphilic porphyrins ($-0.1 < x < 0.4$), none of the porphyrins tested could be considered as amphiphilic according to the results obtained by Chemicalize. Furthermore, Zn(II) chelation experimentally resulted in higher hydrophobicity, in contrast to the Chemicalize results. This suggests that the online tools are not yet sufficient to predict the log*P* values of macrocycles such as porphyrins.

Table 11. clog*P* values determined using Chemicalize from ChemAxon (structure-based analysis).

	clog*P*		clog*P*
13	-5.024	**21**	-5.098
14	-2.101	**22**	-2.488
15	-1.212	**23**	-1.696
16	-0.323	**24**	-0.903
17	0.566	**25**	-0.111
18	1.455	**26**	0.682
19	2.345	**27**	1.475

4.1.10. Time- and temperature-dependent cellular uptake of *N*-methylated free-base porphyrins and their Zn(II) complexes

In addition to the preferred characteristics of PS, there are many factors that determine the outcome of PDT, such as the light intensity and duration of the irradiation, the drug-light interval and the PS concentration. However, it has been shown that the efficient cellular internalization of a PS and its localization within the cells are the most important parameters [75]. Asymmetry of a PS [241–243] and the balance between the lipophilic and hydrophilic character of PS [74], were found to be the most relevant factors for efficient cellular uptake. Therefore, these parameters need to be included in the porphyrin design to study the cellular uptake in a way to achieve the best efficacy for PDT.

As mentioned above, both free base porphyrins and their Zn(II) analogues exhibit fluorescence, which was used as a characteristic feature for measuring the internalization of porphyrins according to the modified protocol of Jensen and colleagues [87]. Experiments were conducted on two melanoma cell lines (MeWo and A375) and human dermal fibroblasts (HDF), where cells were treated with free-base porphyrins **13** to **19**, as well as their Zn(II) complexes **21** to **27**, at a concentration of 1 μM and then kept in the dark at 4 °C or 37 °C for up to 24 hours. The amount of accumulated porphyrin is proportional to the fluorescence intensity measured after solubilization of the cells with 1% SDS in NaOH. Calibration curves for each porphyrin in 1% SDS in NaOH were generated prior to treatment of the cells and used to determine the concentration of porphyrin that entered the cells (**Figure S76** and **S77**).

The kinetics of cellular uptake at 37 °C were investigated by measuring the fluorescence intensity of the solubilized cells after 0.5, 1, 2, 4, 6, 12 and 24 hours of incubation with porphyrin (**Figure 39**). After 24 hours of incubation, the amount of internalized porphyrins **13** to **19** was shown to be proportional to their alkyl chain length, with the exception of

porphyrin **19** (**Figure 39A**, **39C** and **39E**). The concentration of porphyrin **19** was up to 3.7 times higher than the concentration of porphyrin **18**, which has only two C atoms shorter alkyl chain (e.g. ~ 95 nM/10^3 cells (**19**) and ~ 26 nM/10^3 cells (**18**) obtained in the HDF cell line) in all three cell lines. For comparison, the difference between other free-base porphyrins, which also differ in only two C atoms in the alkyl chain length between two porphyrins, was < 10 nM/10^3 cells. Analysis of the kinetics of cellular uptake of free base porphyrin showed that most of the porphyrin entered the cells within the first 6 hours of incubation, compared to the amount of porphyrin internalized during the entire duration of the experiment (24 hours). Again, porphyrin **19** with the longest substituted alkyl chain showed a much lower amount after 6 hours of incubation compared to 24 hours (< 50%), suggesting that the longest alkyl chain, which increases the hydrophobicity of a PS, also slows down the rate of incubation of the porphyrin.

When Zn(II) complexes **21** to **27** were studied, a similar kinetic profile of cellular uptake was observed (**Figure 39B**, **39D** and **39F**). The amount of porphyrin entering the cells was proportional to the length of the alkyl chain, as shown for free-base porphyrins. In contrast to the free-base analogue, the increase in cellular internalization of Zn(II) porphyrin **27**, was shown to be proportional to the length of the alkyl chain. Although the amount of free-base porphyrins and their Zn(II) analogues was similar after 24 hours of incubation, the rate of uptake of the Zn(II) porphyrins was slightly slower. According to the literature, the impact of Zn(II) chelation on cellular uptake depends mainly on the rest of the PS structure. The amount of porphyrins internalized after 24 hours of incubation was observed on two different asymmetric A_3B porphyrins and their Zn(II) analogues. The first work is from Socotoneau and colleagues [244] who studied A_3B porphyrin, 5-(4-hydroxyphenyl)-10,15,20-tris-(4-acetoxy-3-methoxyphenyl) porphyrin and its Zn(II) analogue on colon carcinoma (HT29) and glioblastoma (U-87 MG) cell line, and Bonescu *et al.* who investigated 5-(4-hydroxy-3-methoxyphenyl)-10,15,20-tris-(4-acetoxy-3-metoxyphenyl)porphyrin and its Zn(II) complex also in HT29 and mouse fibroblasts (L929) [242]. In both studies, Zn(II) chelation did not alter the cellular uptake of porphyrins, so that the cellular uptake of Zn(II) and free base porphyrins was similar. The opposite to our results and the findings of Socotoneau and Bonescu was shown by Dabrowski and colleagues by studying the 5,10,15,20-tetrakis[2,6-difluoro-5-(*N*-methylsulfamylo)phenyl]porphyrin and its Zn(II) complex on the human adenocarcinoma (A549) cell line [237]. In their work, they showed that porphyrin chelated with Zn^{2+} is internalized faster (within 6 hours) and in much higher concentration than the free-based analogue. This is due to the formation of a coordination bond between Zn^{2+} and the phosphate group of phospholipids, which plays an essential role in the binding of this photosensitiser to biological membranes [237].

However, compared to the work of Dabrowski and colleagues [237], our free-base porphyrins have three positive charges that can make an electrostatic interaction with negative

phospholipids in the membrane structure, as well as a long alkyl chain that not only increases the hydrophobicity of a molecule, but can also bind to membranes or to transport proteins through hydrophobic interactions, as described in previous chapters, which can facilitate their cellular uptake. This is consistent with the results of Malarcane *et al.* who investigated symmetrical tetrapyridylporphyrins with alkyl chains of different length, and showed that the log*P* value of the PS and the length of their alkyl chain correlate more strongly with cellular uptake than Zn(II) chelation [74].

The long alkyl chain in our work is, as already mentioned, derived from fatty acid and thus there is a possibility that our PS may be internalized also via the fatty acid pathway. The fatty acids are usually present in plasma in the form of lipoprotein triacylglycerols, adipocyte-derived and albumin-bound free fatty acids, and their uptake by endothelial cells may occur via passive diffusion or by membrane-associated transport proteins [79,245] such as fatty acid transport protein 1 (FATP1), which has been shown to be overexpressed in melanomas [79,246], depending on the length of the alkyl chain and its saturation. Another possible route, which has recently been intensively investigated is uptake by endocytosis-type uptake, known as micropinocytosis [79].

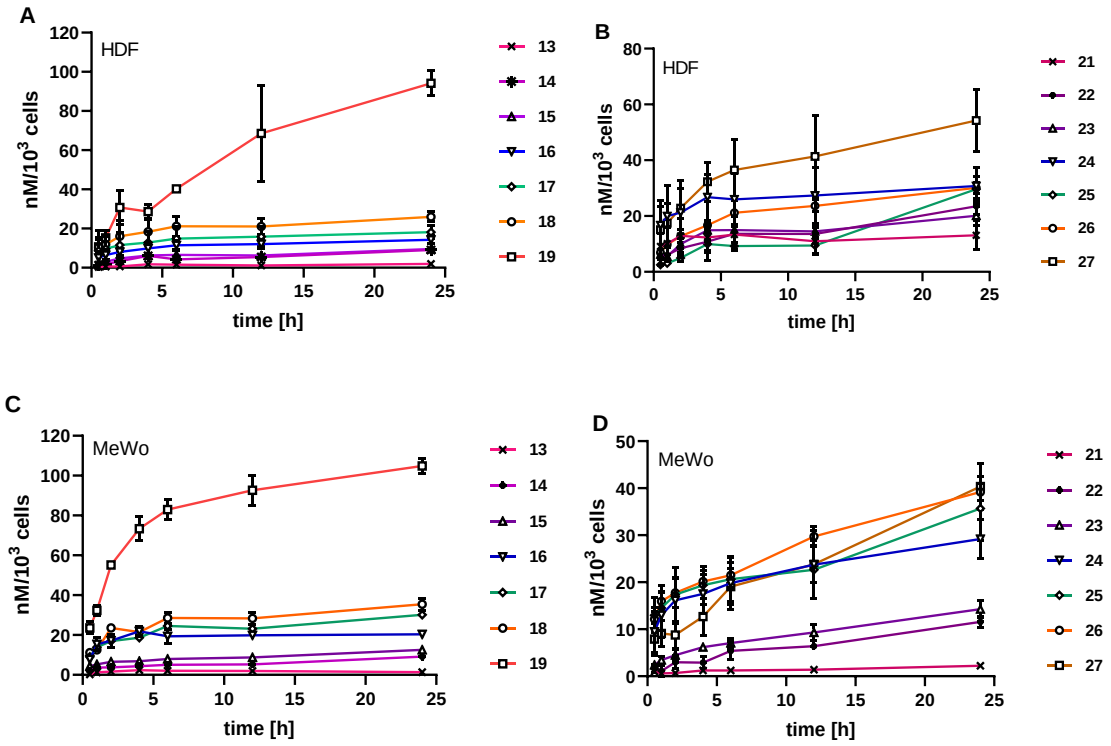

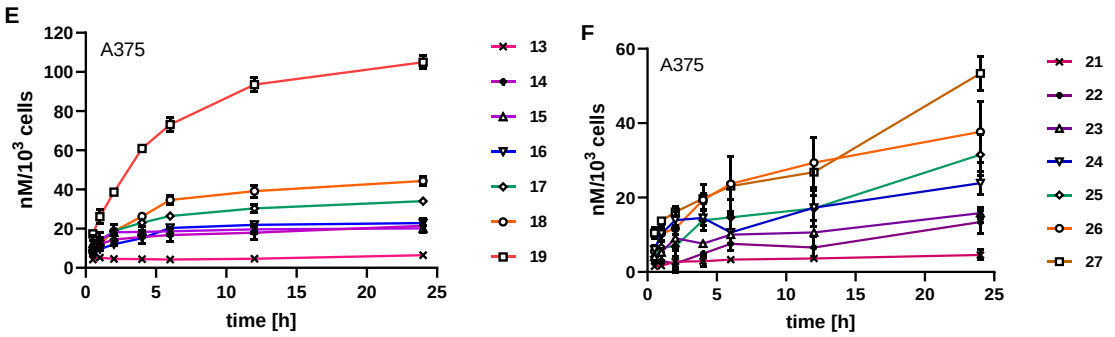

Figure 39. Cellular uptake kinetics, measured by fluorescence intensity, analysed over 24 h of incubation at 37 °C after addition of 1 μM solution of free-base porphyrins (A, C and E) and their Zn(II) complexes (B, D and F) to HDF (A, B), MeWo (C, D) and A375 (E, F) cell line. Results are presented as a mean of calculated concentration per 10^3 cells (nM) obtained after three individual measurements with standard deviations as error bars.

The temperature-dependent cellular uptake of drugs has been extensively studied as the first method to differentiate the passive diffusion from carrier-mediated drug uptake. In these experiments, uptake is measured at two temperature ranges: 0-4 °C and 37 °C. If the uptake is similar at both temperatures, or lower at lower temperatures passive uptake is assumed to be the main process. If the uptake is blocked at 4 °C it can be assumed that major mechanism of uptake is active uptake, as energy consumption is minimal or blocked at lower temperatures [247].

Here, MeWo as a representative of the tumour cell line and HFF as a normal cell line were incubated with free-base porphyrins **13**-**19** and their Zn(II) complexes **21** to **27** at 4 °C and 37 °C for 6 hours (**Figure 40**). As mentioned above, the amount of porphyrin internalized by the cells at 37 °C was proportional to the alkyl chain length. However, this was not observed after incubation at 4 °C. The hydrophilic porphyrin **13**, and its amphiphilic analogues, porphyrins **14** (R = -C_7H_{15}) and **15** (R = -C_9H_{19}), showed similar uptake after incubation at both temperatures, indicating passive transport as the main mechanism of internalization. Similarly, with their Zn(II) complexes, hydrophilic porphyrin **21** and amphiphilic porphyrins **22** and **23**, no statistical difference in cellular uptake was observed in the two cell lines tested as a function of incubation temperature (**Figure 40B** and **40D**). Amphiphilic porphyrins with an R > -$C_{11}H_{23}$, both free base **16** to **19** and their Zn(II) analogues **24** to **27**, showed statistical difference between the incubation at 37 °C and 4 °C indicating that passive transport may not be the only mechanism of cellular internalization. In an example by Vallecorsa and colleagues, who investigated the symmetric 4-(3-*N*,*N*-dimethylaminopropoxy)phenylporphyrin (**TAPP**) the cellular uptake was found to be 60-70% lower at 4 °C than at 37 °C, suggesting that the passive transport is the main mechanism of uptake, as active uptake would be completely blocked [248].

This finding suggests that as the length of an alkyl chain in the structure increases, the rate of the passive transport decreases, and thus the rate of active transport increases. Based on the structure, the majority of drug-fatty acid conjugates are expected to enter cells either by passive diffusion or by facilitated diffusion as another type of passive transport of molecules across the membrane via specialized transport proteins [249]. However, our amphiphilic porphyrins showed strong albumin binding that was shown in the literature to enhance endocytosis type of uptake and inhibits passive diffusion [250]. Furthermore, depending on a charge, size of the molecule and lipophilicity, different types of active transport could also be involved. Pinocytosis, as a type of endocytosis of smaller particles, with the two main mechanisms known as clathrin-mediated and caveolae-mediated endocytosis, is the most common mode of active transport of molecules and small nanoparticles that could be involved. Due to the structure of our compounds, they are expected to favour caveolae mediated endocytosis. They could also undergo clathrin-mediated endocytosis due to their positive charge only, while the presence of the fatty acid chain in the structure and higher lipophilicity are more likely to go through caveolae mediated endocytosis. It has also been shown that drugs that are bound to albumin via hydrophobic interactions of long alkyl chains, like our amphiphilic porphyrins, favour caveolae-mediated endocytosis [251].

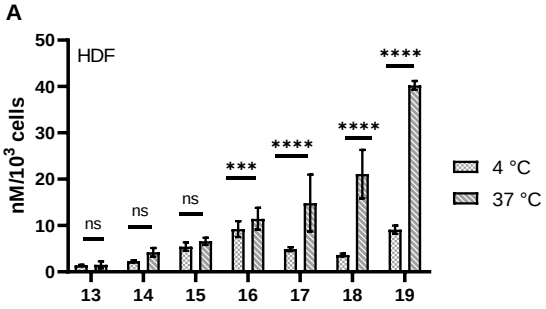

37 °C	13	14	15	16	17	18	19
13							
14							
15	****	*					
16	****	****	****				
17	****	****	****	***			
18	****	****	****	***	ns		
19	****	****	****	****	****	****	

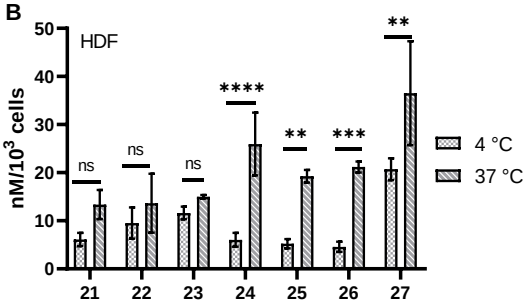

37 °C	21	22	23	24	25	26	27
21							
22	ns						
23	ns	ns					
24	*	*	ns				
25	ns	ns	ns	ns			
26	ns	ns	**	ns	ns		
27	****	****	****	****	***	**	

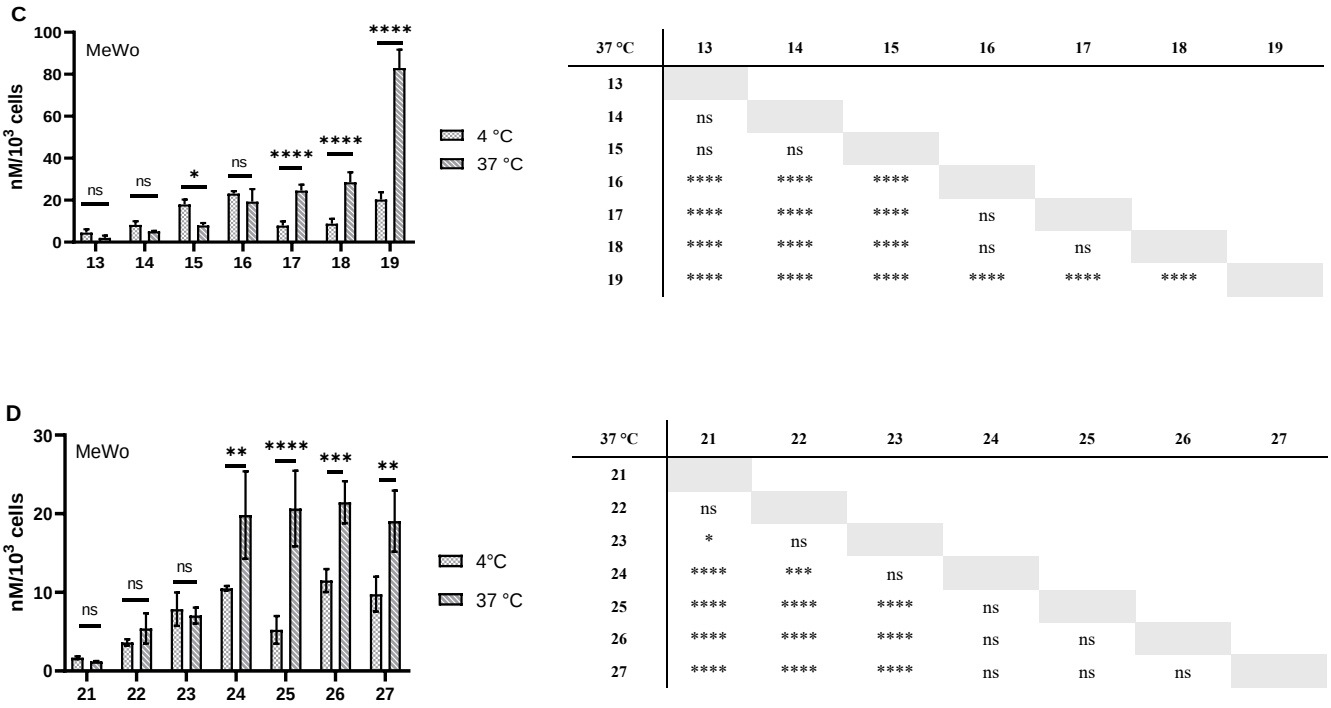

37 °C	13	14	15	16	17	18	19
13							
14	ns						
15	ns	ns					
16	****	****	****				
17	****	****	****	ns			
18	****	****	****	ns	ns		
19	****	****	****	****	****	****	

37 °C	21	22	23	24	25	26	27
21							
22	ns						
23	*	ns					
24	****	***	ns				
25	****	****	****	ns			
26	****	****	****	ns	ns		
27	****	****	****	ns	ns	ns	

Figure 40. Comparison of the cellular uptake at 4 °C and 37 °C after incubation for 6 hours with free-base porphyrins (**13**-**19**) (A and C) and their Zn(II) analogues (**21**-**27**) (B and D) in HDF (A and B) and MeWo (C and D). All results are shown as a mean concentration per 10^3 cells (nM) of measurements in triplicate with standard deviations as error bars. Standard t-tests were used for statistical comparison of cellular uptake at different temperatures (statistics presented on the graph), while two-way ANOVA with Tukey *post-hoc* tests were used to compare the differences on the cellular uptake at 37 °C based on the alkyl chain length (table statistics). In the table, significance was $p < 0.0001$ and it was shown as follows: **** < 0.0001; 0.0001 <*** < 0.001; 0.001 < ** < 0.01; 0.01 < * < 0.1; ns > 0.1 (not significant).

4.1.11. Localization of porphyrins using fluorescence microscopy

In addition to the cellular uptake of the PSs, their localization inside cells is determining factor for the efficiency of PDT [75]. The short lifetime and limited diffusion distance of $^1O_2$ requires the subcellular localization of PS to be near the organelles to efficiently activate the direct cell death mechanism [252]. In addition, the type of photodamage by direct cell death depends on the precise subcellular localization. The determinants of the subcellular localization lie in the structure of PS, such as their hydrophilicity/lipophilicity balance, net charge and structural asymmetry as the key ones [41,83].

It has been shown that positively charged PSs easily cross membranes, and are predominantly localized in mitochondria, due to their electrostatic interactions with negatively charged inner membrane of mitochondria. In addition, it has been shown that the number of charges and their distribution in the PS structure can also influence localization. The PS with one or two charges can localize in Golgi, endoplasmic reticulum (ER) or plasma membranes, while more positively charged tend to be directed toward mitochondria. In addition, PSs of increased lipophilicity, with a long alkyl chain(s), can also enhance localization toward mitochondria [4,37]. Targeting mitochondria has been shown to have more advantages than targeting other cell organelles, such as lysosomes or plasma membrane in PDT, as it induces apoptosis both *in vivo* and *in vitro* [4].

Porphyrins with an alkyl chain of 9, 13 and 17 C-atoms, both in free-base (**15**, **17** and **19**) and Zn(II) complexes (**23**, **25** and **27**), were tested on MeWo (**Figure 41A**) and the HDF cell line (**Figure 41B**) at a concentration of 5 μM with an incubation time of 6 hours and the $DIOC_6(3)$, a marker for the ER and mitochondria, was added for the last 30 minutes as colocalizing agent. The results indicate that all tested porphyrins, free-base and Zn(II) complexes, show strong localization in the mitochondria and ER, mostly with the same localization as $DIOC_6(3)$, which is evident by yellow colour of the merged images. In addition, none of the tested porphyrins localize in the nucleus. The calculated Pearson's correlation coefficient between red channel of porphyrins and green channel of $DIOC_6(3)$ showed an overlap >0.90, which further confirms the localization obtained by overlapping images.

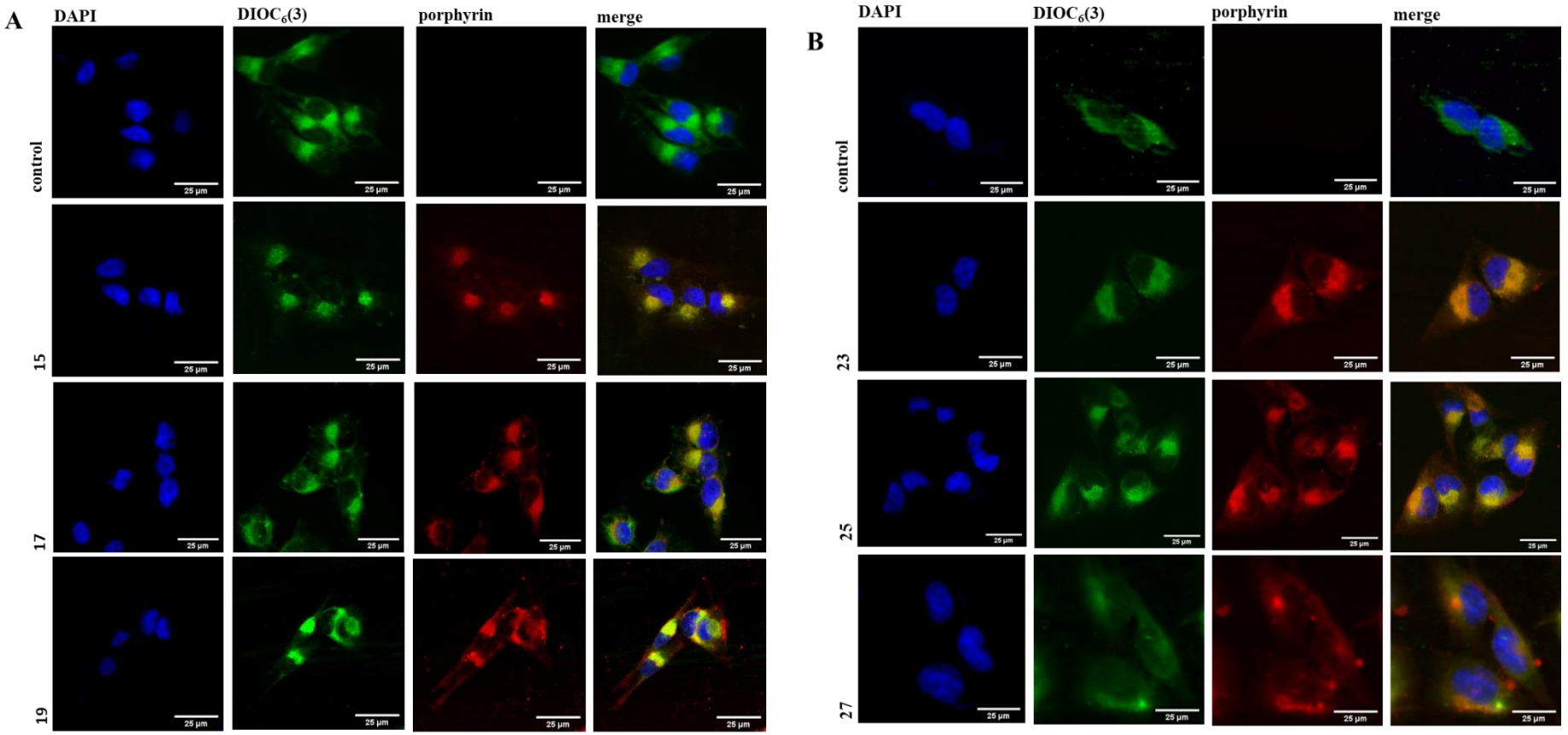

Figure 41. Localization in MeWo cell line of the free-base porphyrins (**15**, **17** and **19**) (A) and their Zn(II) complexes (**23**, **25** and **27**) (B) after incubation with $DIOC_6(3)$, a fluorescent marker for endoplasmic reticulum. The porphyrins were incubated at concentration of 5 µM for 6 hours. All images were taken by fluorescence microscopy at 20× magnification

In addition to microscopy with fluorescent markers as $DIOC_6(3)$, the experiments were performed using antibody type labelling, with GM130, primary antibody targeting the Golgi apparatus, as an example. The difficulties in staining with antibodies lies in the permeabilization step prior to the addition of the primary antibody where Triton X-100 at 5% or 3% concentration is normally used. As already seen, solubilization of cells with detergents causes porphyrin to leave the cells, resulting in lower or negligible concentration of porphyrins that remain inside the cells, i.e. to detect. In our experiments, successful permeabilization of membranes was achieved only with ice-cold MeOH incubated at –20 °C and only with porphyrin **19**, which showed the highest cellular uptake. The yellow coloration in the merged image of **Figure 42** shows the strong overlap of the green fluorescence from the secondary antibody Alexa Fluor 488 targeting Golgi and red fluorescence from porphyrin **19**. This result indicates that free-base porphyrins does not only localize in the ER and mitochondria, but also in the Golgi apparatus.

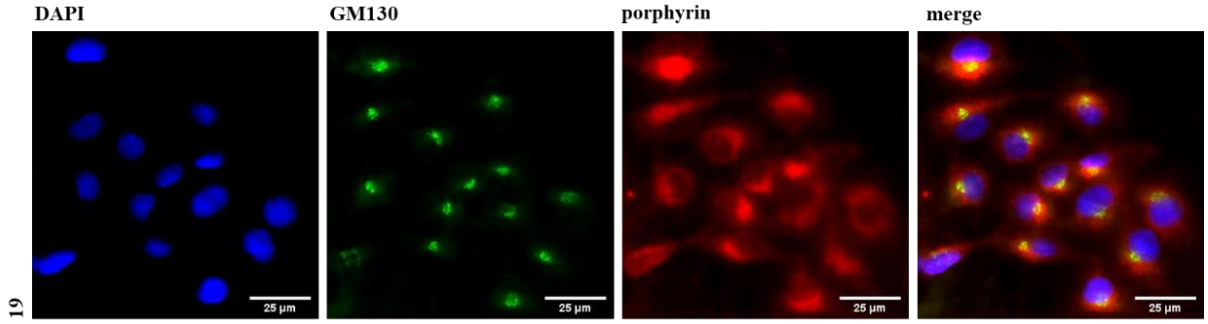

Figure 42. Localization of porphyrin **19** with Golgi apparatus on MeWo cell line, obtained by staining with GM130 as primary antibody and with AlexaFluor 488 secondary antibody. All pictures were taken with fluorescence microscopy at 20× magnification.

4.1.12. Cytotoxicity of *N*-methylated free-base (13-19) and Zn(II) porphyrins on HDF, MeWo and A375 cell lines

The (photo)toxicity of all newly synthesised porphyrins was evaluated using the MTT assay, a colorimetric assay, to evaluate the metabolic activity of cells by determining the living cells capable of reducing MTT (a yellow tetrazolium salt) to formazan (a purple compound) by mitochondrial enzymes [253]. To study toxicity upon irradiation, two LED-based light sources of the same fluence rate (2 mW/cm^2) were used: red light (λ = 643 nm), a standard wavelength in PDT, as it penetrates best into the tissue and does not overlap with the absorption of biomolecules in the cells, and orange light (λ = 606 nm), which matches the absorption properties of both free-base *N*-methylated porphyrins and their Zn(II) complexes.

Two melanoma cell lines, one without the pigment melanin (A375) and one with the melanin (MeWo), and dermal fibroblasts (HDF) were used for the (photo)toxicity experiment, to test the selectivity against melanoma cells. As mentioned in the introduction, the melanoma cell line has proven to be one of the most difficult tumour cell lines to investigate for new anti-cancer therapies. This is due to the numerous resistance mechanisms that the cells exploit, such as dysregulation of the apoptotic pathway and the presence of ABCG5 transporters that act as efflux pumps and eliminate porphyrins outside the cells [8,139]. In addition, melanomas are tumours with melanocytes that can synthesise two melanin pigments: the dark- brown eumelanin and yellow-red pheomelanin. It has been shown that higher levels of melanin, particularly eumelanin, can act as an optical shield by scattering or absorbing light and competing with PS for photons [8].

Furthermore, ROS have been shown to be key parameters in melanin synthesis and melanogenesis by regulating the pro- and anti-apoptotic effect, that seems to be the driving force of melanoma development [138]. Melanosomes can create a relatively hypoxic environment due to increased oxygen consumption, activating hypoxia-induced (HIF1) factor, which is required for the activation of Akt, a serine/threonine kinase that integrates cellular responses to growth factors and is responsible for melanocyte progression [135].

The IC_{50} values were determined in all three cell lines after 30 minutes of irradiation with red and orange light (total light dose 3.6 J/cm^2) (**Table 12**). Cells that were not irradiated and were kept in the dark served as a dark control. None of the porphyrins tested showed significant toxicity to any of the cell lines tested without irradiation at concentrations up to 100 μM. When toxicity was compared between the melanoma cell lines, the IC_{50} value for each porphyrin was found to be lower when tested on the A375 cell line, an amelanotic cell line. For example, the IC_{50} values for free-base porphyrin **17** (R = -$C_{13}H_{27}$) on MeWo, melanotic cell line, were 0.66 and 1.44 μM, after irradiation with red and orange light, respectively, while they were 0.09 and 0.31 μM for A375, an amelanotic cell line, after irradiation with red and orange light, respectively (**Table 12**). These results are consistent with previous reports by Sharma and colleagues showing that amelanotic cell lines are more susceptible to hypericin-PDT and associated oxidative stress than melanotic ones due to the lack of melanin [254].

Two irradiation wavelengths (λ = 606 nm and λ = 643 nm) were used in the determination of cytotoxicity. The difference in irradiation wavelength for free-base porphyrin (**13**-**19**) was the largest among the shorter alkyl chain porphyrins, e.g. porphyrin **15** (R= -C_9H_{19}), that showed a 4.6-fold lower IC_{50} in A375 and 4.3-fold lower in the HDF cell line when irradiated with orange light (λ = 606 nm), or porphyrin **14** (R= -C_7H_{15}), that also showed a 2.3-fold higher toxicity in the MeWo cell line when irradiated with orange light. When analysing cell proliferation at a concentration of 1 μM, the greatest difference based on the irradiation wavelength was observed for porphyrin **17** (R= -$C_{13}H_{27}$) in the MeWo cell line, where 20% lower proliferation was observed after irradiation with red light, and in the HDF cell line, where almost 50% lower proliferation was observed when the irradiation wavelength was

changed from 606 to 643 nm. The difference in cytotoxicity of Zn(II) porphyrins based on the wavelength of irradiation is much larger compared to the free-base analogues. Similar to the free-base porphyrins, the greatest difference was observed for porphyrins substituted with a shorter alkyl chain, such as porphyrins **22** and **23** (R = -C_7H_{15} and R = -C_9H_{19}, respectively), which exhibited up to 8-fold higher IC_{50} values for the A375 cell line upon irradiation with red light. In addition, porphyrin **24** (R = -$C_{11}H_{23}$) showed a 5-fold higher IC_{50} value when irradiation was shifted from orange light to red light. When proliferation at 1 μM concentration of PS was studied, porphyrins **26** and **27** (R = -$C_{15}H_{31}$ and R = -$C_{17}H_{35}$, respectively) were found to show a reduction in cell proliferation to 20% after irradiation with orange light, while the proliferation remained at 80% after irradiation with red light in the HDF cell line. In both melanoma cell lines, a significant reduction in proliferation was observed for all porphyrins with an alkyl chain of more than 11 C atoms when the cells were irradiated with 606 nm, confirming its stronger effect (**Figure 43**).

Table 12. Determined IC_{50} values of *N*-methylated porphyrins (**13**-**19**) and their Zn(II) complexes (**21**-**27**) on HDF, MeWo and A375 cell line. Cells were incubated with porphyrin for 6 hours followed by 30-min irradiation with orange or red light (λ = 606 nm and λ = 643 nm, respectively) of the same fluence rate (2 mW/cm^2, total light dose 3.6 J/cm^2). 'Dark' column represents cells tested with porphyrin without irradiation.

	HDF			**MeWo**			**A375**		
Compound	**dark**	**λ = 643 nm**	**λ = 606 nm**	**dark**	**λ = 643 nm**	**λ = 606 nm**	**dark**	**λ = 643 nm**	**λ = 606 nm**
13	> 100 μM	> 100 μM	> 100 μM	> 100 μM	> 100 μM	> 100 μM	> 100 μM	> 100 μM	> 100 μM
14	> 100 μM	25.68 ± 6.6	32.0 ± 4.29	> 100 μM	8.31 ± 0.51	18.94 ± 3.9	> 100 μM	2.5 ± 0.12	3.22 ± 0.33
15	> 100 μM	7.09 ± 1.14	32.4 ± 5.95	> 100 μM	7.70 ± 0.75	9.77 ± 3.10	> 100 μM	0.91 ± 0.56	3.94 ± 0.72
16	> 100 μM	4.65 ± 0.2	6.26 ± 0.45	> 100 μM	2.36 ± 0.64	4.27 ± 0.98	> 100 μM	0.29 ± 0.04	0.33 ± 0.02
17	> 100 μM	0.78 ± 0.03	4.60 ± 2.19	> 100 μM	0.66 ± 0.11	1.44 ± 0.14	> 100 μM	0.09 ± 0.01	0.31 ± 0.08
18	> 100 μM	0.42 ± 0.03	1.48 ± 0.55	> 100 μM	0.56 ± 0.05	0.79 ± 0.3	> 100 μM	0.1 ± 0.01	0.38 ± 0.04
19	> 100 μM	0.32 ± 0.05	0.67 ± 0.12	> 100 μM	0.35 ± 0.1	0.48 ± 0.1	> 100 μM	0.09 ± 0.01	0.37 ± 0.06
21	> 100 μM	> 100 μM	> 100 μM	> 100 μM	> 100 μM	> 100 μM	> 100 μM	> 100 μM	> 100 μM
22	> 100 μM	73.0 ± 18.4	42.23 ± 9.7	> 100 μM	69.1 ± 7.63	20.8 ± 3.43	> 100 μM	49.8 ± 8.16	6.28 ± 0.91
23	> 100 μM	50 ± 13.75	29.5 ± 12.3	> 100 μM	38.9 ± 2.51	12.1 ± 5.45	> 100 μM	44.8 ± 8.63	3.34 ± 0.75
24	> 100 μM	27.3 ± 10.5	5.71 ± 0.18	> 100 μM	21.1 ± 5.47	5.43 ± 1.20	> 100 μM	7.22 ± 1.33	0.76 ± 0.1
25	> 100 μM	6.75 ± 0.09	5.69 ± 0.08	> 100 μM	4.45 ± 0.82	0.85 ± 0.06	> 100 μM	3.53 ± 1.63	0.31 ± 0.07
26	> 100 μM	5.44 ± 0.51	2.26 ± 0.86	> 100 μM	2.70 ± 0.59	0.39 ± 0.06	> 100 μM	0.79 ± 0.04	0.27 ± 0.07
27	> 100 μM	5.08 ± 0.42	0.68 ± 0.04	> 100 μM	2.01 ± 0.69	0.40 ± 0.08	> 100 μM	0.82 ± 0.11	0.32 ± 0.12

As already mentioned, the results for free-base porphyrins and their Zn(II) complexes agree with the absorption at the desired wavelength, i.e. with the number of photons absorbed. The number of photons was calculated using the equations **3-7**, that is based on the Beer-Lambert law and utilizes both the optical properties of a PS and the physical properties of the

irradiation, such as wavelength, fluence rate and irradiation duration. As expected, the difference in photon number as a function of irradiation wavelength is minimal for free-base porphyrins **13** to **19**, with a 1.2 to 1.5 higher photon absorption observed after irradiation at 606 nm (**Table 13**). For Zn(II) porphyrins **21** to **27**, the difference is much greater and the number of photons absorbed is up to 15 times higher after irradiation at 606 nm than after 643 nm (**Table 13**). Since the number of absorbed protons after irradiation with orange light (λ = 606 nm) is comparable between the two series of porphyrins, the further results are only explained after irradiation with orange light.

Table 13. Number of photons absorbed by *N*-methylated free-base porphyrins (**13**-**19**) and their Zn(II) complexes (**21**-**27**) in concentration 1 μM during their irradiation in MTT assay. Porphyrins were irradiated with orange light (606 nm, 2 mW/cm^2, 3.6 J/cm^2) or red light (643 nm, 2 mW/cm^2, 3.6 J/cm^2) for 30 minutes.

	N_{ph} (x 10^{25}) [ph/cm^2]			N_{ph} (x 10^{25}) [ph/cm^2]	
	606 nm	643 nm		606 nm	643 nm
13	2.1	2.2	**21**	5.2	0.6
14	7.1	5.9	**22**	5.4	0.5
15	5.5	4.0	**23**	5.9	0.2
16	5.6	3.9	**24**	5.9	0.4
17	4.6	3.2	**25**	6.2	0.6
18	5.5	3.7	**26**	5.4	0.4
19	7.9	6.3	**27**	8.4	1.5

Our results showed that the cytotoxicity of porphyrins correlates with the length of a substituted alkyl chain and thus with the cellular uptake of porphyrins (**Figure 39**). The hydrophilic porphyrins **13** and **21**, that exhibited minimal cellular uptake after 6 hours of incubation at 37 °C, showed no toxicity (IC_{50} > 100 μM) in all three cell lines tested. The IC_{50} values < 1 μM indicate relatively high toxicity of porphyrins, and these were shown for both free-base porphyrins and their Zn(II) complexes, substituted with alkyl chains longer the 11 C atoms.

The porphyrins **19** and **27**, substituted with the longest alkyl chain of 17 C atoms showed the highest activity toward all cell lines, including HDF, which suggests that they exhibit low selectivity toward normal cell lines. Among free-base porphyrins, when irradiated with red light, the porphyrin **16** (R = -$C_{11}H_{23}$) showed high selectivity, with a reduction in proliferation of MeWo by 40% and A375 by > 90%, while proliferation of HDF remained ~ 80% (**Figure 43A**). The most pronounced selectivity after irradiation with orange light was observed for porphyrin **17** (R = -$C_{13}H_{27}$), which reduced the proliferation of the cell lines MeWo and A375

by 50 and 90%, while the proliferation of the cell line HDF was only reduced by 20% (**Figure 43B**).

The selectivity index was calculated by dividing the IC_{50} value obtained for the normal cell line, in this case HDF, by the IC_{50} values obtained for the tested tumour cell line, MeWo or A375. The calculation for porphyrin **16** after irradiation with red light gave a value of 2 for MeWo and 16 for A375, while the selectivity index for porphyrin **17** after irradiation with orange light showed selectivity index of 3.2 for MeWo and 14.8 for the A375 cell line. These results suggest that porphyrin **17** may be a preferred candidate for use in PDT among the free-based porphyrins.

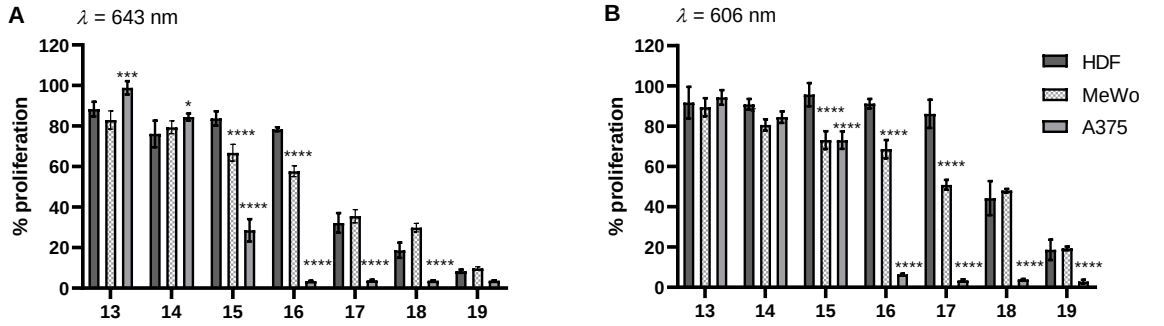

643 nm	HDF	MeWo	A375
14	***	ns	***
15	ns	****	****
16	**	****	****
17	****	****	****
18	****	****	****
19	****	****	****

606 nm	HDF	MeWo	A375
14	ns	***	****
15	ns	****	****
16	ns	****	****
17	ns	****	****
18	****	****	****
19	****	****	****

Figure 43. Comparison of the cytotoxicity of *N*-methylated free-base porphyrins **13** to **19** at concentration of 1 µM after irradiation with 643 nm (A) or 606 nm (B). The statistical analysis in the graph shows the two-way ANOVA analysis of the melanoma cell lines compared to the non-tumour cell line (HDF), while the corresponding tables shows the statistical analysis of the impact of alkyl chain length on the proliferation in comparison to the hydrophilic analogue (**13**) in different cell lines. Significance was $p < 0.0001$ and it was shown using the following signs: **** < 0.0001; 0.0001 <*** < 0.001; 0.001 < ** < 0.01; 0.01 < * < 0.1; ns > 0.1 (not significant).

The selectivity profile of the Zn(II) analogues towards melanoma cell lines was similar to that of the free-base porphyrin (**Figure 44**). The selectivity was observed for porphyrin **24** (R = -$C_{11}H_{23}$), however only against the amelanotic cell line A375 with a reduced

proliferation of 30%, while proliferation of HDF and MeWo cell lines remained at ~80%. Porphyrin **25** (R = -$C_{13}H_{27}$), which has the alkyl chain longer by only two C atoms, showed the highest selectivity towards both the melanotic (MeWo) and the amelanotic (A375) cell line. The proliferation of HDF remained high after the treatment (~80 %), while the proliferation of the melanoma cell lines was strongly reduced, more than 60 % for MeWo and 90% for the A375 cell line (**Figure 44**). When the selectivity index was calculated from the obtained IC_{50} values, the value of 6.8 observed for MeWo and the value of 18.4 observed for A375 suggests that the porphyrin **25** is the most promising candidate when irradiated with orange light, as it exhibits high cytotoxicity and the best selectivity towards melanoma cell lines.

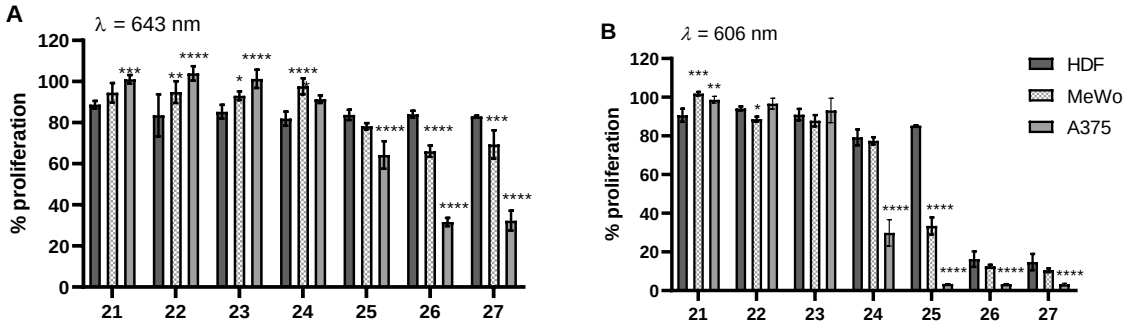

643 nm	HDF	MeWo	A375
22	ns	ns	ns
23	ns	ns	ns
24	ns	ns	*
25	ns	***	****
26	ns	****	****
27	ns	****	****

606 nm	HDF	MeWo	A375
22	ns	****	ns
23	ns	****	ns
24	***	****	****
25	ns	****	****
26	****	****	****
27	****	****	****

Figure 44. Comparison of the cytotoxicity of Zn(II) porphyrins **21** to **27** at concentration of 1 μM after irradiation with 643 nm (A) or 606 nm (B). The statistical analysis in the graph shows the two-way ANOVA analysis of the melanoma cell lines compared to the non-tumour cell line (HDF), while the corresponding tables shows the statistical analysis of the impact of the alkyl chain length on the proliferation compared to the hydrophilic analogue (**21**) in different cell lines. Significance was $p < 0.0001$ and it was shown using the following signs: **** < 0.0001; 0.0001 <*** < 0.001; 0.001 < ** < 0.01; 0.01 < * < 0.1; ns > 0.1 (not significant).

All MTT assays for the evaluation of phototoxicity were performed after incubation of the porphyrins for 6 hours at 37 °C, followed by washing of the unbound cells prior to irradiation. Both free-base porphyrins and their Zn(II) complexes exhibited similar toxicity after

irradiation with orange light wavelength, although it was observed that cellular uptake was much lower after 6 hours compared to the free-base counterparts. These results suggest that the similar phototoxicity is due to the higher amount of Zn(II) porphyrins bound to the cellular membrane. The stronger binding of the Zn(II) porphyrins to the membranes compared to the free-base analogues was previously shown and described as a consequence of the formation of an additional coordination bond between Zn^{2+} and phosphate groups in biological membranes [237]. Furthermore, a slightly higher lipophilicity of the Zn(II) porphyrins could be an additional reason for the enhanced binding to membranes and leading to a slower cellular uptake rate. If the porphyrins are directly bound to the membranes, their irradiation could lead to the production of ROS and consequently lipid oxidation could take place, resulting in increased membrane permeability. The increased permeability allows the porphyrin to enter and indicate oxidative stress in the cells [255]. Although the amount of Zn(II) porphyrins bound to the membranes is not known, these results suggest that Zn(II) porphyrins, although having a lower cellular uptake rate, are likely to strongly bound to the cell membrane and that the increased permeabilization, which is a result of the 30-minute irradiation of PS on the membranes, may increase their internalization and consequently lead to a similar phototoxicity as with the free-base porphyrins, that have been shown to have a faster cellular uptake rate.

4.1.13. Conclusion Part 4.1.

In this part of the work, the two porphyrin groups, the *N*-methylated free-base and their Zn(II) complexes with an acetamido group and substituted with an alkyl chain of different lengths from 7 to 17 C atoms, were synthesised. Both porphyrin groups exhibit preferential properties for use in PDT, however, a longer lifetime of the triplet excited state and a slightly higher production of singlet oxygen was observed for the Zn(II) analogues.

The conjugation of porphyrins with different fatty acids leads to changes in the absorption spectrum indicating the formation of micelle-like aggregates in aqueous solutions with higher ionic strength. However, it has been observed that in cell medium and other solutions containing albumin, the fatty acid in the structure is responsible for binding to albumin. Since the conjugation of the fatty acids increases the hydrophobicity of the molecule, the uptake into the cells is also improved. It has been shown that amphiphilic porphyrins, especially those with a longer substituted alkyl chain, undergo not only by passive but also active uptake, as it is known that compounds bound to albumin can internalize the cells via caveolae-mediated endocytosis.

The balance between hydrophilicity and lipophilicity proved to be an important feature in the design of PSs for PDT. As expected, the cellular uptake of porphyrins increased

proportionally with the length of the alkyl chain. Although Zn(II) porphyrins exhibited higher hydrophobicity, which is expected to increase cellular uptake, their uptake was similar to that of free-base porphyrins, but at a slower uptake rate. The length of the alkyl chain played an important role in the cytotoxicity of the porphyrins. It was observed that the porphyrin with the longest alkyl chain exhibited the highest cytotoxicity in all cell lines tested. When the length of an alkyl chain was shortened, cytotoxicity decreased slightly, but selectivity to both melanoma cell lines increased, with lower cytotoxicity to HDF as the normal cell line.

Among the porphyrins tested, porphyrin **17** and especially porphyrin **25**, both conjugated to an alkyl chain with 13 C atoms, proved to be the most promising candidates for further analysis as PS for PDT. They showed high toxicity with increased selectivity towards melanoma, especially when irradiated with orange light.

4.2. Comparison of *N*-methylated and *N*-oxidized porphyrins with an alkyl chain of different length

4.2.1. Preparation of *N*-oxidised (pyrid-3-yl)porphyrins

A group of porphyrins substituted with *N*-methylated and *N*-oxidised pyridyl groups and with an unsaturated or saturated alkyl chain of 18 C-atoms was recently described by our group, in a study of their potential for use as PSs in PDT [72]. The *N*-oxidation of the pyridyl groups was performed using an excess of *m*-chloroperbenzoic acid (*m*-CPBA) in DCM or DCM-MeOH mixture, where the unreacted *m*-CPBA, upon completion of the reaction was quenched using triethylamine (TEA), following the procedure published by Posakony and colleagues [111]. The reaction resulted in the formation of the desired product; however, purification was difficult due to the presence of triethylammonium oxide as by-product, which remained in the mixture with the product, as evidenced by multiplet at 3.5 ppm in the ^{1}H NMR spectrum (**Figure S88**).

To overcome this issue, modifications of *N*-oxidation were attempted, using some other oxidation procedures, such as by dimethyldioxirane (DMDO). It was shown that the reactivity of this reagent is similar to oxidation with *m*-CPBA, and it usually results in high selectivity and reactivity under mild conditions [256]. The mechanism for the DMDO formation involves the reaction between acetone and OXONE® by nucleophilic attack of the oxygen on the potassium peroxomonosulfate (OXONE®) on the carbonyl carbon, resulting in the loss of potassium sulfate (**Scheme 17**) [256,257]. The rate of DMDO formation has been shown to be mostly influenced by the rate of the oxidant delivery, where the slower addition of OXONE® leads to higher production of the oxidised product. Also, pH of the reaction needs to be adjusted at 7.5-8.0 to maximize the oxidation. Higher pH (pH > 8) usually leads to the degradation of OXONE® while the loss of reactivity occurs at lower pH (pH < 7.0) [257].

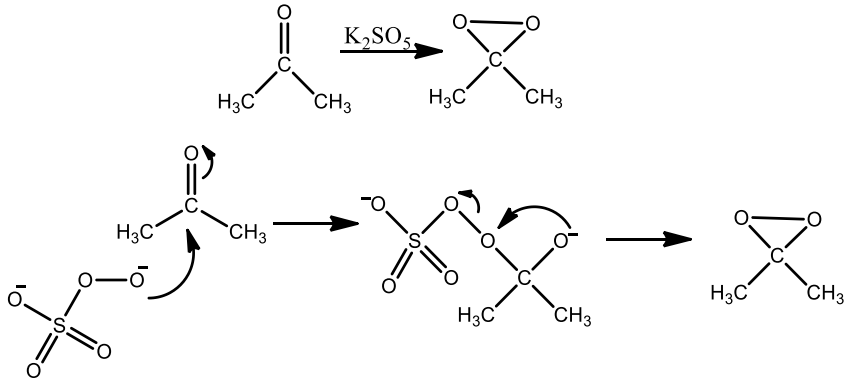

Scheme 17. Formation of dimethydioxirane (DMDO) in the reaction of acetone and potassium peroxomonosulfate (OXONE®) [257].

Here, porphyrin **1** was dissolved in DCM and OXONE®, previously dissolved in H_2O, and acetone were added gradually over one hour (**Scheme 18**). *In situ* formation of DMDO is recommended when biphasic conditions, as here, are used [257]. The pH of the reaction was monitored at the beginning of the reaction and after every addition of acetone, and it was adjusted if needed using 1 M $NaHCO_3$, phosphate buffer (pH = 7.5) or 1 M NaOH.

Unfortunately, oxidation using DMDO resulted in the degradation of the product, shown by TLC (**Figure 45**). In cases where the product was formed, ^{1}H NMR analysis was done. However, ^{1}H NMR spectrum also showed the degradation of the formed product due to overoxidation (**Figure 45**).

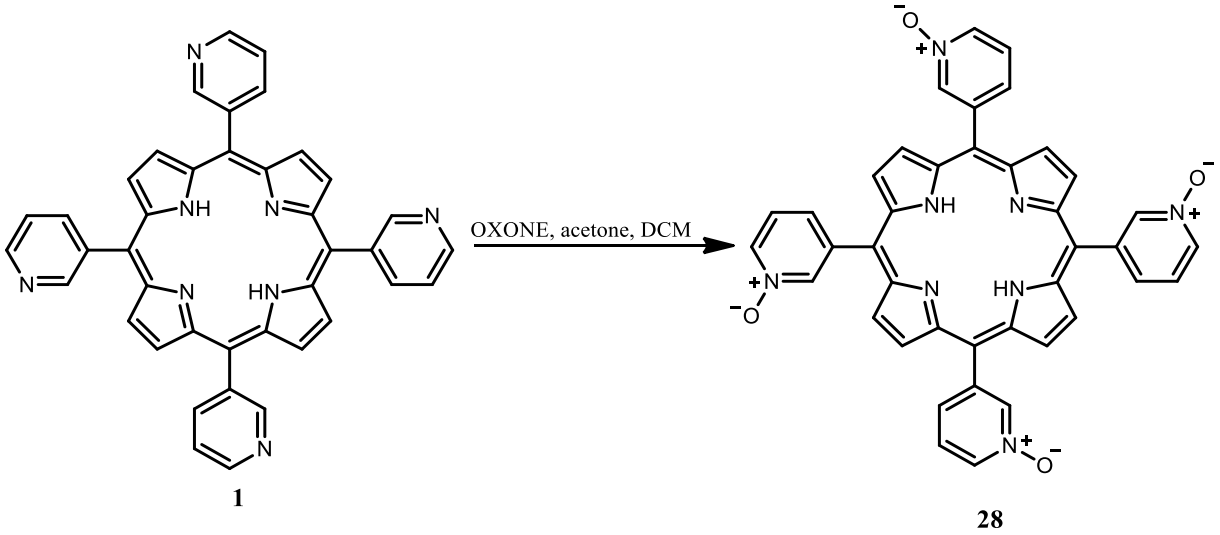

1 **28**

Scheme 18. Oxidation of porphyrin **1** with dimethyldioxirane (DMDO). Conditions of the reaction: OXONE®, acetone, pH = 7.6-7.7, RT, 2 h (method A).

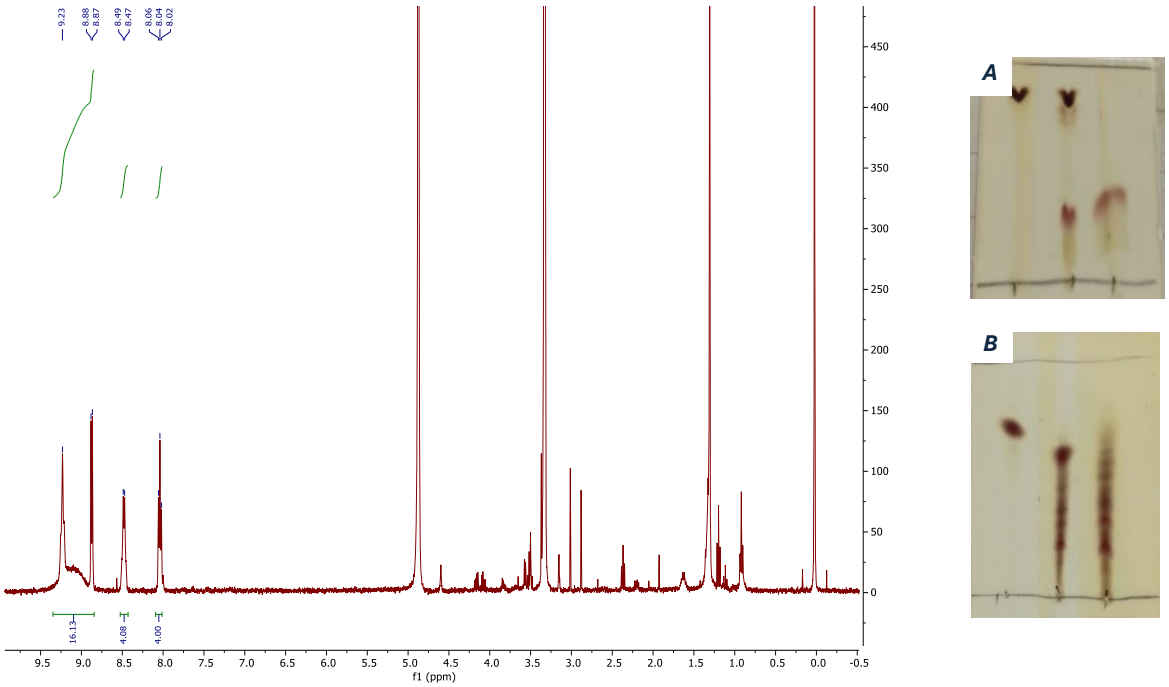

Figure 45. ^{1}H NMR (CD_3OD, 600 MHz) of the unsuccessful reaction (**28**, method A) upon adjustment of pH with 1 M $NaHCO_3$ and TLC chromatograms of the same reaction with the adjustment of pH with 1 M $NaHCO_3$ (A) and phosphate buffer (pH = 7.5) (B).

After an unsuccessful reaction with DMDO, *N*-oxidation with excess *m*-CPBA as an oxidant was tried again, this time using a more hydrophilic agent for quenching, propylamine (PrA). Due to its higher hydrophilicity compared to TEA (log*P* (TEA)= 1.45; log*P* (PrA) = 0.48), oxidized byproducts of PrA are expected to be easier to remove in the purification step, which could result in pure products.

Isolation of pure hydrophilic porphyrin **29** was achieved by column chromatography, which was performed twice with DCM and MeOH in 10:1 ratio, giving yield of 61%. The porphyrin **30,** substituted with an alkyl chain with 9 C-atoms, was successfully purified by washing the reaction mixture in DCM, followed by column chromatography twice with DCM and MeOH with DCM and MeOH in 10:1 ratio, giving yield of 73%. Porphyrins **31** and **32**, which are conjugated to alkyl chains with 13 and 17 C-atoms, respectively, were purified in two steps. The first step involved dissolving the product in a strongly acidic solution with TFA in H_2O (20:1), which led to protonation of the porphyrin and dissolution in aqueous solution. Neutralization of the reaction mixture with 1 M NaOH resulted in precipitation of the product, while the oxidation by-products remained dissolved in H_2O. To remove other by-products, the precipitate was extracted into an organic layer, which was then washed vigorously with water. The final step involved purification by column chromatography twice with different ratios of DCM and MeOH (1st with 15:1 and 2nd 10:1 DCM/MeOH ratio for

porphyrin **31**, and twice with 15:1 ratio for porphyrin **32**), resulting in yield of 79% and 39% for porphyrins **31** and **32**, respectively. The successful *N*-oxidation was confirmed by analysing the structure using ^{1}H and ^{13}C NMR spectroscopy, and by confirming their mass by HMRS. In ^{1}H NMR, successful oxidation was observed by broadening of *β*-pyrrole protons at ~ 9 ppm, as a result of slow tautomerization, as seen in the first part of this work with *N*-methylated porphyrins.

4.2.2. Absorption and fluorescence properties of *N*-oxidised porphyrins (29-32)

Absorption and fluorescence properties of *N*-oxidised porphyrins (**29-32**) were recorded in MeOH and they are summarised in **Table 10**. All porphyrins exhibit characteristic *phyllo*-type free-base porphyrin spectra with the Soret band at 416 nm and high value of molar absorption coefficient varying from 2.8-3.6 × 10^5 $M^{-1}cm^{-1}$ and four Q bands, from 510 nm through 645 nm, varying in the molar absorption coefficient from 1.5-1.9 × 10^4 $M^{-1}cm^{-1}$ observed for Q_y (1-0) to 1.5-2.0 × 10^5 $M^{-1}cm^{-1}$ for Q_x (0-0). Stokes shift was calculated in λ / nm as a distance between Q_x (0-0) in the absorption spectrum and Q (0-0) in the fluorescence spectrum and it is 2-3 nm, similar to one calculated for *N*-methylated porphyrins. Fluorescence spectra recorded in MeOH were also similar to those of *N*-methylated porphyrins and showed two distinct vibrational bands at 648 and 713 nm. (**Figure 46**).

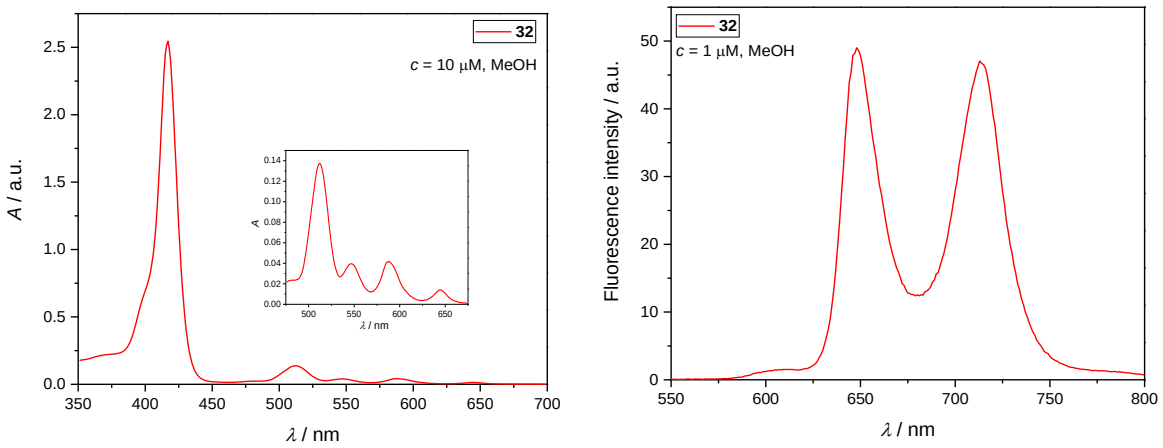

Figure 46. Absorption (left) and fluorescence spectra (right) of porphyrin **32** recorded in MeOH. Soret band wavelength was used for excitation. Inset in the absorption spectrum: enlarged Q bands in region from 480 nm to 680 nm.

Quantum yield of fluorescence (Φ_{FL}) was determined for porphyrins **29** and **32** and it was ~0.05 (**Table 14**) for both porphyrins, calculated following the equation **8** and using a **TPP**

as reference compound, indicating that substitution with a long alkyl chain does not influence the spectroscopic properties of the *N*-oxidized porphyrins measured in MeOH. Compared to *N*-methylated porphyrins **13** and **19**, with Φ_{FL} 0.072 and 0.085, respectively, *N*-oxidized porphyrins exhibit slightly lower Φ_{FL} (**Table 14**).

Table 14. Absorption and fluorescence properties of *N*-oxidised porphyrins **29-32** measured in MeOH. Soret band wavelength was used for excitation when emission spectra were recorded.

	λ_{abs} / nm (ε / × 10^3 $M^{-1}cm^{-1}$)					λ / nm		Φ_{FL}*
	Soret (B)	**Q_y (1-0)**	**Q_y (0-0)**	**Q_x (1-0)**	**Q_x (0-0)**	**Q (0-0)**	**Q (1-0)**	
29	416 (346.9)	510 (18.2)	545 (5.2)	588 (5.8)	645 (1.9)	648	713	0.050 ± 0.002
30	417 (296.4)	512 (15.4)	548 (5.1)	588 (4.9)	645 (1.5)	648	713	-
31	417 (364.6)	512 (19.3)	547 (5.8)	588 (6.0)	646 (2.0)	648	713	-
32	417 (275.4)	512 (15.0)	547 (4.3)	587 (4.5)	646 (1.6)	648	713	0.047 ± 0.002

***** Φ_{FL} is calculated in comparison with **TPP** as a reference compound.

Fluorescence decays, measured by TC-SPC, of porphyrins **29** and **32** were recorded in MeOH purged with N_2 and fit to a sum of two exponents, one of a shorter decay time (< 1 ns) with a smaller contribution (1-2%) and longer decay time (~ 8 ns) with a larger contribution (98-99%) (**Figure 47**).

As seen in the first part with *N*-methylated free-base and Zn(II) porphyrins, there are several plausible explanations for multiexponential decay of porphyrins, and it can be attributed to porphyrin tautomers or rotamers formed by the rotation of the pyridinium groups or the formation of aggregates. The most plausible explanation is formation of aggregates, as previously seen with *N*-methylated porphyrins (**13**, **14** and **19**) obtained in MeOH (**Figure 28**, section 5.1.3). There, a larger contribution of the decay with longer decay time was assigned to the monomer species in the solution, while shorter decay time of smaller contribution is assigned to the plausible porphyrin aggregates. *N*-oxidised porphyrins with three zwitterionic groups showed lower solubility in MeOH than *N*-methylated porphyrins with three positive charges in the structure. Based on the lipophilicity of the molecules, the smaller contribution of the decay may tentatively be assigned to the formation of aggregates in MeOH, while longer contribution are the porphyrins in monomeric state. However, in the porphyrin with the longer alkyl chain, it is expected that the contribution assigned to the aggregated species is larger, similar to the *N*-methylated porphyrin and its Zn(II) analogue (**19** and **27**) (**Table 6,** Section 5.1.3). However, increasing of the contribution of the shorter decay time was not observed when the porphyrin **32**, substituted with an alkyl chain with 17 C-atoms, was analysed (**Figure 47**).

Another possibility that might be assigned to the smaller contribution with shorter decay time of the fluorescence decay is the formation of pyridine-*N*-oxide photoproducts upon irradiation. It was previously shown, by Alkaitas and Calvin, that irradiation of pyridine *N*-oxides in alcohol solution (EtOH or MeOH) for 6 hours with 450-watt mercury lamp can result in the cleveage of the N-O bond and reduction to pyridine, and also in the formation of *N*- formylpyrrole (2-4%) as a result of hydrolysis of unstable photoproduct formed after photolysis of pyridine-*N*-oxide [258,259]. However, the N-O bond in aromatic-*N*-oxides was shown to be very stable, and in alcohols aromatic-*N*-oxides tend to form hydrogen bond, so the hypothesis of formation of photoproducts in a short irradiation is very unlikely [96].

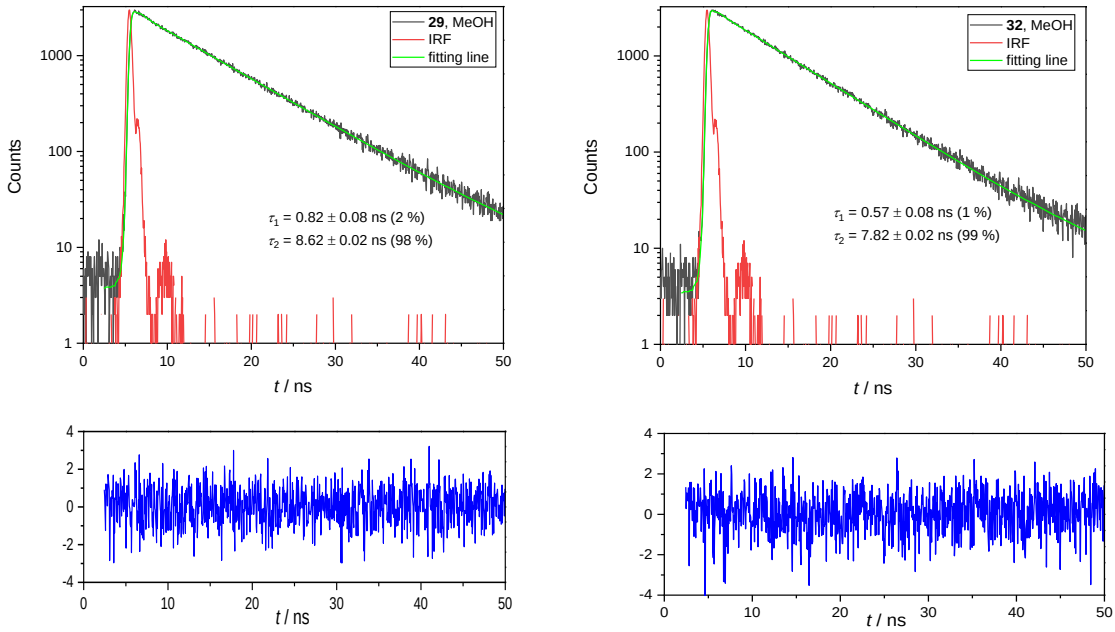

Figure 47. Fluorescence decay of **29** (left) and **32** (right) in MeOH (N_2) obtained using TCSPC (black line) and the fit to a sum of two exponents (green line). λ_{ex} = 405 nm, A_{405nm}(**29**) = 0.096; A_{405nm} (**32**) = 0.11. The bottom panel of the figures correspond to the weighted residuals between the experimental and the fitted values.

Based on results described above, it is difficult to assign the short decay time with certainty. Additional experiments should be performed, such as increasing the porphyrin concentration, temperature-dependent analysis, and measurements without purging the solution with an inert gas.

4.2.3. Triplet lifetime and quantum yield of intersystem crossing of porphyrins 29 and 32 determined by LFP

The triplet-triplet absorption spectra of porphyrin **32** were obtained in N_2 purged MeOH by LFP. The maximum of the absorption for the triplet excited state of *N*-oxidised porphyrins was detected at 440 nm, whereas the maximum of the ground state bleach is detected at 420 nm, both on a slightly lower wavelengths compared to *N*-methylated porphyrins (ground state 440 nm, and triplet maximum 460 nm) (**Figure 48**).

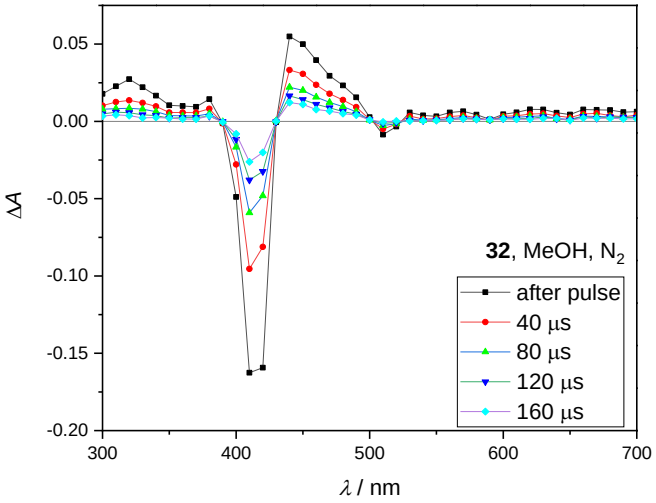

Figure 48. Transient absorption spectra after 355 nm laser excitation of **32** in MeOH saturated with N_2. $A_{355\ nm} = 0.21$, $E_{355\ nm} = 3$ mJ.

The triplet lifetimes were determined by fitting the triplet decays with the first order exponential function or with the mixed first- and second- order exponential function according to the Eq. 11 and 12 [163]. The better fit was obtained when an exponential function with two contributions was used, indicating that there were two contributions to the decay, i.e. that two different processes occurred (**Figure 49**, red line). This indicates that in addition to the detection of the excited triplet state, the formation of reversible or irreversible photoproducts from pyridine-*N*-oxide substituents could also occur.

As mentioned above, possibility of photoproduct formation is small with stabile aromatic-*N*-oxides, and the changes in the absorption spectrum were not detected after the TAS experiments (**Figure S89**). The two contributions are most likely due to the self-quenching upon irradiation due to triplet-triplet annihilation. Therefore, decays were fit to the mixed first- and second- order decay function. When fitting the triplet decays of porphyrins **29** and **32**, estimated lifetimes were 1.11 ms and 0.96 ms, respectively. The observed lifetimes are

longer compared to the *N*-methylated analogues **13** and **19** that were 0.77 and 0.74 ms, respectively (**Figure 49**. blue line, **Table 15**). Long triplet lifetime of *N*-oxidized porphyrins associates with shorter fluorescence decay lifetime (τ_S) observed by TC-SPC.

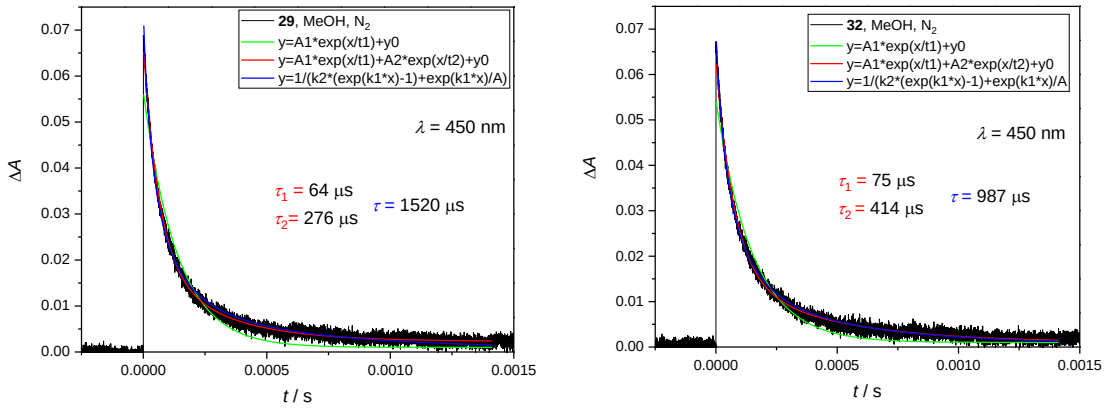

Figure 49. Transient absorption kinetics at 450 nm after 355 nm laser excitation of porphyrins **29** and **32** in MeOH saturated with N_2. $A_{355\ nm}$ (**29**) = 0.22; $A_{355\ nm}$ (**32**) = 0.22, $E_{355\ nm}$ = 3 mJ.

The observed triplets of porphyrins **29** and **32** were quenched with molecular oxygen and the rate of the triplet quenching (*k*q) was calculated using the Stern-Volmer equation (Eq. 15). The observed *k*q for both porphyrins **29** and **32** was similar 1.3 and 1.4 × 10^9 $M^{-1}s^{-1}$ (**Table 11** and **Figure S90**), respectively, and it was also similar to all observed *k*q values for *N*-methylated porphyrin analogues, **14** and **19** (**Figure S87**).

To calculate Φ_{ISC}, the same procedure was used as for *N*-methylated porphyrins, where the molar absorption coefficient using the singlet depletion method (Eq. 13) was used in the first step and comparative method to obtain Φ_{ISC} in the second step (Eq. 14). The obtained values for porphyrins **29** and **32** were 0.66 and 0.51, respectively. The longer τ_T of *N*-oxidised porphyrins compared to *N*-methylated analogues and the higher Φ_{ISC} confirm their favourable photophysical properties as PSs for use in PDT (**Table 15**).

Table 15. Photophysical parameters of tested *N*-oxidised porphyrins (**29** and **32**) in MeOH and a reference compound **TPP** obtained by LFP. Lifetime of the triplet excited state (τ_T), quantum yield of the intersystem crossing (Φ_{ISC}), molar absorption coefficient of the triplet state ($\varepsilon_{T\text{-}T}$), and quenching rate constant of the triplet excited state by O_2 (*k*q (O_2)).

	τ_T / μs	$\varepsilon_{T\text{-}T}$ / $M^{-1}cm^{-1}$	Φ_{ISC}	k_q (O_2) / $M^{-1}s^{-1}$
TPP (C_6H_6) [169]	90	66 600	0.67	/
29	1113 ± 185	47 000	0.66	1.3×10^9
32	962 ± 35	58 300	0.51	1.4×10^9

4.2.4. Singlet oxygen production and lipophilicity of *N*-oxidised porphyrins (29-32)

Production of $^1O_2$ was determined using the photodegradation of DPBF in MeOH, previously described fluorescence dye that reacts with not only singlet oxygen, but with also other ROS produced by PS [234]. Porphyrins **29-32** showed > 70% photodegradation of DPBF after 15-minute irradiation with red light (λ = 647 nm, 9.63 J/cm^2) indicating high production of ROS (**Figure 50**). As with *N*-methylated porphyrins, the length of the alkyl chain did not influence the $^1O_2$ production.

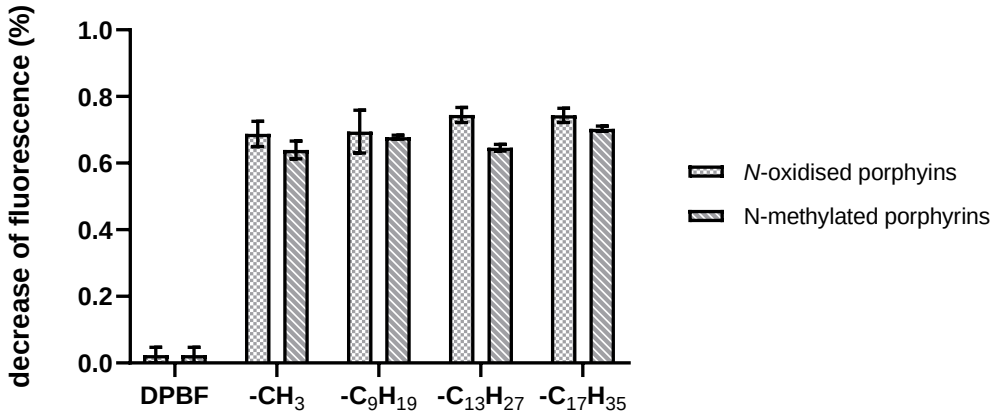

Figure 50. Singlet oxygen ($^1O_2$) production of the *N*-methylated (**13**, **15**, **17** and **19**) and *N*-oxidised porphyrins (**29-32**) (5 μM) obtained by photodegradation of the DPBF (4 μM) in MeOH after irradiation with red light for 15 minutes (λ = 647 nm; 10.7 mW/cm^2, 9.63 J/cm^2).

The decrease in fluorescence observed upon photodegradation of DPBF by *N*-methylated porphyrins was 65-70%, thus *N*-oxidised porphyrins showed similar or slightly higher photodegradation of DPBF than *N*-methylated analogues. These results are consistent with the long triplet lifetimes obtained with LFP, proving preferable photophysical properties of *N*-oxidised porphyrins as PSs for PDT.

The lipophilicity of the *N*-oxidised porphyrins was determined only by theoretical calculations using the aforementioned Chemicalize [240], an online structure-based analysis

program from Chemaxon. According to the data obtained, all *N*-oxidised porphyrins are assumed to be hydrophobic, with calculated clog*P* ranging from 3.03 for porphyrin **29** (R = $-CH_3$) to 10.4 for porphyrin **32** (R= $-C_{17}H_{35}$) (**Table 16**). As mentioned before, these programs are still not suitable for the determination of physicochemical properties, especially for larger molecules such as porphyrins. However, based on the results obtained by Chemicalize, it can be assumed that the change from positively charged *N*-methylated (**Table 11**) to zwitterionic *N*-oxidised (**Table 16**) *meso*-substituents strongly increases the overall lipophilicity of porphyrins.

Table 16. Lipophilicity *N*-oxidised (**29-32**) porphyrins determined using online program Chemicalize from ChemAxon (clog*P*) and compared with *N*-methylated (**13**, **15**, **17** and **19**) porphyrins.

	clog*P*
13	-5.024
15	-1.212
17	0.566
19	2.345
29	3.025
30	6.838
31	8.616
32	10.394

4.2.5. Cellular internalisation of *N*-oxidised porphyrins (29, 30, 31 and 32) in HDF, MeWo and A375 cell lines

Cellular uptake of porphyrins was evaluated by measuring the fluorescence intensity of solubilised solution of cells incubated with porphyrins at 4 or 37 °C for up to 24 hours. As shown in **Figure 51**, substitution of porphyrin with an alkyl chain facilitates entering of the *N*-oxidised porphyrin to the cells. Porphyrin **29** with an acetamido group (R = $-CH_3$) showed very low internalisation compared to porphyrins **30**, **31** and **32**, substituted with an alkyl chain with 9, 13 and 17 C-atoms, respectively. After 24 hours of incubation at 37 °C, the cellular uptake is proportional to the length of the alkyl chain (**Figure 52**). Porphyrins **30** and **31** showed similar kinetics, where the majority of porphyrin that internalised the cell, entered within 6 hours of incubation in HDF and A375, and 12 hours in MeWo cell line. Interestingly, porphyrin **32**, substituted with the longest alkyl chain (R = $-C_{17}H_{35}$), enters cell much slower compared to porphyrins **30** and **31**, with cellular uptake at 6 hour time point slightly lower than cellular uptake of porphyrins **30** and **31**. However, after 24 hour-incubation cellular

uptake was higher than uptake of porphyrins **30** and **31**. This finding indicates that, although hydrophobicity facilitates passage through membranes, too hydrophobic molecules tend to aggregate in aqueous solutions which resulted in slower incubation, most probably *via* active uptake through endocytosis. However, due to the long alkyl chain that can attach to the membranes and the *N*-oxide moiety that reduces membrane permeability, there is also the possibility, similar to the one seen with Zn(II) porphyrins, that these porphyrins are strongly bound to the membranes, resulting in slower uptake. It was already previously shown that hydrophobicity and the kinetics of cellular uptake are not in agreement [226]. Ben Dror and colleagues showed that hydrophobic molecules have lower binding to liposomes of molecules that are not monomeric or do not diffuse properly into the lipid phase [260]. Lower liposome binding can therefore be explained by slower cellular uptake of molecules, as an active uptake is also required for transport [260].

Compared to the cellular incubation of *N*-methylated porphyrins (**Figures 39 and 40**), it has been observed that *N*-oxidised porphyrins, especially **32** conjugated with a longer alkyl chain, enter the cells more slowly and in much smaller amounts (**Figures 51** and **52**). It has already been shown that the length of an alkyl chain is important for better cellular uptake of both porphyrin groups, but the presence of cationic or zwitterionic groups on other *meso*-substituents also plays a role in the cellular uptake of porphyrins. In contrast to the cationic *N*-methylated porphyrins with positive charges that enable binding to the negative sites of the membranes, zwitterionic *N*-oxide groups are known to reduce membrane permeability [96]. In addition to the aggregation of **32** in aqueous media, this could be a possible reason for the overall lower cellular internalization of *N*-oxidised porphyrins.

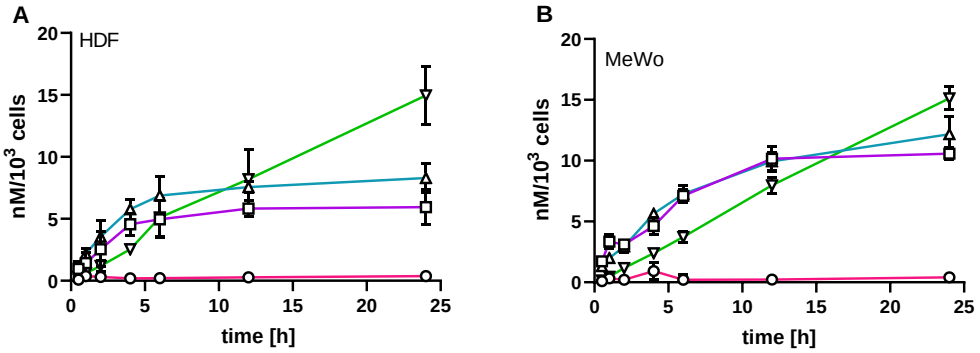

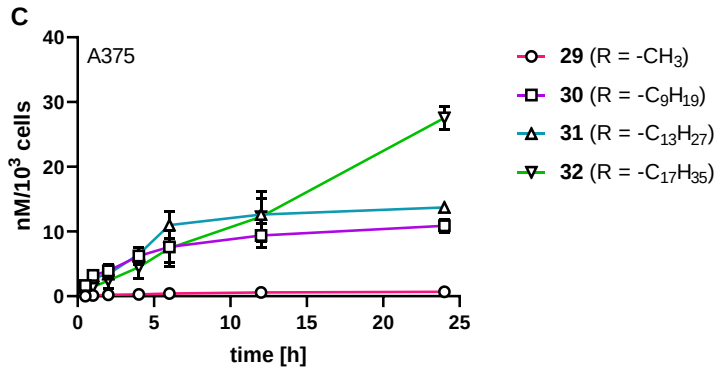

Figure 51. Cellular uptake kinetics measured over 24 hours of incubation at 37 °C of *N*-oxidised porphyrins (**29**-**32**) on HDF (A), MeWo (B) and A375 (C) cell line. Results are presented as a mean of calculated concentration per 10^3 cells (nM) obtained after three individual measurements with standard deviations as error bars.

Temperature-dependent cellular uptake, as described in the Section 4.1.10. is usually used as the first sign to investigate the type of cellular uptake (passive or active) of the porphyrins [247]. To investigate the impact of temperature on cellular uptake, cells (HDF, MeWo and A375 cell lines) were incubated not only at 37 °C but also at 4 °C for 24 hours (**Figure 52**). In contrast to the results after incubation at 37 °C, porphyrin **30** conjugated to an alkyl chain with 9 C-atoms showed the highest internalisation at 4 °C in all cell lines tested, indicating that longer alkyl chain, i.e. molecules with higher lipophilicity, have difficulty penetrating the cells at lower temperatures. As already observed with the *N*-methylated porphyrins, the differences between uptake at higher and lower temperatures are greater with the porphyrin that has a longer alkyl chain. Based on the results, we can assume that porphyrins **29** and **30** are mostly internalised *via* passive process, while porphyrins **31** and **32** can undergo both an active and a passive process, with the proportion of active uptake being higher for porphyrin **32** substituted with a longer alkyl chain.

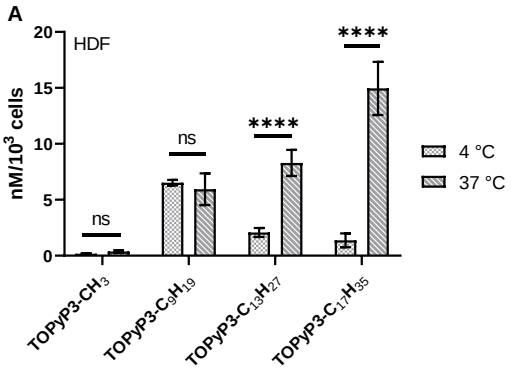

37 °C	29	30	31	32
29				
30	****			
31	****	**		
32	****	****	****	

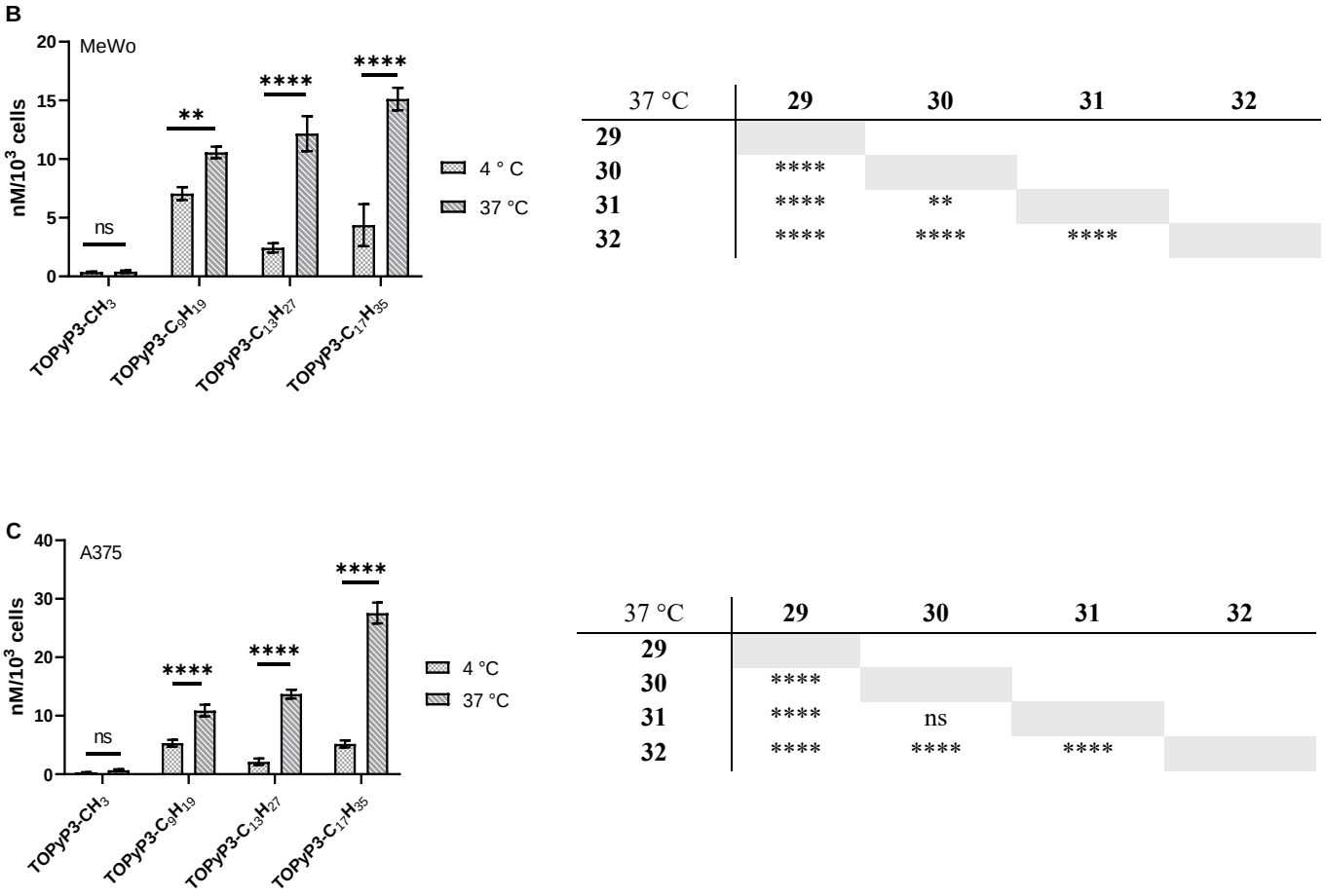

Figure 52. Comparison of the cellular uptake at 4 °C and 37 °C after incubation for 24 hours with *N*-oxidised porphyrins (**29-32**) in HDF (A), MeWo (B) and A375 (C) cell line. All results are shown as a mean concentration per 10^3 cells (nM) with standard deviations as error bars. Standard t-tests were used for statistical comparison of cellular uptake at different temperatures (statistics presented on the graph), while two-way ANOVA with Tukey *post-hoc* tests were used to compare the differences on the cellular uptake at 37 °C based on the alkyl chain length (table statistics). Significance was $p < 0.0001$ and it was shown as follows: **** < 0.0001; 0.0001 <*** < 0.001; 0.001 < ** < 0.01; 0.01 < * < 0.1; ns > 0.1 (not significant).

4.2.6. Localization of *N*-oxidised porphyrins (30-32) using fluorescence microscopy

Localisation of PS in mitochondria and endoplasmic reticulum (ER) is known to promote apoptosis or paraptosis as the main modality of cell death after PDT [4,38,45]. Here, the localization of *N*-oxidised porphyrins (**30**, **31** and **32**) was tested after 6 hours of incubation

using fluorescence microscopy with $DIOC_6(3)$, a marker for mitochondria and ER (**Figure 53**). The results show that porphyrins **30**, **31** and **32** are preferentially located in the ER and mitochondria and none of the tested porphyrins were found in the nucleus. In addition, low solubility and aggregation of porphyrin **32** in biological media was observed in the image. On the overlapping image, arrows are pointing out aggregates of porphyrin **32** that did not enter the cells. This finding agrees with the results of cellular uptake, where porphyrin **32** showed lower cellular uptake compared to **30** and **31**. However, after 24 hours, the cellular uptake of porphyrin **32** is higher than the uptake of the other porphyrins tested. Furthermore, this finding confirms the possibility that part of porphyrin **32** is internalised by an active process, by endocytosis.

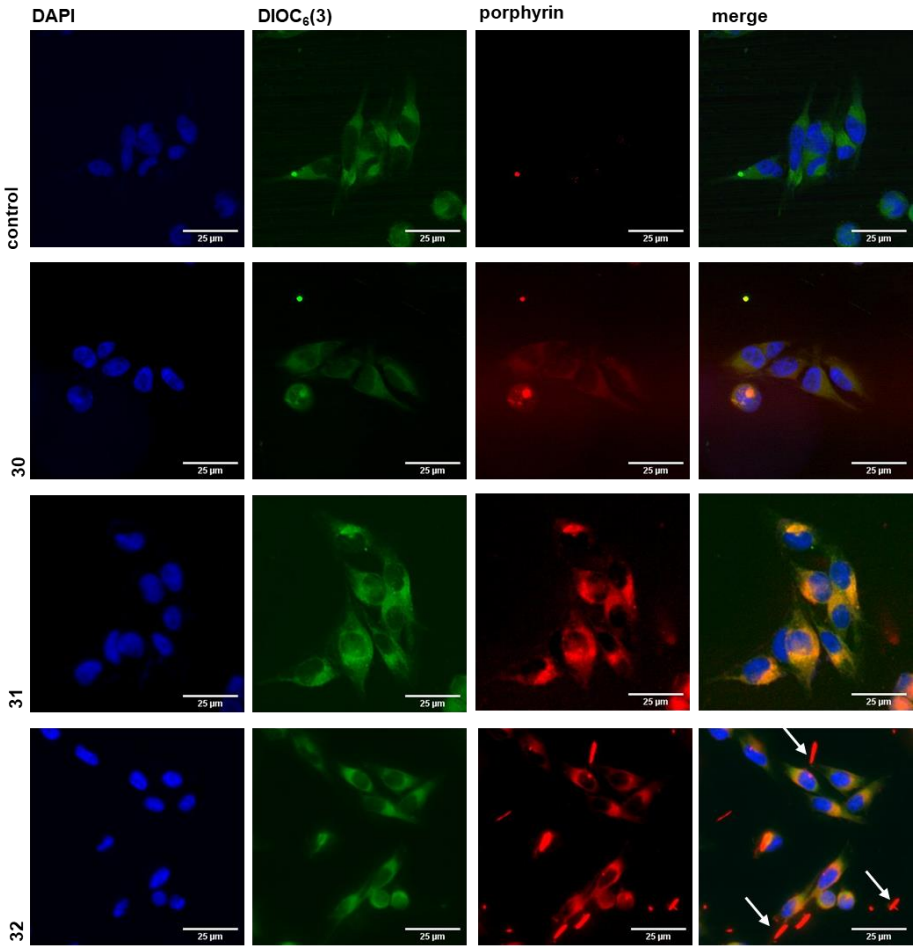

Figure 53. Localisation in MeWo cell line of the *N*-oxidised porphyrins (**30**, **31** and **32**) after incubation with $DIOC_6(3)$. The porphyrins were incubated at concentration of 5 µM for 6 hours. All images were taken by fluorescence microscopy at 20× magnification.

4.2.7. Cytotoxicity of *N*-oxidised porphyrins in conditions of $CoCl_2$-induced hypoxia and normoxia

The cytotoxicity of *N*-methylated (**13**, **15**, **17** and **19**) and *N*-oxidised (**29-32**) porphyrins was determined using the MTT assay under conditions of normoxia and $CoCl_2$-induced hypoxia. Cobalt chloride, $CoCl_2$, is the best-known hypoxia mimetic agent and the most common method to induce hypoxia when a laboratory is not equipped with a hypoxia chamber or an O_2-regulated incubator. The mechanism of $CoCl_2$-induced hypoxia is known as the replacement hypothesis, in which Co^{2+} replaces Fe^{2+} in prolyl hydroxylases (PHDs) and blocks the hydroxylation of hypoxia-inducible factor 1 (HIF-1). Hypoxia-inducible factor (HIF-1) is a transcription factor that regulates oxygen homeostasis in mammalian cells and links the hypoxic stimulus to gene expression. It consists of two main subunits: the oxygen-dependent HIF-1α, which increases under hypoxic conditions, and the oxygen-independent HIF-1β, the aryl hydrocarbon receptor nuclear translocator (ARNT) [98]. Under normoxic conditions, HIF-1α is hydroxylated by the oxygen-dependent degradation domain (ODD) in the PHDs. For successful hydroxylation, the PHDs require O_2, 2-oxoglutarate, ascorbate and iron (Fe^{2+}) as a cofactor. Hydroxylation is the hallmark for ubiquitination by the Von Hippel-Lindau E3 ligase (VHL), a tumour suppressor protein, and consequently for degradation by proteosome 26S [261,262]. In hypoxia, which is achieved either by reducing oxygen levels or, in our case, by replacing a metal cation in prolyl hydroxylases, the hydroxylation step is blocked and the VHL tumour suppressor ligase protein cannot bind and initiate proteasomal degradation, leading to an accumulation of HIF-1α in the cytoplasm [262].

During the experiments, stock solutions were prepared in DMSO, a standard solvent for various pharmacological agents. However, porphyrins were shown to aggregate over time, which made it difficult to obtain reproducible results unless we prepare new stock solutions for each experiment. To avoid this problem, stock solutions were also prepared in polar protic solutions. Alcohols, in our case EtOH, are known to stabilize *N*-oxides [96]. Prior to the experiments with the porphyrins, the toxicity of EtOH was determined at tested concentrations (data not shown). The experiments were carried out with the tumour cell lines A375 and MeWo. It was found that the solvent (EtOH) alone had no effect on the result. Also, the change from polar aprotic to polar protic solvents did not lead to a better stability of the *N*-oxidised porphyrin solutions (**Table 18**). However, EtOH has a lower boiling point than DMSO, so it was possible to evaporate the solvent after the treatment and dissolve it again in EtOH each time the experiment was repeated, which meant that less porphyrin is being wasted than by dissolving it in DMSO.

The maximum concentration tested under both conditions was 100 μM for both *N*-methylated and *N*-oxidised porphyrins at an incubation time of 6 hours (**Figure 54**). No toxicity was observed for any of *N*-oxidised porphyrins even at maximum concentration tested when the

cells (HDF, MeWo and A375) were kept in the dark. The cells were irradiated with red light (643 nm, 2 mW/cm^2) for 30 minutes. For both porphyrin groups, *N*-methylated and *N*-oxidised, substituted with an acetamido group (**13** and **29**, respectively), the IC_{50} was higher than the maximum concentration tested (IC_{50} > 100 µM), indicating low activity, most likely due to low accumulation in the cells (**Table 17**). Substitution with a long alkyl chain increased the cellular uptake and proportionally a higher cytotoxicity of the porphyrins was shown. Porphyrins substituted with a 13 and 17 C-atom alkyl chain, both with the *N*-methylated (**17** and **19**) and in the *N*-oxidised group (**31** and **32**), showed the strongest reduction in proliferation after the treatment with 1 µM porphyrin and subsequent irradiation with red light (**Figure 54**), whereas porphyrins substituted with a 9 C-atom alkyl chain (**15** and **30**) showed little or negligible reduction. Only in A375, the *N*-methylated porphyrin **15** also showed a strong reduction in proliferation, by > 50% under the same conditions (**Figure 54**). The IC_{50} values obtained are in agreement with the proliferation results, with IC_{50} < 1 µM observed for porphyrins **17**, **19** (*N*-methylated), **31** and **32** (*N*-oxidised) in all cell lines tested and for porphyrin **15** in A375 (**Table 17**). When mentioning the relationship between cellular uptake and cytotoxicity, it should be noted that all porphyrins, *N*-methylated and *N*-oxidised, were incubated for 6 hours. Among the tested *N*-oxidised porphyrins with an alkyl chain (**30**, **31** and **32**), porphyrin **32** had either the lowest internalisation (MeWo) or similar to porphyrin **30** (HDF and A375). However, the results of the MTT assay show a much higher cytotoxicity compared to porphyrin **30** in the HDF and A375 cell lines and even the highest reduction of proliferation in the MeWo cell line. Since porphyrin **32** shows the highest cellular uptake after 24 hours of incubation, this result could be explained by the fact that the porphyrin could attach the cell membranes with the long alkyl chain within 6 hours of incubation and upon irradiation, lipid oxidation can take place. Consequently, lipid oxidation leads to increased permeabilization of the membrane and easier penetration of the PS into the cell [255], which leads to ROS production within the cells and higher cytotoxicity of the PS.

Compared to the *N*-methylated porphyrins (**17** and **19**), the *N*-oxidised porphyrins (**31**, **32**) showed lower photocytotoxicity under both conditions, normoxia and $CoCl_2$-induced hypoxia, and in all cell lines tested (**Figure 54**). In addition, porphyrin **15** showed significantly lower proliferation of A375 compared to the **30**, *N*-oxidised analogue (**Figure 54C**). Although better photophysical properties such as higher Φ_{ISC} and longer τ_T that were observed for *N*-oxidised porphyrins, the lower cellular uptake proved to be a decisive factor for the outcome of PDT.

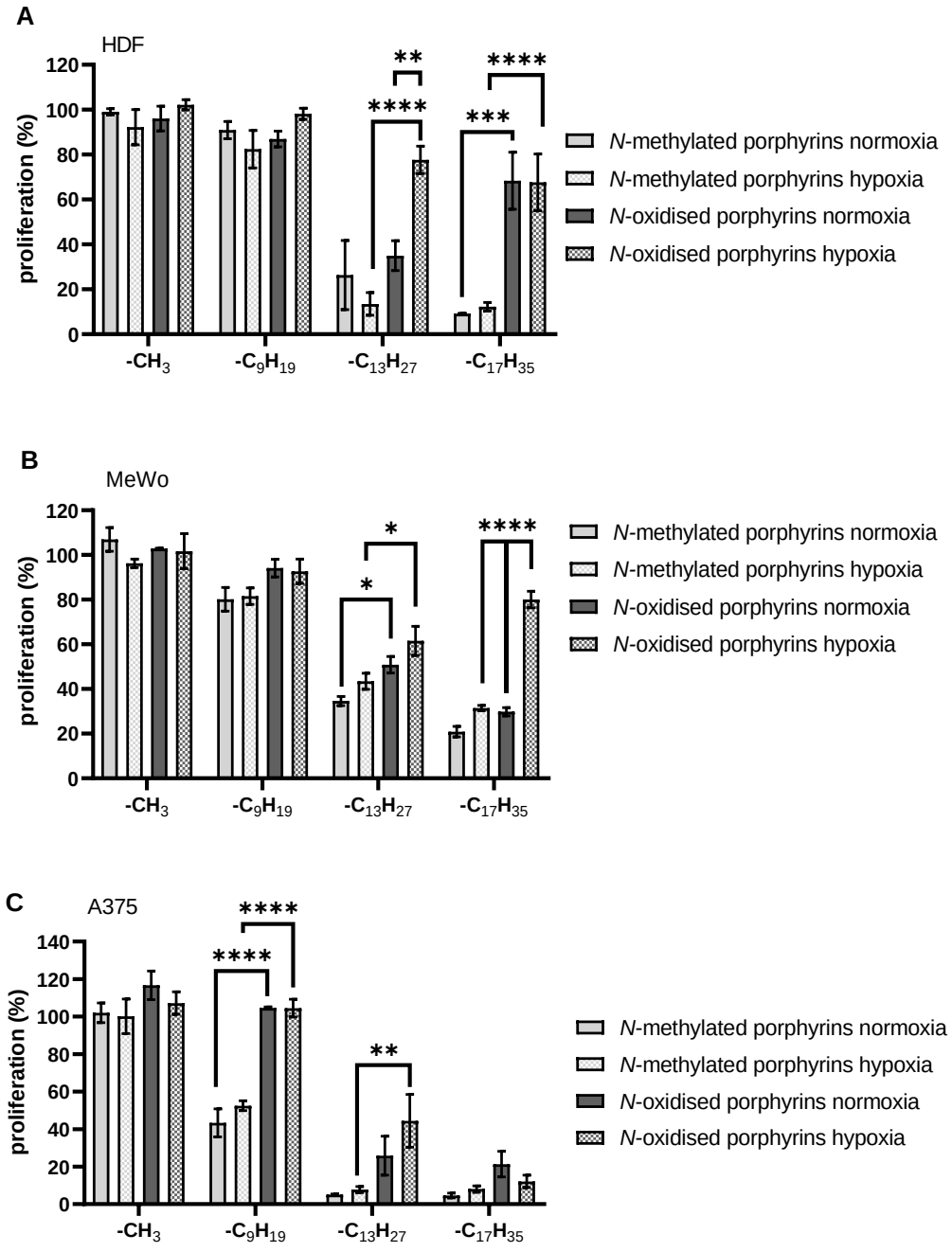

Figure 54. Comparison of the proliferation at 1 μM concentration of *N*-methylated (**13** (R =-CH_3), **15** (R = -C_9H_{19}), **17** (R = -$C_{13}H_{27}$) and **19** (R = -$C_{17}H_{35}$), and *N*-oxidised porphyrin (**29** (R = -CH_3), **30** (R = -C_9H_{19}), **31** (R = -$C_{13}H_{27}$) and **32** (R = -$C_{17}H_{35}$)) in the conditions of normoxia and $CoCl_2$ induced hypoxia on HDF, MeWo and A375 cell lines. Statistical analysis was performed using two-way ANOVA with Tuckey *post-hoc* test to compare each group of porphyrins under the condition of normoxia and $CoCl_2$-induced hypoxia and to

compare the two groups of porphyrins under the same condition. Significance was $p < 0.0001$ and it was shown using the following signs: **** < 0.0001; 0.0001 <*** < 0.001; 0.001 < ** < 0.01; 0.01 < * < 0.1; ns > 0.1 (not significant).

The use of *N*-oxide substituents in the porphyrin structure as a moiety of hypoxia-activated prodrugs (HAPs) is a strategy to overcome hypoxia. However, hypoxia conditions were achieved by adding $CoCl_2$ at a concentration of 100 μM at least two hours before the treatment with porphyrins. In this way, as explained above, hypoxia was not achieved by reducing oxygen levels in the cells, but by the accumulation of HIF-1α, a transcription protein that regulates oxygen homeostasis. Although oxygen levels remained the same, a reduction in proliferation was observed when cells were treated with *N*-oxidised porphyrins under condition of $CoCl_2$-induced hypoxia. For example, a significant reduction in proliferation was observed for porphyrin **31** in the HDF cell line, while a smaller reduction was seen in MeWo and A375 (**Figure 54**). The IC_{50} values are compared for porphyrin **31**, where an increase of 1.8 μM can be seen in HDF, 0.75 μM in MeWo and 0.1 μM in A375. A reduction in proliferation was also observed with *N*-methylated porphyrins, but their activity was much stronger compared to *N*-oxidised porphyrins in normoxia, so the inhibition effects of $CoCl_2$ hypoxia conditions were much smaller. The calculated IC_{50} values for porphyrin **17**, substituted with 13 C-atom alkyl chain, were 0.18 μM higher in the HDF and MeWo cell lines and 0.07 μM in A373 under $CoCl_2$-induced hypoxia (**Table 17**).

These results are consistent with previous from literature describing that $CoCl_2$ induces hypoxia leading to increased proliferation due to the accumulation of HIF-1α, which alters the expression of vascular endothelial growth factor (VEGF), which in turn promotes angiogenesis, and increases the expression of p53 that is involved in cell survival [263]. Resistance to PDT after treating cells with $CoCl_2$ was previously demonstrated in Het-1A (non-cancerous endothelial cell line) with 5-aminolevulinic acid (5-ALA) as PS [264]. It was observed that accumulation of HIF-1α can reduce photosensitivity *in vitro*, which is partly due to inhibition of the PDT-induced apoptosis. A role of HIF-1α accumulation and apoptosis inhibition has been described by the overexpression of pro-apoptotic genes such as BAX and the accumulation of p53 [263,265]. In another study by Rodriguez and colleagues, resistance to PDT employing 5-aminolevulinic acid methyl ester (Me-ALA) as PS was described by the induction of autophagy as a survival mechanism, by the accumulation of HIF-1α and the production of ROS, which subsequently led to the overexpression of vacuole membrane protein 1 (VMP-1), a protein that plays an important role in the formation of autophagosomes [266]. In addition, increased ROS production in hypoxia contributes to the stabilization of HIF-1α via cytokines in a ROS-dependent mechanism that also has an impact on PDT resistance on $CoCl_2$-treated cells [265]. All this information suggests that the obtained lower

decrease in proliferation of $CoCl_2$-treated cells after treatment with both *N*-oxidised and *N*-methylated porphyrins are the result of induced accumulation of HIF-1α and therefore increased resistance to ROS, cell survival and increased proliferation of hypoxia-induced cells *in vitro*.

Table 17. Calculated IC_{50} values of *N*-methylated porphyrins (**13**, **15**, **17** and **19**) and *N*-oxidised porphyrins (**29**-**32**) after irradiation with red light for 30 minutes (λ = 643 nm, 2 mW/cm^2, 3.6 J/cm^2) on HDF, MeWo and A375 cell lines. Stock solutions (20 mM) were prepared in dimethylsulfoxide (DMSO). Hypoxia conditions were achieved by adding 100 μM hypoxia-mimetic agent $CoCl_2$ for minimum two hours before treatment with porphyrins.

	HDF		**MeWo**		**A375**	
IC_{50} [μM]	No $CoCl_2$	100 μM $CoCl_2$	No $CoCl_2$	100 μM $CoCl_2$	No $CoCl_2$	100 μM $CoCl_2$
13	> 100	> 100	> 100	> 100	> 100	> 100
15	7.09 ± 0.66	8.87 ± 0.02	3.52 ± 0.65	6.81 ± 1.36	0.67 ± 0.03	0.99 ± 0.13
17	0.81 ± 0.05	0.99 ± 0.05	0.43 ± 0.03	0.61 ± 0.16	0.15 ± 0.06	0.22 ± 0.08
19	0.33 ± 0.03	0.46 ± 0.14	0.33 ± 0.04	0.47 ± 0.02	0.15 ± 0.08	0.23 ± 0.07
29	> 100	> 100	> 100	> 100	> 100	> 100
30	3.49 ± 0.45	7.65 ± 0.06	5.46 ± 1.08	6.28 ± 0.82	3.87 ± 0.45	5.46 ± 1.48
31	0.86 ± 0.04	2.62 ± 0.19	1.04 ± 0.09	1.79 ± 0.37	0.78 ± 0.17	0.86 ± 0.06
32	1.31 ± 0.57	1.09 ± 0.29	0.66 ± 0.14	0.68 ± 0.19	0.77 ± 0.08	0.94 ± 0.15

Changes in the alkyl chain length of free-base *N*-methylated porphyrin and their Zn(II) complexes were shown to result in higher selectivity towards the melanoma cell lines (**Figures 43** and **44**). Here, the same results with *N*-methylated porphyrins were also shown in $CoCl_2$-induced hypoxia, where higher selectivity was observed for porphyrins **17** and **15** compared to porphyrin **19**, which is substituted with the longest alkyl chain containing 17C atoms. In the group of *N*-oxidised porphyrins, as discussed before, a decrease in cytotoxicity was observed when the alkyl chain was shorter. However, based on the IC_{50} values obtained, no selectivity towards melanoma cells was observed for any of the *N*-oxidised porphyrins tested (**Table 17**).

In addition, melanin is known as the main defence mechanism in the PDT of melanomas as it mainly acts as oxygen scavenger [8]. The difference in the proliferation experiments based on the type of melanoma cells was shown after treatment with *N*-methylated porphyrins, as with MeWo as melanotic and A375 as amelanotic cell lines (**Figure 43**). Here, lower proliferation of A375 after treatment with 1μM porphyrin **31** and **32** was observed (**Figure**

54C). However, IC_{50} results obtained for A375 were similar to the results on both MeWo and HDF cell lines, showing that impact of the melanin did not serve as a strong defendant as it was seen with *N*-methylated porphyrins implying that some other cytotoxic mechanisms might be involved when the *N*-oxidised porphyrins are used (**Table 17**).

Table 18. Calculated IC_{50} values of *N*-methylated porphyrins (**13**, **15**, **17** and **19**) and *N*-oxidised porphyrins (**29**-**32**) after irradiation with red light for 30 minutes (λ = 643 nm, 2 mW/cm^2, 3.6 J/cm^2) on MeWo and A375 cell lines. Stock solutions (20 mM) were prepared in EtOH. Hypoxia conditions were achieved by adding 100 μM $CoCl_2$ for minimum two hours before treatment with porphyrins.

	MeWo		**A375**	
IC_{50} [μM]	No $CoCl_2$	100 μM $CoCl_2$	No $CoCl_2$	100 μM $CoCl_2$
13	> 100	> 100	> 100	> 100
15	4.76 ± 0.06	6.10 ± 2.12	0.87 ± 0.31	1.25 ± 0.61
17	0.43 ± 0.00	0.55 ± 0.16	0.21 ± 0.04	0.23 ± 0.06
19	0.23 ± 0.11	0.33 ± 0.06	0.09 ± 0.01	0.13 ± 0.05
29	> 100	> 100	> 100	> 100
30	3.78 ± 1.21	4.77 ± 1.87	3.68 ± 1.48	5.68 ± 2.01
31	0.82 ± 0.36	0.94 ± 0.04	1.68 ± 1.11	3.04 ± 0.54
32	0.93 ± 0.01	0.84 ± 0.02	0.82 ± 0.02	2.35 ± 0.71

4.2.8. Conclusion of the part 4.2.

In this part of the work, *N*-oxidised porphyrins (**29**-**32**) were successfully synthesised in a reaction with *m*-CPBA, and the purification for each porphyrin was optimised based on their alkyl chain length. All porphyrins exhibited preferential photophysical properties for use in PDT, with high Φ_{ISC} and ~ 1 ms long τ_T. However, the cellular uptake of the *N*-oxidised porphyrins was significantly lower compared to the *N*-methylated analogues and consequently a lower cytotoxicity of the *N*-oxidised porphyrins was observed. Moreover, hypoxia in the cells was achieved by treating the cells with $CoCl_2$, a hypoxia-mimetic agent that does not reduce the amount of oxygen in the cells but stabilises the hypoxia-inducible factor (HIF-1α), leading to its accumulation in the cells. Although the *N*-oxides were synthesised to be activated and lead to better activity under hypoxia, no “true" hypoxia was achieved with $CoCl_2$, thus no increased activity was observed.

Furthermore, no selectivity towards melanoma cell lines was observed. However, the difference in activity was much less in the two melanoma cell lines differing in melanin content than in the *N*-methylated analogues, suggesting that *N*-oxide moiety plays a role in the cytotoxicity of porphyrin overcoming melanin resistance.

Overall, amphiphilic *N*-oxidised porphyrins, especially porphyrin **31**, which showed relatively rapid cellular uptake with desirable toxicity towards cell lines, proved to be potential PSs for use in PDT. In further studies, the synthesised PSs should be tested under "true" hypoxia conditions, i.e. with a reduced amount of oxygen in the culture, which could be achieved by using "hypoxia incubators" or enzymatic systems (glutathione oxidase (GOX)/ catalase (CAT) system) to reduce amount of oxygen in cellular culture.

4.3. Synthesis of chlorins by reduction of porphyrins

The porphyrin structure is a highly stable extended macrocyclic π-electron system which can be chemically modified to achieve better optical properties. The macrocycle of porphyrin itself has 22 π-electrons, 18 of which are delocalised and follow Huckel's rule for the aromaticity. By reducing one or two peripheral double bonds on the porphyrins, the number of π-electrons is reduced to 20 and to 18, preserving the aromaticity of the ring, but leading to the better optical properties of a PS for PDT [44,63,89,197].

As can be seen in Sections 4.1. and 4.2. of this thesis, a typical absorption spectrum of a free-base porphyrin consists of the Soret band at 420 nm, showing the $S_0 \rightarrow S_2$ transition, and four Q bands in the range of 480 nm to 660 nm, showing the $S_0 \rightarrow S_1$ transition upon excitation. The last Q band, Q_x (0-0), normally occurs at 650 nm with the lowest absorption coefficient ($\sim 10^3$ $M^{-1}cm^{-1}$). The reduction of one peripheral double bond leads to chlorin (dihydroporphyrin) with a higher absorption of the Q-band at 650 nm and the reduction of two opposite peripheral double bonds forms bacteriochlorin (tetrahydroporphyrin), which forms the absorption peak in the region around 720 nm. Better absorption in the optical part of the EM spectrum is one of the properties that scientists are trying to achieve for an ideal PS, as the red light can penetrate the tissue better without interfering with the absorption of the molecules already present in the tissue [63,147].

Theoretical calculations have shown that the reduction of a number of π-electrons in the porphyrin macrocycle has no effect on the LUMO energies, but the HOMO energies systematically increase due to the destabilisation caused by the D_{2h} distortion of the ring. The reduction thus leads to a decrease in the HOMO-LUMO gaps, resulting in a bathochromic shift of the last Q-band and increasing the molar absorption coefficient [63,199].

Some of the reduction mechanisms that have been studied on porphyrins include various hydrogenation reactions such as the use of sodium in isoamyl alcohol, catalytic hydrogenation over Pd/C or reduction with Raney nickel in dioxane and Whitlock's diimide reduction [267]. Other tested reduction mechanisms of porphyrins include the use of osmium tetroxide (OsO_4) as an oxidative electrophile on porphyrins bearing alkyl groups at *β-β*' pyrrole positions, leading to the formation of vicinal dihydroxychlorin, which undergoes a pinacol-pinacolone rearrangement to give the final geminal dialkyloxochlorin [268]. In contrast to OsO_4, reductive alkylation was studied only on *meso*-substitued porphyrins with reagents like *n*-alkyllithium in the presence of palladium. Among mentioned, Whitlock's diimide was studied in this work on porphyrin **2**, with the three pyridyl substituents and one acetamidophenyl group, due to the mild reaction conditions and as it has proven to be the most prominent method for the reduction of numerous *meso*- or *β*-substituted porphyrins [268].

4.3.1. Reduction of the porphyrin 2 by Whitlock's diimide reduction

The reduction of double or triple bonds in the presence of diimide has been widely studied in organic chemistry. Diimide can be generated at low temperature by a gas-phase electric discharge in hydrazine or, as done in this work, by the thermal decomposition of metal salts of *p*-toluenesulfonyl hydrazide [269]. When generated, diimide can occur in three potential structures: *trans*-, *cis*- and 1,1-diimide, among which *trans*-diimide has the lowest energy. Although mainly *trans*-diimide is formed, stereochemical studies have shown that the *cis*-isomer is responsible for the transfer of hydrogen. *Cis-trans* isomerization in solution probably occurs through a catalysed process involving a rapid protonation-deprotonation sequence. The reduction of diimide occurs by *syn* addition of hydrogen from *cis*-diimide to a symmetrical double bond via a cyclic transition state (**Scheme 19**) [269].

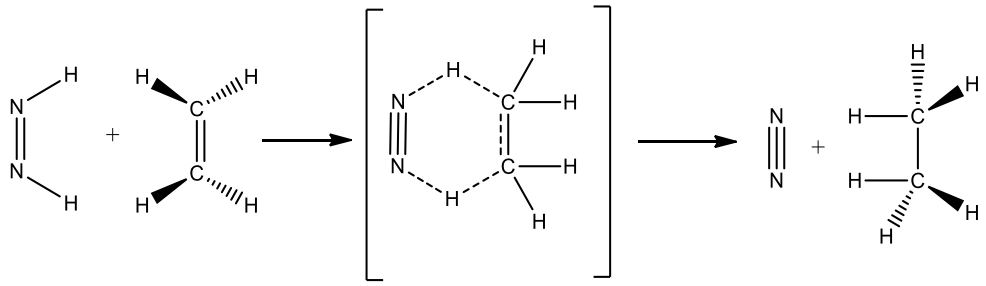

Scheme 19. The mechanism of diimide reduction [269].

The first attempts at diimide reduction of porphyrins were undertaken by Whitlock and colleagues in 1969, where it was applied to **TPP** and 1,2,3,4,5,6-octaethylporphyrin [270]. The reduction of **TPP**, a representative of the *meso*-substituted porphyrins as porphyrins synthesised in this work, was achieved by *in situ* generation of diimide in a reaction of *p*-toluenesulfonylhydrazide (*p*-TSH), anhydrous potassium carbonate in a hot solution of dry pyridine (105 °C) in nitrogen atmosphere for 6.5 hours. The reaction resulted in the formation of a mixture of chlorine, bacteriochlorin and isobacteriochlorin. Bacteriochlorin and isobacteriochlorin were successfully removed by adding an oxidising agent, *p*-chloranil, and washing with a solution containing benzene and phosphoric acid of varying acidity. Finally, *meso*-tetraphenyl chlorin (TPC) was isolated in 72% yield [268,270]. Numerous chlorins have been synthesized using Whitlock's method, including a widely known, commercially available *m*-tetra(3-hydroxyphenyl)-2,3-dihydroporphyrin used for photodynamic therapy of squamous cell carcinoma of the head and neck, known by the trade name FOSCAN® or Temoporfin [271].

Here, a reduction of porphyrin **2** was performed by dissolving porphyrin in hot, dry pyridine (105 °C) and adding anhydrous potassium carbonate together with *p*-TSH (8 equiv.) to the

reaction. During the reaction, *p*-TSH was added in two further sets (8 and 4 equiv.). After 6.5 hours, the reaction was checked using TLC and UV-Vis, and the formation of chlorine **37** was observed along with bacteriochlorin **38** (**Scheme 20**).

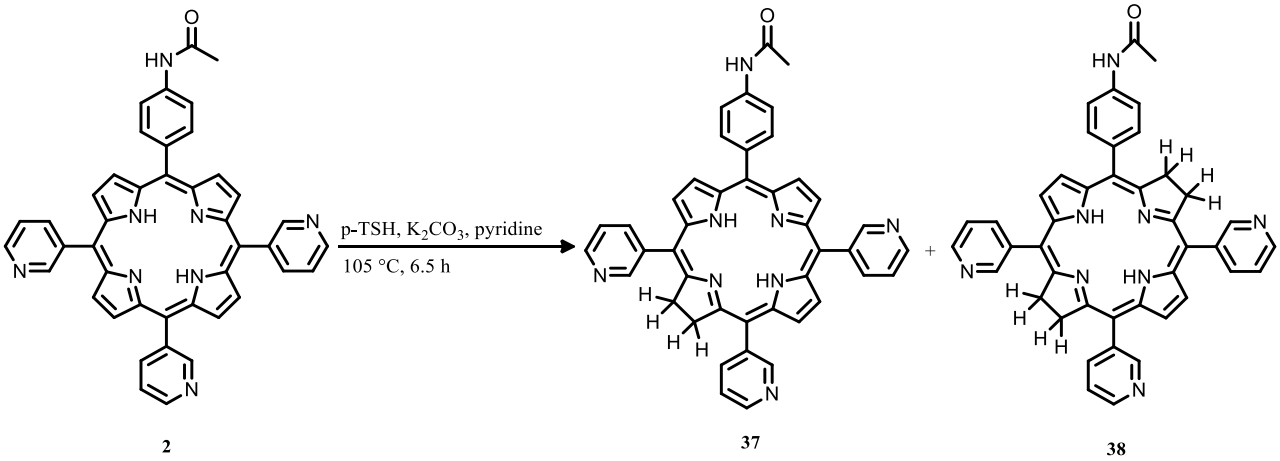

2 **37** **38**

Scheme 20. Diimide reduction of porphyrin **2** results in chlorin **37** and bacteriochlorin **38** as products.

Since it was difficult to separate these tetrapyrrolic products, the reaction was oxidized with an oxidising reagent, 2,3-dichloro-5,6-dicyano-1,4-benzoquinone (DDQ), to remove bacteriochlorin **38** from the reaction mixture. The solid obtained from the reaction mixture after removing the solvent by evaporation under pressure was dissolved in DCM and DDQ (dissolved in DCM), which was gradually added. After each addition, the reaction mixture was stirred for 10 minutes at room temperature and then checked by TLC and UV-Vis spectroscopy. The addition of DDQ was stopped upon the disappearance of the peak at ~720 nm, that corresponds to bacteriochlorin (**Figure 55**). Finally, the excess of DDQ was removed by washing the DCM solution with H_2O and the product was purified twice by column chromatography.

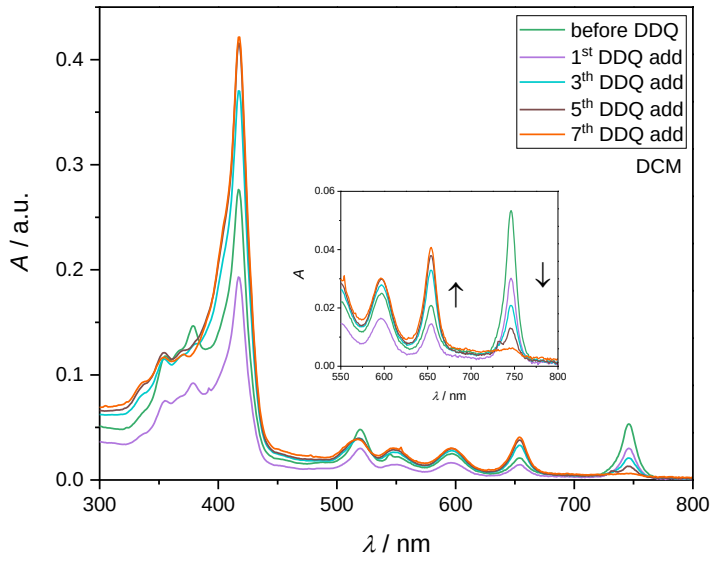

Figure 55. UV-Vis spectrum showing the changes in spectrum upon addition of DDQ of the reaction mixture after process diimide reduction of porphyrin **2**.

Finally, product **37** was isolated from the reaction, which was confirmed by ^{1}H NMR. In the spectrum, a multiplet at 3.39-4.41 ppm, characteristic for the four *β*-protons on the pyrrole ring with reduced double bond, and a singlet at −1.40 ppm, characteristic for the two inner pyrrole atoms of chlorine, were observed (**Figure S91**). However, the ^{1}H NMR spectrum shows high contamination of the product with the parent porphyrin **2**, almost in 1:1 ratio, as evidenced by the peaks at 9.38 (Py-2-*H*), 9.09 (Py-4-*H*), 8.55 (Py-6-*H*), 8.20 (Ar-2,6-*H*) and 7.80 (Ar-3,5-*H*) ppm in the aromatic part of the spectrum and at 2.80 ppm (inner pyrrole protons). Other unidentified impurities are observed in the spectrum between 6.90-7.55 ppm and 0.5-2.5 ppm (**Figure S91**). Due to the structural similarity, the compound obtained was difficult to separate from other tetrapyrrolic impurities using column chromatography, which can be attributed to the π-π interactions. In addition, column chromatography on silica gel was not the most adequate method for the purification of the chlorin obtained, as it was not stable and it easily oxidised back into the corresponding porphyrin.

4.3.2. Reduction of the porphyrin 2 using tin (II) chloride ($SnCl_2$)

In 2019, Bregier and colleagues proposed a new, one-step method for the reduction of pyridylporphyrins to the corresponding dihydroporphyrins (chlorins) using tin(II) chloride in hot acidic solution. Tin(II) chloride is frequently used in organic chemistry for the reduction of nitro compounds to the corresponding amines [272]. However, it was found that in a reaction where the tin(II) chloride is used in a reduction of the nitro group in 5-(4-

aminophenyl)-10,15,20-tris(pyridyl)porphyrin to amino group, the resulting compound was not the expected porphyrin but the corresponding chlorine.

To investigate the $SnCl_2$ reduction of porphyrin **2**, the protocol of Breiger et al. [273] was applied. Porphyrin **2** was dissolved in 6M HCl and 2 equiv. of $SnCl_2 \times 2\ H_2O$ were added. The reaction was heated at 65 °C for two hours and then stirred overnight at room temperature. The next day, the reaction mixture was neutralized using sodium carbonate and extracted in DCM. When the reaction mixture was checked, a new dot with higher R_f value in TLC chromatogram and a strong absorption peak at ~ 650 nm in the UV-VIS spectrum were observed, both characteristic of chlorins indicating the formation of the product of interest (**Figure 56**). The obtained compound was purified by washing the DCM layer with H_2O to remove the salts after neutralisation and by column chromatography with DCM:MeOH (20:1) as eluent.

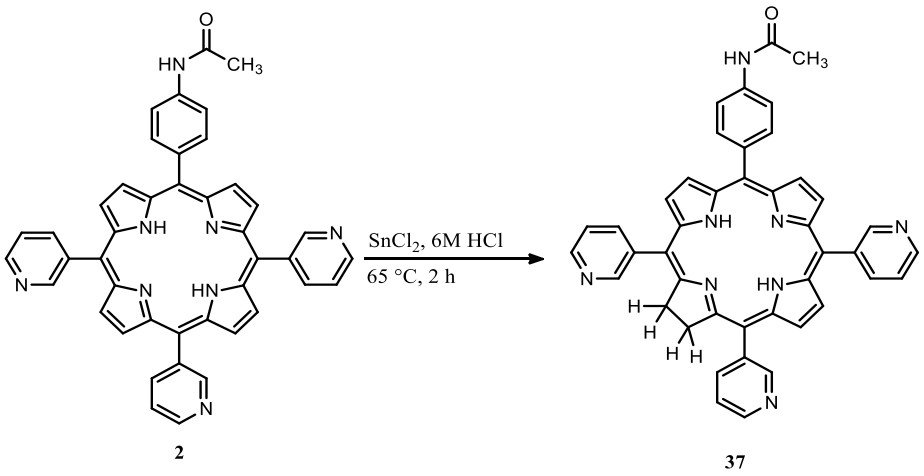

2 **37**

Scheme 21. Regioselective $SnCl_2$ reduction of porphyrin **2** in boiling HCl results in a formation of chlorin **37**.

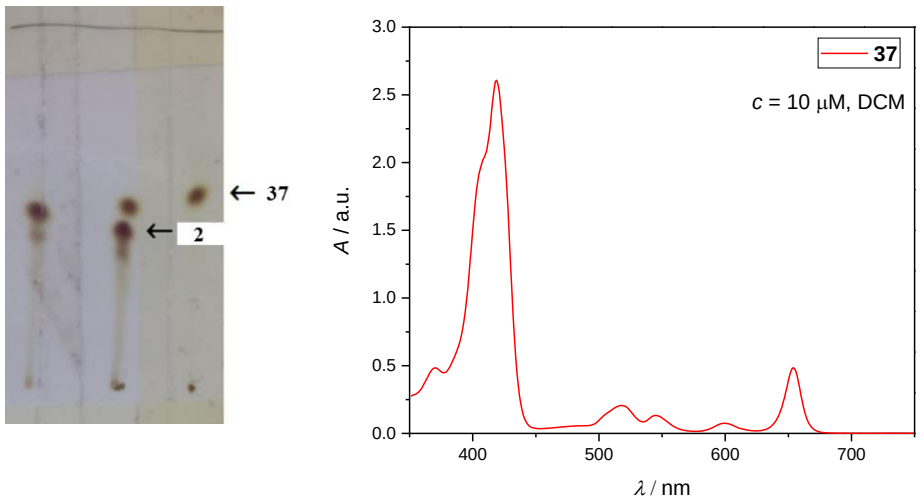

Figure 56. TLC chromatogram and UV-VIS spectrum of obtained chlorin **37** by $SnCl_2$ reduction of porphyrin **2**.

The successful synthesis of chlorin **37** was confirmed by ^{1}H NMR spectroscopy (**Figure 57**), with a peak at 1.43 ppm characteristic of two pyrrolic *N*-protons and a peak at ~ 4.20 ppm characteristic of four *β*-protons at positions 17 and 18 of the chlorin ring in the aliphatic part of the spectrum, both of which are characteristic of chlorin. Unfortunately, impurities of porphyrin **2** were also present after the reaction with $SnCl_2$, but to a much lesser extent than after the diimide reduction. Characteristic peak of porphyrin **2** observed in the ^{1}H NMR spectrum was at 2.80 ppm (inner pyrrole protons), peak at 0.90 ppm ($COCH_3$), and small peaks in the aromatic part of the spectrum with the *δ*/ppm similar to that of porphyrin **2**.

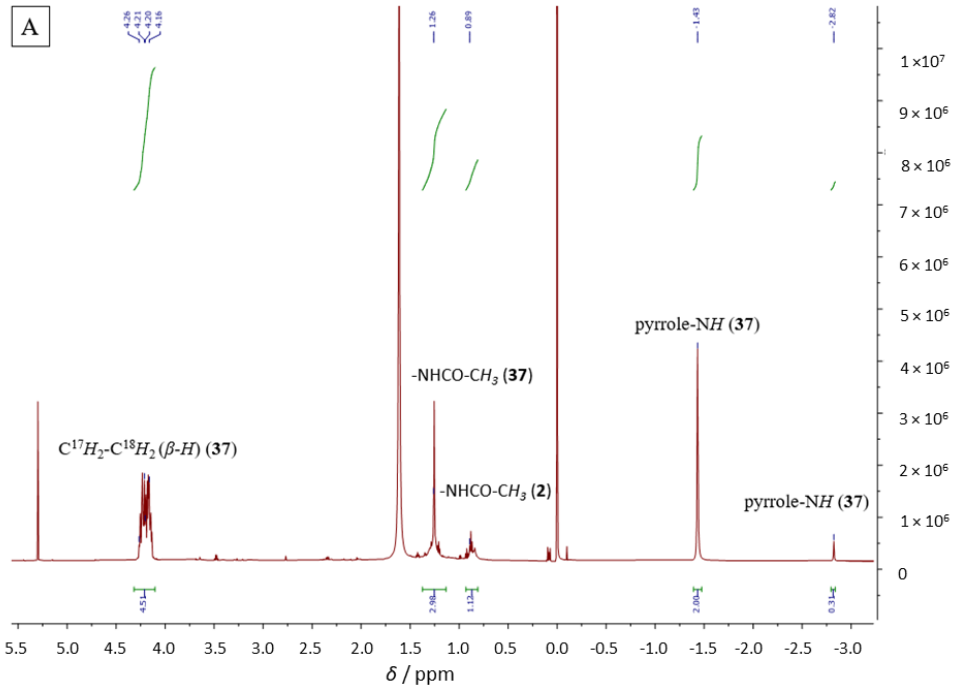

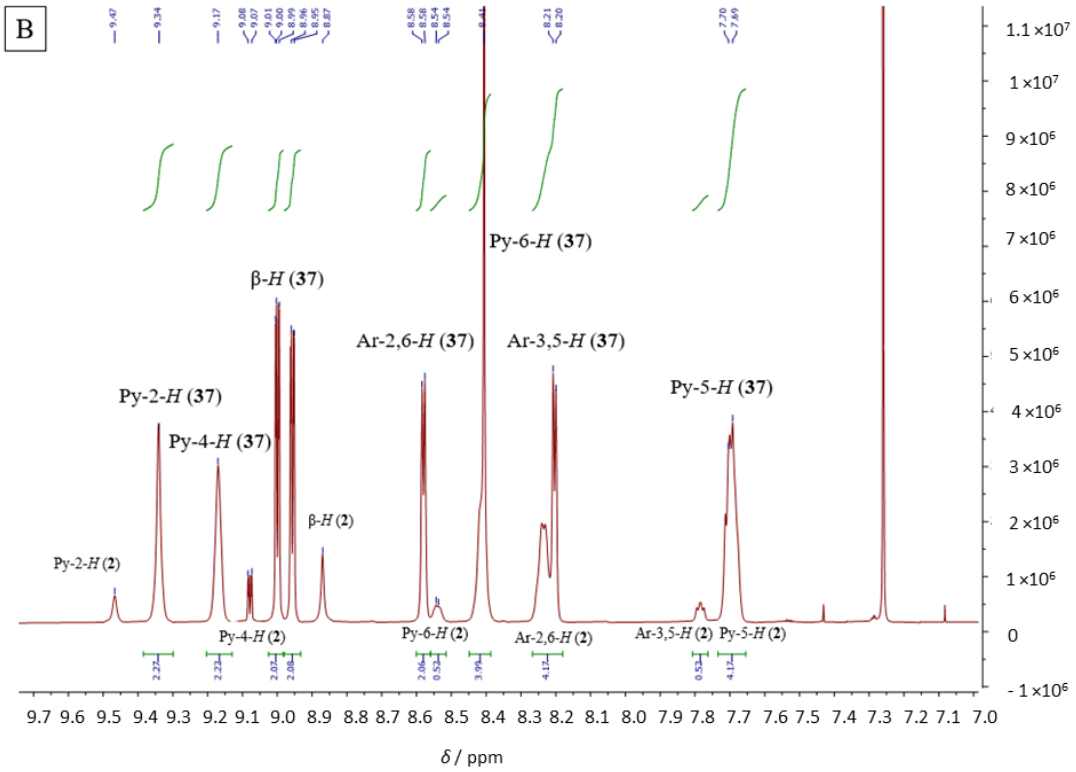

Figure 57. ^{1}H NMR (CD_3Cl, 600 MHz) spectrum of chlorin **37**, obtained by $SnCl_2$ reduction of porphyrin **2** shown in the A) aliphatic (-3.0 to 5.5 ppm) part of the spectrum, B) aromatic part of the spectrum (0.0 ppm to 4.8 ppm). Peaks that correspond to chlorin are shown as **37**, and impurities from the remained starting porphyrin are shown as **2**.

Compared to Whitlock's diimide reduction, the $SnCl_2$ reduction led to a higher yield of the reaction (20%) with a lower amount of impurities in the final product. Furthermore, $SnCl_2$ reduction is known to be a regioselective reduction in which the reduction of the *β-β'* bond occurs only within the two pyridyl groups at the *meso*-positions of the ring, whereas diimide reduction is known to form different chlorin isomers.

4.3.3. Conclusion part 4.3.

In this part, the reduction of porphyrin **2** was investigated to obtain the corresponding chlorin, which absorbs stronger in the red part of the EM spectrum. Two methods were studied, a two-step diimide reduction in which *p*-TSH and potassium carbonate were first dissolved in hot pyridine (105 °C) for 6.5 hours, and the second step involved reaction with DDQ to oxidise the obtained bacteriochlorin back to chlorin. The second method involved a regioselective reduction with tin(II) chloride dihydrate in hot acidic solution, followed by neutralisation with sodium carbonate.

Although both reactions resulted in the formation of chlorin **37**, the reaction with $SnCl_2$ gave a higher yield and a lower amount of starting porphyrin impurities in the ^1H NMR spectrum. In addition, the $SnCl_2$ reduction proved to be regioselective according to the literature [273], whereas the diimide reduction can lead to the formation of isomers that would be difficult to separate [268].

Unfortunately, the chlorins obtained from both reactions could not be isolated without impurities of the corresponding porphyrins, so they were not investigated further. Therefore, no *in vitro* analysis was performed in this section. In addition, the chlorins obtained showed low stability due to facile oxidation back to the parent porphyrin. Further work in this field might include investigation of the other purification methods, probably based on different basicity of porphyrins and chlorins, to obtain a pure compound for further studies.

4.4. Biodistribution of [^{68}Ga]gallium radiolabelled porphyrins with alkyl chains of different length measured using PET-CT scanning.

4.4.1. Radiolabelling of porphyrins 13, 15, 17 and 19 with [^{68}Ga]gallium chloride

The first step in radiolabelling of porphyrins involves the elution and preparation of the radionuclide, in our case ^{68}Ga. In addition to the aforementioned advantageous properties of ^{68}Ga for PET imaging, the preparation of the ^{68}Ga radionuclide requires only a ^{68}Ge/^{68}Ga generator with a long shelf life ($t_{½}$(^{68}Ge) 271 days), which is facile on-site generation of radionuclide ^{68}Ga. The ^{68}Ge/^{68}Ga generators are produced by immobilizing the cyclotron-generated ^{68}Ge (from the stable parent Ga-69 isotope) on a column with inorganic (usually TiO_2) or organic matrix [155]. The ^{68}Ge in a column spontaneously decays into daughter ^{68}Ga, which can then be repeatedly eluted from the column. ^{68}Ga decays in its turn to stable ^{68}Zn. To elute the ^{68}Ga, most generators use a dilute acidic eluent, such as 0.05 M HCl in our case, as it provides cationic Ga^{3+} that can be used for further chemistry [274].

$$^{68}_{32}Ge + {}^{0}_{-1}e \rightarrow {}^{68}_{31}Ga + \upsilon$$

$$^{68}_{31}Ga \rightarrow {}^{68}_{30}Zn + \beta^{+} + \upsilon$$

Scheme 22. Radionuclide decays within the ^{68}Ge/^{68}Ga generators [274].

In our work, the ^{68}Ga is eluted from the column with 4 mL HCl (0.05 M), followed by purification of the obtained radionuclide using the SCX cartridge. The excess of non-decayed parent [^{68}Ge], and over-decayed Zn^{2+}, was removed with the acetone/HCl eluent containing 20% HCl and the SCX column was then washed with acetone/HCl containing only 2% HCl to collect the pure $^{68}Ga^{3+}$ for reaction with porphyrins. After drying Ga^{3+} at 80 °C under argon flow, the porphyrins (100 µg in 2 mg/mL water) were prepared in a sodium acetate (pH = 4.3) according to the procedure of Bhadwal and colleagues done for radiolabelling of **TMPyP4** (**Figure 58**) [160]. Moreover, the radiolabelling with $^{68}Ga^{3+}$ with the highest efficiency in buffered solutions is when the pH is ~4, since it precipitates as $Ga(OH)_3$ and forms colloidal solutions when the pH is ≥ 6. In addition to the acetate buffer, the HEPES buffer has also been shown to be advantageous as both are biocompatible, non-toxic and provide a relevant pH stabilizing radiolabelling agent [274].

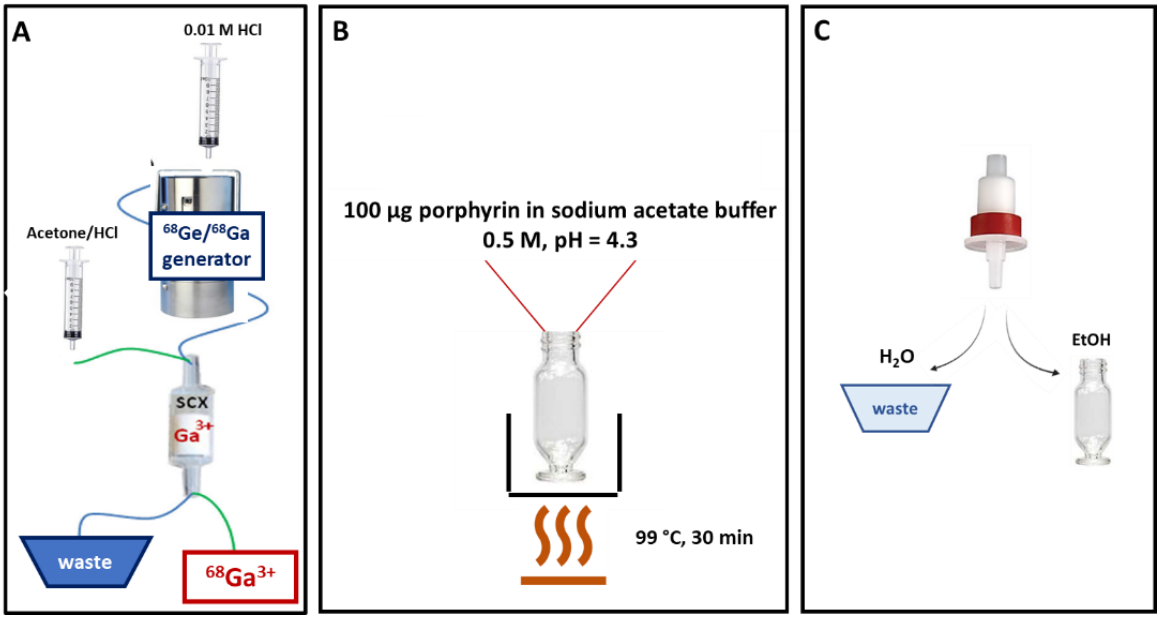

Figure 58. Schematic representation of a tri-step protocol in radiolabelling with ^{68}Ga: A) Elution of the ^{68}Ga/^{68}Ge generator and purifying of $^{68}Ga^{3+}$ over SCX cartridge, B) Radiolabelling of porphyrin with $^{68}Ga^{3+}$ in 0.5 M sodium acetate solution (pH = 4.3) C) Purification of the radiolabelled porphyrin using tBu-SepPak cartridge.

After mixing the porphyrin and radionuclide, the reaction mixture was left to stir for 30 minutes at 99 °C. Both radio-TLC and radio-HPLC confirmed the successful radiolabelling of all four porphyrins (**33-36**) with ~80% efficiency (**Table 14**, RCE). Radiochemical efficiency (RCE), or also known as radiochemical purity (RCP), is the proportion of the radioactivity which is present in the desired chemical form compared to the non-labelled radionuclide. Usually, it is calculated by dividing the AUC of the radiolabelled product with the sum of the AUC of the radiolabelled product and the radionuclide in the free form. Complete purification of the reaction, resulting in > 99% RCE, was achieved by purification on the tBu-C18 SepPak cartridge. Unreacted [^{68}Ga]$GaCl_3$ was removed by washing the column with H_2O, and the radiolabelled porphyrin was then eluted with EtOH.

Radiochemical yield (**Table 19**, RCY) of the reaction is the amount of activity in the product expressed as the percentage (%) of related starting activity that was used in the synthesis. Therefore, a RCY can be determined as a function of the chemical yield of the reaction and the time needed to perform the reaction. As the half-life of the ^{68}Ga is relatively short ($t_{1/2}$ = 68 min), the corresponding radiochemical yields, after the 1-hour protocol that includes elution of the radionuclide, the reaction and purification resulted in a 50% RCY.

Table 19. Radiochemical yields (RCY) and radiochemical efficiency (RCE) obtained after radiolabelling of porphyrins **13, 15, 17** and **19**.

	RCY	**RCE**
[^{68}Ga]**33**	51%	78%
[^{68}Ga]**34**	44%	82%
[^{68}Ga]**35**	57%	82%
[^{68}Ga]**36**	51%	80%

Although the radiochemical efficiency was relatively high, most of the free-base porphyrin in the sample remained non-radiolabelled. To obtain a product containing only Ga(III) porphyrins, two approaches were used for each porphyrin. The first approach, called “hot labelling”, involved purification of the obtained product by preparative HPLC and subsequent purification of the product with tBu-C18SepPak columns. In the second approach, called “hot-cold radiolabelling” or “carrier added system", the $GaCl_3$ was added to the reaction after radiolabelling and the reaction was stirred for 15 minutes. If necessary, the reaction mixture was further purified by preparative HPLC to obtain only Ga(III) porphyrins in the product. The first method, in which only the hot radionuclide is observed, is preferable in cases where only PET imaging is performed, while for theranostic PET/PDT agents the second method is preferable as there is a large difference in the amount used in each technique. PET imaging requires small nanomolar quantities of a radiotracer, whereas PDT generally uses PS in the micromolar range. Therefore, if ”hot-cold labelled” radiotracer is used, the treatment can easily be performed without the need to add the second dose of theranostic agent [156].

Porphyrin **13** substituted with an acetamidophenyl group was successfully radiolabelled with 82% efficiency (**Figure 59A**). However, obtaining only Ga(III) porphyrin as a radionuclide was successful only using the “hot-cold radiolabelling” method. The purification of the radionuclide after only radiolabelling was not successful because porphyrin was very soluble in water and the small amounts of porphyrin purified by preparative HPLC did not retain on the SepPak column after the H_2O wash. On the other hand, “hot-cold” radiolabelling with the addition of 3 equiv. $GaCl_3$ resulted in 100% chelation of free-base porphyrin within 15 minutes of the reaction (**Figure 59B**). The radionuclide was successfully purified, however, a loss of the radionuclide in the H_2O wash was also observed after purification on the SepPak column.

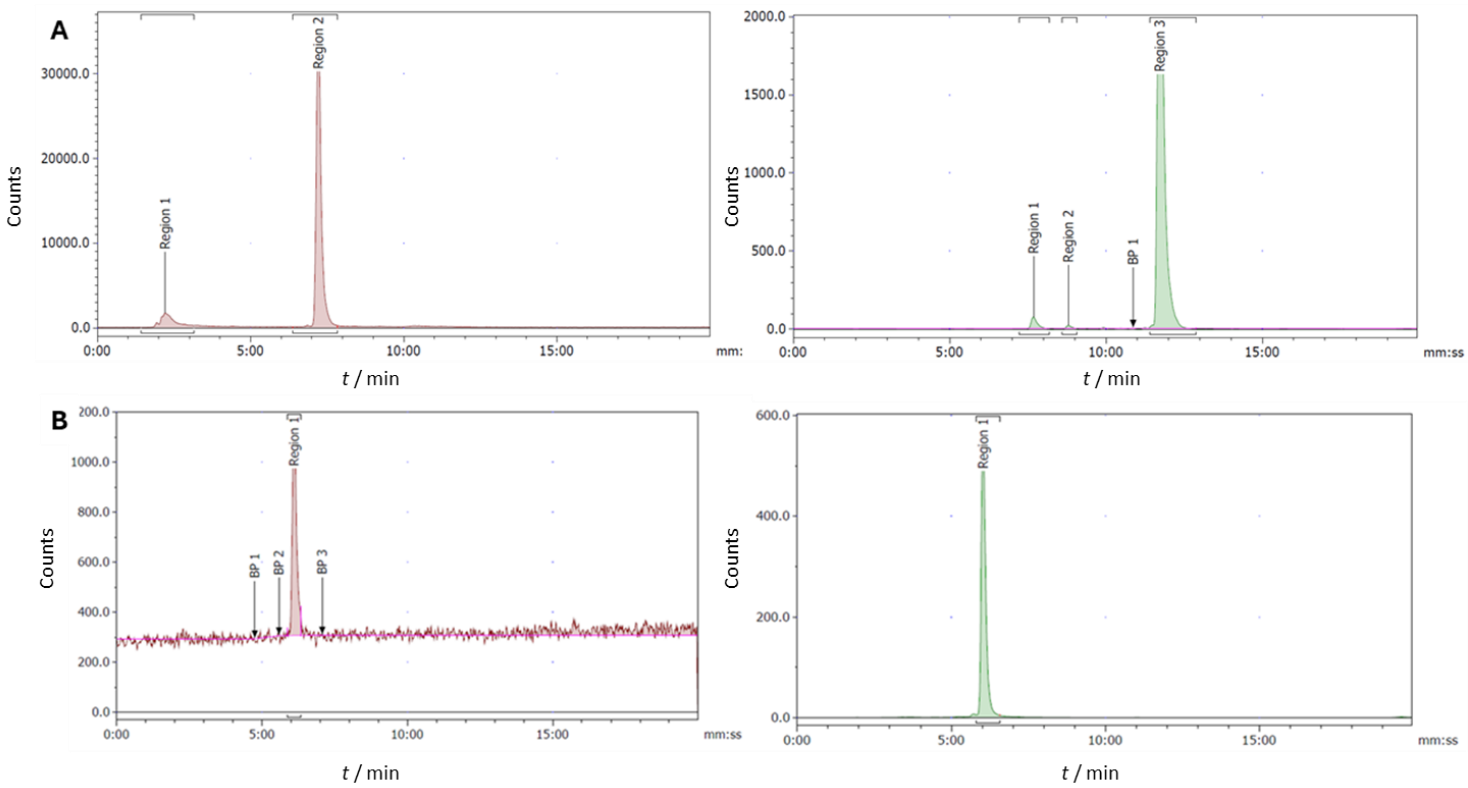

Figure 59. Radiochromatogram (pink) and UV-chromatogram (green) of the radiolabelled porphyrin **13 ([^{68}Ga]34)**: A) results after the radiolabelling step B) "hot-cold" radiolabelled radionuclide, with added 3 equiv. of $GaCl_3$.

In contrast to porphyrin **13**, the radiolabelled porphyrins **15** (**[^{68}Ga]34**) and **17** (**[^{68}Ga]35**) were successfully isolated with both methods due to the long alkyl chain in the structure and the associated higher lipophilicity of the molecule (**Figure 60, Figure 61**). After "hot labelling" and purification of the radiolabelled porphyrin by preparative HPLC, **[^{68}Ga]34** was isolated, and the specific activity of a sample was calculated to be 15.4 GBq/µg or 14.1 MBq/pmol, determined as “high specific activity” (high SA) (**Figure 60B**). The “hot-cold labelling" method was successfully performed with 3 equiv. $GaCl_3$, resulting in 91 % chelated porphyrin. The specific activity obtained with this method was determined as “low specific activity” (low SA) after purification by preparative HPLC and calculated as 0.58 MBq/µg or 8.45 MBq/µmol ((**Figure 60C**). The specific activity (SA) of a radionuclide is determined as the amount of its radioactivity per unit mass or concentration of a sample [275]. It was calculated using the calibration curve obtained by comparing the AUC and the concentration of the porphyrin tested.

The purification of **[^{68}Ga]35** after radiolabelling of porphyrin **17** was successful and the high SA obtained was 6.9 GBq/µg or 13.9 MBq/pmol (**Figure 61B**). When carrier added method was used, 65% of a porphyrin was chelated with Ga^{3+} using 3 equiv. $GaCl_3$ within 15 minutes of the reaction. When a reaction was carried out with a higher excess of $GaCl_3$, no changes in the amount of Ga(III) complex were observed. After the “hot-cold radiolabelling” successful purification by HPLC was observed and a low SA of 0.22 MBq/µg and 9.06 MBq/µmol was determined ((**Figure 61C**).

Unfortunately, none of the methods were successful for obtaining pure radio tracer or carrier added radiotracer. Radiolabelling of a porphyrin **19** resulted in 80% RCE and purification via SepPak column resulted in a pure radionuclide (**Figure 62A**). However, purification of a radiotracer to remove non-labelled porphyrin using preparative HPLC resulted in retaining of a tracer inside the column. Furthermore, adding of 3 equiv. of $GaCl_3$ in a “hot-cold radiolabelling” procedure resulted in 44% chelation with Ga^{3+}, however, as with the “hot procedure” purification resulted in a trapping of the porphyrin inside the HPLC column. Although porphyrin **[^{68}Ga]36** was not used in *in vivo* experiments on mice, some of the properties of the radiolabelled porphyrins, as log*P* and serum and *apo*-transferrin stability, were investigated.

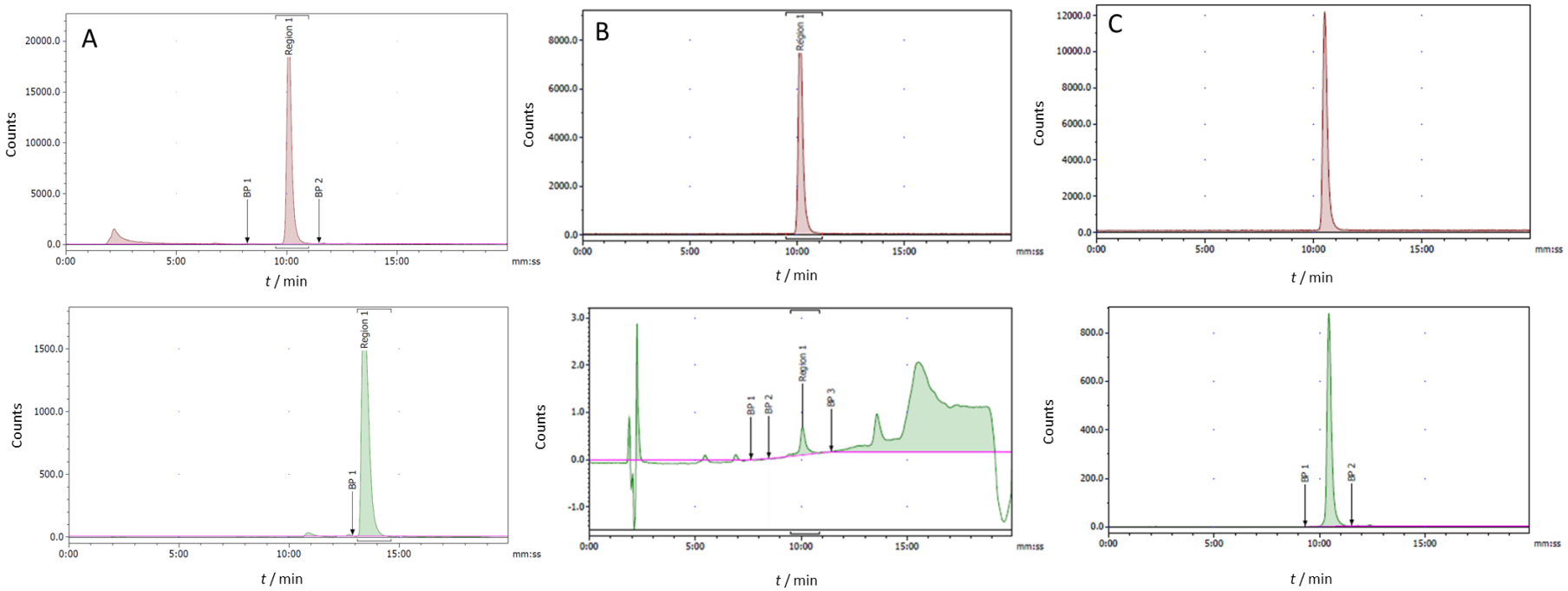

Figure 60. Radiochromatogram (pink) and UV-chromatogram (green) of the radiolabelled porphyrin **15 ([^{68}Ga]34)**: A) results after the radiolabelling step B) "hot" radiolabelled radionuclide, after the purification by preparative HPLC C) "hot-cold" radiolabelled radionuclide, with added 3 equiv. of $GaCl_3$, after the purification by preparative HPLC.

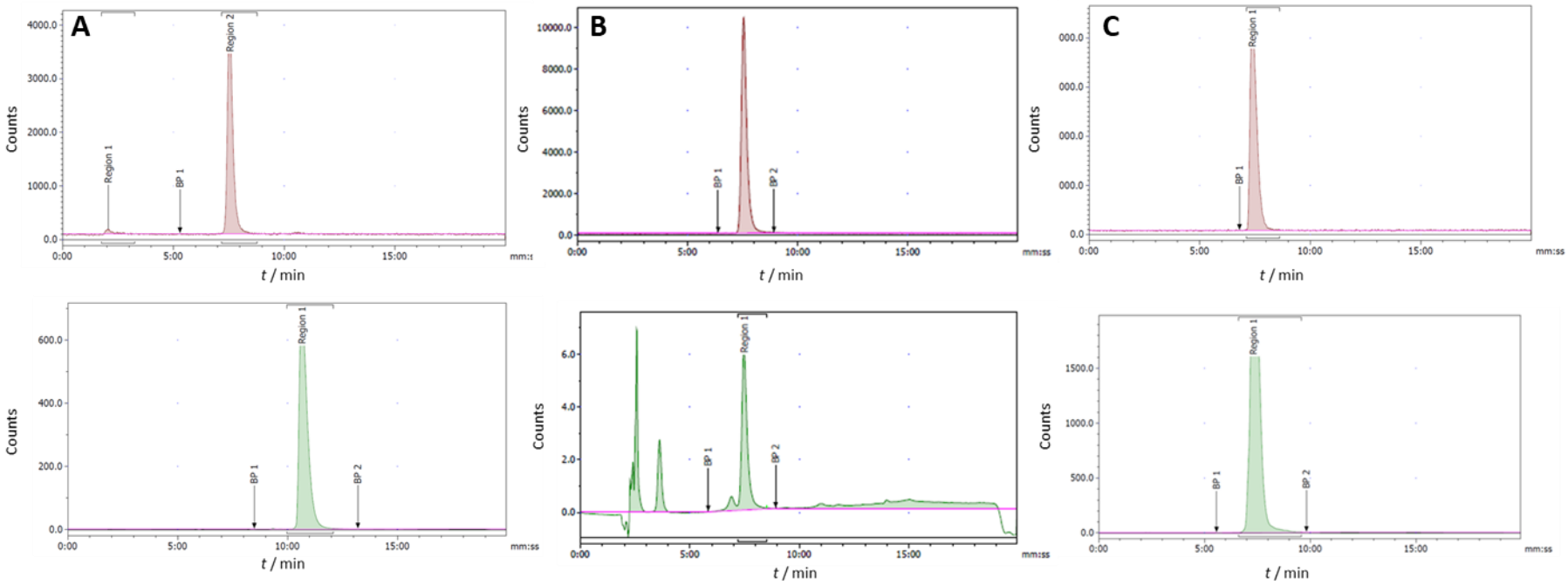

Figure 61. Radiochromatogram (pink) and UV-chromatogram (green) of the radiolabelled porphyrin **17** (**[^{68}Ga]35**): A) results after the radiolabelling step B) "hot" radiolabelled radionuclide, after the purification by preparative HPLC C) "hot-cold" radiolabelled radionuclide, with added 3 equiv. of $GaCl_3$, after the purification by preparative HPLC.

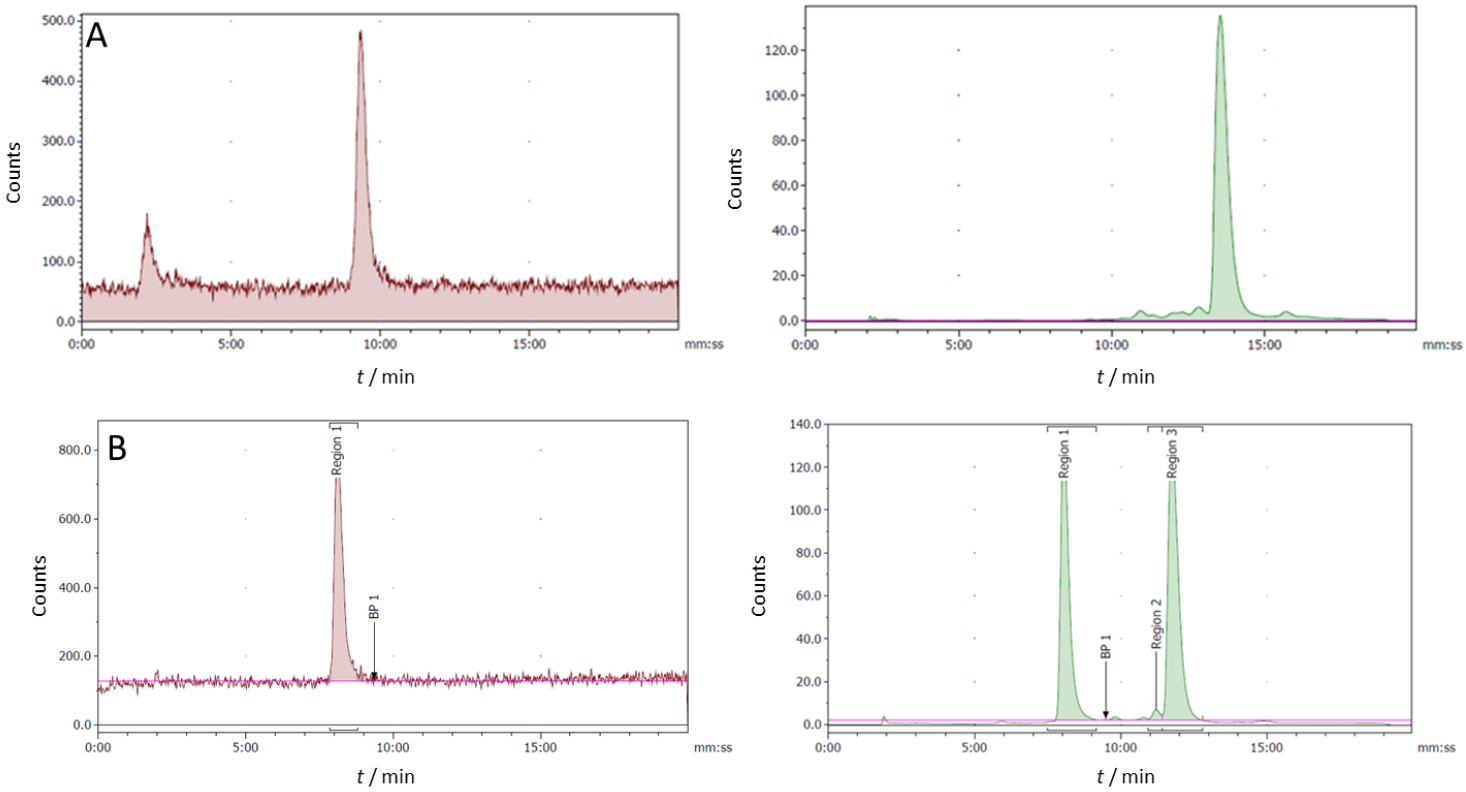

Figure 62. Radiochromatogram (pink) and UV-chromatogram (green) of the radiolabelled porphyrin **19** (**[^{68}Ga]36**): A) results after the radiolabelling step B) "hot-cold" radiolabelled radionuclide, with added 3 equiv. of $GaCl_3$, before the purification by preparative HPLC

4.4.2. Synthesis of ^{nat}Ga(III)porphyrins substituted with an alkyl chain with 1, 9, 13 and 17 C atoms- porphyrins 33, 34, 35 and 36

In parallel to radiolabelling, porphyrins **13**, **15**, **17** and **19** were chelated with $GaCl_3$ to obtain ^{nat}Ga(III) porphyrins, which were then used in *in vitro* analyses to investigate their therapeutic potential as PSs for PDT. Ga^{3+} chelation was performed following a similar protocol as for cold step in "hot-cold" radiolabelling. The porphyrins were dissolved in 0.5 M sodium acetate buffer and the excess of $GaCl_3$ (10 equiv. for porphyrin **13** and 20 equiv. for amphiphilic porphyrins) was added and the pH was adjusted to 4.3. The reaction was stirred at 99 °C for 30 minutes and the reaction was monitored by HPLC ($MeOH/H_2O$ + 0.1 % TFA) and TLC on silica gel (8:1:1 MeCN: H_2O: $KNO_{3(sat.)}$) (**Scheme 23**).

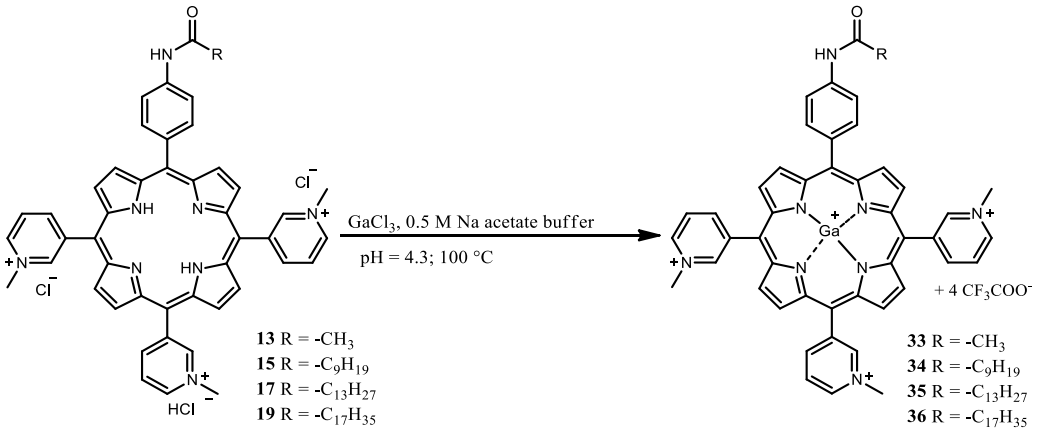

Scheme 23. Ga(III)chelation of *N*-methylated free-base porphyrins **13**, **15**, **17** and **19** using $GaCl_3$ to obtain porphyrins **33**-**36**.

Similar to the results of the "hot-cold" radiolabelling of porphyrins, only the porphyrin **33** substituted with an acetamidophenyl group was completely chelated with $GaCl_3$, while the ratio of the complexed porphyrin compared to the parent porphyrin decreased with the length of the alkyl chain. Increasing the excess of $GaCl_3$ did not lead to a significant improvement in chelation. In addition, too high excess of $GaCl_3$ precipitated into $Ga(OH)_3$ due to the change from pH, making the reaction more difficult to purify. Removal of the unreacted porphyrins was achieved by preparative HPLC, as the Ga(III) porphyrins were found to be more hydrophilic and had a shorter retention time, allowing them to elute as the first fraction from the columns. Although the chloride counterions proved to be beneficial in drug design [181], due to the low amount of porphyrins observed after preparative HPLC, further analyses were performed with trifluoroacetate as counterions in Ga(III) porphyrins. Only in the case of porphyrin **33**, which was not purified by preparative HPLC, a change of counterions with precipitations by NH_4PF_6 and TBAC were successfully performed, as done with the Zn(II) porphyrins **21** to **27** (Section 5.1.1.).

The porphyrins **33**-**36** were obtained in yields depending on the length of the substituted alkyl chain, with the highest yield of 84% observed for porphyrin **33**, decreasing to 38% for porphyrin **34**, 28% for porphyrin **35** and 20% for porphyrin **36**. The successful Ga(III) chelation of the porphyrins was confirmed by ^{1}H NMR spectroscopy and the mass of the product by MALDI-MS. In ^{1}H NMR spectroscopy, the successful Ga(III) chelation was evident in the recovery of sharp signals of the *β*-protons in the porphyrin ring as a result of the no longer present slow tautomerism [203], since the inner pyrrole protons are substituted with metal (**Figure 63**, porphyrins **17** and **35** used as examples). The similar changes were shown in the Section 5.1.1. of this thesis when the free-base *N*-methylated (pyridinium-3-yl)porphyrins were chelated with Zn^{2+}. In MALDI-MS spectrum, characteristic $[M–3H]^{+}$, $[M–2H–CH_3]^{+}$ or $[M\text{-}2CH_3\text{-}H]^{+}$ were observed for porphyrins **33**-**36**, similar to ions previously described for free-base N-methylated pyridiniumporphyrins by our research group [72].

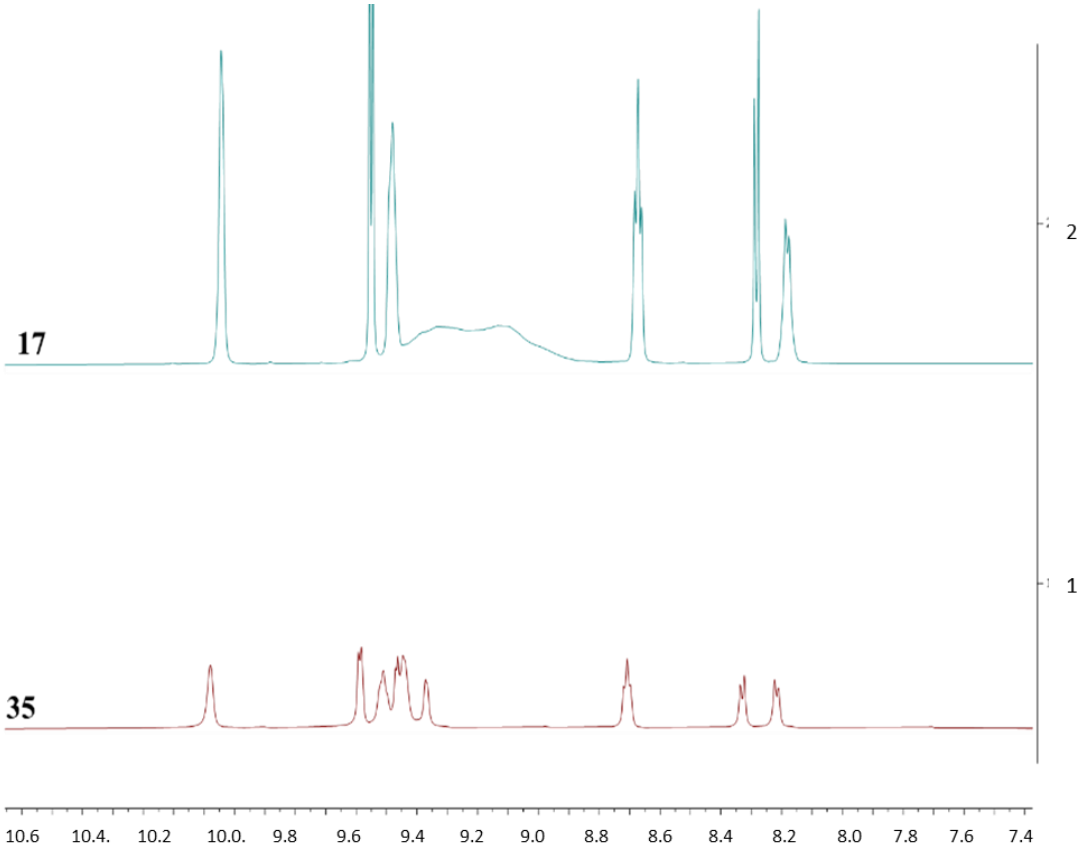

Figure 63. Comparison of the ^{1}H NMR (CD_3OD, 600 MHz) spectra of the free-base *N*-methylated porphyrin **17** and its Ga(III) complex, porphyrin **35**.

4.4.3. Absorption and fluorescence properties of ^{nat}Ga(III) (pyridinium-3-yl) porphyrins 33-36

The absorption and fluorescence properties of the synthesised ^{nat}Ga(III) porphyrins **33** to **36** were observed in MeOH and in PBS (**Figure 64**, **Table 20**). In MeOH, the spectra of the porphyrins resemble typical metalloporphyrin spectra with a Soret band at 425 nm and a calculated molar absorption coefficient of ε = 2.6 – 3.0 × 10^5 $M^{-1}cm^{-1}$ and two Q bands at 555 nm (Q (1-0)) and 594 nm (Q (0-0)) with observed molar absorption coefficients of ε = 1.5- 1.9 × 10^4 $M^{-1}cm^{-1}$ for Q (1-0) and ε = 2.6 – 3.5 × 10^3 $M^{-1}cm^{-1}$ for Q (0-0). The observed Stokes shift was ~11 nm, calculated as λ in nm, by subtracting the λ of Q (0-0) in the fluorescence spectrum with the λ Q (0-0) in the absorption spectrum. The observed data correspond to the data already shown for Zn(II) porphyrins, another representative of metalloporphyrins, in Section 5.1.3. of this thesis.

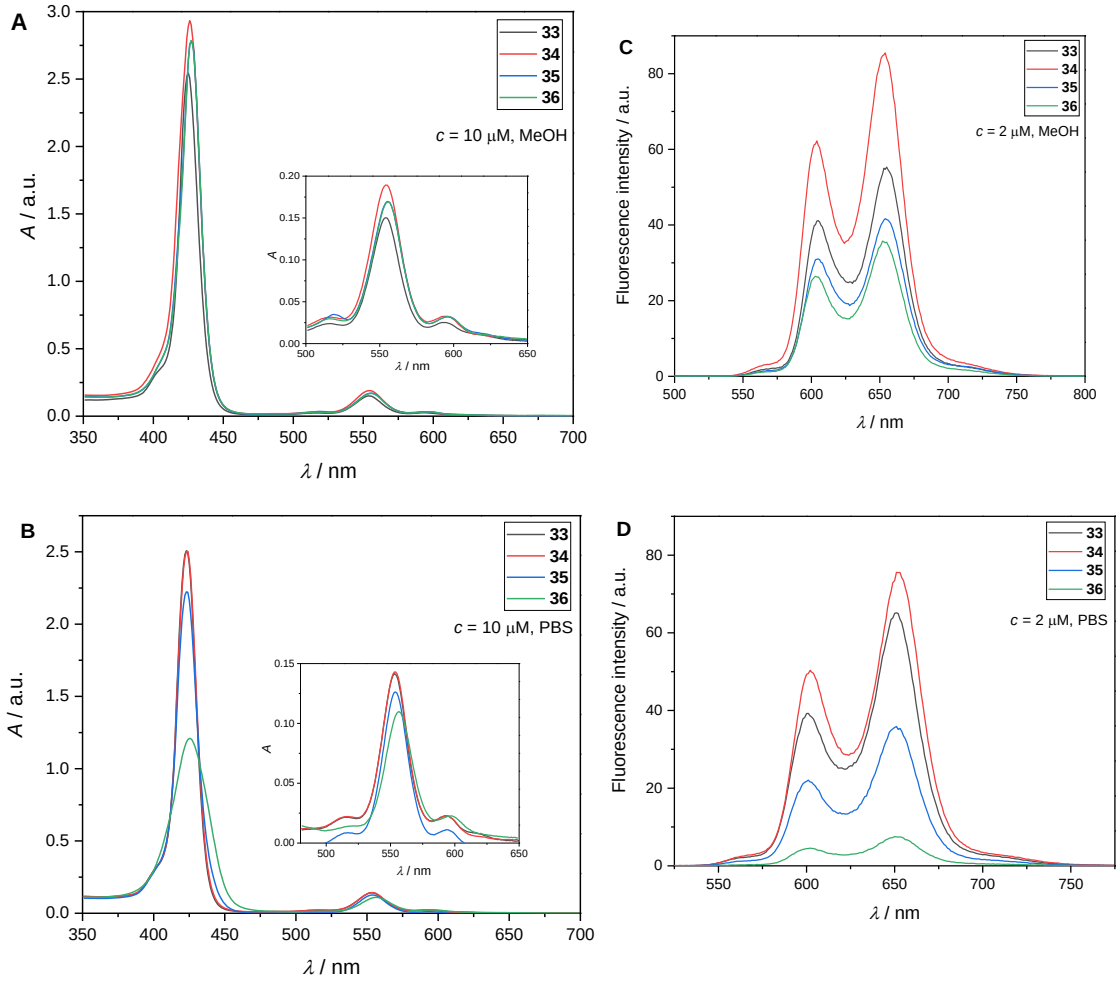

Figure 64. Absorption and fluorescence spectra of ^{nat}Ga(III) porphyrins **33-36** observed in MeOH (A,C) and PBS (B,D). Soret band wavelength was used for excitation of samples.

In PBS, a small hypsochromic shift of the Soret band of 2 nm, compared to the Soret band detected in MeOH, (λ = 423 nm) was observed for porphyrins **33** to **35**, which is due to the solvation effect, similar to the Zn(II) porphyrins (**Figure 64B**). Porphyrin **36**, substituted with the longest alkyl chain, showed a broadening of the Soret band and a decrease in its intensity compared to the other porphyrins tested. In addition, a bathochromic shift of 4 nm was observed for the Soret band (λ = 427 nm) and a bathochromic shift of ~ 3 nm for both Q-band wavelengths compared to other Ga(III) porphyrins tested. As we have already seen, the broadening of the Soret band and a decrease in its intensity are characteristic changes in the spectrum assigned for plausible porphyrin aggregates. Since Ga(III) porphyrins are similar in structure to *N*-methylated free-base porphyrins and their Zn(II) complexes, also with them it seems that the aggregation occurs when the ionic strength of the solution is increased and the porphyrins form vesicle-type aggregates, like micelles, due to the increased hydrophobic interactions [204].

Table 20. Absorption and fluorescence properties of Ga(III) porphyrins (**33-36**) recorded in MeOH and PBS. *Soret band wavelength was used for the excitation.

MeOH	λ_{abs} / nm (ε / $\times 10^3$ $M^{-1}cm^{-1}$)			λ_{em}/nm*	
	Soret (B)	**Q (1-0)**	**Q (0-0)**	**Q (0-0)**	**Q (1-0)**
33	425 (263.2)	554 (15.4)	594 (2.6)	605	655
34	425 (299.2)	554 (19.3)	593 (3.2)	604	653
35	427 (284.1)	555 (17.0)	594 (3.0)	605	652
36	427 (287.9)	556 (17.3)	596 (3.5)	603	652

PBS	λ_{abs} / nm (ε / $\times 10^3$ $M^{-1}cm^{-1}$)			λ_{em}/nm*	
	Soret (B)	**Q (1-0)**	**Q (0-0)**	**Q (0-0)**	**Q (1-0)**
33	423 (263.5)	553 (13.9)	593 (2.2)	600	651
34	423 (266.9)	553 (15.1)	593 (2.5)	603	653
35	423 (248.5)	555 (15.4)	595 (3.6)	601	651
36	427 (126.3)	556 (11.7)	597 (2.5)	602	652

4.4.4. Physical and chemical properties of [^{68}Ga]gallium radiolabelled porphyrins

4.4.4.1. Log*D* of radiollabeled porphyrins [^{68}Ga] 33-36

The partition coefficient of the radiolabelled porphyrins was calculated by dissolving the [^{68}Ga]gallium porphyrins (~5 MBq) in 1× PBS (pH = 7.45) and adding the same amount of 1-octanol. After shaking vigorously for 15 min, the samples were centrifuged for 5 min, and the activity in each layer was monitored using a γ-counter. As expected, the log*D* values obtained increase proportionally with the length of the substituted alkyl chain, with a log*D* value of –3.37 calculated for the hydrophilic porphyrin **[^{68}Ga]33** with an acetamido groups, and a log*D* value of –0.51 for the porphyrin **[^{68}Ga]36**, substituted with an alkyl chain with

17 C atoms (**Table 21**). However, due to the highly positively charged structure (four positive charges), the calculated log*D* indicates the hydrophilic nature of the synthesised porphyrins, with the exception of porphyrin **[^{68}Ga]36**, which could be considered amphiphilic. The results obtained are in agreement with data from the literature, where log*D* –4.30 was observed for symmetric **TMPyP4** [160] and –1.55 for its A_3B analogue in which one *N*-methylpyridinium group was substituted by a carboxymethylenoxyphenyl group [161,276].

Table 21. Partition coefficient (log*D*) determined using shake-flask method with 1-octanol and PBS. Prior mixing, activity (~1 MBq) was dissolved in PBS. After separation of layers, activity in each layer was observed using γ-counter.

	log*D* calculated
[^{68}Ga]33	-3.37 ± 0.24
[^{68}Ga]34	-1.63 ± 0.01
[^{68}Ga]35	-1.14 ± 0.01
[^{68}Ga]36	-0.51 ± 0.02

4.4.4.2. Serum stability of radiollabeled porphyrins [^{68}Ga] 33-36

Serum stability is a crucial aspect in the development of new radiotracers and a relevant information when the radiolabelled compounds are translated to *in vivo*, as well as their stability in other biological media such as *apo*-transferrin, superoxide dismutase or hydroxyapatite [277]. The stability of the chelate *in vivo* affects its pharmacokinetic and pharmacodynamic properties as well as toxicity. It is known that highly stable compounds have a high clearance rate from the body via the kidneys and bladder or the digestive system, depending on their polarity. On the other hand, unstable complexes have been shown to be taken up for a prolonged period of time in organs or tissues known to self-associate with unbound radiometal (e.g. ^{68}Ga-EDTA in brain lesions, ^{68}Ga-citrate in bones and joints) [274,277]. To investigate serum stability, the radiolabelled porphyrins **[^{68}Ga]33-36** were dissolved in mouse serum and incubated for up to 2 hours. At the desired time point, an aliquot of the samples was mixed with MeCN at a ratio of 1:2 (time points up to 60 minutes) or 1:1 (60 and 120 minutes). After precipitation, the sample was centrifuged and the supernatant was analysed by radio-HPLC and radio-TLC (**Figure 65**).

As shown in **Figure 65**, the radiolabelled porphyrins **[^{68}Ga]33** (R = $-CH_3$) and **[^{68}Ga]34** (R= $-C_9H_{19}$) were stable in serum over an incubation period of 2 hours, with the strong decrease in the activity intensity of **[^{68}Ga]34,** presumably due to ^{68}Ga decay. Porphyrins **[^{68}Ga]35** (R =$-C_{13}H_{27}$) and **[^{68}Ga]36** (R = $-C_{17}H_{35}$) showed a complete loss of radiolabelled porphyrin signal, where for porphyrin **[^{68}Ga]35** was observed after two hours of incubation, while for porphyrin **[^{68}Ga]36** the intensity of the signal was weak at the beginning of the experiment and a complete disappearance of the peak was observed after 60 minutes of incubation. The

whole sample of porphyrin **[^{68}Ga]36** was analysed and the activity obtained was 1.17 MBq. When divided, the activity of the supernatant was 0.138 MBq and of the pellet 1.07 MBq, indicating that the disappearance of the peak is due to the strong binding of the radiolabelled porphyrin to proteins in the serum. The activity observed in the supernatant is the free **[^{68}Ga]acetate** remaining in serum, which confirms the peak that was observed in the radio-chromatogram within the first 5 minutes of analysis (**Figure 65**, **[^{68}Ga]36** 60 and 120 min). The potential binding to serum albumin and its use as a potential carrier is investigated in the next chapter.

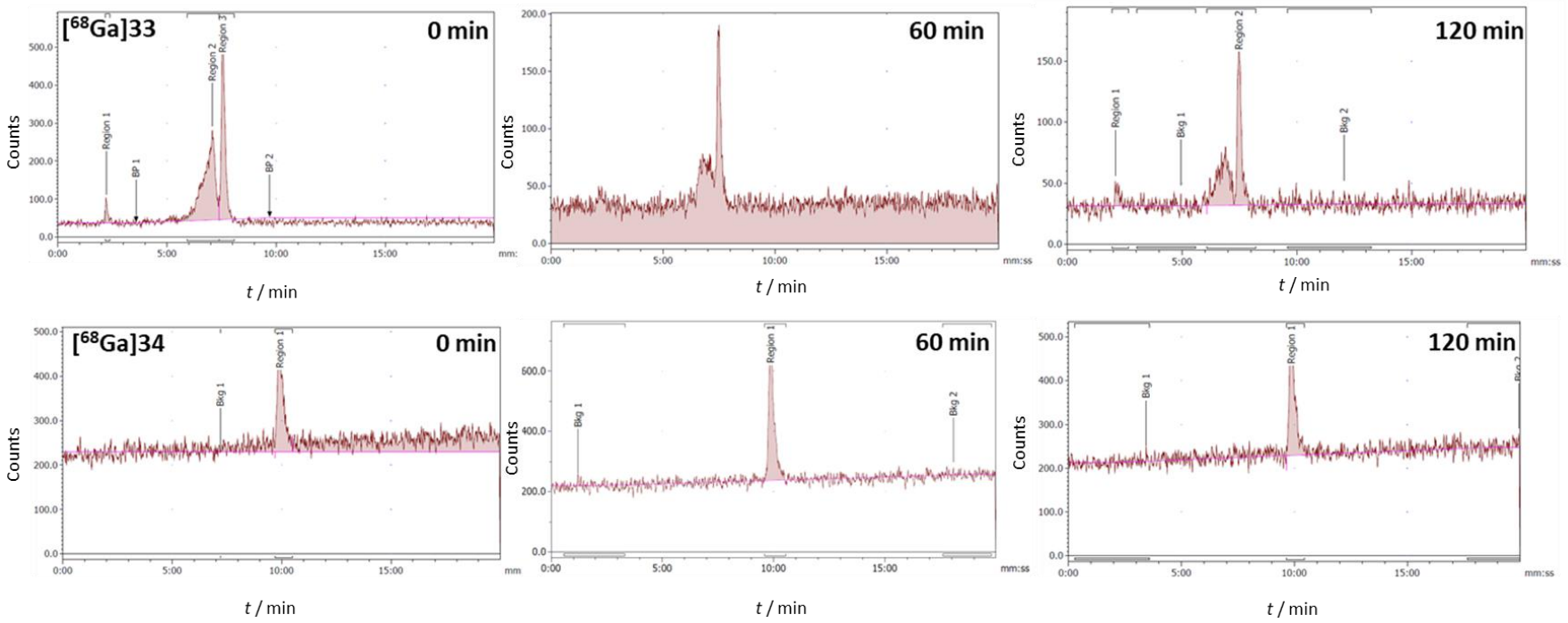
[68Ga]33
0 min
60 min
120 min
[68Ga]34
0 min
60 min
120 min
Counts
t / min
Region 1
Region 2
Region 3
BP 1
BP 2
Bkg 1
Bkg 2

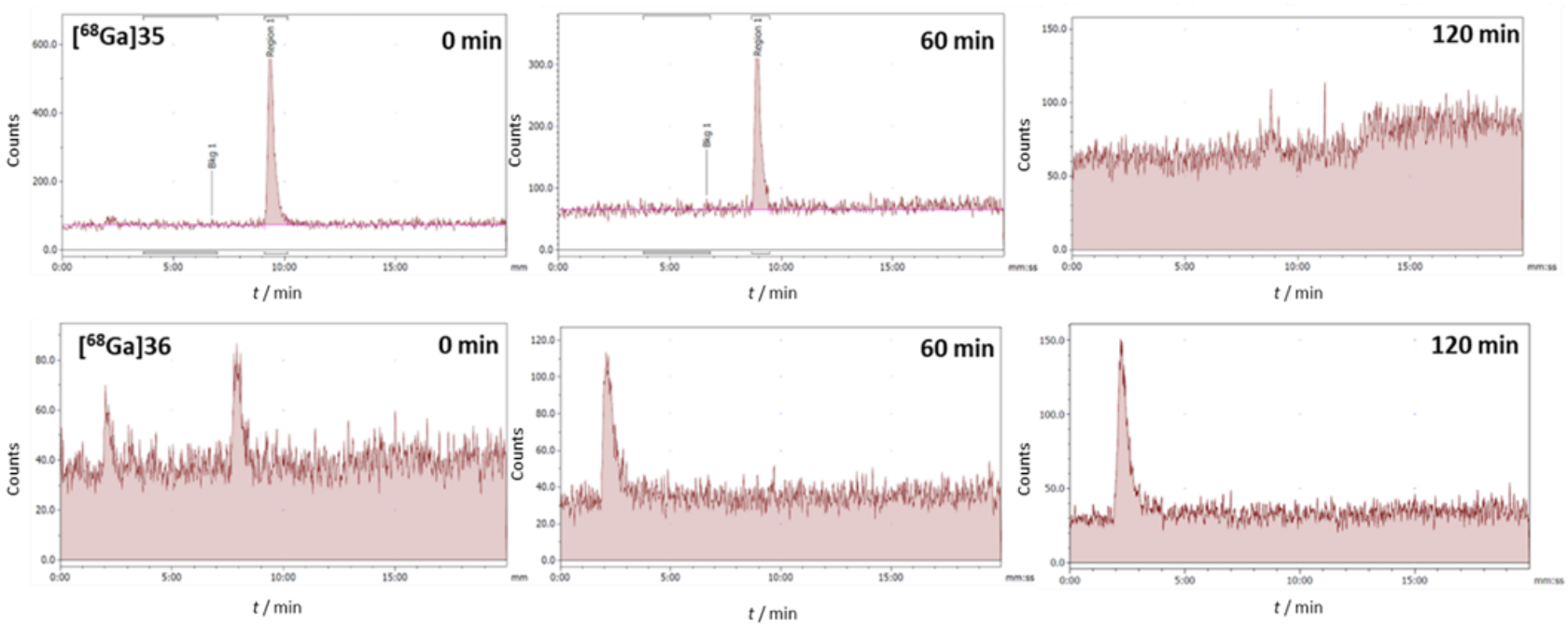

Figure 65. HPLC radio-chromatograms of radiolabelled porphyrins **[^{68}Ga]33, [^{68}Ga]34**, **[^{68}Ga]35** and **[^{68}Ga]36** after the incubation in the mouse serum for 2 hours at 37 °C. Radio-chromatograms are showing stability at the beginning of the experiment (0 min) and after 60 minutes and 120 minutes of incubatio

4.4.4.3. *Apo*-Transferrin chelator challenge study with [^{68}Ga]gallium radiolabelled porphyrins

In addition to serum stability, stability in the solution containing *apo*-transferrin was studied. *Apo*-transferrin, also known as iron-free transferrin, is a protein part of the serum that is involved in the transfer of an iron to the cells and binds free-iron in the cell medium. It is a single chain glycoprotein which may bind up to two ferric (Fe^{3+}) ions [278]. As the Fe^{3+} ion has similar chemistry to the $^{68}Ga^{3+}$, it was seen that *apo*-transferrin successfully binds Ga^{3+} [277], thus it can be investigated as a potential biological competing chelator of Ga^{3+}.

The similar protocol, as done in serum stability was carried out in *apo*-transferrin chelator challenge study [279]. Radiolabelled porphyrins **[^{68}Ga]34** and **[^{68}Ga]35** were dissolved in *apo*-transferrin solution (1 mg/mL) and the solution was incubated for 3 hours at 37 °C. At the desired time point, the solution was precipitated in MeCN (1:1) and the supernatant was investigated by radio-HPLC and radio-TLC. As seen in the **Figure 66**, both radiolabelled porphyrins proved to be strongly chelated to $^{68}Ga^{3+}$ as they showed stability of the chelate toward *apo*-transferrin competing chelation up to 3 hours of incubation at 37 °C.

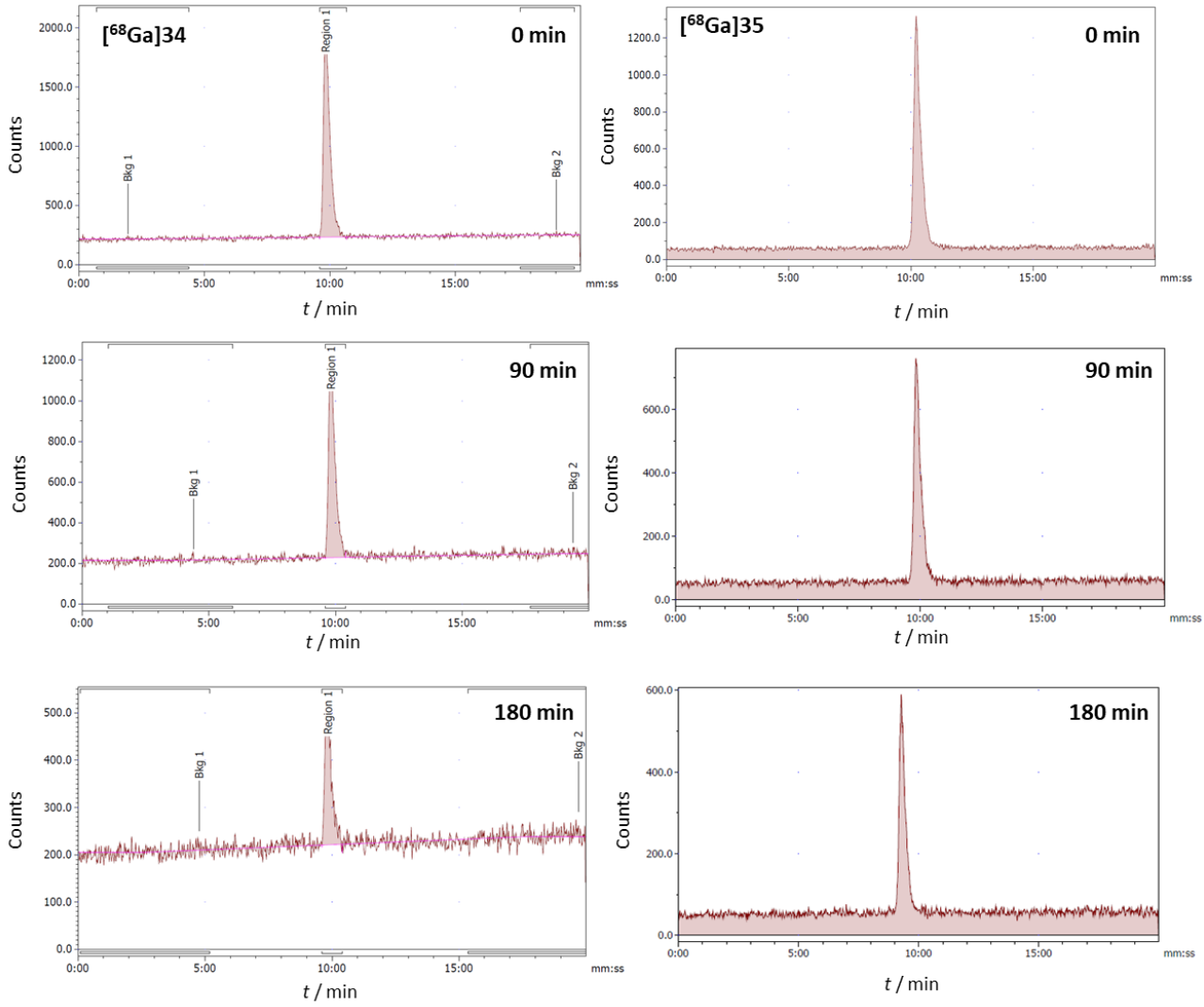

Figure 66. HPLC radio-chromatograms of radiolabelled porphyrins **[^{68}Ga]34** and **[^{68}Ga]35** after the incubation with *apo*-transferrin (1 mg/mL) for 3 hours at 37 °C. Radio-chromatograms are showing stability at the beginning of the experiment (0 min) and after 90- and 180-minute incubation.

4.4.5. Bovine serum albumin (BSA) and low-density lipoprotein (LDL) binding studies with [^{68}Ga]gallium radiolabelled porphyrins

As described in section 5.1.7, albumin is the most abundant and tumour cells have a higher turnover rate of human serum albumin (HSA) due to increased metabolism and proliferation rate [25]. To investigate the albumin binding properties, radiolabelled porphyrins **[^{68}Ga]33-36** were dissolved in 3% BSA in PBS solution and the potential binding was investigated by size exclusion chromatography (SE-HPLC) with PBS as eluent (flow 0.5 mL/min). In addition, the radiolabelled porphyrin-BSA complexes were incubated at 37 °C up to 4 hours to investigate the stability of the radiotracer in serum.

Binding was investigated by both UV and radio-chromatogram, and the [^{68}Ga]gallium acetate was used as a control (**Figure 67**). In the control, one peak with a retention time (R_t) of 40 minutes in the radio-chromatogram shows the peak of free [^{68}Ga]gallium acetate, while in the UV-chromatogram three peaks with retention times of 18, 20 and 25 minutes correspond to the BSA in the solution. When the peaks in the UV-chromatogram and the radio-chromatogram did not overlap, as in the control [^{68}Ga]gallium acetate, the binding did not occur (**Figure 67**, [^{68}Ga]acetate). A similar situation to the control was seen with the hydrophilic porphyrin **[^{68}Ga]33**, where the peaks observed in the radio-chromatogram with retention times of 38 and 41 minutes did not overlap with the UV-chromatogram with BSA peaks with an R_t ~ 20 minutes.

On the other hand, all tested porphyrins substituted with an alkyl chain, **[^{68}Ga]34**, **[^{68}Ga]35**, and **[^{68}Ga]36**, showed significant binding of the radiolabelled porphyrin with BSA already after 30-minute incubation, as evidenced by the overlap of the UV- and radio-chromatogram, which both show the retention peaks at 18, 20, and 25 minutes. The structures of the radiolabelled porphyrins are similar to the already tested metalloporphyrins, the Zn(II) porphyrins. In Section 5.1.4. the binding of the two free-base pyridiniumporphyrins and their Zn(II) complexes to BSA is described, showing that the main binding of BSA with the amphiphilic porphyrins **[^{68}Ga]34**, **[^{68}Ga]35** and **[^{68}Ga]36** occurs through the hydrophobic interactions of the long alkyl chain in their structure (**34** R= -C_9H_{19}, **35** R = -$C_{13}H_{27}$ and **35** R = -$C_{17}H_{35}$), as the moiety of fatty acids, and the hydrophobic pockets in the BSA structure. In addition, electrostatic interactions may occur with the additional bonding between positively charged [^{68}Ga]gallium. However, these interactions are not strong and reversible, as evidenced by the hydrophilic porphyrin **[^{68}Ga]33**, which showed no binding to BSA after SE-HPLC analysis.

Furthermore, the stability of the radiolabelled porphyrins in serum was again observed by SE-HPLC after incubation at 37 °C in BSA solution for 2 and 4 hours (**Figure S92**). All amphiphilic porphyrins exhibited high stability, with no unbound porphyrin present in the formulation. These results show that the porphyrins will be stable when injected *in vivo*. However, they will circulate in the bloodstream as protein-bound BSA radiotracers.

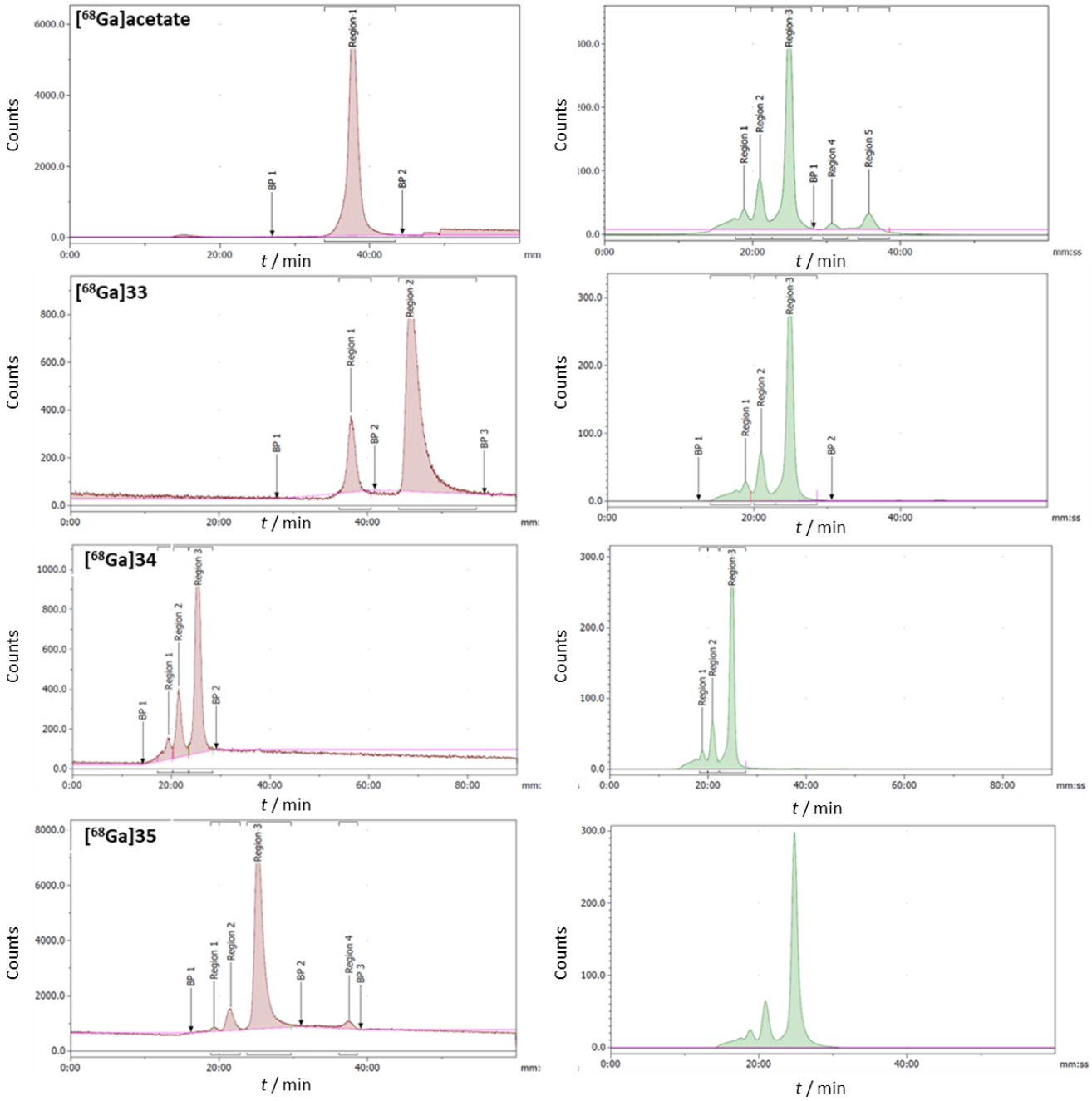
[68Ga]acetate
Counts
t / min
BP 1
BP 2
Region 1
[68Ga]33
BP 3
Region 2
[68Ga]34
Region 3
[68Ga]35
Region 4
Region 5

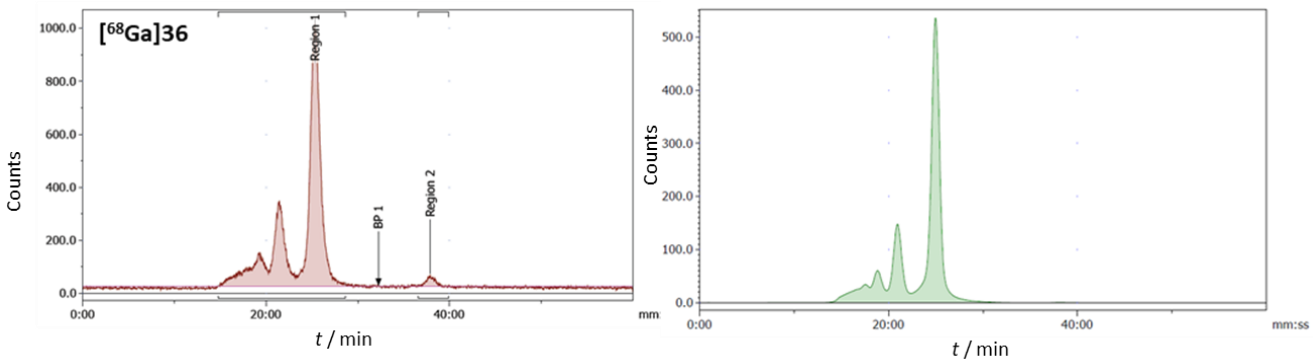

Figure 67. Radio-chromatograms (pink) and UV-chromatograms (green) of the size exclusion chromatography (PBS, flow: 0.5 mL/min) investigating binding of the radiolabelled porphyrins **[^{68}Ga]33**, **[^{68}Ga]34** and **[^{68}Ga]35** to BSA (3% in PBS). **[^{68}Ga]acetate** was used as control. The chromatograms are showing the results after 30-minute incubation with BSA solution.

Low density lipoprotein (LDL) serves as another potential carrier in PDT, although its primary role is cholesterol delivery to cells. Since the cancer cells have an increased need for lipids to synthesize new membranes, low-density lipoprotein receptors (LDLR) are overexpressed in tumours. This allows a higher accumulation of LDL-drug complexes in tumour cells compared to normal cells. Further advantages of LDL bio-nanoparticles are the possibility to bind hydrophobic drugs to the hydrophobic core as well as amphiphilic drugs to the amphiphilic shell of LDL. They can extend the half-life of the bound drugs in the bloodstream to up to 4 days and are biocompatible and relatively easily biodegradable[280]. In PDT, pharmacokinetic studies with tumour-bearing mice showed that various liposome-associated porphyrins loaded on LDL exhibited significant tumour uptake and improved PDT outcome [281].

A similar procedure as for BSA was carried out with LDL, however, with the high SA formulation of the amphiphilic porphyrins **[^{68}Ga]34** and **[^{68}Ga]35** and the low SA formulation of the hydrophilic porphyrin **[^{68}Ga]33**, since a low concentration of LDL was used (0.5 mg/mL), which mimics the body concentration of LDL (**Figure 68**). As expected, both [^{68}Ga]acetate, used as control, and **[^{68}Ga]33** showed no binding to LDL, as the R_t of LDL in the UV-chromatogram was 18 minutes and did not overlap with the radio-chromatogram of the radiotracers [^{68}Ga]acetate and **[^{68}Ga]33**, which were observed at 39 and 44 minutes, respectively. Amphiphilic porphyrins, **[^{68}Ga]34** and **[^{68}Ga]35**, showed minimal binding to LDL, as evidenced by an overlap of signals in the radio-chromatogram and UV-chromatogram (**Figure 68**, **[^{68}Ga]34** and **[^{68}Ga]35**). However, only a small signal bound to

LDL was detected compared to the injected radioactivity and no signal from unbound porphyrins was detected on the radio-chromatogram. The results obtained could be due to the fact that only a small amount of the radiolabelled porphyrin is bound to LDL and travels through the column and that the unbound porphyrin could not be detected because it is trapped on the column and thus not possible to detect.

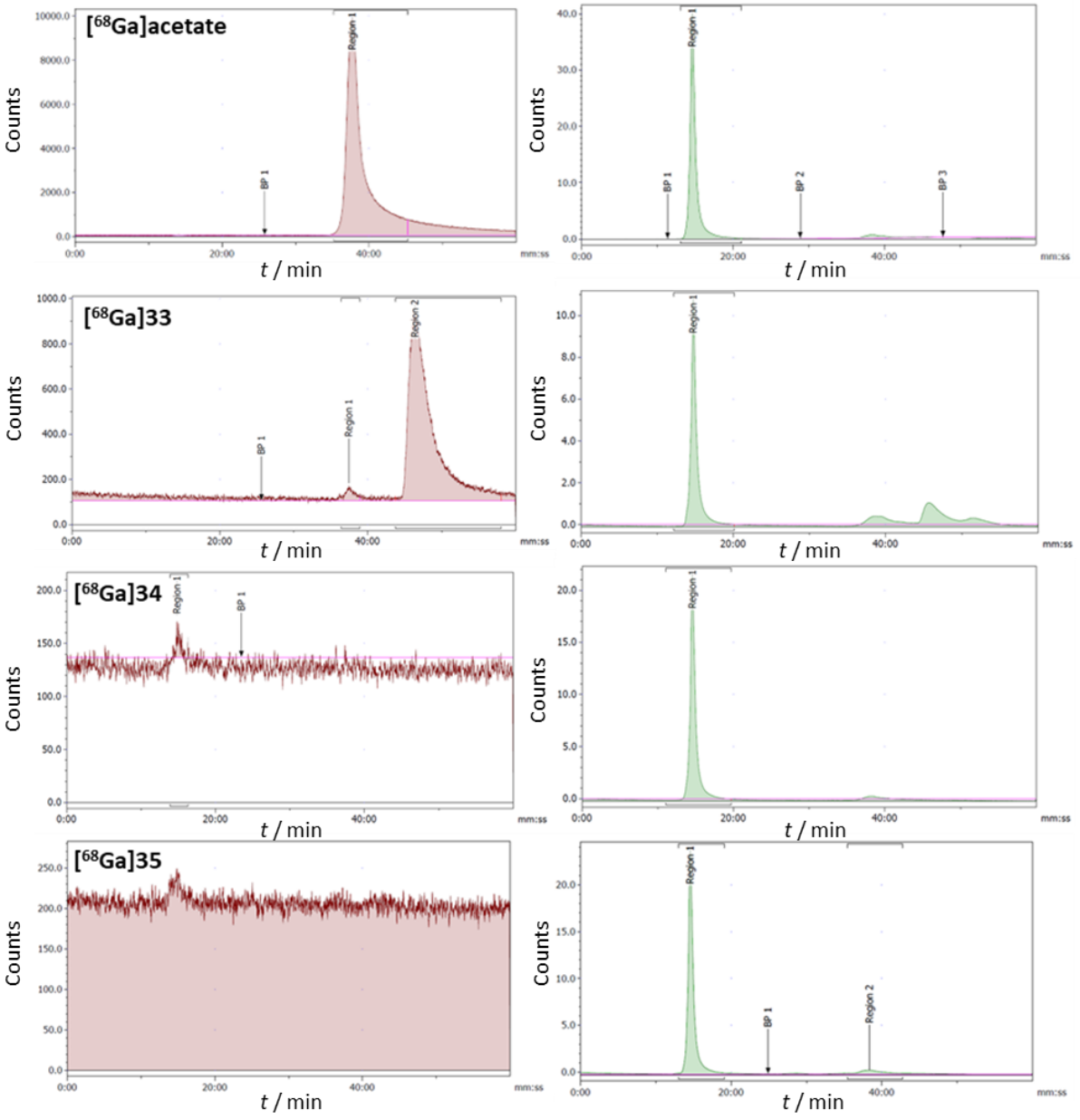

Figure 68. Radio-chromatograms (pink) and UV-chromatograms (green) of the size exclusion chromatography (PBS, flow: 0.5 mL/min) investigating binding of the radiolabelled porphyrins **[^{68}Ga]33**, **[^{68}Ga]34** and **[^{68}Ga]35** to LDL (0.5 mg/mL). Both amphiphilic porphyrins were used in their high SA formulation, while porphyrin **[^{68}Ga]33** was used as low SA formulation. **[^{68}Ga]acetate** was used as control.

4.4.6. *In vitro* studies of ^{nat}Ga(III) porphyrins 33-36 on MDA-MB 231 cell line

4.4.6.1. Cellular uptake of Ga(III) porphyrins 33-36

The cellular uptake of porphyrins **33-36** was evaluated by measuring the fluorescence intensity of the solubilized cells after the incubation with porphyrins, using the same protocol as for the *N*-methylated and *N*-oxidised porphyrins in the previous sections of this thesis. The breast cancer cell line MDA-MB 231 was used and the cells were incubated with 1 μM porphyrin for up to 24 hours at 4 °C and 37 °C. As can be seen in **Figure 69A**, the amount of porphyrin internalised by the cells is proportional to the length of the alkyl chain. Furthermore, comparing to the amount of porphyrin internalised within 24 hours, the porphyrins internalised the cells in the highest concentration within 6 hours. Similar to the previously obtained results with *N*-methylated free-base pyridiniumporphyrins in Section 5.1., porphyrin **36** (R= -$C_{17}H_{35}$) showed somewhat slower uptake rate compared to the other analogues tested. Unfortunately, the porphyrins that were successfully obtained as low SA or high SA, porphyrins **33** to **35**, showed minimal internalisation within 2 hours, suggesting that only a relatively small amount of each porphyrin is expected to internalise the cells during a PET-CT scan, thus only a relatively small amount can be detected inside tumours.

As already described, the temperature-dependent analysis was used as the first insight into the type of cellular uptake of porphyrins - passive or active [247]. The porphyrins were incubated at 4 °C or 37 °C for 6 hours and the intensity of the porphyrins was measured by its fluorescence (**Figure 69B**). Porphyrins **33** and **34** showed similar cellular internalisation after incubation at both temperatures, suggesting that passive or facilitated uptake is the major mechanism of uptake of these two porphyrins. For porphyrins **35** and **36**, significantly increased internalisation of the porphyrins was observed after incubation at 37 °C. However, due to the smaller difference in cellular uptake at different temperatures, it is assumed that porphyrin **35** is only internalised by passive uptake, whereas porphyrin **36** can be taken up by both passive and active uptake.

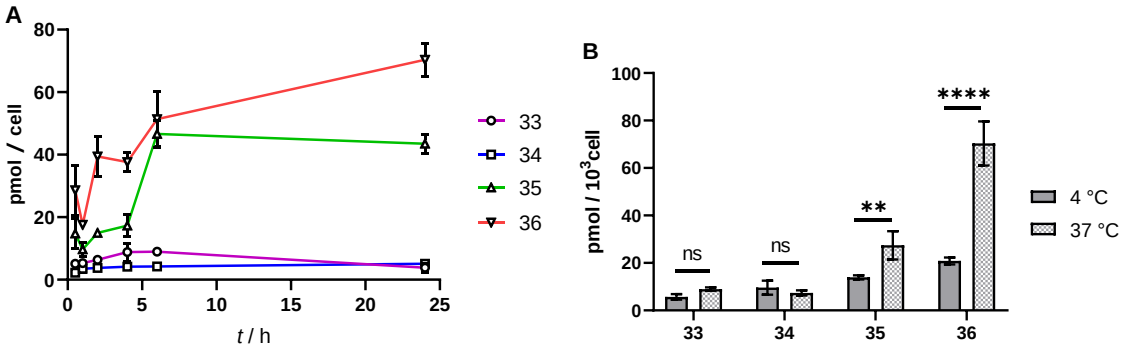

Figure 69. Time dependent (A) and temperature dependent (B) cellular uptake of ^{nat}Ga(III) porphyrins **33-36** on MDA-MB 231 cell line. Time dependent analysis shows the kinetics of a cellular uptake over 24 hours at 37 °C, while in temperature dependent analysis,

porphyrins were incubated for 6 hours at 4 °C or 37 °C. Results are shown as an average of three experiments with standard deviation in error bars. Statistical analysis was done using the Two-way ANOVA with Sidak's *post-hoc* test. Significance was $p < 0.0001$ and it was shown using the following signs: **** < 0.0001; 0.0001 <*** < 0.001; 0.001 < ** < 0.01; 0.01 < * < 0.1; ns > 0.1 (not significant).

In addition, after incubation with porphyrins, the washing protocol included a wash with ice-cold glycine buffer (pH = 2.8) and incubation on ice for 5 minutes to collect all molecules that were bound to the membrane and thus not internalised. **Figure 70** shows a comparison of the membrane-bound porphyrins and the porphyrins in the cells after 6 hours of incubation at 37 °C and 4 °C. After incubation at 37 °C, it can be seen that the amount of porphyrins **33**, **34** and **35** bound to membrane is higher than the amount of internalised porphyrins (**Figure 70A**). Furthermore, a reverse situation was observed for the most lipophilic porphyrin, porphyrin **36**, which showed a significantly higher accumulation within the cells than the porphyrins bound to the membrane. When the cells were incubated at 4 °C, all four porphyrins tested showed a much higher concentration of membrane-bound porphyrins compared to porphyrins that had internalised the cells (**Figure 70B**). This result is a further confirmation that porphyrin **36** is the only one that can enter the cells by both passive and active uptake, while other porphyrins are internalised by passive uptake.

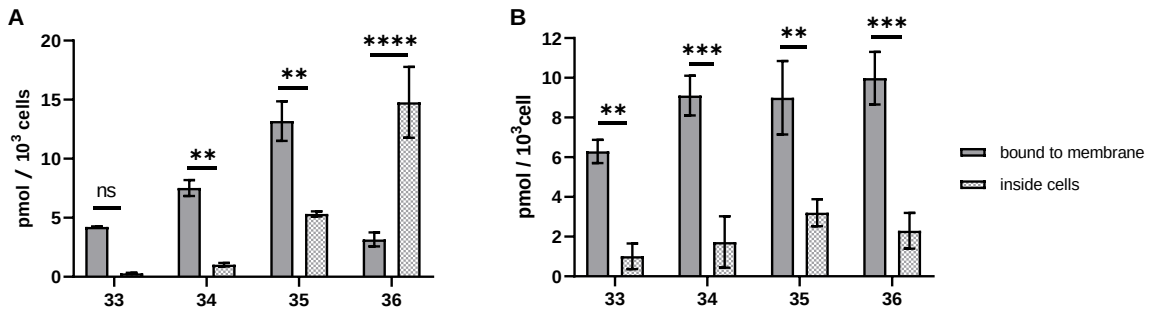

Figure 70. Comparison of the amount of porphyrin attached to the cell wall of the MDA-MB 231 cell line removed by ice-cold glycine buffer and the amount of the porphyrin inside the cells determined after solubilization of the cells with the 1% SDS in 0.1M NaOH after the incubation at 37 °C (A) and 4 °C (B). Results are shown as an average of three experiments with standard deviation in error bars. The statistical analysis was done using the Two-way ANOVA with Sidak's *post-hoc* test. Significance was $p < 0.0001$ and it was shown using the following signs: **** < 0.0001; 0.0001 <*** < 0.001; 0.001 < ** < 0.01; 0.01 < * < 0.1; ns > 0.1 (not significant).

Additional confirmation of the cellular uptake of porphyrins **33**- **36** was provided by fluorescence microscopy. As in the previous microscopy experiments, the porphyrins were incubated with MDA-MB 231 cell line at a concentration of 5 μM for 6 hours. The fluorescence microscopy images confirm that the porphyrins have internalized the cells and,

based on the fluorescence intensity, the amount of internalized porphyrin is in line with the length of the substituted alkyl chain (**Figure 71**).

Colocalization markers, such as $DIOC_6(3)$, used for previous porphyrins were not used in this experiment, so the final localisation of the porphyrins cannot be determined. However, based on the structure of porphyrin, which is asymmetric, has 4 positive charges and is amphiphilic, with a long alkyl chain substituted, and based on the previous localisation experiments performed with the porphyrins of similar structure, it could be expected that these porphyrins could mainly localise mitochondria, the ER and the Golgi apparatus.

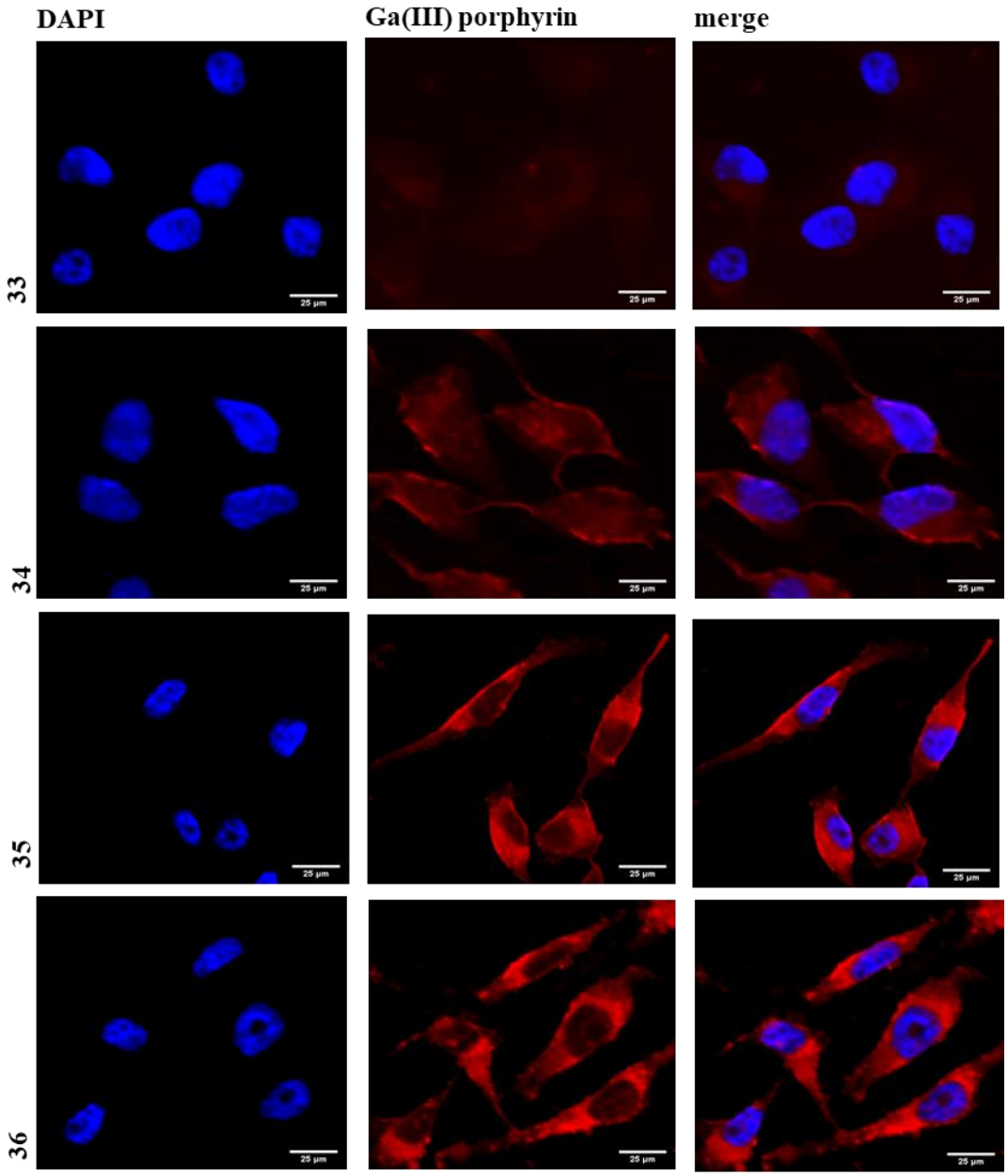

Figure 71. Cellular uptake of ^{nat}Ga(III) porphyrins **33-36** in MDA-MB 231 cell line determined after the incubation of porphyrins for 6 hours at 37 °C. Images were observed by fluorescence microscopy at magnification 20×. Scale bare = 25 μm.

4.4.6.2. Cytotoxicity of Ga(III) porphyrins 33-36

The cytotoxicity of Ga(III)-porphyrins **33** to **36** was investigated using an MTT assay on the cell lines MDA-MB 231 and HDF. In contrast to the previous sections, a breast cancer cell line was used here as a tumour cell line in order to use the same cell line as in PET-CT scans and to have the proof of concept that Ga(III) porphyrins can be used simultaneously for diagnostic purposes (PET-CT scan) and have a therapeutic effect when accumulation in the tumour is observed. Human dermal fibroblasts (HDF) were used as a represent of a normal cell line. The LED-based red-light setup (λ = 643 nm, 2 mW/cm^2) was used to irradiate the treated cells, while non-irradiated cells served as a dark control.

The cells were incubated for 6 hours with porphyrins at a concentration of up to 100 μM. The cells were then washed to remove all unbound cells. The cells were then irradiated for 30 or 60 minutes and the amount of dead cells was determined by measuring the intensity of formazan dye ~36 hours after treatment. Negligible toxicity was observed after treatment with porphyrins at a concentration of 100 μM without irradiation. Furthermore, no toxicity was observed for hydrophilic porphyrin in both the HDF and MDA-MB 231 cell lines, even after the prolonged irradiation of 60 minutes. The determined IC_{50} values for porphyrins **34** to **36** show low to moderate phototoxicity of the tested Ga(III) porphyrins, with the increasing phototoxicity being proportional to the length of the alkyl chain. The results indicate that the phototoxicity of the Ga(III) porphyrins is proportional to the cellular uptake into the cells. Although moderate phototoxicity was observed for porphyrins **35** and **36**, they showed selectivity towards tumour cell line, especially for porphyrin **35** after both 30 and 60 minutes of irradiation (75 μM for HDF and 31 μM for MDA-MB 231 after 30 minutes of irradiation), while porphyrin **36** showed selectivity only after 30 minutes of irradiation (58 μM for HDF and 19 μM for MDA-MB 231) (**Table 22**).

Table 22. Determined IC_{50} values of ^{nat}Ga(III)porphyrins **33-36** on HDF and MDA-MB 231 cell line. Cells were incubated with porphyrin for 6 hours followed by irradiation with red light (λ = 643 nm, 2 mW/cm^2) for 30 (3.6 J/cm^2) or 60 minutes (7.2 J/cm^2). 'Dark' column represents cells tested with porphyrin without irradiation.

IC_{50} / μM	HDF			MDA-MB 231		
λ = 643 nm	**DARK**	**3.6 J/cm^2**	**7.2 J/cm^2**	**DARK**	**3.6 J/cm^2**	**7.2 J/cm^2**
33	> 100	> 100	> 100	> 100	> 100	> 100
34	> 100	> 100	> 100	> 100	83.7 ± 2.65	71.03 ± 5.66
35	> 100	75.29 ± 2.55	56.06 ± 3.72	> 100	31.92 ± 1.82	26.84 ± 0.99
36	> 100	57.49 ± 3.49	22.92 ± 0.89	> 100	18.34 ± 0.28	13.88 ± 0.46

A reduced IC_{50} value after prolonged irradiation was observed for porphyrins **35** and **36** in the HDF cell line as well as for porphyrins **34**-**36** in the MDA-MB 231 cell line (**Table 17**). When analysing proliferation after treatment with 50 μM, it was found that the greatest statistical difference in the time of irradiation was observed for porphyrins **35** and **36** in the HDF cell line and for **34** and **35** in MDA-MB 231 (**Figure 72**). All tested amphiphilic porphyrin showed strong binding to membranes after 6 hours of incubation, thus is not surprising that prolonged irradiation caused higher cytotoxicity of a porphyrin to both MDA-MB 231 and HDF cell lines.

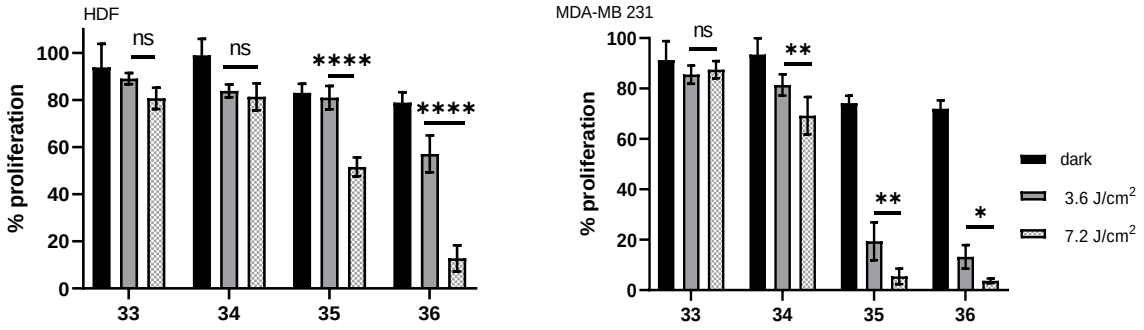

Figure 72. Comparison of the cytotoxicity of ^{nat}Ga(III) pyridiniumporphyrins on HDF (left) and MDA-MB 231 (right) at concentration of 50 μM after irradiation for 30 minutes (3.6 J/cm^2) and 60 minutes (7.2 J/cm^2). The statistical analysis in the graph shows the two-way ANOVA analysis between two light doses applied to the cell lines. Significance was $p <$ 0.0001 and it was shown using the following signs: **** < 0.0001; 0.0001 <*** < 0.001; 0.001 < ** < 0.01; 0.01 < * < 0.1; ns > 0.1 (not significant).

In addition to the MTT assay after irradiation with red light, the cytotoxicity of porphyrin **35** was examined after irradiation with orange light (λ = 606 nm) for 30 (3.6 J/cm^2) and 60 (7.2 J/cm^2) minutes. Compared to red light, orange light is more suitable for the optical properties of metalloporphyrins such as Zn(II) and Ga(III), which were tested in this work, as they have minimal absorption in the wavelengths > 610 nm.

Surprisingly, no changes in phototoxicity were observed after irradiation with orange light (**Table 23**). When the cytotoxicity of porphyrin **35** was tested after irradiation with orange light, IC_{50} values were even higher than after irradiation with red light (IC_{50} = 31 μM after irradiation with red light, and IC_{50} = 50 μM after 30 min irradiation with orange light on MDA-MB 231). This indicates that the wavelength of irradiation has a small or negligible impact on the toxicity of Ga(III)-porphyrins.

Table 23. Determined IC_{50} values of ^{nat}Ga(III) porphyrin **35** on HDF and MDA-MB 231 cell lines. Cells were incubated with porphyrin for 6 hours followed by 30-min and 60-min irradiation with orange light (λ = 606 nm, 2 mW/cm^2, total light dose 3.6 J/cm^2 (30-minute irr.) and 7.2 J/cm^2 (60-minute irr.). 'Dark' column represents cells tested with porphyrin without irradiation.

IC_{50} / μM	HDF		MDA-MB 231	
λ = 606 nm	3.6 J/cm^2	7.2 J/cm^2	3.6 J/cm^2	7.2 J/cm^2
35	74.33 ± 3.06	46.34 ± 4.32	50.03 ± 11.98	37.18 ± 3.98

Compared to the previously tested porphyrins in this work, the Ga(III) porphyrins did not show high toxicity towards tumour cell line. These results are consistent with the literature in which PET-PDT gallium porphyrin also showed mild to low toxicity to tumour cells. In a study by Guleria and colleagues, the porphyrins **Ga(III)-TMPyP4** and its analogue with a carboxymethyleneoxyphenyl peripheral group (**TriMPyCOOHP**) were tested as potential PET-PDT agents and their phototoxicity was investigated in the human lung adenocarcinoma cell line A549 [161]. Among the concentrations tested, a reduced proliferation of 65% and 45% was observed only at 50 μM and 100 μM, respectively. At a higher light dose (from 10 to 40 J/cm^2, white light), a slight increase in phototoxicity was observed, but the IC_{50} value determined was never below 40 μM.

As mentioned in the introduction, Ga(III)-porphyrins are generally used in PDI as they mimic Fe^{3+} due to their similar chemistry, however, this is more investigated as antibacterial strategy than anti-tumour. At a low Fe^{3+} concentration in bacteria, gallium porphyrins could be taken up by bacteria via iron-regulated surface determinants (Isd) or the haeme transport system (Hts) and block iron metabolism in bacteria, which is known as a Trojan horse strategy. However, both Ga^{3+}mesoporphyrin IX (**Ga^{3+}MPIX**) and photoporphyrin IX (**Ga^{3+}PpIX**) were tested against endothelial cell lines, **Ga^{3+}MPIX** against keratinocytes (HaCaT) [282] and **Ga^{3+}PpIX** against HaCaT cell line and human colon cancer cell line (HT-29) [283]. No toxicity was observed in either cell lines after treatment with **Ga^{3+}PpIX**. However, phototoxicity of **Ga^{3+}MPIX** was only observed at a concentration of 100 μM (40% proliferation observed), while the PDI concentrations required for eradication of *S. aureus* were much lower (10 μM). However, the results showed that although there was minimal effect on phototoxicity to the cells, cells treated with **Ga^{3+}MPIX** exhibited a lower proliferation rate after the treatment than untreated cells [282]. When comparing the Ga(III) porphyrin to other porphyrins in this this thesis, they might seem produce lower cytotoxic effect. However, comparing to the literature data, these results, especially for amphiphilic porphyrins with longer alkyl chain, porphyrins **35** and **36**, show to be promising when used as PDT agents.

4.4.7. *In vivo* biodistribution studies of [^{68}Ga]gallium porphyrins using PET-CT scanning

Positron emission computed tomography (PET-CT) scanning was performed by John D. Wright, an animal laboratory technician at the PET Research Centre at the University of Hull in the United Kingdom. Mice were anaesthetized with isoflurane prior to the measurements, and radiolabelled porphyrins **[^{68}Ga]33**, **[^{68}Ga]34**, and **[^{68}Ga]35** were injected through a lateral tail vein at an activity of ~3 MBq of high SA for porphyrins **34** and **35** and of low SA for porphyrin **33**. After the injection, a standard 90 min dynamic scan was performed, followed by a whole-body CT scan. The obtained 3D images of PET-CT scans of the [^{68}Ga]gallium porphyrins were shown in **Figure 73**.

The hydrophilic porphyrin **[^{68}Ga]33** showed moderate uptake in the kidneys and high uptake in the bladder, due to its high hydrophilicity and the stability of the radiotracer both in blood serum and in the presence of a biological chelator, *apo*-transferrin. These results are consistent with the literature, which found that for symmetrical **[^{68}Ga]TMPyP4**, most of the radiotracer was excreted after 1 hour of *in vivo* incubation (54%), while ~15% was detected in the kidneys, which is much higher compared to other organs tested [160]. In addition, as shown in the right image of hydrophilic porphyrin, a small amount of radioactivity, represented as light blue coloration, was observed in the stifle joints of the lower legs of a mouse. Although accumulation of the [^{68}Ga]gallium porphyrin radiotracer in the bones or joints has not been observed in the literature, some formulations of free [^{68}Ga]gallium radionuclides are known to accumulate in the bones [277]. Thus, the low accumulation in the stifle joints could be due to the fact that the free [^{68}Ga]gallium radionuclide contained in the formulation was either injected in a low percentage in the formulation or the [^{68}Ga]porphyrin is de-chelated by some biological competing chelators *in vivo*.

However, the amphiphilic porphyrin **[^{68}Ga]34** (R = -C_9H_{19}) shows moderate accumulation both in the kidneys and liver with a clear cardiac signal separate from the liver with accumulation in the neck carotid arteries (**Figure 73**), indicating its preferential blood pool retention. With increasing alkyl chain length, preferential accumulation of porphyrin **[^{68}Ga]35** (R = -$C_{13}H_{27}$) was observed in the liver. Based on the scan, it does not appear that porphyrin **[^{68}Ga]35** has a high accumulation in the heart, however, uptake in the heart could be mistaken for spill-over signal from the liver. These results demonstrate a lipophilicity-dependent shift in the biodistribution of porphyrins, from preferential liver accumulation for the most lipophilic compound to renal excretion observed for the most hydrophilic porphyrin, by way of extending blood pool retention of porphyrin of moderate lipophilicity.

The changes in biodistribution after PET-CT scanning of a porphyrin with similar structure and higher lipophilicity were observed in a previously mentioned work by Guleira and colleagues [161], where a change in only one peripheral group increased lipophilicity from -4.30 to -1.55. The change in lipophilicity also showed a small change in the ratio between kidney and liver accumulation, with higher lipophilicity porphyrin showing similar uptake in

kidney and liver, whereas highly hydrophilic porphyrin accumulated almost exclusively in kidney and bladder.

The PET-CT scan of a porphyrin **[^{68}Ga]35** was performed on a mouse with tumour (MDA-MB 231). The tumour grew on the left shoulder of the mice pointed to by the arrow in the scan of porphyrin **[^{68}Ga]35** (**Figure 73**, right). Unfortunately, no detectable tumour uptake of porphyrin **[^{68}Ga]35** could be determined from the scan results. This result is in agreement with the cellular uptake results, which show that a minimal amount of porphyrin is internalised in the cells within 90 minutes of incubation. However, it should be noted that the uptake of porphyrin in the tumours is usually analysed in biodistribution studies in % IA/g (% of injected activity per gram) by measuring the radioactivity with a γ-counter in the individual organs after sacrificing a mouse, whereas here the biodistribution is analysed by PET-CT scans to avoid sacrificing mice.

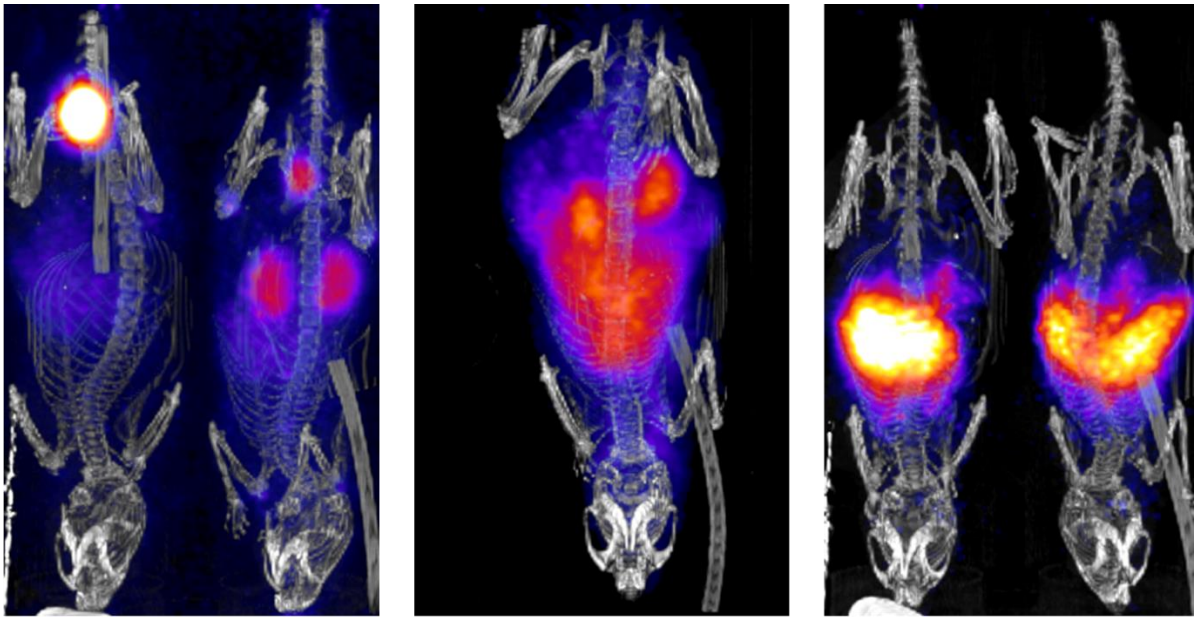

Figure 73. 3D images of *in vivo* biodistribution of [^{68}Ga]gallium porphyrins **33**, **34** and **35** observed using dynamic 90 min PET/CT scan. Dynamic imaging was performed in naive or tumour (MDA-MD 231) bearing mouse (CD1 strain-female) with the start time coinciding with intravenous injection of radiotracer into the tail vein via catheter.

The determination of the activity concentrations of the tested porphyrins **[^{68}Ga]34** and **[^{68}Ga]35** was performed by converting the count rates from reconstructed PET-CT scan images. Regions of interest (ROI) were drawn around the liver, kidneys, bladder, heart, and sections of quadriceps muscle, and SUV/mean data were generated using AMIDE software (**Figure 74**). From the results, porphyrin with higher lipophilicity has higher uptake in the liver and heart as shown by the PET-CT scan. The uptake in the heart cannot be confirmed

because the heart and liver overlap in the PET scan, so the accumulation in these organs sometimes cannot be separated by the scan image. However, the higher accumulation in the kidneys and bladder after treatment with **[^{68}Ga]34** confirms the difference in biodistribution due to the lipophilicity of the two porphyrins tested.

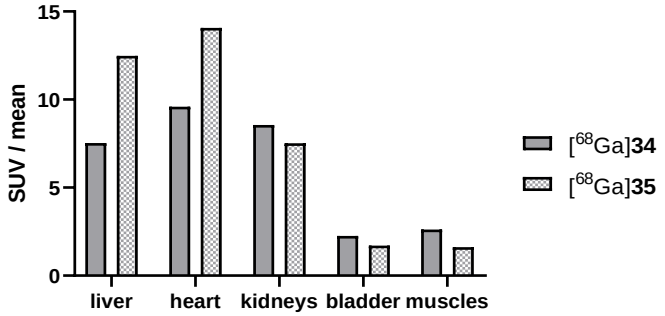

Figure 74. Biodistribution pattern over the selected organs (liver, heart, kidneys, bladder and muscles), determined by analysis of PET-CT scans with the radiolabelled porphyrins **[^{68}Ga]34** and **[^{68}Ga]35** in the AMIDE program.

The metabolites were analysed by HPLC after the 90-minute PET-CT scan with **[^{68}Ga]35** (R = -$C_{13}H_{27}$) by sacrificing a mouse (**Figure 75**). The stability of the radiotracer was examined in urine, blood and liver and a HPLC scan of the injected formulation was used as a control. A small amount of the radiotracer was detected in urine at the retention time of the formulation (20% of the total AUC), while the majority of the radiotracer was metabolised and detected in urine as free **[^{68}Ga]gallium** (80% AUC) (**Figure 75B**). The liver is analysed by mixing the MeCN with the liver sample in 1:1 ratio and analysing the MeCN sample by HPLC after separation from the pellet by centrifugation. As expected, the majority of the porphyrin in the liver was bound to proteins and were not extracted by MeCN, so that no signal could be detected in the liver sample (**Figure 75C**). In blood, the radiotracer proved to be stable, as only the signal at the R_t of the formulation was detected (**Figure 75D**). These results confirm the stability of our radiolabelled porphyrin *in vivo*, which, however, is strongly bound to serum proteins and is only metabolised by the renal system upon extraction. However, based on the results of lipophilicity and metabolite analysis, it can be assumed that these porphyrins can remain in the blood system, resulting in prolonged sensitivity of the patient.

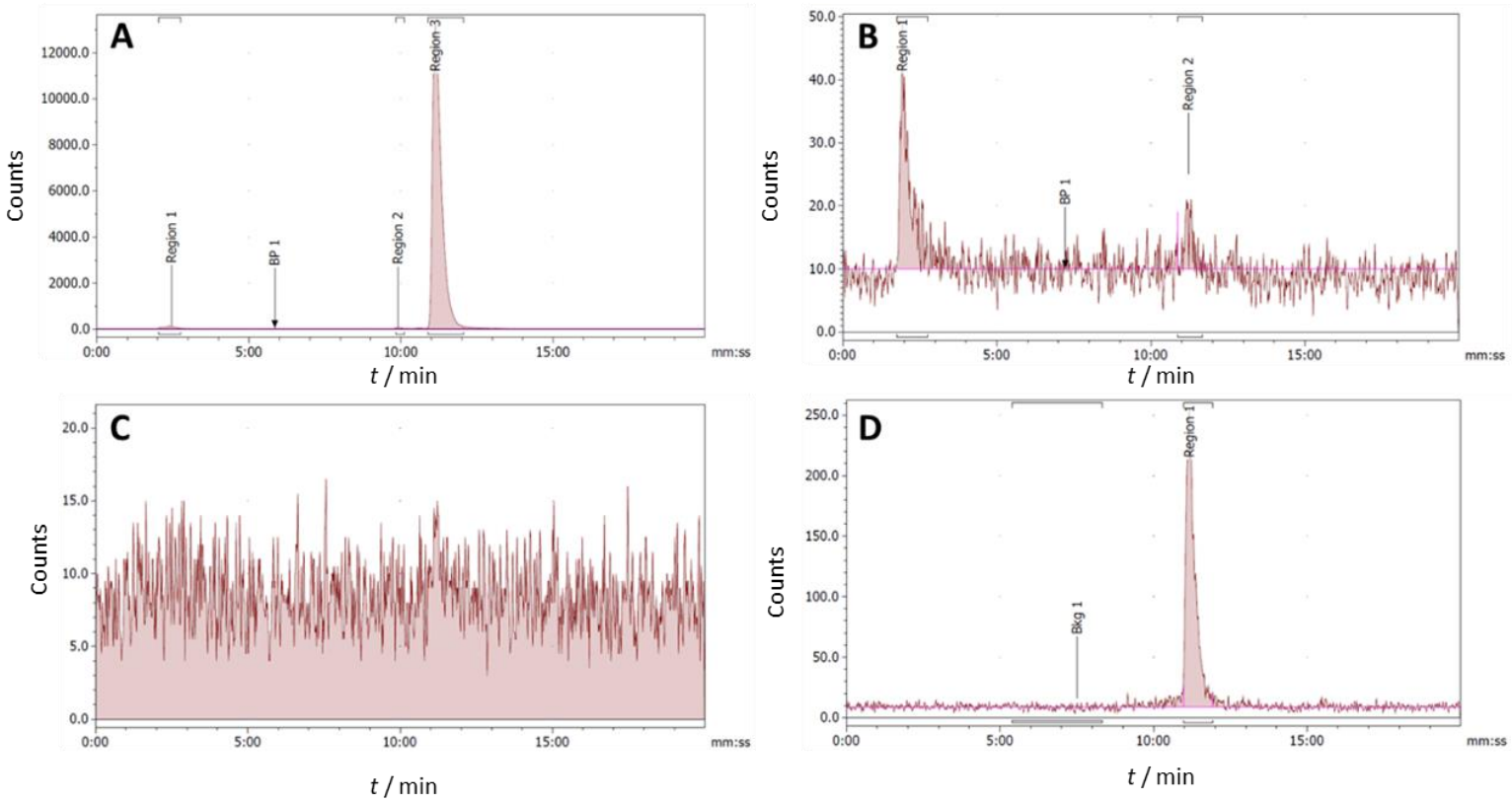

Figure 75. Radiochromatograms of the metabolites in urine (B), liver (C) and blood (D) of the HPLC analysis after the standard 90-minute PET-CT scan with porphyrin **[^{68}Ga]35**. A radiochromatogram of the formulation (A) is shown as a control.

4.4.8. Conclusion Part 4.4.

The potential of the synthesised porphyrins to be used as theranostic compounds as PET-PDT agents was investigated by radiolabelling of porphyrins with [^{68}Ga]gallium for PET imaging and chelating with $GaCl_3$ to evaluate the PDT outcome. Successful radiolabelling occurred within the 30-min reaction with [^{68}Ga]Ga^{3+} in acidic buffer with > 80% RCE. The porphyrin **[^{68}Ga]33** was formulated only as low SA formulations, while the porphyrins **[^{68}Ga]34** and **[^{68}Ga]35** were formulated as both low SA and high SA formulations. Together with the radiolabelled porphyrins, the Ga(III)-porphyrins **33** to **36** were synthetised and their activity on the cell lines MDA-MB 231 and HDF was investigated. The hydrophilic porphyrin **33** showed no activity against the cell lines, while the activity of porphyrins **34** to **36** corresponded to their cellular uptake, with moderate overall efficiency against the tested cell lines. In addition, porphyrin **35** showed selectivity towards the cell line MDA-MB 231. PET-CT scans of the tested porphyrins **[^{68}Ga]33**, **[^{68}Ga]34** and **[^{68}Ga]35** showed a lipophilicity-dependent biodistribution of porphyrins, with the most lipophilic porphyrin showing preferential accumulation in the liver. The porphyrin with moderate lipophilicity showed high uptake in the blood pool, while the most hydrophilic porphyrin showed high uptake in the renal system, i.e. kidneys and bladder. Tumour uptake of porphyrin **[^{68}Ga]35** was not discernible, probably due to the low cellular uptake of porphyrins within the time of the dynamic PET-CT scan (90 minutes).

Overall, the tested amphiphilic porphyrins have shown potential for use as PET-PDT agents as they exhibited toxicity towards cells and successful radiolabelling of porphyrin was achieved with high RCE. However, for these porphyrins, [^{68}Ga]gallium may not be the best radionuclide for use, as its short half-life of 68 minutes does not correlate with the slower cellular uptake of porphyrins, so tumour uptake was not detected.

5. Conclusion

In this doctoral thesis several series of amphiphilic pyridylporphyrins were designed and synthesised to obtain PSs with various alkyl chain length and quaternisation of the pyridyl substituent to achieve different hydrophilic-lipophilic ratio. Furthermore, their (photo)physicochemical properties and *in vitro* characteristics were evaluated proving that hydrophilic-lipophilic balance has a strong impact in the achieving the best outcome of the PDT treatment of melanoma cell lines.

Therefore, the main hypothesis proposed in the beginning of the work that the more optimal lipophilicity-hydrophilicity ratio in the structure of the newly synthesised amphiphilic PSs will increase cellular uptake and selectivity towards the melanoma cell line and thus improve PDT efficiency in melanoma was confirmed.

Following the sections of this thesis, the main conclusions were drawn based on the obtained results and findings:

1. Two groups, free-base and Zn(II) of amphiphilic *N*-methylated (pyridinium-3-yl)porphyrins with alkyl chains of different lengths (7, 9, 11, 13,15 and 17 C atoms) were synthesised and their photophysical and photochemical properties were evaluated. In addition, *in vitro* properties were evaluated on two melanoma cell lines, as well as on fibroblasts used as a normal cell line.

- Zn(II) pyridinium-3-ylporphyrins showed **improved photophysical properties, slightly higher lipophilicity and higher singlet oxygen production compared to their metal-free analogues**. However, Zn(II) porphyrins internalised the cells at slower rates and in overall lower amounts which resulted in similar cytotoxicity as their metal-free analogues.
- Zn(II) pyridinium-3-ylporphyrin with 13 C-atom chain, **25**, showed the high cytotoxicity, lower than 1 μM and high selectivity towards both melanoma cell line. Therefore, **Zn(II) porphyrins of optimal hydrophilic-lipophilic balance could be better PSs than free-base analogues**.
- **The change from the red light irradiation to orange light resulted in higher photon absorption for both, Zn(II) porphyrins and metal free analogues**, resulting in higher cytotoxicity towards tested cell lines.

2. Synthesis and study of the group of *N*-oxidised pyrid-3-ylporphyrins with alkyl chains of 9, 13 and 17 C atoms enabled their comparison with *N*-methylated analogues *in vitro*, against melanoma cell lines in conditions of normoxia and $CoCl_2$-induced hypoxia.

- *N*-oxidised porphyrins **showed better photophysical properties, with longer triplet state lifetime and higher Φ_{ISC}**. Unfortunately, the significantly lower cellular uptake

resulted in lower cytotoxicity to all cell lines tested compared to *N*-methylated analogues. Moreover, under the condition of $CoCl_2$-induced hypoxia, the *N*-oxidised porphyrins resulted in lower cytotoxicity to all cell lines tested. Lower cytotoxicity was observed not only for *N*-oxidised, but also for *N*-methylated porphyrins.

- *N*-oxidised porphyrins with the moiety of HAPs did not show a decrease in cytotoxicity when the pigmented melanoma cell line (MeWo) was tested in comparison to the amelanotic cell line (A375). This indicates that **melanin, which is a ROS scavenger, may be less of an obstacle for the *N*-oxidised porphyrins**.

3.The reduction of porphyrin **2** by Whitlock's diimide reduction or $SnCl_2$ reduction in hot acid was tested.

- The aim in this part could not be fully achieved since **the pure chlorin was not successfully isolated**. The formation of chlorin obtained by both $SnCl_2$ and diimide reduction was confirmed by ^{1}H NMR, however the product was heavily contaminated and not stabile, since it easily oxidised back to the parent porphyrin. Therefore, further spectroscopy and *in vitro* studies were not performed.

4. The design and synthesis of the group of *N*-methylated ^{68}Ga- and Ga(III)-(pyridinium-3-yl)porphyrins was performed to obtain PSs as potential PET/PDT agents. In this part, free-base *N*-methylated pyridinium-3-ylporphyrins were successfully radiolabelled with [^{68}Ga]gallium chloride and prepared formulation showed high stability in serum and against biological chelators proving that these porphyrins can serve as potential PET agents. In addition, the synthesised Ga(III)porphyrins showed moderate cytotoxicity against breast cancer cell line (MDA-MB 231) proving their use for PDT.

- The combination of a both PET and PDT agents in a single formulation with Ga(III) porphyrin was successfully performed with **hydrophilic porphyrin, as well as amphiphilic porphyrins with 9 and 13 C-atom chain**, therefore, they have a potential to **serve as PET/PDT agents**. Furthermore, studying the biodistribution of ^{68}Ga *N*-methylated porphyrins observed by PET-CT scan **showed strong impact of the hydrophilic-lipophilic balance in the biodistribution of a porphyrin radiotracer**.

Overall, the findings obtained in this thesis show that amphiphilic A_3B pyridylporphyrins have a high potential for use as PSs in PDT against melanoma cell lines. This work has pointed out the importance of studying the (photo)physical and (photo)chemical properties of new PSs and in particular the hydrophilic-lipophilic balance of the molecule, which may be crucial for the cellular internalisation of PSs and thus for a better PDT outcome.

Furthermore, the amphiphilic porphyrins studied in this work with the best hydrophilic-lipophilic balance have been shown to be potent molecules that should be further investigated as “ideal PSs” for PDT against melanoma tumours.

6. Literature

[1] D.E.J.G.J. Dolmans, D. Fukumura, R.K. Jain, Photodynamic therapy for cancer, Nat Rev Cancer 3 (2003) 380–387. https://doi.org/10.1038/nrc1071.

[2] P. Agostinis, K. Berg, K.A. Cengel, T.H. Foster, A.W. Girotti, S.O. Gollnick, S.M. Hahn, M.R. Hamblin, A. Juzeniene, D. Kessel, M. Korbelik, J. Moan, P. Mroz, D. Nowis, J. Piette, B.C. Wilson, J. Golab, Photodynamic therapy of cancer: An update, CA Cancer J Clin 61 (2011) 250–281. https://doi.org/10.3322/caac.20114.

[3] L.G. Arnaut, Design of porphyrin-based photosensitizers for photodynamic therapy, in: Rudi van Eldik, Grazyna Stochel (Eds.), Adv Inorg Chem, 2011: pp. 187–233. https://doi.org/10.1016/B978-0-12-385904-4.00006-8.

[4] N. Malatesti, I. Munitic, I. Jurak, Porphyrin-based cationic amphiphilic photosensitisers as potential anticancer, antimicrobial and immunosuppressive agents, Biophys Rev 9 (2017) 149–168. https://doi.org/10.1007/s12551-017-0257-7.

[5] N. Mehraban, H.S. Freeman, Developments in PDT Sensitizers for Increased Selectivity and Singlet Oxygen Production, Materials (Basel) 8 (2015) 4421–4456. https://doi.org/10.3390/ma8074421.

[6] I. Baldea, L. Giurgiu, I.D. Teacoe, D.E. Olteanu, F.C. Olteanu, S. Clichici, G.A. Filip, Photodynamic Therapy in Melanoma - Where do we Stand?, Curr Med Chem 25 (2017) 5540–5563. https://doi.org/10.2174/0929867325666171226115626.

[7] C.N. Honors, C.A. Kruger, H. Abrahamse, Photodynamic therapy for metastatic melanoma treatment: A review, Technol Cancer Res Treat (2018). https://doi.org/10.1177/1533033818791795.

[8] Y.-Y. Huang, D. Vecchio, P. Avci, R. Yin, M. Garcia-Diaz, M.R. Hamblin, Melanoma resistance to photodynamic therapy: new insights, Biol Chem 394 (2013) 239–250. https://doi.org/doi:10.1515/hsz-2012-0228.

[9] J. Dang, H. He, D. Chen, L. Yin, Manipulating tumor hypoxia toward enhanced photodynamic therapy (PDT), Biomater Sci (2017). https://doi.org/10.1039/c7bm00392g.

[10] R.L. Siegel, A.N. Giaquinto, A. Jemal, Cancer statistics, 2024, CA Cancer J Clin 74 (2024) 12–49. https://doi.org/10.3322/caac.21820.

[11] J.H. Correia, J.A. Rodrigues, S. Pimenta, T. Dong, Z. Yang, Photodynamic therapy review: Principles, photosensitizers, applications, and future directions, Pharmaceutics 13 (2021). https://doi.org/10.3390/pharmaceutics13091332.

[12] Á. Juarranz, P. Jaén, F. Sanz-Rodríguez, J. Cuevas, S. González, Photodynamic therapy of cancer. Basic principles and applications, Clinical and Translational Oncology 10 (2008) 148–154. https://doi.org/10.1007/s12094-008-0172-2.

[13] R.R. Allison, K. Moghissi, Photodynamic Therapy (PDT): PDT Mechanisms, Clin Endosc 46 (2013) 24–29. https://doi.org/10.5946/ce.2013.46.1.24.

[14] Dabrowski M Janusz, Arnaut G. Luis, Photodynamic Therapy (PDT)of Cancer: From a Local to a Systemic Treatment, Photochemical & Photobiological Sciences 14 (2015) 1765–1780. https://doi.org/https://doi.org/10.1039/C5PP00132C.

[15] H. Abrahamse, M.R. Hamblin, New photosensitizers for photodynamic therapy, Biochemical Journal 473 (2016) 347–364. https://doi.org/10.1042/BJ20150942.

[16] U. Chilakamarthi, L. Giribabu, Photodynamic Therapy: Past, Present and Future, The Chemical Record 17 (2017) 775–802. https://doi.org/https://doi.org/10.1002/tcr.201600121.

[17] K. Plaetzer, B. Krammer, J. Berlanda, F. Berr, T. Kiesslich, Photophysics and photochemistry of photodynamic therapy: Fundamental aspects, Lasers Med Sci 24 (2009) 259–268. https://doi.org/10.1007/s10103-008-0539-1.

[18] M.S. Baptista, J. Cadet, P. Di Mascio, A.A. Ghogare, A. Greer, M.R. Hamblin, C. Lorente, S.C. Nunez, M.S. Ribeiro, A.H. Thomas, M. Vignoni, T.M. Yoshimura, Type I and Type II Photosensitized Oxidation Reactions: Guidelines and Mechanistic Pathways, Photochem Photobiol 93 (2017) 912–919. https://doi.org/https://doi.org/10.1111/php.12716.

[19] Joseph R. Lakowitz, Introduction to Fluorescence, in: Principles of Fluorescence Spectroscopy, 3rd ed., 2006: pp. 1–26.

[20] J.M. Dąbrowski, Reactive Oxygen Species in Photodynamic Therapy: Mechanisms of Their Generation and Potentiation, in: Adv Inorg Chem, Academic Press Inc., 2017: pp. 343–394. https://doi.org/10.1016/bs.adioch.2017.03.002.

[21] M.C. Derosa, R.J. Crutchley, Photosensitized singlet oxygen and its applications, Coord Chem Rev 233–234 (2002) 351–371. https://doi.org/https://doi.org/10.1016/S0010-8545(02)00034-6.

[22] S. Jockusch, N.J. Turro, E.K. Thompson, M. Gouterman, J.B. Callis, G.E. Khalil, Singlet molecular oxygen by direct excitation, Photochemical and Photobiological Sciences 7 (2008) 235–239. https://doi.org/10.1039/b714286b.

[23] D. Kessel, Critical PDT Theory VI: Detection of Reactive Oxygen Species: Trials and Errors, Photochem Photobiol 99 (2023) 1216–1217. https://doi.org/10.1111/php.13778.

[24] M. Garcia-Diaz, Y.Y. Huang, M.R. Hamblin, Use of fluorescent probes for ROS to tease apart Type I and Type II photochemical pathways in photodynamic therapy, Methods 109 (2016) 158–166. https://doi.org/10.1016/j.ymeth.2016.06.025.

[25] L.B. Josefsen, R.W. Boyle, Unique diagnostic and therapeutic roles of porphyrins and phthalocyanines in photodynamic therapy, imaging and theranostics, Theranostics 2 (2012) 916–966. https://doi.org/10.7150/thno.4571.

[26] P. Attri, Y.H. Kim, D.H. Park, J.H. Park, Y.J. Hong, H.S. Uhm, K.N. Kim, A. Fridman, E.H. Choi, Generation mechanism of hydroxyl radical species and its lifetime prediction during the plasma-initiated ultraviolet (UV) photolysis, Sci Rep 5 (2015). https://doi.org/10.1038/srep09332.

[27] Nonell Santi, Flors Christina, Singlet Oxygen Applications in Biosciences and Nanosciences, 2014. https://doi.org/10.1039/9781782622130-FP007.

[28] P. Di Mascio, G.R. Martinez, S. Miyamoto, G.E. Ronsein, M.H.G. Medeiros, J. Cadet, Singlet Molecular Oxygen Reactions with Nucleic Acids, Lipids, and Proteins, Chem Rev 119 (2019) 2043–2086. https://doi.org/10.1021/acs.chemrev.8b00554.

[29] I.O.L. Bacellar, T.M. Tsubone, C. Pavani, M.S. Baptista, Photodynamic efficiency: From molecular photochemistry to cell death, Int J Mol Sci 16 (2015) 20523–20559. https://doi.org/10.3390/ijms160920523.

[30] E.N. Frankel, Photooxidation of unsaturated fats, in: Lipid Oxidation, Elsevier, 2012: pp. 51–66. https://doi.org/10.1533/9780857097927.51.

[31] T.P.A. Devasagayam, K.P. Jayashree, Biological significance of singlet oxygen, Indian J Exp Biol 40 (2002) 680–692.

[32] B. Epe, Genotoxicity of singlet oxygen, Chem.-Biol. Interactions 80 (1991) 239–260. https://doi.org/https://doi.org/10.1016/0009-2792(91)90086-M.

[33] M.-F. Zuluaga, N. Lange, Combination of Photodynamic Therapy with Anti-Cancer Agents, Curr Med Chem 15 (2008) 1655–1673. https://doi.org/10.2017/09298708784872401.

[34] P. Mroz, A. Yaroslavsky, G.B. Kharkwal, M.R. Hamblin, Cell death pathways in photodynamic therapy of cancer, Cancers (Basel) 3 (2011) 2516–2539. https://doi.org/10.3390/cancers3022516.

[35] C. Donohoe, M.O. Senge, L.G. Arnaut, L.C. Gomes-da-Silva, Cell death in photodynamic therapy: From oxidative stress to anti-tumor immunity, Biochim Biophys Acta Rev Cancer 1872 (2019). https://doi.org/10.1016/j.bbcan.2019.07.003.

[36] T. Mishchenko, I. Balalaeva, A. Gorokhova, M. Vedunova, D. V. Krysko, Which cell death modality wins the contest for photodynamic therapy of cancer?, Cell Death Dis 13 (2022). https://doi.org/10.1038/s41419-022-04851-4.

[37] D. van Straten, V. Mashayekhi, H.S. de Bruijn, S. Oliveira, D.J. Robinson, Oncologic photodynamic therapy: Basic principles, current clinical status and future directions, Cancers (Basel) 9 (2017). https://doi.org/10.3390/cancers9020019.

[38] Plaetzer Kristjan, The Modes of Cell Death Induced by PDT: An Overview, Med.Laser Appl. 18 (2003) 7–19. https://doi.org/1615-1615/03/18/01-007.

[39] R. Alzeibak, T.A. Mishchenko, N.Y. Shilyagina, I. V. Balalaeva, M. V. Vedunova, D. V. Krysko, Targeting immunogenic cancer cell death by photodynamic therapy: Past, present and future, J Immunother Cancer 9 (2021). https://doi.org/10.1136/jitc-2020-001926.

[40] Y. Sun, D. Zhao, G. Wang, Y. Wang, L. Cao, J. Sun, Q. Jiang, Z. He, Recent progress of hypoxia-modulated multifunctional nanomedicines to enhance photodynamic therapy: opportunities, challenges, and future development, Acta Pharm Sin B 10 (2020) 1382–1396. https://doi.org/10.1016/j.apsb.2020.01.004.

[41] S. Bonneau, C. Vever-Bizet, Tetrapyrrole photosensitisers, determinants of subcellular localisation and mechanisms of photodynamic processes in therapeutic approaches, Expert Opin Ther Pat 18 (2008) 1011–1025. https://doi.org/10.1517/13543776.18.9.1011.

[42] R. Falk-Mahapatra, S.O. Gollnick, Photodynamic Therapy and Immunity: An Update, Photochem Photobiol 96 (2020) 550–559. https://doi.org/10.1111/php.13253.

[43] R.K. Pandey, Recent advances in photodynamic therapy, n.d.

[44] L.B. Josefsen, R.W. Boyle, Photodynamic therapy and the development of metal-based photosensitisers, Met Based Drugs 2008 (2008) 276109. https://doi.org/10.1155/2008/276109.

[45] M. Ethirajan, Y. Chen, P. Joshi, R.K. Pandey, The role of porphyrin chemistry in tumor imaging and photodynamic therapy, Chem Soc Rev 40 (2011) 340–362. https://doi.org/10.1039/b915149b.

[46] M.R. Hamblin, Photodynamic Therapy for Cancer: What's Past is Prologue, Photochem Photobiol 96 (2020) 506–516. https://doi.org/10.1111/php.13190.

[47] A.P. Castano, T.N. Demidova, M.R. Hamblin, Mechanisms in photodynamic therapy: Part one - Photosensitizers, photochemistry and cellular localization,

Photodiagnosis Photodyn Ther 1 (2004) 279–293. https://doi.org/10.1016/S1572-1000(05)00007-4.

[48] A.T.P.C. Gomes, M.G.P.M.S. Neves, J.A.S. Cavaleiro, Cancer, Photodynamic Therapy and Porphyrin-Type Derivatives., An Acad Bras Cienc 90 (2018) 993–1026. https://doi.org/10.1590/0001-3765201820170811.

[49] Shirasu Naoto, Ouk Nam Sung, Kuroki Masahide, Tumor-targeted Photodynamic Therapy, Anticancer Res 33 (2013) 2823–2832. https://doi.org/0250-7005/2013.

[50] F. Danhier, O. Feron, V. Préat, To exploit the tumor microenvironment: Passive and active tumor targeting of nanocarriers for anti-cancer drug delivery, Journal of Controlled Release 148 (2010) 135–146. https://doi.org/10.1016/j.jconrel.2010.08.027.

[51] M.A. Rajora, J.W.H. Lou, G. Zheng, Advancing porphyrin's biomedical utility: Via supramolecular chemistry, Chem Soc Rev 46 (2017) 6433–6469. https://doi.org/10.1039/c7cs00525c.

[52] B.P. George, H. Abrahamse, Passive and Active Tumor Targeting in Photodynamic Therapy of Cancer: Mini-Review, J Biomed Photonics Eng 10 (2024) 040201. https://doi.org/10.18287/jbpe24.10.040201.

[53] J. Wu, The enhanced permeability and retention (Epr) effect: The significance of the concept and methods to enhance its application, J Pers Med 11 (2021). https://doi.org/10.3390/jpm11080771.

[54] A.M. Bugaj, Targeted photodynamic therapy - A promising strategy of tumor treatment, Photochemical and Photobiological Sciences 10 (2011) 1097–1109. https://doi.org/10.1039/c0pp00147c.

[55] B.P. George, H. Abrahamse, Passive and Active Tumor Targeting in Photodynamic Therapy of Cancer: Mini-Review, J Biomed Photonics Eng 10 (2024) 040201. https://doi.org/10.18287/jbpe24.10.040201.

[56] P. Sarbadhikary, B.P. George, H. Abrahamse, Recent Advances in Photosensitizers as Multifunctional Theranostic Agents for Imaging-Guided Photodynamic Therapy of Cancer, Theranostics 11 (2021) 9054–9088. https://doi.org/10.7150/thno.62479.

[57] K. Berg, P.K. Selbo, A. Weyergang, A. Dietze, L. Prasmickaite, A. Bonsted, B.Q. Engesaeter, E. Angell-Petersen, T. Warloe, N. Frandsen, A. Hogset, Porphyrin-related photosensitizers for cancer imaging and therapeutic applications, J Microsc 218 (2005) 133–147. https://doi.org/10.1111/j.1365-2818.2005.01471.x.

[58] R. Giovannetti, L. Alibabaei, L. Petetta, Aggregation behaviour of a tetracarboxylic porphyrin in aqueous solution, J Photochem Photobiol A Chem 211 (2010) 108–114. https://doi.org/10.1016/j.jphotochem.2010.02.003.

[59] A.R. Battersby, Tetrapyrroles: The pigments of life, Nat Prod Rep 17 (2000) 507–526. https://doi.org/10.1039/b002635m.

[60] T.P. Wijesekera, D. Dolphin, Some preparations and properties of porphyrins., Adv Exp Med Biol (1985). https://doi.org/10.1007/978-1-4613-2165-1_25.

[61] Y. Lin, T. Zhou, R. Bai, Y. Xie, Chemical approaches for the enhancement of porphyrin skeleton-based photodynamic therapy, J Enzyme Inhib Med Chem 35 (2020) 1080–1099. https://doi.org/10.1080/14756366.2020.1755669.

[62] M.G. Vicente, K. Smith, Porphyrins and Derivatives Synthetic Strategies and Reactivity Profiles, Curr Org Chem 4 (2005) 139–174. https://doi.org/10.2174/1385272003376346.

[63] J.M. Dąbrowski, B. Pucelik, A. Regiel-Futyra, M. Brindell, O. Mazuryk, A. Kyzioł, G. Stochel, W. Macyk, L.G. Arnaut, Engineering of relevant photodynamic processes through structural modifications of metallotetrapyrrolic photosensitizers, Coord Chem Rev 325 (2016) 67–101. https://doi.org/10.1016/j.ccr.2016.06.007.

[64] S. Pisarek, K. Maximova, D. Gryko, Strategies toward the synthesis of amphiphilic porphyrins, Tetrahedron 70 (2014) 6685–6715. https://doi.org/https://doi.org/10.1016/j.tet.2014.05.090.

[65] M. Luciano, C. Br ckner, Modifications of porphyrins and hydroporphyrins for their solubilization in aqueous media, Molecules 22 (2017). https://doi.org/10.3390/molecules22060980.

[66] A.M. Odeh, J.D. Craik, R. Ezzeddine, A. Tovmasyan, I. Batinic-Haberle, L.T. Benov, Targeting Mitochondria by Zn(II)N-Alkylpyridylporphyrins: The Impact of Compound Sub-Mitochondrial Partition on Cell Respiration and Overall Photodynamic Efficacy, PLoS One 9 (2014). https://doi.org/10.1371/journal.pone.0108238.

[67] R. Ezzeddine, A. Al-Banaw, A. Tovmasyan, J.D. Craik, I. Batinic-Haberle, L.T. Benov, Effect of molecular characteristics on cellular uptake, subcellular localization, and phototoxicity of Zn(2) N-Alkylpyridylporphyrins, Journal of Biological Chemistry 288 (2013) 36579–36588. https://doi.org/10.1074/jbc.M113.511642.

[68] R. Hudson, H. Savoie, R.W. Boyle, Lipophilic cationic porphyrins as photodynamic sensitisers—Synthesis and structure–activity relationships, Photodiagnosis Photodyn

Ther 2 (2005) 193–196. https://doi.org/https://doi.org/10.1016/S1572-1000(05)00065-7.

[69] A. Martinez De Pinillos Bayona, P. Mroz, C. Thunshelle, M.R. Hamblin, Design features for optimization of tetrapyrrole macrocycles as antimicrobial and anticancer photosensitizers, Chem Biol Drug Des 89 (2017) 192–206. https://doi.org/10.1111/cbdd.12792.

[70] V. Rapozzi, S. Zorzet, M. Zacchigna, E. Della Pietra, S. Cogoi, L.E. Xodo, Anticancer activity of cationic porphyrins in melanoma tumour-bearing mice and mechanistic in vitro studies, Mol Cancer 13 (2014) 75. https://doi.org/10.1186/1476-4598-13-75.

[71] M. Rojkiewicz, P. Kuś, P. Kozub, M. Kempa, The synthesis of new potential photosensitizers [1]. Part 2. Tetrakis-(hydroxyphenyl)porphyrins with long alkyl chain in the molecule, Dyes and Pigments 99 (2013) 627–635. https://doi.org/https://doi.org/10.1016/j.dyepig.2013.06.029.

[72] M. Jelovica, P. Grbčić, M. Mušković, M. Sedić, S.K. Pavelić, M. Lončarić, N. Malatesti, In Vitro Photodynamic Activity of N-Methylated and N-Oxidised Tripyridyl Porphyrins with Long Alkyl Chains and Their Inhibitory Activity in Sphingolipid Metabolism, ChemMedChem 13 (2018) 360–372. https://doi.org/10.1002/cmdc.201700748.

[73] N. Malatesti, A. Harej, S. Kraljević Pavelić, M. Lončarić, H. Zorc, K. Wittine, U. Andjelkovic, D. Josic, Synthesis, characterisation and in vitro investigation of photodynamic activity of 5-(4-octadecanamidophenyl)-10,15,20-tris(N-methylpyridinium-3-yl)porphyrin trichloride on HeLa cells using low light fluence rate, Photodiagnosis Photodyn Ther 15 (2016) 115–126. https://doi.org/https://doi.org/10.1016/j.pdpdt.2016.07.003.

[74] M.C. Malacarne, M.B. Gariboldi, E. Marras, E. Caruso, Could the Length of the Alkyl Chain Affect the Photodynamic Activity of 5,10,15,20-Tetrakis(1-alkylpyridinium-4-yl)porphyrins?, Molecules 29 (2024) 1285. https://doi.org/10.3390/molecules29061285.

[75] A.M. Burloiu, D.P. Mihai, G. Manda, D. Lupuliasa, I.V. Neagoe, R.P. Socoteanu, M. Surcel, L.-I. Anghelache, L. Olariu, C.E. Gîrd, R. Boscencu, In Silico and In Vitro Studies on an Asymmetrical Porphyrin Derivative with Therapeutic Potential in Skin Disorders, Pharmaceuticals 17 (2024) 688. https://doi.org/10.3390/ph17060688.

[76] M. Bhat, R. Jatyan, A. Mittal, R.I. Mahato, D. Chitkara, Opportunities and challenges of fatty acid conjugated therapeutics, Chem Phys Lipids 236 (2021). https://doi.org/10.1016/j.chemphyslip.2021.105053.

[77] M.G.V. Heiden, L.C. Cantley, C.B. Thompson, Understanding the warburg effect: The metabolic requirements of cell proliferation, Science (1979) 324 (2009) 1029–1033. https://doi.org/10.1126/science.1160809.

[78] L. Zhang, Y. Yao, S. Liu, Targeting fatty acid metabolism for cancer therapy, Fundamental Research (2024). https://doi.org/10.1016/j.fmre.2024.09.011.

[79] S.R. Nagarajan, L.M. Butler, A.J. Hoy, The diversity and breadth of cancer cell fatty acid metabolism, Cancer Metab 9 (2021). https://doi.org/10.1186/s40170-020-00237-2.

[80] L. Pellerin, L. Carrié, C. Dufau, L. Nieto, B. Ségui, T. Levade, J. Riond, N. Andrieu-Abadie, Lipid metabolic reprogramming: Role in melanoma progression and therapeutic perspectives, Cancers (Basel) 12 (2020) 1–33. https://doi.org/10.3390/cancers12113147.

[81] D. Innocenzi, P.L. Alò, A. Balzani, V. Sebastiani, V. Silipo, G. La Torre, G. Ricciardi, C. Bosman, S. Calvieri, Fatty acid synthase expression in melanoma, J Cutan Pathol 30 (2003) 23–28. https://doi.org/10.1034/j.1600-0560.2003.300104.x.

[82] S. Bonsall, S. Hubbard, U. Jithin, J. Anslow, D. Todd, C. Rowding, T. Filarowski, G. Duly, R. Wilson, J. Porter, S. Turega, S. Haywood-Small, Water-Soluble Truncated Fatty Acid–Porphyrin Conjugates Provide Photo-Sensitizer Activity for Photodynamic Therapy in Malignant Mesothelioma, Cancers (Basel) 14 (2022). https://doi.org/10.3390/cancers14215446.

[83] B.P.P. McCormick, M.F. Pansa, L.N.M. Sanabria, C.M.B. Carvalho, M.A.F. Faustino, M.G.P.M.S. Neves, J.A.S. Cavaleiro, N.B.R. Vittar, V.A. Rivarola, Cationic porphyrin derivatives for application in photodynamic therapy of cancer, Laser Phys 24 (2014). https://doi.org/10.1088/1054-660X/24/4/045603.

[84] Y.E. Yegorov, K.S. Vishnyakova, X. Pan, A.E. Egorov, K. V. Popov, L.L. Tevonyan, G. V. Chashchina, D.N. Kaluzhny, Mechanisms of Phototoxic Effects of Cationic Porphyrins on Human Cells In Vitro, Molecules 28 (2023). https://doi.org/10.3390/molecules28031090.

[85] J.W. Snyder, J.D.C. Lambert, P.R. Ogilby, 5,10,15,20-Tetrakis(N-Methyl-4-Pyridyl)-21 H,23H-Porphine (TMPyP) as a Sensitizer for Singlet Oxygen Imaging in Cells: Characterizing the Irradiation-dependent Behavior of TMPyP in a Single Cell†, Photochem Photobiol 82 (2006) 177–184. https://doi.org/10.1562/2005-05-30-RA-553.

[86] F.M. Engelmann, I. Mayer, D.S. Gabrielli, H.E. Toma, A.J. Kowaltowski, K. Araki, M.S. Baptista, Interaction of cationic meso-porphyrins with liposomes, mitochondria and erythrocytes, J Bioenerg Biomembr 39 (2007) 175. https://doi.org/10.1007/s10863-007-9075-0.

[87] T.J. Jensen, M.G.H. Vicente, R. Luguya, J. Norton, F.R. Fronczek, K.M. Smith, Effect of overall charge and charge distribution on cellular uptake, distribution and phototoxicity of cationic porphyrins in HEp2 cells, J Photochem Photobiol B 100 (2010) 100–111. https://doi.org/10.1016/j.jphotobiol.2010.05.007.

[88] G. Abbas, F. Alibrahim, R. Kankouni, S. Al-Belushi, D.A. Al-Mutairi, A. Tovmasyan, I. Batinic-Haberle, L. Benov, Effect of the nature of the chelated metal on the photodynamic activity of metalloporphyrins, Free Radic Res 57 (2023) 487–499. https://doi.org/10.1080/10715762.2023.2288997.

[89] J. Sandland, N. Malatesti, R. Boyle, Porphyrins and related macrocycles: Combining photosensitization with radio- or optical-imaging for next generation theranostic agents, Photodiagnosis Photodyn Ther 23 (2018) 281–294. https://doi.org/10.1016/j.pdpdt.2018.06.023.

[90] C. Pavani, A.F. Uchoa, C.S. Oliveira, Y. Iamamoto, M.S. Baptista, Effect of zinc insertion and hydrophobicity on the membrane interactions and PDT activity of porphyrin photosensitizers, Photochemical & Photobiological Sciences 8 (2009) 233–240. https://doi.org/10.1039/B810313E.

[91] G. Klein Couto, J.C. Rodrigues, B.S. Pacheco, L. Damé Simões, J.D. Paschoal, F.K. Seixas, T. V. Acunha, B.A. Iglesias, T. Collares, Zinc(II), copper(II) and nickel(II) ions improve the selectivity of tetra-cationic platinum(II) porphyrins in photodynamic therapy and stimulate antioxidant defenses in the metastatic melanoma lineage (A375), Photodiagnosis Photodyn Ther 31 (2020). https://doi.org/10.1016/j.pdpdt.2020.101942.

[92] L. Benov, Photodynamic Therapy: Current Status and Future Directions, Medical Principles and Practice 24(suppl 1 (2015) 14–28. https://doi.org/10.1159/000362416.

[93] L. Benov, J. Craik, I. Batinic-Haberle, The Potential of Zn(II) N-Alkylpyridylporphyrins for Anticancer Therapy, Anticancer Agents Med Chem 11 (2012) 233–241. https://doi.org/10.2174/187152011795255975.

[94] X.X. Peng, S. Gao, J.L. Zhang, Gallium (III) Complexes in Cancer Chemotherapy, Eur J Inorg Chem 2022 (2022). https://doi.org/10.1002/ejic.202100953.

[95] T.H.S. Souza, J.F. Sarmento-Neto, S.O. Souza, B.L. Raposo, B.P. Silva, C.P.F. Borges, B.S. Santos, P.E. Cabral Filho, J.S. Rebouças, A. Fontes, Advances on antimicrobial photodynamic inactivation mediated by Zn(II) porphyrins, Journal of Photochemistry and Photobiology C: Photochemistry Reviews 49 (2021). https://doi.org/10.1016/j.jphotochemrev.2021.100454.

[96] M. Kobus, T. Friedrich, E. Zorn, N. Burmeister, W. Maison, Medicinal Chemistry of Drugs with N-Oxide Functionalities, J Med Chem 67 (2024) 5168–5184. https://doi.org/10.1021/acs.jmedchem.4c00254.

[97] D. Bernier, U.K. Wefelscheid, S. Woodward, Properties, preparation and synthetic uses of amine n-oxides. An update, Org Prep Proced Int 41 (2009) 173–210. https://doi.org/10.1080/00304940902955756.

[98] M.J.Dp. Brown, Exploiting the hypoxic cancer cell: mechanisms and therapeutic strategies, Mol Med Today 6 (2000) 157–162. https://doi.org/10.1016/s1357-4310(00)01677-4.

[99] W.A. Denny, The role of hypoxia-activated prodrugs in cancer therapy, Lancet Oncology 1 (2000) 25–29. https://doi.org/10.1016/S1470-2045(00)00006-1.

[100] C.P. Guise, A.M. Mowday, A. Ashoorzadeh, R. Yuan, W.H. Lin, D.H. Wu, J.B. Smaill, A. V. Patterson, K. Ding, Bioreductive prodrugs as cancer therapeutics: Targeting tumor hypoxia, Chin J Cancer 33 (2014) 80–86. https://doi.org/10.5732/cjc.012.10285.

[101] J. Dang, H. He, D. Chen, L. Yin, Manipulating tumor hypoxia toward enhanced photodynamic therapy (PDT), Biomater Sci 5 (2017) 1500–1511. https://doi.org/10.1039/c7bm00392g.

[102] H. Cerecetto, M. González, N-Oxides as Hypoxia Selective Cytotoxins, Mini Rev Med Chem 1 (2001) 219–231. https://doi.org/10.2174/1389557013406891.

[103] A.M. Mfuh, O. V Larionov, Heterocyclic N-Oxides-An Emerging Class of Therapeutic Agents, n.d.

[104] W.R. Wilson, M.P. Hay, Targeting hypoxia in cancer therapy, Nat Rev Cancer 11 (2011) 393–410. https://doi.org/10.1038/nrc3064.

[105] X. Li, S. Kolemen, J. Yoon, E.U. Akkaya, Activatable Photosensitizers: Agents for Selective Photodynamic Therapy, Adv Funct Mater 27 (2017) 1604053. https://doi.org/10.1002/adfm.201604053.

[106] B. Pucelik, A. Sułek, A. Barzowska, J.M. Dąbrowski, Recent advances in strategies for overcoming hypoxia in photodynamic therapy of cancer, Cancer Lett 492 (2020) 116–135. https://doi.org/10.1016/j.canlet.2020.07.007.

[107] Z. Shen, Q. Ma, X. Zhou, G. Zhang, G. Hao, Y. Sun, J. Cao, Strategies to improve photodynamic therapy efficacy by relieving the tumor hypoxia environment, NPG Asia Mater 13 (2021). https://doi.org/10.1038/s41427-021-00303-1.

[108] Y. Dai, B. Wang, Z. Sun, J. Cheng, H. Zhao, K. Wu, P. Sun, Q. Shen, M. Li, Q. Fan, Multifunctional Theranostic Liposomes Loaded with a Hypoxia-Activated Prodrug for Cascade-Activated Tumor Selective Combination Therapy, ACS Appl Mater Interfaces 11 (2019) 39410–39423. https://doi.org/10.1021/acsami.9b11080.

[109] L. Feng, L. Cheng, Z. Dong, D. Tao, T.E. Barnhart, W. Cai, M. Chen, Z. Liu, Theranostic Liposomes with Hypoxia-Activated Prodrug to Effectively Destruct Hypoxic Tumors Post-Photodynamic Therapy, ACS Nano 11 (2017) 927–937. https://doi.org/10.1021/acsnano.6b07525.

[110] Ü. Anık, S. Timur, Z. Dursun, Recent pros and cons of nanomaterials in drug delivery systems, International Journal of Polymeric Materials and Polymeric Biomaterials 69 (2020) 1090–1100. https://doi.org/10.1080/00914037.2019.1655753.

[111] J.J. Posakony, R.C. Pratt, S.J. Rettig, B.R. James, K.A. Skov, Porphyrins incorporating heterocyclic N-oxides: (oxidopyridyl)porphyrins, porphyrin-N-oxides, and a tirapazamine-porphyrin conjugate, Can J Chem 77 (1999) 182–198.

[112] L.E. Andrews, R. Bonnett, R.J. Ridge, E.H. Appelman, The Preparation and Reactions of Porphyrin N-Oxides, Journal of the Chemical Society, Perkin Transactions I (1983) 103–107. https://doi.org/10.1039/P19830000103.

[113] M.M. Kim, A.A. Ghogare, A. Greer, T.C. Zhu, On the in vivo photochemical rate parameters for PDT reactive oxygen species modeling, Phys Med Biol 62 (2017) R1–R48. https://doi.org/10.1088/1361-6560/62/5/R1.

[114] M.M. Kim, A. Darafsheh, Light Sources and Dosimetry Techniques for Photodynamic Therapy, Photochem Photobiol 96 (2020) 280–294. https://doi.org/10.1111/php.13219.

[115] S. Mallidi, S. Anbil, A.L. Bulin, G. Obaid, M. Ichikawa, T. Hasan, Beyond the barriers of light penetration: Strategies, perspectives and possibilities for photodynamic therapy, Theranostics 6 (2016) 2458–2487. https://doi.org/10.7150/thno.16183.

[116] G. Gunaydin, M.E. Gedik, S. Ayan, Photodynamic Therapy for the Treatment and Diagnosis of Cancer–A Review of the Current Clinical Status, Front Chem 9 (2021). https://doi.org/10.3389/fchem.2021.686303.

[117] I. Ratkaj, M. Mušković, N. Malatesti, Targeting Microenvironment of Melanoma and Head and Neck Cancers in Photodynamic Therapy, Curr Med Chem 29 (2021) 3261–3299. https://doi.org/10.2174/0929867328666210709113032.

[118] F.R. Balkwill, M. Capasso, T. Hagemann, The tumor microenvironment at a glance, J Cell Sci 125 (2012) 5591–5596. https://doi.org/10.1242/jcs.116392.

[119] A.J. Sorrin, M. Kemal Ruhi, N.A. Ferlic, V. Karimnia, W.J. Polacheck, J.P. Celli, H.C. Huang, I. Rizvi, Photodynamic Therapy and the Biophysics of the Tumor Microenvironment, Photochem Photobiol 96 (2020) 232–259. https://doi.org/10.1111/php.13209.

[120] F.R. Balkwill, M. Capasso, T. Hagemann, The tumor microenvironment at a glance, J Cell Sci 125 (2012) 5591–5596. https://doi.org/10.1242/jcs.116392.

[121] R.K. Jain, Normalizing tumor microenvironment to treat cancer: Bench to bedside to biomarkers, in: Journal of Clinical Oncology, American Society of Clinical Oncology, 2013: pp. 2205–2218. https://doi.org/10.1200/JCO.2012.46.3653.

[122] R.K. Jain, J.D. Martin, T. Stylianopoulos, The role of mechanical forces in tumor growth and therapy, Annu Rev Biomed Eng 16 (2014) 321–346. https://doi.org/10.1146/annurev-bioeng-071813-105259.

[123] R. Burgos-Panadero, F. Lucantoni, E. Gamero-Sandemetrio, L. de la Cruz-Merino, T. Álvaro, R. Noguera, The tumour microenvironment as an integrated framework to understand cancer biology, Cancer Lett 461 (2019) 112–122. https://doi.org/10.1016/j.canlet.2019.07.010.

[124] M. Kalli, T. Stylianopoulos, Defining the role of solid stress and matrix stiffness in cancer cell proliferation and metastasis, Front Oncol 8 (2018). https://doi.org/10.3389/fonc.2018.00055.

[125] P. Purkayastha, M.K. Jaiswal, T.P. Lele, Molecular cancer cell responses to solid compressive stress and interstitial fluid pressure, Cytoskeleton 78 (2021) 312–322. https://doi.org/10.1002/cm.21680.

[126] J.P. Piret, D. Mottet, M. Raes, C. Michiels, CoCl2, a chemical inducer of hypoxia-inducible factor-1, and hypoxia reduce apoptotic cell death in hepatoma cell line HepG2, in: Ann N Y Acad Sci, New York Academy of Sciences, 2002: pp. 443–447. https://doi.org/10.1111/j.1749-6632.2002.tb04680.x.

[127] L. Larue, B. Myrzakhmetov, A. Ben-Mihoub, A. Moussaron, N. Thomas, P. Arnoux, F. Baros, R. Vanderesse, S. Acherar, C. Frochot, Fighting hypoxia to improve PDT, Pharmaceuticals 12 (2019). https://doi.org/10.3390/ph12040163.

[128] K. Saginala, A. Barsouk, J.S. Aluru, P. Rawla, A. Barsouk, Epidemiology of Melanoma, Med Sci (Basel) 9 (2021). https://doi.org/10.3390/medsci9040063.

[129] P. Koczkodaj, U. Sulkowska, J. Didkowska, P. Rutkowski, M. Mańczuk, Melanoma Mortality Trends in 28 European Countries: A Retrospective Analysis for the Years 1960–2020, Cancers (Basel) 15 (2023). https://doi.org/10.3390/cancers15051514.

[130] Arnold Melina, Singh Deependra, Laversanne Mathiew, Global Burden of Cutaneous Melanoma in 2020 and Projections to 2040, JAMA Dermatol 158 (2022) 495–503.

[131] F. Solano, Photoprotection and skin pigmentation: Melanin-related molecules and some other new agents obtained from natural sources, Molecules 25 (2020). https://doi.org/10.3390/molecules25071537.

[132] D. Schadendorf, A.C.J. van Akkooi, C. Berking, K.G. Griewank, R. Gutzmer, A. Hauschild, A. Stang, A. Roesch, S. Ugurel, Melanoma, The Lancet 392 (2018) 971–984. https://doi.org/10.1016/S0140-6736(18)31559-9.

[133] M. Cichorek, M. Wachulska, A. Stasiewicz, Heterogeneity of neural crest-derived melanocytes, Cent Eur J Biol 8 (2013) 315–330. https://doi.org/10.2478/s11535-013-0141-1.

[134] R.M. Slominski, T. Sarna, P.M. Płonka, C. Raman, A.A. Brożyna, A.T. Slominski, Melanoma, Melanin, and Melanogenesis: The Yin and Yang Relationship, Front Oncol 12 (2022). https://doi.org/10.3389/fonc.2022.842496.

[135] H.G.M. Wittgen, L. On, C.L.T. Van Kempen, Reactive oxygen species in melanoma and its therapeutic implications Reactive oxygen species, Wolters Kluwer Health | Lippincott Williams & Wilkins, 2007.

[136] K.G. Chen, J.C. Valencia, J.P. Gillet, V.J. Hearing, M.M. Gottesman, Involvement of ABC transporters in melanogenesis and the development of multidrug resistance of melanoma, Pigment Cell Melanoma Res 22 (2009) 740–749. https://doi.org/10.1111/j.1755-148X.2009.00630.x.

[137] R.E. Vera, M.J. Lamberti, V.A. Rivarola, N.B. Rumie Vittar, Developing strategies to predict photodynamic therapy outcome: the role of melanoma microenvironment, Tumor Biology 36 (2015) 9127–9136. https://doi.org/10.1007/s13277-015-4059-x.

[138] P.R. Upadhyay, R.J. Starner, V.B. Swope, K. Wakamatsu, S. Ito, Z.A. Abdel-Malek, Differential Induction of Reactive Oxygen Species and Expression of Antioxidant Enzymes in Human Melanocytes Correlate with Melanin Content: Implications on the Response to Solar UV and Melanoma Susceptibility, Antioxidants 11 (2022). https://doi.org/10.3390/antiox11061204.

[139] I. Baldea, L. Giurgiu, I.D. Teacoe, D.E. Olteanu, F.C. Olteanu, S. Clichici, G.A. Filip, Photodynamic Therapy in Melanoma - Where do we Stand?, Curr Med Chem 25 (2017) 5540–5563. https://doi.org/10.2174/0929867325666171226115626.

[140] M. Rozanowska, T. Sarna, E.J. Land, T. George Truscott, Free radical scavenging properties of melanin interaction of eu- and pheo-melanin models with reducing and oxidising radicals, Free Radic Biol Med 26 (1999) 518–522.

[141] I. Baldea, D.E. Olteanu, P. Bolfa, R.M. Ion, N. Decea, M. Cenariu, M. Banciu, A.V. Sesarman, A.G. Filip, Efficiency of photodynamic therapy on WM35 melanoma with synthetic porphyrins: Role of chemical structure, intracellular targeting and antioxidant defense, J Photochem Photobiol B 151 (2015) 142–152. https://doi.org/10.1016/j.jphotobiol.2015.07.019.

[142] I. Baldea, D.E. Olteanu, P. Bolfa, F. Tabaran, R.M. Ion, G.A. Filip, Melanogenesis and DNA damage following photodynamic therapy in melanoma with two meso-substituted porphyrins, J Photochem Photobiol B 161 (2016) 402–410. https://doi.org/10.1016/j.jphotobiol.2016.06.012.

[143] G. Kramer-Marek, C. Serpa, A. Szurko, M. Widel, A. Sochanik, M. Snietura, P. Kus, R.M.D. Nunes, L.G. Arnaut, A. Ratuszna, Spectroscopic properties and photodynamic effects of new lipophilic porphyrin derivatives: Efficacy, localisation and cell death pathways, J Photochem Photobiol B 84 (2006) 1–14. https://doi.org/10.1016/j.jphotobiol.2005.12.011.

[144] N. Tsolekile, O. Oluwafemi, S. Nelana, Porphyrin as diagnostic and therapeutic agent, Molecules 24 (2019) 2669. https://doi.org/10.3390/molecules24142669.

[145] P. Mikuš, M. Melník, A. Forgácsová, D. Krajčiová, E. Havránek, Gallium compounds in nuclear medicine and oncology, Main Group Metal Chemistry 37 (2014) 53–65. https://doi.org/10.1515/mgmc-2014-0009.

[146] S.Y. Yap, T.W. Price, H. Savoie, R.W. Boyle, G.J. Stasiuk, Selective radiolabelling with 68Ga under mild conditions: A route towards a porphyrin PET/PDT theranostic agent, Chemical Communications 54 (2018) 7952–7954. https://doi.org/10.1039/c8cc03897j.

[147] P. Sarbadhikary, B.P. George, H. Abrahamse, Recent advances in photosensitizers as multifunctional theranostic agents for imaging-guided photodynamic therapy of cancer, Theranostics 11 (2021) 9054–9088. https://doi.org/10.7150/thno.62479.

[148] P.A. Waghorn, Radiolabelled porphyrins in nuclear medicine, J Labelled Comp Radiopharm 57 (2014) 304–309. https://doi.org/10.1002/jlcr.3166.

[149] F. Bryden, R.W. Boyle, Metalloporphyrins for Medical Imaging Applications, in: Adv Inorg Chem, Academic Press Inc., 2016: pp. 141–221. https://doi.org/10.1016/bs.adioch.2015.09.003.

[150] Dirac Paul, Quantised singularities in the electromagnetic field, Proceedings of the Royal Society of London. Series A, Containing Papers of a Mathematical and Physical Character 133 (1931) 60–72. https://doi.org/10.1098/rspa.1931.0130.

[151] V. Kapoor, B.M. McCook, F.S. Torok, An introduction to PET-CT imaging, Radiographics 24 (2004) 523–543. https://doi.org/10.1148/rg.242025724.

[152] M.D. Farwell, D.A. Pryma, D.A. Mankoff, PET/CT imaging in cancer: Current applications and future directions, Cancer 120 (2014) 3433–3445. https://doi.org/10.1002/cncr.28860.

[153] K. Pyrzynska, K. Kilian, M. Pęgier, Porphyrins as Chelating Agents for Molecular Imaging in Nuclear Medicine, Molecules 27 (2022). https://doi.org/10.3390/molecules27103311.

[154] Z. Li, P.S. Conti, Radiopharmaceutical chemistry for positron emission tomography, Adv Drug Deliv Rev 62 (2010) 1031–1051. https://doi.org/10.1016/j.addr.2010.09.007.

[155] F. Rösch, 68Ge/68Ga Generators: Past, present, and future, Recent Results in Cancer Research 194 (2013) 3–16. https://doi.org/10.1007/978-3-642-27994-2_1.

[156] F. Bryden, H. Savoie, E. V. Rosca, R.W. Boyle, PET/PDT theranostics: Synthesis and biological evaluation of a peptide-targeted gallium porphyrin, Dalton Transactions 44 (2015) 4925–4932. https://doi.org/10.1039/c4dt02949f.

[157] B. Behnam Azad, C.F. Cho, J.D. Lewis, L.G. Luyt, Synthesis, radiometal labeling and in vitro evaluation of a targeted PPIX derivative, Applied Radiation and Isotopes 70 (2012) 505–511. https://doi.org/10.1016/j.apradiso.2011.11.054.

[158] Y. Fazaeli, M.A. Hosseini, F. Shahabinia, S. Feizi, 68Ga-5, 10, 15, 20-Tetrakis (2, 4, 6-trimethoxy phenyl) porphyrin: a novel radio-labeled porphyrin complex for positron emission tomography, J Radioanal Nucl Chem 320 (2019) 201–207. https://doi.org/10.1007/s10967-019-06465-1.

[159] Y. Fazaeli, A.R. Jalilian, M.M. Amini, K. Ardaneh, A. Rahiminejad, F. Bolourinovin, S. Moradkhani, A. Majdabadi, Development of a 68Ga-Fluorinated Porphyrin Complex as a Possible PET Imaging Agent, Nucl Med Mol Imaging 46 (2012) 20–26. https://doi.org/10.1007/s13139-011-0109-5.

[160] M. Bhadwal, T. Das, H. Dev Sarma, S. Banerjee, Radiosynthesis and Bioevaluation of [68Ga]-Labeled 5,10,15,20-Tetra(4-methylpyridyl)-porphyrin for Possible Application as a PET Radiotracer for Tumor Imaging, Mol Imaging Biol 17 (2015) 111–118. https://doi.org/10.1007/s11307-014-0760-1.

[161] M. Guleria, S.K. Suman, J.B. Mitra, S.B. Shelar, J. Amirdhanayagam, H.D. Sarma, A. Dash, T. Das, Effect of structural variation on tumor targeting efficacy of cationically charged porphyrin derivatives: Comparative in-vitro and in-vivo evaluation for possible potential in PET and PDT, Eur J Med Chem 213 (2021). https://doi.org/10.1016/j.ejmech.2021.113184.

[162] M. Mušković, I. Ćavar, A. Lesar, M. Lončarić, N. Malatesti, I. Gobin, Photodynamic Inactivation of Legionella pneumophila Biofilm Formation by Cationic Tetra- and Tripyridylporphyrins in Waters of Different Hardness, Int J Mol Sci 22 (2021) 9095. https://doi.org/10.3390/ijms22169095.

[163] M. Mušković, I. Džeba, I. Antol, N. Basarić, N. Malatesti, Photophysical properties of 5-(4-acetamidophenyl)-10,15,20-tris(N-methylpyridinium-3-yl)porphyrin trichloride and its Zn(II) complex, J Photochem Photobiol A Chem 444 (2023) 114939. https://doi.org/10.1016/j.jphotochem.2023.114939.

[164] F.A. Schaberle, Assessment of the actual light dose in photodynamic therapy, Photodiagnosis Photodyn Ther 23 (2018) 75–77. https://doi.org/10.1016/j.pdpdt.2018.06.009.

[165] Novak, Laser photolysis and spectroscopy: a new technique for the study of rapid reactions in the nanosecond time range, Proc R Soc Lond A Math Phys Sci 308 (1968) 95–110. https://doi.org/10.1098/rspa.1968.0210.

[166] I. Carmichael, G.L. Hug', Triplet-Triplet Absorption Spectra of Organic Molecules in Condensed Phases, J. Phys.Chem.Ref. Dara 15 (1986) 1–250. https://doi.org/10.1063/1.555770.

[167] R.V.. Bensasson, E.J.. Land, T.G.. Truscott, Flash photolysis and pulse radiolysis : contributions to the chemistry of biology and medicine, Pergamon, 1983.

[168] R.V.. Bensasson, E.J.. Land, T.G.. Truscott, Flash photolysis and pulse radiolysis : contributions to the chemistry of biology and medicine, Pergamon, 1983.

[169] R. Bonnett, D.J. McGarvey, A. Harriman, E.J. Land, T.G. Truscott, U. -J Winfield, Photophysical Properties of meso-tetrephanylporphyrin and Some meso-tetra(hydroxyphenyl)porphyrins, Photochem Photobiol 48 (1988) 271–276. https://doi.org/10.1111/j.1751-1097.1988.tb02820.x.

[170] T.H. Tran-Thi, C. Desforge, C. Thiec, S. Gaspard, Singlet-Singlet and Triplet-Triplet Intramolecular Transfer Processes in a Covalently Linked Porphyrin-Phthalocyanine Heterodimer, J. Phys. Chem 93 (1989) 1226–1233.

[171] I. Kos, J.S. Rebouças, G. DeFreitas-Silva, D. Salvemini, Z. Vujaskovic, M.W. Dewhirst, I. Spasojević, I. Batinić-Haberle, Lipophilicity of potent porphyrin-based antioxidants: Comparison of ortho and meta isomers of Mn(III) N-alkylpyridylporphyrins, Free Radic Biol Med 47 (2009) 72–78. https://doi.org/https://doi.org/10.1016/j.freeradbiomed.2009.04.002.

[172] P. Kanellopoulos, E. Lymperis, A. Kaloudi, M. de Jong, E.P. Krenning, B.A. Nock, T. Maina, [99mTc]Tc-DB1 mimics with different-length PEG spacers: Preclinical comparison in GRPR-positive models, Molecules 25 (2020) 3418. https://doi.org/10.3390/molecules25153418.

[173] A.A. Hörmann, M. Klingler, C. Rangger, C. Mair, C. Decristoforo, C. Uprimny, I.J. Virgolini, E. von Guggenberg, Radiopharmaceutical formulation and preclinical

testing of68ga-labeled dota-mgs5 for the regulatory approval of a first exploratory clinical trial, Pharmaceuticals 14 (2021) 575. https://doi.org/10.3390/ph14060575.

[174] D. Satpati, R. Sharma, H.D. Sarma, A. Dash, Comparative evaluation of 68 Ga-labeled NODAGA, DOTAGA, and HBED-CC-conjugated cNGR peptide chelates as tumor-targeted molecular imaging probes, Chem Biol Drug Des 91 (2018) 781–788. https://doi.org/10.1111/cbdd.13143.

[175] P. Rothemund, A New Porphyrin Synthesis. The Synthesis of Porphin, Journal Od the American Chemical Society 58 (1936) 625–627. https://doi.org/10.1021/ja'1295a027.

[176] P. Rothemund, A. Menotti, Porphyrin Studies. IV.1 The Synthesis of α,β,γ,δ-Tetraphenylporphine, Journal of the American Society 63 (1941) 267–270. https://doi.org/10.1021/JA1846A065.

[177] Adler D Alan, Longo Frederick, Finarelli John, A Simplified Synthesis for meso-Tetraphenylporphin, J Org Chem 32 (1967) 467–477. https://doi.org/10.1021/JO01288A053.

[178] B.M. Amos-Tautua, S.P. Songca, O.S. Oluwafemi, Application of porphyrins in antibacterial photodynamic therapy, Molecules 24 (2019). https://doi.org/10.3390/molecules24132456.

[179] J.S. Lindsey, I.C. Schreiman, H.C. Hsu, P.C. Kearney, A.M. Marguerettaz, Rothemund and Adler-Longo Reaction Revisited: Synthesis of Tetraphenylporphyrins under Equilibrium Conditions, J Org Chem 52 (1987) 827–836. https://doi.org/10.1021/jo00381a022.

[180] E. Fagadar-Cosma, E. Fagadar-Cosma, I. Creanga, B. Maranescu, A. Palade, A. Lőrinczi, G. Fagadar-Cosma, M. Popescu, Dependence of Optical Response on Ph Of A Water-Soluble Zn(II)-Metalloporphyrin, Dig J Nanomater Biostruct 6 (2011) 75–80. https://www.researchgate.net/publication/261173412.

[181] S.S. Bharate, Recent developments in pharmaceutical salts: FDA approvals from 2015 to 2019, Drug Discov Today 26 (2021) 384–398. https://doi.org/10.1016/j.drudis.2020.11.016.

[182] E.B. Fleischer, A.M. Shachter, Coordination Oligomers and a Coordination Polymer of Zinc Tetraarylporphyrins, Inorg Chem 30 (1991) 3763–3769. https://doi.org/10.1021/ic00019a038.

[183] E. V. Ermakova, I.N. Meshkov, Y. Yu. Enakieva, A.I. Zvyagina, A.A. Ezhov, A.A. Mikhaylov, Y.G. Gorbunova, V. V. Chernyshev, M.A. Kalinina, V. V. Arslanov, Effect of metalation-demetalation reactions on the assembly and properties of 2D

supramolecular arrays of tetrapyridylporphyrin and its Zn(II)-complex, Surf Sci 660 (2017) 39–46. https://doi.org/10.1016/j.susc.2017.02.007.

[184] G.M. Entract, F. Bryden, J. Domarkas, H. Savoie, L. Allott, S.J. Archibald, C. Cawthorne, R.W. Boyle, Development of PDT/PET Theranostics: Synthesis and Biological Evaluation of an 18F-Radiolabeled Water-Soluble Porphyrin, Mol Pharm 12 (2015) 4414–4423. https://doi.org/10.1021/acs.molpharmaceut.5b00606.

[185] G.P. Gurinovich, A.N. Sevchenko, K.N. Solov'ev, The Spectroscopy of Porphyrins, Soviet Physics Uspekhi 6 (1963) 173–234. http://iopscience.iop.org/0038-5670/6/1/R04.

[186] M. Ste˛pień, L. Latos-Graz.yński, Aromaticity and Tautomerism in Porphyrins and Porphyrinoids, in: 2008. https://doi.org/10.1007/7081_2008_4.

[187] K. Kano, H. Minamizono, T. Kitae, S. Negi, Self-Aggregation of Cationic Porphyrins in Water. Can π-π Stacking Interaction Overcome Electrostatic Repulsive Force?, Journal of Physical Chemistry 101 (1997) 6118–6124. https://doi.org/10.1021/jp9710446.

[188] R.W. Seidel, R. Goddard, C. Hoch, J. Breidung, I.M. Oppel, On the structure of unsolvated free-base 5,10,15,20-tetra(3-pyridyl)porphyrin, J Mol Struct 985 (2011) 307–315. https://doi.org/https://doi.org/10.1016/j.molstruc.2010.11.011.

[189] M. Gouterman, G.H. Wagniere, L.C. Snyder, Spectra of Porphyrins Part II. Four Orbital Model, J Mol Spectrosc 11 (1963) 108–127. https://doi.org/10.1016/0022.2852(63)90011-0.

[190] M. Gouterman, Spectra of Porphyrins*, J Mol Spectrosc 6 (1961) 138–163. https://doi.org/10.1016/0022-2852(61)90236-3.

[191] Milgrom L.R, The Colours of Life: An Introduction to the Chemistry of Porphyrins and Related Compounds, Oxford Academic Books, 1997. https://doi.org/10.1093/oso/9780198553809.001.0001.

[192] J.M.S. Lopes, J.R.T. Reis, A.E.H. Machado, T.H.O. Leite, A.A. Batista, T. V. Acunha, B.A. Iglesias, P.T. Araujo, N.M. Barbosa Neto, Influence of the meso-substituents on the spectral features of free-base porphyrin, Spectrochim Acta A Mol Biomol Spectrosc 238 (2020) 118389. https://doi.org/10.1016/j.saa.2020.118389.

[193] R.J.P. Williams, The Properties of Metalloporphyrins, Chem Rev 56 (1955) 299–326. https://doi.org/10.1021/cr50008a004.

[194] W. Zheng, N. Shan, L. Yu, X. Wang, UV-visible, fluorescence and EPR properties of porphyrins and metalloporphyrins, Dyes and Pigments 77 (2008) 153–157. https://doi.org/10.1016/j.dyepig.2007.04.007.

[195] Z. Valicsek, M.P. Kiss, M.A. Fodor, M. Imran, O. Horváth, Formation, Photophysics, Photochemistry and Quantum Chemistry of the Out-of-Plane Metalloporphyrins, Hungarian Journal of Industry and Chemistry 45 (2018) 29–36. https://doi.org/10.1515/hjic-2017-0006.

[196] R. Giovannetti, The Use of Spectrophotometry UV-Vis for the Study of Porphyrins, in: Macro To Nano Spectroscopy, 2012. https://doi.org/10.5772/38797.

[197] N.C.M. Magdaong, M. Taniguchi, J.R. Diers, D.M. Niedzwiedzki, C. Kirmaier, J.S. Lindsey, D.F. Bocian, D. Holten, Photophysical Properties and Electronic Structure of Zinc(II) Porphyrins Bearing 0-4 meso-Phenyl Substituents: Zinc Porphine to Zinc Tetraphenylporphyrin (ZnTPP), Journal of Physical Chemistry A 124 (2020) 7776–7794. https://doi.org/10.1021/acs.jpca.0c06841.

[198] M. Taniguchi, J.S. Lindsey, D.F. Bocian, D. Holten, Comprehensive review of photophysical parameters (ε, Φf, τs) of tetraphenylporphyrin (H2TPP) and zinc tetraphenylporphyrin (ZnTPP) – Critical benchmark molecules in photochemistry and photosynthesis, Journal of Photochemistry and Photobiology C-Photochemistry Reviews 46 (2021) 100401.

[199] A. Harriman, Luminescence of porphyrins and metalloporphyrins. Part 1. - Zinc(II), nickel(II) and manganese(II) porphyrins, Journal of the Chemical Society, Faraday Transactions 1: Physical Chemistry in Condensed Phases 76 (1980) 1978–1985. https://doi.org/10.1039/F19807601978.

[200] P.J. Gonalves, P.L. Franzen, D.S. Correa, L.M. Almeida, M. Takara, A.S. Ito, S.C. Zílio, I.E. Borissevitch, Effects of environment on the photophysical characteristics of mesotetrakis methylpyridiniumyl porphyrin (TMPyP), Spectrochim Acta A Mol Biomol Spectrosc 79 (2011) 1532–1539. https://doi.org/10.1016/j.saa.2011.05.012.

[201] R.F. Khairutdinov, N. Serpone, Photoluminescence and transient spectroscopy of free base porphyrin aggregates, Journal of Physical Chemistry B 103 (1999) 761–769. https://doi.org/10.1021/jp980869s.

[202] U. Siggel, U. Bindig, C. Endisch, T. Komatsu, E. Tsuchida, J. Voigt, J.-H. Fuhrhop, Photophysical and photochemical properties of porphyrin aggregates, Berichte Der Bunsengesellschaft Fur Physikalische Chemie 100 (1996) 2070–2075. https://doi.org/10.1002/bbpc.19961001225.

[203] K. Kano, K. Fukuda, H. Wakami, R. Nishiyabu, R.F. Pasternack, Factors influencing self-aggregation tendencies of cationic porphyrins in aqueous solution, J Am Chem Soc 122 (2000) 7494–7502. https://doi.org/10.1021/ja000738g.

[204] S. Chauhan, A. Kumar, K.A. Srinivas, M.K. Mishra, Effect of side chain length on the aggregation of amphiphilic 5,10,15-tris (1-methylpyridinium-4-yl)-20-[4-

(alkoxy) phenyl] 21H, 23H porphyrin tritosylates, Indian J Biochem Biophys 40 (2003) 429–438.

[205] F.J. Vergeldt, R.B.M. Koehorst, A. van Hoek, T.J. Schaafsma, Intramolecular Interactions in the Ground and Excited States of Tetrakis(N-methylpyridyl)porphyrins, J Phys Chem 99 (1995) 4397–4405. https://doi.org/10.1021/j100013a007.

[206] W. Becker, A. Bergmann, M.A. Hink, K. König, K. Benndorf, C. Biskup, Fluorescence Lifetime Imaging by Time-Correlated Single-Photon Counting, Microsc Res Tech 63 (2004) 58–66. https://doi.org/10.1002/jemt.10421.

[207] W. Becker, A. Bergmann, G. Biscotti, A. Rück, Advanced time-correlated single photon counting technique for spectroscopy and imaging in biomedical systems, 2004.

[208] R. Bonnett, D.J. McGarvey, A. Harriman, E.J. Land, T.G. Truscott, U.-J. Winfield, Photophysical Properties of meso-tetraphenylporphyrin and some meso-tetra(hydroxyphenyl)porphyrins, Photochem Photobiol 48 (1988) 271–276. https://doi.org/https://doi.org/10.1111/j.1751-1097.1988.tb02820.x.

[209] Z.H. Mazumder, D. Sharma, D. Sengupta, A. Mukherjee, J.S. Boruah, S. Basu, P.K. Shukla, T. Jha, Photodynamic activity attained through the ruptured π-conjugation of pyridyl groups with a porphyrin macrocycle: Synthesis and the photophysical and photobiological evaluation of 5-mono-(4-nitrophenyl)-10,15,20-tris-[4-(phenoxymethyl)pyridine]-porphyrin and its Zn(ii) complex, Photochemical and Photobiological Sciences 19 (2020) 1776–1789. https://doi.org/10.1039/d0pp00319k.

[210] K. Kalyanasundaram, Photochemistry of Water-Soluble Porphyrins: Comparative Study of Isomeric Tetrapyridyl-and Tetrakis(N-Methylpyridiniumy1)porphyrins, 1984.

[211] J.C. Scaiano, Nanosecond Laser Flash Photolysis: A Tool for Physical Organic Chemistry, in: Reactive Intermediate Chemistry, Wiley, 2003: pp. 847–871. https://doi.org/10.1002/0471721492.ch18.

[212] L.M. Moreira, F.V. Dos Santos, J.P. Lyon, M. Maftoum-Costa, C. Pacheco-Soares, N. Soares Da Silva, Photodynamic therapy: Porphyrins and phthalocyanines as photosensitizers, Aust J Chem 61 (2008) 741–754. https://doi.org/10.1071/CH08145.

[213] P.S. Santiago, D. de S. Neto, S.C.M. Gandini, M. Tabak, On the localization of water-soluble porphyrins in micellar systems evaluated by static and time-resolved frequency-domain fluorescence techniques, Colloids Surf B Biointerfaces 65 (2008) 247–256. https://doi.org/10.1016/j.colsurfb.2008.04.010.

[214] M.A. Gradova, O. V Gradov, K.A. Zhdanova, N.A. Bragina, A. V Lobanov, Self-assembly of amphiphilic meso-aryl-substituted porphyrin derivatives in the presence of surfactants, J Porphyr Phthalocyanines 24 (2019) 505–514. https://doi.org/10.1142/S108842461950175X.

[215] C.M.R. Almeida, B.F.O. Nascimento, M. Pineiro, A.J.M. Valente, Thermodynamic study of the interaction between 5,10,15,20-tetrakis-(N-methyl-4-pyridyl)porphyrin tetraiodine and sodium dodecyl sulfate, Colloids Surf A Physicochem Eng Asp 480 (2015) 279–286. https://doi.org/10.1016/j.colsurfa.2014.12.030.

[216] W.G. Qiu, Z.F. Li, G.M. Bai, S.N. Meng, H.X. Dai, H. He, Interaction of water-soluble cationic porphyrin with anionic surfactant, Spectrochim Acta A Mol Biomol Spectrosc 68 (2007) 1164–1169. https://doi.org/10.1016/j.saa.2007.01.015.

[217] X. Li, D. Li, M. Han, Z. Chen, G. Zou, Neutral porphyrin J-aggregates in premicellar SDS solution, Colloids Surf A Physicochem Eng Asp 256 (2005) 151–156. https://doi.org/10.1016/j.colsurfa.2005.01.006.

[218] N.C. Maiti, S. Mazumdar, N. Periasamy, J-and H-Aggregates of Porphyrin-Surfactant Complexes: Time-Resolved Fluorescence and Other Spectroscopic Studies †, J Phys Chem B 102 (1998) 1528–1538. https://doi.org/10.1021/jp9723372.

[219] P.J. Gonçalves, D.S. Corrêa, P.L. Franzen, L. De Boni, L.M. Almeida, C.R. Mendonça, I.E. Borissevitch, S.C. Zílio, Effect of interaction with micelles on the excited-state optical properties of zinc porphyrins and J-aggregates formation, Spectrochim Acta A Mol Biomol Spectrosc 112 (2013) 309–317. https://doi.org/10.1016/j.saa.2013.04.065.

[220] T. Ackermann, S. Tardito, Cell Culture Medium Formulation and Its Implications in Cancer Metabolism, Trends Cancer 5 (2019) 329–332. https://doi.org/10.1016/j.trecan.2019.05.004.

[221] P. Rahimizadeh, S. Yang, S.I. Lim, Albumin: An Emerging Opportunity in Drug Delivery, Biotechnology and Bioprocess Engineering 25 (2020) 985–995. https://doi.org/10.1007/s12257-019-0512-9.

[222] N. Muller, F. Lapicque, E. Drelon, P. Netter, Binding Sites of Fluorescent Probes on Human Serum Albumin, Journal of Pharmacy and Pharmacology 46 (1994) 300–304. https://doi.org/10.1111/j.2042-7158.1994.tb03798.x.

[223] E.N. Hoogenboezem, C.L. Duvall, Harnessing albumin as a carrier for cancer therapies, Adv Drug Deliv Rev 130 (2018) 73–89. https://doi.org/10.1016/j.addr.2018.07.011.

[224] Li Xuechen, Li Xinyue, Park Suyoung, Wu Shinig, Guo Yongxian, Nam Ki Taek, Kwon Nahyun, Yoon Juyoung, Hu Qiungzheng, Photodynamic and Photothermal therapy via human serum albumin delivery, Coord Chem Rev 520 (2024) 216142.

[225] S. Curry, P. Brick, N.P. Franks, Fatty acid binding to human serum albumin: new insights from crystallographic studies, Biochim Biophys Acta 1441 (1999) 131–140. https://doi.org/10.1016/S1388-1981(99)00148-1.

[226] S. Ben Dror, I. Bronshtein, H. Weitman, K.M. Smith, W.G. O'Neal, P.A. Jacobi, B. Ehrenberg, The binding of analogs of porphyrins and chlorins with elongated side chains to albumin, European Biophysics Journal 38 (2009) 847–855. https://doi.org/10.1007/s00249-009-0444-y.

[227] P. Zhao, J.W. Huang, L.N. Ji, Cationic pyridinium porphyrins appending different peripheral substituents: Spectroscopic studies on their interactions with bovine serum albumin, Spectrochim Acta A Mol Biomol Spectrosc 88 (2012) 130–136. https://doi.org/10.1016/j.saa.2011.12.017.

[228] N.S. Lebedeva, Y.A. Gubarev, E.S. Yurina, S.A. Syrbu, Features of interaction of tetraiodide meso-tetra(N-methyl-3-pyridyl)porphyrin with bovine serum albumin, J Mol Liq 265 (2018) 664–667. https://doi.org/10.1016/j.molliq.2018.06.030.

[229] Karapetyan N. H., Madakyan V. N., Karapetyan (2004)-New pyridylporphyrins with BSA, Russ J Bioorg Chem 30 (2004) 172–177.

[230] O.A. Chaves, L.B. Menezes, B.A. Iglesias, Multiple spectroscopic and theoretical investigation of meso-tetra-(4-pyridyl)porphyrin-ruthenium(II) complexes in HSA-binding studies. Effect of Zn(II) in protein binding, J Mol Liq 294 (2019). https://doi.org/10.1016/j.molliq.2019.111581.

[231] V. Timoshenko, Singlet Oxygen Generation and Detection for Biomedical Applications, in: M.-I. Baraton (Ed.), Sensors for Environment, Health and Security, Springer Science, 2009: pp. 295–309. https://doi.org/10.1007/978-1-4020-9009-7_19.

[232] E.L. Clennan, A. Pace, Advances in singlet oxygen chemistry, Tetrahedron 61 (2005) 6665–6691. https://doi.org/10.1016/j.tet.2005.04.017.

[233] P. Carloni, E. Damiani, L. Greci, P. Stipa, F. Tanfani, E. Tartaglini, M. Wozniak, On the use of 1,3-diphenylisobenzofuran (DPBF). Reactions with carbon and oxygen centered radicals in model and natural systems, Research on Chemical Intermediates 19 (1993) 395–405. https://doi.org/10.1163/156856793X00181.

[234] K. Żamojć, M. Zdrowowicz, P.B. Rudnicki-Velasquez, K. Krzymiński, B. Zaborowski, P. Niedziałkowski, D. Jacewicz, L. Chmurzyński, The development of 1,3-diphenylisobenzofuran as a highly selective probe for the detection and

quantitative determination of hydrogen peroxide, Free Radic Res 51 (2017) 38–46. https://doi.org/10.1080/10715762.2016.1262541.

[235] T. Entradas, S. Waldron, M. Volk, The detection sensitivity of commonly used singlet oxygen probes in aqueous environments, J Photochem Photobiol B 204 (2020) 111787. https://doi.org/https://doi.org/10.1016/j.jphotobiol.2020.111787.

[236] A.P.H. Schenning, M.C. Feiters, R.J.M. Nolte, An Amphiphilic Porphyrin with Unexpected Aggregation Behaviour, Tetrahedron Lett 34 (1993) 7077–7080.

[237] J.M. Dąbrowski, B. Pucelik, M.M. Pereira, L.G. Arnaut, G. Stochel, Towards tuning PDT relevant photosensitizer properties: Comparative study for the free and Zn2+ coordinated meso -tetrakis[2,6-difluoro-5-(N -methylsulfamylo)phenyl]porphyrin, J Coord Chem 68 (2015) 3116–3134. https://doi.org/10.1080/00958972.2015.1073723.

[238] A. Wiehe, E.J. Simonenko, M.O. Senge, B. RÖder, Hydrophilicity vs hydrophobicity - Varying the amphiphilic structure of porphyrins related to the photosensitizer m-THPC, J Porphyr Phthalocyanines 5 (2001) 758–761. https://doi.org/10.1002/jpp.389.

[239] V.N. Viswanadhan, A.K. Ghose, G.R. Reyankar, R.K. Robins, Atomic Physicochemical Parameters for Three Dimensional Structure Directed Quantitative Structure-Activity Relationships. 4. Additional Parameters for Hydrophobic and Dispersive Interactions and Their Application for an Automated Superposition of Certain Naturally Occurring Nucleoside Antibiotics, 1989.

[240] M. Swain, chemicalize.org, J Chem Inf Model 52 (2012) 613–615. https://doi.org/10.1021/ci300046g.

[241] C.-L. Peng, P.-S. Lai, M.-J. Shieh, Influence of Substitutions in Asymmetric Porphyrins ON Intracellular Uptake, Subcellular Localization and Phototoxicity in HeLa Cells, Biomed Eng (Singapore) 20 (2008) 9–17. https://doi.org/10.1142/S1016237208000556.

[242] R. Boscencu, G. Manda, N. Radulea, R.P. Socoteanu, L.C. Ceafalan, I.V. Neagoe, I.F. MacHado, S.H. Basaga, L.F.V. Ferreira, Studies on the synthesis, photophysical and biological evaluation of some unsymmetrical meso-tetrasubstituted phenyl porphyrins, Molecules 22 (2017). https://doi.org/10.3390/molecules22111815.

[243] A. Martinez De Pinillos Bayona, P. Mroz, C. Thunshelle, M.R. Hamblin, Design features for optimization of tetrapyrrole macrocycles as antimicrobial and anticancer photosensitizers, Chem Biol Drug Des 89 (2017) 192–206. https://doi.org/10.1111/cbdd.12792.

[244] R.P. Socoteanu, R. Boscencu, G. Manda, M. Anastasescu, I.V. Neagoe, I. Ferreira Machado, O. Dinca, A. Bucur, L.F. Vieira Ferreira, Morphologic evaluation of some promising A3B porphyrinic type compounds designed for theranostic applications in cancer, Chem Phys 544 (2021) 111115. https://doi.org/https://doi.org/10.1016/j.chemphys.2021.111115.

[245] R. Mallick, P. Bhowmik, A.K. Duttaroy, Targeting fatty acid uptake and metabolism in cancer cells: A promising strategy for cancer treatment, Biomedicine and Pharmacotherapy 167 (2023). https://doi.org/10.1016/j.biopha.2023.115591.

[246] Y. Matsushita, H. Nakagawa, K. Koike, Lipid metabolism in oncology: Why it matters, how to research, and how to treat, Cancers (Basel) 13 (2021) 1–24. https://doi.org/10.3390/cancers13030474.

[247] E. Cocucci, J.Y. Kim, Y. Bai, N. Pabla, Role of Passive Diffusion, Transporters, and Membrane Trafficking-Mediated Processes in Cellular Drug Transport, Clin Pharmacol Ther 101 (2017) 121–129. https://doi.org/10.1002/cpt.545.

[248] P. Vallecorsa, G. Di Venosa, M.B. Ballatore, D. Ferreyra, L. Mamone, D. Sáenz, G. Calvo, E. Durantini, A. Casas, Novel meso-substituted porphyrin derivatives and its potential use in photodynamic therapy of cancer, BMC Cancer 21 (2021) 547. https://doi.org/10.1186/s12885-021-08286-6.

[249] B. Sun, C. Luo, W. Cui, J. Sun, Z. He, Chemotherapy agent-unsaturated fatty acid prodrugs and prodrug-nanoplatforms for cancer chemotherapy, Journal of Controlled Release 264 (2017) 145–159. https://doi.org/10.1016/j.jconrel.2017.08.034.

[250] C. Donohoe, F.A. Schaberle, F.M.S. Rodrigues, N.P.F. Gonçalves, C.J. Kingsbury, M.M. Pereira, M.O. Senge, L.C. Gomes-Da-Silva, L.G. Arnaut, Unraveling the Pivotal Role of Atropisomerism for Cellular Internalization, J Am Chem Soc 144 (2022) 15252–15265. https://doi.org/10.1021/jacs.2c05844.

[251] S. Mazumdar, D. Chitkara, A. Mittal, Exploration and insights into the cellular internalization and intracellular fate of amphiphilic polymeric nanocarriers, Acta Pharm Sin B 11 (2021) 903–924. https://doi.org/10.1016/j.apsb.2021.02.019.

[252] C.A. Robertson, D.H. Evans, H. Abrahamse, Photodynamic therapy (PDT): A short review on cellular mechanisms and cancer research applications for PDT, J Photochem Photobiol B 96 (2009) 1–8. https://doi.org/10.1016/j.jphotobiol.2009.04.001.

[253] F. Denizot, R. Lang, Rapid colorimetric assay for cell growth and survival Modifications to the tetrazolium dye procedure giving improved sensitivity and reliability, 1986.

[254] K. V. Sharma, N. Bowers, L.M. Davids, Photodynamic therapy-induced killing is enhanced in depigmented metastatic melanoma cells, Cell Biol Int 35 (2011) 939–944. https://doi.org/10.1042/cbi20110103.

[255] I.O.L. Bacellar, M.C. Oliveira, L.S. Dantas, E.B. Costa, H.C. Junqueira, W.K. Martins, A.M. Durantini, G. Cosa, P. Di Mascio, M. Wainwright, R. Miotto, R.M. Cordeiro, S. Miyamoto, M.S. Baptista, Photosensitized Membrane Permeabilization Requires Contact-Dependent Reactions between Photosensitizer and Lipids, J Am Chem Soc 140 (2018) 9606–9615. https://doi.org/10.1021/jacs.8b05014.

[256] H. Mikula, D. Svatunek, D. Lumpi, F. Glöcklhofer, C. Hametner, J. Fröhlich, Practical and efficient large-scale preparation of dimethyldioxirane, Org Process Res Dev 17 (2013) 313–316. https://doi.org/10.1021/op300338q.

[257] S.E. Denmark, D.C. Forbes, D.S. Hays, J.S. Depue, R.G. Wilde, Catalytic Epoxidation of Alkenes with Oxone, Journal of Organic Chemistry 60 (1996) 1391–1407. https://doi.org/10.1021/jo00110a049.

[258] J.S. Poole, Recent Advances in the Photochemistry of Heterocyclic N-Oxides and Their Derivatives, in: O. Larionov (Ed.), Heterocyclic N-Oxides, Springer, Cham, 2017: pp. 111–151. https://doi.org/10.1007/7081_2017_4.

[259] B. Algis Alkaitis, M. Calvin, The photochemistry of pyridine N-oxide, Chemical Communications (1968) 292–294. https://doi.org/10.1039/C19680000292.

[260] S. Ben-Dror, I. Bronshtein, A. Wiehe, B. Röder, M.O. Senge, B. Ehrenberg, On the Correlation Between Hydrophobicity, Liposome Binding and Cellular Uptake of Porphyrin Sensitizers, Photochem Photobiol 82 (2006) 695–701. https://doi.org/10.1562/2005-09-01-ra-669.

[261] H. Rinderknecht, S. Ehnert, B. Braun, T. Histing, A.K. Nussler, C. Linnemann, The Art of Inducing Hypoxia, Oxygen 1 (2021) 46–61. https://doi.org/10.3390/oxygen1010006.

[262] J. Muñoz-Sánchez, M.E. Chánez-Cárdenas, The use of cobalt chloride as a chemical hypoxia model, Journal of Applied Toxicology 39 (2019) 556–570. https://doi.org/10.1002/jat.3749.

[263] N.K. Rana, P. Singh, B. Koch, CoCl2 simulated hypoxia induce cell proliferation and alter the expression pattern of hypoxia associated genes involved in angiogenesis and apoptosis, Biol Res 52 (2019) 12. https://doi.org/10.1186/s40659-019-0221-z.

[264] Z. Ji, G. Yang, S. Shahzidi, K. Tkacz-Stachowska, Z. Suo, J.M. Nesland, Q. Peng, Induction of hypoxia-inducible factor-1α overexpression by cobalt chloride enhances cellular resistance to photodynamic therapy, Cancer Lett 244 (2006) 182–189. https://doi.org/10.1016/j.canlet.2005.12.010.

[265] A.B. Zepeda, A. Pessoa, R.L. Castillo, C.A. Figueroa, V.M. Pulgar, J.G. Farías, Cellular and molecular mechanisms in the hypoxic tissue: Role of HIF-1 and ROS, Cell Biochem Funct 31 (2013) 451–459. https://doi.org/10.1002/cbf.2985.

[266] M.E. Rodríguez, C. Catrinacio, A. Ropolo, V.A. Rivarola, M.I. Vaccaro, A novel HIF-1α/VMP1-autophagic pathway induces resistance to photodynamic therapy in colon cancer cells, Photochemical and Photobiological Sciences 16 (2017) 1631–1642. https://doi.org/10.1039/c7pp00161d.

[267] W. Flitsch, Hydrogenated Porphyrin Derivatives: Hydroporph yrins, 1988.

[268] M. Taniguchi, J.S. Lindsey, Synthetic chlorins, possible surrogates for chlorophylls, prepared by derivatization of porphyrins, Chem Rev 117 (2017) 344–535. https://doi.org/10.1021/acs.chemrev.5b00696.

[269] D.J. Pasto, R.T. Taylor, Reduction with Diimide, in: L. Paquette (Ed.), Organic Reactions, John Wiley & Sons, Int., 1991: pp. 91–155. https://doi.org/10.1002/0471264180.or040.02.

[270] H.W. Whitlock, R. Hanauer, M.Y. Oester, B.K. Bower, Diimide Reduction of Porphyrins, J Am Chem Soc 91 (1969) 74885–7489. https://doi.org/10.1021/ja01054a044.

[271] M.O. Senge, MTHPC - A drug on its way from second to third generation photosensitizer?, Photodiagnosis Photodyn Ther 9 (2012) 170–179. https://doi.org/10.1016/j.pdpdt.2011.10.001.

[272] F.D. Bellamy, K. Ou, Selective Reduction of Aromatic Nitro Compounds With Stannous Chloride in non Acidic and non Aqueous Medium, Tetrahedron Lett 25 (1984) 839–842. https://doi.org/10.1016/S0040-4039(01)80041-1.

[273] F. Brégier, J. Godard, J. Thiais, S. Bouramtane, A. Moulin, Y. Champavier, A. Mailleau, V. Chaleix, V. Sol, Regioselective reduction of 5-aryl-10,15,20-tris(pyridyl) porphyrin to 5-aryl-10,15,20-tris(pyridyl)dihydroporphyrin (chlorin), in: Porphyrin Science by Women, WORLD SCIENTIFIC, 2021: pp. 568–585. https://doi.org/10.1142/9789811223556_0045.

[274] I. Velikyan, 68Ga-based radiopharmaceuticals: Production and application relationship, Molecules 20 (2015) 12913–12943. https://doi.org/10.3390/molecules200712913.

[275] Gunnar Antoni, Thw Radiopharmaceutical Chemistry of Carbon-11: Basic Principles, in: Springer, 2019: pp. 207–220.

[276] M. Guleria, C. Kumar, T. Das, J. Amirdhanayagam, R. Sharma, H.D. Sarma, A. Dash, Studies towards elucidating the potential of 5,10,15,20-tetrakis(: P -carboxy-

methyleneoxyphenyl)porphyrin as a theranostic agent for applications in PET and PDT, Medchemcomm 9 (2018) 657–666. https://doi.org/10.1039/c7md00433h.

[277] E.W. Price, C. Orvig, Matching chelators to radiometals for radiopharmaceuticals, Chem Soc Rev 43 (2014) 260–290. https://doi.org/10.1039/c3cs60304k.

[278] P.T. Gomme, K.B. McCann, J. Bertolini, Transferrin: structure, function and potential therapeutic actions, Drug Discov Today 10 (2005) 267–273. https://doi.org/10.1016/S1359-6446(04)03333-1.

[279] T.W. Price, J. Gallo, V. Kubíček, Z. Böhmová, T.J. Prior, J. Greenman, P. Hermann, G.J. Stasiuk, Amino Acid Based Gallium-68 Chelators Capable of Radiolabeling at Neutral pH, 2017.

[280] G.I. Harisa, F.K. Alanazi, Low density lipoprotein bionanoparticles: From cholesterol transport to delivery of anti-cancer drugs, Saudi Pharmaceutical Journal 22 (2014) 504–515. https://doi.org/10.1016/j.jsps.2013.12.015.

[281] T. Kanda, T. Sugihara, T. Takata, Y. Mae, H. Kinoshita, T. Sakaguchi, T. Hasegawa, H. Kurumi, Y. Ikebuchi, T. Murakami, H. Isomoto, Low-density lipoprotein receptor expression is involved in the beneficial effect of photodynamic therapy using talaporfin sodium on gastric cancer cells, Oncol Lett (2019). https://doi.org/10.3892/ol.2019.10004.

[282] K. Michalska, M. Rychłowski, M. Krupińska, G. Szewczyk, T. Sarna, J. Nakonieczna, Gallium Mesoporphyrin IX-Mediated Photodestruction: A Pharmacological Trojan Horse Strategy to Eliminate Multidrug-Resistant Staphylococcus aureus, Mol Pharm 19 (2022) 1434–1448. https://doi.org/10.1021/acs.molpharmaceut.1c00993.

[283] A. V. Morales-De-Echegaray, T.R. Maltais, L. Lin, W. Younis, N.R. Kadasala, M.N. Seleem, A. Wei, Rapid Uptake and Photodynamic Inactivation of Staphylococci by Ga(III)-Protoporphyrin IX, ACS Infect Dis 4 (2018) 1564–1573. https://doi.org/10.1021/acsinfecdis.8b00125.

7. Lists

7.1. List of figures

Figure 15. The melanin synthesis pathway (left) [131] and the four-stage process of melanogenesis (right) and maturation of melanosomes [8].

Figure 16. Structures of several porphyrins tested in the treatment of melanoma.

Figure 17. The basic principle of positron emission tomography (PET) scanning. Figure adapted from [154].

Figure 18. The structures of porphyrin ligands (with the abbreviations used in the text) from the literature complexed with ^{68}Ga(III) for use in PET imaging.

Figure 19. Comparison of the ^{1}H NMR spectra after using $ZnCl_2$ for 1 hour and $Zn(CH_3COO)_2$ for metalation of porphyrin **12** to obtain porphyrin **20**.

Figure 20. Comparison of the ^{1}H NMR spectra of *N*-methylated free-base porphyrin (**13**) and its Zn(II) complex (**21**).

Figure 21. The aromatic part of the ^{1}H NMR ($CDCl_3$, 400 MHz) spectrum of porphyrin **2** (upper spectrum) and enlarged part of the spectrum between 6.95 and 8.30 ppm (lower spectrum) measured first at 25 °C (red line), then after cooling to 5 °C (green line), followed by heating to 50 °C (blue line) and cooling back to 25 °C (purple line).

Figure 22. Perspective view of four possible conformations of porphyrin **1** [188].

Figure 23. Comparison of the normalised absorption (A) and fluorescence (B) spectrum of *N*-methylated free-base and Zn(II) porphyrins on the example of porphyrins **19** and **27**, both conjugated with an alkyl chain with 17 C atoms. Measurements were performed in MeOH and Soret band wavelength (λ = 419 nm (**19**) and λ = 432 nm (**27**)) was used for the excitation.

Figure 24. Comparison of the absorption spectra of *N*-methylated free-base porphyrins **13** (A) and **19** (C) and their Zn(II) complexes **21** (B) and **27** (D) in MeOH, H_2O and 0.05 M phosphate buffer.

Figure 25. Comparison of the temperature effect (5 °C, 25 °C and 60 °C) on the fluorescence spectra of porphyrin **13** (A, B and C) and its Zn(II) complex **21** (D, E and F) (1 μM) in MeOH (A, D), H_2O (B, E) and 0.05 M phosphate buffer (C, F).

Figure 26. Absorption spectra of the *N*-methylated free-base porphyrins (**13**, **15**, **17** and **19**) (A) and their Zn(II) complexes (**21**, **23**, **25** and **27**) (B) recorded in 1× PBS.

Figure 27. Emission spectra of the free-base porphyrins (**13**, **15**, **17** and **19**) (A) and their Zn(II) complexes (**21**, **23**, **25** and **27**) (B) recorded in PBS. Excitation wavelength used for free-base *N*-methylated porphyrins was 420 nm, and for Zn(II) complexes 430 nm.

Figure 28. Fluorescence decay at 650 nm (λ_{ex} = 405 nm) for free-base porphyrins **13** (A), **14** (C) and **19** (E) their Zn(II) complexes **21** (B), **22** (D) and **27** (F) measured in MeOH (N_2)

using time-correlated single photon counting (TC-SPC) (black line) and fit to a sum of two exponents (red line). The bottom panel of the figures correspond to the weighted residuals between the experimental and the fitted values.

Figure 29. Triplet-triplet absorption spectra or Transient absorption spectra after laser excitation of free-base *N*-methylated porphyrins **13** (A), **14** (C) and **19** (E) and their Zn(II) complexes **21** (B), **22** (D) and **27** (F). ^{3}PS* of **13** and **21** were recorded in MeOH after laser excitation at 266 nm ($E_{266\ nm}$ = 2 mJ. $A_{266\ nm}$ = 0.20), ^{3}PS* of **14** and **22** in phosphate buffer (0.05 M, pH = 7) after laser excitation at 355 nm ($E_{355\ nm}$ = 2 mJ. $A_{355\ nm}$ (14) = 0.23; $A_{355\ nm}$ (22) = 0.25) and ^{3}PS* **19** and **27** in MeOH after laser excitation at 355 nm ($E_{355\ nm}$ = 2 mJ. $A_{355\ nm}$ = 0.25).

Figure 30. Transient absorption kinetics of *N*-methylated free-base porphyrins **13**, **14** and **19** (A, C and E) and their Zn(II) complexes **21**, **22** and **27** (B, D and F) at 450 nm (free-base porphyrins) or 460 nm (Zn(II) porphyrins) after 355 nm laser excitation in MeOH saturated with N_2. $A_{355\ nm}$ = 0.2; $E_{355\ nm}$ = 3 mJ.

Figure 31. Absorption spectra of free base porphyrins 13 (A) and 19 (B) and their Zn(II) complexes 21 (C) and 27 (D) in PBS alone and after addition of TX-100 in different concentrations to the PBS solution.

Figure 32. Absorption spectra of free base porphyrins (**13** (A) and **19** (B)) and their Zn(II) complexes (**21** (C) and **27** (D)) in PBS alone and after addition of SDS in different concentrations to the PBS solution.

Figure 33. Absorption spectra of free-base porphyrin **13** (A) and porphyrin **19** (B) in pure DMEM cell medium and DMEM medium after completion of the medium with 1 % penicillin/streptomycin solution, 1 % L-glutamine and 10 % fetal bovine serum (FBS) (DMEM 2). Spectra were compared at 10 μM concentration.

Figure 34. Absorption spectra of free-base porphyrins **13** and **19** (A and B) and their Zn(II) complexes, **21** and **27** (C and D) measured in PBS with the addition of bovine serum albumin (BSA).

Figure 35. Singlet oxygen production ($^1O_2$) of the *N*-methylated free-base (**13**-**19**) porphyrins and their Zn(II) complexes (**21**-**28**) determined by photodegradation of DPBF after irradiation for 15 min with red light (λ = 647 nm, 10.7 mW/cm^2, 9.63 J/cm^2) (A), and orange light (λ = 606 nm, 2 mW/cm^2, 1.8 J/cm^2) (B). Results are presented as percentage of fluorescence decrease calculated from area under the curve after the photodegradation of DPBF. All results are presented as an average of measurements in triplicate with the standard deviation in error bars.

Figure 36. Singlet oxygen production ($^1O_2$) of the *N*-methylated free-base (**13**, **15**, **17** and **19**) and Zn(II) porphyrins (**21**, **23**, **25** and **27**) (1 μM) determined by photodegradation of ABMDMA in PBS after irradiation with violet light (λ = 411 nm, 3.5 mW/cm^2, 1.05 J/cm^2). Results are presented as average of measurements in triplicate showing a percentage of fluorescence decrease calculated from area under the curve after the photodegradation of 1,3-diphenylisobenzofurane (DPBF).

Figure 37. Obtained logP_{BW} (A) and logP_{OW} (B) with corresponding tables showing calculated values obtained by modified shake-flask method. log*P*ow was calculated from the logP_{BW} values using a correlation formula **19**. All results are shown as an average of duplicate measurements with standard deviation in error bars.

Figure 38. R_f values determined by thin layer chromatography (TLC) on silica gel plates with MeCN: H_2O: $KNO_{3(sat.)}$ (8:1:1) used as a mobile phase. Results represent an average of measurements in duplicate with standard deviation in error bars.

Figure 39. Cellular uptake kinetics, measured by fluorescence intensity, analysed over 24 h of incubation at 37 °C after addition of 1 μM solution of free-base porphyrins (A, C and E) and their Zn(II) complexes (B, D and F) to HDF (A, B), MeWo (C, D) and A375 (E, F) cell line. Results are presented as a mean of calculated concentration per 10^3 cells (nM) obtained after three individual measurements with standard deviations as error bars.

Figure 40. Comparison of the cellular uptake at 4 °C and 37 °C after incubation for 6 hours with free-base porphyrins (**13**-**19**) (A and C) and their Zn(II) analogues (**21**-**27**) (B and D) in HDF (A and B) and MeWo (C and D). All results are shown as a mean concentration per 10^3 cells (nM) of measurements in triplicate with standard deviations as error bars. Standard t-tests were used for statistical comparison of cellular uptake at different temperatures (statistics presented on the graph), while two-way ANOVA with Tukey *post-hoc* tests were used to compare the differences on the cellular uptake at 37 °C based on the alkyl chain length (table statistics). In the table, significance was $p < 0.0001$ and it was shown as follows: **** < 0.0001; 0.0001 <*** < 0.001; 0.001 < ** < 0.01; 0.01 < * < 0.1; ns > 0.1 (not significant).

Figure 41. Localization in MeWo cell line of the free-base porphyrins (**15**, **17** and **19**) (A) and their Zn(II) complexes (**23**, **25** and **27**) (B) after incubation with $DIOC_6(3)$, a fluorescent marker for endoplasmic reticulum. The porphyrins were incubated at concentration of 5 μM for 6 hours. All images were taken by fluorescence microscopy at 20× magnification.

Figure 42. Localization of porphyrin **19** with Golgi apparatus on MeWo cell line, obtained by staining with GM130 as primary antibody and with AlexaFluor 488 secondary antibody. All pictures were taken with fluorescence microscopy at 20× magnification.

Figure 43. Comparison of the cytotoxicity of *N*-methylated free-base porphyrins **13** to **19** at concentration of 1 μM after irradiation with 643 nm (A) or 606 nm (B). The statistical analysis in the graph shows the two-way ANOVA analysis of the melanoma cell lines compared to the non-tumour cell line (HDF), while the corresponding tables shows the statistical analysis of the impact of alkyl chain length on the proliferation in comparison to the hydrophilic analogue (**13**) in different cell lines. Significance was $p < 0.0001$ and it was shown using the following signs: **** < 0.0001; 0.0001 <*** < 0.001; 0.001 < ** < 0.01; 0.01 < * < 0.1; ns > 0.1 (not significant).

Figure 44. Comparison of the cytotoxicity of Zn(II) porphyrins **21** to **27** at concentration of 1 μM after irradiation with 643 nm (A) or 606 nm (B). The statistical analysis in the graph shows the two-way ANOVA analysis of the melanoma cell lines compared to the non-tumour cell line (HDF), while the corresponding tables shows the statistical analysis of the impact of the alkyl chain length on the proliferation compared to the hydrophilic analogue (**21**) in different cell lines. Significance was $p < 0.0001$ and it was shown using the following signs: **** < 0.0001; 0.0001 <*** < 0.001; 0.001 < ** < 0.01; 0.01 < * < 0.1; ns > 0.1 (not significant).

Figure 45. ^{1}H NMR (CD_3OD, 600 MHz) of the unsuccessful reaction (**28**, method A) upon adjustment of pH with 1 M $NaHCO_3$ and TLC chromatograms of the same reaction with the adjustment of pH with 1 M $NaHCO_3$ (A) and phosphate buffer (pH = 7.5) (B).

Figure 46. Absorption (left) and fluorescence spectra (right) of porphyrin **32** recorded in MeOH. Soret band wavelength was used for excitation. Inset in the absorption spectrum: enlarged Q bands in region from 480 nm to 680 nm.

Figure 47. Fluorescence decay of **29** (left) and **32** (right) in MeOH (N_2) obtained using TCSPC (black line) and the fit to a sum of two exponents (green line). λ_{ex} = 405 nm, A_{405nm}(**29**) = 0.096; A_{405nm} (**32**) = 0.11. The bottom panel of the figures correspond to the weighted residuals between the experimental and the fitted values.

Figure 48. Transient absorption spectra after 355 nm laser excitation of **32** in MeOH saturated with N_2. $A_{355\ nm}$ = 0.21, $E_{355\ nm}$ = 3 mJ.

Figure 49. Transient absorption kinetics at 450 nm after 355 nm laser excitation of porphyrins **29** and **32** in MeOH saturated with N_2. $A_{355\ nm}$ (**29**) = 0.22; $A_{355\ nm}$ (**32**) = 0.22, $E_{355\ nm}$ = 3 mJ.

Figure 50. Singlet oxygen ($^1O_2$) production of the *N*-methylated (**13**, **15**, **17** and **19**) and *N*-oxidised porphyrins (**29**-**32**) (5 μM) obtained by photodegradation of the DPBF (4 μM) in MeOH after irradiation with red light for 15 minutes (λ = 647 nm; 10.7 mW/cm^2, 9.63 J/cm^2).

Figure 51. Cellular uptake kinetics measured over 24 hours of incubation at 37 °C of *N*-oxidised porphyrins (**29**-**32**) on HDF (A), MeWo (B) and A375 (C) cell line. Results are

presented as a mean of calculated concentration per 10^3 cells (nM) obtained after three individual measurements with standard deviations as error bars.

Figure 52. Comparison of the cellular uptake at 4 °C and 37 °C after incubation for 24 hours with *N*-oxidised porphyrins (**29**-**32**) in HDF (A), MeWo (B) and A375 (C) cell line. All results are shown as a mean concentration per 10^3 cells (nM) with standard deviations as error bars. Standard t-tests were used for statistical comparison of cellular uptake at different temperatures (statistics presented on the graph), while two-way ANOVA with Tukey *post-hoc* tests were used to compare the differences on the cellular uptake at 37 °C based on the alkyl chain length (table statistics). Significance was $p < 0.0001$ and it was shown as follows: **** < 0.0001; 0.0001 <*** < 0.001; 0.001 < ** < 0.01; 0.01 < * < 0.1; ns > 0.1 (not significant).

Figure 54. Comparison of the proliferation at 1 μM concentration of *N*-methylated (**13** (R =-CH_3), **15** (R = -C_9H_{19}), **17** (R = -$C_{13}H_{27}$) and **19** (R = -$C_{17}H_{35}$), and *N*-oxidised porphyrin (**29** (R = -CH_3), **30** (R = -C_9H_{19}), **31** (R = -$C_{13}H_{27}$) and **32** (R = -$C_{17}H_{35}$)) in the conditions of normoxia and $CoCl_2$ induced hypoxia on HDF, MeWo and A375 cell lines. Statistical analysis was performed using two-way ANOVA with Tuckey *post-hoc* test to compare each group of porphyrins under the condition of normoxia and $CoCl_2$-induced hypoxia and to compare the two groups of porphyrins under the same condition. Significance was $p < 0.0001$ and it was shown using the following signs: **** < 0.0001; 0.0001 <*** < 0.001; 0.001 < ** < 0.01; 0.01 < * < 0.1; ns > 0.1 (not significant).

Figure 55. UV-Vis spectrum showing the changes in spectrum upon addition of DDQ of the reaction mixture after process diimide reduction of porphyrin **2**.

Figure 56. TLC chromatogram and UV-VIS spectrum of obtained chlorin **37** by $SnCl_2$ reduction of porphyrin **2**.

Figure 57. ^1H NMR (CD_3Cl, 600 MHz) spectrum of chlorin **37**, obtained by $SnCl_2$ reduction of porphyrin **2** shown in the A) aliphatic (-3.0 to 5.5 ppm) part of the spectrum, B) aromatic part of the spectrum (0.0 ppm to 4.8 ppm). Peaks that correspond to chlorin are shown as **37**, and impurities from the remained starting porphyrin are shown as **2**.

Figure 58. Schematic representation of a tri-step protocol in radiolabelling with ^{68}Ga: A) Elution of the $^{68}Ga/^{68}Ge$ generator and purifying of $^{68}Ga^{3+}$ over SCX cartridge, B) Radiolabelling of porphyrin with $^{68}Ga^{3+}$ in 0.5 M sodium acetate solution (pH = 4.3) C) Purification of the radiolabelled porphyrin using tBu-SepPak cartridge.

Figure 59. Radiochromatogram (pink) and UV-chromatogram (green) of the radiolabelled porphyrin **13** (**[^{68}Ga]34**): A) results after the radiolabelling step B) “hot-cold” radiolabelled radionuclide, with added 3 equiv. of $GaCl_3$.

Figure 60. Radiochromatogram (pink) and UV-chromatogram (green) of the radiolabelled porphyrin **15 ([^{68}Ga]34)**: A) results after the radiolabelling step B) "hot" radiolabelled radionuclide, after the purification by preparative HPLC C) "hot-cold" radiolabelled radionuclide, with added 3 equiv. of $GaCl_3$, after the purification by preparative HPLC.

Figure 61. Radiochromatogram (pink) and UV-chromatogram (green) of the radiolabelled porphyrin **17** (**[^{68}Ga]35**): A) results after the radiolabelling step B) "hot" radiolabelled radionuclide, after the purification by preparative HPLC C) "hot-cold" radiolabelled radionuclide, with added 3 equiv. of $GaCl_3$, after the purification by preparative HPLC.

Figure 62. Radiochromatogram (pink) and UV-chromatogram (green) of the radiolabelled porphyrin **19** (**[^{68}Ga]36**): A) results after the radiolabelling step B) "hot-cold" radiolabelled radionuclide, with added 3 equiv. of GaCl3, before the purification by preparative HPLC.

Figure 63. Comparison of the ^{1}H NMR (CD_3OD, 600 MHz) spectra of the free-base *N*-methylated porphyrin **17** and its Ga(III) complex, porphyrin **35**.

Figure 64. Absorption and fluorescence spectra of ^{nat}Ga(III) porphyrins **33**-**36** observed in MeOH (A,C) and PBS (B,D). Soret band wavelength was used for excitation of samples.

Figure 65. HPLC radio-chromatograms of radiolabelled porphyrins **[^{68}Ga]33**, **[^{68}Ga]34**, **[^{68}Ga]35** and **[^{68}Ga]36** after the incubation in the mouse serum for 2 hours at 37 °C. Radio-chromatograms are showing stability at the beginning of the experiment (0 min) and after 60 minutes and 120 minutes of incubation.

Figure 66. HPLC radio-chromatograms of radiolabelled porphyrins **[^{68}Ga]34** and **[^{68}Ga]35** after the incubation with *apo*-transferrin (1 mg/mL) for 3 hours at 37 °C. Radio-chromatograms are showing stability at the beginning of the experiment (0 min) and after 90- and 180-minute incubation.

Figure 67. Radio-chromatograms (pink) and UV-chromatograms (green) of the size exclusion chromatography (PBS, flow: 0.5 mL/min) investigating binding of the radiolabelled porphyrins **[^{68}Ga]33**, **[^{68}Ga]34** and **[^{68}Ga]35** to BSA (3% in PBS). **[^{68}Ga]acetate** was used as control. The chromatograms are showing the results after 30-minute incubation with BSA solution.

Figure 68. Radio-chromatograms (pink) and UV-chromatograms (green) of the size exclusion chromatography (PBS, flow: 0.5 mL/min) investigating binding of the radiolabelled porphyrins **[^{68}Ga]33**, **[^{68}Ga]34** and **[^{68}Ga]35** to LDL (0.5 mg/mL). Both amphiphilic porphyrins were used in their high SA formulation, while porphyrin **[^{68}Ga]33** was used as low SA formulation. **[^{68}Ga]acetate** was used as control.

Figure 69. Time dependent (A) and temperature dependent (B) cellular uptake of ^{nat}Ga(III) porphyrins **33**-**36** on MDA-MB 231 cell line. Time dependent analysis shows the kinetics of a cellular uptake over 24 hours at 37 °C, while in temperature dependent analysis, porphyrins were incubated for 6 hours at 4 °C or 37 °C. Results are shown as an average of three

experiments with standard deviation in error bars. Statistical analysis was done using the Two-way ANOVA with Sidak's *post-hoc* test. Significance was $p < 0.0001$ and it was shown using the following signs: **** < 0.0001; 0.0001 <*** < 0.001; 0.001 < ** < 0.01; 0.01 < * < 0.1; ns > 0.1 (not significant).

Figure 70. Comparison of the amount of porphyrin attached to the cell wall of the MDA-MB 231 cell line removed by ice-cold glycine buffer and the amount of the porphyrin inside the cells determined after solubilization of the cells with the 1% SDS in 0.1M NaOH after the incubation at 37 °C (A) and 4 °C (B). Results are shown as an average of three experiments with standard deviation in error bars. The statistical analysis was done using the Two-way ANOVA with Sidak's *post-hoc* test. Significance was $p < 0.0001$ and it was shown using the following signs: **** < 0.0001; 0.0001 <*** < 0.001; 0.001 < ** < 0.01; 0.01 < * < 0.1; ns > 0.1 (not significant).

Figure 71. Cellular uptake of ^{nat}Ga(III) porphyrins **33**-**36** in MDA-MB 231 cell line determined after the incubation of porphyrins for 6 hours at 37 °C. Images were observed by fluorescence microscopy at magnification 20×. Scale bare = 25 μm.

Figure 72. Comparison of the cytotoxicity of ^{nat}Ga(III) pyridiniumporphyrins on HDF (left) and MDA-MB 231 (right) at concentration of 50 μM after irradiation for 30 minutes (3.6 J/cm^2) and 60 minutes (7.2 J/cm^2). The statistical analysis in the graph shows the two-way ANOVA analysis between two light doses applied to the cell lines. Significance was $p < 0.0001$ and it was shown using the following signs: **** < 0.0001; 0.0001 <*** < 0.001; 0.001 < ** < 0.01; 0.01 < * < 0.1; ns > 0.1 (not significant).

Figure 73. 3D images of *in vivo* biodistribution of [^{68}Ga]gallium porphyrins **33**, **34** and **35** observed using dynamic 90 min PET/CT scan. Dynamic imaging was performed in naive or tumour (MDA-MD 231) bearing mouse (CD1 strain-female) with the start time coinciding with intravenous injection of radiotracer into the tail vein via catheter.

Figure 74. Biodistribution pattern over the selected organs (liver, heart, kidneys, bladder and muscles), determined by analysis of PET-CT scans with the radiolabelled porphyrins **[^{68}Ga]34** and **[^{68}Ga]35** in the AMIDE program.

Figure 75. Radiochromatograms of the metabolites in urine (B), liver (C) and blood (D) of the HPLC analysis after the standard 90-minute PET-CT scan with porphyrin **[^{68}Ga]35**. A radiochromatogram of the formulation (A) is shown as a control.

7.2. List of schemes

7.3. List of tables

Table 9. Number of photons absorbed by *N*-methylated free-base (**13**-**19**) and their Zn(II) complexes (**21**-**27**) during the measurement of $^1O_2$ production, calculated according to the equations **3-7.** Porphyrins were tested in 5 μM concentration dissolved in MeOH and irradiated with orange light (606 nm, 2 mW/cm^2, 1.8 J/cm^2) or red light (647 nm, 10.7 mW/cm^2, 9.63 J/cm^2) for 15 minutes.

Table 10. Number of photons absorbed by *N*-methylated free-base (**13**, **15**, **17** and **19**) and their Zn(II) complexes (**21**, **23**, **25** and **27**) during the measurement of singlet oxygen production. Porphyrins (1 μM) were dissolved in PBS and irradiated with violet light (λ = 411 nm, 3.5 mW/cm^2, 1.05 J/cm^2) for 5 min.

Table 11. clog*P* values determined using Chemicalize from ChemAxon (structure-based analysis).

Table 12. Determined IC_{50} values of *N*-methylated porphyrins (**13**-**19**) and their Zn(II) complexes (**21**-**27**) on HDF, MeWo and A375 cell line. Cells were incubated with porphyrin for 6 hours followed by 30-min irradiation with orange or red light (λ = 606 nm and λ = 643 nm, respectively) of the same fluence rate (2 mW/cm^2, total light dose 3.6 J/cm^2). 'Dark' column represents cells tested with porphyrin without irradiation.

Table 13. Number of photons absorbed by *N*-methylated free-base porphyrins (**13**-**19**) and their Zn(II) complexes (**21**-**27**) in concentration 1 μM during their irradiation in MTT assay. Porphyrins were irradiated with orange light (606 nm, 2 mW/cm^2, 3.6 J/cm^2) or red light (643 nm, 2 mW/cm^2, 3.6 J/cm^2) for 30 minutes.

Table 14. Absorption and fluorescence properties of *N*-oxidised porphyrins **29**-**32** measured in MeOH. Soret band wavelength was used for excitation when emission spectra were recorded.

Table 15. Photophysical parameters of tested *N*-oxidised porphyrins (**29** and **32**) in MeOH and a reference compound **TPP** obtained by LFP. Lifetime of the triplet excited state (τ_T), quantum yield of the intersystem crossing (Φ_{ISC}), molar absorption coefficient of the triplet state ($\varepsilon_{T\text{-}T}$), and quenching rate constant of the triplet excited state by O_2 (kq (O_2)).

Table 16. Lipophilicity *N*-oxidised (**29**-**32**) porphyrins determined using online program Chemicalize from ChemAxon (clog*P*) and compared with *N*-methylated (**13**, **15**, **17** and **19**) porphyrins.

Table 17. Calculated IC_{50} values of *N*-methylated porphyrins (**13**, **15**, **17** and **19**) and *N*-oxidised porphyrins (**29**-**32**) after irradiation with red light for 30 minutes (λ = 643 nm, 2 mW/cm^2, 3.6 J/cm^2) on HDF, MeWo and A375 cell lines. Stock solutions (20 mM) were prepared in dimethylsulfoxide (DMSO). Hypoxia conditions were achieved by adding 100 μM hypoxia-mimetic agent $CoCl_2$ for minimum two hours before treatment with porphyrins.

Table 18. Calculated IC_{50} values of *N*-methylated porphyrins (**13**, **15**, **17** and **19**) and *N*-oxidised porphyrins (**29**-**32**) after irradiation with red light for 30 minutes (λ = 643 nm, 2 mW/cm^2, 3.6 J/cm^2) on MeWo and A375 cell lines. Stock solutions (20 mM) were prepared in EtOH. Hypoxia conditions were achieved by adding 100 μM $CoCl_2$ for minimum two hours before treatment with porphyrins.

Table 19. Radiochemical yields (RCY) and radiochemical efficiency (RCE) obtained after radiolabelling of porphyrins **13, 15, 17** and **19**.

Table 20. Absorption and fluorescence properties of Ga(III) porphyrins (**33**-**36**) recorded in MeOH and PBS. *Soret band wavelength was used for the excitation.

Table 21. Partition coefficient (log*D*) determined using shake-flask method with 1-octanol and PBS. Prior mixing, activity (~1 MBq) was dissolved in PBS. After separation of layers, activity in each layer was observed using γ-counter.

Table 22. Determined IC_{50} values of ^{nat}Ga(III)porphyrins **33**-**36** on HDF and MDA-MB 231 cell line. Cells were incubated with porphyrin for 6 hours followed by irradiation with red light (λ = 643 nm, 2 mW/cm^2) for 30 (3.6 J/cm^2) or 60 minutes (7.2 J/cm^2). 'Dark' column represents cells tested with porphyrin without irradiation.

Table 23. Determined IC_{50} values of ^{nat}Ga(III) porphyrin **35** on HDF and MDA-MB 231 cell lines. Cells were incubated with porphyrin for 6 hours followed by 30-min and 60-min irradiation with orange light (λ = 606 nm, 2 mW/cm^2, total light dose 3.6 J/cm^2 (30-minute irr.) and 7.2 J/cm^2 (60-minute irr.). 'Dark' column represents cells tested with porphyrin without irradiation.

7.4. List of abbreviations

***** Abbreviations are listed in alphabetical order

5-ALA	5-aminolevulinic acid
ABC	ATP-binding cassette
ABMDMA	9,10-anthracenediyl-bis(methylene)dimalonic acid
ACN	acetonitrile
AKR1C3	aldo-keto reductase 1C3
APAF-1	apoptosis protease-activation factor 1
ATG	autophagy related genes
ATP	adenozine triphosphate
ATR-IR	Attenuated total reflection-infrared spectroscopy
AUC	area under the curve
BCL-2	B-cell lymphoma 2 family

BDP-MA	benzoporphyrin derivative, monoacid ring A
BSA	bovine-serum albumin
BuOH	buthanol
CAC	critical aggregation concentration
Ce6	chlorine e6
CMC	critical micelization concentration
CRT	calreticulin 1
CT	computed tomography
CT	charge transfer
CYP	cytochrome P450 oxidoreductase
DAMP	damage associated molecular patterns
DAPI	4′,6-diamidino-2-phenylindole
DC	dendritic cells
DCM	dichloromethane
DDQ	2,3-dichloro-5,6-dicyano-1,4-benzoquinone
DEMI H_2O	demineralised H_2O
DHI	5,6-dihydroxylindole
DHICA	5,6-dihydroxyindole-2-carboxylic acid
$DIOC_6(3)$	3,3’-dihexyloxacarbocyanine iodide
DKK1	Dickkopf-related protein 1
DLI	drug-light interval
DMEM	Dulbecco’s modified Eagle medium
DMF	dimethylformamide
DMSO	dimethylsulfoxide
DPBF	1,3- diphenylisobenzofuran
ECM	extracellular matrix
EGFR	endothelial growth factor receptor
eIF2	eukaryotic translocation initiation factor 2 subunit α
EM	electromagnetic
EMC	endogenous melanogenic cytotoxicity
EPR	enhanced permeability and retention
ER	endoplasmic reticulum
Et_2O	diethyl-ether
EtOH	ethanol
FBS	fetal bovine serum
GSH	glutathione
HA-Ce6	hyaluronic acid-chlorin e6
HAP	hypoxia activated prodrug
HDL	high-density lipoprotein

HER 2	human epidermal growth factor receptor 2
HIF-1	hypoxia-inducible factor 1
HMGB1	high mobility groups Box 1
HpD	hematoporphyrin derivative
HPLC	high-resolution mass spectrometer
HPLC	high-pressure liquid chromatography
HSA	human serum albumin
IC	internal conversion
ICD	immunogenic cell death
ICG	indocyanine green
IFP	interstitial fluid stress
IRF	instrument response function
ISC	intersystem crossing
LDL	low density lipoprotein
L-DOPA	3,4-dihydroxyphenylalanine
LED	light-emitting diode
LFP	laser flash photolysis
LOOH	lipid hydroperoxides
m-CPBA	meta-chloroperbenzoic acid
MDR	multidrug resistance
MeOH	methanol
MHC-1	major histocompatibility complex class 1
MITF	microphthalmia-associated transcription factor
MRI	magnetic-resonance imaging
m-THPC	tetra-(*m*-hydroxylphenyl)chlorin
MTT	3-(4,5-dimethylthiazol-2-yl)-2,5-diphenyltetrazolium bromide
MV	microvascular stress
NF-Kb	nuclear factor Kb
NIR	near infrared region
NMR	nuclear magnetic resonance
NQO1	DT-diaphorase
NRF2	nuclear factor E2 related factor 2
NRG 1	neureoregulin 1
PAI	photoacoustic imaging
PBS	phosphate buffered saline
PDT	photodynamic therapy
PEI−ANI	polyethylenimine−alkyl nitroimidazole
PET	positron emission tomography
PI	photodynamic index
PIK3C3	phosphatidylinositol-3-kinase catalitic subunit type 3
PMT	photomultiplier tube

PPIX	protoporphyrin IX
PrA	propylamine
PRR	pattern recognition receptors
PS	photosensitiser
p-TSH	*p*-toluenesulfonylhydrazide
RCF	radichemical efficiency
ROS	reactive oxygen species
SA	specific activity
SAR	structure-activity relationship
SDS	sodium duodecyl sulfate
SOD	suberoxide dismutase
SPARC	secreted protein acidic and rich in cysteine
SPECT	single-photon emission computed tomography
TA	transient absorption
TAC	time-to-amplitude converter
TBAC	tetrabutylammonium chloride
TC-SPC	time-correlated single photon counting method
TEA	triethylamine
TFA	trifluoroacetic acid
THOMPP	5-(4-hydroxyphenyl)-10,15,20-methoxyphenyl)porphyrin
THOPP	5,10,15,20-tetrakis(4-hydroxyphenyl)porphyrin
TLC	thin-layer chromatography
TME	tumour microenvironment
TMPyP4	5,10,15,20-tetrakis(*N*-methylpyridinium-4-yl)porphyrin
TPP	tetraphenylporphyrin
TPZ	tirapazamine
TRP 1	tyrosinase related protein 1
ULK 1	unc-51-like autophagy-activating kinase 1
Zn(II) TPP	zinc(II) tetraphenylporphyrin

8. Supporting information

8.1. Supporting information to the Section 3.2.

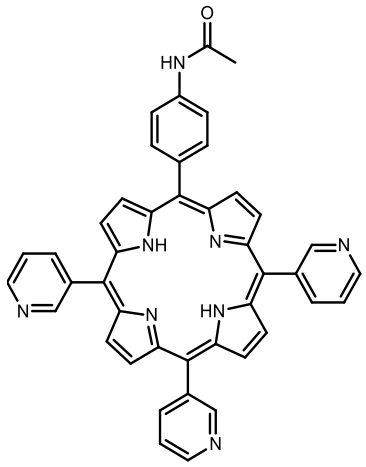

2

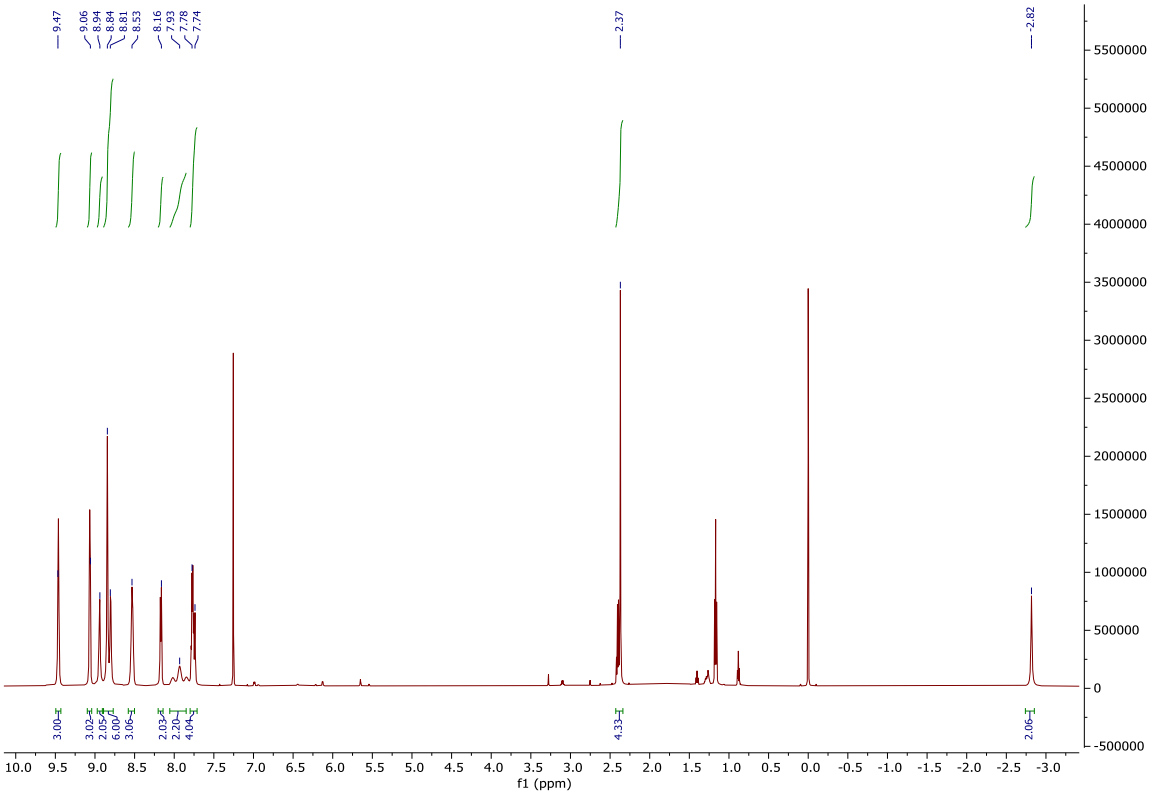

Figure S1. ^{1}H NMR ($CDCl_3$, 600 MHz) spectrum of porphyrin **2**.

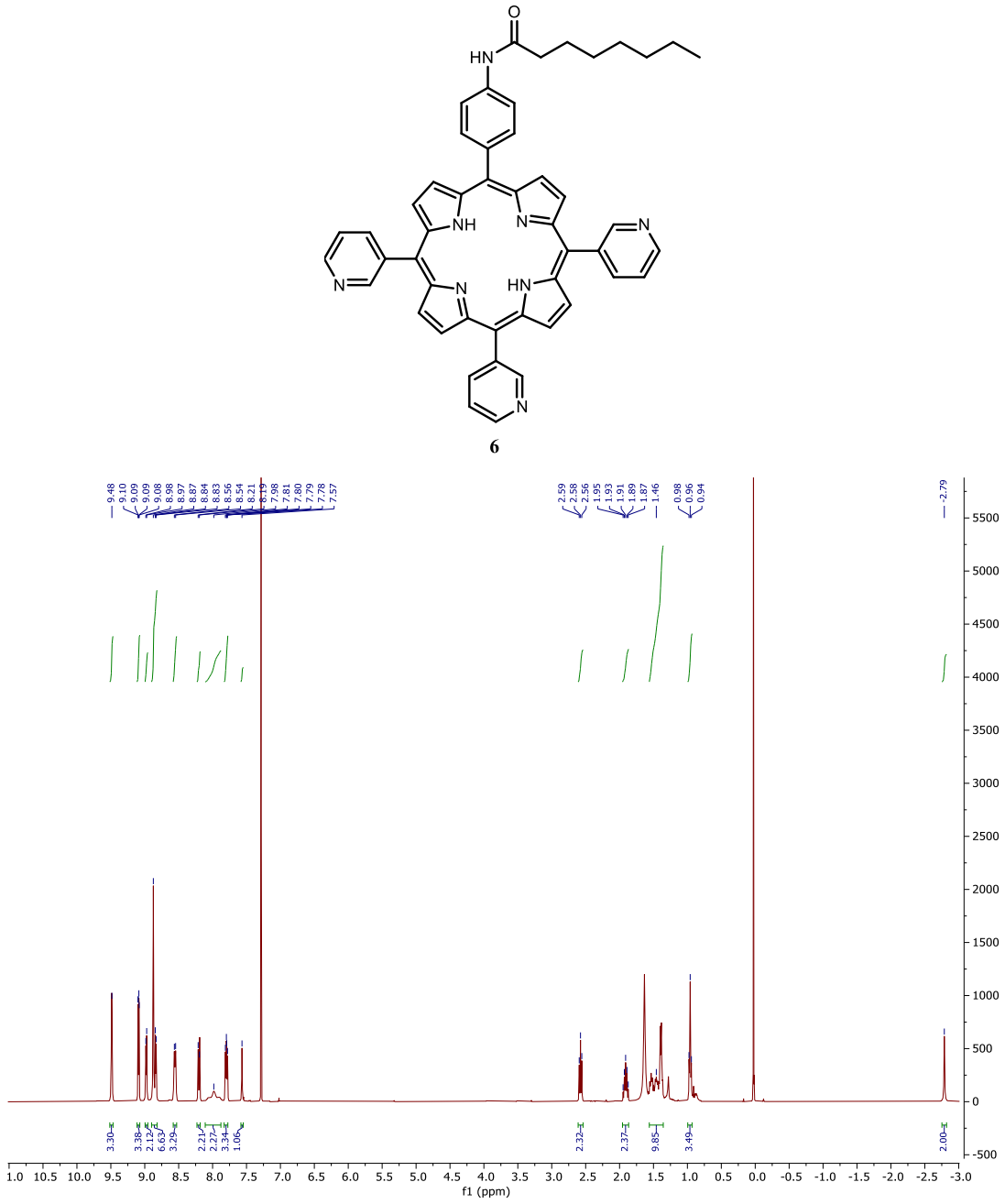

Figure S2. ^{1}H NMR ($CDCl_3$, 400 MHz) spectrum of **6**.

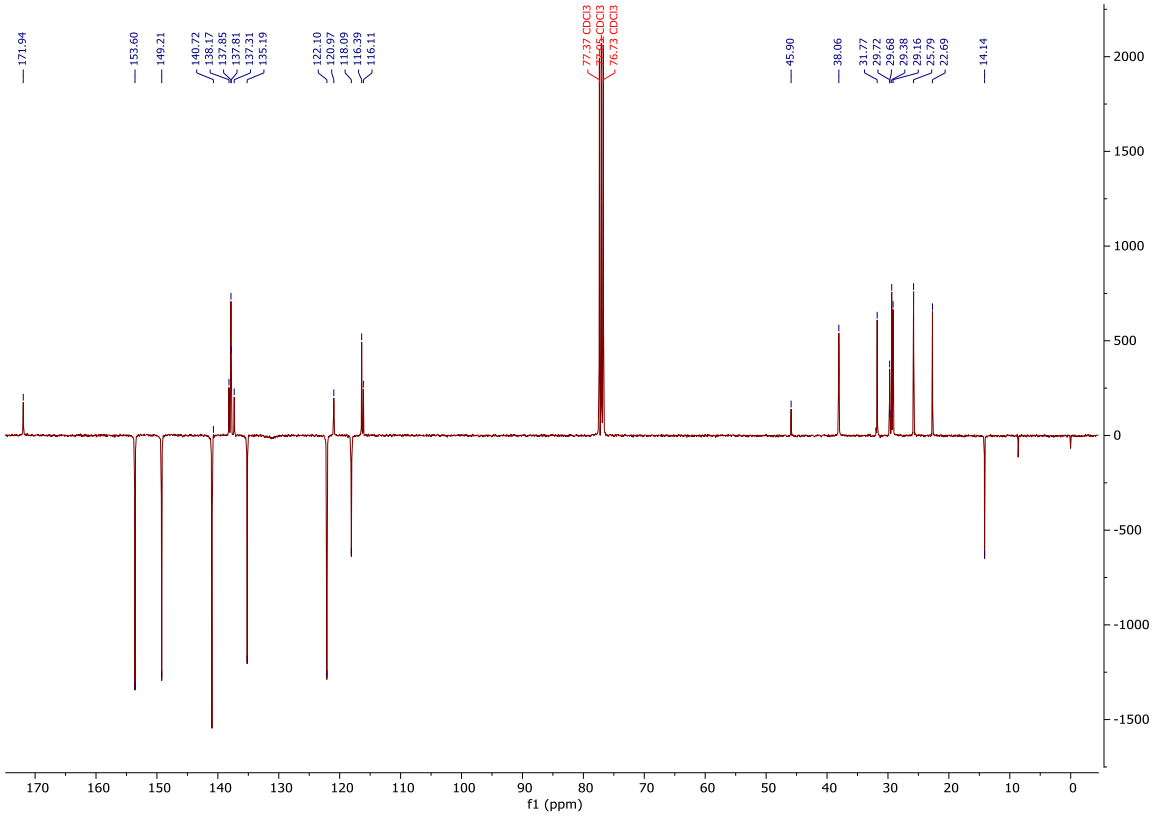

Figure S3. ^{13}C NMR ($CDCl_3$, 100 MHz) spectrum of **6**.

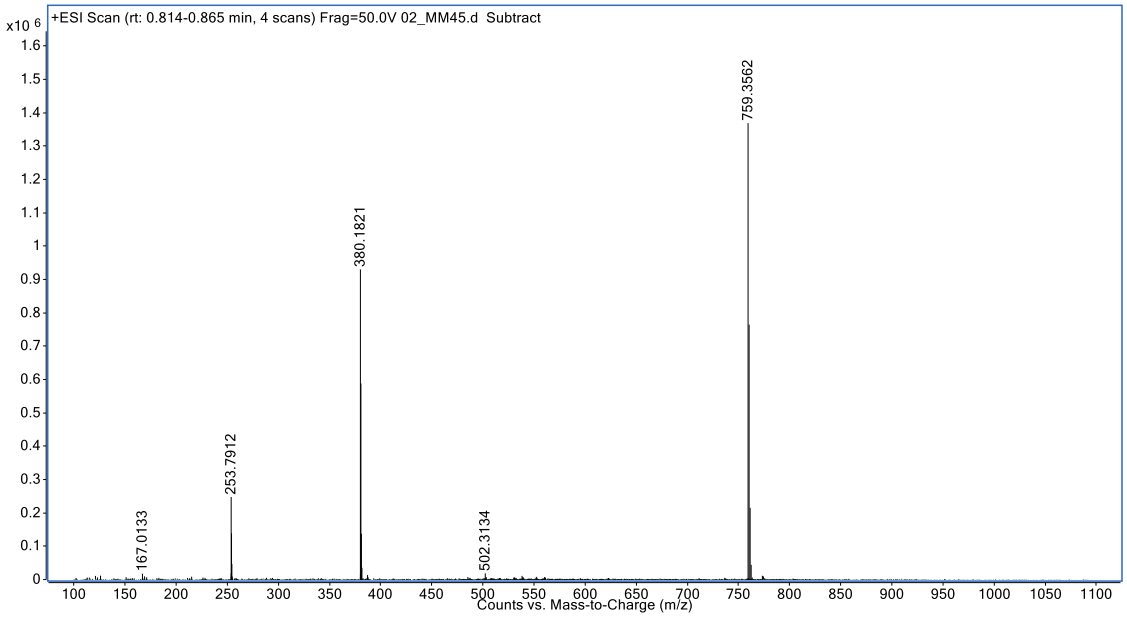

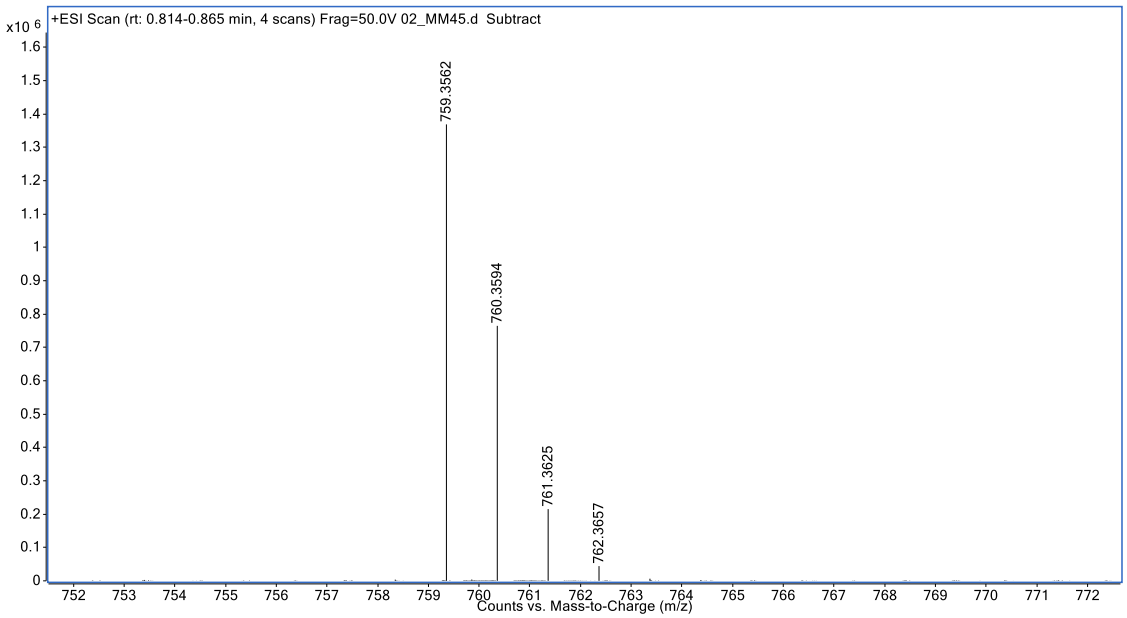

Figure S4. Mass spectrum of **6** in m/z region 100-1100 (upper spectrum) and enlarged spectrum in region m/z 752 – 772 (lower spectrum).

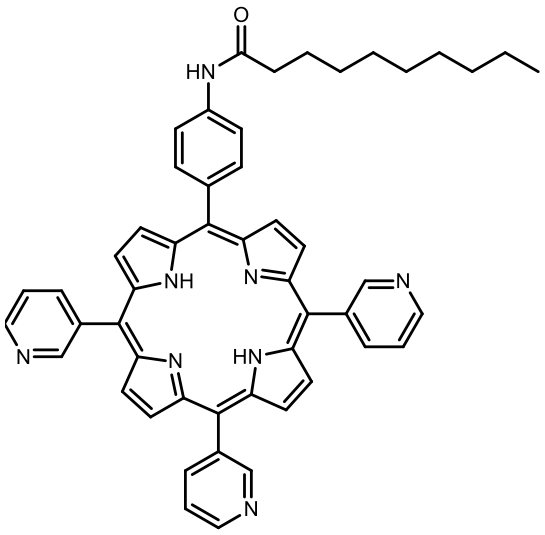

7

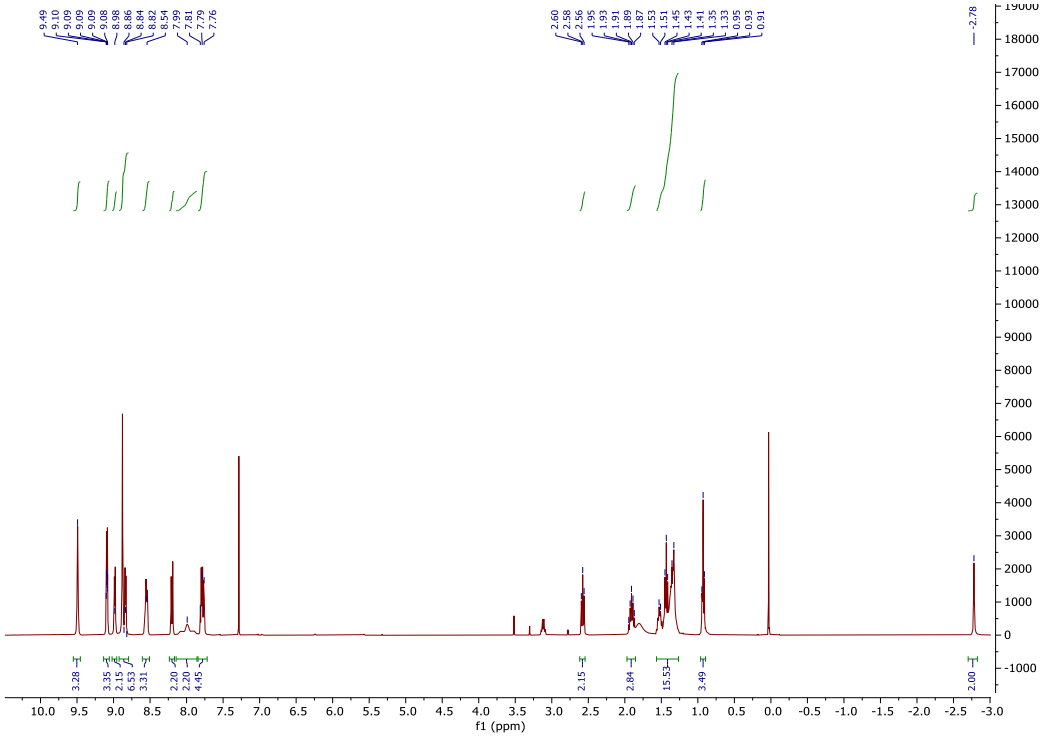

Figure S5. ^{1}H NMR ($CDCl_3$, 400 MHz) spectrum of **7**.

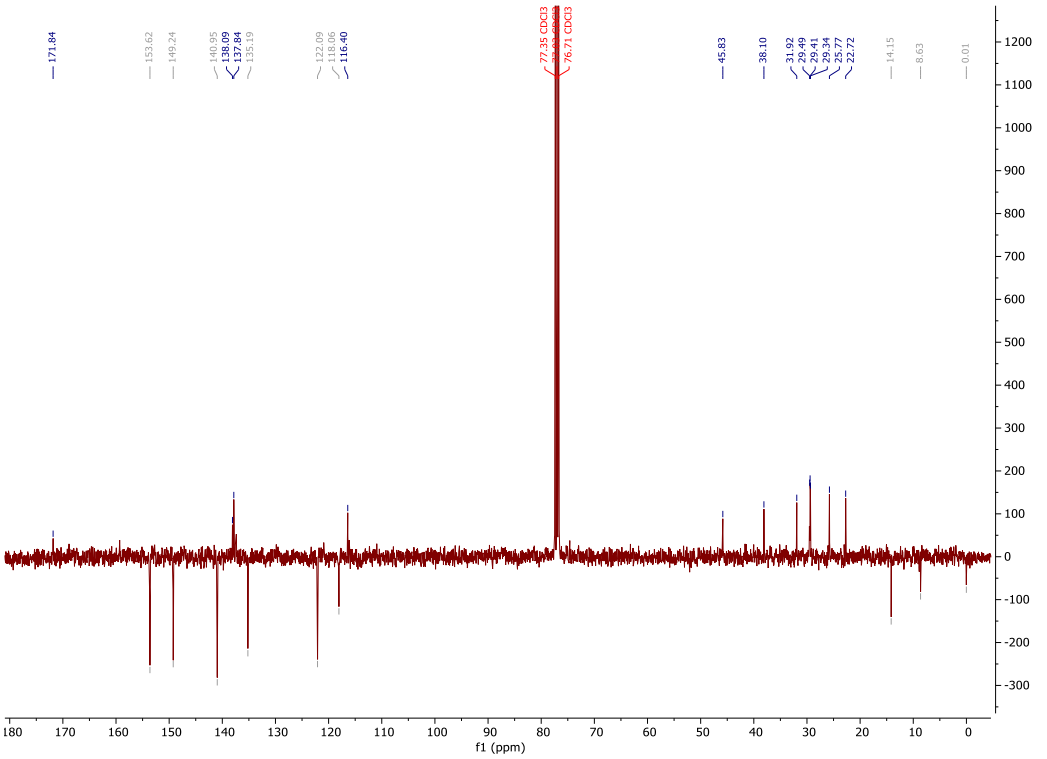

Figure S6. ^{13}C NMR ($CDCl_3$, 100 MHz) spectrum of **7**.

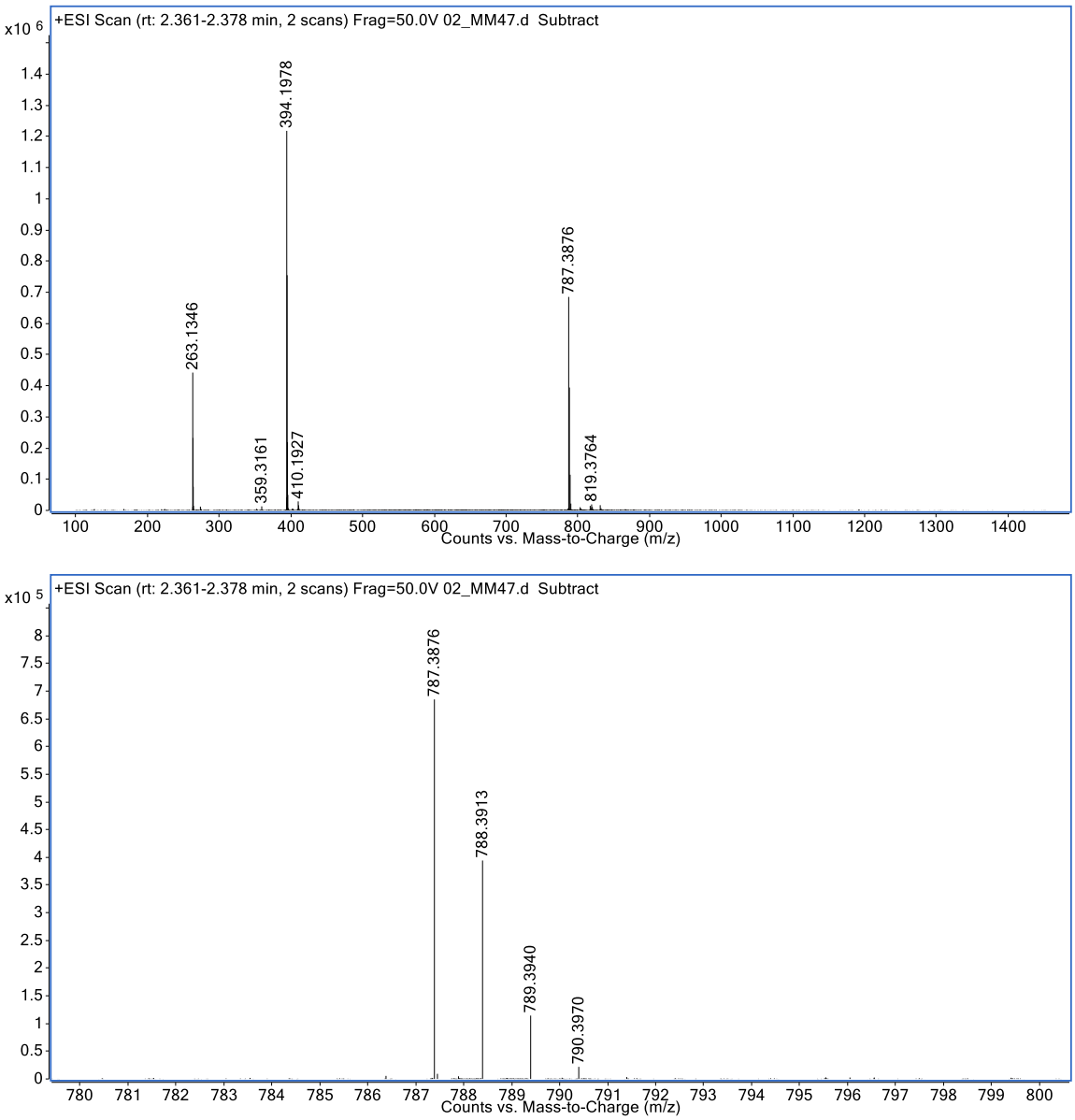

Figure S7. Mass spectrum of **7** in m/z region 100-1500 (upper spectrum) and enlarged spectrum in region m/z 780 – 800(lower spectrum).

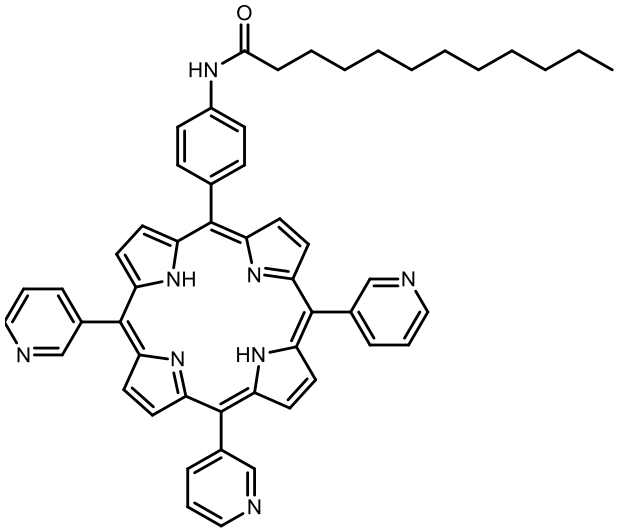

8

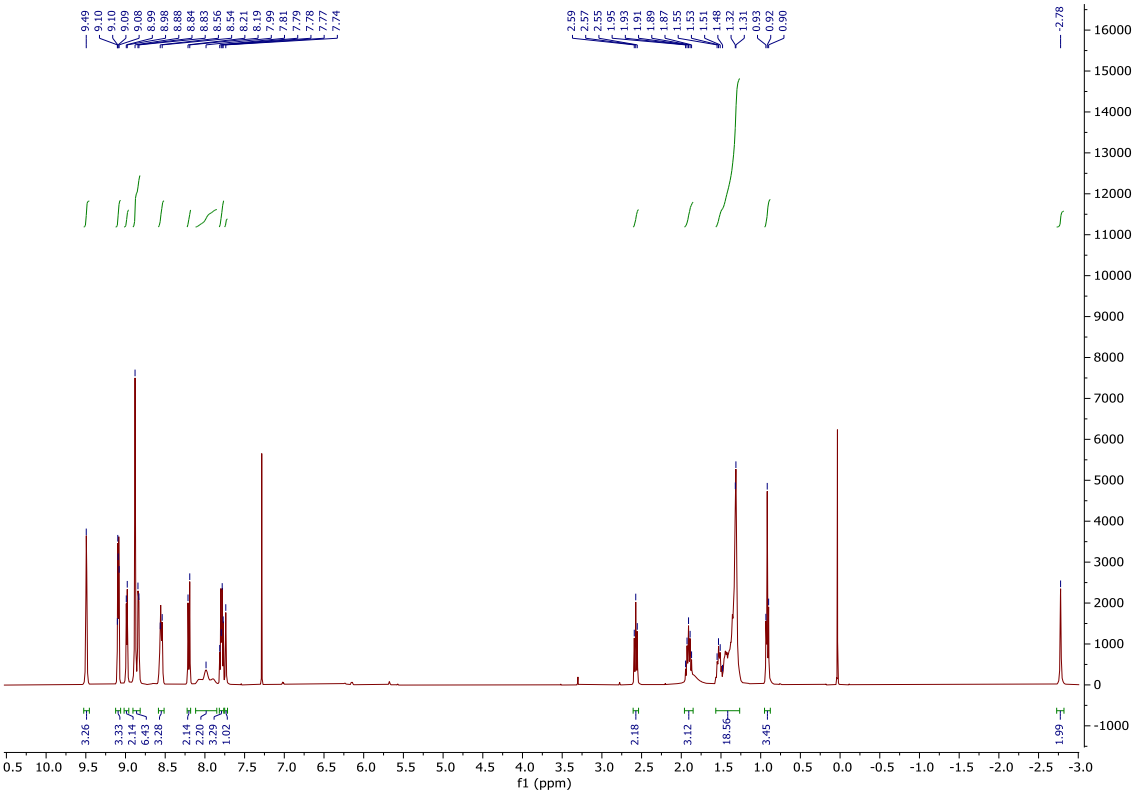

Figure S8. ^{1}H NMR ($CDCl_3$, 400 MHz) spectrum of **8**.

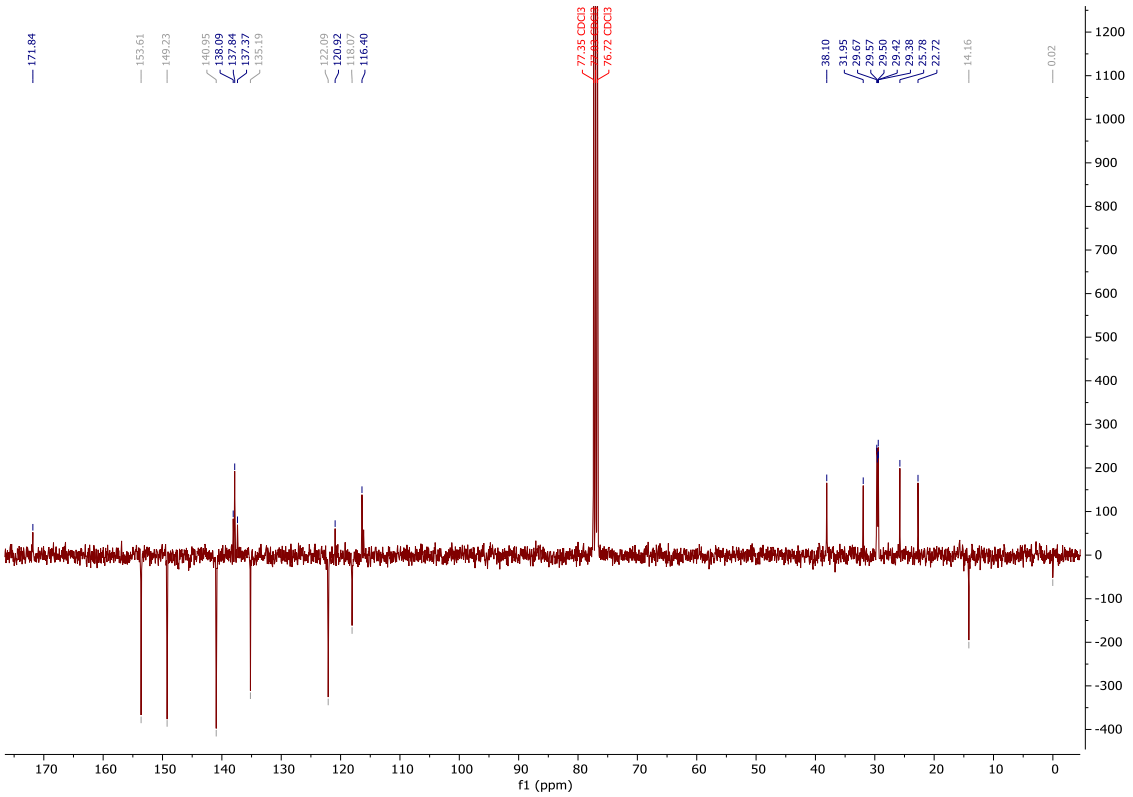

Figure S9. ^{13}C NMR ($CDCl_3$, 100 MHz) spectrum of **8**.

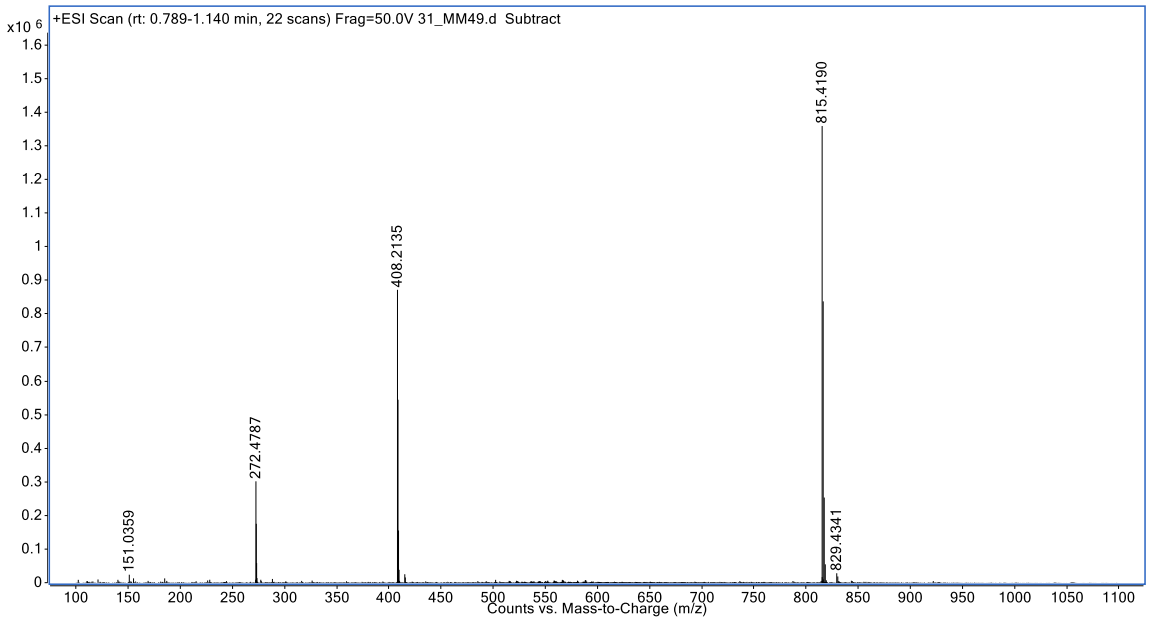

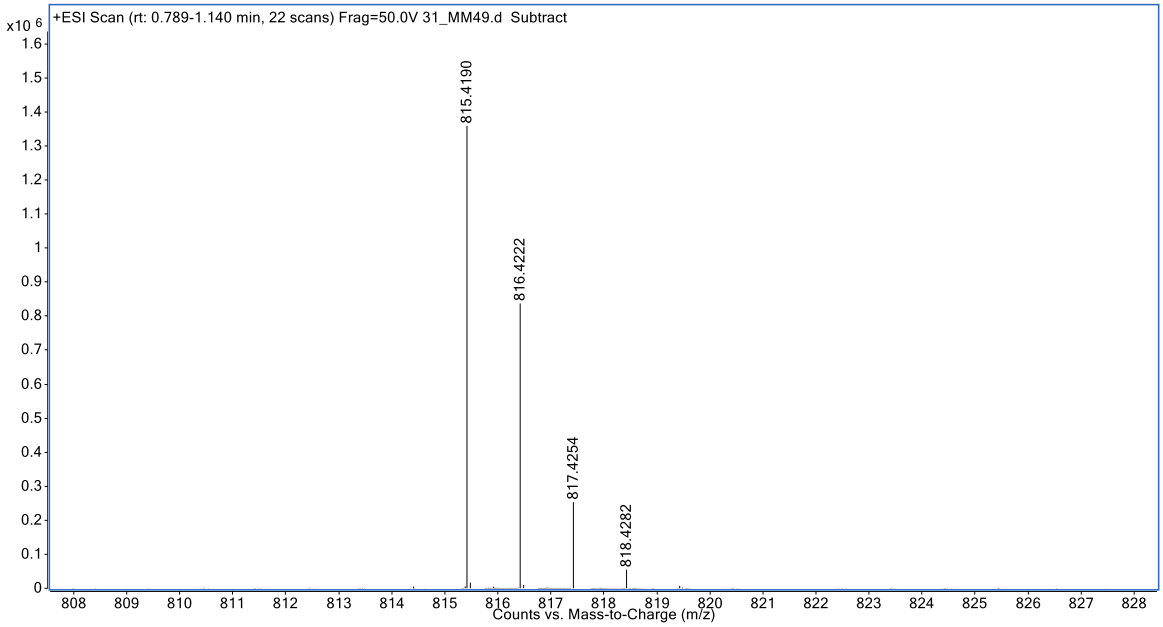

Figure S10. Mass spectrum of **8** in m/z region 100-1100 (upper spectrum) and enlarged spectrum in region m/z 808 – 828(lower spectrum).

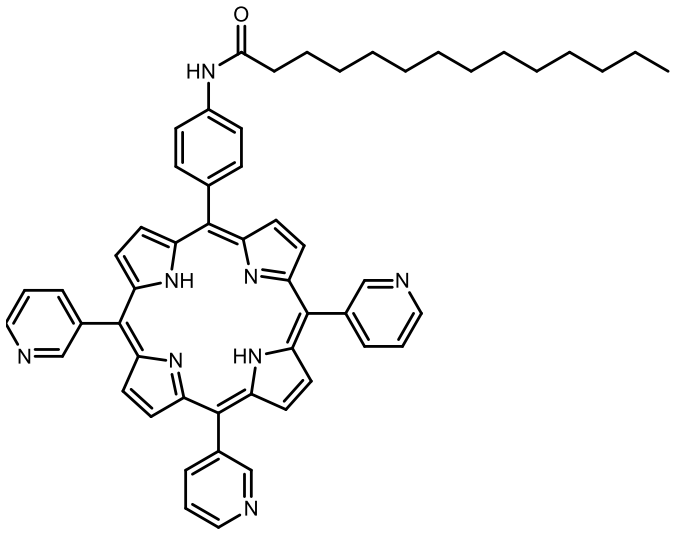

9

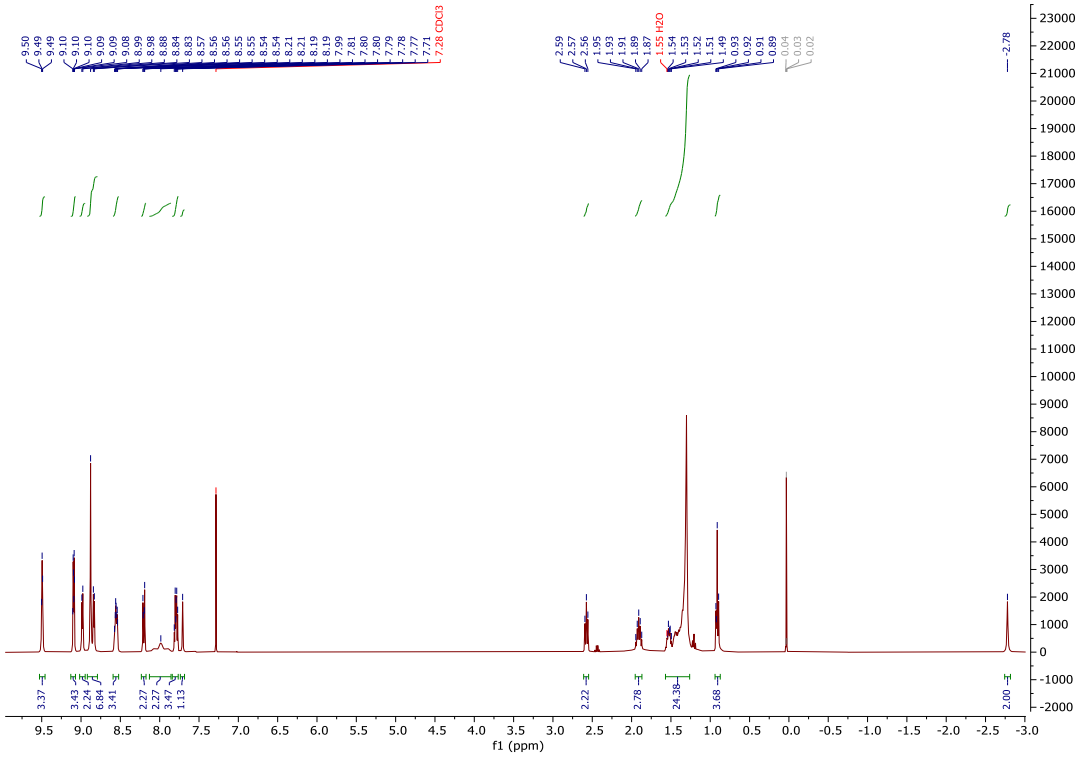

Figure S11. ^{1}H NMR ($CDCl_3$, 400 MHz) spectrum of **9**.

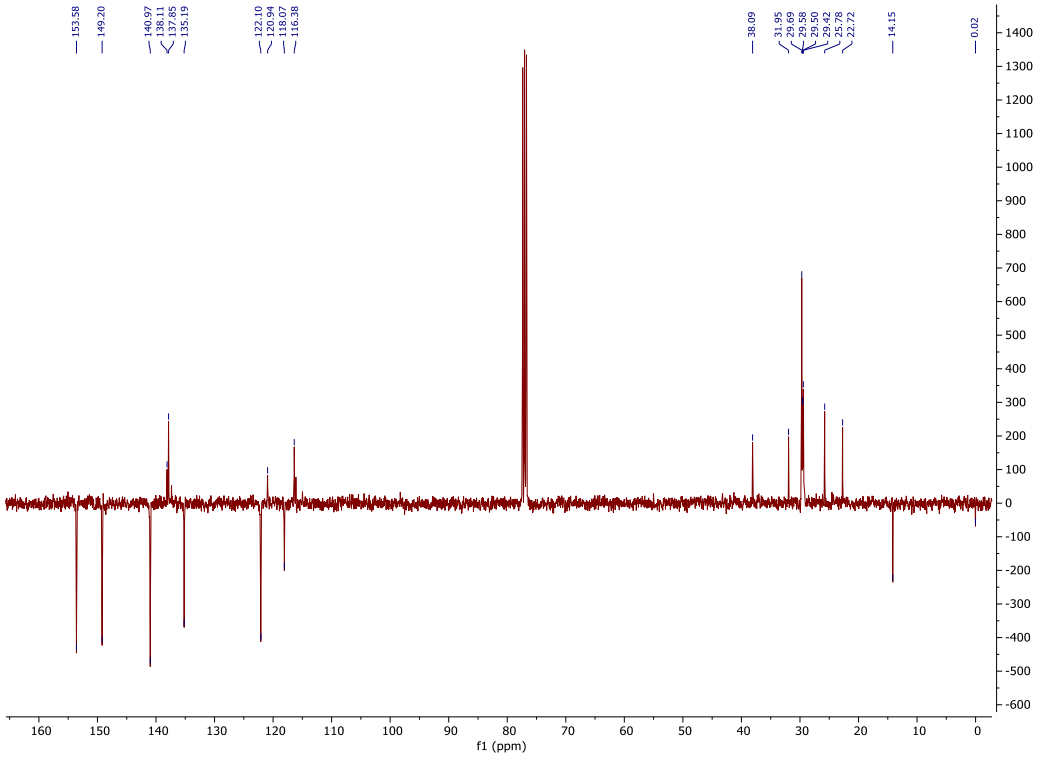

Figure S12. ^{13}C NMR ($CDCl_3$, 100 MHz) spectrum of **9**.

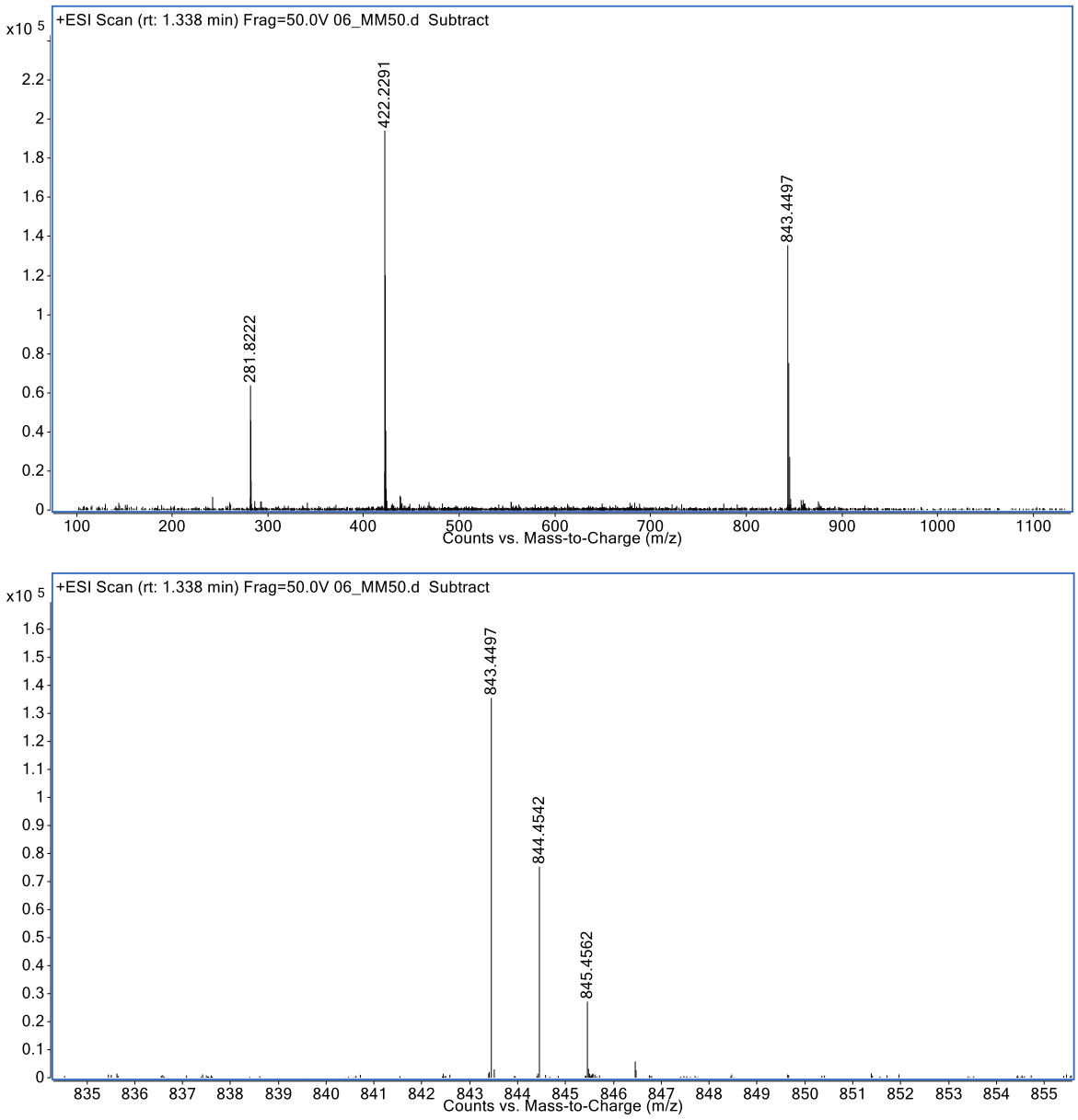

Figure S13. Mass spectrum of **9** in m/z region 100-1100 (upper spectrum) and enlarged spectrum in region m/z 835 – 855(lower spectrum).

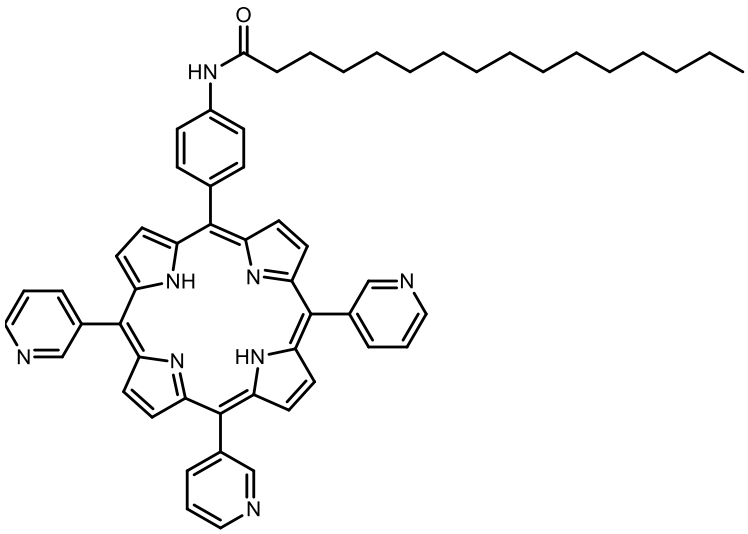

10

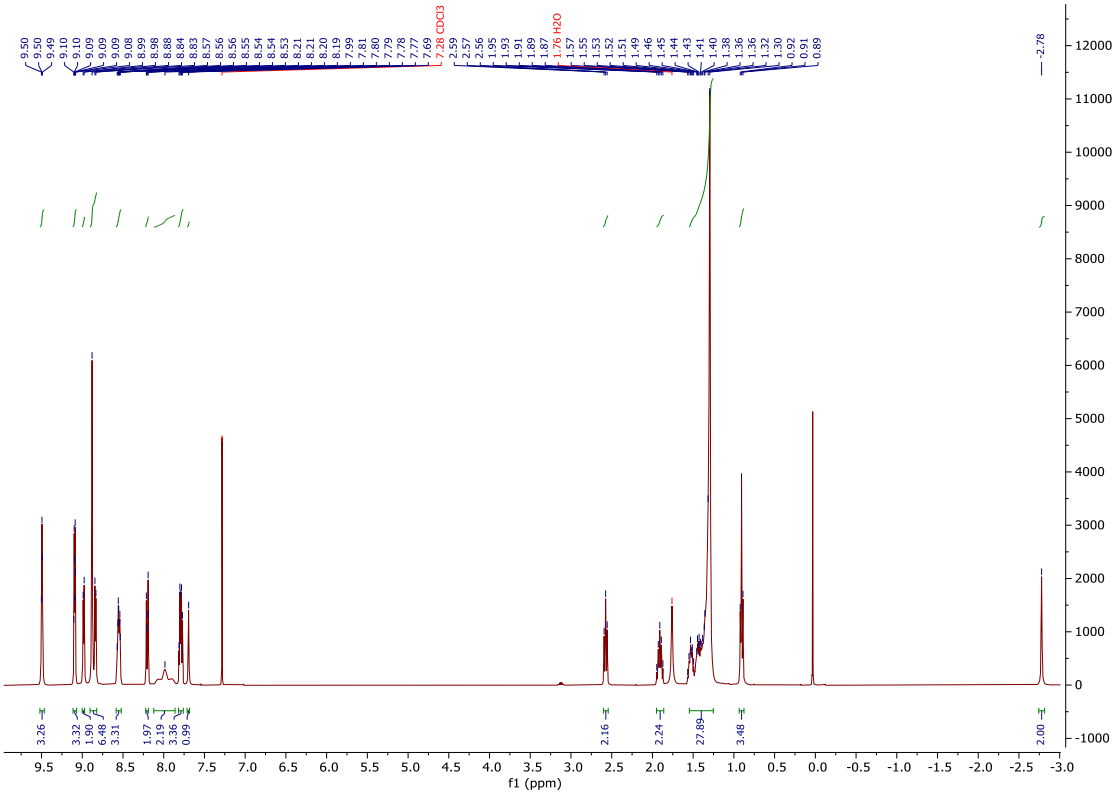

Figure S14. ^{1}H NMR ($CDCl_3$, 400 MHz) spectrum of **10**.

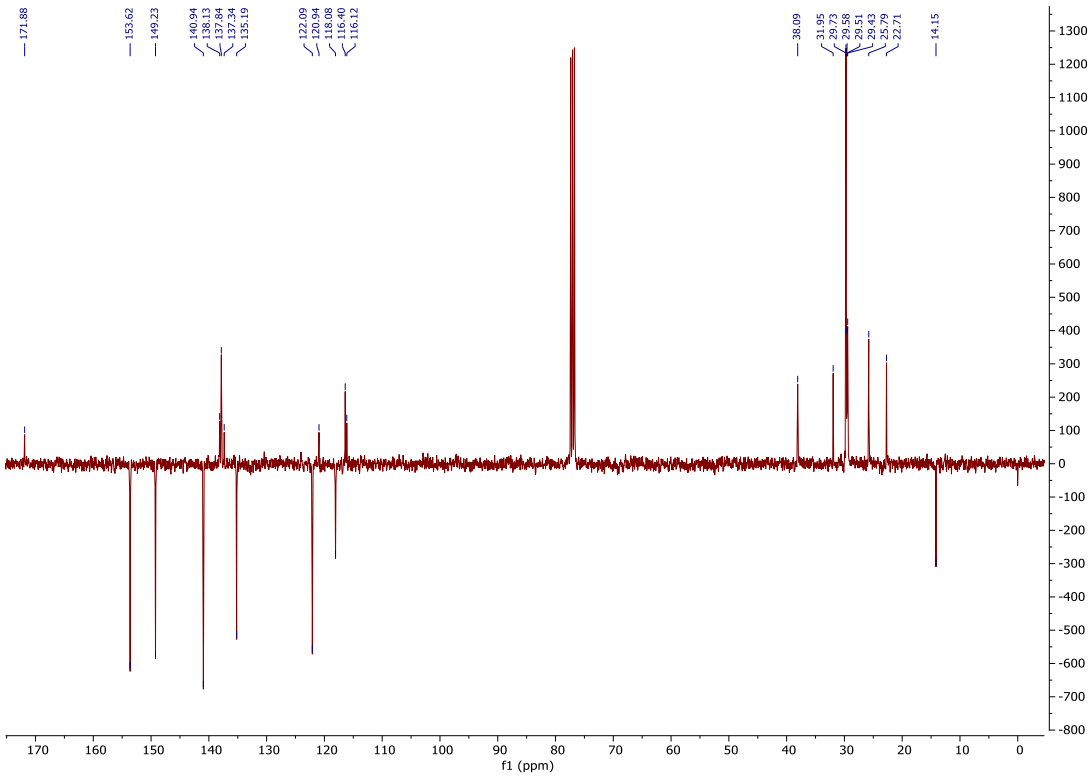

Figure S15. ^{13}C NMR ($CDCl_3$, 100 MHz) spectrum of **10**.

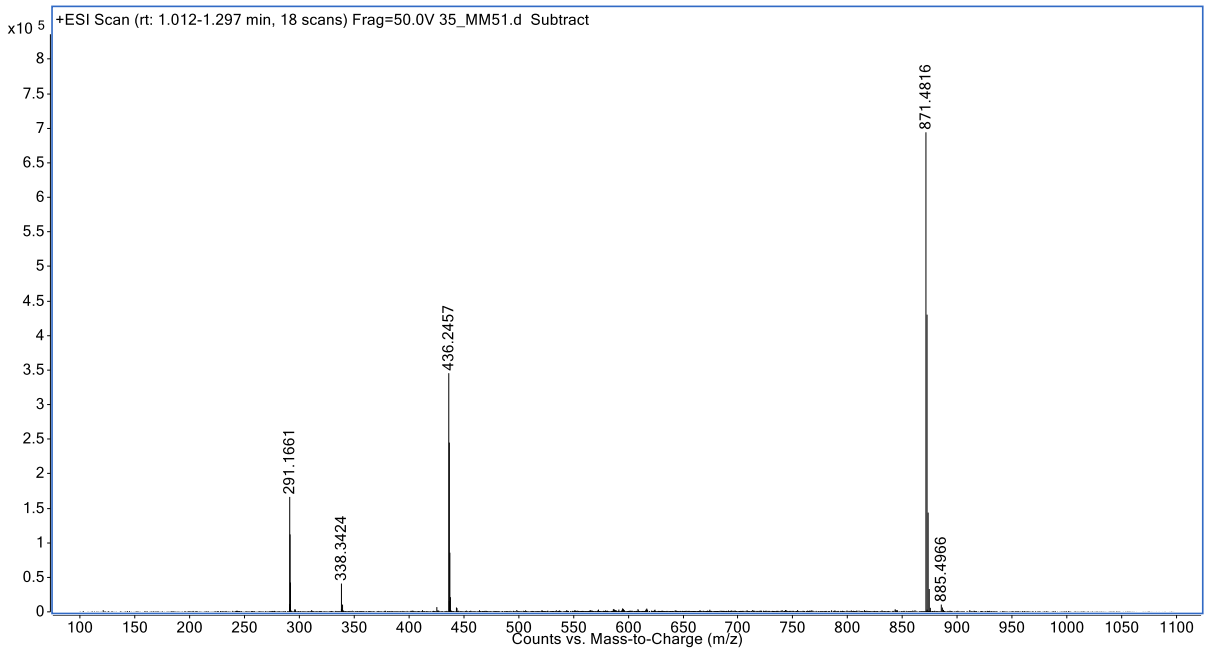

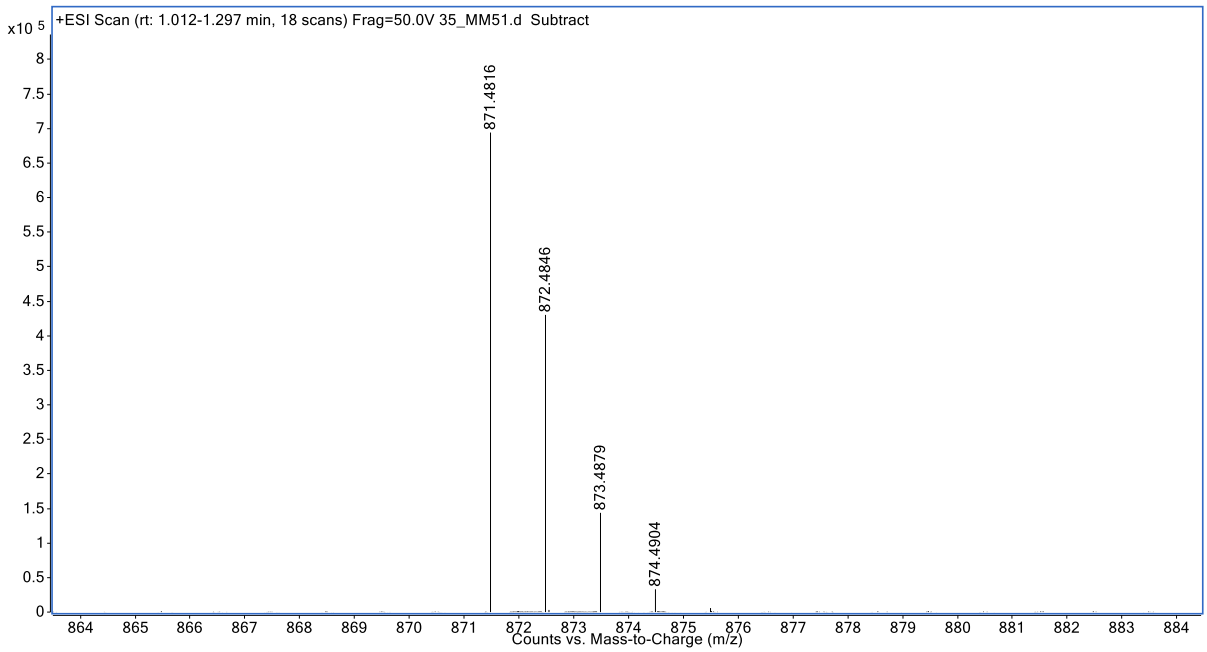

Figure S16. Mass spectrum of **10** in m/z region 100-1100 (upper spectrum) and enlarged spectrum in region m/z 864 – 884(lower spectrum).

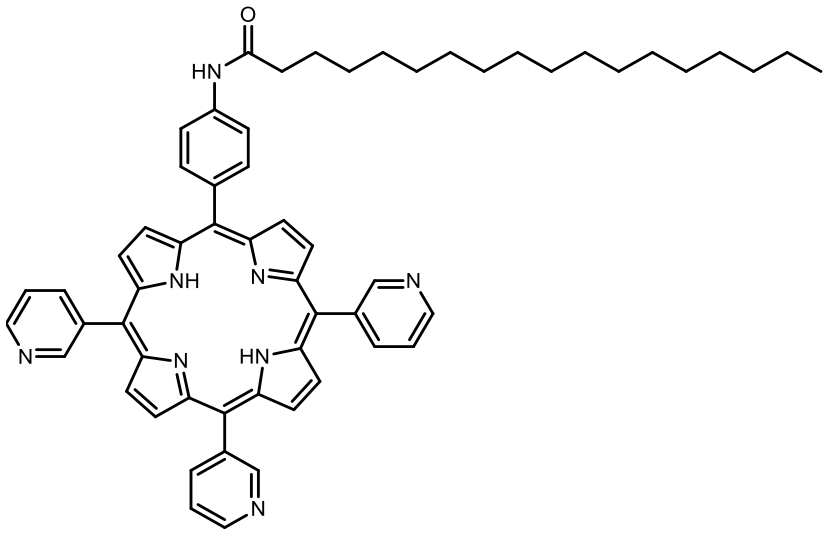

11

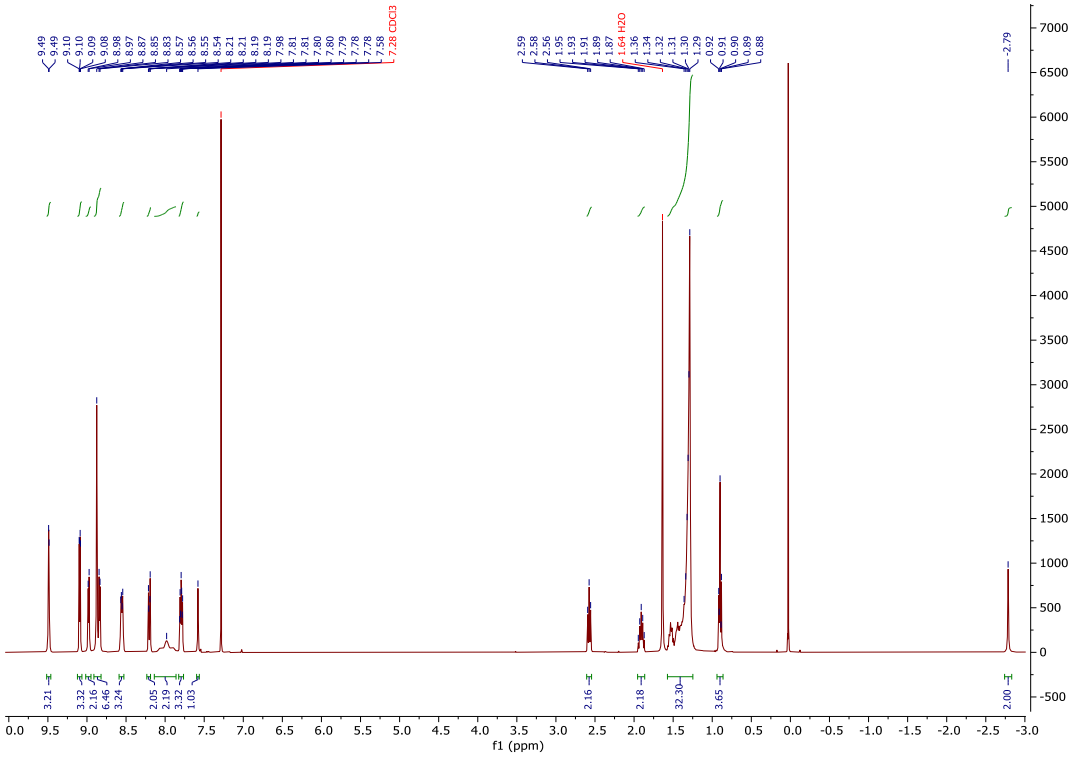

Figure S17. ^{1}H NMR ($CDCl_3$, 400 MHz) spectrum of **11**.

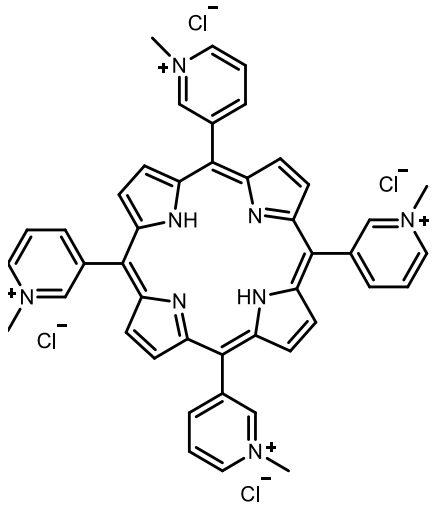

12

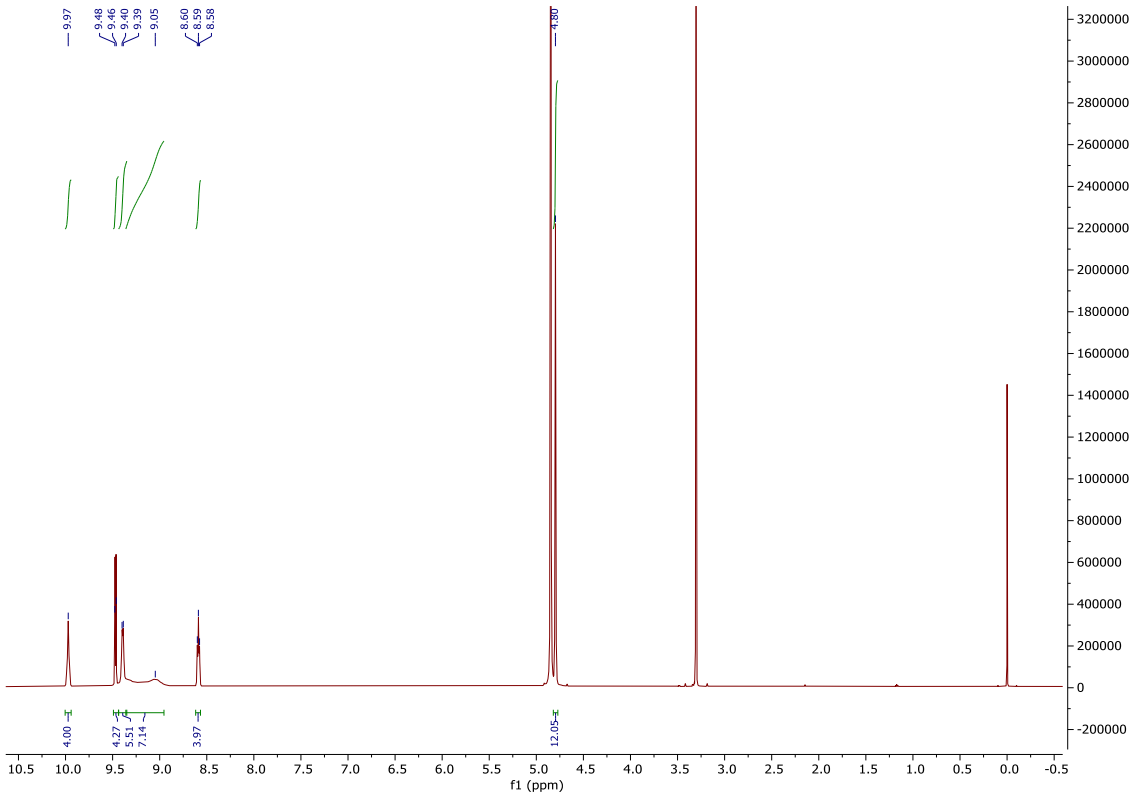

Figure S18. ^{1}H NMR (CD_3OD, 600 MHz) spectrum of **12**.

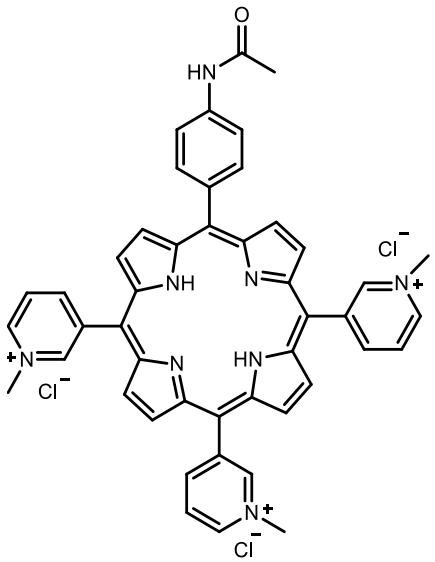

13

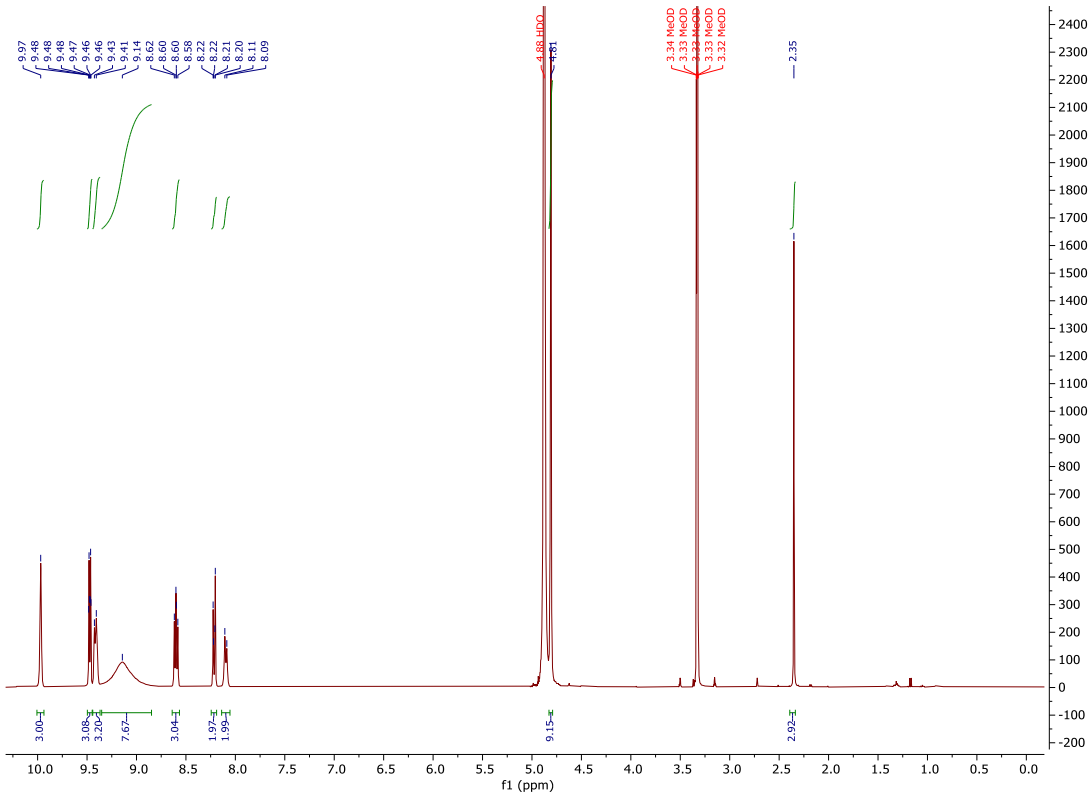

Figure S19. ^{1}H NMR (CD_3OD, 400 MHz) of **13**.

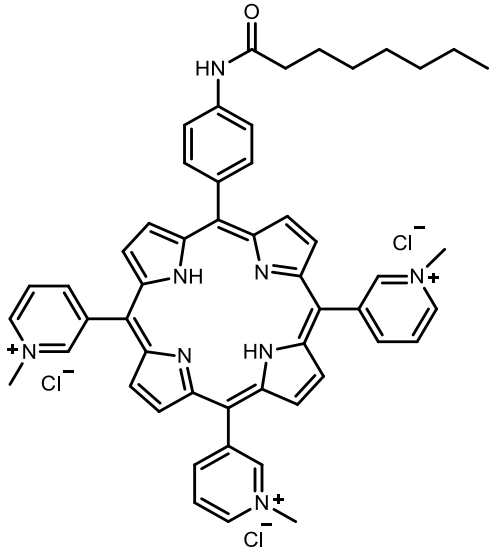

14

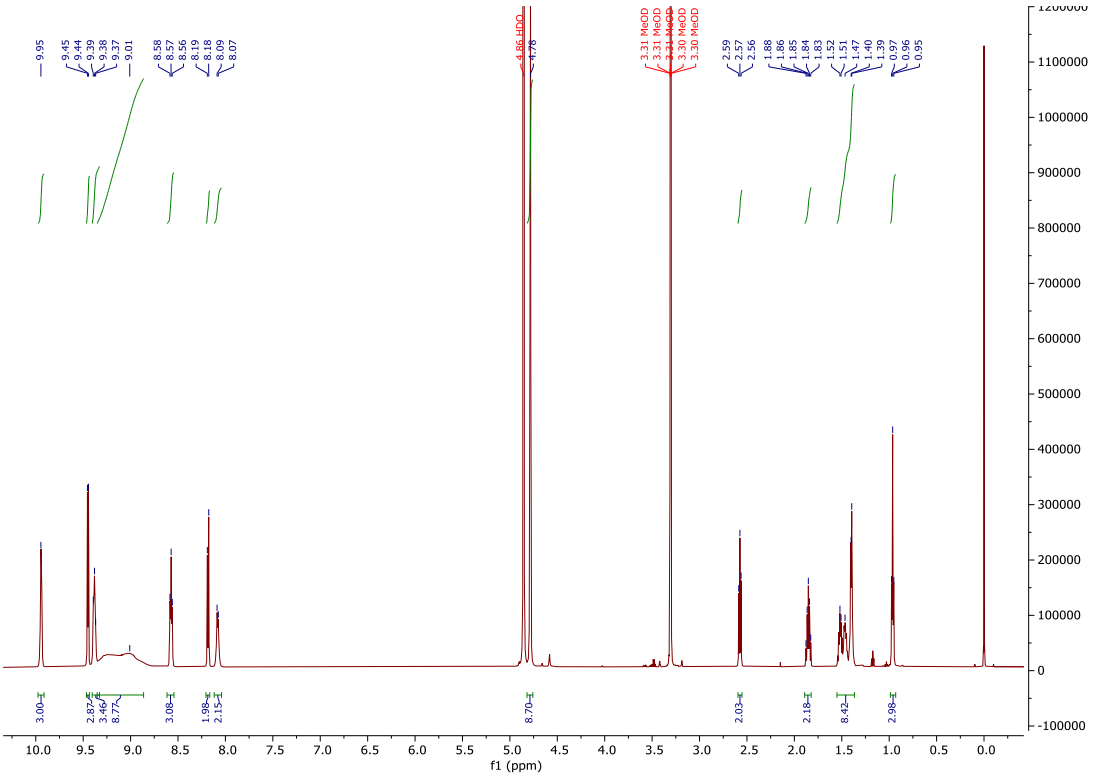

Figure S20. ^{1}H NMR (CD_3OD, 600 MHz) spectrum of **14**.

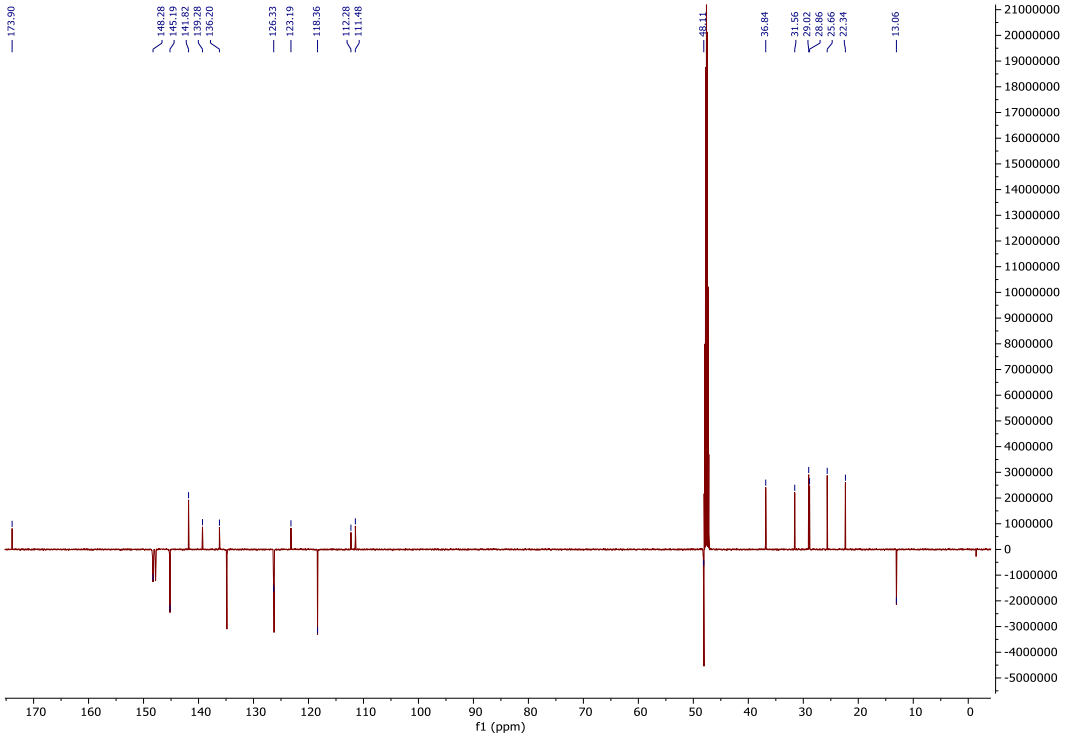

Figure S21. ^{13}C NMR (CD_3OD, 150 MHz) spectrum of **14**.

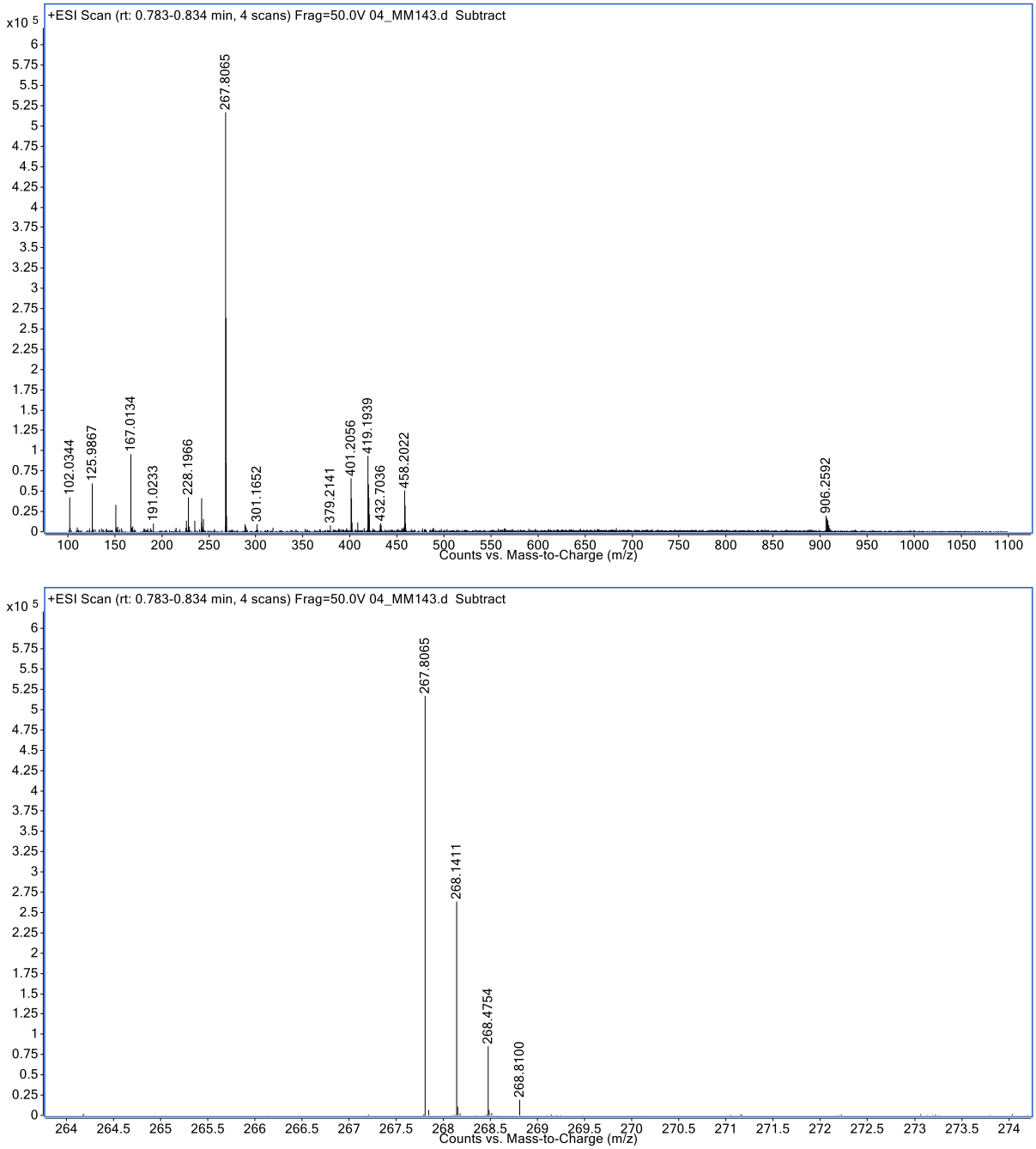

Figure S22. Mass spectrum of **14** in m/z region 100-1100 (upper spectrum) and enlarged spectrum in region m/z 264 – 274(lower spectrum).

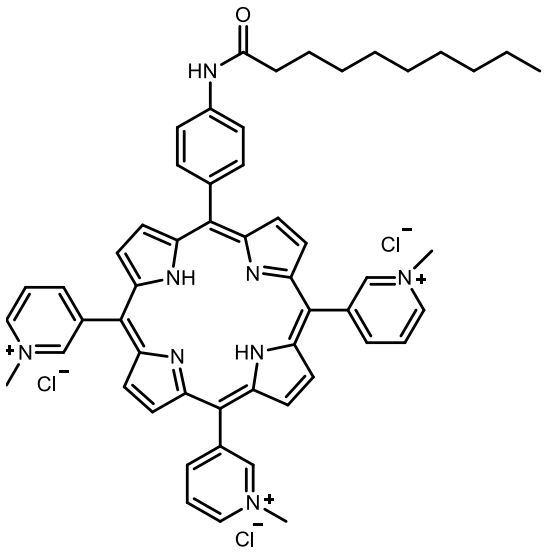

15

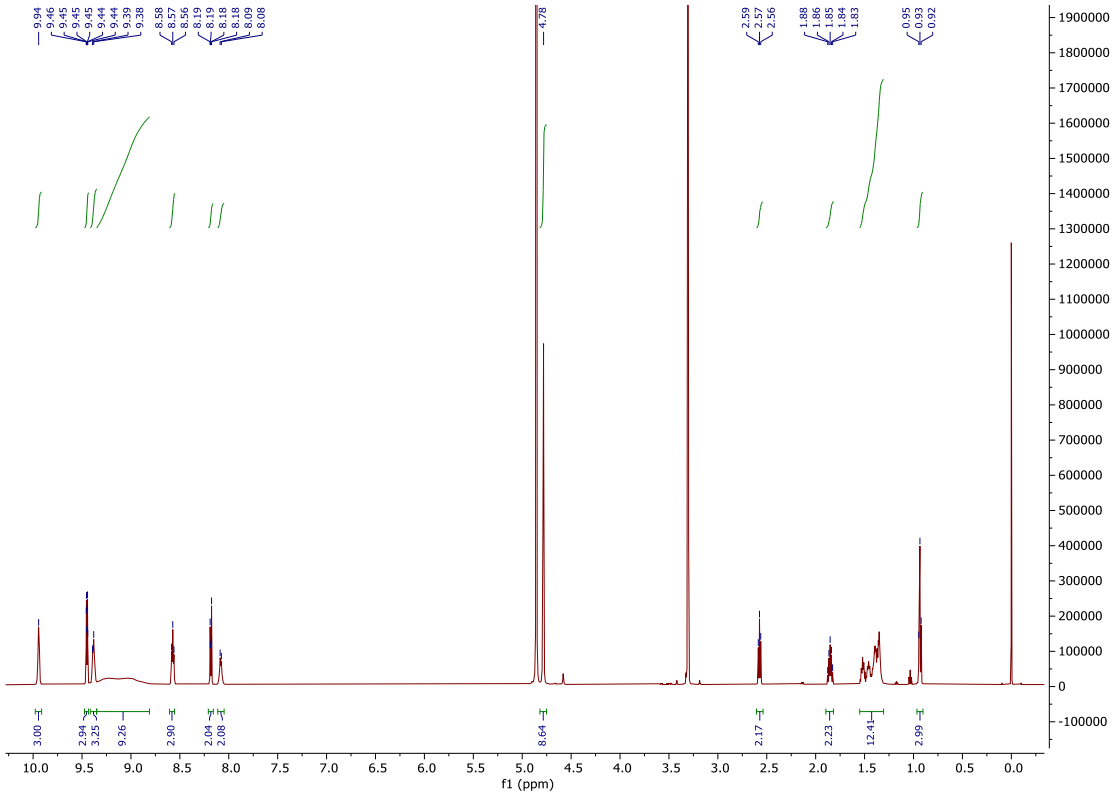

Figure S23. ^{1}H NMR (CD_3OD, 600 MHz) spectrum of **15**.

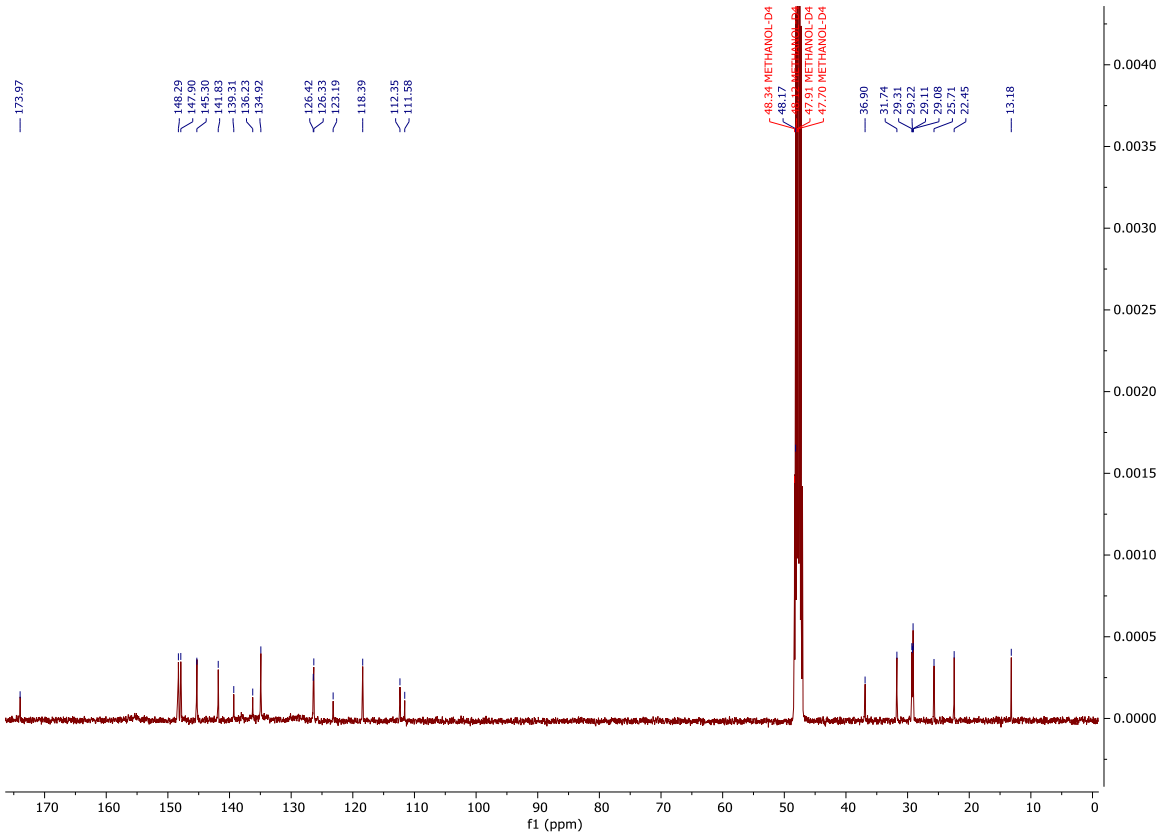

Figure S24. ^{13}C NMR (CD_3OD, 100 MHz) spectrum of **15**.

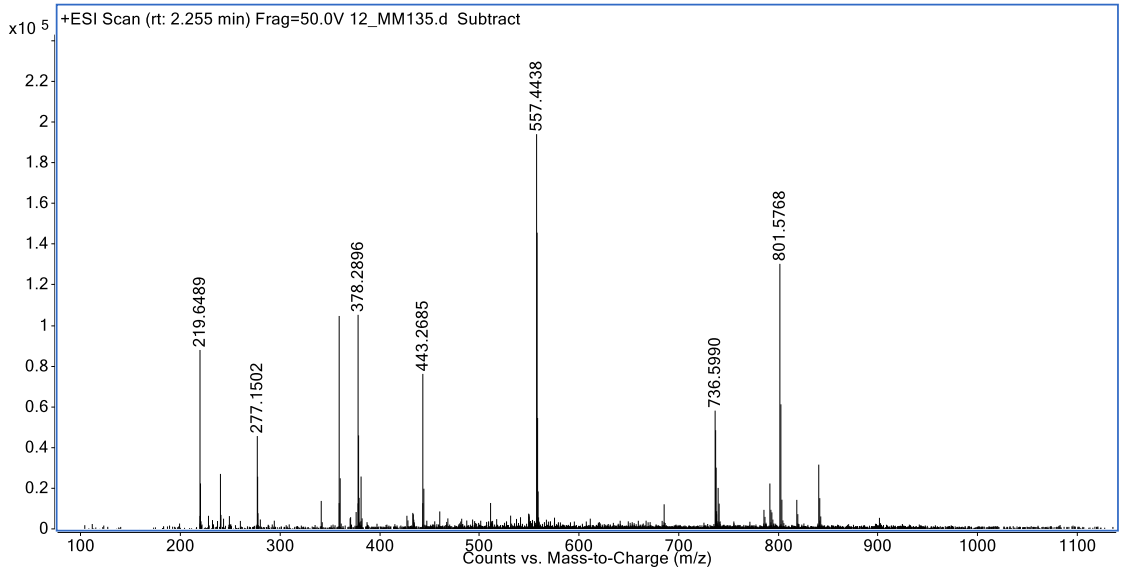

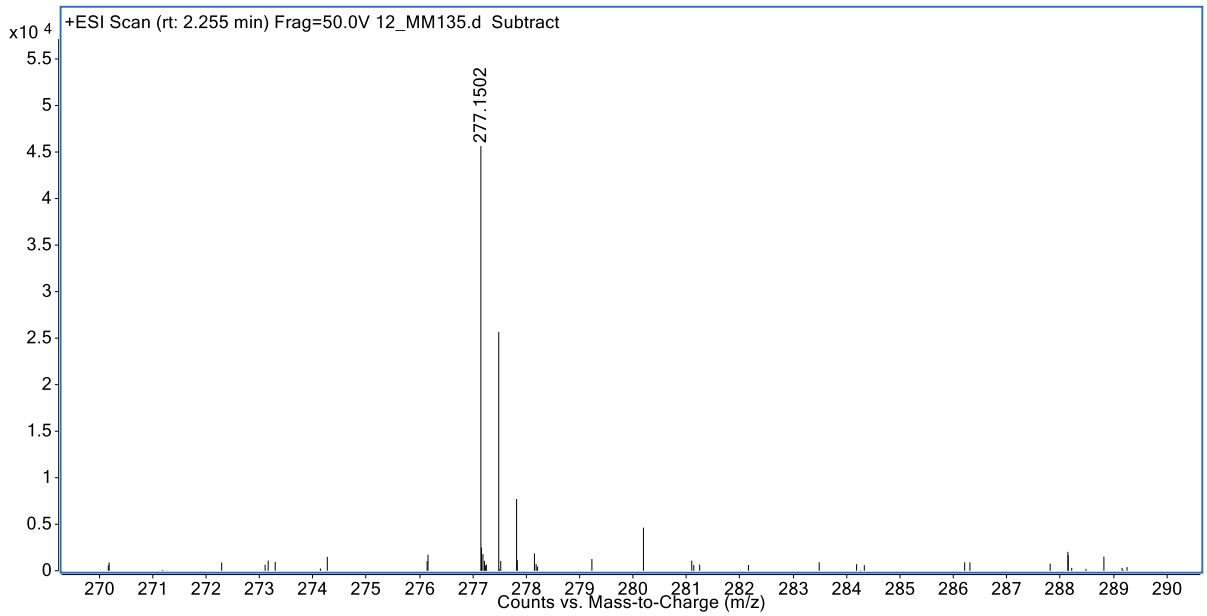

Figure S25. Mass spectrum of **15** in m/z region 100-1100 (upper spectrum) and enlarged spectrum in region m/z 270 – 290 (lower spectrum).

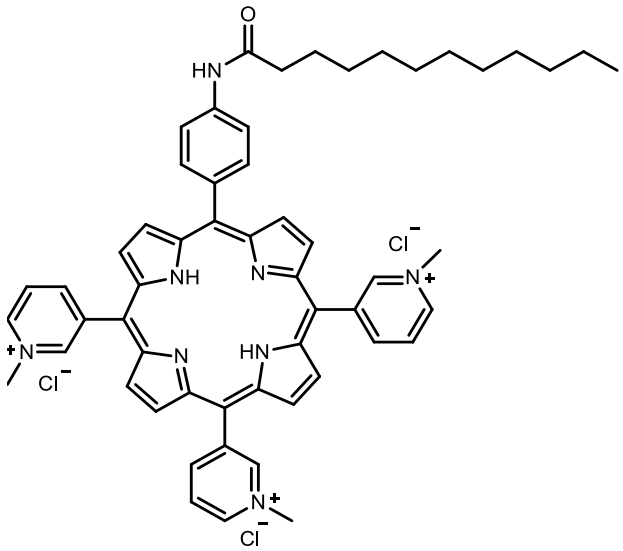

16

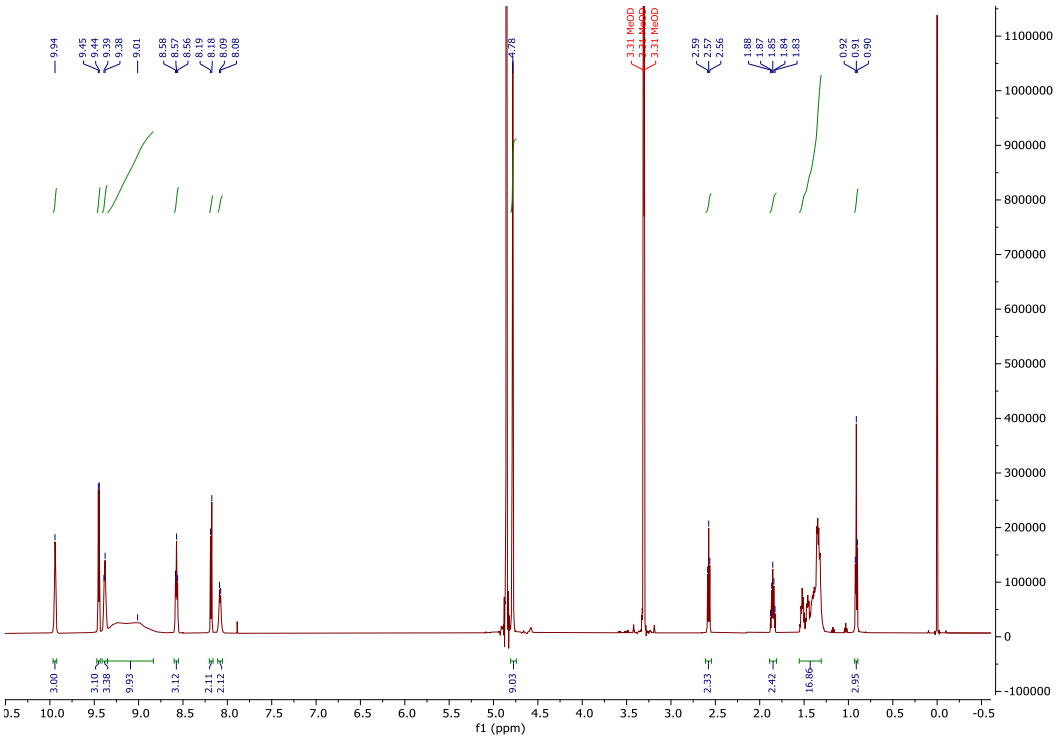

Figure S26. ^{1}H NMR (CD_3OD, 600 MHz) spectrum of **16**.

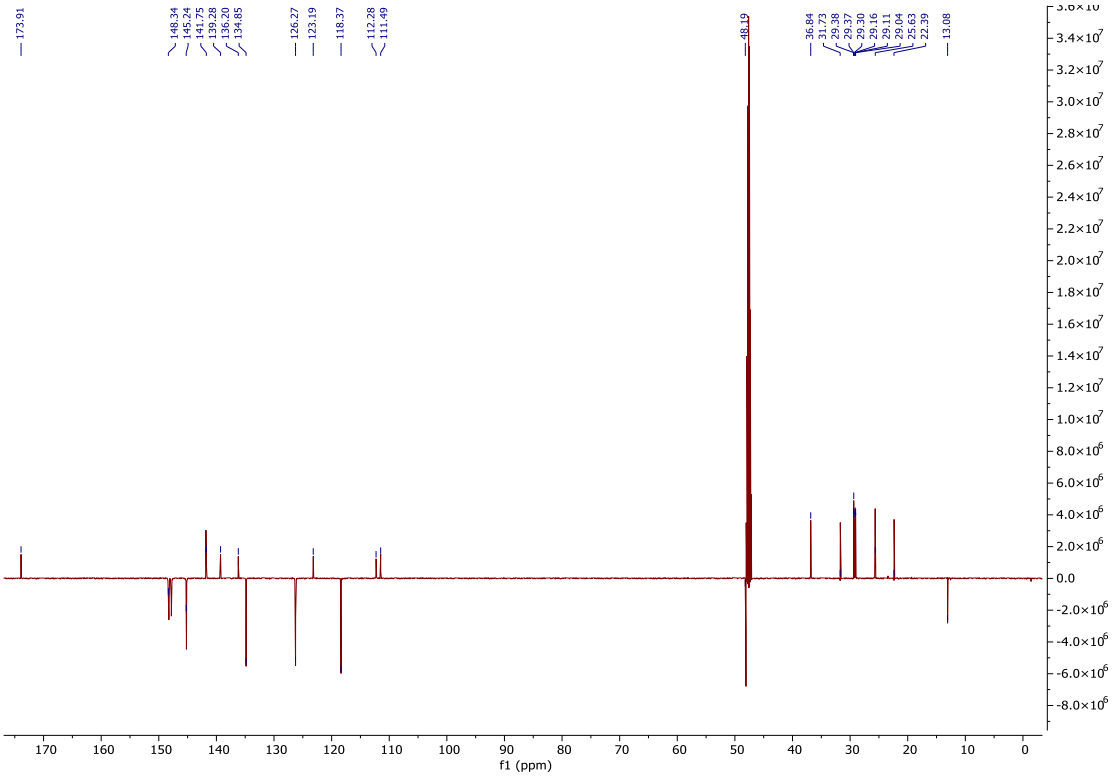

Figure S27. ^{13}C NMR (CD_3OD, 150 MHz) spectrum of **16**.

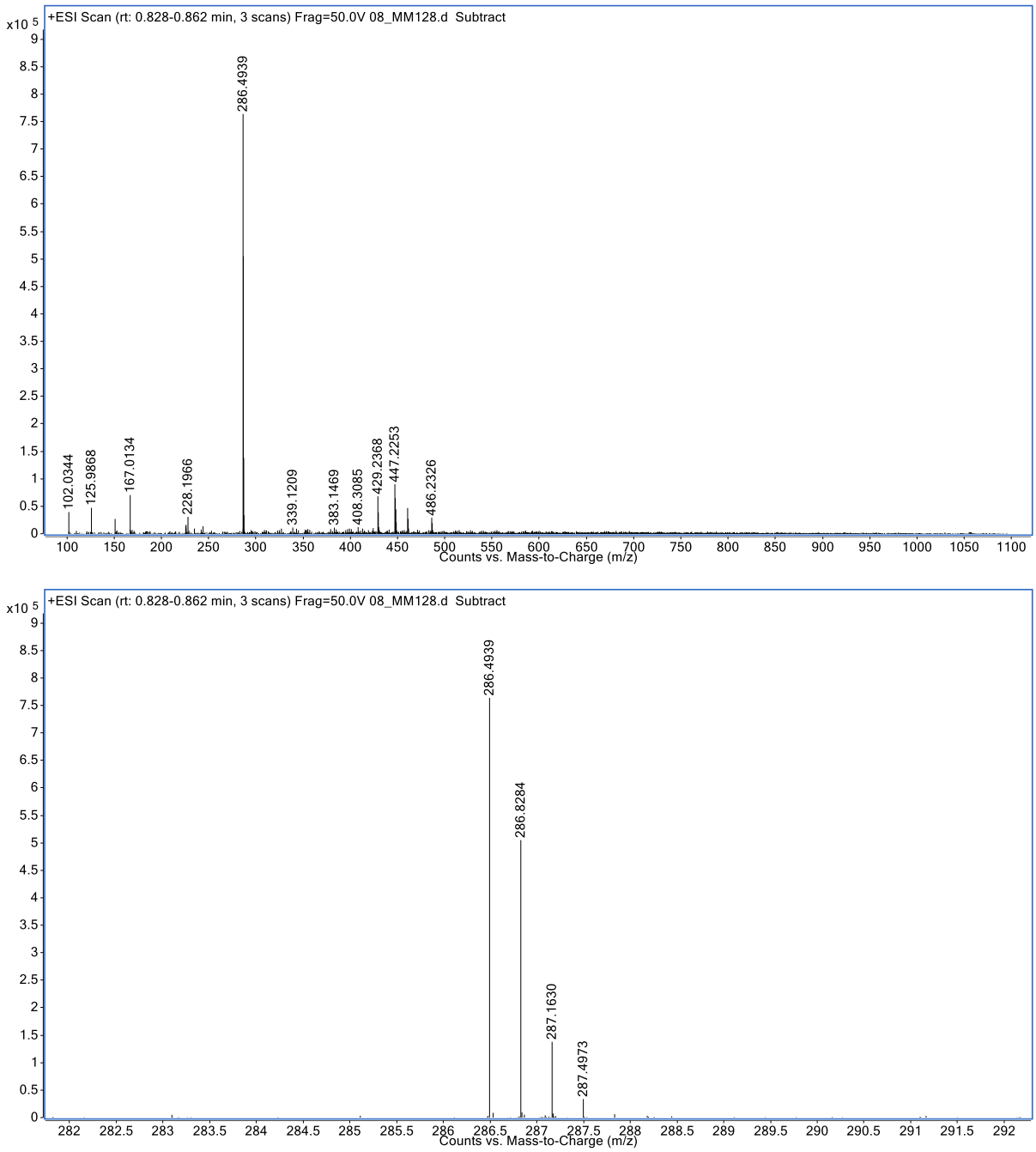

Figure S28. Mass spectrum of **16** in m/z region 100-1100 (upper spectrum) and enlarged spectrum in region m/z 282 – 292 (lower spectrum).

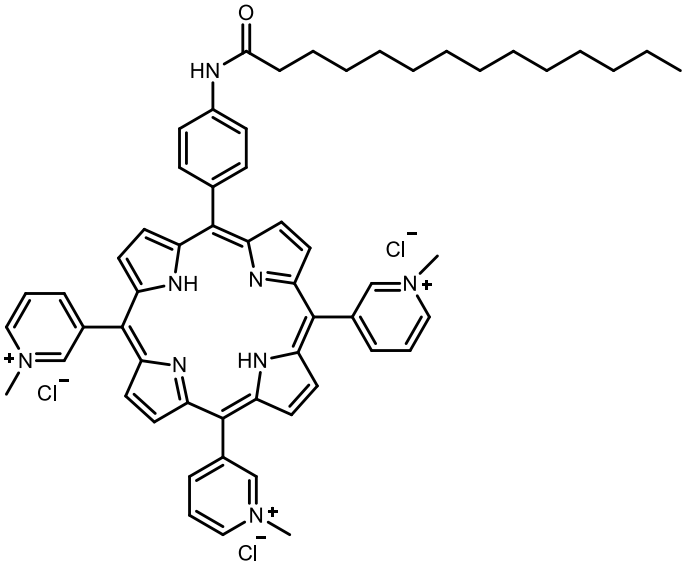

17

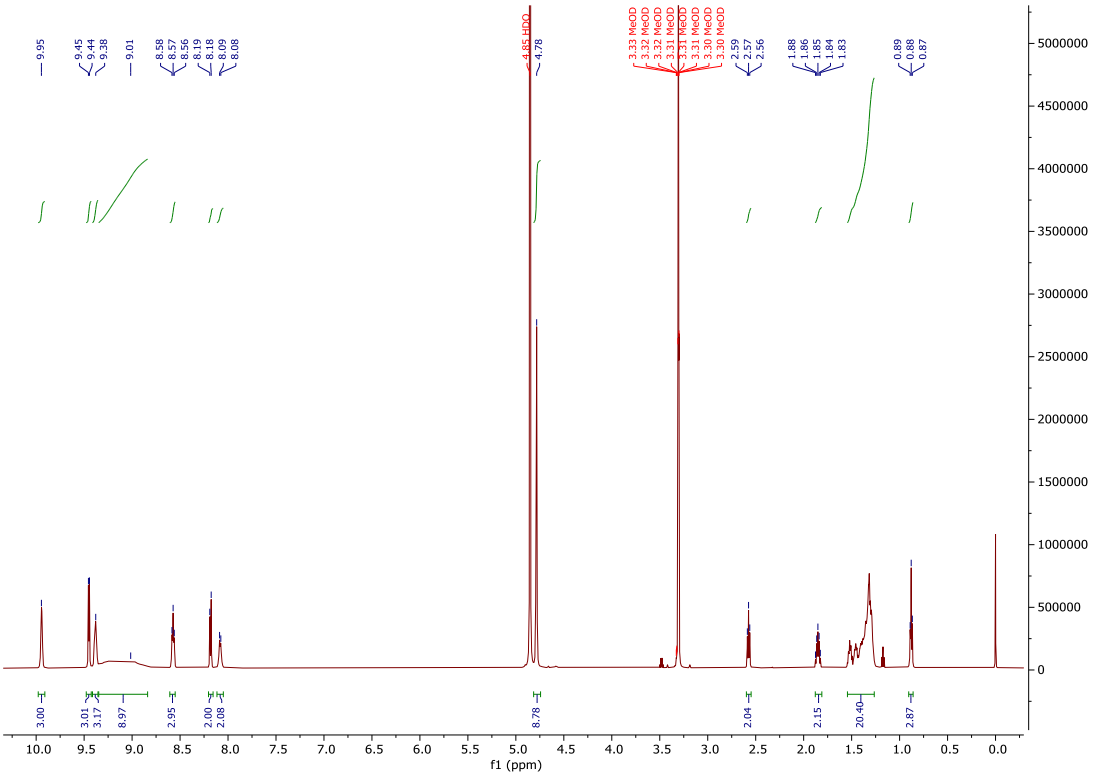

Figure S29. ^{1}H NMR (CD_3OD, 600 MHz) spectrum of **17.**

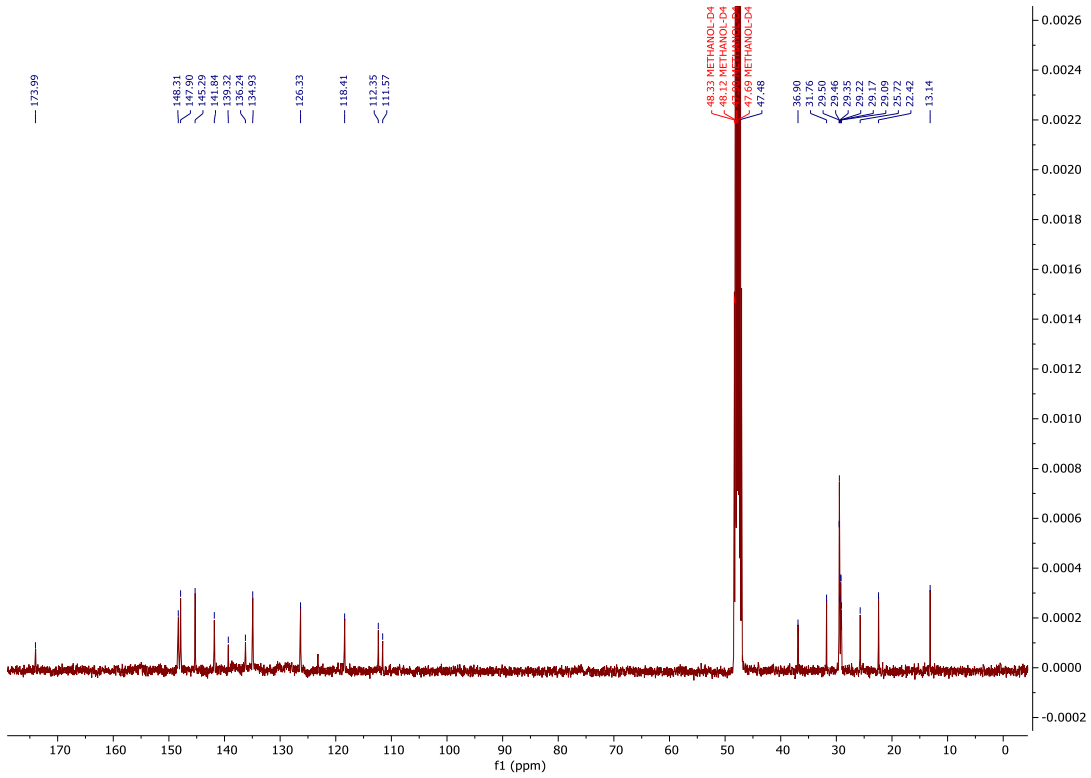

Figure S30. ^{13}C NMR (CD_3OD, 100 MHz) spectrum of **17.**

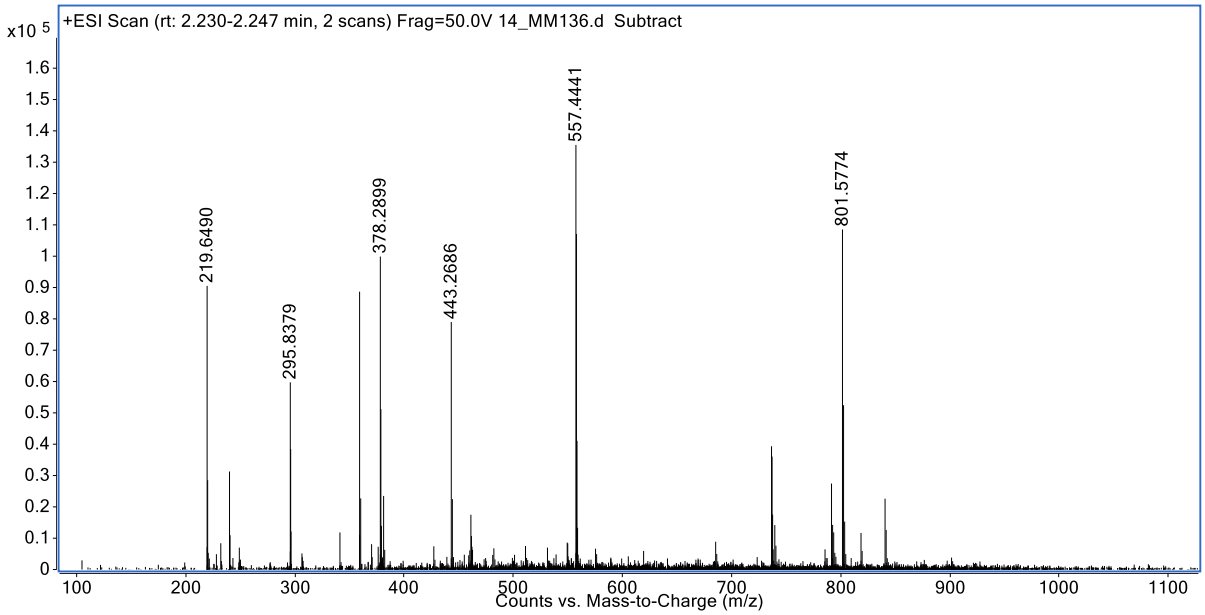

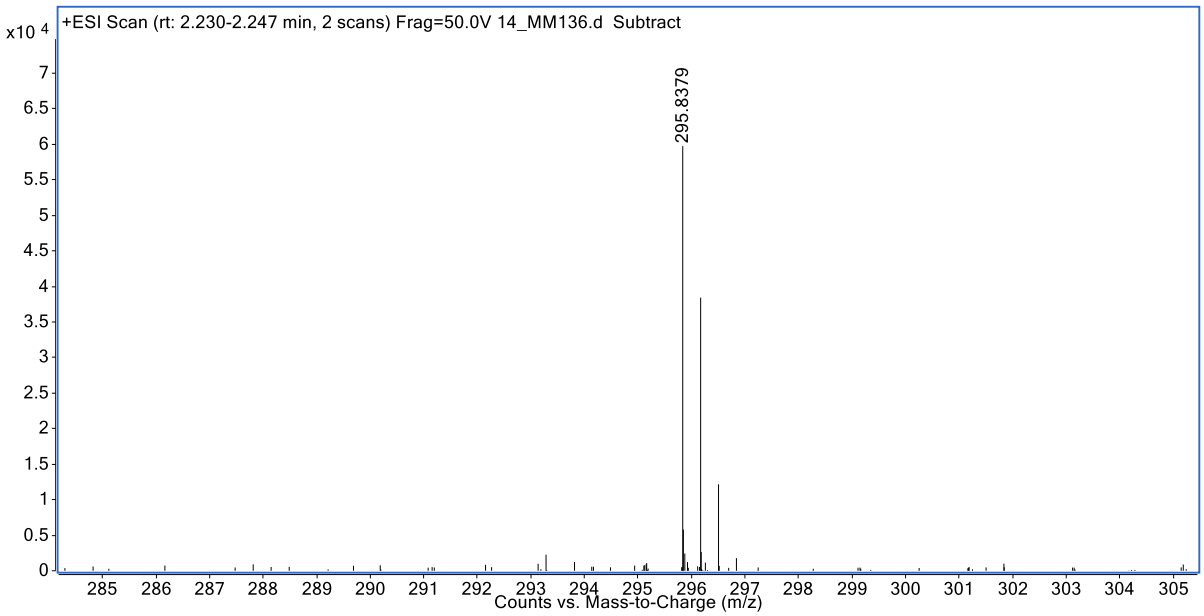

Figure S31. Mass spectrum of **17** in m/z region 100-1100 (upper spectrum) and enlarged spectrum in region m/z 285 – 305 (lower spectrum).

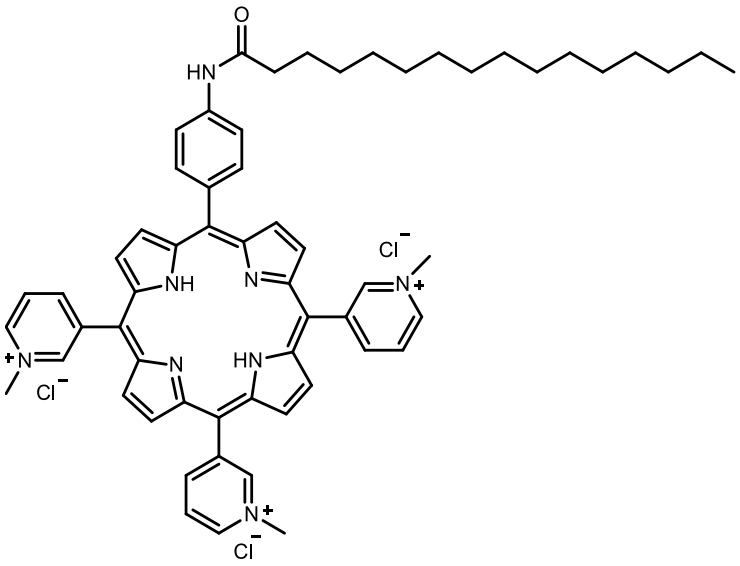

18

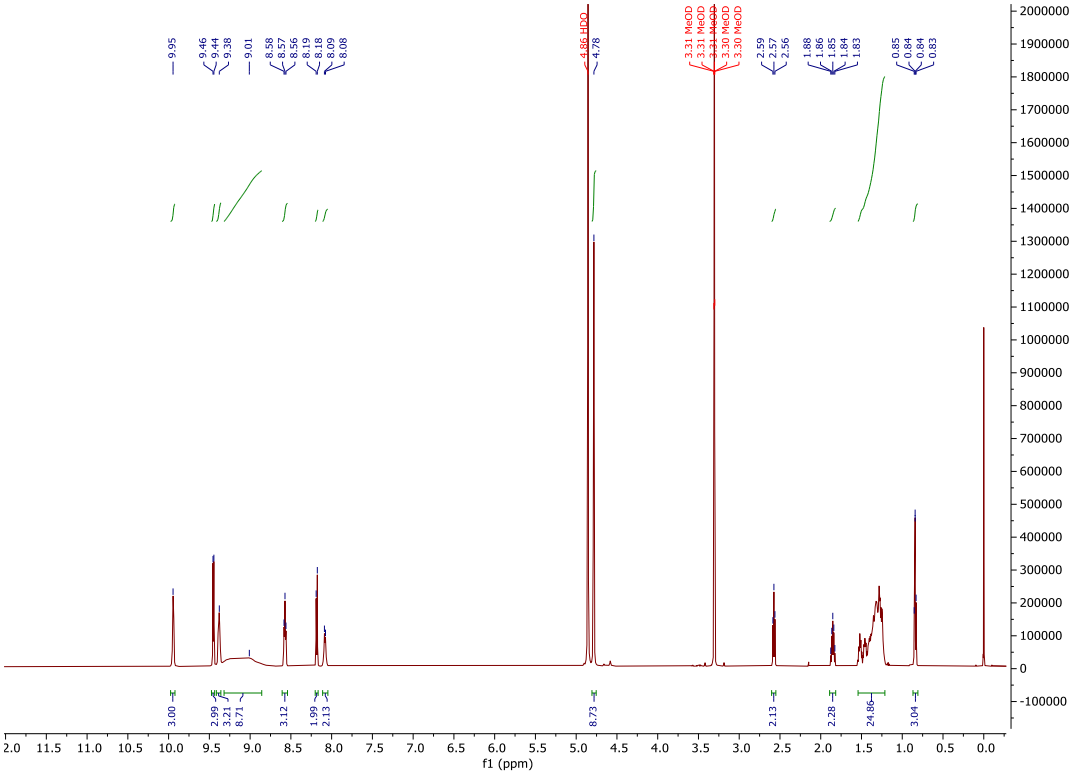

Figure S32. ^{1}H NMR (CD_3OD, 600 MHz) spectrum of **18.**

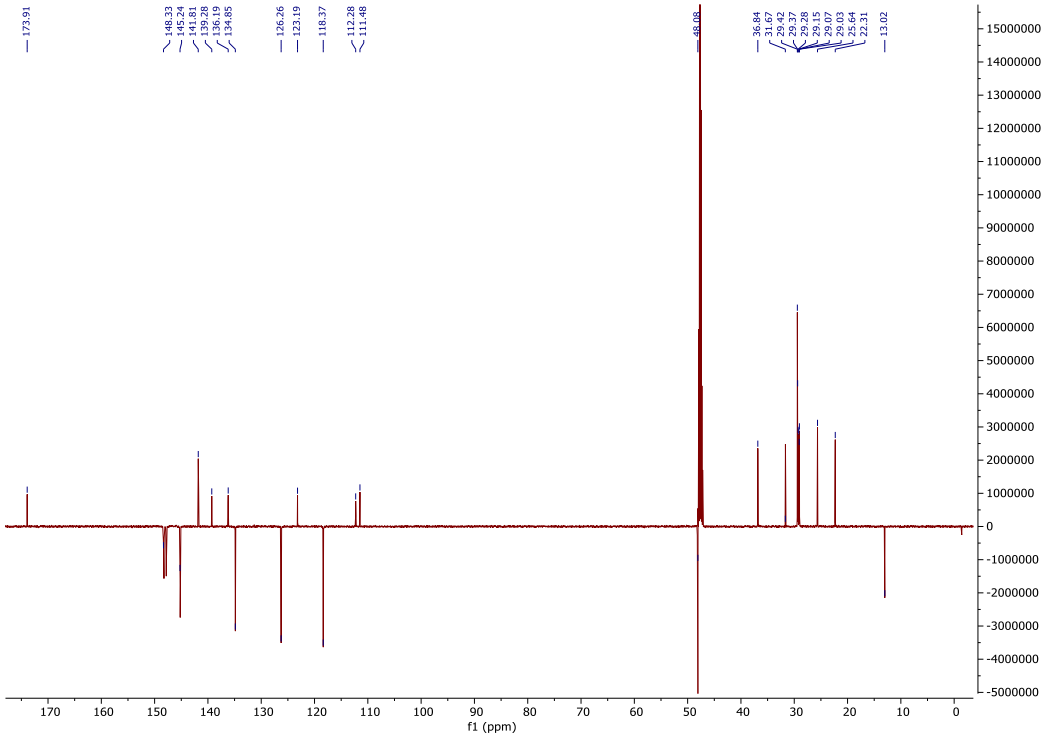

Figure S33. ^{13}C NMR (CD_3OD, 150 MHz) spectrum of **18.**

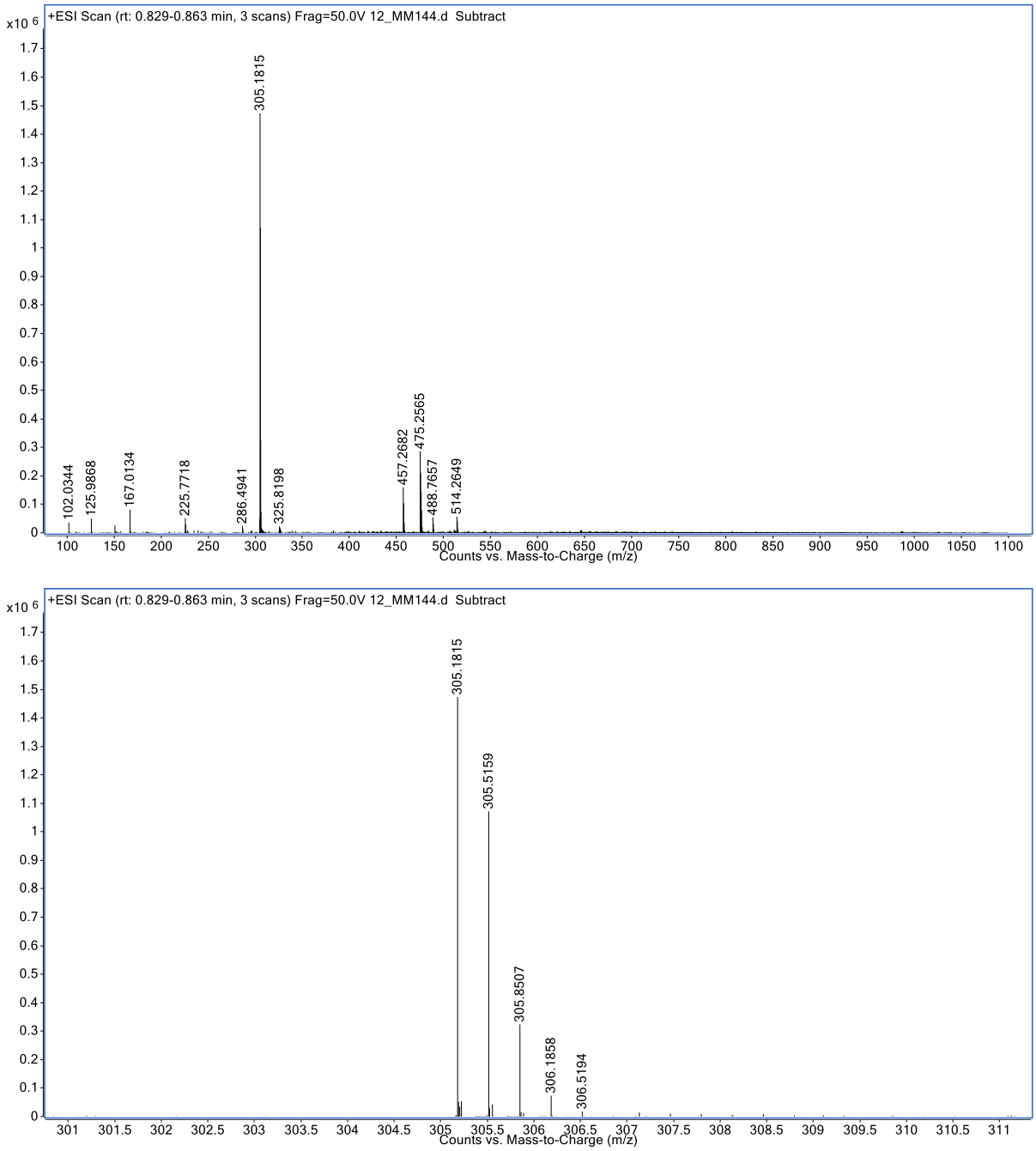

Figure S34. Mass spectrum of **18** in m/z region 100-1100 (upper spectrum) and enlarged spectrum in region m/z 301 – 311 (lower spectrum).

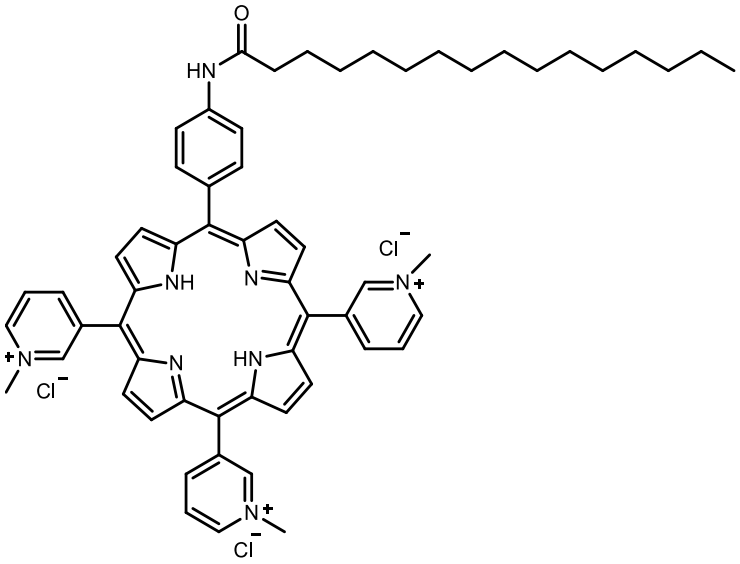

19

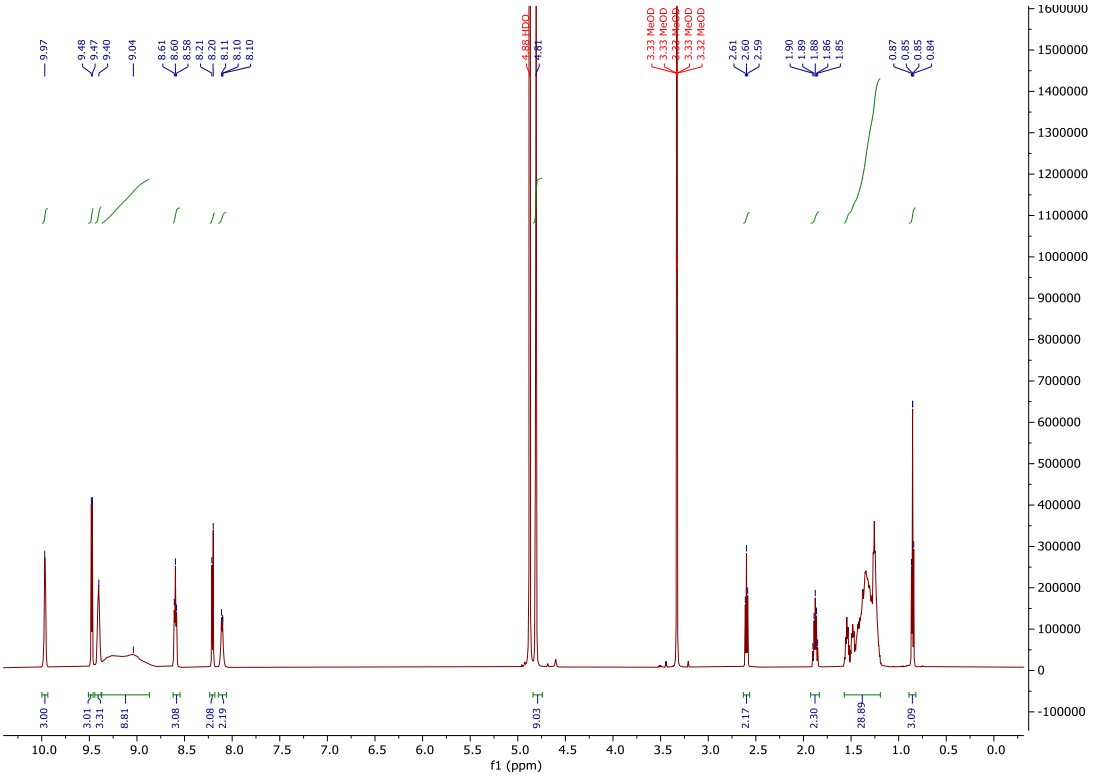

Figure S35. ^{1}H NMR (CD_3OD, 600 MHz) spectrum of **19.**

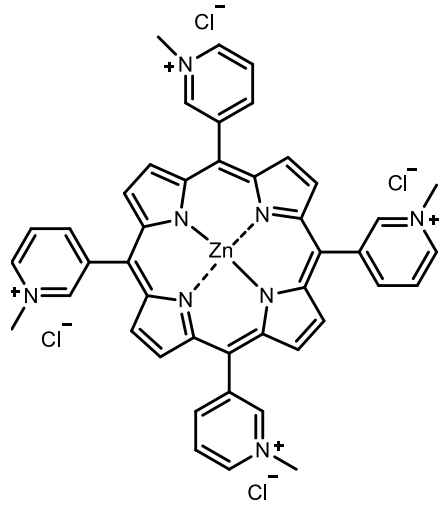

20

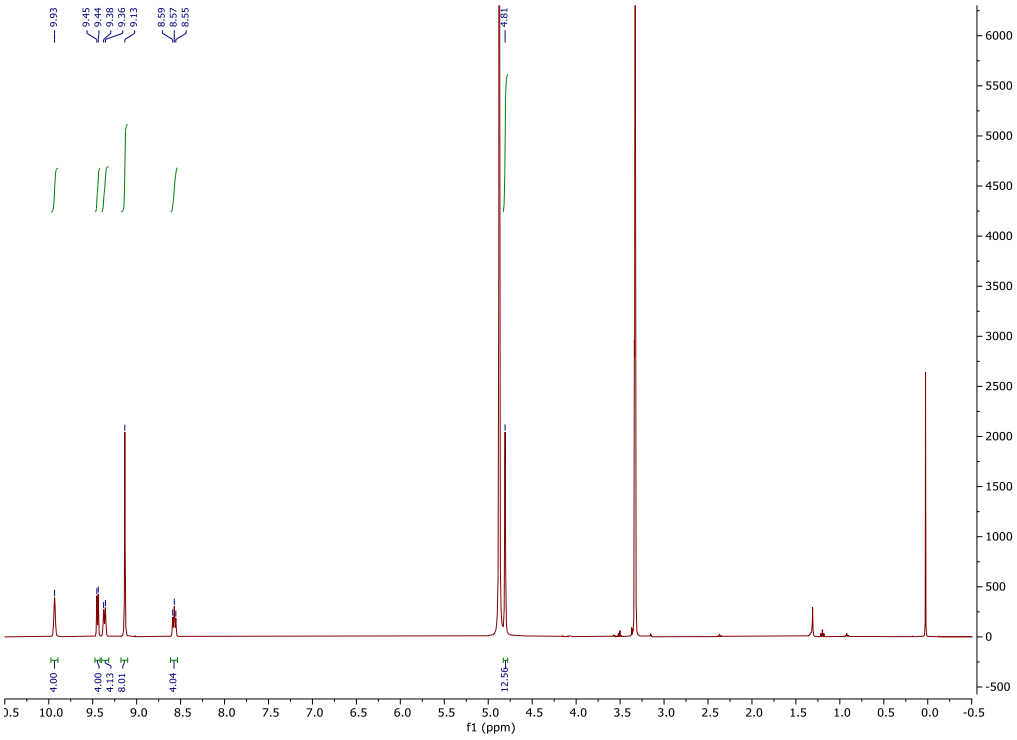

Figure S36. ^{1}H NMR (CD_3OD, 400 MHz) spectrum of **20**.

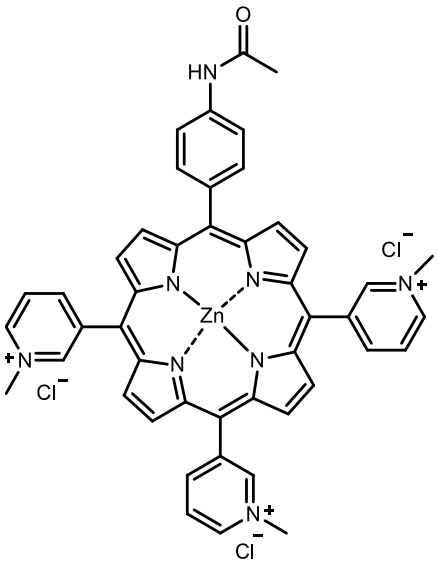

21

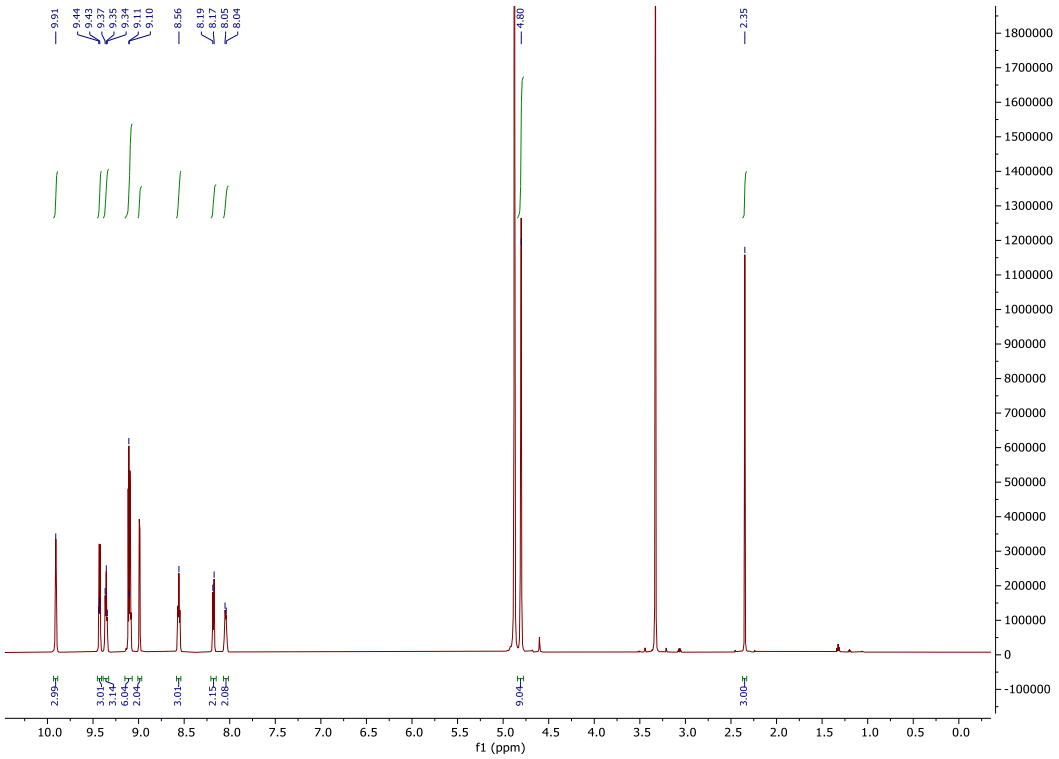

Figure S36. ^{1}H NMR (CD_3OD, 600 MHz) spectrum of **21**.

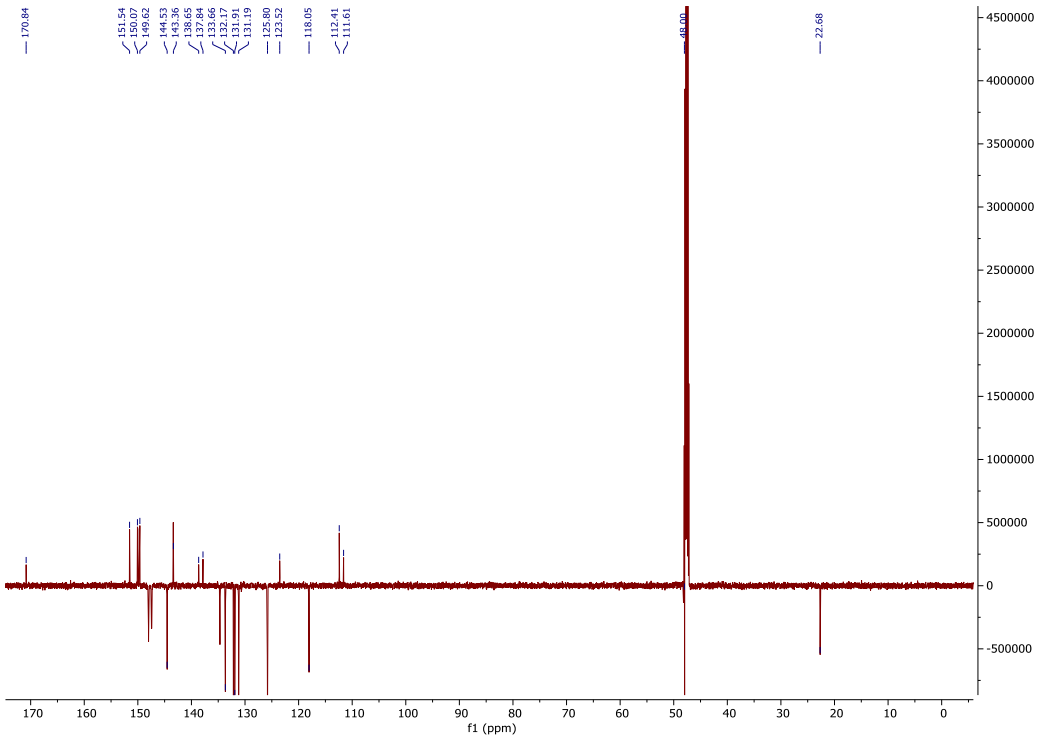

Figure S37. ^{13}C NMR (CD_3OD, 150 MHz) spectrum of **21**.

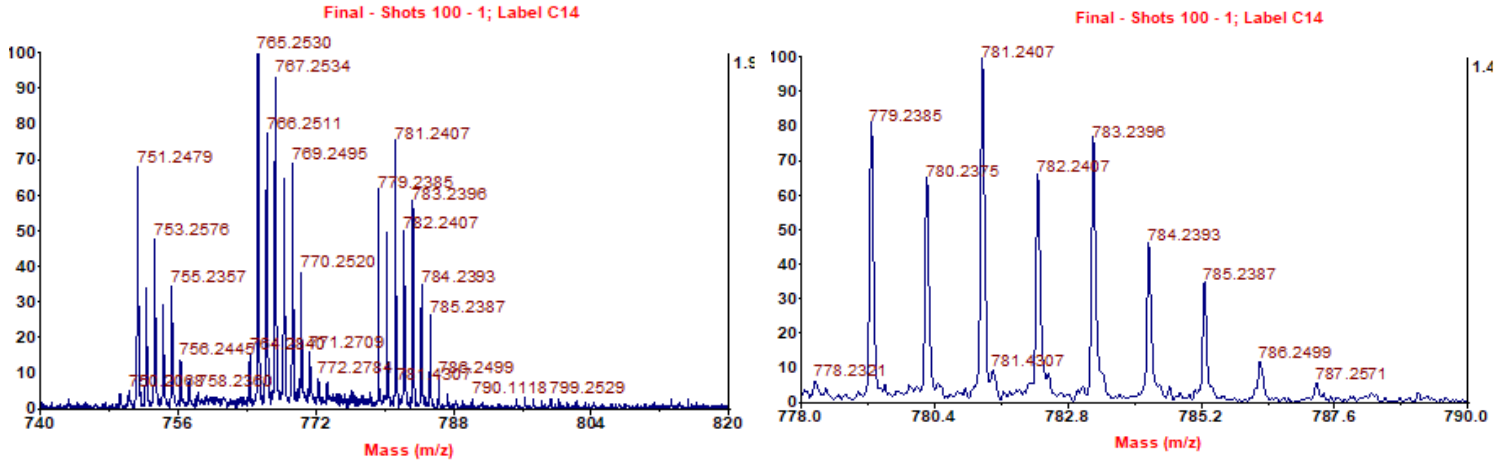

Figure S38. MALDI-MS mass spectrum of porphyrin **21** in region *m/z* 740 – 820 (left) and the enlarged part of the spectrum *m/z* 778 – 790 (right).

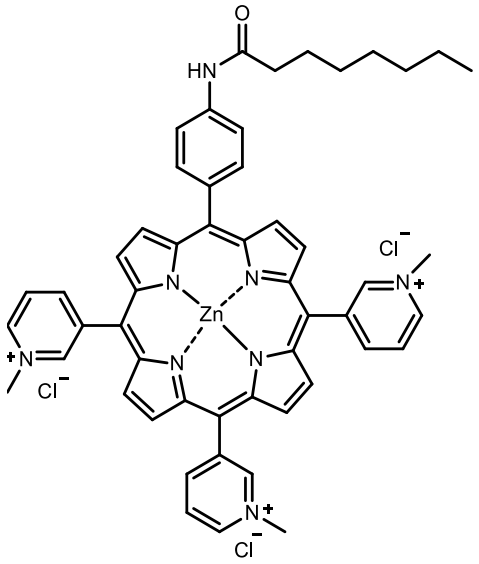

22

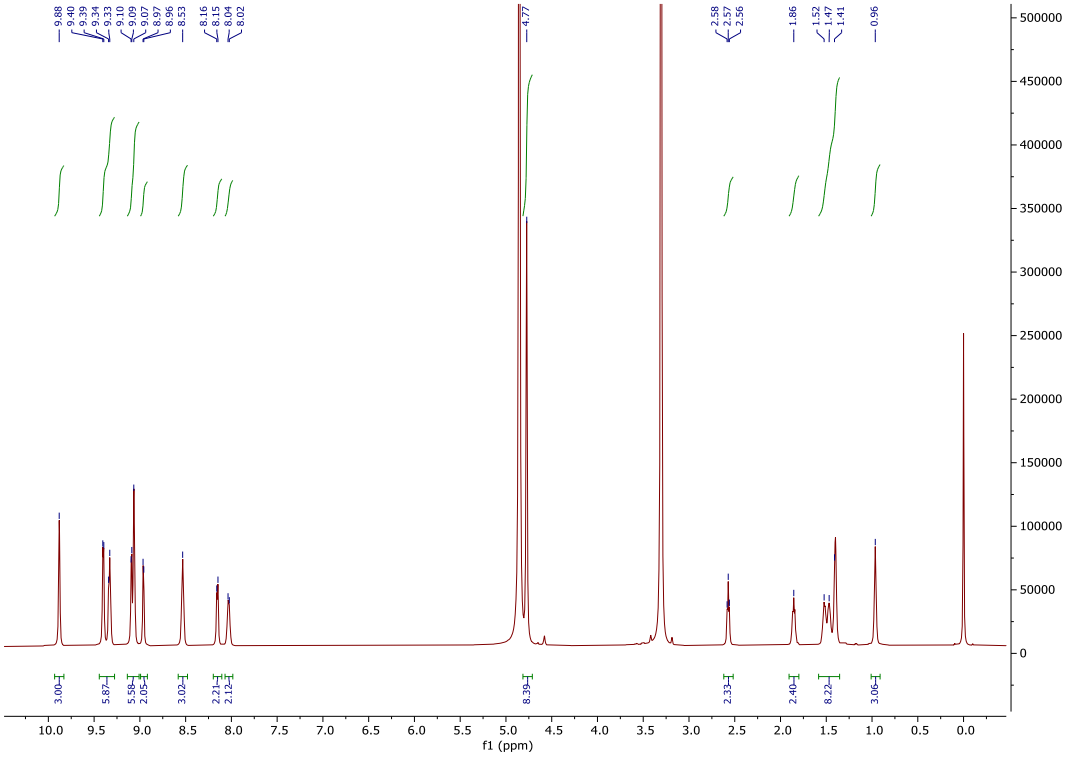

Figure S39. ^{1}H NMR (CD_3OD, 600 MHz) spectrum of **22**.

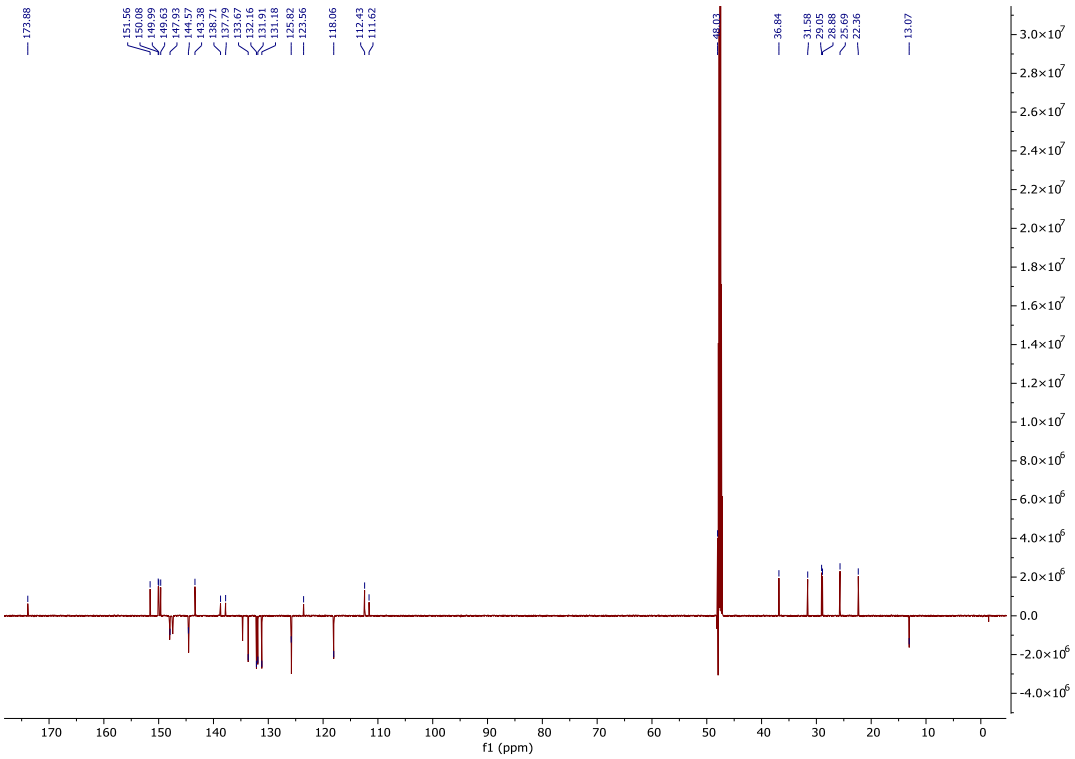

Figure S40. ^{13}C NMR (CD_3OD, 150 MHz) spectrum of **22**.

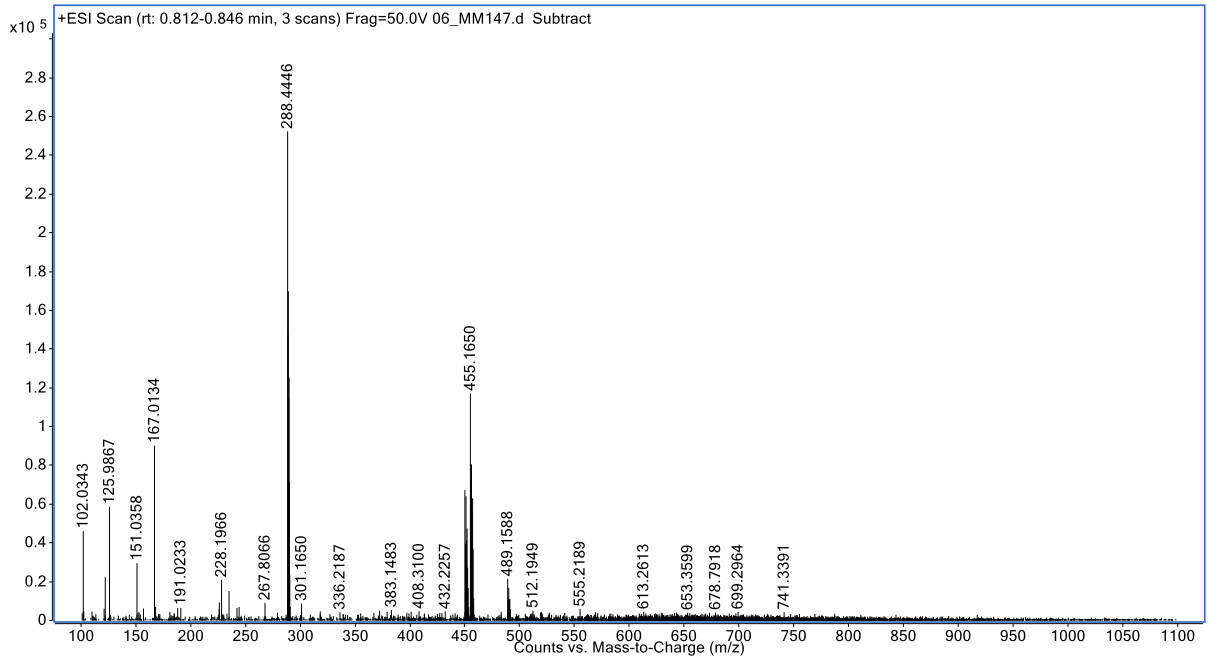

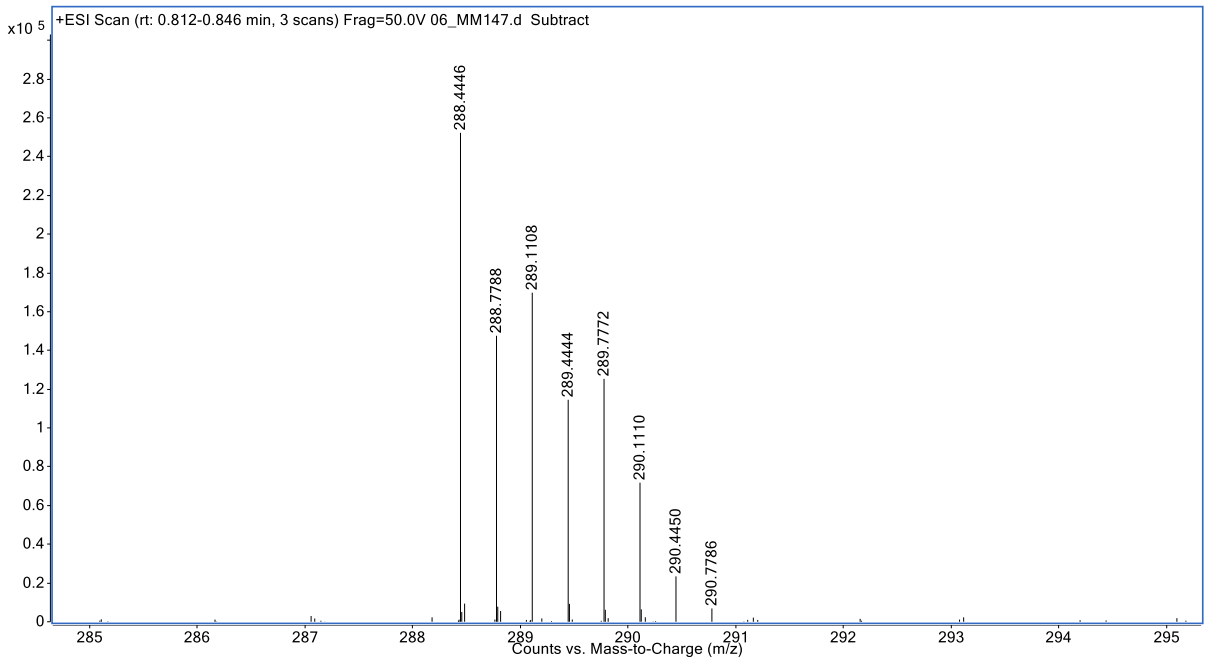

Figure S41. Mass spectrum of **22** in m/z region 100-1100 (upper spectrum) and enlarged spectrum in region m/z 285 – 295 (lower spectrum).

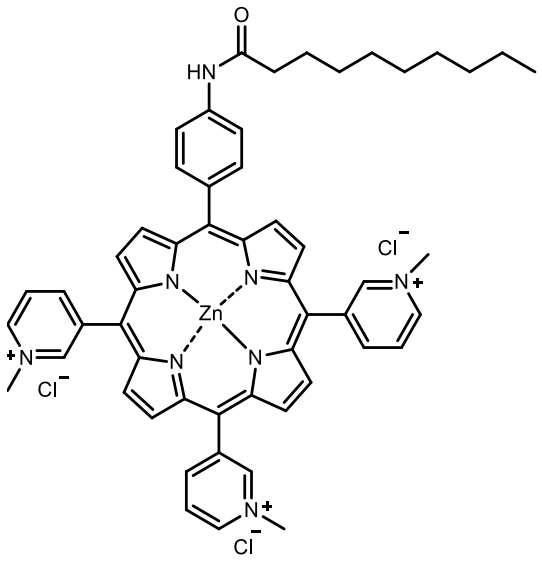

23

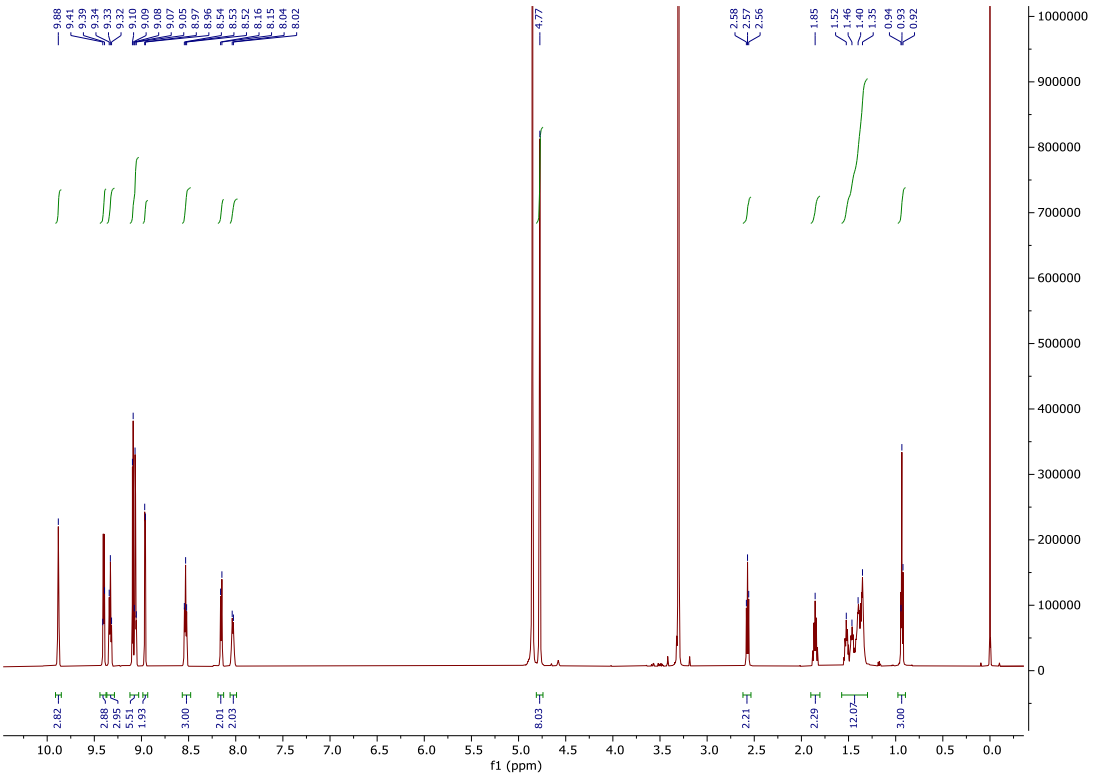

Figure S42. ^{1}H NMR (CD_3OD, 600 MHz) spectrum of **23**.

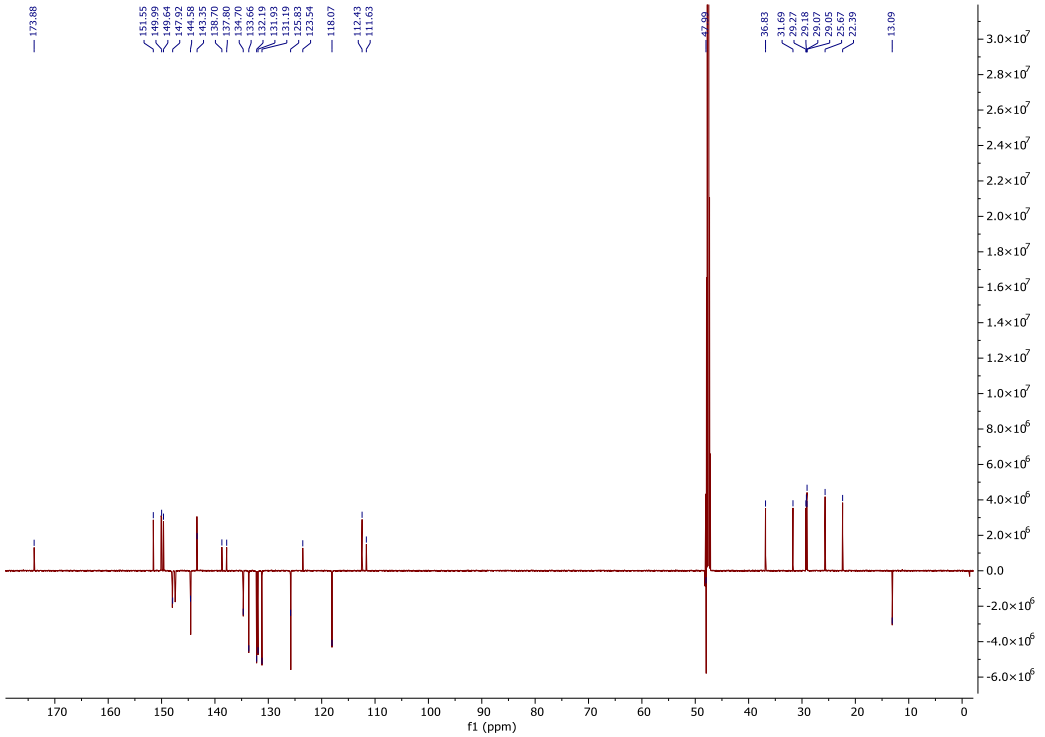

Figure S43. ^{13}C NMR (CD_3OD, 150 MHz) spectrum of **23**.

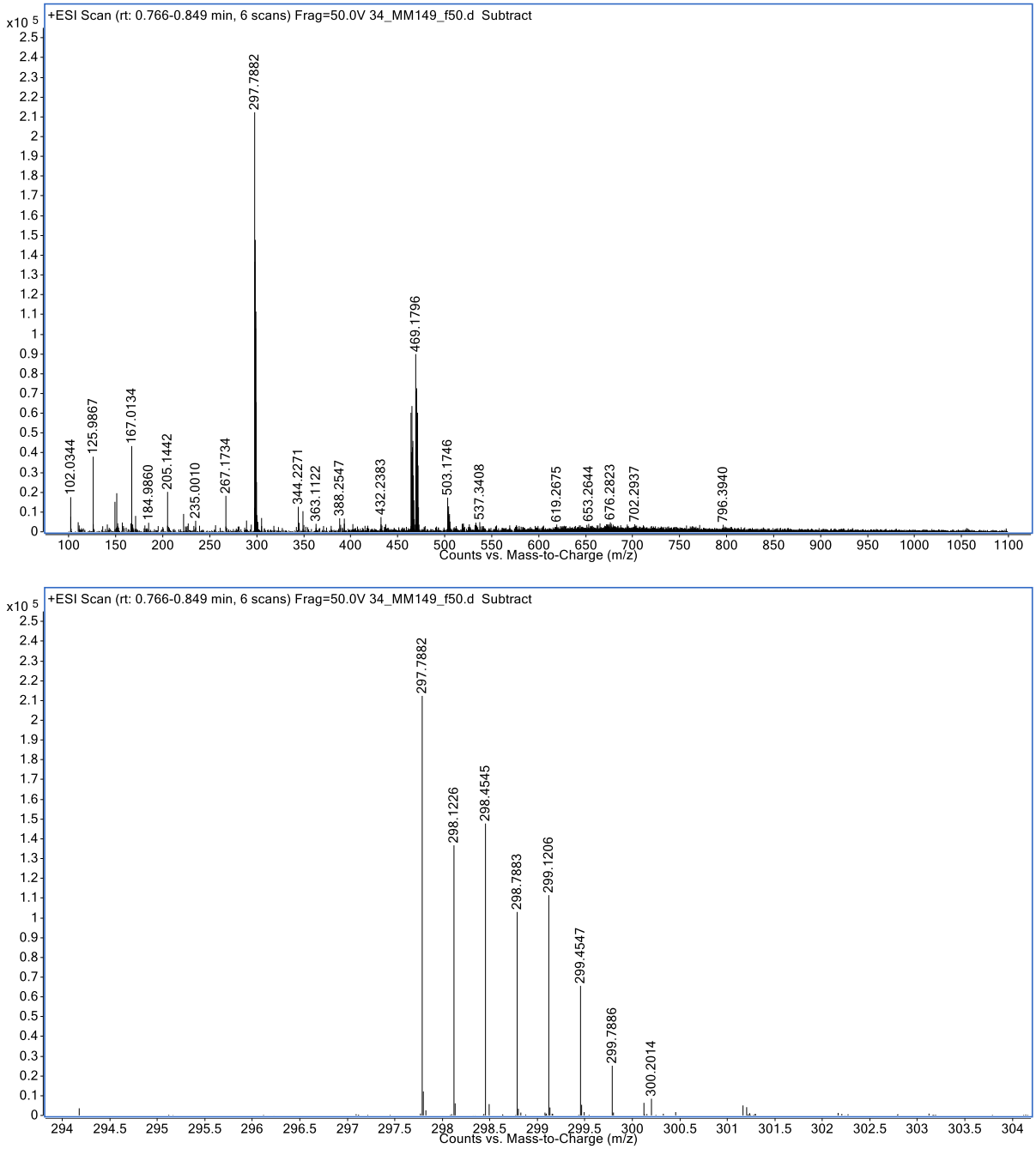

Figure S44. Mass spectrum of **23** in m/z region 100-1100 (upper spectrum) and enlarged spectrum in region m/z 294 – 304 (lower spectrum).

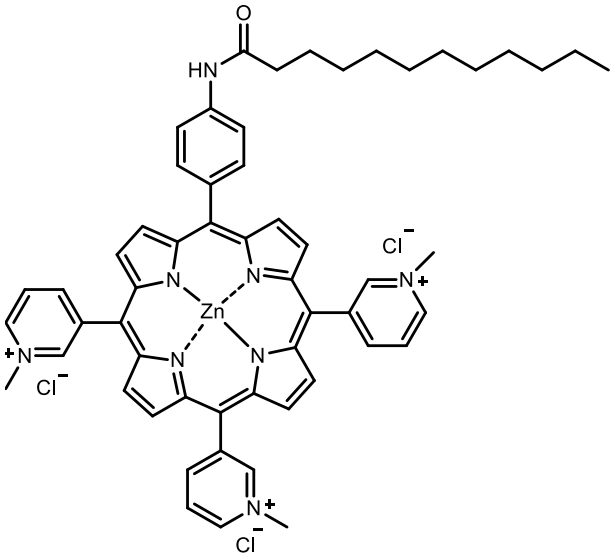

24

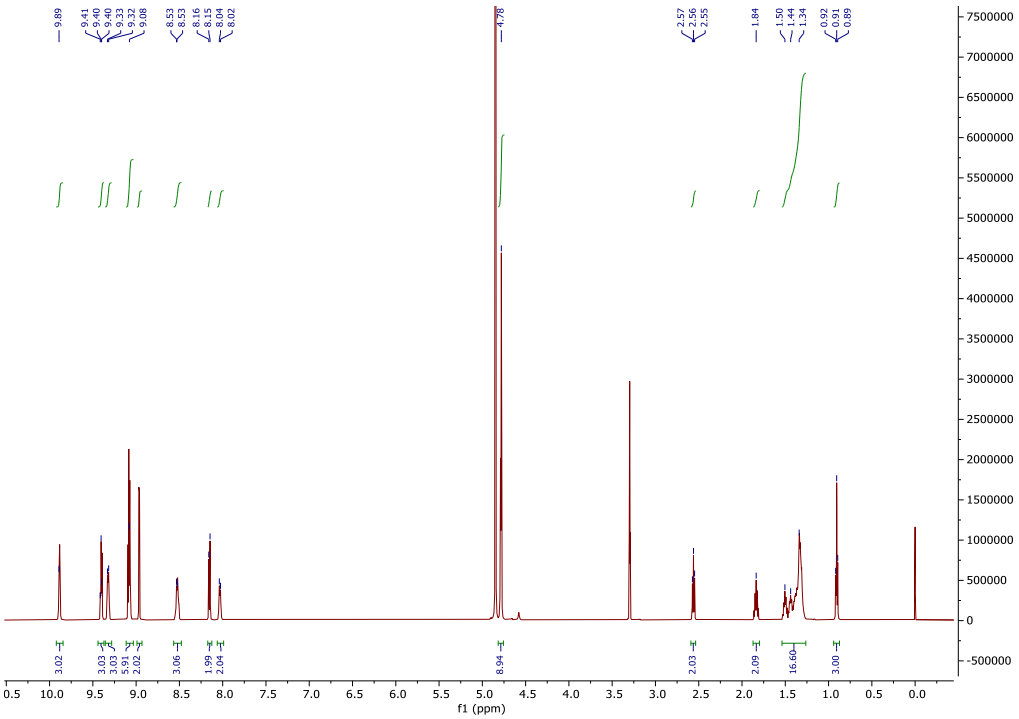

Figure S45. ^{1}H NMR (CD_3OD, 600 MHz) spectrum of **24**.

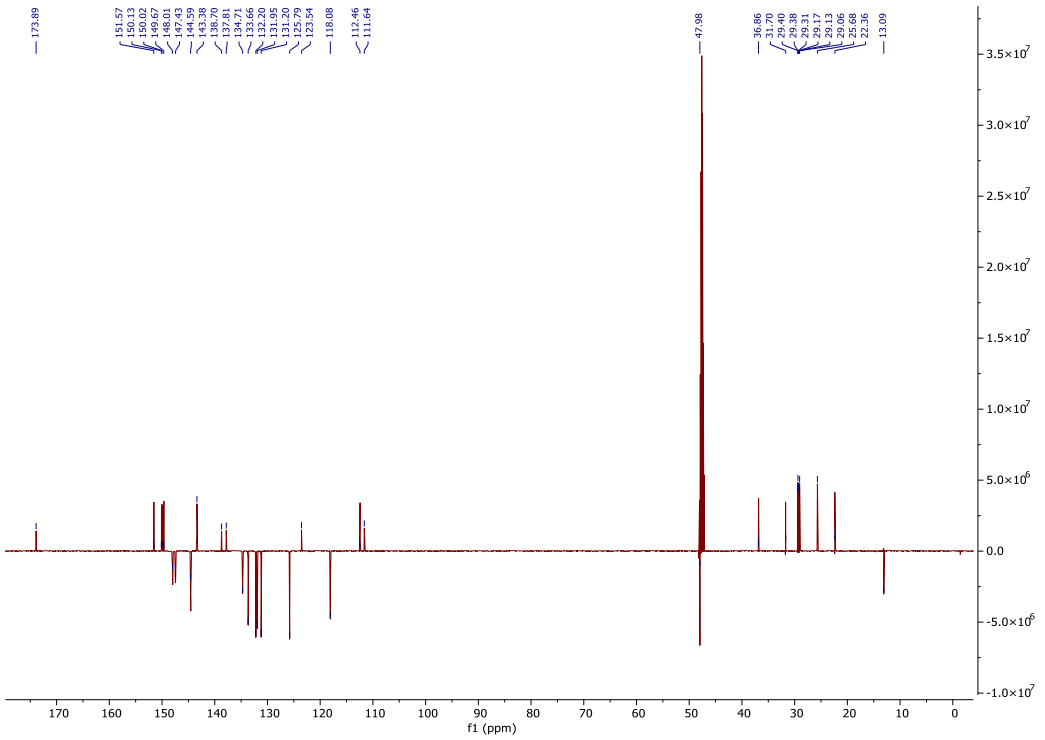

Figure S46. ^{13}C NMR (CD_3OD, 150 MHz) spectrum of **24**.

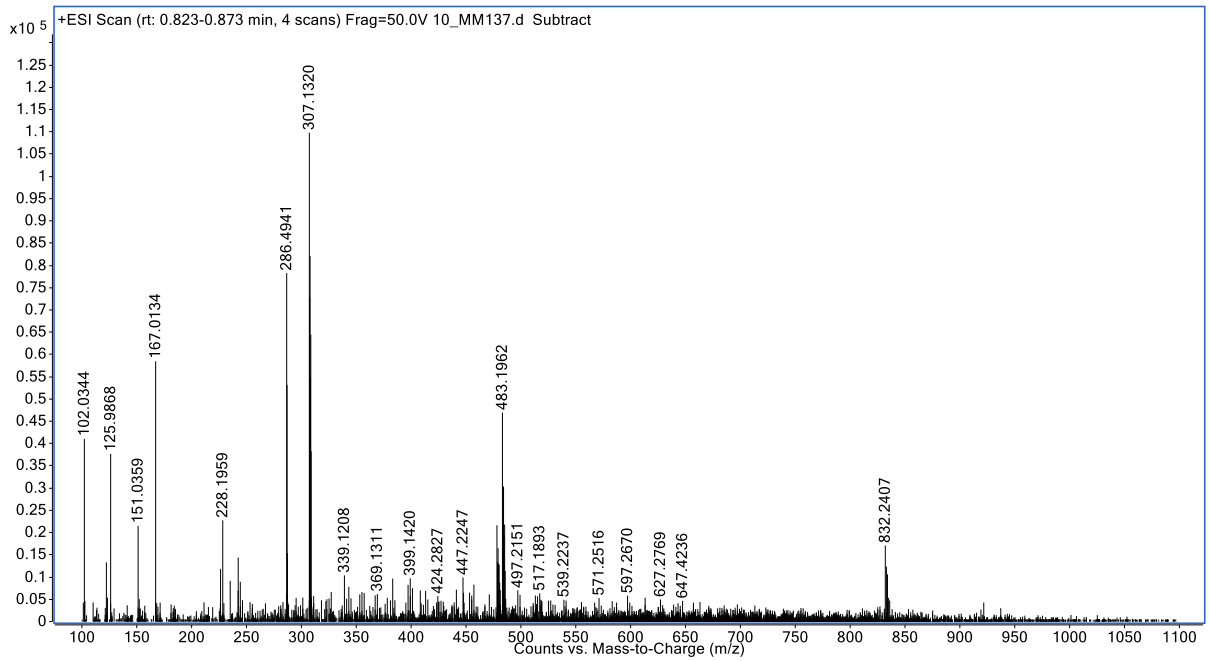

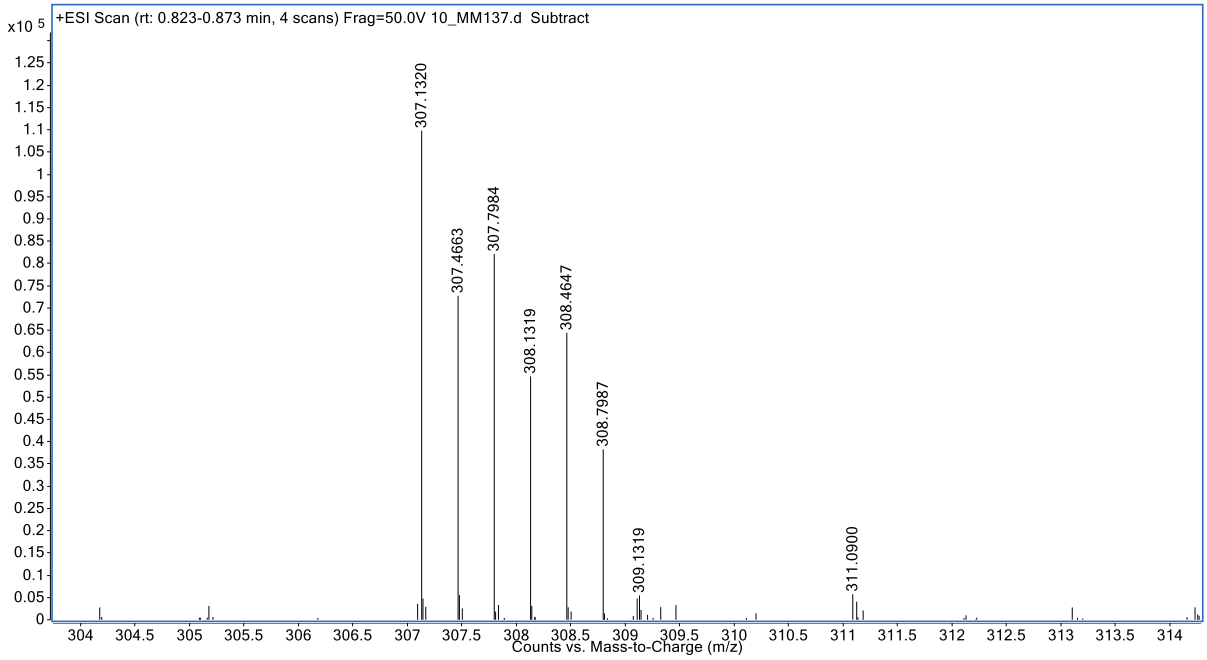

Figure S47. Mass spectrum of **24** in m/z region 100-1100 (upper spectrum) and enlarged spectrum in region m/z 304 – 314 (lower spectrum).

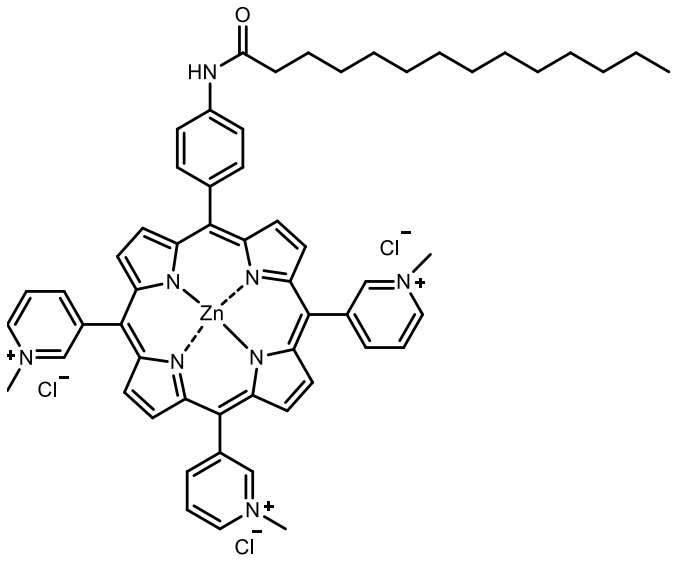

25

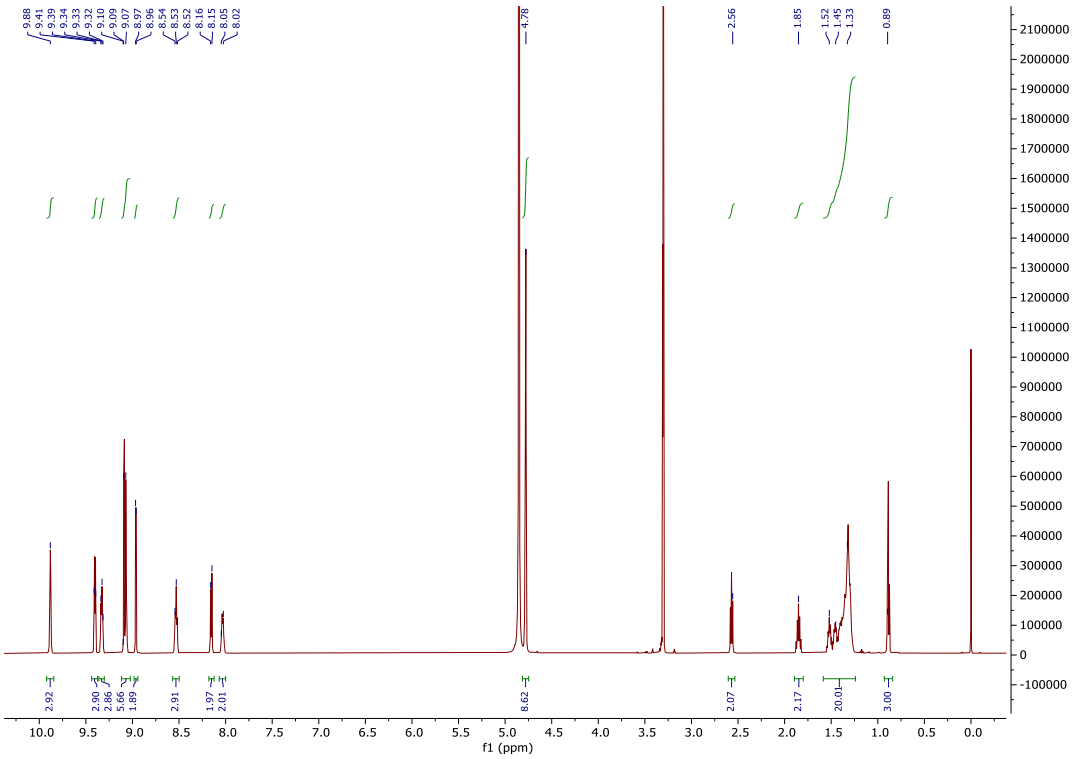

Figure S48. ^{1}H NMR (CD_3OD, 600 MHz) spectrum of **25**.

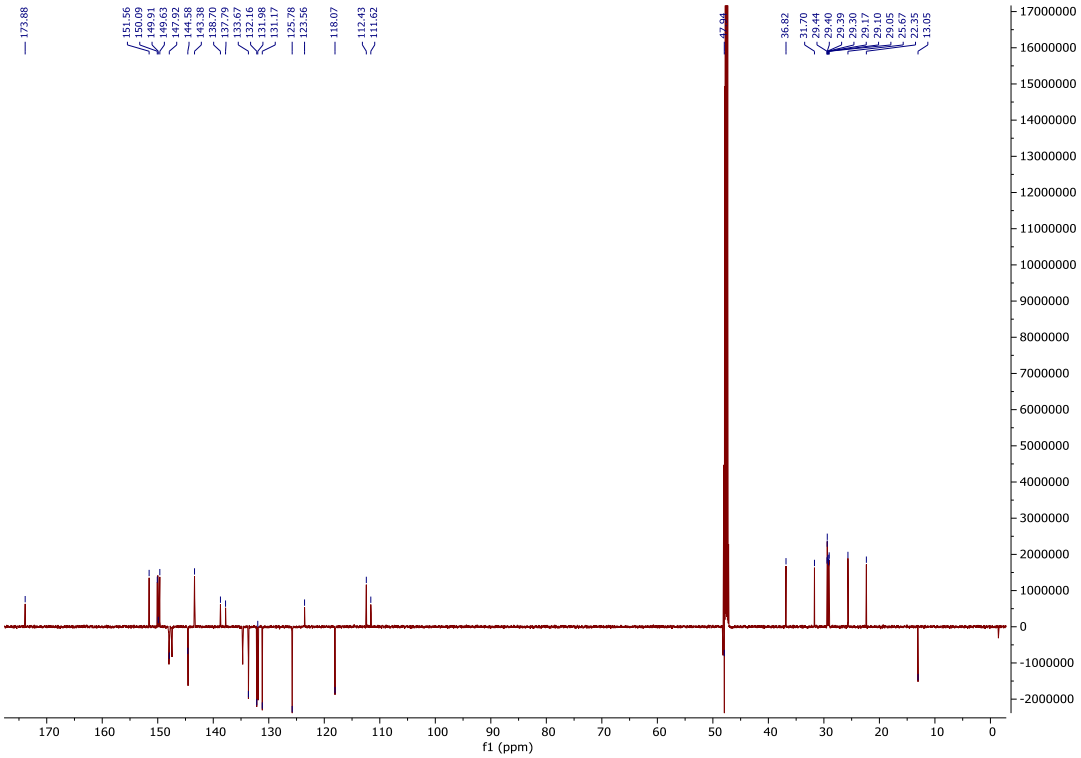

Figure S49. ^{13}C NMR (CD_3OD, 150 MHz) spectrum of **25**.

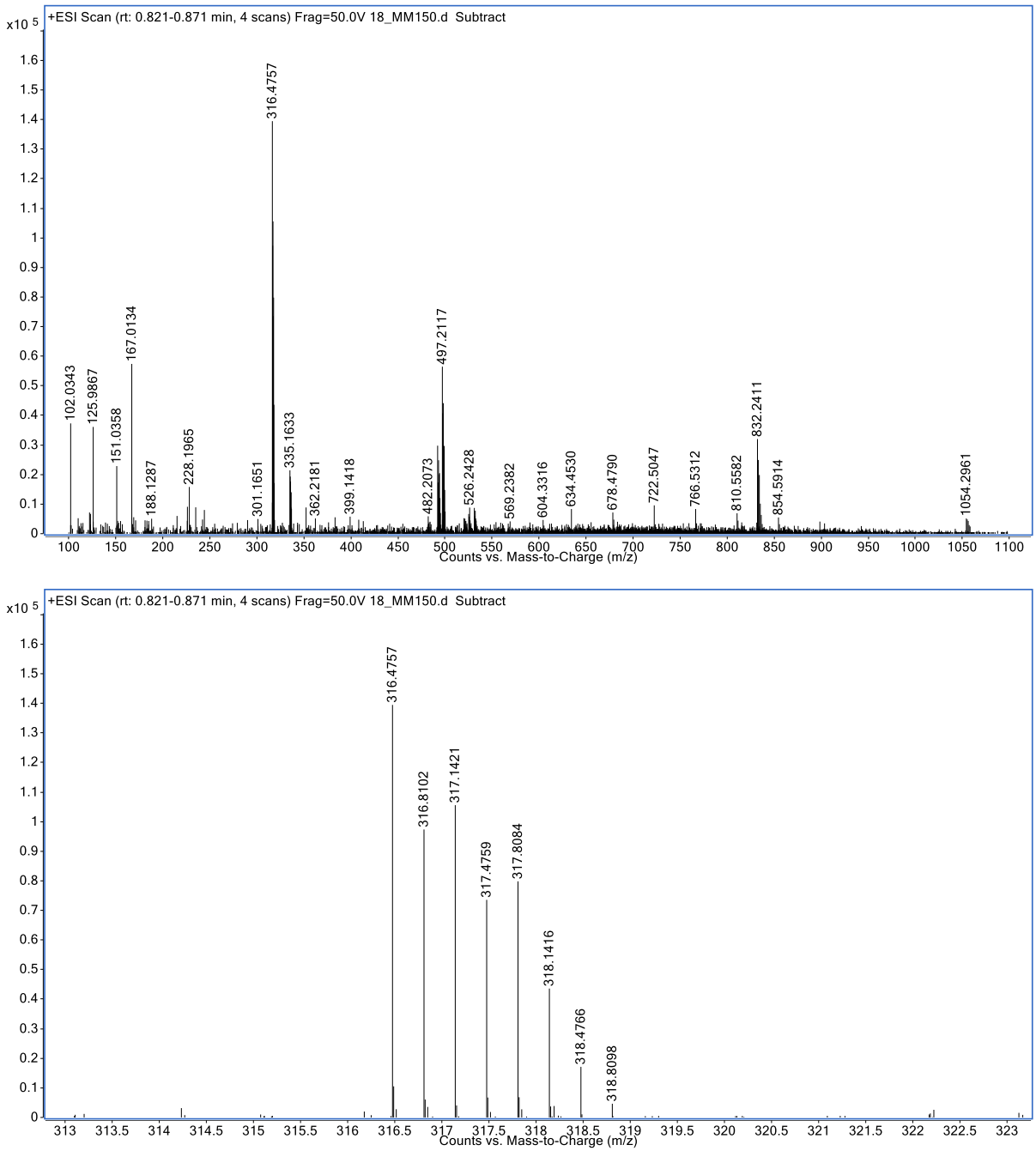

Figure S50. Mass spectrum of **25** in m/z region 100-1100 (upper spectrum) and enlarged spectrum in region m/z 313 – 323 (lower spectrum).

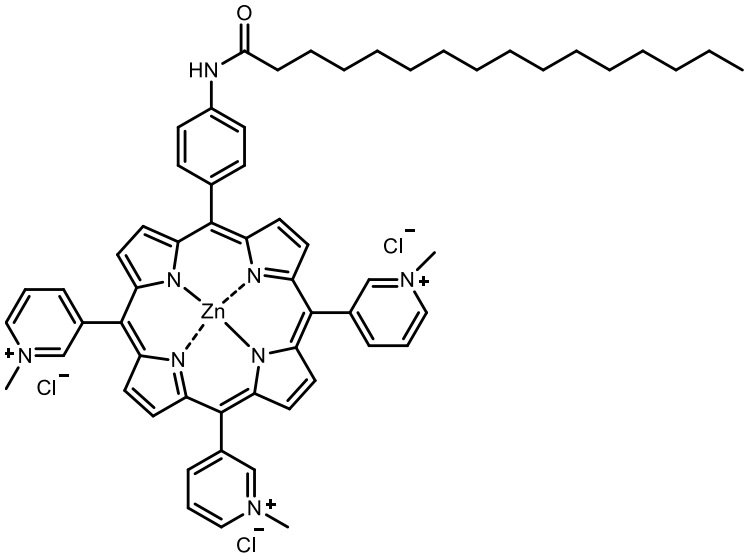

26

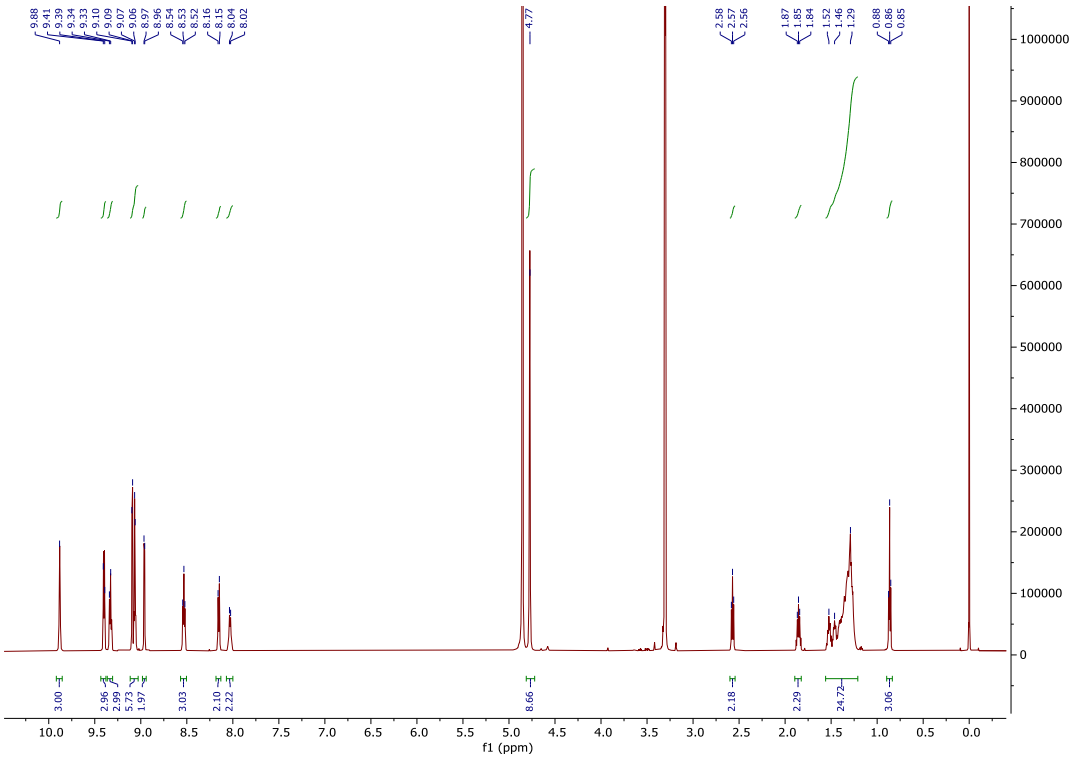

Figure S51. ^{1}H NMR (CD_3OD, 600 MHz) spectrum of **26**.

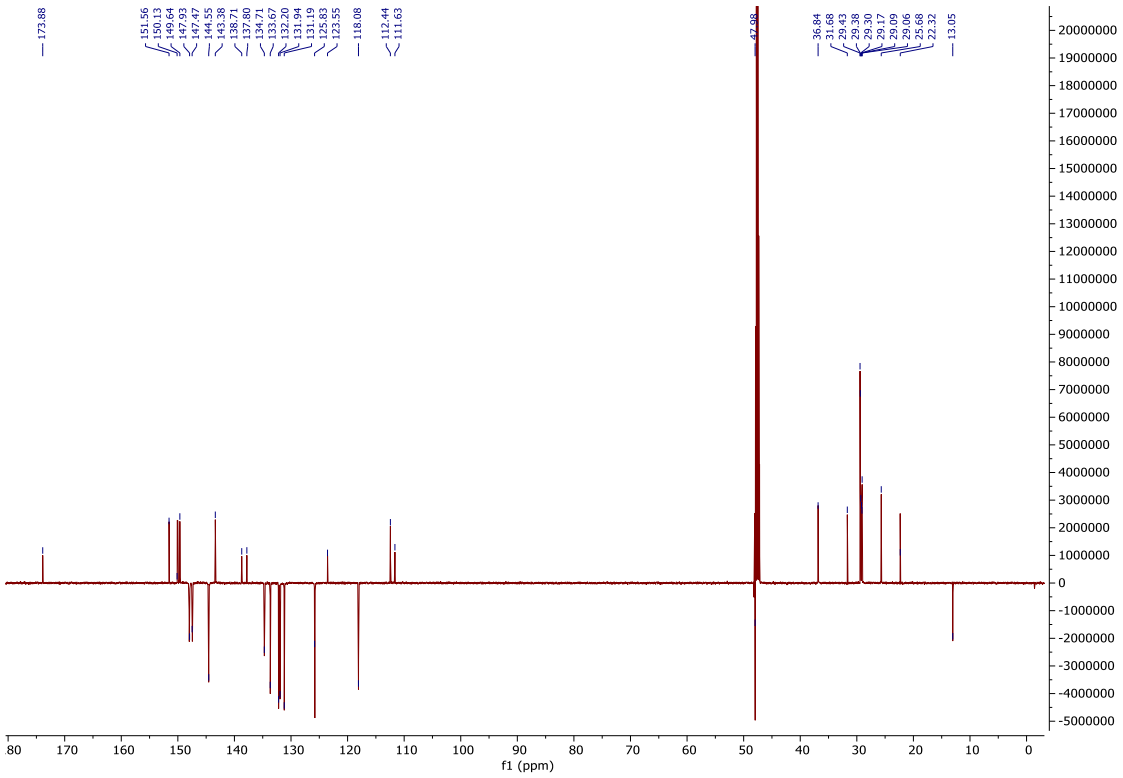

Figure S52. ^{13}C NMR (CD_3OD, 150 MHz) spectrum of **26**.

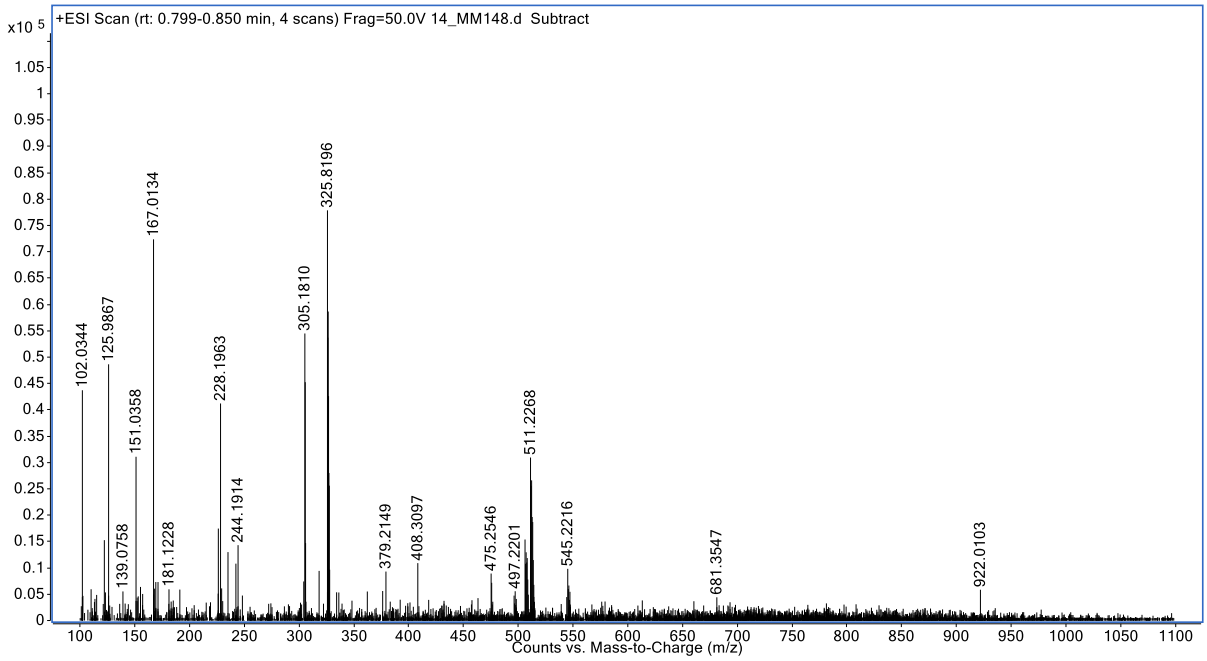

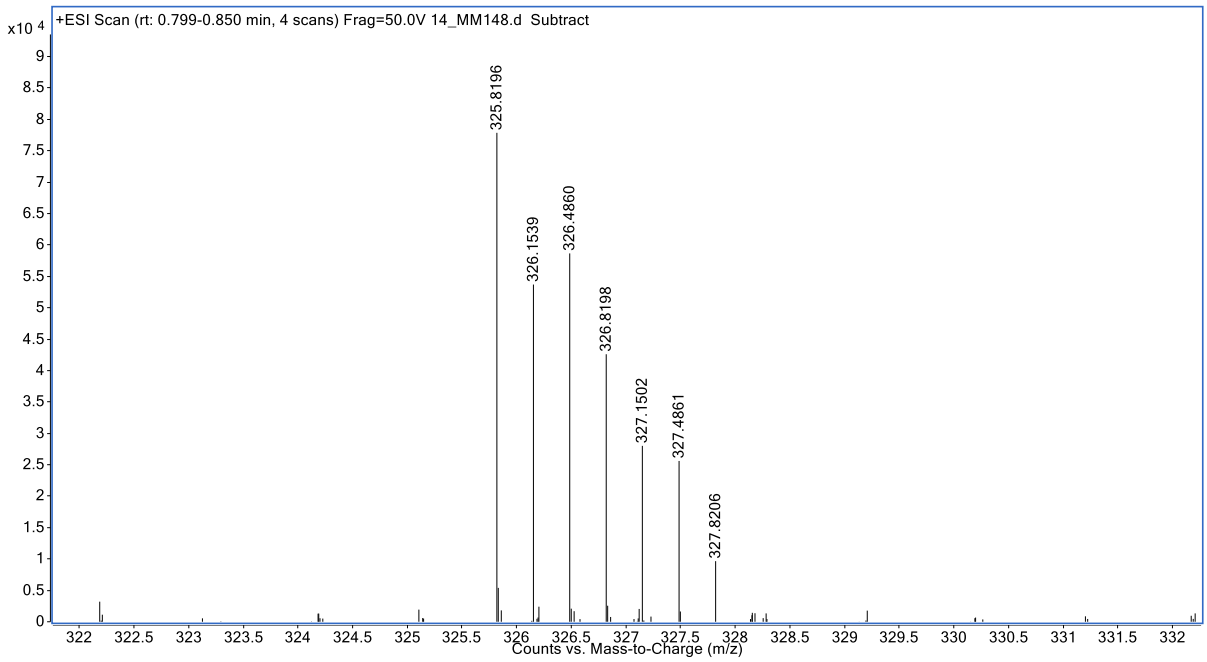

Figure S53. Mass spectrum of **26** in m/z region 100-1100 (upper spectrum) and enlarged spectrum in region m/z 322 – 332 (lower spectrum).

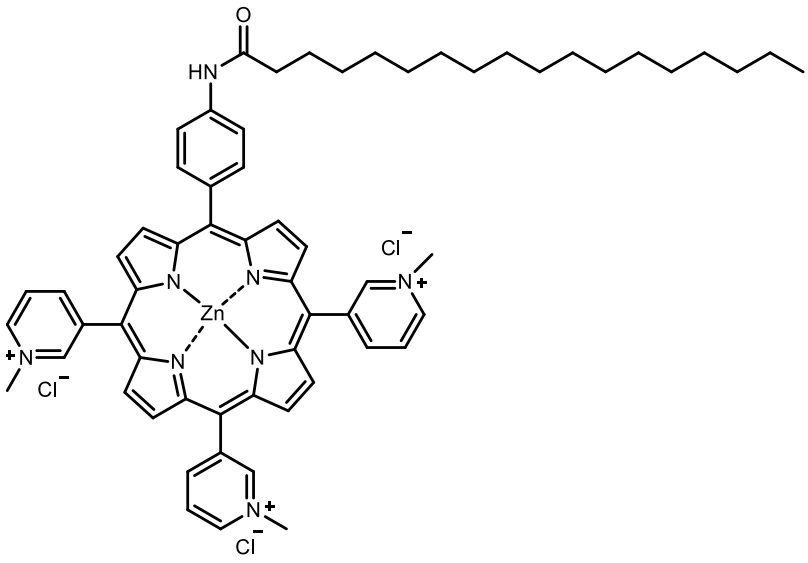

27

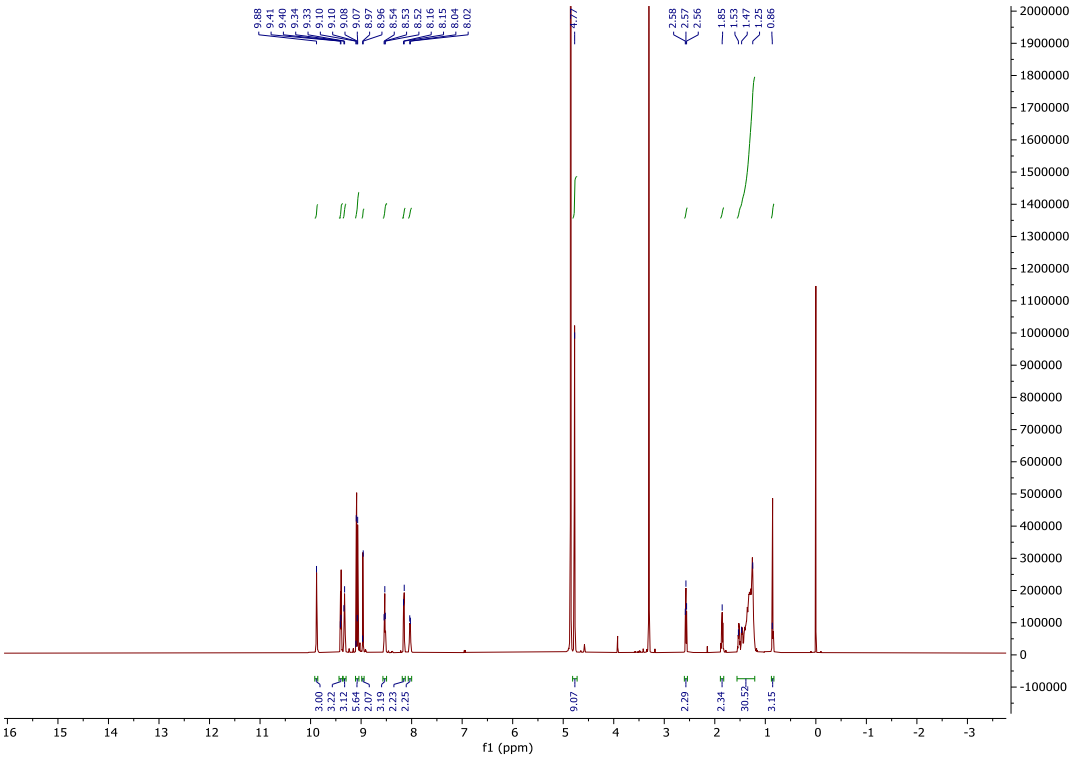

Figure S54. ^{1}H NMR (CD_3OD, 600 MHz) spectrum of **27**.

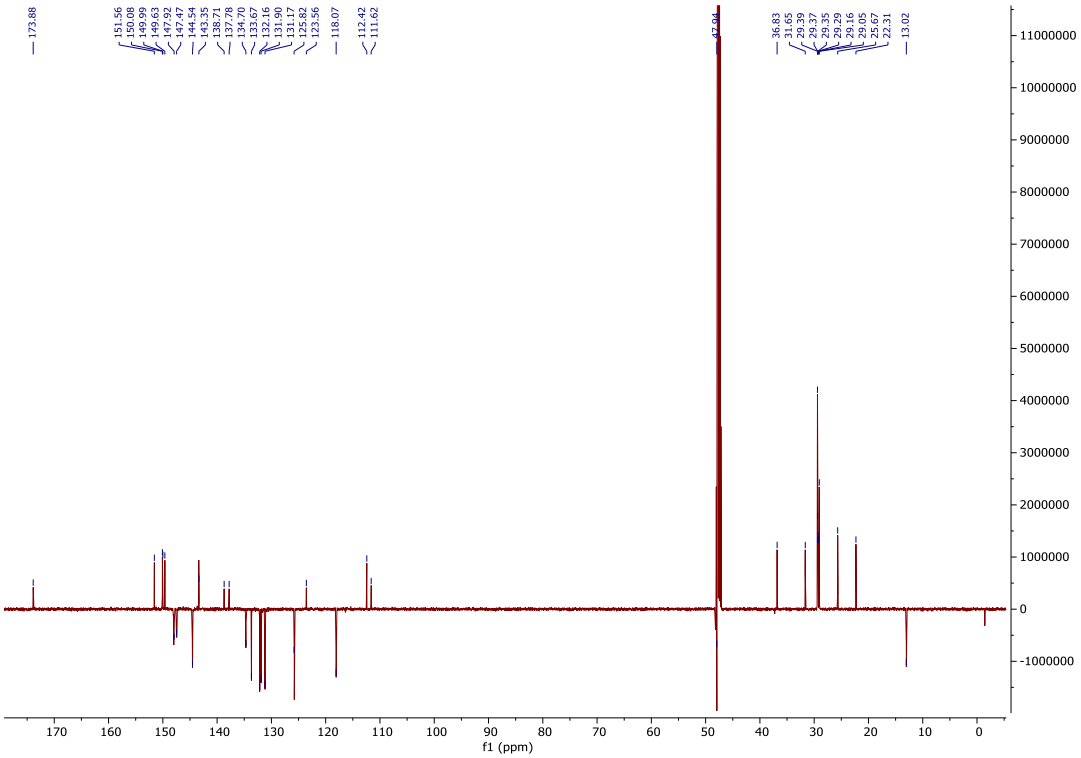

Figure S55. ^{13}C NMR (CD_3OD, 150 MHz) spectrum of **27**.

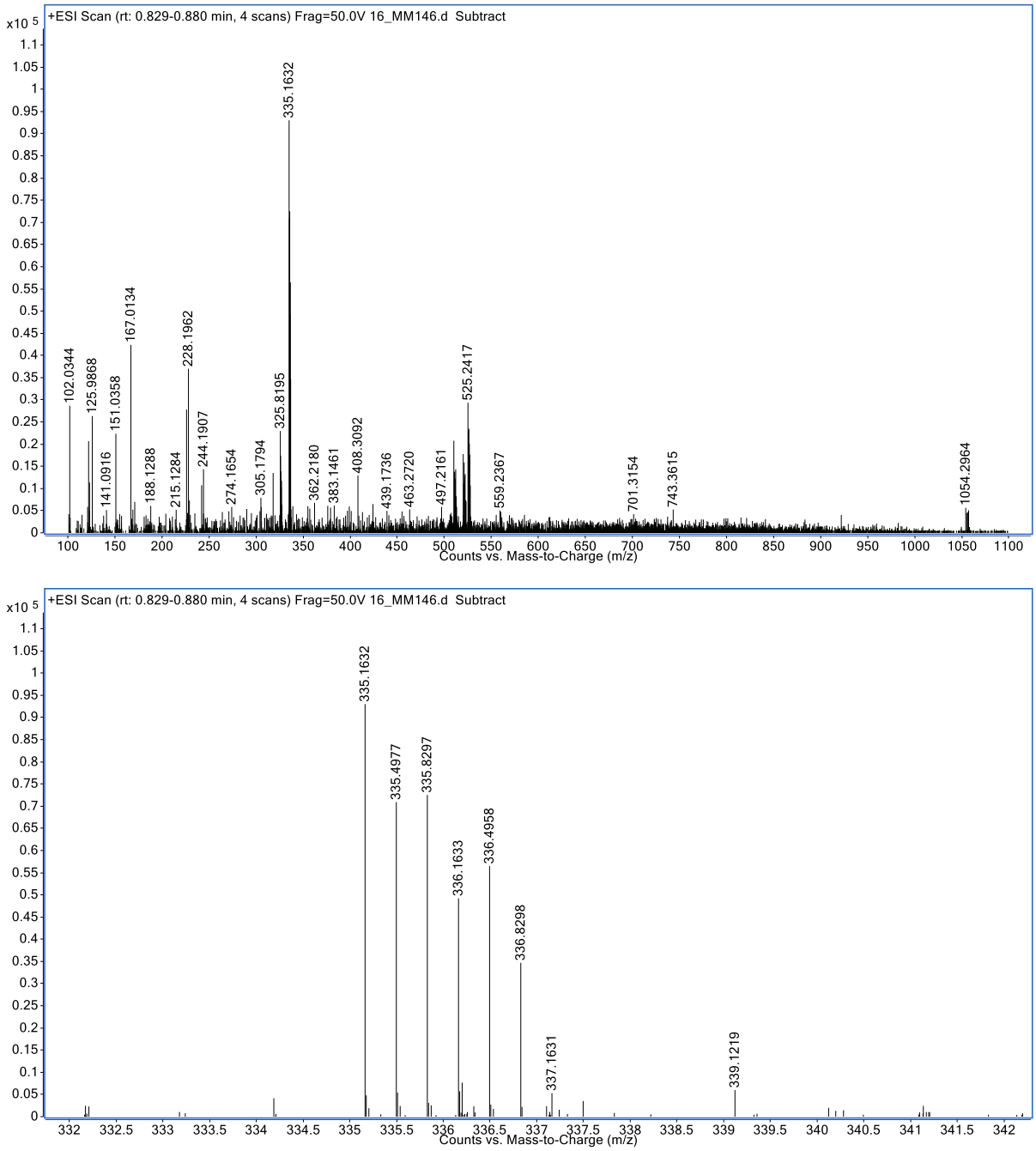

Figure S56. Mass spectrum of **27** in m/z region 100-1100 (upper spectrum) and enlarged spectrum in region m/z 332 – 342 (lower spectrum).

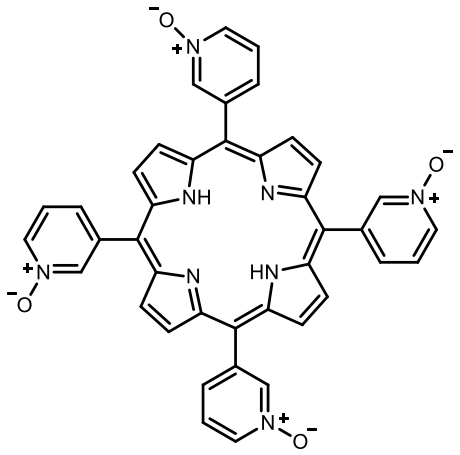

28

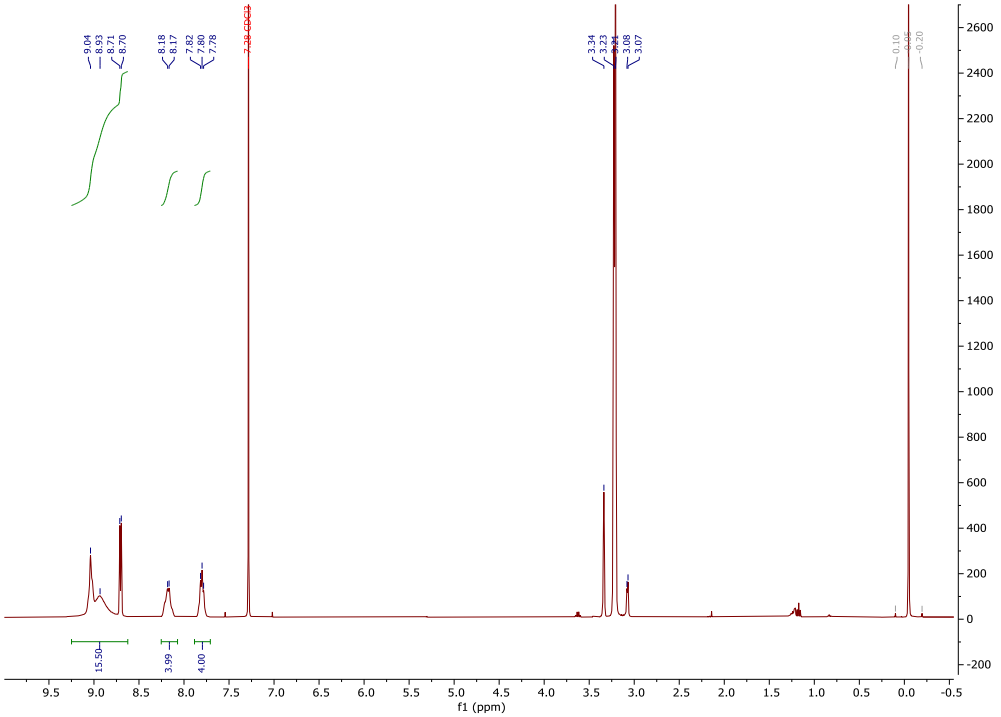

Figure S57. ^{1}H NMR (CD_3OD + $CDCl_3$, 600 MHz) spectrum of **28.**

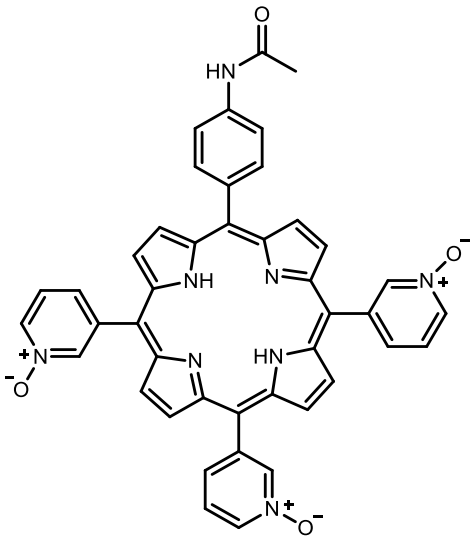

29

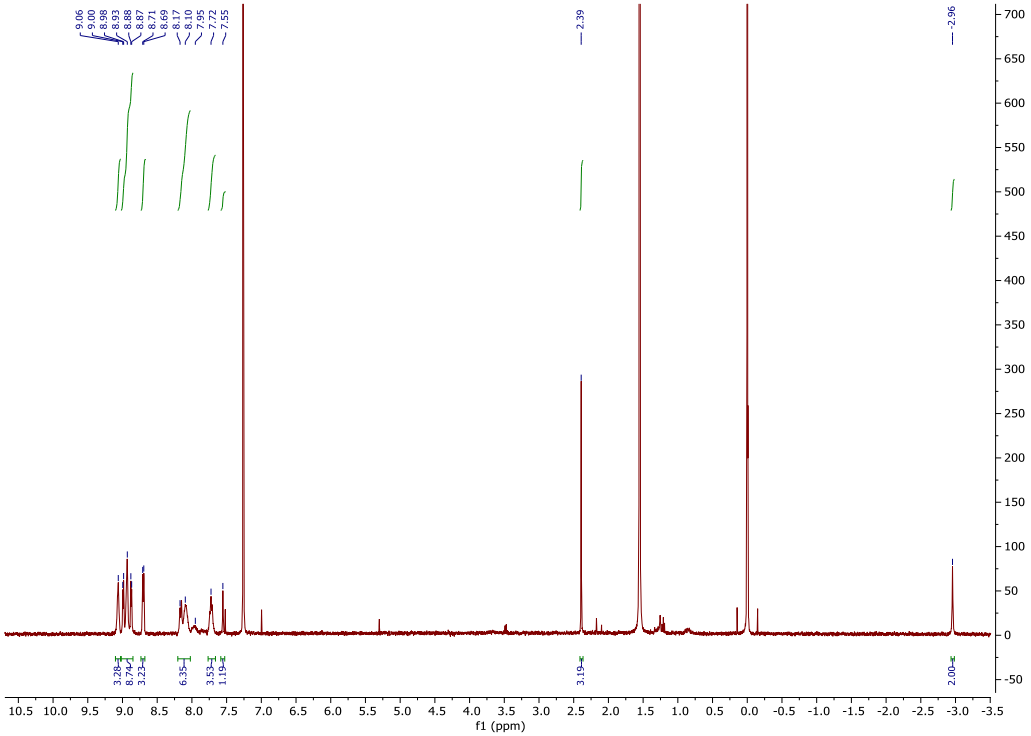

Figure S58. ^{1}H NMR ($CDCl_3$, 400 MHz) spectrum of **29**.

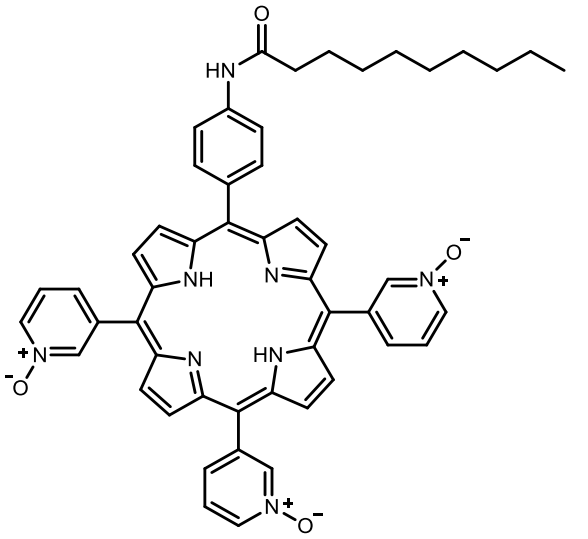

30

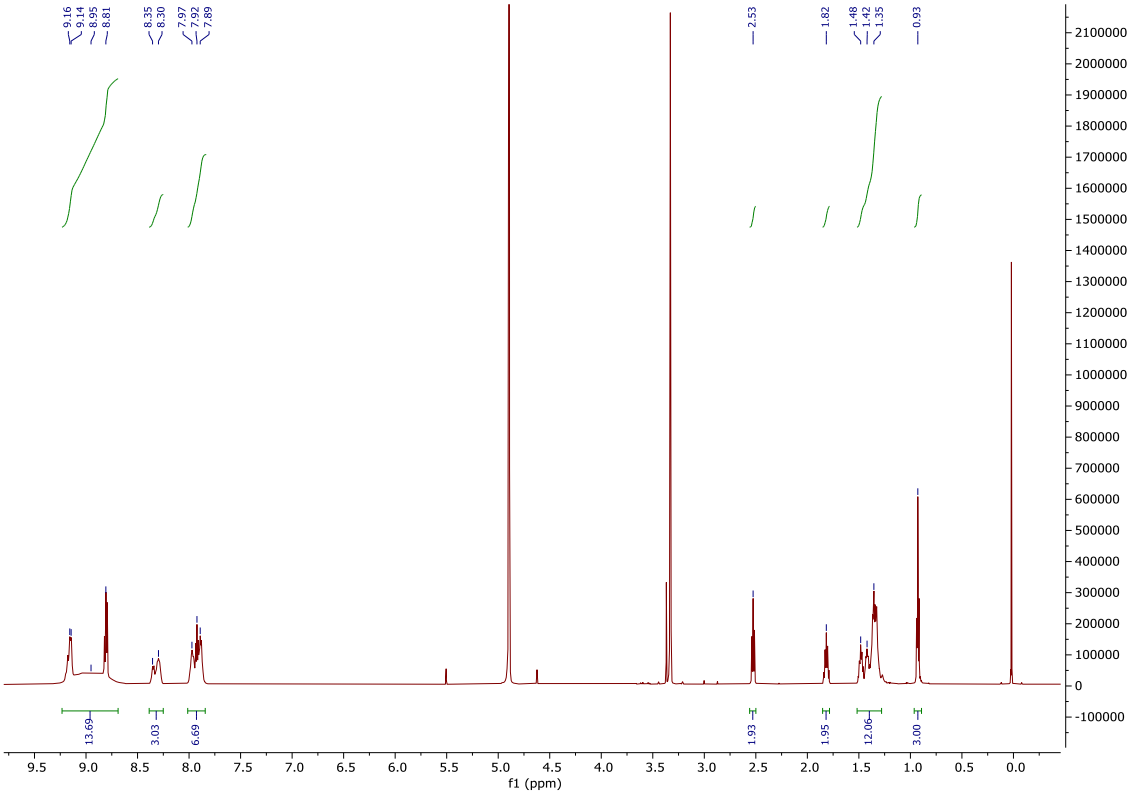

Figure S59. ^{1}H NMR (CD_3OD, 600 MHz) spectrum of **30**.

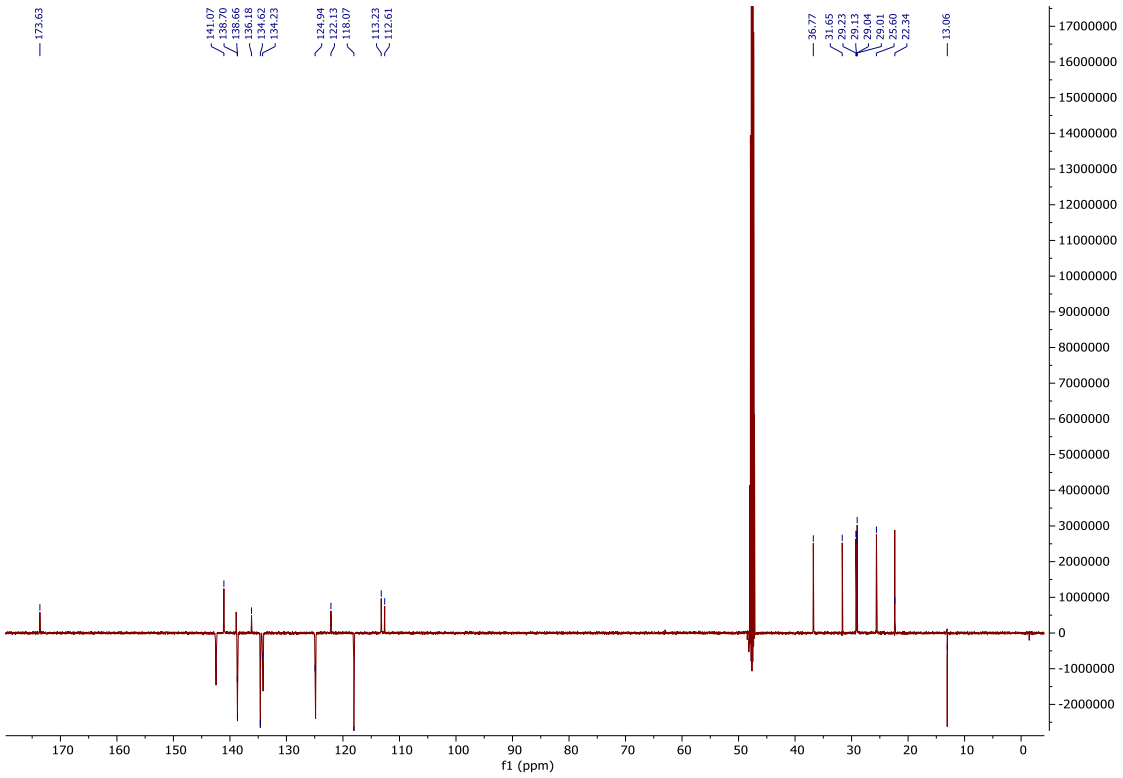

Figure S60. ^{13}C NMR (CD_3OD, 151 MHz) spectrum of **30**.

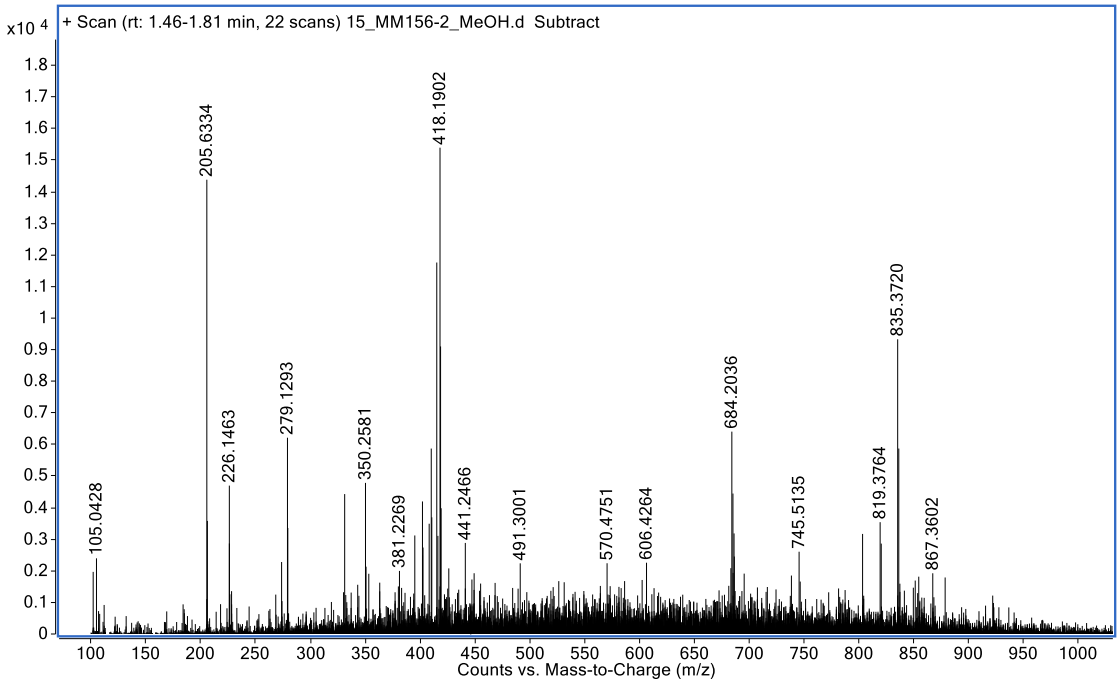

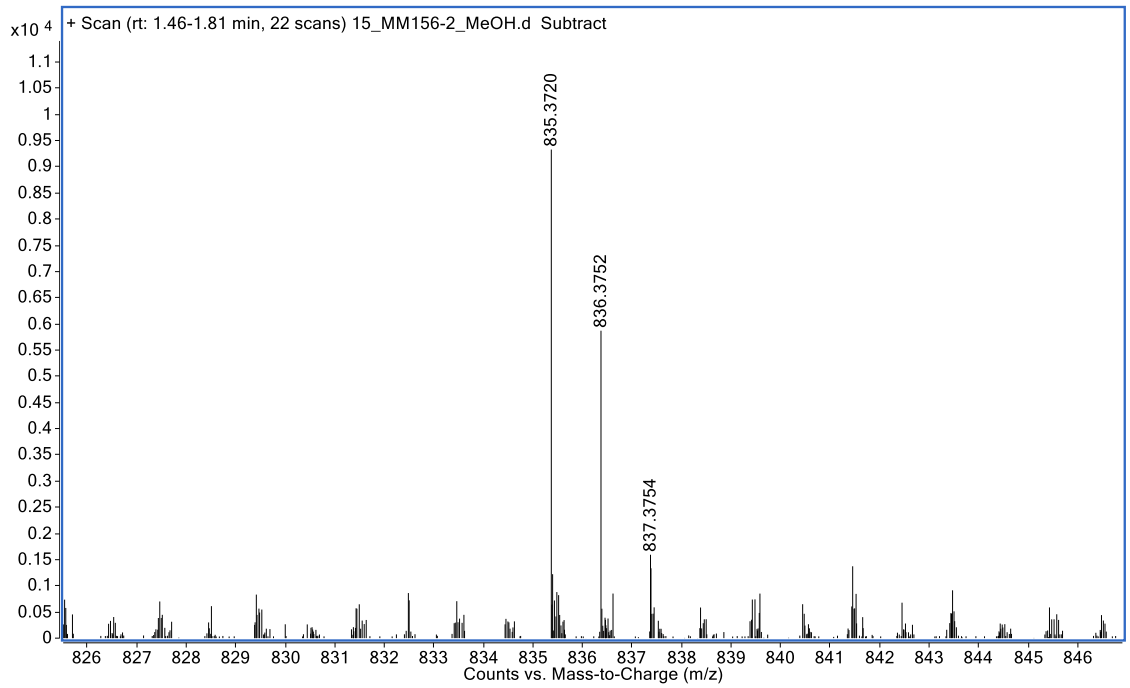

Figure S61. Mass spectrum of **30** in m/z region 100-1100 (upper spectrum) and enlarged spectrum of $[M+H]^+$ species detected in region m/z 826 – 846 (lower spectrum).

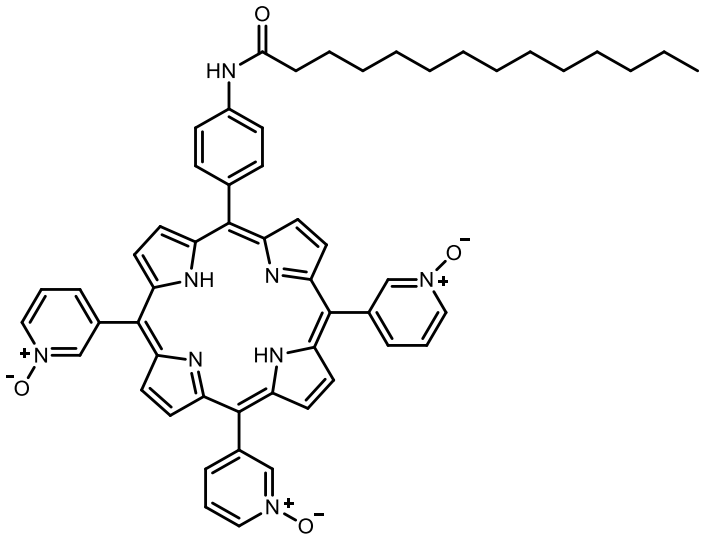

31

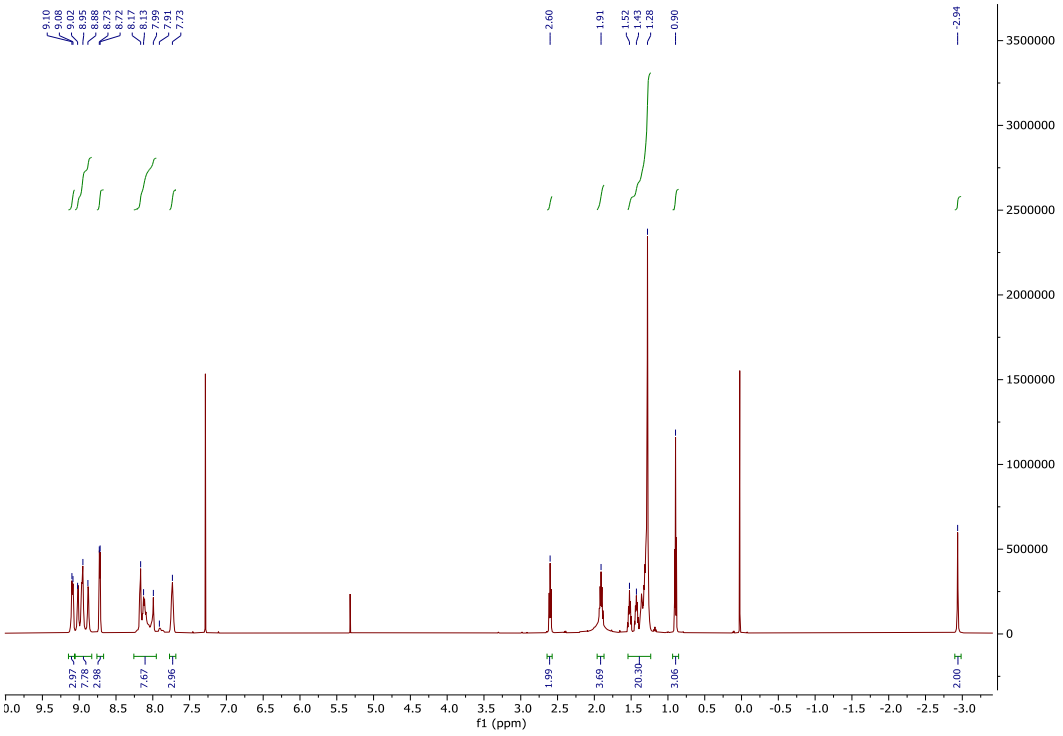

Figure S62. ^{1}H NMR (CD_3OD, 600 MHz) spectrum of **31**.

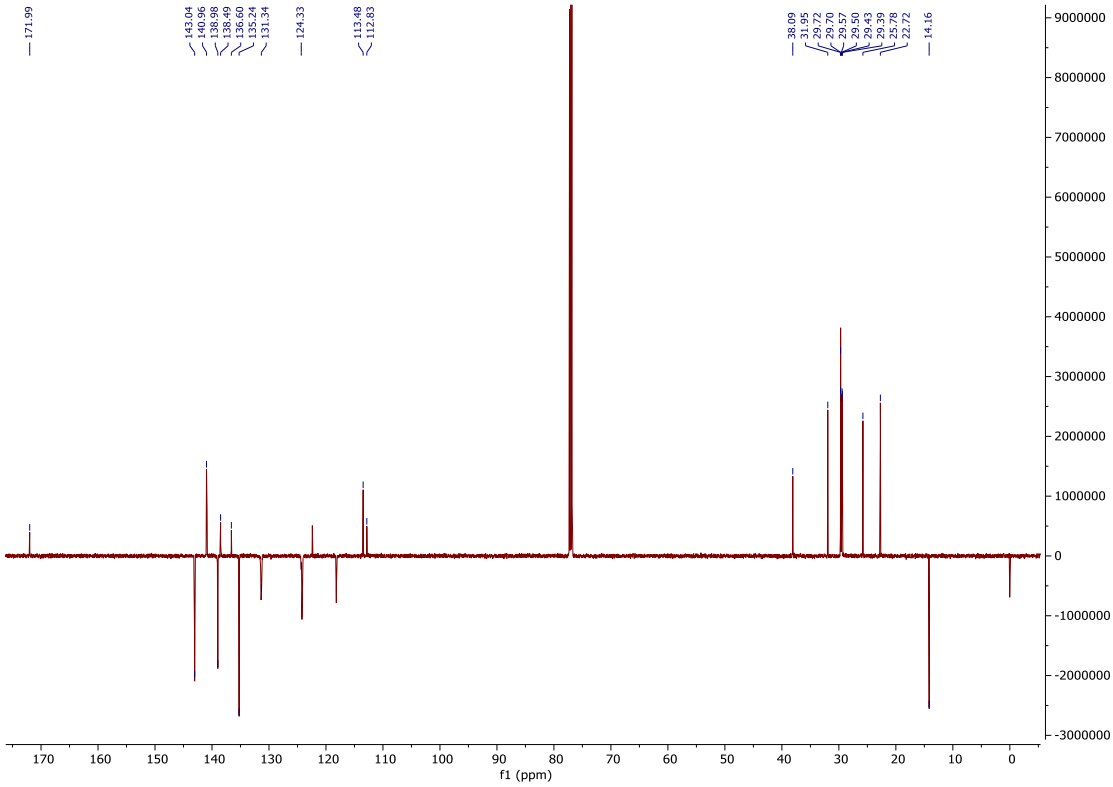

Figure S63. ^{13}C NMR (CD_3OD, 151 MHz) spectrum of **31**.

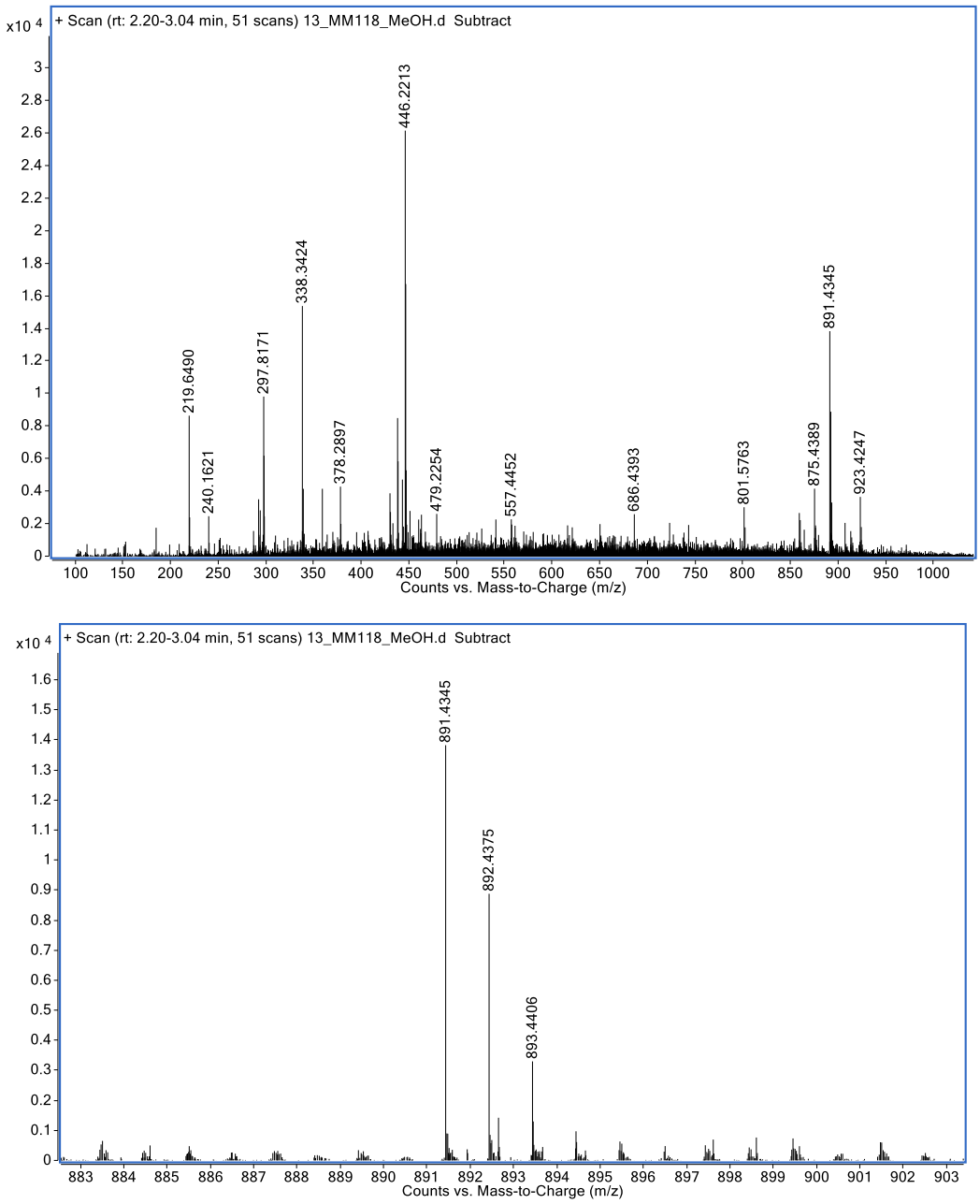

Figure S64. Mass spectrum of **31** in m/z region 100-1100 (upper spectrum) and enlarged spectrum of $[M+H]^+$ species detected in region m/z 883 – 903 (lower spectrum).

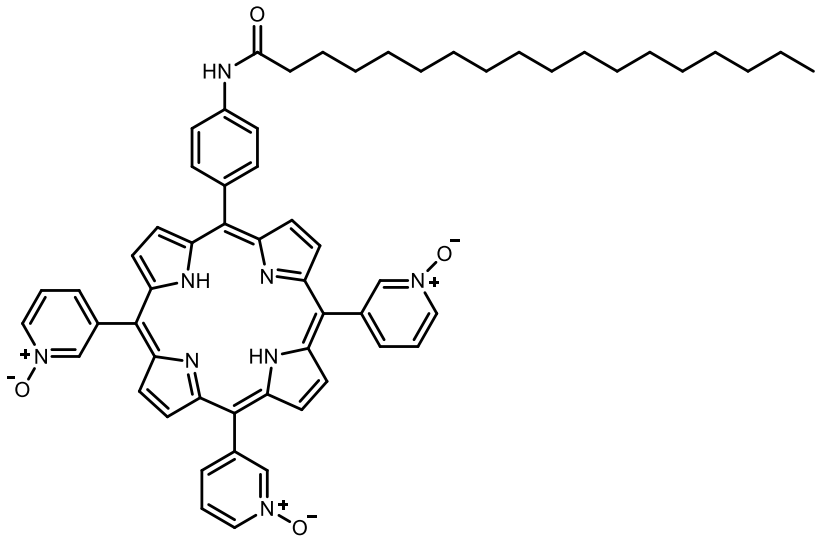

32

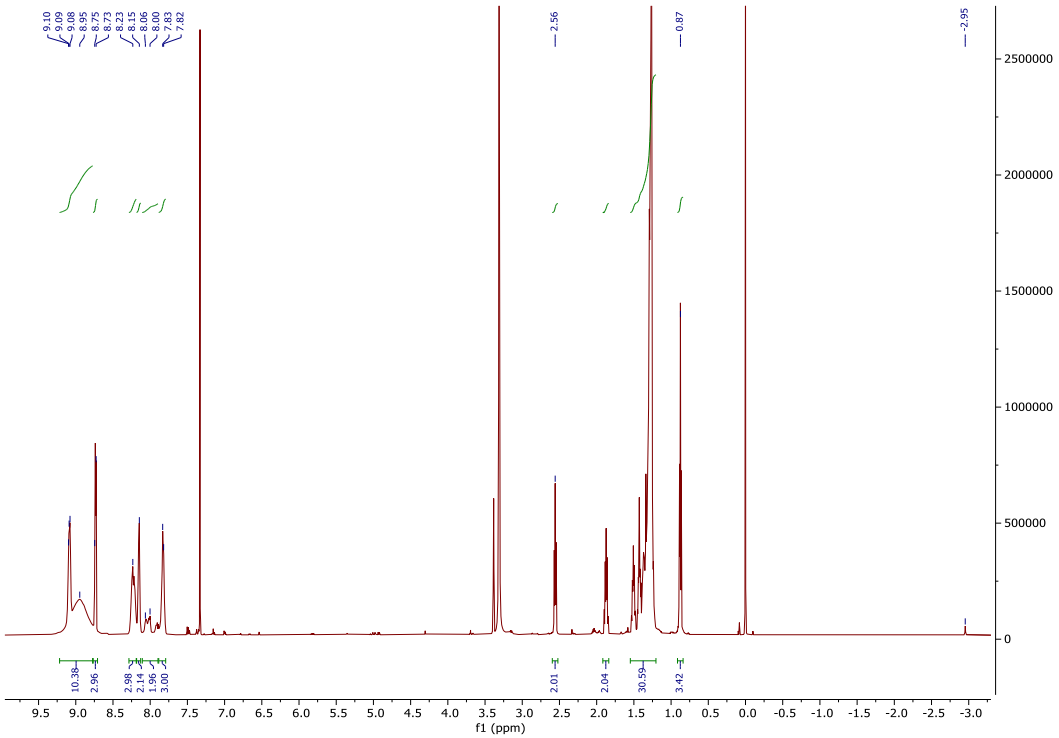

Figure S65. ^{1}H NMR (CD_3OD + $CDCl_3$, 600 MHz) spectrum of **32**.

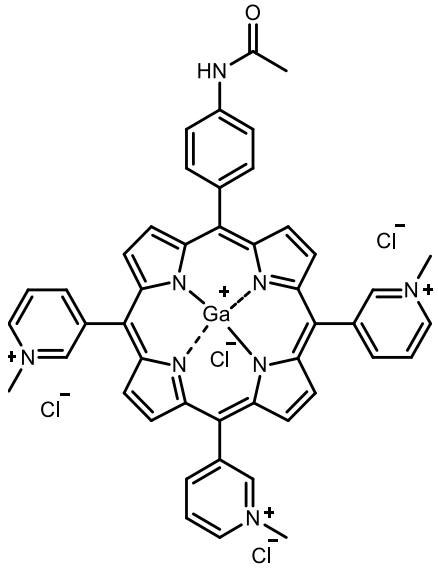

33

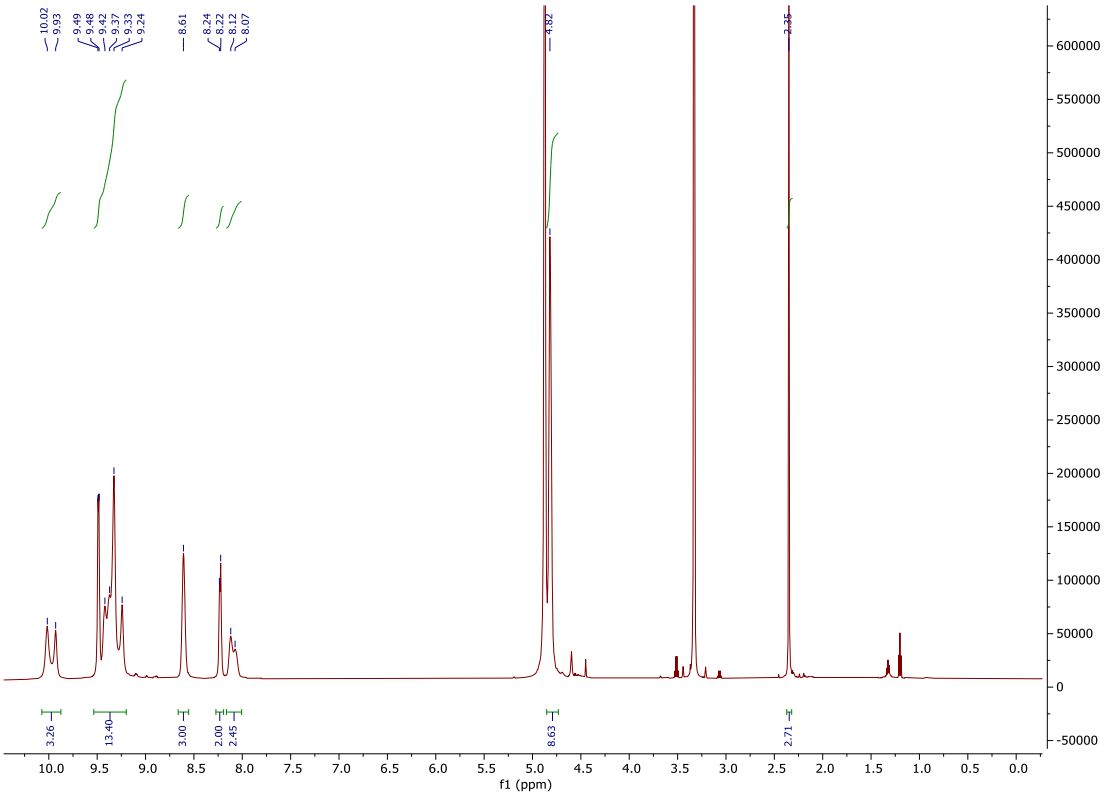

Figure S66. ^{1}H NMR (CD_3OD, 600 MHz) spectrum of **33**.

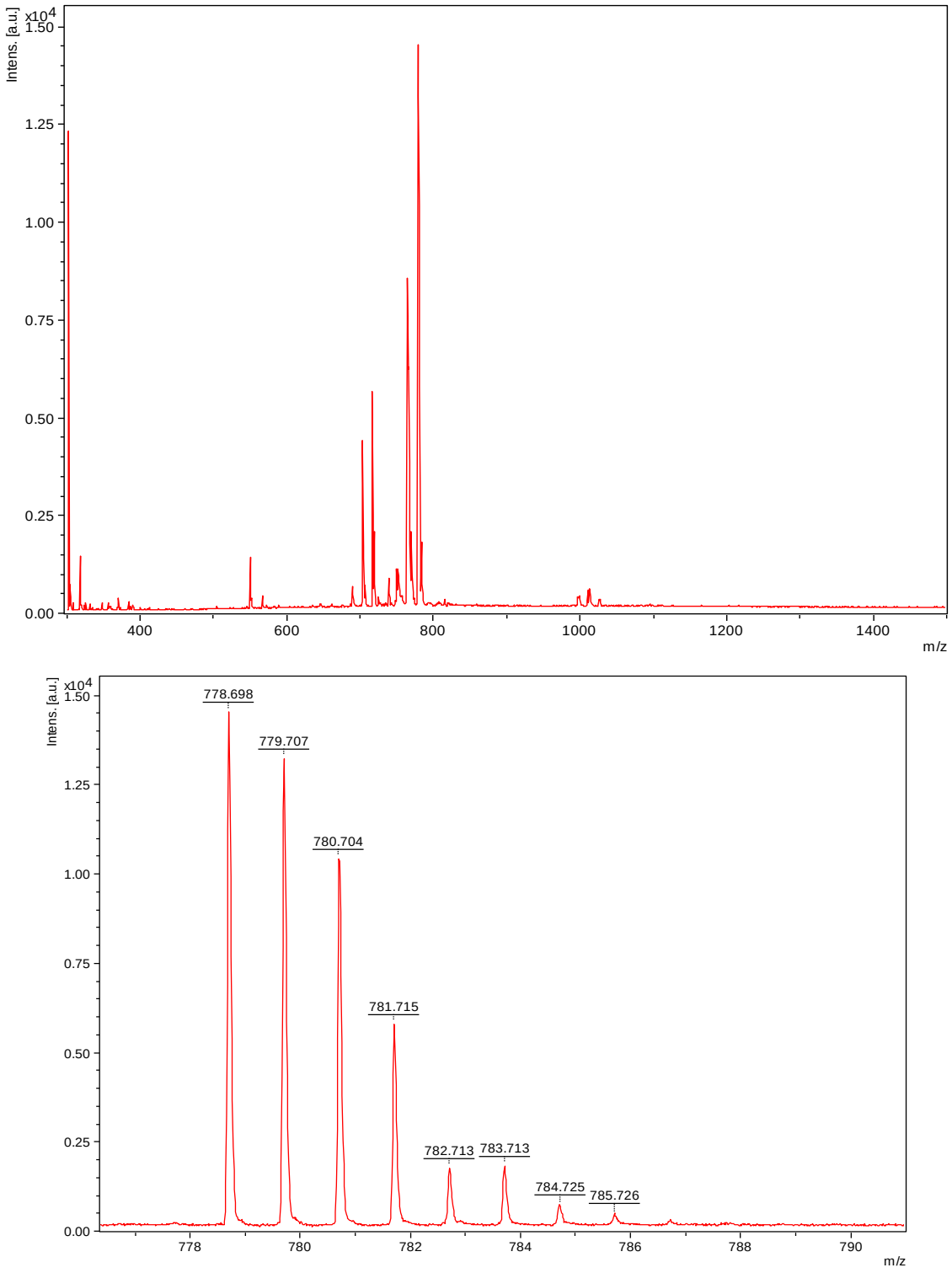

Figure S67. MALDI-MS spectrum of **33** in m/z region 400-1400 (upper spectrum) and enlarged part of the spectrum 778-790 (lower spectrum).

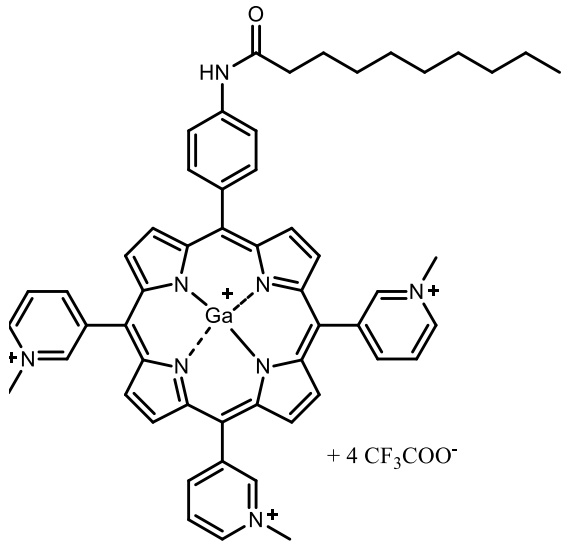

34

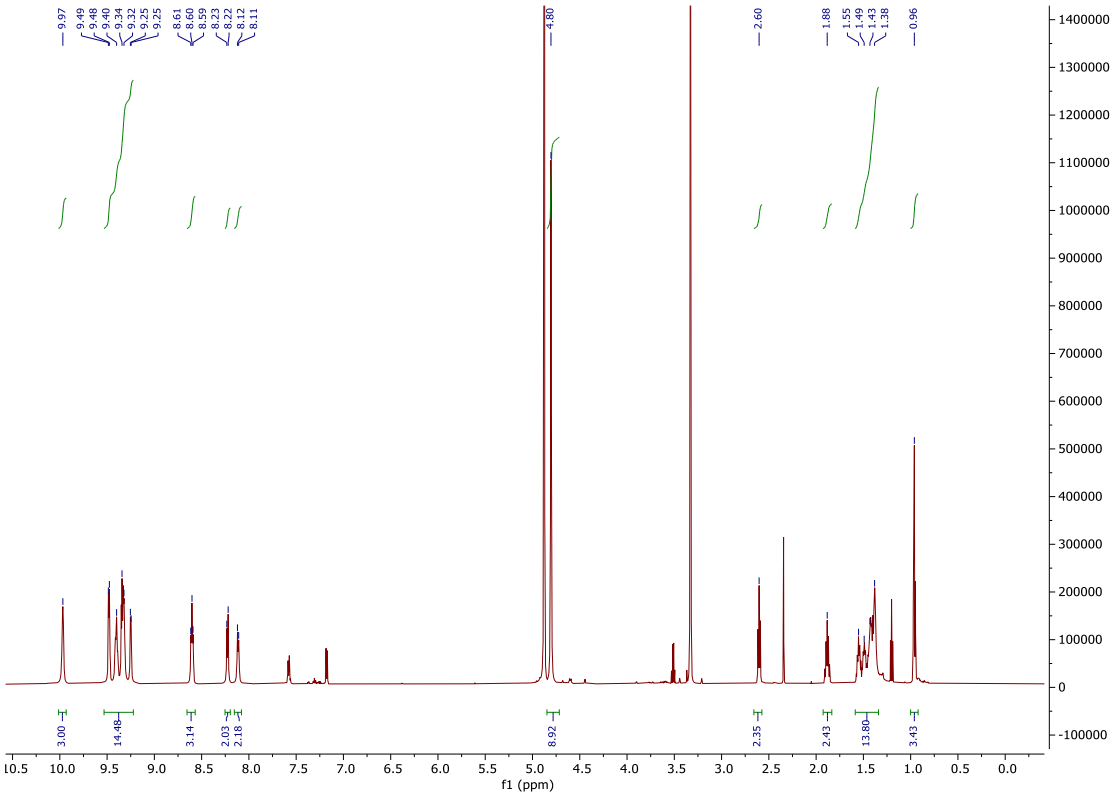

Figure S68. ^{1}H NMR (CD_3OD, 600 MHz) spectrum of **34**.

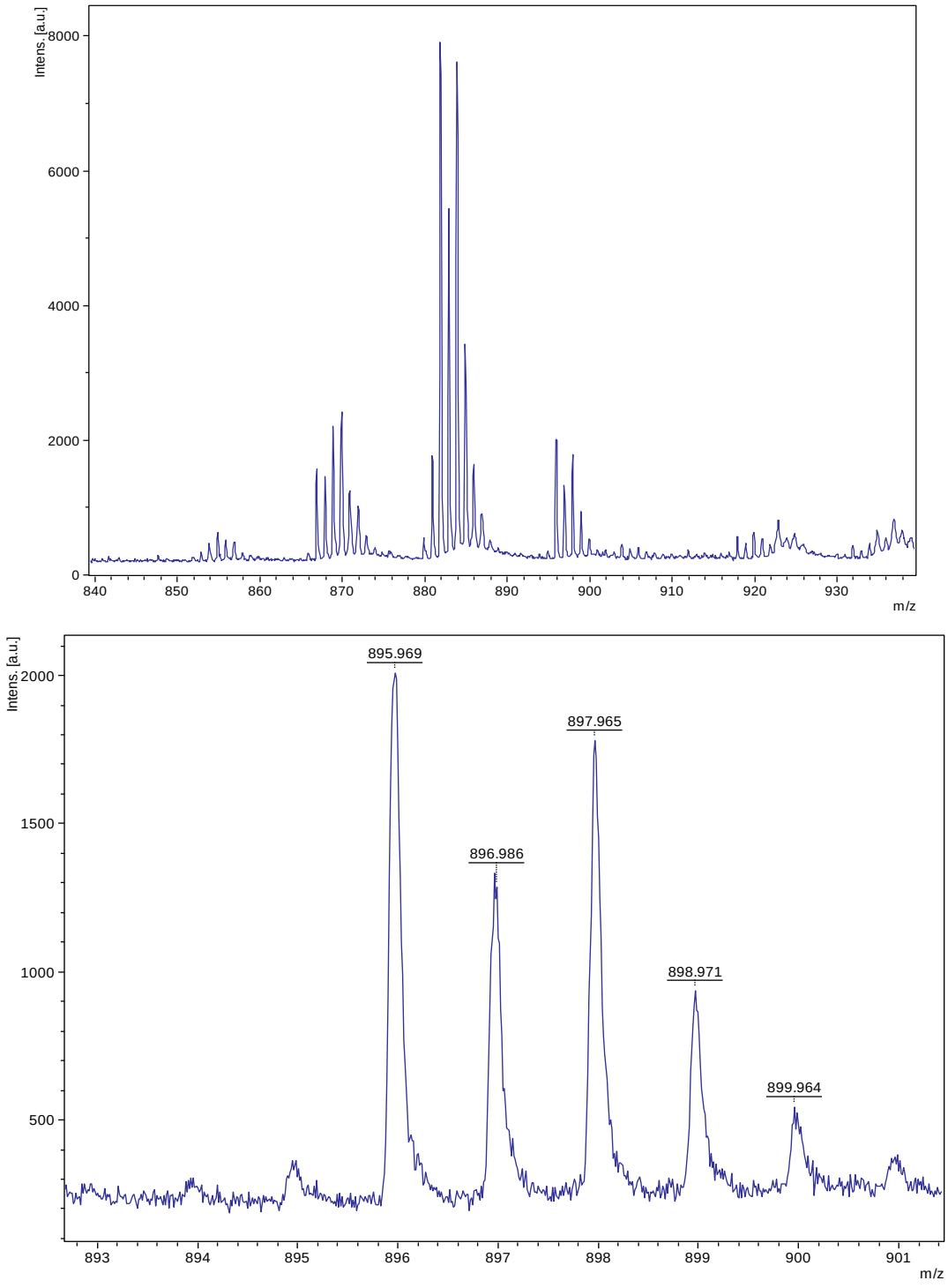

Figure S69. MALDI-MS spectrum of **34** in m/z region 840-930 (upper spectrum) and enlarged part of the spectrum 893-901 (lower spectrum).

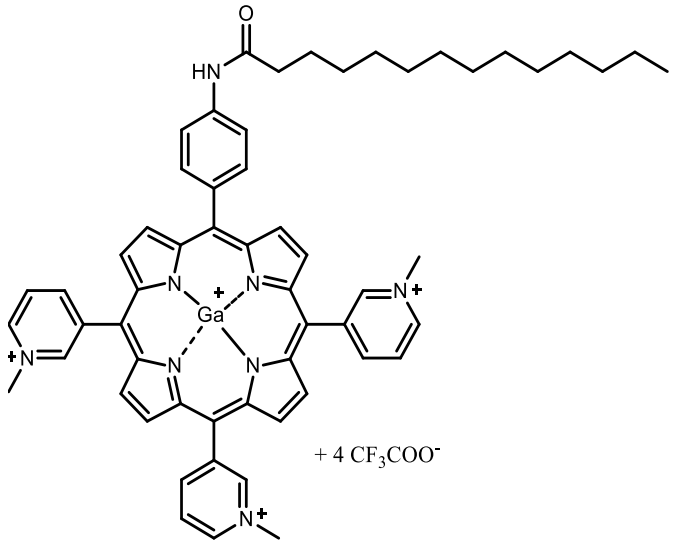

35

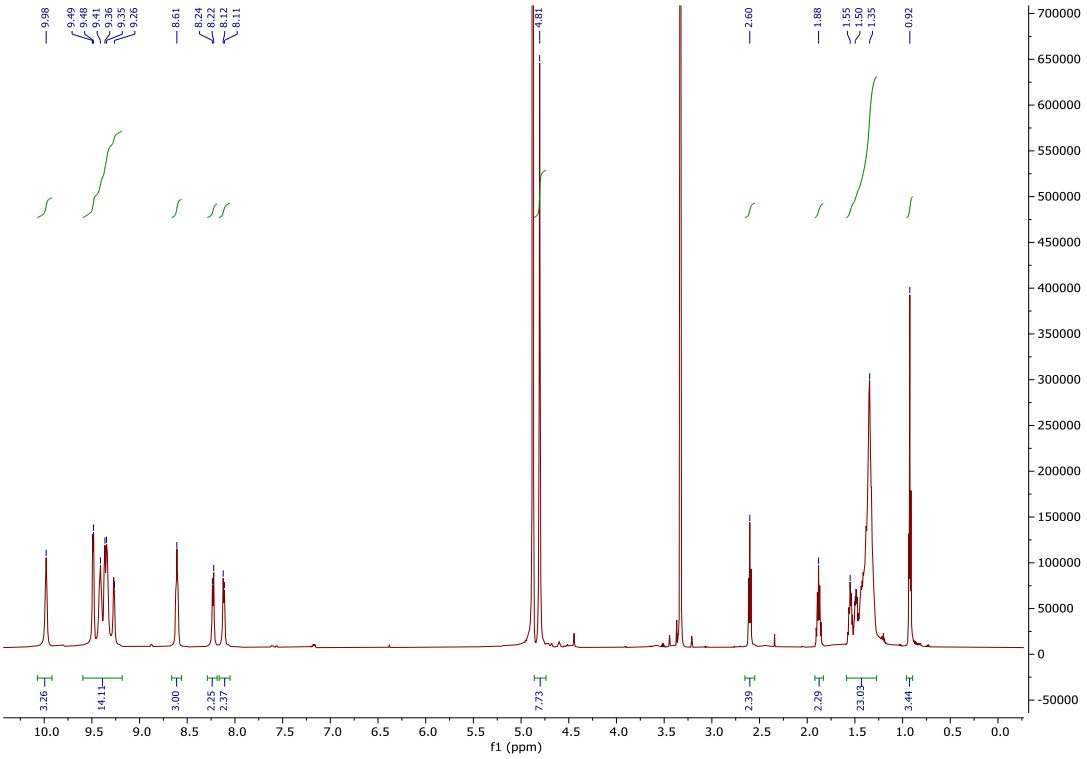

Figure S70. ^{1}H NMR (CD_3OD, 600 MHz) spectrum of **35**.

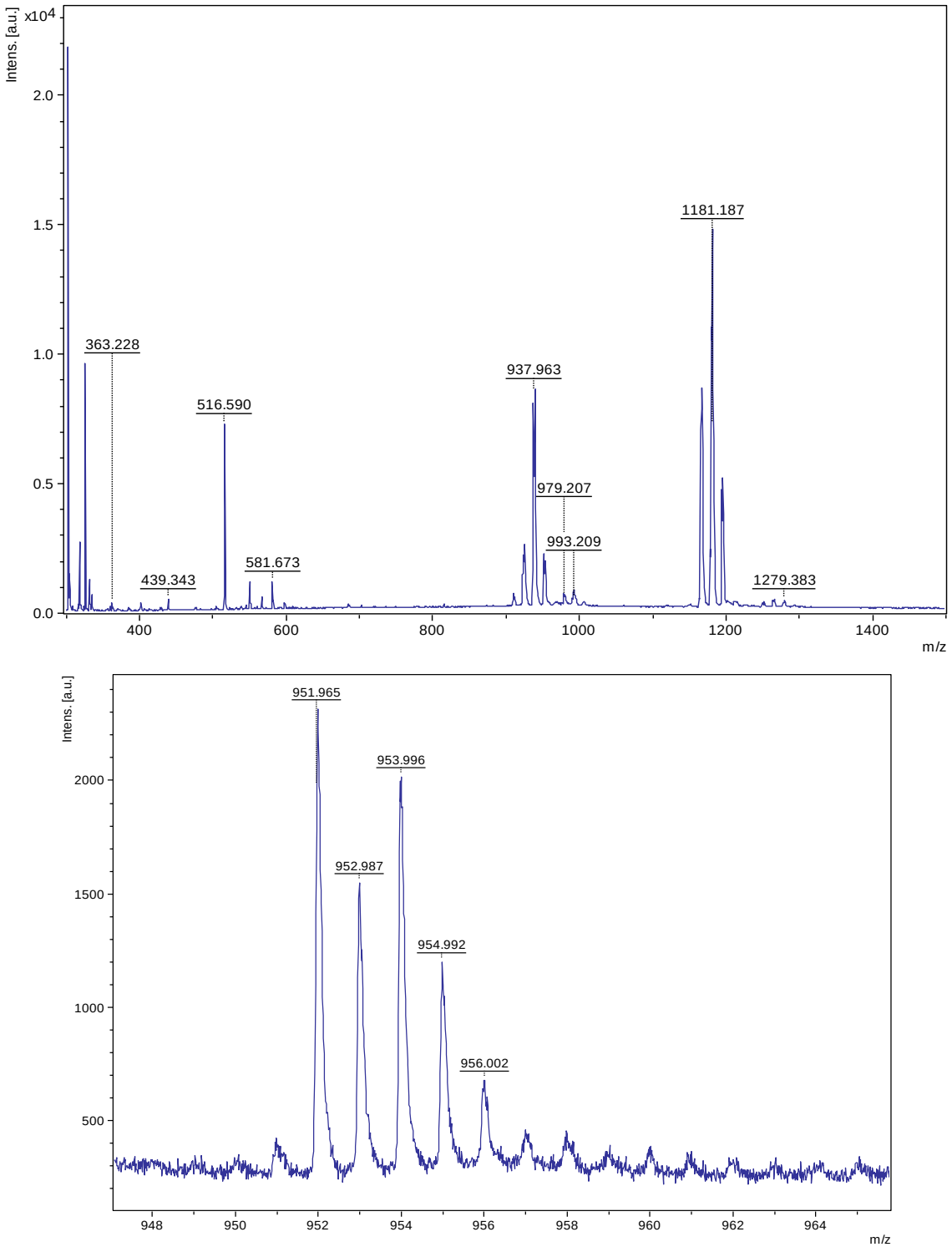

Figure S71. MALDI-MS spectrum of **35** in m/z region 400-1400 (upper spectrum) and enlarged part of the spectrum 948-964 (lower spectrum).

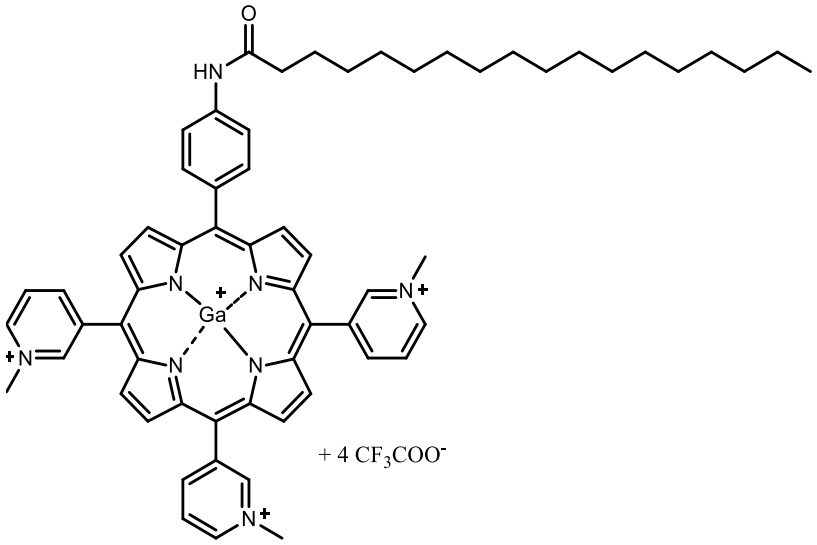

36

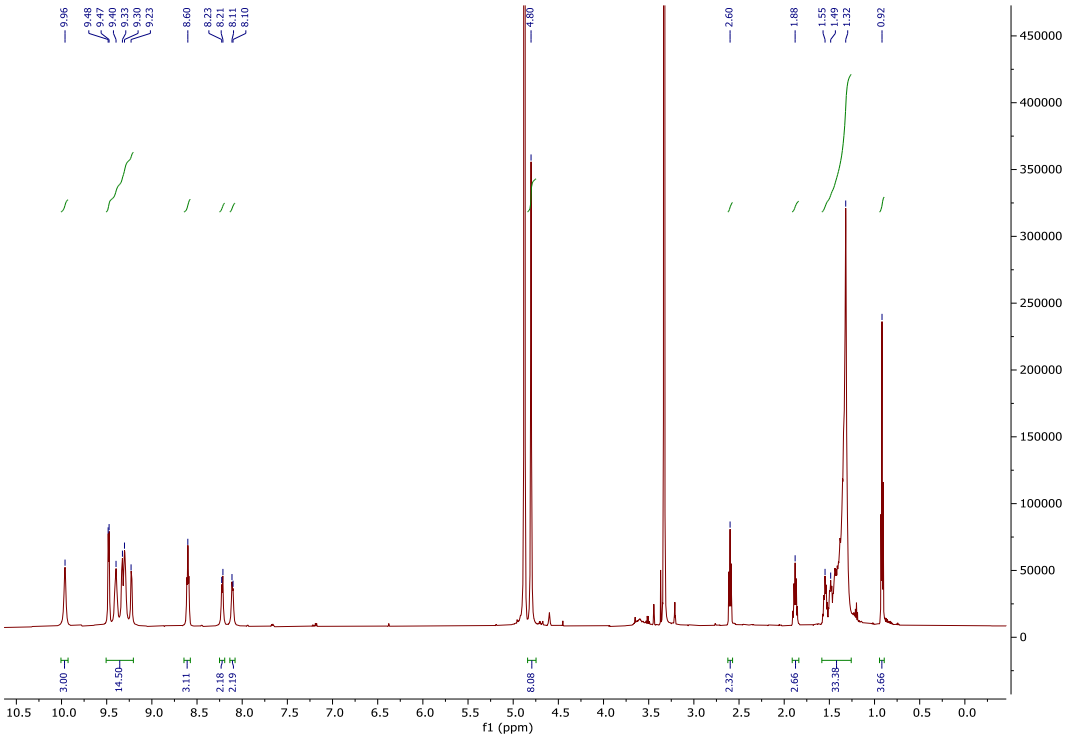

Figure S72. ^{1}H NMR (CD_3OD, 600 MHz) spectrum of **36**.

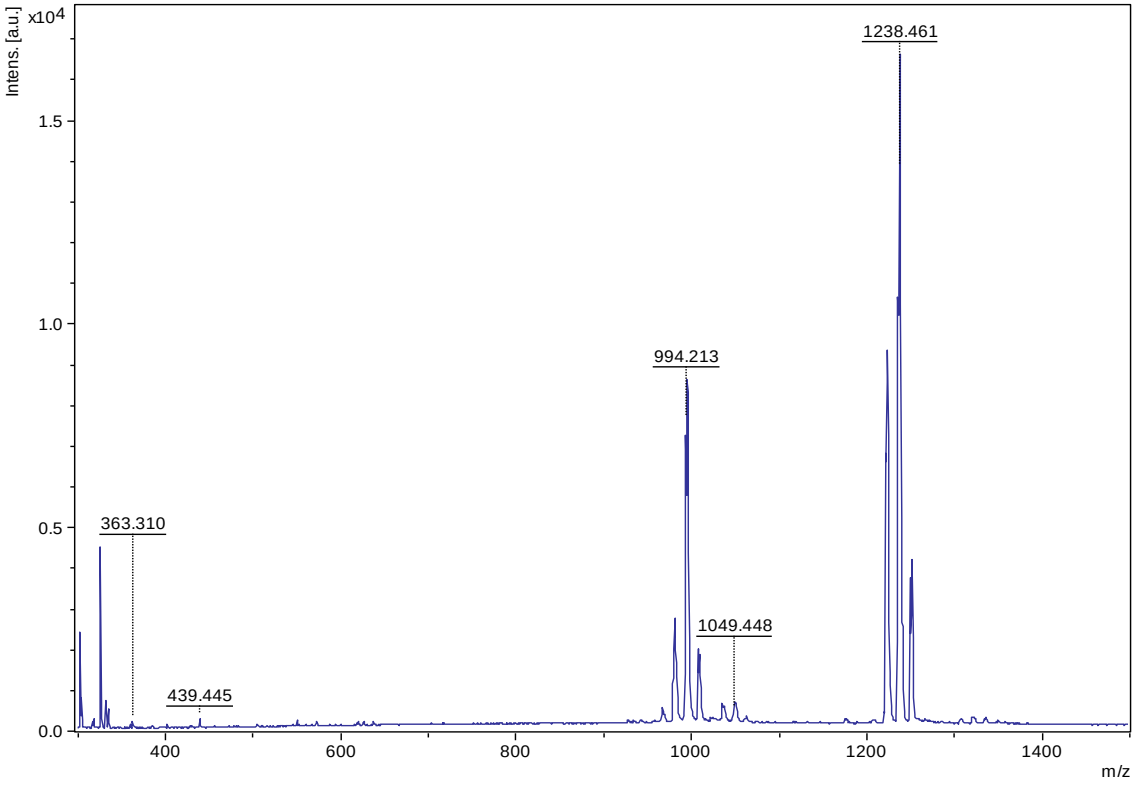

Figure S73. MALDI-MS spectrum of **36** in m/z region 400-1400.

8.2. Supporting information to the Section 3.4.

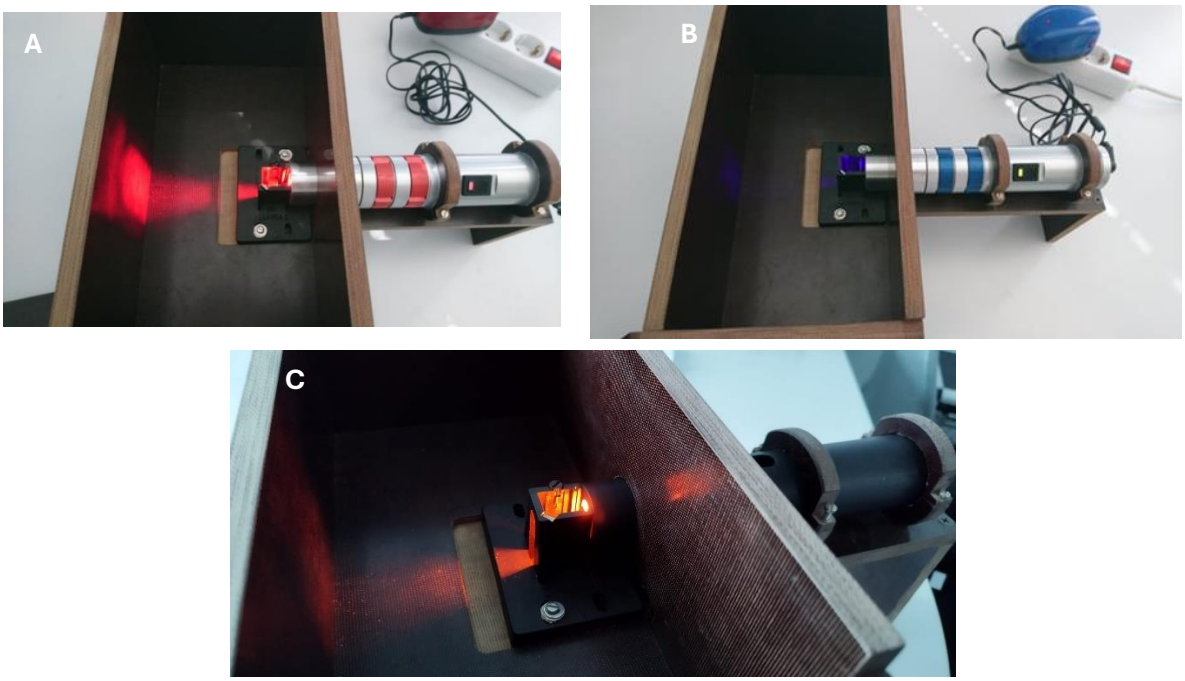

Figure S74. Light sources used for the measurements in the cuvette. Picture A shows the set-up for irradiation with red light (λ = 647 nm, variable fluence rate 10.7, 15.3, 22.0 or 38.0 mW/cm^2), picture B with violet light (λ = 411 nm, variable fluence rate 3.5, 7.0, 11.0 mW/cm^2) and on picture C a set-up with orange light (λ = 606 nm, 2 mW/cm^2).

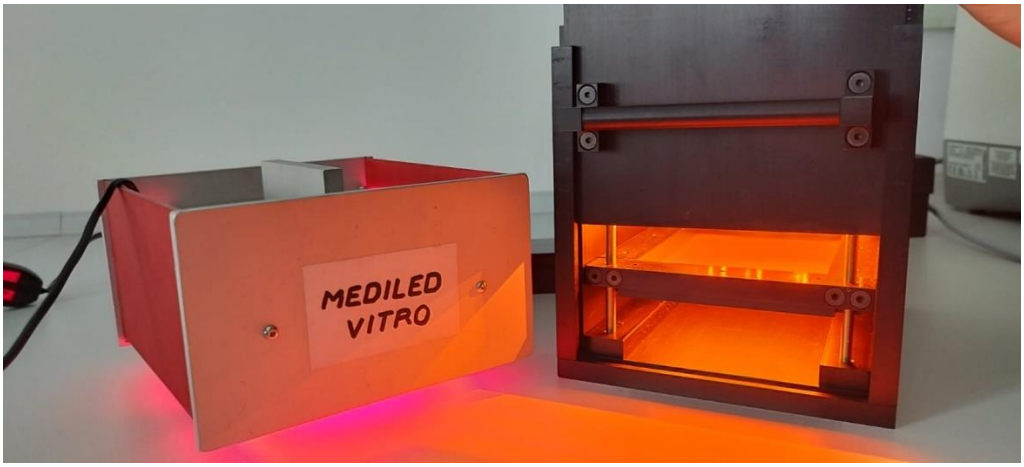

Figure S75. Light sources used in phototoxicity experiments for the irradiation on 96-well microtiter plate with red light (λ = 643 nm, 2 mW/cm^2) and orange light (λ = 606 nm, 2 mW/cm^2).

8.3. Supporting information to the 3.11.2. Cellular uptake

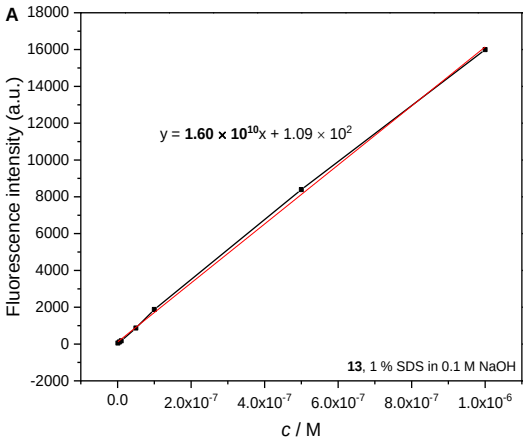

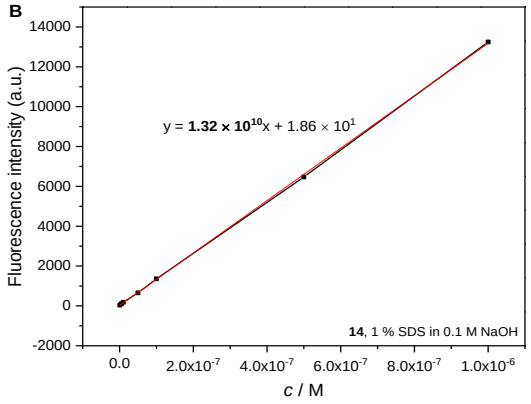

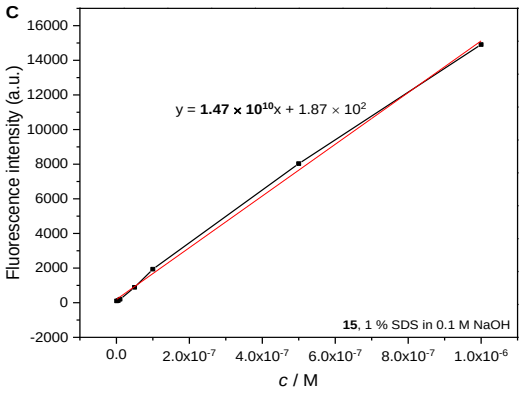

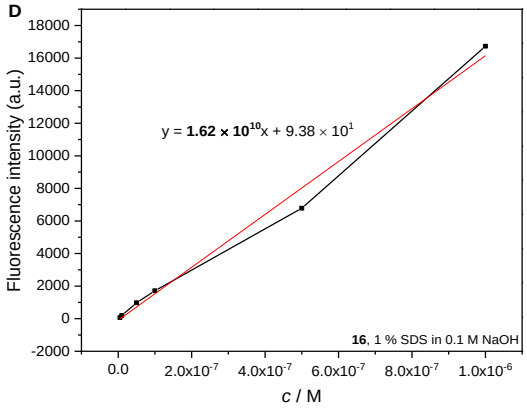

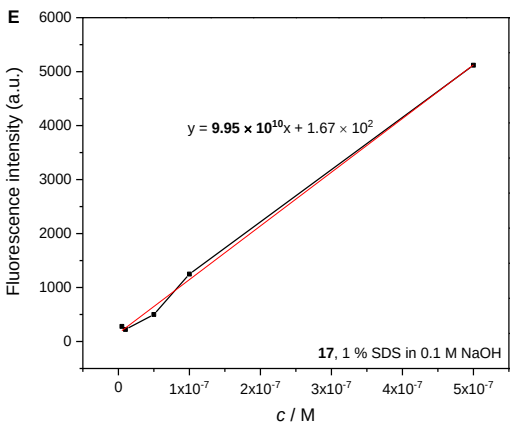

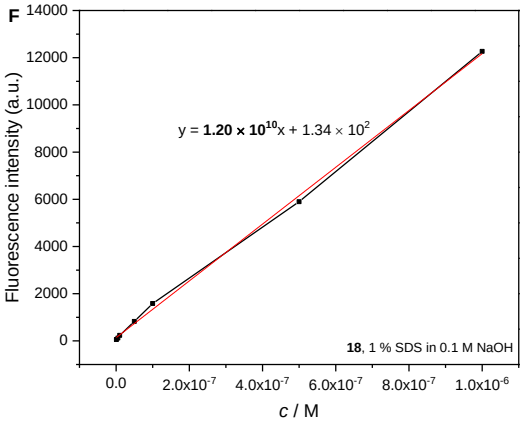

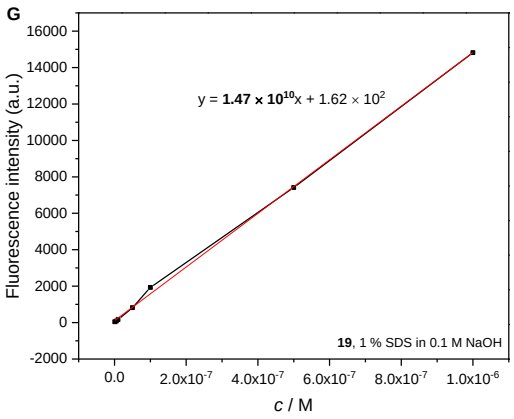

Figure S76. Calibration curves in 1% SDS in 0.1 M NaOH used for calculation of concentration of *N*-methylated porphyrins (**13**-**19**) in cellular uptake.

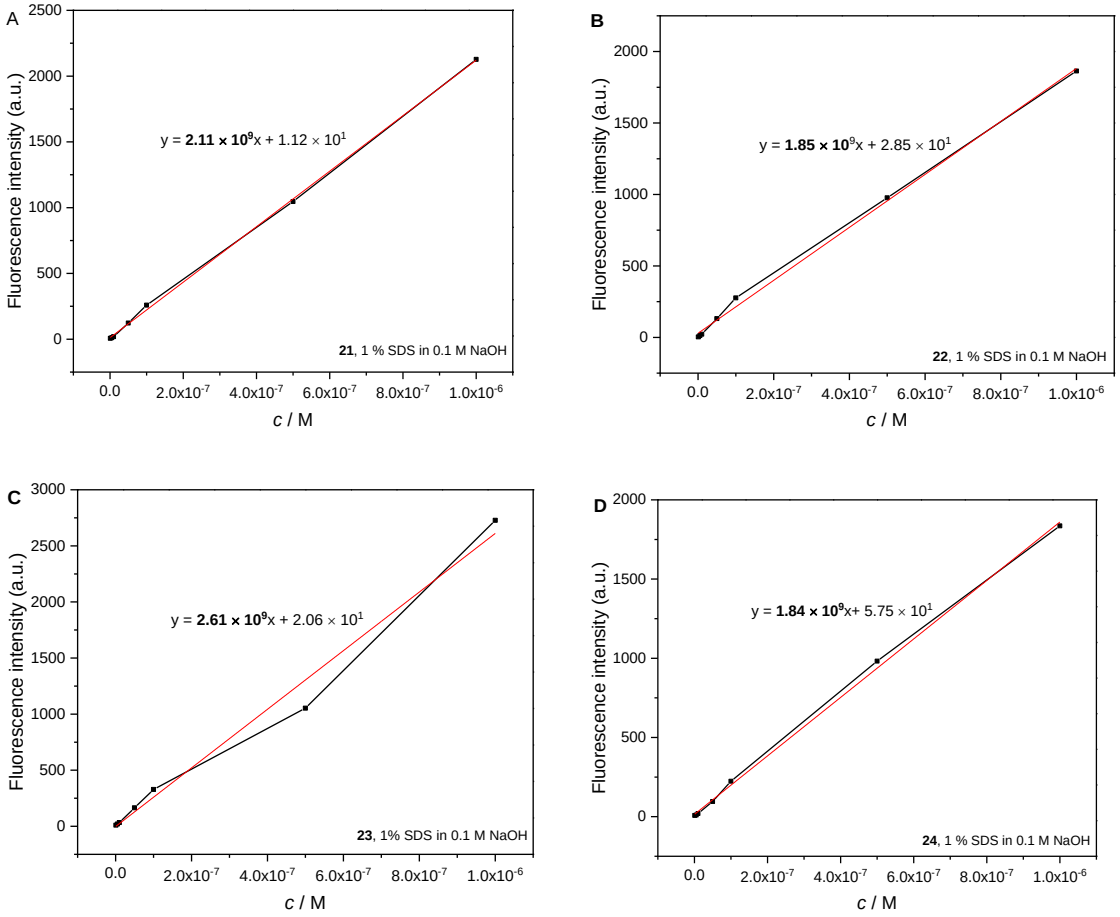

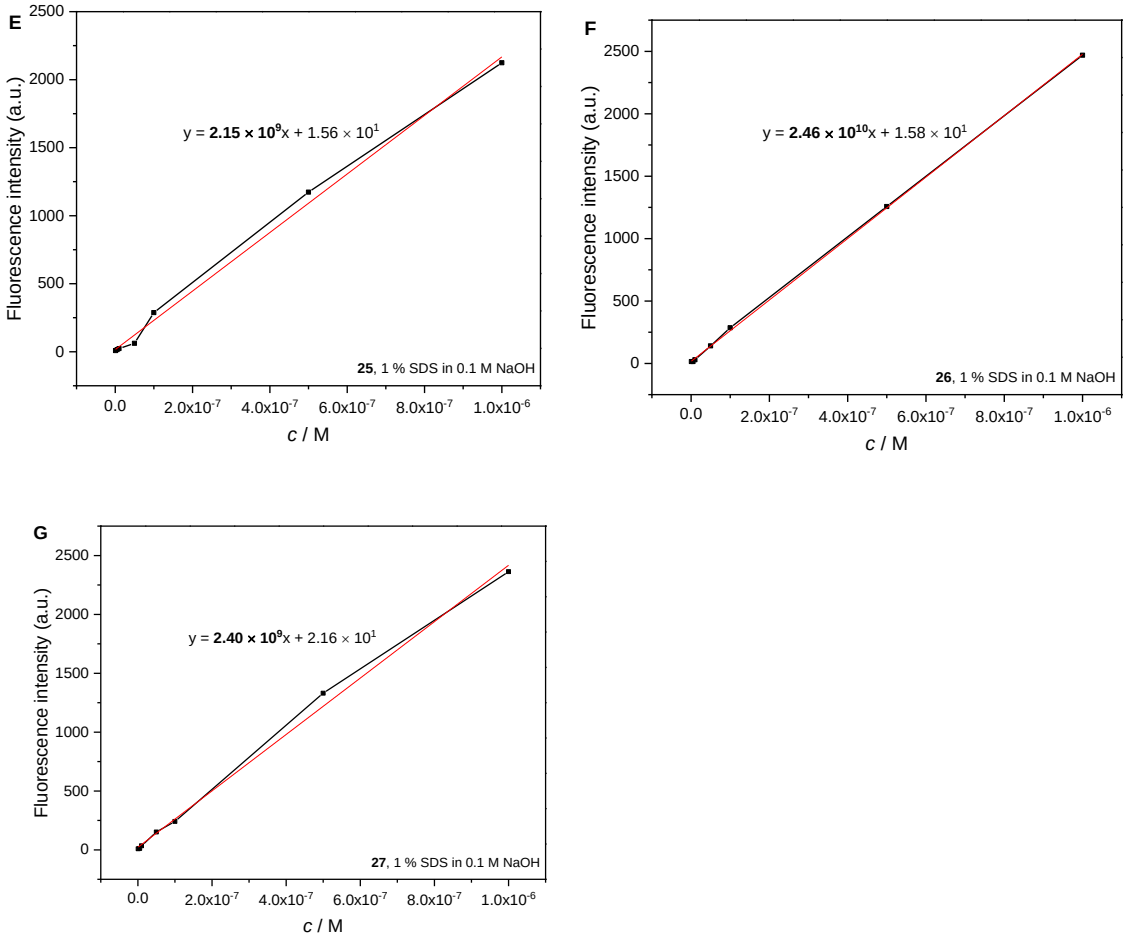

Figure S77. Calibration curves in 1% SDS in 0.1 M NaOH used for calculation of concentration of Zn(II) (*N*-methylpyridinium-3-yl)porphyrins (**21**-**27**) in cellular uptake.

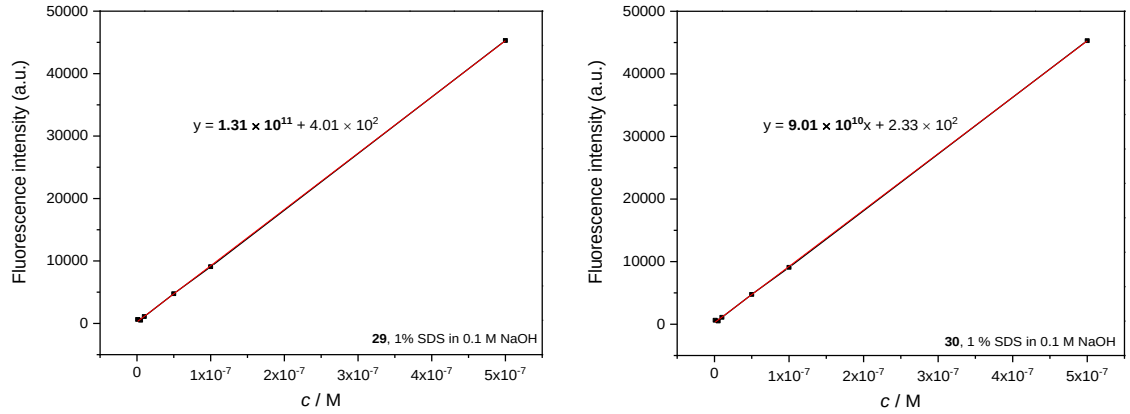

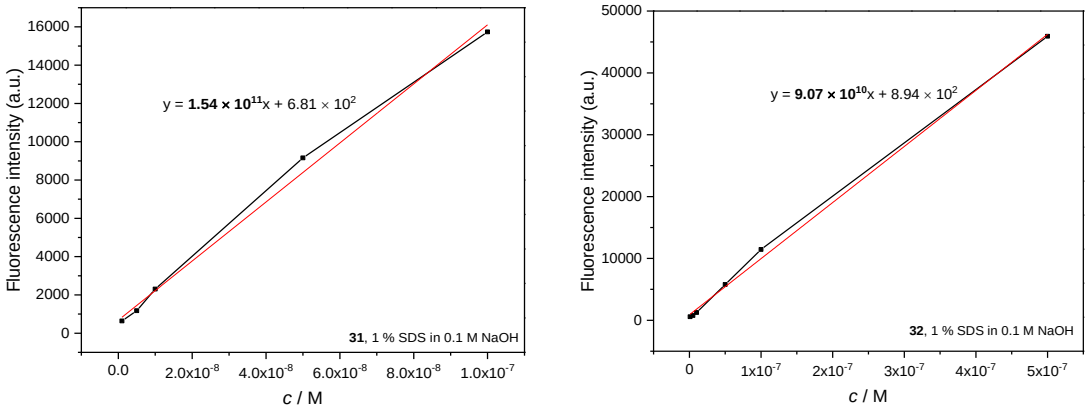

Figure S78. Calibration curves in 1 % SDS in 0.1 M NaOH used for calculation of concentration of *N*-oxidised (pyrid-3-yl)porphyrins (**29**-**32**) in cellular uptake.

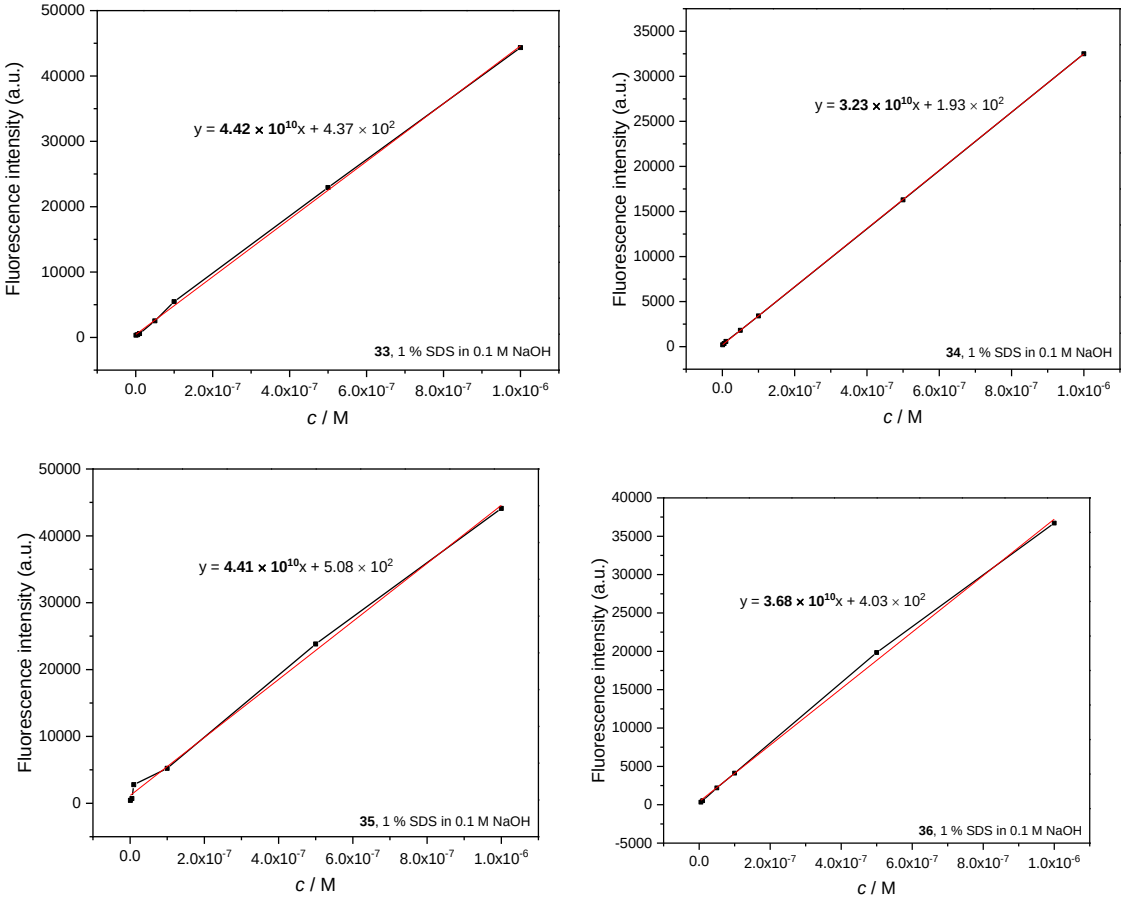

Figure S79. Calibration curves in 1 % SDS in 0.1 M NaOH used for calculation of concentration of Ga(III) *N*-methylpyridiniumporphyrins (**29**-**32**) in cellular uptake.

8.4. Supporting information to the Section 5.1.

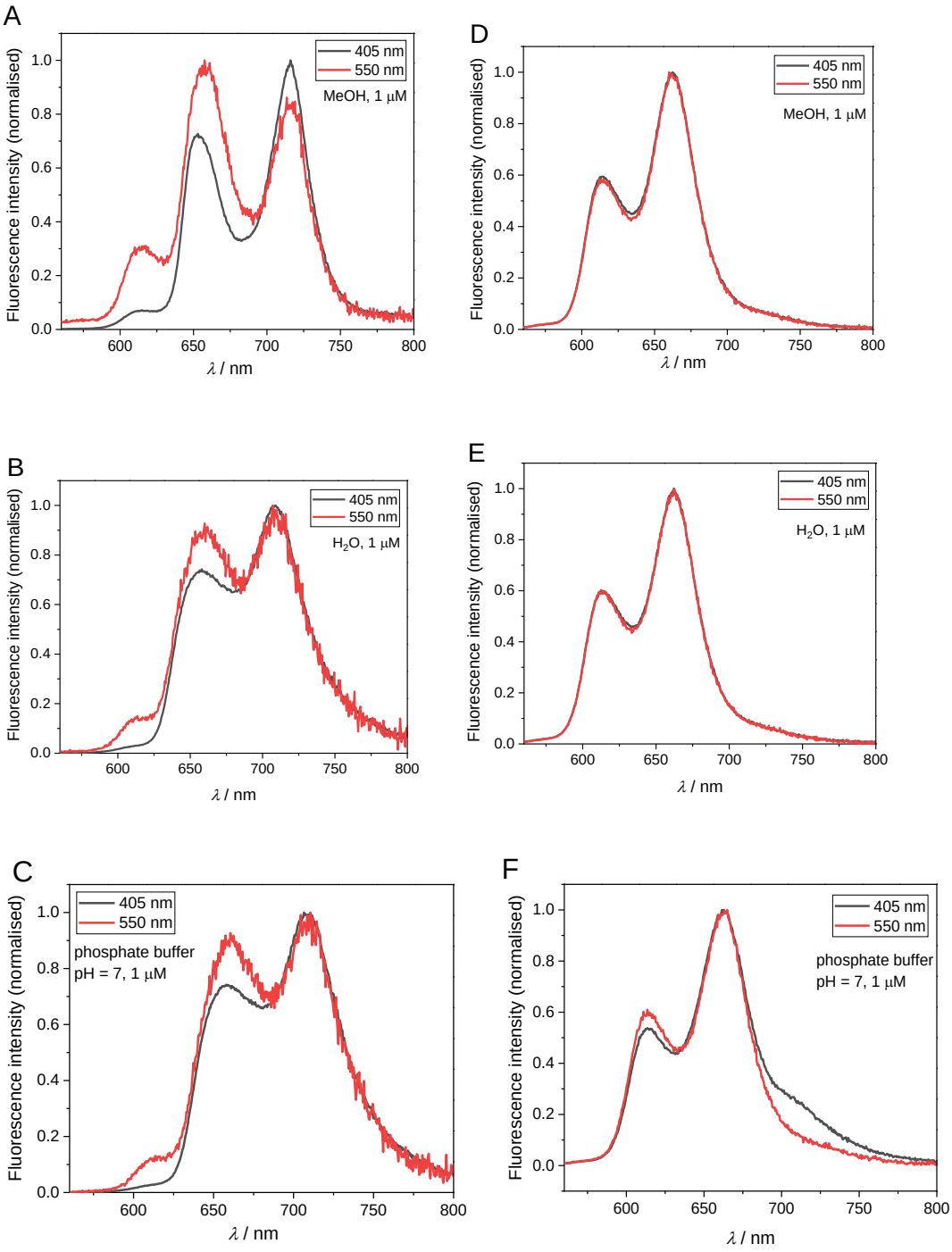

Figure S80. Comparison of the fluorescence spectra of **1** (A-C) and **2** (D-F) measured after excitation at 405 nm and 550 nm of 1 μM solution of **1** and **2** in MeOH, H_2O and 0.05 M phosphate buffer, pH=7.

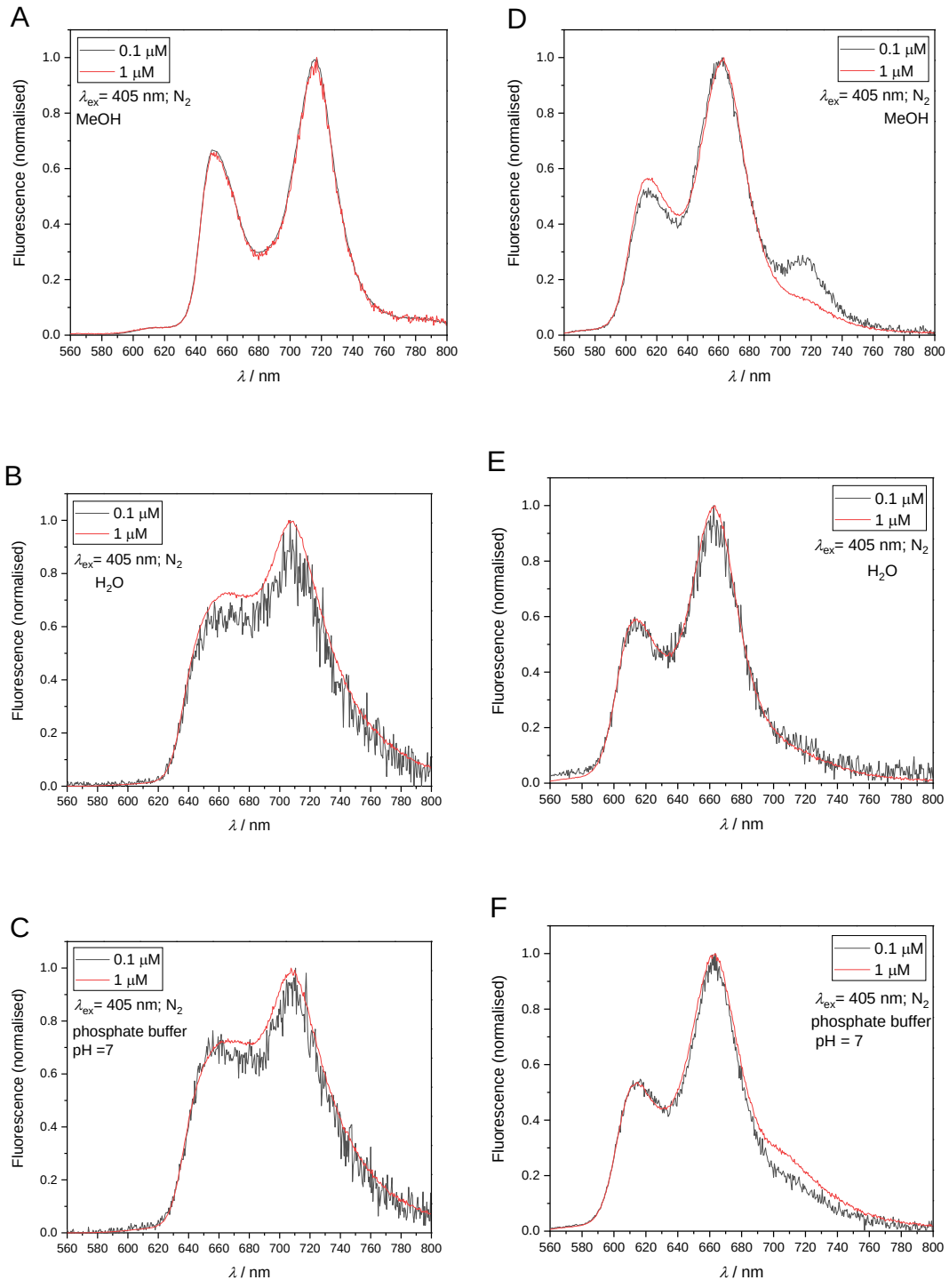

Figure S81. Comparison of fluorescence spectra of **1** (A-C) and **2** (D-F) measured after excitation at 405 nm of 0.1 and 1 μM solution of **1** and **2** in MeOH, H_2O and 0.05 M phosphate buffer, pH=7 at 25 °C.

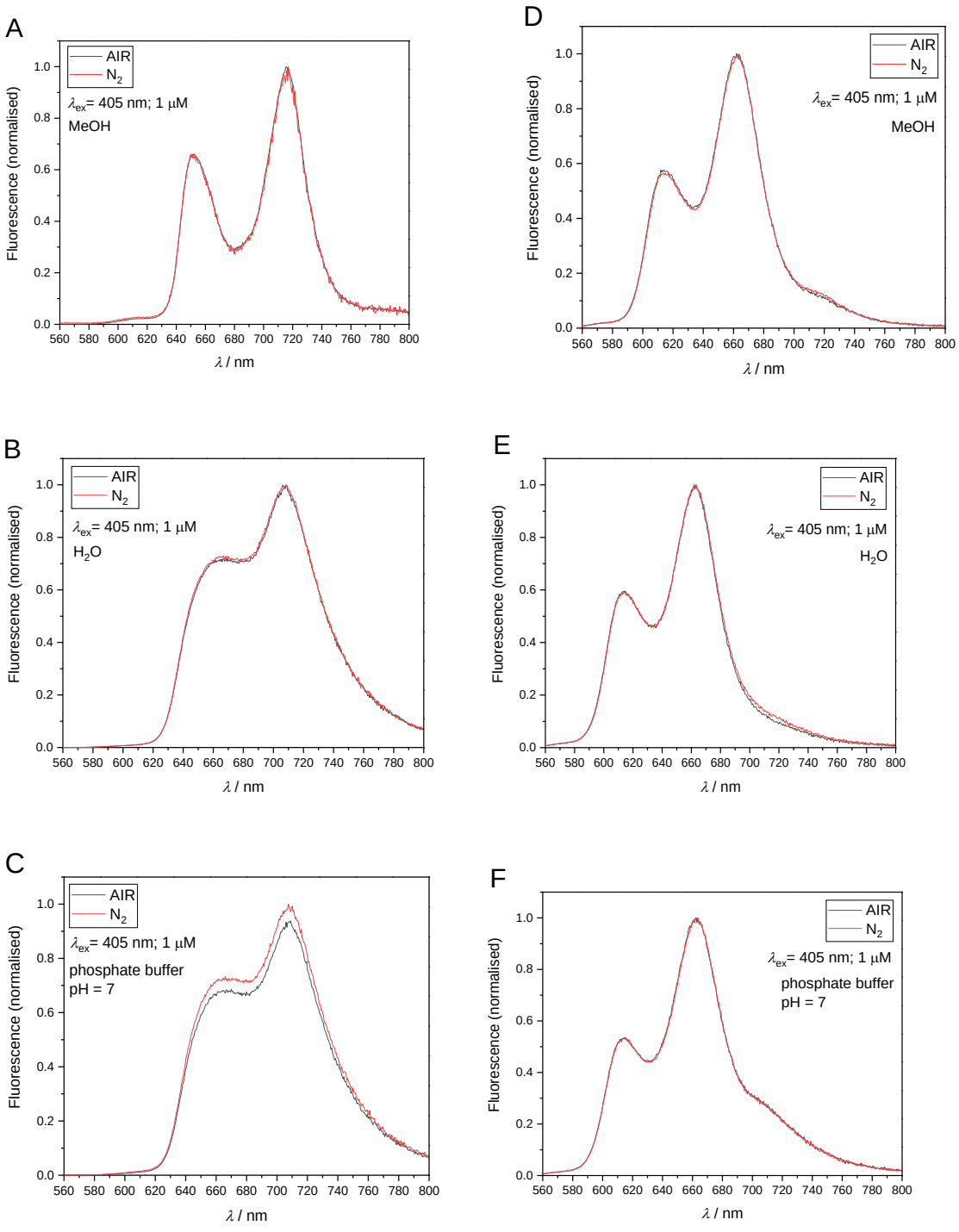

Figure S82. Comparison of the fluorescence spectra of porphyrin **1** (A-C) and porphyrin **2** (D-F) measured after excitation at 405 nm of 1 μM solution of **1** and **2** in MeOH, H_2O and 0.05 M phosphate buffer, pH=7, before and after purging the solution with N_2.

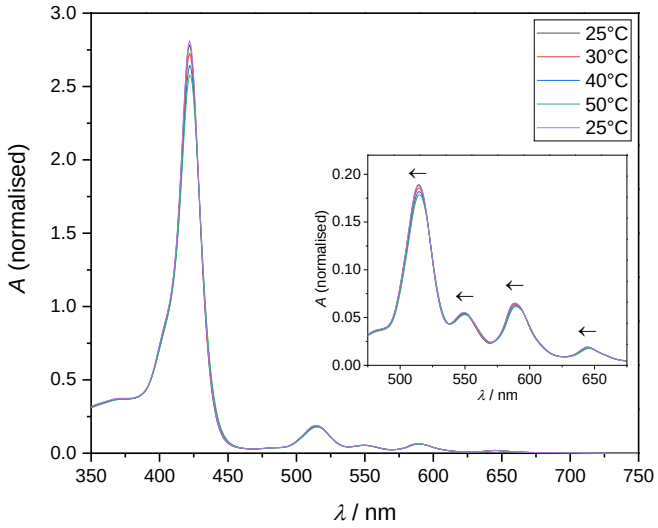

Figure S83. Absorption spectra of > 10 μM porphyrin **13** in MeOH at different temperatures (temperature was increased from 25 °C to 30, 40, and 50 °C and then cooled back to 25 °C).

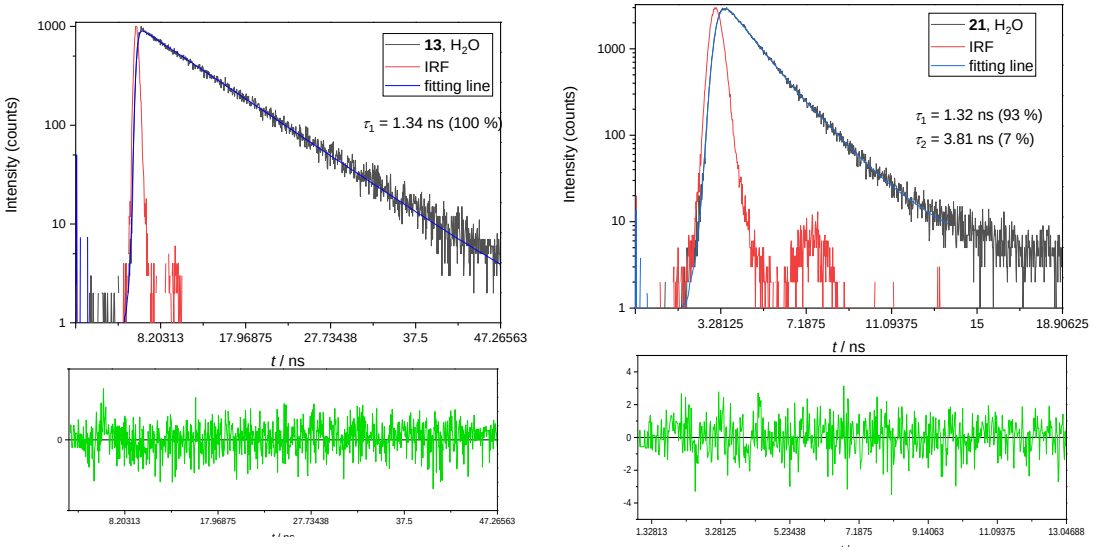

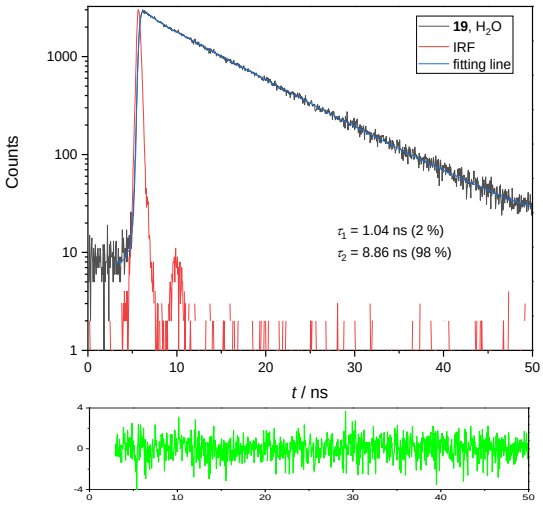

Figure S85. Fluorescence decay at 650 nm (λ_{ex} = 405 nm) for *N*-methylated porphyrins **13** and **19** and the Zn(II)analogue **21** in H_2O at 1 μM concentration measured by time-correlated single photon counting TC-SPC method. The bottom panel of the Figs correspond to the weighted residuals between the experimental and the fitted values.

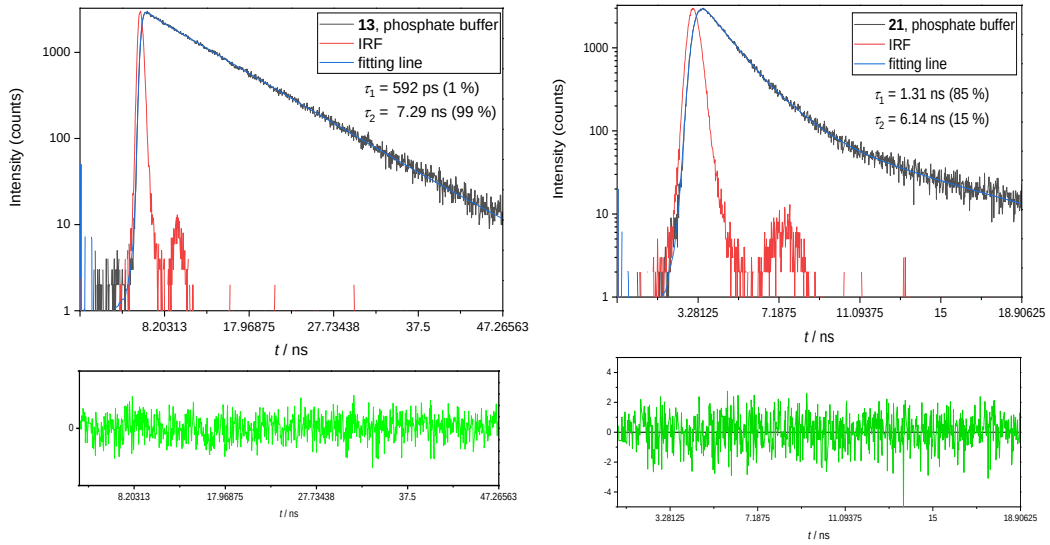

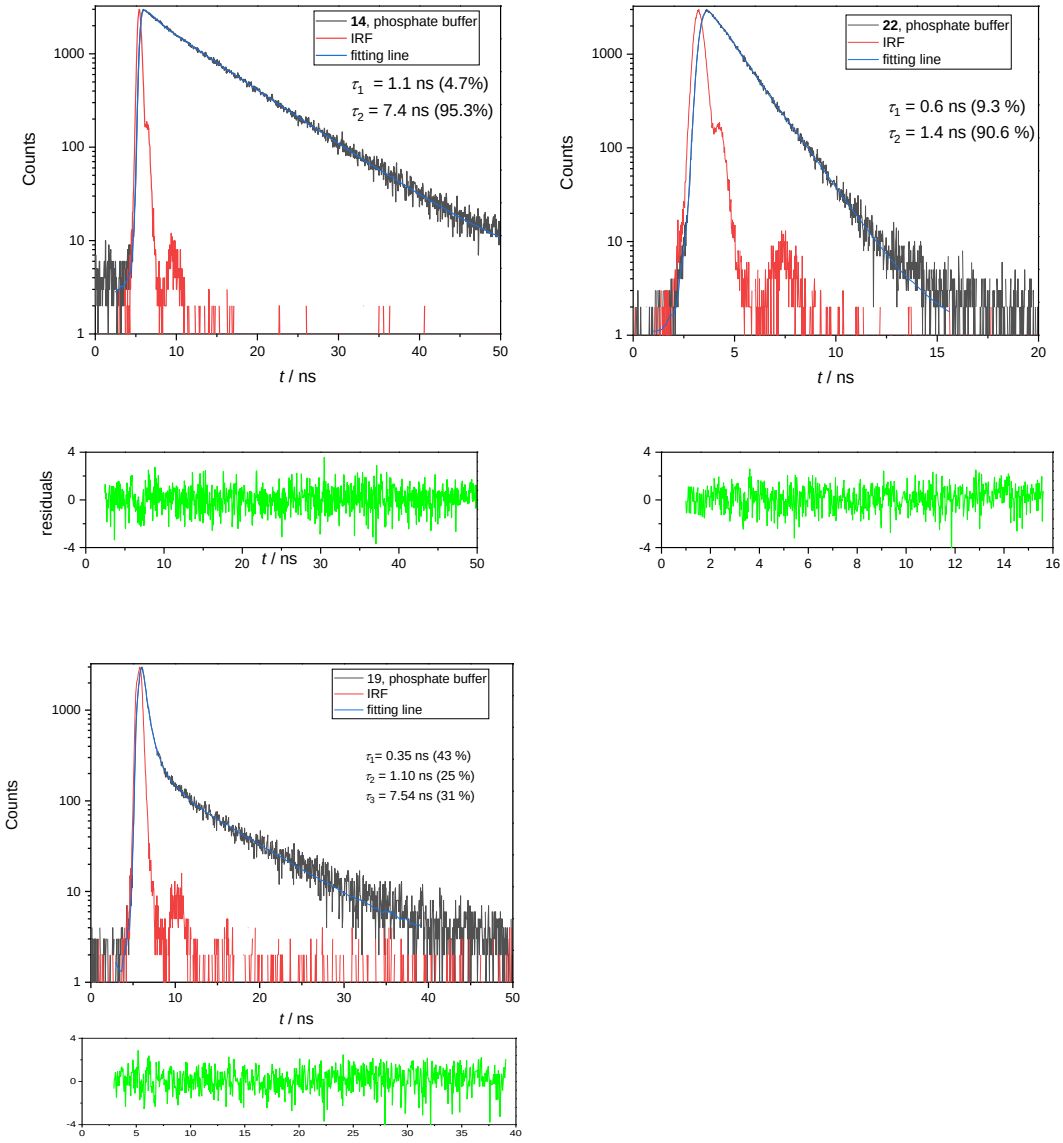

Figure S86. Fluorescence decay at 650 nm (λ_{ex} = 405 nm) for *N*-methylated porphyrins **13, 14 and 19** and their Zn(II)analogues **21 and 22** in 0.05 M phosphate buffer at 1 μM concentration measured by time-correlated single photon counting TC-SPC method. The bottom panel of the Figs correspond to the weighted residuals between the experimental and the fitted values.

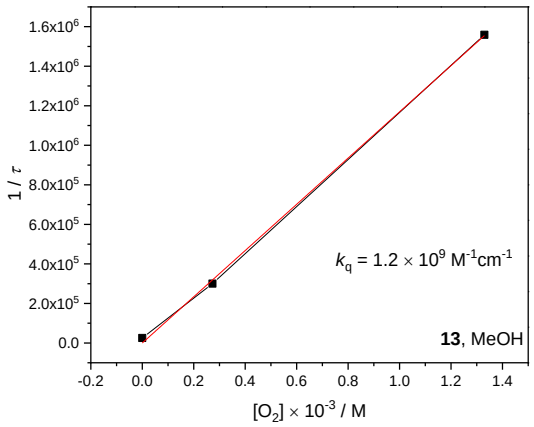
1 / τ
k_q = 1.2 × 10^9 M^{-1}cm^{-1}
13, MeOH
[O$_2$] × 10^{-3} / M

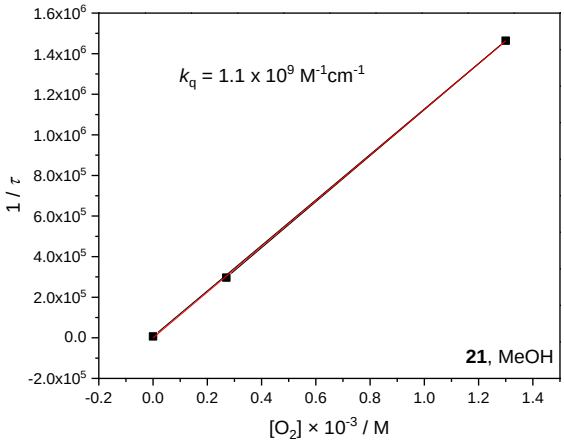
1 / τ
k_q = 1.1 x 10^9 M^{-1}cm^{-1}
21, MeOH
[O$_2$] × 10^{-3} / M

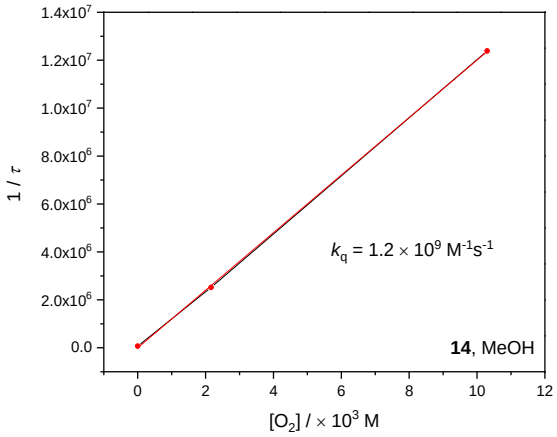
1 / τ
k_q = 1.2 × 10^9 M^{-1}s^{-1}
14, MeOH
[O$_2$] / × 10^3 M

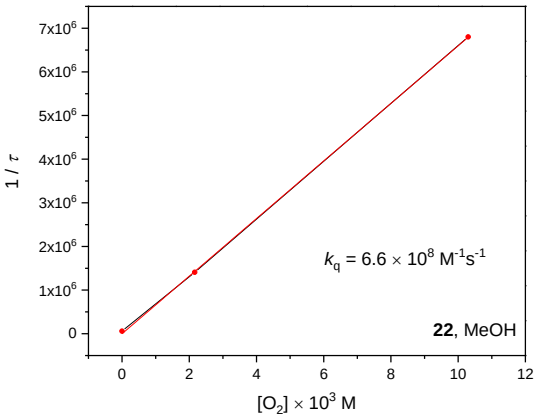
1 / τ
k_q = 6.6 × 10^8 M^{-1}s^{-1}
22, MeOH
[O$_2$] × 10^3 M

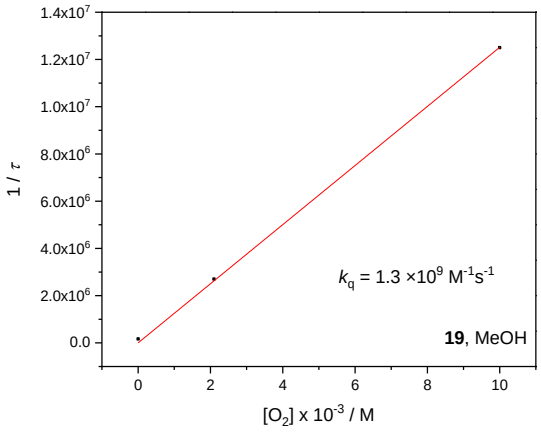
1 / τ
k_q = 1.3 ×10^9 M^{-1}s^{-1}
19, MeOH
[O$_2$] x 10^{-3} / M

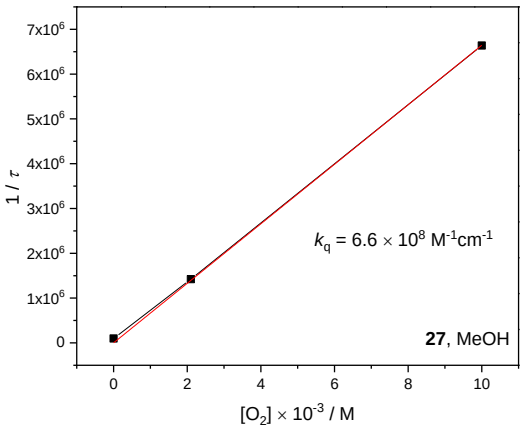
1 / τ
k_q = 6.6 × 10^8 M^{-1}cm^{-1}
27, MeOH
[O$_2$] × 10^{-3} / M

Figure S87. The quenching rate constant of the *N*-methylated porphyrins **13**, **14** and **19** (left column) and their Zn(II) analogues **21**, **22** and **27** (right column) triplet quenching with molecular oxygen in MeOH. A_{355} = 0.2, E_{355} nm = 3 mJ

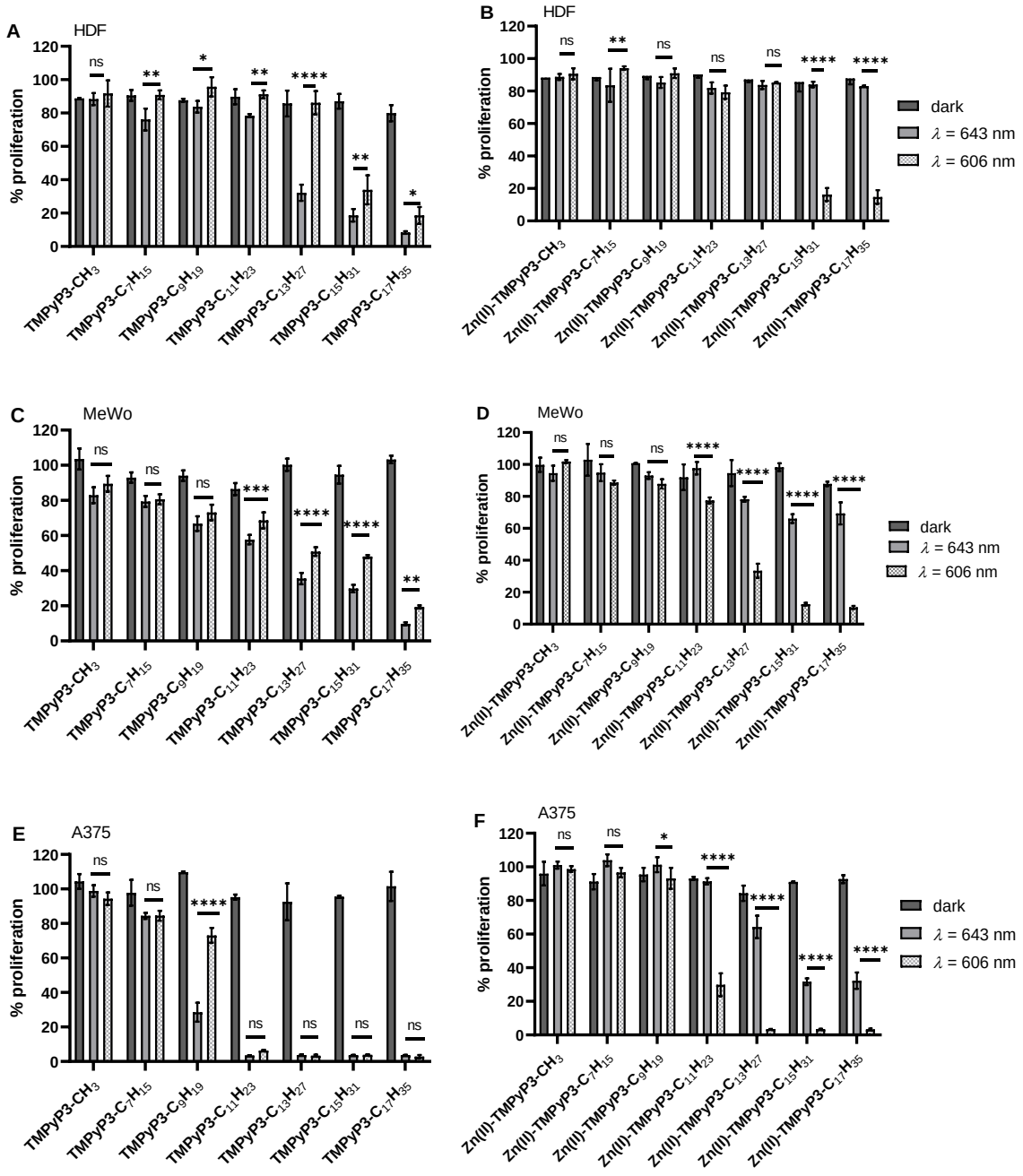

Figure S88. Comparison of the cytotoxicity of free-base (A, C and E) and Zn(II) (B, D and F) pyridiniumporphyrins at concentration of 1 μM after irradiation of 643 nm or 606 nm on

HDF (A and B), MeWo (C and D) and A375 (E and F) cell lines. Results are shown as an average of triplicate measurements with standard deviations in error bars. The statistical analysis in the graph shows the two-way ANOVA analysis for the comparison of cytotoxicity after irradiation with 643 and 606 nm.

8.5. Supporting information to the Section 5.2.

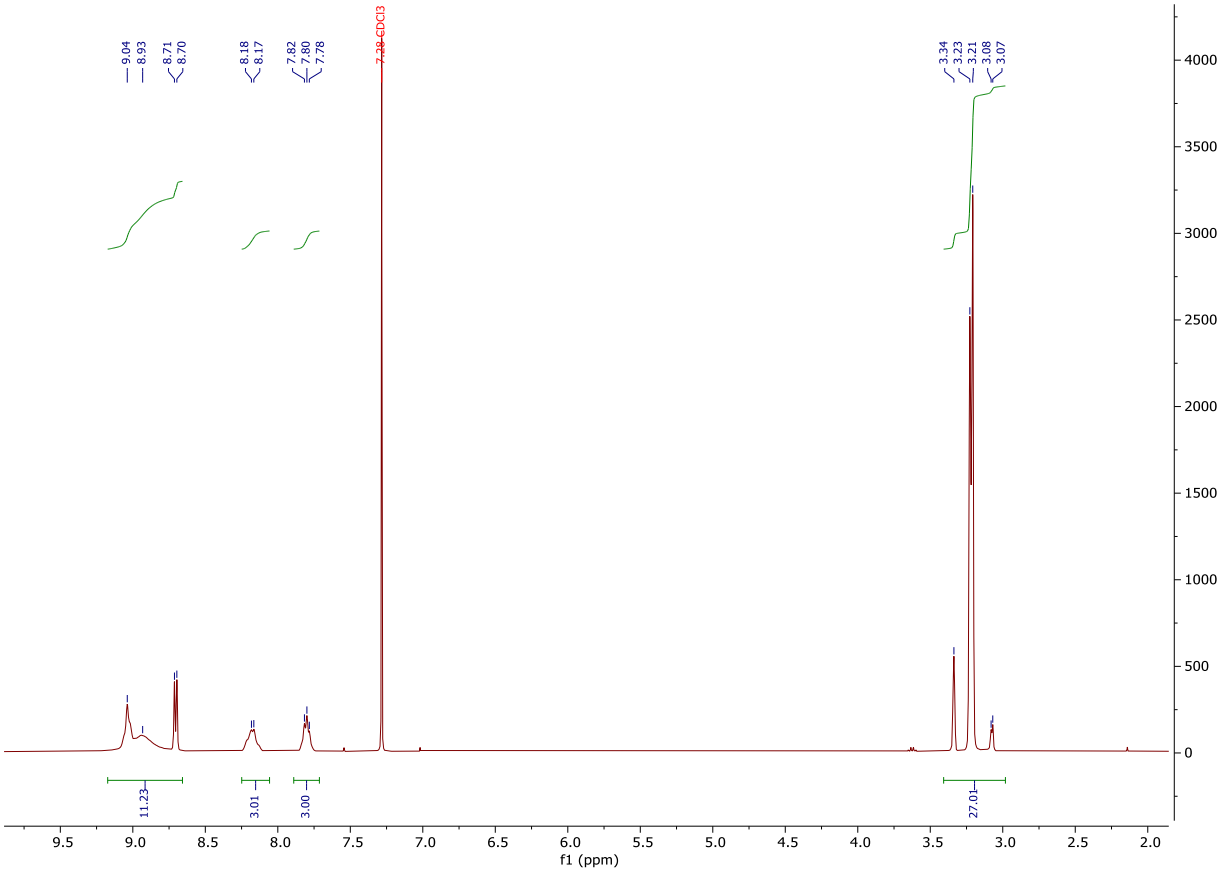

Figure S89. ^{1}H NMR (600 MHz, CD_3Cl+ CD_3OD) spectrum of porphyrin 29 after the *m*-CPBA oxidation reaction that was quenched with triethylamine (TEA). Impurities in the region 3.0-3.5 ppm are attributed to the impurities from the triethylammonium oxide remained in the spectrum.

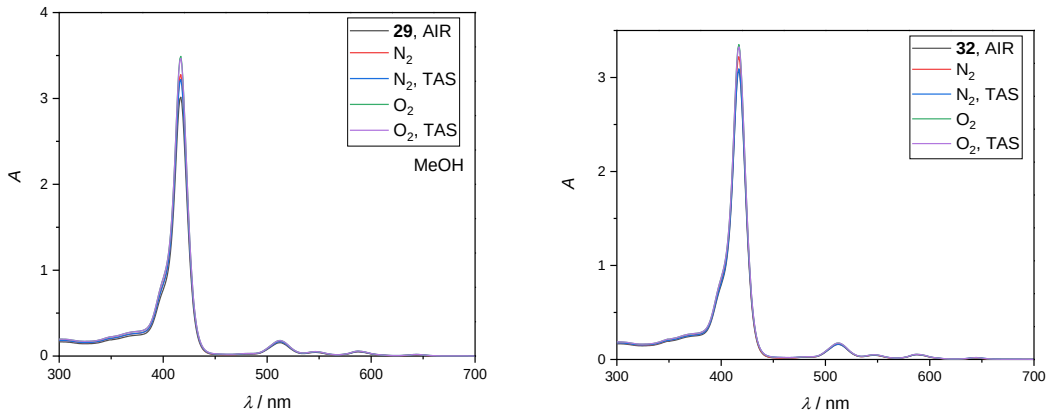

Figure S90. Ground absorption spectra of porphyrins **29** (left) and **32** in MeOH (right) in air and after purging with nitrogen and oxygen and after TAS measurements.

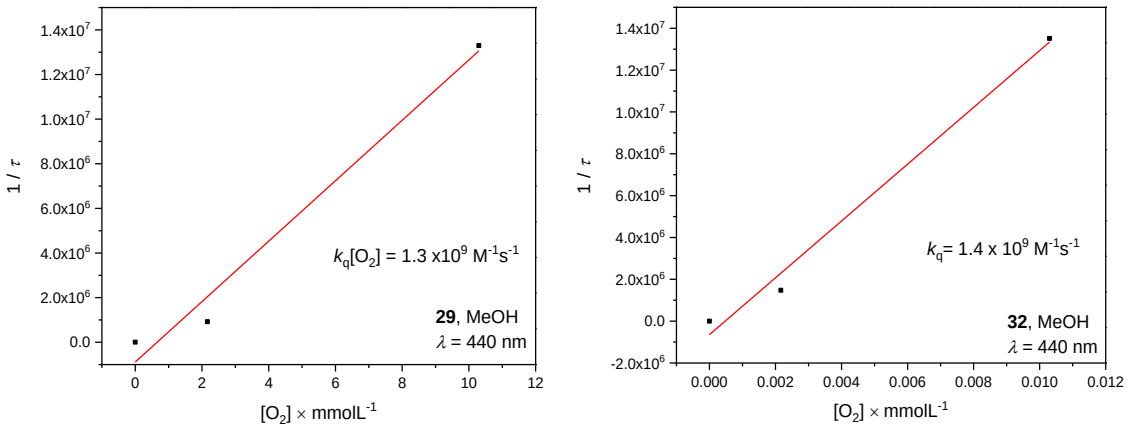

Figure S91. The quenching rate constant of the porphyrins' 29 (left) and 32 (440 nm) triplet quenching with molecular oxygen in MeOH. A_{355} (**29**)= 0.22, A_{355} (**32**)= 0.21, E_{355} nm = 3 mJ

8.6. Supporting information to the Section 5.3.

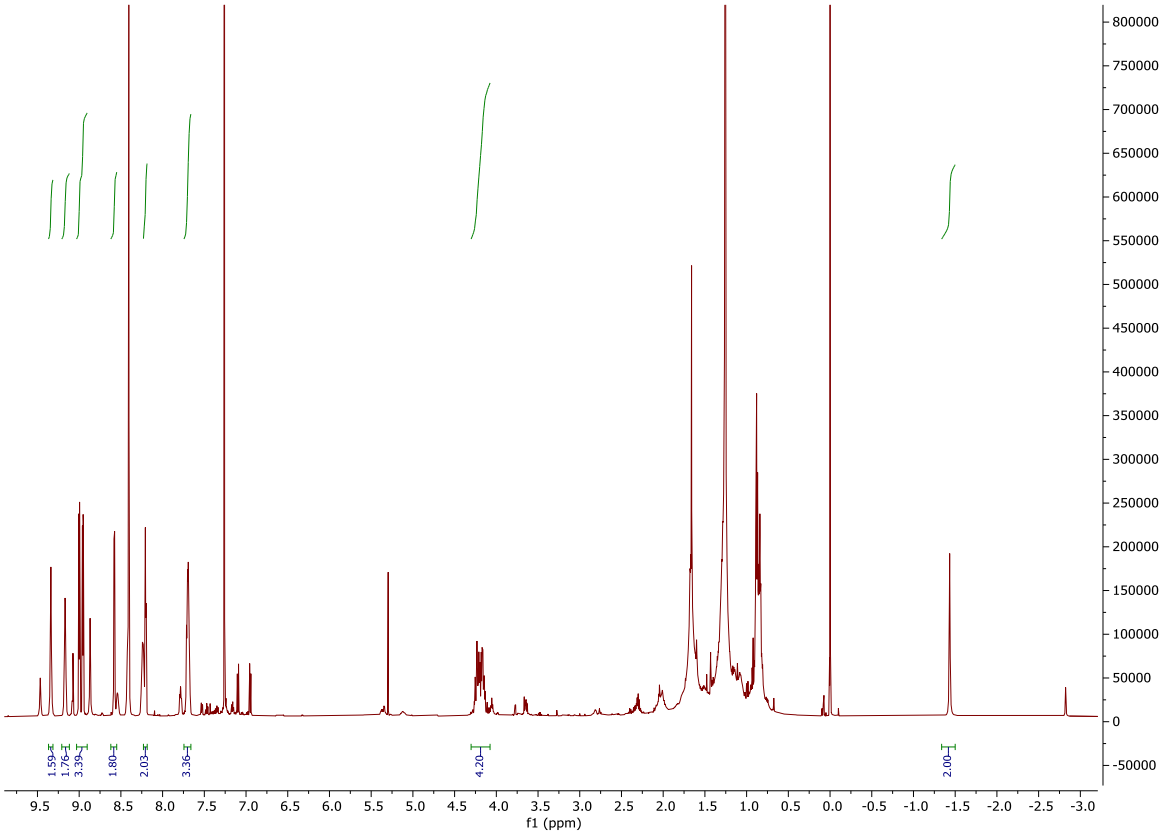

Figure S92. ^{1}H NMR (600 MHz, $CDCl_3$) spectrum of the reduction of porphyrin **2** following the Whitlock's diimide reduction. The integrated signals correspond to the characteristic chlorin peaks found in the reaction mixture.

8.7. Supporting information to the Section 5.4.

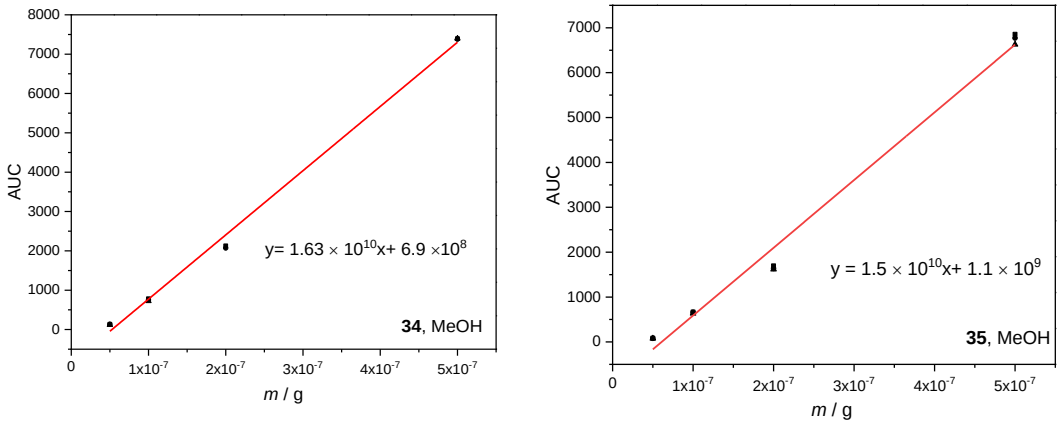

Figure S93. Calibration curves (AUC/mass) of porphyrins **34** and **35** for the determination of low SA and high SA concentrations.

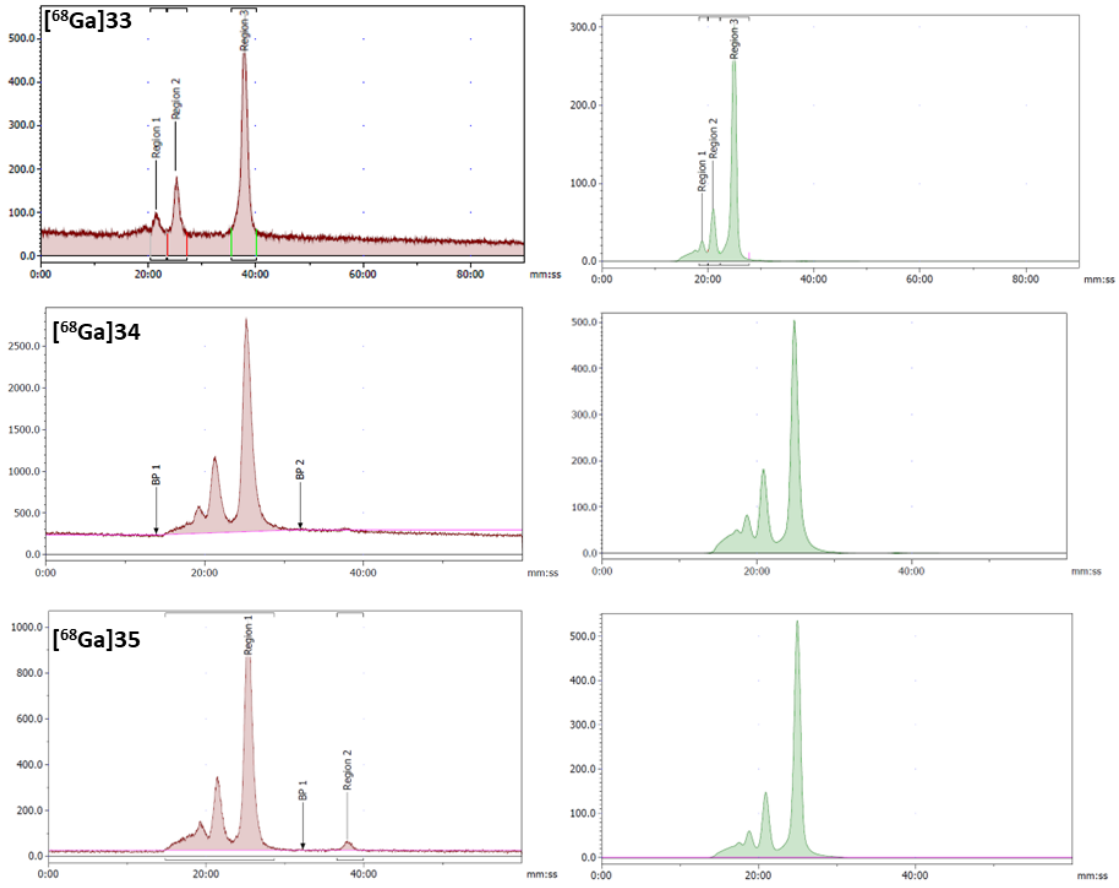

Figure S93. Stability of the BSA formulation after 3 hours of the incubation with porphyrin radiotracers **[^{68}Ga]33, [^{68}Ga]34 and [^{68}Ga]35.** Y axis: Counts; X axis: t / min.

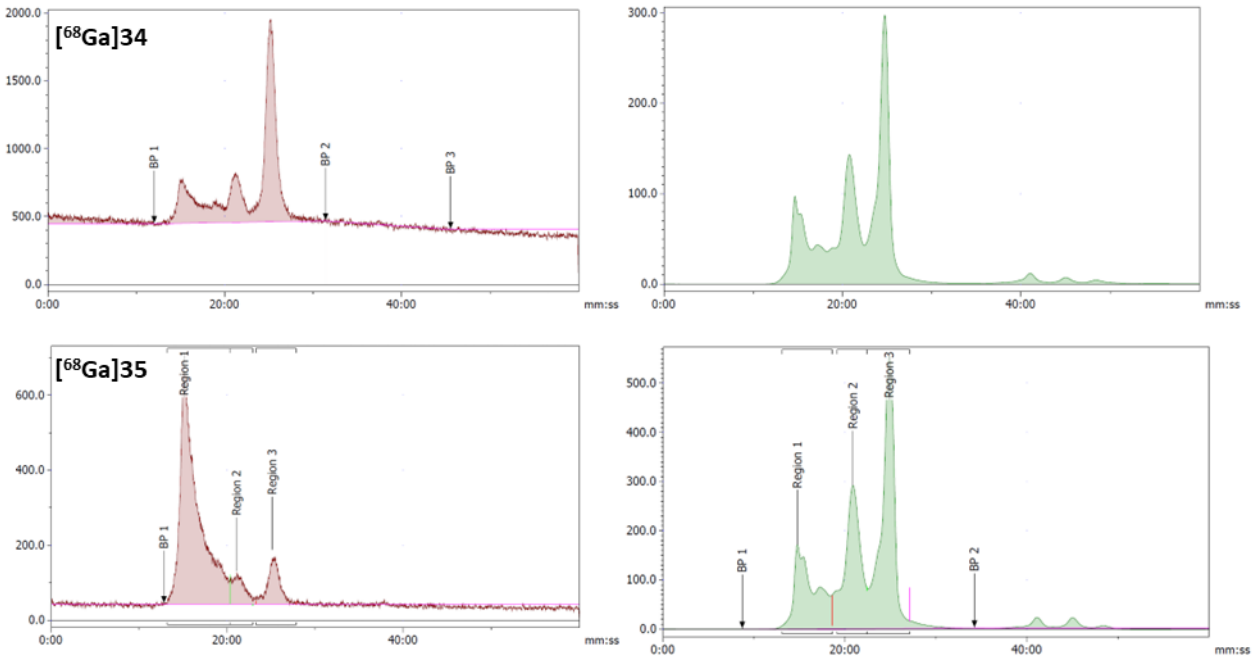

Figure S94. Serum stability of the BSA formulation of porphyrin radiotracers **[^{68}Ga]34** and **[^{68}Ga]35** after 2 hours of the incubation at RT. Y axis: Counts; X axis: t / min.

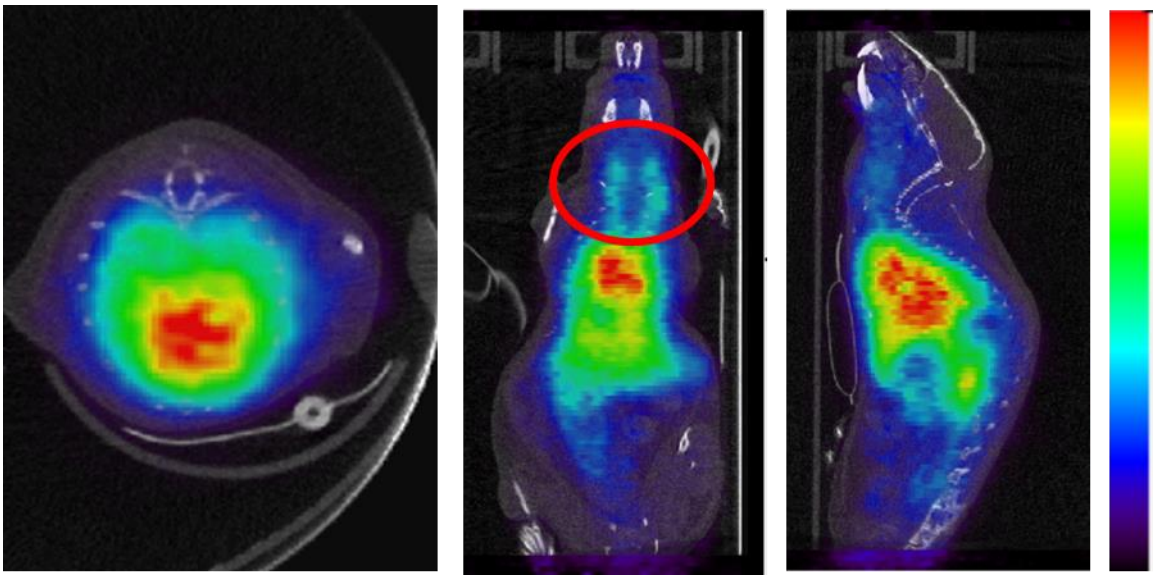

Figure S95. PET-CT scan images of *in vivo* biodistribution of **[^{68}Ga]34** radionuclide observed using dynamic 90 min scan. Dynamic imaging was performed in naïve mouse with the start time coinciding with intravenous injection of radiotracer into the tail vein via catheter.

9. Curriculum vitae

Mušković Martina
mag.med.chem
martina.muskovic@biotech.uniri.hr
+385917974976

WORK EXPERIENCE

04/2019-ongoing	**Assistant** Department of Biotechnology, Division of Medicinal Chemistry University of Rijeka Radmile Matejčić 2, 51000 Rijeka (Croatia) Courses: Organic chemistry and Analytical chemistry
09/2018-04/2019	**Science teacher** Elementary school Turnić, Franje Čandeka 20, 51000 Rijeka (Croatia)
01/2019- 03/2019	**Chemistry and biology teacher** Elementary school Turnić, Franje Čandeka 20, 51000 Rijeka (Croatia)
11/2018-12/2018	**Science and biology teacher** Elementary school Pećine, Šetalište 13. Divizije 25, 51000 Rijeka (Croatia)
12/2018	**Laboratory practice demonstrator (Organic chemistry)** University of Rijeka, Department of biotechnology Radmile Matejčić 2, 51000 Rijeka (Croatia)
12/2017	**Laboratory practice demonstrator (Organic chemistry)** University of Rijeka, Department of biotechnology Radmile Matječić 2, 51000 Rijeka (Croata)

12/2016	**Laboratory practice demonstrator (Organic chemistry)** University of Rijeka, Department of biotechnology Radmile Matječić 2, 51000 Rijeka (Croatia)
01/2016	**Laboratory practice demonstrator (Organic chemistry)** University of Rijeka, Department of biotechnology Radmile Matječić 2, 51000 Rijeka (Croatia)
01/2015	**Laboratory practice demonstrator** University of Rijeka, Department of biotechnology Radmile Matječić 2, 51000 Rijeka (Croatia)
EDUCATION AND TRAINING	
2008-2012	Prva Riječka Hrvatska gimnazija, Rijeka (Croatia)
10/2012-07/2015	**Bachelor of Science (BSc) in Biotechnology and drug development** University of Rijeka, Department of biotechnology (Croatia)
10/2015-12/2017	**Master of Science (MSc) in Medicinal Chemistry** University of Rijeka, Department of Biotechnology (Croatia) The title of Master's thesis: "Synthesis and properties of new (oxido)pyridylporphyrins for use in photodynamic therapy" Supervisor: Nela Malatesti, PhD
01/2018-	**PhD sudent of Doctoral programmme „Medicinal Chemistry“** University of Rijeka, Department of Biotechnology (Croatia) Topic of experimental work at postgraduate study: *" Amphiphilic fatty acid conjugates of pyridylporphyrins as potential photosensitizers for use in photodynamic therapy of melanoma*” Supervisor: Nela Malatesti, PhD
05/2017-08/2017	**Erasmus Internship** University of Hull, Faculty of Science and Engineering Title of experimental work: Synthesis of new BODIPY’s and conjugation with fetal bovine serum (BSA) for imaging using confocal microscope on HeLa cells Laboratory: Laboratory for photochemistry and photobiology Supervisor: Prof Ross W. Boyle, PhD

08/2021-11/2021	**Internship in UK** • Scholarship from British Scholarship Trust Laboratory of photobiology and photomedicine and Positron tomography emission (PET) research center, University of Hull, UK Supervisors: Prof Ross W Boyle, Prof Steve J Archibald
06/2015	**Laboratory practice in industry** Jadran Galenski laboratorij (JGL) Svilno 20, 51 000 Rijeka (Croatia)

PUBLICATIONS

M.Mušković, I. Ratkaj, M. Lončarić & N. Malatesti, Impact of the hydrophilic-lipophilic balance of free-base and Zn(II) tricationic pyridiniumporphyrins and irradiation wavelength in PDT against the melanoma cell lines, European Journal of Medicinal Chemistry, 282, 2025, 117063. DOI: 10.1016/j.ejmech.2024.117063

A. Filošević Vujnović, S. Čabrijan, **M. Mušković**, N. Malatesti & R. Andretic Waldovski, Systemic Effects of Photoactivated 5,10,15,20-tetrakis(N-methylpyridinium-3-yl) Porphyrin on Healthy Drosophila melanogaster, *Biotech*, 13(3), 2024, 23. DOI: 10.3390/biotech13030023

M. Mušković, I. Gobin & N. Malatesti, Photodynamic Inactivation of Opportunistic Premise Plumbing
Pathogens and Their Biofilms, *Processes*, 11(2023), 3074. DOI: 10.3390/pr11113074

M. Mušković, M. Planinić, A. Crepulja, M. Lušić, M. Glad, M. Lončarić, N. Malatesti & I. Gobin, Photodynamic inactivation of multidrug resistant strains of Klebsiella pneumoniae and Pseudomonas aeruginosa in municipal wastewater by tetracationic porphyrin and violet-blue light: The impact of wastewater constituents, *PLoS ONE*, 18 (2023), e0290080. DOI: 10.1371/journal.pone.0290080

M. Mušković, I. Džeba, I. Antol, N. Basarić & N. Malatesti, Photophysical properties of 5-(4-acetamidophenyl)-10,15,20-tris(N-methylpyridinium-3-yl)porphyrin trichloride and its Zn(II) complex, *Journal of Photochemistry and Photobiology, A: Chemistry*, 444 (2023), 114939. DOI: 10.1016/j.jphotochem.2023.114939

M. Mušković, R. Pokrajac & N. Malatesti, Combination of Two Photosensitisers in Anticancer, Antimicrobial and Upconversion Photodynamic Therapy, *Pharmaceuticals*, 16 (2023), 613. DOI: 10.3390/ph16040613

I. Ratkaj, **M. Mušković** & N. Malatesti, Targeting Microenvironment of Melanoma and Head and Neck Cancers in Photodynamic Therapy, Curr. Med. Chem., *29*(18), 2022, 3261-3299. https://doi.org/10.2174/0929867328666210709113032

M. Mušković, I. Ćavar, A. Lesar, M. Lončarić, N. Malatesti, I.Gobin, Photodynamic Inactivation of Legionella pneumophila Biofilm Formation by Cationic Tetra- and Tripyridylporphyrins in Waters of Different Hardness, *Int. J. Mol. Sci. 22*(16), (2020), 9095. https://doi.org/10.3390/ijms22169095

A. Lesar, **M. Mušković**, G. Begić, M. Lončarić, D.T. Linšak, N. Malatesti, I. Gobin, Cationic porphyrins as effective agents in photodynamic inactivation of opportunistic plumbing pathogen legionella pneumophila, *Int. J. Mol. Sci. 21*, (2020) 5367. https://doi.org/10.3390/ijms21155367.

M. Jelovica, P. Grbčić, **M. Mušković**, M. Sedić, S. Kraljević-Pavelić, M. Lončarić, N. Malatesti: In Vitro Photodynamic Activity of N-Methylated and *N*-Oxidised Tripyridyl Porphyrins with Long Alkyl Chains and Their Inhibitory Activity in Sphingolipid Metabolism, *ChemMedChem,* 13(4), (2018), 360372. https://doi.org/10.1002/cmdc.201700748

CONFERENCES AND SYMPOSIA

- 35th Annual Congress of the Italian Society for Photobiology, Messina, Italy, 9th to 11th September, 2024

Oral presentation:
Synthesis, physicochemical properties and in vitro evaluation of amphiphilic pyridiniumporphyrins with N-oxide moiety for use in photodynamic therapy (PDT)
Authors: Martina Mušković, Martin Lončarić, Ivana Ratkaj, Nela Malatesti
http://www.sifb.it/congress-call/

- 20th Congress of the European Society for Photobiology, Lyon, France, 27th to 31st August, 2023.

Poster presentation:
Amphiphilic cationic tripyridiniumporphyrins and their Zn(II) complexes: the influence of the irradiation wavelength and the length of the alkyl chain
Authors: *Martina Mušković, Martin Lončarić, Ivana Ratkaj and Nela Malatesti*
https://photobiolyon.sciencesconf.org/

- 34th Annual Conference of the Italian Society of Photobiology Lecce, Italy, 26th to 30th June, 2023.

Poster presentations:
1. *Photoinactivation of L. pneumophila in municipal wastewater with two tetracationic porphyrins*
Authors: Marko Lušić, Martina Mušković, Marin Glad, Martin Lončarić, Ivana Gobin and Nela Malatesti
2. *Amphiphilic cationic tripyridiniumporphyrins and their Zn(II) complexes: the influence of the irradiation wavelength and the length of the alkyl chain*
Authors: Martina Mušković, Martin Lončarić, Ivana Ratkaj and Nela Malatesti
http://www.sifb.it/congress-call/

- 5th Symposium of Section for Medicinal and Pharmaceutical Chemistry of Croatian Chemical Society in Zagreb, Croatia

Organization: Croatian Chemical Society and Fidelta d.o.o.
Oral presentation:

First in vivo positron emission tomography biodistribution study of [^{68}Ga]gallium radiolabelled amphiphilic cationic porphyrins with potential applications in photodynamic therapy
Authors: *Martina Mušković, Juozas Domarkas, John D Wright, Nela Malatesti, Ross W Boyle, Steve J Archibald*

- 49th Congress Synthesis and Analysis of Drugs, Faculty of Pharmacy, Charles University, Czech Republic

Oral presentation:
Synthesis, photophysical, photochemical and photobiological properties of amphiphilic Zn(II) and free based tripyridylporphyrins
Authors: *Martina Mušković, Iva Džeba, Nikola Basarić, Martin Lončarić, Ivana Ratkaj and Nela Malatesti*

- 19th Congress of European Society for Photobiology, Salzburg, Austria (online)

Poster presentation:
1. "*Zn(II) and free base N-methylated tripyridylporphyrins: impact of solubility and light excitation wavelength*"
Authors: *Martina Mušković, Iva Džeba, Nikola Basarić, Martin Lončarić, Branka Mihaljević, Ivana Ratkaj, Nela Malatesti*
2. "*Water hardness shows strong impact on the photodynamic activity on the Legionella pneumophila biofilm*"
Authors: *Iva Ćavar, Martina Mušković, Ivana Gobin, Nela Malatesti*

- 5th Photodynamic Day, International scientific symposium, University Acibadem Mehmet Ali Aydinlar

Poster presentation:
Cationic tripyridylporphyrins and their Zn(II) complexes: a comparison of 645 nm and 605 nm light irradiation for PDT
Authors: *Martina Mušković, Ivana Ratkaj, Martin Lončarić and Nela Malatesti*

- International Scientific Conference 18. Ružička Days "Toady Science – Tomorrow Industry" in Vukovar, Croatia organized by Croatian Society of Chemical engineers (HDKI) and Faculty of Food Technology in Osijek

Poster presentation:
1. *Photodynamic activity of N-methylated and N-oxidised tripyridylporphyrins bearing long alkyl chain on melanoma cells*
Autori: *A. Cindrić, L. Penić-Ivanko, M. Mušković, I. Ratkaj, N. Malatesti*
2. *PDT potential of amphiphilic free-base and Zn(II) tripyridylporphyrins*
Authors: *Martina Mušković, Ivana Ratkaj, Nela Malatesti*

- 6th *EFMC-Young Medicinal Chemists Symposium (EFMC-YMCS)* in Athens, Greece

Organization: European Federation for Medicinal Chemistry
Poster presentation: *"Photodynamic activity of free-base and Zn(II) complexes of N-methylated tetra-and tripyridylporphyrins"*
Authors*: Martina Mušković, Ivana Ratkaj, Nela Malatesti*

- 26th *Croatian meeting of Chemists and Chemical engineers* (26th HSKIKI) and 4th Vladimir Prelog Symposium, Šibenik (Solaris), Croatia organized by Croatian Chemical Society and Croatian Society of Chemist and Chemical Engineers

Poster presentation: *„Photophysical and photochemical characteristics of free-base and Zn(II) complexes of N-methylated tetra- and tripyridylporphyrins"*
Authors: *Martina Mušković and Nela Malatesti, PhD*

- 2nd *Mini symposium of Young Medicinal Chemists in Croatia*, Zagreb, Fidelta, Croatia organized by Croatian Chemical Society

Oral presentation *"The singlet oxygen production and lipophilicity of N-methylated and N-oxidised pyridylporphyns for photodynamic therapy"*
Authors: *Martina Mušković, Andrija Lesar, Ivana Gobin, Martin Lončarić and Nela Malatesti*

- 2nd *PhD Day (Doctoral programme Medicinal Chemistry)*, Rijeka, Department of Biotehnology

Oral presentation *"The effect of singlet oxygen production and lipophilicity of the photosensitiser in photodynamic activity of N-methylated and N-oxidised pyridylporphyrins"*
Authors: *Martina Mušković* and *Nela Malatesti*

- 5th *EFMC-Young Medicinal Chemists Symposium (EFMC-YMCS)* in Ljubljana, Slovenia

Organization: European Federation for Medicinal Chemistry

- winner of young medicinal chemists in Croatia

Oral presentation: "The effect of singlet oxygen production and lipophilicity of the photosensitiser in photodynamic activity of *N*-methylated and *N*-oxidised pyridylporphyrins"
Authors: *Martina Mušković, Andrija Lesar, Ivana Gobin, Martin Lončarić and Nela Malatesti*

WORKSHOPS AND SCHOOLS

- 6th Photobiology School held in Brixen, Italy (August 2022.)

HONOURS AND AWARDS

- **Erasmus scholarship** for Internship at University of Hull, England (2017.)
- **Scholarship from European Federation of Medicinal Chemistry** for oral presentation on 5th EFMC-YMCS (European Federation of Medicinal Chemistry-Young Medicinal Chemists Symposium) (2018.)
- **IUPAC Scholarship** for participation on. 26th Croatian meeting of Chemists and Chemical engineers and 4th Vladimir Prelog Symposium, Šibenik, Solaris (Croatia) April 2019 (2019.)
- **Scholarship from Croatian Chemical Society** for participation on EFMC-ASMC (European Federation for Medicinal Chemistry- International Symposium on Advances in Synthetic and Medicinal Chemistry) and 6th EFMC-YMCS (EFMC- Young Medicinal Chemists Symposium)
- **Award** for excellence in teaching **from University of Rijeka**, May 2021.
- **Scholarship from British Scholarship Trust** for study and research at University of Hull under supervision of Prof Ross W Boyle,

- **2nd best oral presentation at 49th Conference of Synthesis and Analysis of Drugs**, organization: Faculty of Pharmacy, Charles University, Czech Republic
- **Researcher Development and Travel Grant** by Royal Society of Chemistry to attend the 20th Congress of the European Society for Photobiology held in Lyon, France from 27th to 31st August, 2023.
- **University of Rijeka Foundation- Trust fund "Prometej"** – for the participation of the 35th Congress of the Italian Society for Photobiology, Messina, Sicily Italy, 9th- 11th September 2024.

PROJECTS

- **2024.-** Priprema *N*-oksida piridilporfirina, njihova karakterizacija i fotodinamička aktivnost", mjesto troška- grant by University of Rijeka (UNIRI) awarded to dr.sc. Nela Malatesti- **project associate**
- **1.1.2023.- 30.9.2023.** *Novi fotosenzibilizator za upotrebu u fotodinamičkoj terapiji (*N-PROM 26/2022)- grant by University of Rijeka Foundation-Trust fund "Prometej"- **project manager** (fund: 1325 €)
- **2022.-2023.** *Ispitivanje protumikrobnog fotodinamičkog učinka profirina za razvoj novih metoda dezinfekcije otpadnih voda*- UNIRI-INOVA grant awarded to dr.sc. Nela Malatesti- **project associate, PhD student**
- **2021.-2022.** *Sinteza novih amfifilnih tripiridilklorina za upotrebu u fotodinamičkoj terapiji melanoma*- grant by Croatian Academy of Sciences and Arts- **project manager** (4000 kn-530 €)
- **2019.-2023**. *Priprema lipidnih konjugata piridilporfirina, njihova karakterizacija i fotodinamička aktivnost*- grant by University of Rijeke (UNIRI) awarded to dr.sc. Nela Malatesti- **project associate, PhD student**

MEMBERSHIP

2019- today: Croatian Chemical Society

2019- today: European Federation of Medicinal Chemistry-Young Scientist Network (EFMC-YSN)

2020-today: European Society for Photobiology

- today: member of the Communication work group in the ESP committee (ESP Work Groups | ESP - European Society for Photobiology)

2023-today: Royal Chemical Society: Spectroscopy and Organic Chemistry group

SCIENCE POPULARIZATION

01/2017-01/2019

DVD with chemistry experiments for final exam in Chemistry

- author and project leader
- collaboration with publishing house "Školska knjiga"

Vidematerials published in books:
Turčinović, D.; „Pokusi iz kemije za državnu maturu“,Školska knjiga, Zagreb, February 2018
Lukić, S., Marić Zerdun, I., Trenčevska, N., Varga, M.: „Kemija 7“, chemistry textbook for 7th grade of elementary school
Luetić, M., Preočanin, T., Petrović Peroković, V., Rupčić Petelinc, S., Turčinović, D.: „Kemija 1“, chemistry textbook for 1st grade of gimnasium

04/2014- today

Open days of Department of Biotechnology and Tetragon

- part of the organization team (2020-2022- head organizer)

University of Rijeka, Department of Biotechnology, Rijeka (Croatia)

- from 2022.- workshop titled: Kemija boja i svjetlost (Chemistry of colour and light)

09/2022- today

European Researchers' Night- Project: "Reconnecting Science with the Blue Society – Blue-connect"

- Station: Chemistry of colours and light